Evaluation of the DFT/MRCI Method in the Contexts of Singlet Fission and Photodetachment–Photoelectron Spectroscopy

Inaugural-Dissertation

zur

Erlangung des Doktorgrades der

Mathematisch-Naturwissenschaftlichen Fakultät

der Heinrich Heine Universität Düsseldorf

vorgelegt von

Timo Schulz

aus Donaueschingen

Köln, 29. Juni 2024

aus dem Institut für Theoretische Chemie und Computerchemie
der Heinrich Heine Universität Düsseldorf

Gedruckt mit der Genehmigung der
Mathematisch-Naturwissenschaftlichen Fakultät der
Heinrich Heine Universität Düsseldorf

Berichterstatter:

1. Univ.-Prof. Dr. Christel M. Marian
2. Univ.-Prof. Dr. Shirin Faraji

Tag der mündlichen Prüfung: 17.10.2024

Eidesstattliche Erklärung

Ich versichere an Eides Statt, dass die Dissertation von mir selbständig und ohne unzulässige fremde Hilfe unter Beachtung der Grundsätze zur Sicherung guter wissenschaftlicher Praxis an der Heinrich Heine Universität Düsseldorf erstellt worden ist. Die aus fremden Quellen direkt oder indirekt übernommenen Gedanken sind als solche gekennzeichnet. Die Dissertation wurde in der vorliegenden oder in ähnlicher Form noch bei keiner anderen Prüfungsbehörde eingereicht. Es wurden keine früheren erfolglosen Promotionsversuche unternommen.

Düsseldorf, den

Meinen Großeltern und Eltern

All models are wrong,
some are useful

George Box

Danksagung

Zuvorderst möchte ich mich bei meiner Doktormutter, Frau Prof. Dr. Christel M. Marian, für die Unterstützung, das in mich gesetzte Vertrauen und die Ermöglichung dieser Promotion bedanken.

Weiterhin, bedanke ich mich herzlich bei Frau Prof. Dr. Shirin Faraji für die Übernahme des Zweitgutachtens.

Dem Arbeitskreis am Institut für theoretische Chemie und Computerchemie, danke ich für die vielen netten Arbeitstage und vorallem die gemeinsamen Festivitäten.

Ein besonderes Dankeschön an Dr. Martin Kleinschmidt, Dr. Dennis Dombrowski und Jeremy Kaminksy für das Korrekturlesen dieser Arbeit und die hilfreichen Anmerkungen.

Auch bei PD Dr. Oliver Weingart und meinem Bürokollegen Simon Hédé möchte ich mich für den freundschaftlichen Umgang miteinander bedanken.

Mein größter Dank gilt meiner Familie, die mich in allen Fragen und Entscheidungen unterstützt hat. Besonders, meiner Eherfrau Nora danke ich für Ihre Geduld und Unterstützung.

Für die finanzielle Förderung des Projekts MA-1051/20-1 in dessen Rahmen diese Arbeit entstanden ist möchte ich mich bei der Deutschen Forschungsgemeinschaft bedanken.

Zusammenfassung

Das Ziel dieser Arbeit war es, die Rolle des ferromagnetisch gekoppelten Bi-Triplett-Zustands ^{5}(TT) in der Singulettspaltung zu untersuchen. Insbesondere war die mögliche Kopplung von ^{5}(TT) und seinem antiferromagnetisch gekoppelten Gegenstück ^{1}(TT), vermittelt durch Spin-Spin-Dipol-Wechselwirkungen, von Interesse. Da sowohl ^{5}(TT) als auch ^{1}(TT) Doppelanregungen in Bezug auf den geschlossenschaligen Singulett-Grundzustand der untersuchten Moleküle sind, war es notwendig, eine Elektronenstrukturtheorie zu verwenden, die solche Zustände beschreiben kann. Daher konnte die sehr verbreitete zeitabhängige Dichtefunktionaltheorie nicht verwendet werden. Stattdessen wurde die DFT/MRCI-Methode verwendet, um eine angemessene Beschreibung von ^{5}(TT) und ^{1}(TT) zu erhalten. Bei DFT/MRCI dient eine geschlossenschalige Determinante aus der Kohn-Sham (KS) Dichtefunktionaltheorie als Ankerkonfiguration und die zugrundeliegenden KS-Molekülorbitale werden als Ein-Teilchen-Basis für eine Entwicklung der Wellenfunktion im Sinne des Multireferenz-Konfigurationswechselwirkungs-Ansatzes verwendet. Entgegen den Erwartungen stellte sich heraus, dass die Methode in ihren bisherigen Formulierungen völlig ungeeignet ist, diese Zustände zu beschreiben. Glücklicherweise konnten die Probleme identifiziert werden, und es wurde ein neuer DFT/MRCI Modell-Hamilton-Operator formuliert und parametrisiert, mit dem Zustände wie ^{5}(TT) und ^{1}(TT) beschrieben werden können. Die Leistungsfähigkeit des neu entwickelten Hamilton-Operators wurde an Photodetachment-Photoelektronen-Spektroskopie Daten von *oligo-para*-phenylenen, Anthracen und den Anthracen-Derivaten 2,6-di-Phenyl-, 9,10-di-Phenyl-, 9-Phenyl-, 9-(1-Naphthyl)- und 9,9′-bis-Anthracen getestet.
Untersuchungen im Kontext der Singulettspaltung wurden an den literaturbekannten Materialien Pentacen, 6,13-bis(triisopropylsilylethynyl)-Pentacen und den drei Regioisomeren eines kovalent verknüpften Pentacen Dimers durchgeführt. Da alle diese Moleküle aus rechnerischer Sicht recht groß sind, wurden das `SPOCK.sistr` und `mrci` Programm mithilfe des OpenMP Application Programming Interface (API) parallelisiert. In den Untersuchungen wurde festgestellt, dass weder in den in der Gasphase un-

tersuchten kovalent verknüpften Pentacen-Dimeren, noch in den in kristalliner Umgebung eingebetteten Pentacen oder 6,13-bis(triisopropylsilylethynyl)-Pentacen ^{5}(TT) energetisch nahe an ^{1}(TT) liegt, was eine Kopplung durch den Breit-Pauli Spin-Spin Dipol Operator sehr unwahrscheinlich macht. Dennoch wurden Breit-Pauli-Spin-Spin-Matrixelemente für ein Pentacen-Dimer berechnet, um die Programme zu testen und den geringen Einfluss der Spin-Spin-Dipol-Wechselwirkungen abzusichern.

Abstract

The aim of this thesis was to elucidate the role of the ferromagnetically coupled bi-triplet state ^{5}(TT) in the singlet exciton fission (SF) process. In particular, the possible coupling of ^{5}(TT) and its anti-ferromagnetically coupled counterpart ^{1}(TT), mediated through spin-spin dipole interactions was of interest. As both ^{5}(TT) and ^{1}(TT), are double excitations with respect to the singlet, closed-shell ground state of the investigated molecules it is necessary to use an electronic structure theory able to describe such states. Therefore, the very common time-dependent density functional theory (TD-DFT) method could not be employed. Instead, the DFT/MRCI method was used to obtain proper descriptions of ^{5}(TT) and ^{1}(TT). In DFT/MRCI a closed-shell Kohn-Sham (KS)-density functional theory (DFT)-determinant serves as an anchor configuration and the underlying molecular orbitals (MOs) are used as the one-particle basis for a multi-reference configuration interaction (MRCI)-like expansion of the wave function. Contrary to the expectations, it turned out that the method in its previous formulations is completely unsuitable for describing these states. Fortunately, the problems could be identified, and a new DFT/MRCI model Hamiltonian was formulated, allowing to treat states like ^{5}(TT) and ^{1}(TT) concisely. The performance of the newly developed Hamilton operator was tested on photodetachment-photoelectron spectroscopy (PD-PES) data of *oligo-para*-phenylenes, anthracene and the anthracene-derivatives 2,6-di-phenyl-, 9,10-di-phenyl-, 9-phenyl-, 9-(1-naphthyl)- and 9,9′-bis-anthracene. Investigations in the context of SF were carried out on the literature known materials pentacene (PT), 6,13-bis(triisopropylsilylethynyl)pentacene (TIPS-PT) and three regio-isomers of a covalently linked PT dimer. Since all of these molecules are quite large from a computational point of view, the `SPOCK.sistr` and `mrci` programs were parallelized using the OpenMP application programming interface (API). The investigations revealed that neither in the covalently linked PT dimers investigated in the gas phase, nor in PT or TIPS-PT embedded in a crystalline environment ^{5}(TT) is energetically close to ^{1}(TT), which makes a coupling *via* spin-spin dipole interactions very unlikely. Nevertheless, Breit-Pauli spin-spin matrix elements

were calculated for a PT dimer in order to test the program and to validate the small influence of the spin-spin-dipole interactions.

Introductory Remarks

In some passages of this work the reader will encounter a notation, which might be unfamiliar at first sight, however has proven useful in distinguishing states effectively in discussions. It is derived from the common way to denote excited determinants in literature, e.g. $|\Psi_{ij}^{ab}\rangle$ often denotes generic doubly excited configurations. In the derived notation, single excitations are symbolized by their overall multiplicity, e.g. S for singlet and T for triplet, a subscript denoting the orbitals out of which the particle is taken and a superscript denoting its destination. To give an example, S_h^l denotes a singlet state, dominated by a configuration in which the highest occupied orbital was substituted by the lowest unoccupied orbital. $\mathrm{T}_{h-1;h}^{l;l+1}$ denotes a triplet state built from two configurations. In the first the second-highest occupied molecular orbital is substituted by the lowest unoccupied orbital and in the second the highest occupied is substituted with the second lowest unoccupied molecular orbital. The notation is most useful in differentiating between different doubly excited configurations, which play a fundamental role in singlet fission. A configuration with four open shells is denoted by a V, one with two by a Z, and zero open shell with an N. The letters are motivated by the German words Vier (four), Zwei (two) and Null (zero), respectively. A state dominated by a doubly excited configuration with four, two and no open-shells would be denoted $\mathrm{V}_{h-1;h}^{l;l+1}/\mathrm{N}_h^l/\mathrm{Z}_h^{l;l+1}$. Note, that it is not necessary to repeat certain indices in this notation, as this information is contained in the symbols. If necessary, explicit reference to the multiplicity will be made in such cases. However, most of the time it is clear from the context, which multiplicity is discussed. Publications to which the author contributed are prefixed with a capital 'P'. Furthermore, they were put into a separate bibliography found right before the table of contents. Figures, tables, equations, sections and algorithms are abbreviated as Fig., Tab., Eq., Sec. and Alg. respectively. A glossary with definitions of common and uncommon terms was compiled and can be found right after the last chapter of the thesis.

Own Publications

[P1] D. Dombrowski, T. Schulz, M. Kleinschmidt, C. Marian, "R2022: A DFT/MRCI Ansatz with Improved Performance for Double Excitations", *The Journal of Physical Chemistry A* **2023**, *127*, 2011–2025,

Author's contributions: Large parts of the draft and the final publication were written by the author. The author provided figures, suggested the investigated carotenoids as test molecules, and provided raw and processed data of the Buckminsterfullerene investigated in the paper. Furthermore, he participated in and contributed to discussions leading to the new model Hamiltonian.

[P2] T. Schulz, C. M. Marian, "Simulating the Full Spin Manifold of Triplet-Pair States in a Series of Covalently Linked TIPS-Pentacenes", *Journal of Computational Chemistry* **Under Revision**,

Author's contributions: All computations were carried out by the author. All Tables and figures were created by the author. The inital draft of the manuscript was provided by the author. Furthermore, he supported reviewing the final, submitted manuscript and played an active role in the submission process.

[P3] T. Schulz, P. Konieczny, D. R. Dombrowski, S. Metz, C. M. Marian, R. Weinkauf, "Electron Affinities and Lowest Triplet and Singlet State Properties of *para*-Oligophenylenes (n = 3–5): Theory and Experiment", *Physical Chemistry Chemical Physics* **2023**, *25*, 29850–29866,

Author's contributions: Most of the electronic structure calculations, as well as Franck-Condon simulations on the three investigated molecules were carried out by the author. Furthermore, the author contributed python and Shell-scripts to generate the figures and tables and created figures and tables of his own. He was actively involved in discussing the manuscript drafts and reviewing drafts and the final manuscript.

[P4] T. Schulz, S. Hédé, O. Weingart, C. M. Marian, "Multiexcitonic and Optically Bright States in Subunits of Pentacene Crystals: A Hybrid DFT/MRCI and Molecular Mechanics Study", *The Journal of Chemical Physics* **2024**, *160*, 144114,

Author's contributions: The author initated and managed the project. All electronic structure calculations on the DFT/MRCI level on the embedded pentacenes were done by the author. All gas-phase simulations including geometry optimizations and electronic structure calculations were done by the author. All figures and tables were provided by the author. The inital draft was written by the author and he supported reviewing the final manuscript.

Contents

1 Introduction

The observation that light can interact with matter is one of the most important observations made in modern human history. It has led to unrivaled progress in all areas of science and is ultimately the basis of countless technical achievements that have become commonplace. Particularly fruitful was the discovery[5] that materials like selenium are capable of generating electricity on light exposure, nowadays known as photovoltaic effect. In 2023 the impressive amount of 59.9 TW h electric energy were produced using photovoltaic devices in Germany alone[6]. Over 90% of the employed cells were based on silicon (Si) wafers[7], which is likely rooted in the easy availability of the materials needed in their construction. A downside of employing Si based cells is their relatively low efficiency of $\approx 24\%$[8], which is reasonably close to the theoretical best estimate of $\approx 28\%$[9–11] It would appear that there is a strong desire to construct cells that benefit from the properties of silicon-based cells, while also being more efficient. A potential solution was put forth in 2006. Hanna and Nozik [12] calculated the maximum power conversion efficiency in photovoltaic cells when carrier multiplication is exploited. They modeled drastic increases of $> 10\%$ compared to a standard single gap solar cell, of which Si devices are representatives, when coupled to a layer capable of singlet exciton fission (SF). SF is a process in which an initially excited singlet exciton evolves into an uncoupled pair of triplet excitons, which means the number of available charge-carriers is doubled. Though, there are comprehensive reviews[13–20] from different perspectives, all possible mechanistic steps have not been fully elucidated, yet. However, important intermediates have been identified[21, 22]. An overview of the possible steps connecting them is given in Fig. 1.1. Initially, a photo excited singlet state is formed, decaying rapidly into other states. The anti-ferromagnetically coupled triplet pair ^{1}(TT), whose simplified electronic configuration is sketched as the result of steps 2 or 3 in Fig. 1.1, makes the initial step spin-allowed and potentially fast. Furthermore, it serves as the starting point of the disentanglement into separated triplets $T_1 + T_1$. The suspected mechanism of this step involves the spin-decorrelation of a triplet pair state, which

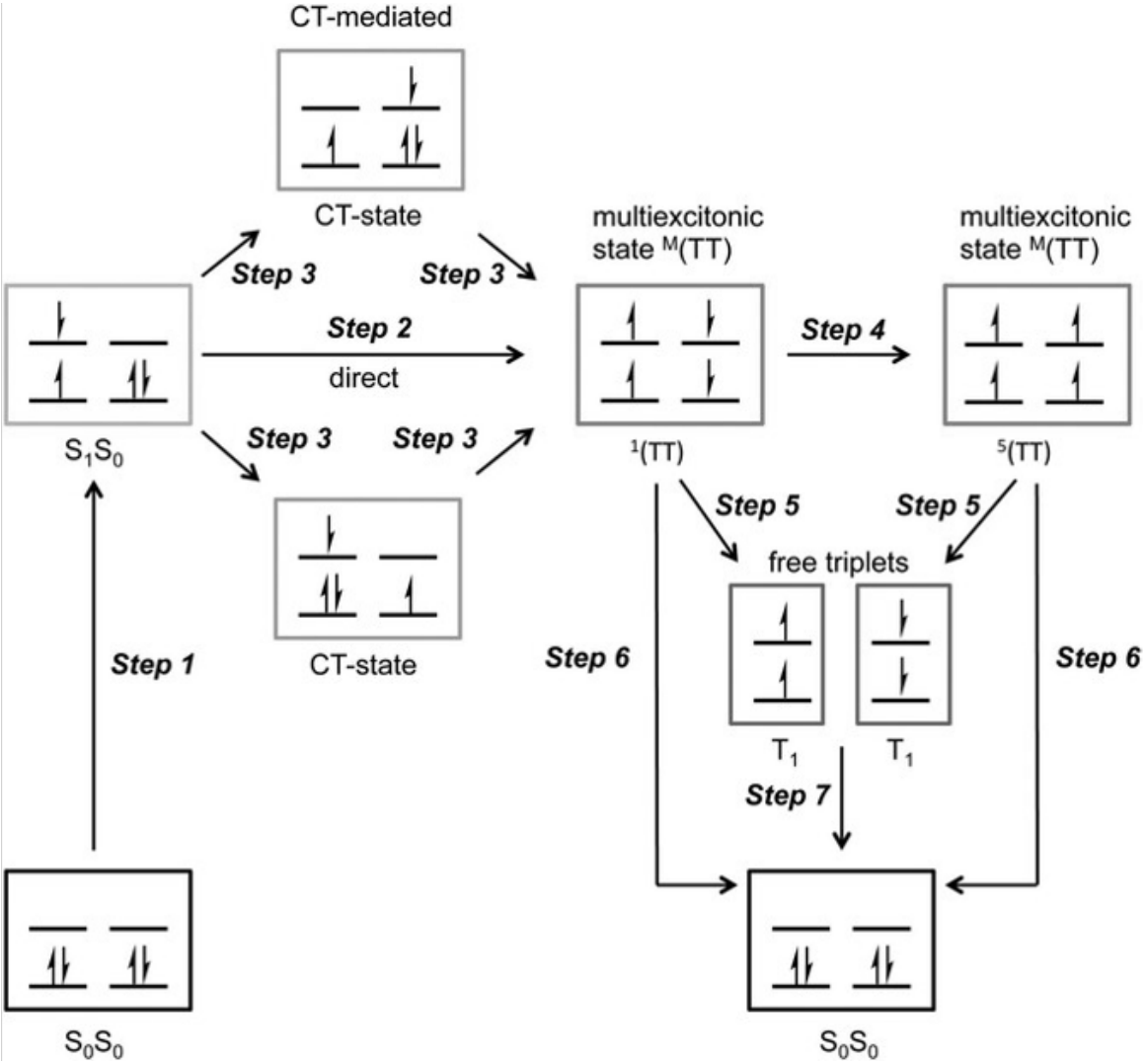

Figure 1.1: Different possible mechanism for the SF process. Copied with permission from Hetzer et al. [19].

comprises two spatially pure triplet states. This is backed by observations of Grieco et al. [21] and Chan et al. [23] using time-resolved spectroscopies. However, a route *via* the ferromagnetically coupled form of the triplet pair ^{5}(TT), i.e. involving step 4 in Fig. 1.1, is not ruled out[24] as (time-dependent) electronic spin resonance experiments[25][26] suggest. A first order effect able to interconnect ^{1}(TT) to ^{5}(TT) is the spin-spin dipole interaction, which will be one of the topics of this work. Calculating matrix elements of the Breit-Pauli spin-spin dipole operator for different multiplicities is not an easy endeavor and density functional theory combined with multi-reference configuration interaction (DFT/MRCI) is one of the few methods, that offer this

possibility.

Unfortunately, materials known to undergo SF are relatively scarce. Surely, this is rooted in the fact that the mechanism enabling a material to show SF is not fully understood, yet. Consequently, it is mostly unclear what molecular building blocks are beneficial and which structures need to be manipulated to obtain an efficient SF material. Though, pentacene[19, 27–29] and perylene diimide[30, 31] have been deemed good foundations. Nowadays, computational chemistry is a valuable tool to design new materials or gain insight into properties of molecules. It is used on a general basis to aid interpreting spectroscopic data and elucidate mechanistic details. Consequently, it serves as an indispensable tool in elucidating the mechanistic details of SF and exploring new materials to maximize the yield of triplet pairs. It is clear that the employed methods must have a certain degree of accuracy to do so. More importantly, they must be able to give a balanced description of the plethora of states possibly contributing to the process (see Fig. 1.1). The present work will deal in large parts with such a method and properties computed based on it. Furthermore, it will be investigated whether the method is suited to be employed in the simulation of SF materials and if mechanistic insight can be gained. The thesis is structured as follows: First, an introduction of the elementary theories needed for this work is given. The author has tried to be as detailed and complete as necessary. Special reference should be made to the glossary, where short explanations of commonly used terms are collected. Secondly, a short technical part follows. A newly implemented parallelization scheme for two program modules used in the computer chemistry group of the Heinrich Heine University (HHU) Düsseldorf will be presented. Thirdly, it will be investigated how previous methods developed in the same group perform in simulating the necessary states for SF. Afterwards, a new method will be introduced, whose performance was evaluated on anthracene derivatives and *oligo-para*-phenylenes for which high-quality, gas-phase spectroscopic data is available. Finally, work in the context of SF will be presented. Investigations on pentacene (PT) and 6,13-bis(triisopropylsilylethynyl)pentacene (TIPS-PT) embedded in a crystalline environment will be discussed, focusing as well on the ^{5}(TT) state and its possible role in SF. Finally, a conclusion will be drawn, and an outlook will be given.

2 Theory

The basic task to solve In the beginning of the last century it became apparent that physics and consequently chemistry are not governed by the (more or less) simple deterministic laws of classical mechanics formulated in a continuous configuration space, but are governed by something quantized and non-deterministic. One of the most convincing experimental evidences for this quantization was found by Stern and Gerlach[32]. Nowadays, the experiment is interpreted as proof of one of the most 'quantum' phenomena known, namely a particle's spin. From a mathematical point-of-view spin owns a similar underlying structure as angular momentum. However, the physical consequences of its existence are very different, and it is necessary to dive into the fascinating world of quantum field theory[33] to try to understand why spin emerges and in what physical picture it might be cast[34]. For the purpose presented in the following it will suffice to simply accept the fact that particle spin can be introduced into quantum mechanics, i.e. into a picture, which assumes that particles or *vice versa* their associated waves are the fundamental quantity needed to describe physical processes. Furthermore, we will restrict ourselves to a picture, which will emerge if the expectation values of the observables are constant in time, i.e. we will only treat stationary states. The language of quantum mechanics is based on the language of Hilbert spaces and the key axioms are that physical observables are associated with the eigenvalues of linear operators and degrees of freedom can be added by taking the tensor product between Hilbert spaces. In the following sections the physical framework used in this work will be discussed, starting with a very short overview of the general equations used in electronic structure theory, followed by a discussion of the consequences of introducing a spin dependency into these equations. Based on this, the framework of rotations in quantum mechanics will be introduced, closing with an introduction to the formalism of second quantization.

2.1 The Molecular Hamiltonian and its Eigenfunctions

Though quantum physics has been around for quite some time and it is nowadays accepted in chemistry that the laws governing the chemical regime are of quantum mechanical nature, it is still a remarkable challenge to make accurate predictions based on these. Even more so if relativistic approaches are taken to tackle the problem, as outlined in the monograph of Kutzelnigg [35]. The central quantity to be computed is the energy, E_S, of a system S, which is fully described by a wave function Ψ_S. Derivatives of E_S with respect to external fields or internal moments, such as the magnetic moment arising from nuclear spin, gives access to central properties of molecules, e.g. polarizability, hyperfine coupling or optical rotation.[1] The full time-independent molecular Schrödinger-Hamiltonian for a system of N electrons and P nuclei is shown in Eq. (2.1) in atomic units. Terms one and two express the kinetic energies of the electrons (lower case indexing) and the nuclei (upper case indexing), where the latter includes the nuclear masses M. The fourth, fifth and sixth term represent the Coulomb interaction of the charges carried by the electrons and nuclei (Z), respectively. $\vec{\nabla}$ denotes the Nabla operator.

$$\begin{aligned}\hat{H} &= -\sum_{i}^{N}\frac{1}{2}\vec{\nabla}_i^{\,2} - \sum_{A}^{P}\frac{1}{2M_A}\vec{\nabla}_A^{\,2} - \sum_{i,A}^{N,P}\frac{Z_A}{r_{Ai}} + \sum_{A>B}^{P}\frac{Z_A Z_B}{r_{AB}} + \sum_{i>j}^{N}\frac{1}{r_{ij}} \\ &= \hat{T}^{nuc.} + \hat{V}^{nuc.} + \hat{T}_{el.} + \hat{V}_{el.} + \hat{V}_{el.}^{nuc.}\end{aligned} \tag{2.1}$$

Obviously, Eq. (2.1) can be grouped into terms linked to coordinates of the nuclei and terms containing only electronic degrees of freedom. It is evident that a separation of nuclear and electronic coordinates represents a desirable solution, as it markedly simplifies the underlying complexity of the problem. Fortunately, a good approximation can be found in the product ansatz $\Psi(r,R) = \Phi(r;R)\,\Theta(R)$ of the wave function, where $\Phi(r;R)$ is associated with all electronic coordinates r and a fixed nuclear arrangement R and $\Theta(R)$ deals with variable nuclear coordinates[37]. Acting with the

[1] An exemplary list of properties derivable from the electronic energy can be found in the book of Jensen [36, p. 320]

Hamiltonian defined in Eq. (2.1)

$$\begin{aligned}\hat{H}\Psi(r,R) = \Theta(R)\left[\sum_{i>j}^{N}\frac{1}{r_{ij}} - \sum_{i}^{N}\frac{1}{2}\vec{\nabla}_i^{\,2} - \sum_{i,A}^{N,M}\frac{Z_A}{r_{Ai}}\right]\Phi(r;R) \\ + \Phi(r;R)\left[-\sum_{A}^{M}\frac{1}{2M_A}\vec{\nabla}_A^{\,2} + \sum_{A>B}^{M}\frac{Z_A Z_B}{r_{AB}}\right]\Theta(R) \\ - \sum_{A}^{M}\frac{1}{M_A}\vec{\nabla}_A\Phi(r;R)\,\vec{\nabla}_A\Theta(R) - \Theta(R)\sum_{A}^{M}\frac{1}{2M_A}\vec{\nabla}_A^{\,2}\Phi(r;R)\end{aligned} \tag{2.2}$$

gives rise to terms containing only electronic and nuclear coordinates and coupling terms originating from the divergence of the nuclear gradient. Solving the electronic problem, i.e.

$$\left[\sum_{i>j}^{N}\frac{1}{r_{ij}} - \sum_{i}^{N}\frac{1}{2}\vec{\nabla}_i^{\,2} - \sum_{i,A}^{N,M}\frac{Z_A}{r_{Ai}}\right]\Phi(r;R) = E(R)\,\Phi(r;R) \tag{2.3}$$

is the main task of quantum chemistry. Unfortunately, no closed solutions exist for systems with more than two particles and further approximations discussed in latter sections must be made. Peculiarly, spin, a concept whose discovery led to the acceptance of quantum theory in the first place, is not included in the equation. To introduce it, one has to consider either special representations of the Galilei-group or start from the relativistic treatment of a free particle and investigate the limits of the underlying relativistic Hamiltonian on letting the speed of light go to infinity $c \to \infty$, i.e. taking the non-relativistic limit.

2.1.1 Introducing Spin

As mentioned in the preceding paragraph it is possible to introduce spin by linearization of Eq. (2.1) and considering group theoretical arguments. The derivation was given by Lévy-Leblond [38], and it can be concluded that spin itself is not a relativistic quantity. As the procedure is a bit tedious, the interested reader is referred to the original publication[38] or the work of Kutzelnigg [39] for a derivation. Here, the more common way will be presented which starts from the relativistic Dirac-equation Eq. (2.4), and ends in taking its non-relativistic limit. Many-body effects will be introduced in form of the Breit operator, which will lead to the operator for electronic spin dipole-dipole coupling used as the basis of this and earlier work[40]. As there are

a plethora of textbooks discussing this derivation in a more or less detailed way, e.g. Reiher and Wolf [41, p. 185 ff.], Dyall [42, p. 49 ff.] or Sakurai [43, p. 85 ff.], we refrain from giving any detailed derivations and content ourselves with a short introduction in the sprit of Barysz and Ishikawa [44, chap. 4] and the final result, commonly called the Pauli equation (Eq. (2.10)). The free-particle Dirac-equation (Eq. (2.4)) reads

$$\begin{aligned}\hat{H}_D\Psi_4 &= \left[c\vec{\alpha}\vec{p} + \beta mc^2\right]\Psi_4 \\ &= \left[c\begin{pmatrix}0_2 & \vec{\sigma}\\ \vec{\sigma} & 0_2\end{pmatrix}\vec{p} + \begin{pmatrix}\mathbf{1}_2 & 0_2\\ 0_2 & -\mathbf{1}_2\end{pmatrix}mc^2\right]\begin{pmatrix}\xi\\ \psi\end{pmatrix} = \begin{pmatrix}E & 0_2\\ 0_2 & E\end{pmatrix}\begin{pmatrix}\xi\\ \psi\end{pmatrix} \\ &\overset{\epsilon=E-mc^2}{\Leftrightarrow} \begin{cases}\left[c\vec{\sigma}\vec{p}\psi - \epsilon\xi\right] = 0\\ \left[c\vec{\sigma}\vec{p}\xi - \left(2mc^2+\epsilon\right)\psi\right] = 0\end{cases},\end{aligned} \tag{2.4}$$

where $\hat{H}_D$ is an operator acting on a four-component spinor wave function Ψ_4, consisting of two subcomponents ψ and ξ. In the last equation, the energy spectrum was shifted by $-mc^2$ to align the energy origin associated with the electronic solutions to the origin of the non-relativistic spectrum. Apparently, a relativistic theory leads to coupled positive and negative energy solutions. While the former are associated with the electron and are most relevant for chemistry, the negative solutions can be associated with a particle called positron. $\hat{H}_D$ makes use of 4×4 matrices $\vec{\alpha}$ and β each consisting of 2×2 sub-blocks of the form

$$\mathbf{0}_2 = \begin{pmatrix}0 & 0\\ 0 & 0\end{pmatrix} \quad \mathbf{1}_2 = \begin{pmatrix}1 & 0\\ 0 & 1\end{pmatrix} \quad \sigma_1 = \begin{pmatrix}0 & 1\\ 1 & 0\end{pmatrix} \quad \sigma_2 = \begin{pmatrix}0 & -i\\ i & 0\end{pmatrix} \quad \sigma_3 = \begin{pmatrix}1 & 0\\ 0 & -1\end{pmatrix},$$

where $\vec{\sigma}$ is a vector of the Pauli spin-matrices $\sigma_\mathbf{1}, \sigma_\mathbf{2}$ and $\sigma_\mathbf{3}$. Furthermore, the canonical momentum operator $\vec{p} = -i\hbar\nabla$, the speed of light c and the rest mass m are used in Eq. (2.4). If atoms, molecules or any other entities in which electromagnetic fields are present shall be described, it is necessary to introduce the electromagnetic potential, which consists of a scalar field $\phi(\vec{r},t)$ and a vector field $\vec{A}(\vec{r},t)$. This necessitates a modification of the canonical momentum according to the principle of minimal coupling[45] $\vec{p} \to \vec{p} - e\vec{A}$ and introducing the electric field $e\phi$ by substituting $\epsilon \to \epsilon - e\phi$[46] in Eqs (2.4), yielding the expressions

$$(2.4) = \begin{cases}c\vec{\sigma}\left(\vec{p} - e\vec{A}\right)\psi - \left(\epsilon - e\phi\right)\xi = 0 & \text{(2.5a)}\\ c\vec{\sigma}\left(\vec{p} - e\vec{A}\right)\xi - \left(2mc^2 + \epsilon - e\phi\right)\psi = 0 & \text{(2.5b)}\end{cases}$$

Obviously, ψ and ξ are related through[2]

$$\psi = \frac{c\vec{\sigma}\left(\vec{p} - e\vec{A}\right)}{(2mc^2 + \epsilon - e\phi)}\xi \tag{2.6}$$

Inserting into Eq. (2.5a) and factoring out $\frac{1}{2mc^2}$ gives

$$\begin{aligned} &\left[\vec{\sigma}\left(\vec{p} - e\vec{A}\right)\frac{c^2}{(2mc^2 + \epsilon - e\phi)}\vec{\sigma}\left(\vec{p} - e\vec{A}\right) - (\epsilon - e\phi)\right]\xi = 0 \\ &= \left[\vec{\sigma}\left(\vec{p} - e\vec{A}\right)\frac{1}{2m\left(1 + \frac{\epsilon - e\phi}{2mc^2}\right)}\vec{\sigma}\left(\vec{p} - e\vec{A}\right) - (\epsilon - e\phi)\right]\xi = 0 \end{aligned} . \tag{2.7}$$

For obvious reasons, the procedure is called elimination of the small component. It introduces some problems into the theory, as extensively discussed by Kutzelnigg [47][48, 49], and despite their irrelevance to the investigations carried out in this work, it should not remain unmentioned for the sake of completeness. Taking the non-relativistic limit of Eq. (2.7), i.e. letting $c \to \infty$, leads to a vanishing second term in the denominator leaving

$$(2.7) \overset{c\to\infty}{=} \left[\frac{\vec{\sigma}\left(\vec{p} - e\vec{A}\right)\vec{\sigma}\left(\vec{p} - e\vec{A}\right)}{2m} - (\epsilon - e\phi)\right]\xi = 0, \tag{2.8}$$

where in the last step the Dirac relation was used and ϕ has been chosen to be a central potential caused by a charge Z, e.g. a nucleus. Choosing the Coulomb gauge, introducing the magnetic field strength as $\vec{\nabla} \times \vec{A} = \vec{B}$ and letting m and e be the mass and charge of an electron, yields the non-relativistic Pauli-Schrödinger Hamiltonian

$$\hat{H} = \frac{1}{2}\vec{\nabla}^2 - \frac{Z}{r} - i\vec{\nabla} \cdot \vec{A} + A^2 - \vec{\sigma} \cdot \vec{B}$$

with correction terms for the interaction of a charged particle with a magnetic field. Obviously, letting $\vec{A} = 0$, leaves us with the Schrödinger equation of a particle in a central potential. Expanding the denominator of Eq. (2.7) in a geometrical series

$$\left(1 + \frac{\epsilon - e\phi}{2mc^2}\right)^{-1} = \left(1 - \frac{e\phi - \epsilon}{2mc^2}\right)^{-1} = 1 + \frac{e\phi - \epsilon}{2mc^2} + \frac{(e\phi - \epsilon)^2}{4m^2c^4} + \cdots \tag{2.9}$$

[2]Formally this is only true if $\left(2mc^2 + \epsilon - e\phi\right) > 0$, however this can be guaranteed for chemically relevant potentials as discussed by Dyall [42, p. 50]

and reinserting of the first two terms into Eq. (2.7) gives

$$\begin{aligned}
\left[\vec{\sigma}\left(\vec{p}-e\vec{A}\right)\left(1+\frac{e\phi-\epsilon}{2mc^2}\right)\vec{\sigma}\left(\vec{p}-e\vec{A}\right)-(\epsilon-e\phi)\right]\xi &= 0 \\
\underbrace{\left[\frac{1}{8m^3c^2}\nabla^4+\frac{\nabla^2 e\phi}{8m^2c^2}-\frac{i}{4m^2c^2}\vec{\sigma}\left(\left(\vec{\nabla}e\phi\right)\times\vec{\nabla}\right)-\frac{\nabla^2}{2m}+e\phi\right]}\xi &= \epsilon\xi \\
\frac{\vec{p}^{\,2}}{2m}+e\phi-\frac{1}{8m^3c^2}\vec{p}^{\,4}+\frac{\pi\hbar^2 Z}{2m^2c^2}\delta(\mathbf{r})+\frac{Z}{2m^2c^2r^3}\vec{s}\cdot\vec{l} &= \hat{\mathcal{H}}^{\text{Pauli}},
\end{aligned} \tag{2.10}$$

where the Dirac relation was used to simplify the σ dependent terms and in the last equality $\phi = Z/r$ was assumed, $\sigma = \frac{1}{2}\vec{s}$ exploited and the orbital angular momentum operator $\vec{l} = \vec{r}\times\vec{p}$ introduced. Eq. (2.10) is the so-called Pauli-Hamiltonian and is nowadays mostly used for educational purposes and finding improvements based on failures of Eq. (2.10). However, the general way sketched here to obtain it, is directly transferable to a many-electron Hamiltonian, which is of more use for chemical problems of light elements and will be introduced in the following.

2.1.2 Treating Many–Spin Systems

While Eq. (2.10) is a sound way of introducing magnetic field or spin effects as perturbations into non-relativistic Schrödinger theory, it is not very useful for chemistry as it deals only with a single electron. A many-body extension is needed, and it turns out quickly that this is not a simple extension as it is in the non-relativistic Schrödinger theory, but considerable work has to be put into finding a suitable approximate(!) Hamiltonian. The details will not be laid out here, but the author recommends the mini-review of Saue [50], the discussions given by Liu [51] or Kutzelnigg [47][35], and the text books of Reiher and Wolf [41] and Dyall [42]. In short, one cannot simply use the Coulomb-potential $\sum r_{ij}^{-1}$ to couple the sub-systems as this form assumes instantaneous interactions, which does not harmonize with relativistic theories[44]. Furthermore, in Dirac theory the electronic spectrum cannot simply be treated by itself as it is always coupled to its positronic counterpart (pair theory). Fortunately, neglecting these effects does not hamper the application of approximate relativistic Hamiltonians in quantum chemistry as discussed by Liu [51]. Breit [52][53, 54] proposed an approximate relativistic many-body Hamiltonian of the form

$$\hat{H}_{DCB} = \sum_i \hat{h}_D^i + \sum_{i>j} g_{ij} = \sum_i \hat{h}_D^i + \sum_{i>j} \left[g_{ij}^{Coulomb} + g_{ij}^{Breit} \right] \tag{2.11}$$

$$\hat{h}_D^i = c\vec{\alpha}\vec{p} + mc^2\beta + V_{ext} = c\vec{\alpha}\vec{p} + mc^2\beta - \sum_A \frac{Z_A}{r_{Ai}}, \tag{2.12}$$

where $\hat{h}_D^i$ is the Dirac-Hamiltonian[55] of the i-th particle, consisting of the Dirac-matrices $\vec{\alpha}$ and β and the external potential V_{ext}. For atoms and molecules V_{ext} is simply the electric field caused by the nuclei with charge Z_A. g_{ij} collects all two-particle interactions and can be approximated by the classical, non-relativistic Coulomb interaction $g_{ij}^{Coulomb}$ and correction terms of the necessary relativistic corrections g_{ij}^{Breit} in Coulomb gauge

$$\hat{g}_{ij} \approx \frac{1}{r_{ij}} \underbrace{-\frac{1}{2}\left[\frac{\vec{\alpha}_1\vec{\alpha}_2}{r_{ij}} + \frac{(\vec{r}_{ij}\cdot\vec{\alpha}_1)(\vec{r}_{ij}\cdot\vec{\alpha}_2)}{r_{ij}^3} \right]}_{\equiv g_{ij}^{Breit}}. \tag{2.13}$$

As shown in the classic book of Bethe and Salpeter [56, Sec. 39] and in great detail by Reiher and Wolf [41, Chap. 13], the non-relativistic limit of the g_{ij} term and neglect

of all external-vector potentials leads to

$$\hat{\mathcal{H}}^{\mathrm{BP}} = \sum_i \left[\frac{\vec{p}_i{}^2}{2m} - \frac{Z}{r_i} - \frac{\vec{p}_i{}^4}{8m^3c^2} + \frac{\pi\hbar^2 Z}{2m^2c^2}\delta\left(\vec{r}_i\right) \right] \tag{2.14}$$

$$+ \frac{1}{2}\sum_{i\neq j}\left[\frac{1}{r_{ij}} - \frac{1}{2m^2c^2}\left(\frac{1}{r_{ij}}\vec{p}_i\cdot\vec{p}_j + \frac{1}{r_{ij}^3}\left(\vec{r}_{ij}\left(\vec{r}_{ij}\cdot\vec{p}_j\right)\cdot\vec{p}_i\right)\right) - \frac{\pi\hbar^2}{m^2c^2}\delta\left(\vec{r}_{ij}\right) \right. \tag{2.15}$$

$$+ \frac{Z}{2m^2c^2r^3}\vec{s}_i\cdot\vec{\ell_i} - \frac{1}{m^2c^2r_{ij}^3}\left(\vec{s}_i + 2\vec{s}_j\right)\cdot\vec{r}_{ij}\times\vec{p}_i \tag{2.16}$$

$$\left. - \frac{8\pi}{3m^2c^2}\left(\vec{s}_i\cdot\vec{s}_j\right)\delta\left(\vec{r}_{ij}\right) + \frac{1}{m^2c^2}\left(\frac{\left(\vec{s}_i\cdot\vec{s}_j\right)}{r_{ij}^3} - \frac{3\left(\vec{s}_i\cdot\vec{r}_{ij}\right)\left(\vec{s}_j\cdot\vec{r}_{ij}\right)}{r_{ij}^5}\right)\right] \tag{2.17}$$

for an atom of with a nuclear charge of Z. Apparently, it is possible to group relativistic correction into spin-dependent (Eqs. (2.16) / (2.17)) and -independent parts (Eqs. (2.14)/(2.15)). For this work, only the last group, comprised of spin orbit (Eq. (2.16)) and electron spin-spin dipole interactions (Eq. (2.17)), is of interest. As all of these effects originate in observables linked to rotation, the next section is dedicated to rotations in quantum mechanics and how investigating the underlying structure introduces great simplifications in computing the expectation values of such quantities.

2.2 Rotating Quantum Mechanical Systems

Rotating the whole system under investigation must not lead to a different physical picture, which is clear from intuition and more formally follows from the isotropy of space[57]. Associated with this intuitive statement is a rather unintuitive quantity called angular momentum. Generally, angular momentum operators transform similar to vectors under rotation and are defined through the relations[58–60]

$$\mathcal{D}\left(\vec{n},\delta\theta\right) = 1 - i\vec{J}\vec{n}\delta\theta \tag{2.18}$$

$$\mathcal{D}\left(\vec{n},\theta\right) = \lim_{N\to\infty}\left[1 - i\vec{J}\vec{n}\frac{\theta}{N}\right]^N = e^{\left(-i\vec{J}\vec{n}\theta\right)} \tag{2.19}$$

$$\left[J_i, B_j\right] = i\sum_{k=1}^{3}\epsilon_{ijk}B_j, \tag{2.20}$$

where $\mathcal{D}$ denotes a rotation operator, $\vec{n}$ determines the direction of the rotation axis, $(\delta)\theta$ the (infinitesimal) rotation angle, $\vec{B}$ an arbitrary vector-, $\vec{J}$ the total angular

momentum operator, B_j and J_i their components, and ϵ_{ijk} the Levi-Civita symbol. A rotation about an arbitrary unit vector $\vec{n}$ by an angle θ, can clearly be understood as a composition of infinitely many infinitesimal rotations of magnitude $\delta\theta$. This is expressed in Eqs. (2.18) and (2.19), where the occurrence of $\vec{J}$ is rooted in its role as the generator[3] of rotations. Note that $\vec{J}$ is a hermitian operator, while in the defining equation of the rotation operator Eq. (2.19) its anti-hermitian $i\vec{J}$ counterpart occurs. The explanation is simple. A rotation into the other direction must lead to a change of sign, which coincides with taking the conjugate in the operator formalism. As already mentioned in the preceding section, spin behaves like an angular momentum and is coupled to orbital-angular momentum $\vec{\ell}$ through Eqs (2.16). Consequently, it does not suffice to investigate the orbital-angular momentum only, if the associated observables shall be discussed, which is in stark contrast to classical mechanics. One can define the total electronic angular momentum

$$\vec{J} = \vec{L} + \vec{S}.$$

Due to the principles of quantum mechanics, one can only investigate a single component of the angular momentum vector as, according to the defining Eq. (2.20), any two of its components are non-compatible observables. By convention the z-component J_z is chosen. Defining the Casimir operator[64]

$$J^2 = J_x J_x + J_y J_y + J_z J_z, \tag{2.21}$$

which commutes with every component of $\vec{J}$ by definition and is recognized as the magnitude of the total angular momentum vector. Therefore, one needs two quantum numbers j and m_j to fully characterize an angular momentum state $|j, m_j\rangle$. It is often very helpful to switch to the Cartan-Weyl form[63, 64] of the underlying Lie-algebra, which leads to the commutators

$$[J_z, J_z] = 0 \quad [J_z, J_\pm] = \pm J_\pm \quad [J_-, J_+] = 2J_z$$

[3]The angular momenta can be used to express every rotation and therefore fully determine the transformation properties of the system under rotation. More formally a generator is a member of a group algebra, i.e. we can use it to generate all the group-elements by acting with the generator on the group members[61–63]

and operators

$$\begin{aligned} J_z = J_z; \quad J_- = J_x - iJ_y; \quad J_+ = J_x + iJ_y \\ J^2 = J_+ J_- + J_z \left(J_z + 1\right), \end{aligned} \tag{2.22}$$

where $J_\pm$ are called ladder- or raising- and lowering-operators, respectively. Deriving their matrix elements in the basis $|j, m_j\rangle$ is straightforward. Noting that[59]

$$J_+ \left|j; m_j = j\right\rangle = \left|j; m_j = j+1\right\rangle = 0 \quad J_{-1} \left|j; m_j = -j\right\rangle = \left|j; m_j = -j-1\right\rangle = 0$$

leads to the matrix elements[65]

$$\begin{aligned} \langle j'; m_j' | J^2 | j; m_j \rangle &= j(j+1)\delta_{jj'}\delta_{m_j;m_j'} \\ \langle j'; m_j' | J_z | j; m_j \rangle &= m_j \delta_{jj'}\delta_{m_j;m_j'} \\ \langle j'; m_j' | J_+ | j; m_j \rangle &= \sqrt{(j-m_j)\left(j+m_j+1\right)}\delta_{jj'}\delta_{m_j';m_j+1} \\ \langle j'; m_j' | J_- | j; m_j \rangle &= \sqrt{(j+m_j)\left(j-m_j+1\right)}\delta_{jj'}\delta_{m_j';m_j-1}. \end{aligned}$$

What remains to be done to obtain expressions for many-body systems is to couple all angular momenta appropriately. This requires a formalism which is intimidating on first encounter, especially for more than two angular momenta, because of the unusual notation and plethora of indices. Thorough discussions of the topic can be found in the textbooks by Sakurai and Napolitano [59, Chap. 3], Rose [66] Tinkham [60] or Jeevanjee [58]. As the operators used in this work do not necessitate to couple more than two angular momenta at a time the introduction given here will be limited to this case. An obvious but useful statement is

$$[J_{Ai}, J_{Bj}] = 0,$$

which is intuitive as the linear maps of angular momentum states belonging to the subspace A have no bearing on vectors of B and *vice versa*. This necessitates to construct a composite map, acting on any two states of A and B, i.e. one needs a map acting on the Cartesian product space $C = A \times B$. Such a map is realized utilizing the tensor product

$$J_i = J_{Ai} \otimes \mathbb{I}_B + \mathbb{I}_A \otimes J_{Bi}, \tag{2.23}$$

where $\mathbb{I}_A$ and $\mathbb{I}_B$ denote the identities of the vector spaces A and B, respectively. From the given definition it is clear that two equivalent choices of characterizing states can be made. Either, one utilizes eigenkets of the set $J_{Az}, J_{Bz}, J_{Az}^2, J_{Bz}^2, \{\ |\ j_A, j_B; m_{jA}, m_{jB}\rangle\ \}$ or the set $\{\ |\ j_A, j_B; J, M_J\rangle\ \}$, where $|J; M_J\rangle$ are eigenvectors of the composite maps J^2 and J_z generated in the spirit of Eq. (2.23) The two bases are related through[67]

$$|j_A, j_B; J, M_J\rangle = \sum_{\substack{m_{jA} \\ m_{jB}=M_J-m_{jA}}} |j_A, j_B; m_{jA}, m_{jB}\rangle \underbrace{\langle j_A, j_B; m_{jA}, m_{jB}|j_A, j_B; J, M_J\rangle}_{\text{Clebsch–Gordan coefficient}} \tag{2.24}$$

and the amplitudes, dubbed Clebsch-Gordan coefficients, appear frequently in representation theory, e.g. in expanding rotation matrices. They have the nice property to vanish if either

$$M_J \neq m_{jA} + m_{jB} \quad \text{or} \tag{2.25}$$

$$J < |j_A - j_B| \qquad \text{or} \qquad J > j_A + j_B. \tag{2.26}$$

Furthermore, they are elements of a unitary matrix, which implies a symmetry with the inverse coefficient and orthogonality of different coefficient vectors. They might be interpreted as a connection between different 'geometries' of angular momentum, as they link the quantum numbers characterising the projection to the z-axis m_A, m_B and M_J. A second observation can be made, which links Eq. (2.23) to a more general treatment of the subject. While the vectors of the 'length' operator of the individual momenta j_X^2 are obviously bounded from below by 0, which makes them uni-directional in a sense, the compound operator J^2 has eigenkets, characterized by the quantum numbers

$$J = |j_A - j_B|\,, |j_A - j_B| + 1, \cdots, j_A + j_B - 1, j_A + j_B,$$

as already implied by Eq.(2.26). The eigenkets of the compound operator J^2 are apparently bidirectional. As a consequence, they must be related to a quantity, which is linked to vector operators, but itself is a higher dimensional object. Such a quantity is called tensor operator. In the case of two vectors being coupled it is called a second rank tensor or dyad in which case Eq. (2.23) is called the dyadic product. It can be shown quite generally[65, 68] that the representations belonging to such an operator are reducible, i.e. it can be decomposed into components each transforming differently.

Irreducible representations can be obtained on decomposition of the tensor into a spherical basis, leading to a set of spherical tensor operators denoted as $T_q^{(k)}$. The superscript (k) denotes the rank of the tensor, and simply measures how many vectors are needed in its construction, while the subscript q can be understood as a label for the basis vectors used in setting up its representation. The algebra of such operators was worked out by Racah [69][70, 71] and is central in many areas of physics. They can be defined[59] using the commutators

$$\left[J_z, T_q^{(k)}\right] = qT_q^{(k)} \tag{2.27}$$

$$\left[J_\pm, T_q^{(k)}\right] = \sqrt{\{(k \mp q)(k \pm q + 1)\}} T_k^{q\pm 1}, \tag{2.28}$$

where the relation to Eqs. (2.20) is understood. Evaluating matrix elements of $T_q^{(k)}$ brings us to one of the most useful theorems from representation theory for quantum mechanics, namely the Wigner-Eckart Theorem (WET). Assume a set of angular momentum eigenstates $\{ \mid N, J, M_J\rangle \}$, where N is a collection of quantum numbers needed to fully characterize the state. One can show using Eq. (2.28) that

$$\langle N, J', M'_J|T_q^{(k)}|N, J, M_J\rangle = \langle Jk; M_j q|Jk; J'M'_J\rangle \frac{\langle N'J'||T^{(k)}||NJ\rangle}{\sqrt{2J'+1}}, \tag{2.29}$$

where $\langle Jk; M_J q|Jk; J'M'_J\rangle$ is a Clebsch-Gordan coefficient and $\langle N'J'||T^{(k)}||NJ\rangle$ is the so-called reduced matrix element. This means, every matrix element of an irreducible tensor operator evaluated on angular momentum eigenkets can be obtained by multiplying a constant geometric factor and a matrix element, which only depends on the magnitude and the remaining quantum numbers specifying the system. Since the reduced matrix element only depends on the J values one can interpret the theorem from a group theoretical point of view, as the statement that every irreducible representation occurs only once in the reduction of the tensor product. Due to the properties of the Clebsch-Gordan coefficients presented before (Eq. (2.25)) one can immediately deduce that the matrix element on the left-hand side (LHS) vanishes unless $M'_J = M_J + q$ and $|J - J'| \leq k \leq J + J'$. To construct expressions for the components of the spherical tensor operator one can exploit the analogy to spherical[60] $Y_l^m(\theta, \phi)$ or solid[68] harmonics $\mathcal{Y}_l^m(\vec{r})$, which transform exactly like the $T_q^{(k)}$ under rotation. An important example is the representation of a second rank tensor operator, i.e. constructed from two vector operators, which decomposes into a sum of spherical tensor operators of rank 0, 1 and 2. While $k = 0$ corresponds to a scalar,

Table 2.1: Components of the rank 1 and rank 2 spherical tensors used in the decomposition of a general rank 2 tensor operator. A and B labels arbitrary vector-like entities, which transform appropriately under rotation, e.g. the $Y_l^m(\theta,\phi)$ $\mathcal{Y}_l^m(\vec{r})$ or $J_z, J_\pm$ mentioned in the text.

	k	
q	1	2
2	-	$A_1^1 B_1^1$
1	$\sqrt{\frac{1}{2}}\left(A_1^1 B_0^1 - A_0^1 B_1^1\right)$	$\sqrt{\frac{1}{2}}\left(A_1^1 B_0^1 + A_0^1 B_1^1\right)$
0	$\sqrt{\frac{1}{2}}\left(A_1^1 B_{-1}^1 - A_{-1}^1 B_1^1\right)$	$\sqrt{\frac{1}{6}}\left(A_1^1 B_{-1}^1 + A_{-1}^1 B_1^1 + 2A_0^1 B_0^1\right)$
-1	$\sqrt{\frac{1}{2}}\left(A_0^1 B_{-1}^1 - A_{-1}^1 B_0^1\right)$	$\sqrt{\frac{1}{2}}\left(A_{-1}^1 B_0^1 + A_0^1 B_{-1}^1\right)$
-2	-	$A_{-1}^1 B_{-1}^1$

i.e. a quantity invariant under rotation, rank 1 and 2 behave antisymmetric and symmetric on rotation, respectively. Tab. 2.1 compiles a collection of q components for $k = 1, 2$ of $T_q^{(k)}$. Accordingly, the operator defined in Eq. (2.17) can be written as[72, 73]

$$\hat{\mathcal{H}}_{SS} = C\left(\frac{(\vec{s}_i\cdot\vec{s}_j)}{r_{ij}^3} - \frac{3\,(\vec{s}_i\cdot\vec{r}_{ij})\,(\vec{s}_j\cdot\vec{r}_{ij})}{r_{ij}^5}\right) \tag{2.30}$$

$$= C\sum_i^N\sum_{j<i}^N\left[\frac{1}{2}\left\{\frac{2\vec{z}_{ij}^{\,2} - \vec{x}_{ij}^{\,2} - \vec{y}_{ij}^{\,2}}{r_{ij}^5}\right\}\left\{2\vec{s}_i^{\,0}\vec{s}_j^{\,0} + \vec{s}_i^{\,+1}\vec{s}_j^{\,-1} + \vec{s}_i^{\,-1}\vec{s}_j^{\,+1}\right\}\right. \tag{2.31}$$

$$+\frac{3}{2}\left\{\frac{\vec{x}_{ij}^{\,2} - \vec{y}_{ij}^{\,2}}{r_{ij}^5}\right\}\left\{\vec{s}_i^{\,-1}\vec{s}_j^{\,-1} + \vec{s}_i^{\,+1}\vec{s}_j^{\,+1}\right\} \tag{2.32}$$

$$+\,i\left\{\frac{3\vec{x}_{ij}\vec{y}_{ij}}{r_{ij}^5}\right\}\left\{\vec{s}_i^{\,-1}\vec{s}_j^{\,-1} - \vec{s}_i^{\,+1}\vec{s}_j^{\,+1}\right\} \tag{2.33}$$

$$+\frac{1}{\sqrt{2}}\left\{\frac{3\vec{x}_{ij}\vec{z}_{ij}}{r_{ij}^5}\right\}\left\{\vec{s}_i^{\,-1}\vec{s}_j^{\,0} + \vec{s}_i^{\,0}\vec{s}_j^{\,-1} - \vec{s}_i^{\,+1}\vec{s}_j^{\,0} - \vec{s}_i^{\,0}\vec{s}_j^{\,+1}\right\} \tag{2.34}$$

$$\left.+i\frac{1}{\sqrt{2}}\left\{\frac{3\vec{y}_{ij}\vec{z}_{ij}}{r_{ij}^5}\right\}\left\{\vec{s}_i^{\,-1}\vec{s}_j^{\,0} + \vec{s}_i^{\,0}\vec{s}_j^{\,-1} + \vec{s}_i^{\,+1}\vec{s}_j^{\,0} + \vec{s}_i^{\,0}\vec{s}_j^{\,+1}\right\}\right], \tag{2.35}$$

where C is a constant depending on the chosen unit system and the spatial tensor components are given as cartesian components, in spirit of the relations known for

the spherical harmonics

$$\begin{aligned}
\frac{1}{2}(\vec{x}+i\vec{y})\,(\vec{x}+i\vec{y}) &\equiv T_2^{(2)},\\
\frac{1}{2}\,(\vec{z}\,(\vec{x}+i\vec{y})+(\vec{x}+i\vec{y})\vec{z}) &\equiv T_1^{(2)},\\
\frac{1}{\sqrt{6}}\,(2\vec{z}\vec{z}-\vec{x}\vec{x}-\vec{y}\vec{y}) &\equiv T_0^{(2)},\\
-\frac{1}{2}\,(\vec{z}\,(\vec{x}-i\vec{y})+(\vec{x}-i\vec{y})\vec{z}) &\equiv T_{-1}^{(2)},\\
\frac{1}{2}(\vec{x}-i\vec{y})\,(\vec{x}-i\vec{y}) &\equiv T_{-2}^{(2)}.
\end{aligned}$$

By introducing spherical tensor operators one can determine straight away, which angular momentum states might be coupled by this operator based on the WET. Furthermore, it can be seen that the spin and space parts can be treated separately as no mixed products occur. Before discussing methods for computing such states, it is useful to introduce another formalism, dealing with the representation of the states.

2.3 The Formalism of Second Quantization

At the heart of second quantization lies the ideas that every one-particle state $|n_q\rangle$ might be generated from a common ground state $|\mathbf{0}\rangle$ by application of special operators. Further, the so constructed one-particle states serve as a basis of a many-particle state. It is deemed sufficient to label how often a $|n_q\rangle$ appears, i.e. how many particles occupy a certain state. Due to latter point of view, the term *occupation number representation* is intrinsically linked with the concept. For thorough discussions on why this is a valid way of representing quantum mechanics at all, see the discussion given by Rollnik [74, chap. 2]. Generally, most authors[74–76] treat the annihilation and creation operators used to generate the $|n_q\rangle$ in great detail. However, this is only really necessary if one dwells further into field theories for which they were originally intended. For quantum chemistry it is usually sufficient to acknowledge their existence and the usefulness of their algebra for manipulating many-electron systems. In the following the basic concepts are introduced. Starting with the expression of states in the formalism and ending with expressions for operator equations using the language of second quantization.

2.3.1 Expressing States

The first quantity to be introduced is the occupation number vector (ONV) $|\mathbf{k}\rangle$, which for fermions is simply a collection of ones and zeros determining whether a spin-molecular orbital (MO) ϕ_i, occurs in the many-body state or not.

$$\begin{aligned} |\mathbf{k}\rangle &= |k_1, k_2, \cdots, k_N\rangle \quad k_i = 0, 1 \\ &= -\,|k_2, k_1, \cdots k_N\rangle\,, \end{aligned} \tag{2.36}$$

where the anti-symmetry of $|\mathbf{k}\rangle$ is implied. As an example one might have chosen a one-particle basis of dimension three $\{\,\phi_{r\sigma}, \phi_{s\tau}, \phi_t\,\}$. Constructing an ONV for two electrons can be done in three different ways

$$|1_{r\sigma}, 1_{s\tau}, 0_t\rangle \quad |1_{r\sigma}, 0_{s\tau}, 1_t\rangle \quad |0_{r\sigma}, 1_{s\tau}, 1_t\rangle\,. \tag{2.37}$$

The construction can be thought of as the subsequent application of so-called creation operators $a_i^\dagger$ to the base vector $|\mathbf{0}\rangle$, which is assumed to be normalized $\langle\mathbf{0}|\mathbf{0}\rangle = 1$. As the rightmost operator acts first, and antisymmetric functions are used as a basis, the

order of application matters

$$a^\dagger_{s\tau}a^\dagger_{r\sigma}\left|\mathbf{0}\right\rangle = a^\dagger_{s\tau}\left|1_{r\sigma}\right\rangle = \left|1_{s\tau},1_{r\sigma}\right\rangle \tag{a}$$

$$a^\dagger_{r\sigma}a^\dagger_{s\tau}\left|\mathbf{0}\right\rangle = a^\dagger_{r\sigma}\left|1_{s\tau}\right\rangle = \left|1_{r\sigma},1_{s\tau}\right\rangle = -\left|1_{s\tau},1_{r\sigma}\right\rangle \tag{b}$$

$$\xrightarrow{\text{(a)+(b)}} \left(a^\dagger_{s\tau}a^\dagger_{r\sigma} + a^\dagger_{r\sigma}a^\dagger_{s\tau}\right)\left|\mathbf{0}\right\rangle = \left|1_{s\tau},1_{r\sigma}\right\rangle - \left|1_{s\tau},1_{r\sigma}\right\rangle = 0.$$

From the last step, the basic anti-commutation relation of the fermionic creation operators for arbitrary spin orbitals $r\sigma, s\tau$ can be concluded to be

$$\left[a^\dagger_{r\sigma}, a^\dagger_{s\tau}\right]_+ = a^\dagger_{r\sigma}a^\dagger_{s\tau} + a^\dagger_{s\tau}a^\dagger_{r\sigma} = 0, \tag{2.38}$$

where $[\cdot,\cdot]_+$ denotes the anti-commutator. Furthermore, it immediately follows that $a^\dagger_{r\sigma}a^\dagger_{r\sigma}|\mathbf{0}\rangle = 0$, i.e. the Pauli-principle is a built-in property of the formalis., Consequently, every ONV in which the i-th state is already occupied is part of the kernel ker of $a^\dagger_{r\sigma}$. As a result, a general formulation for the application of an arbitrary creation operator on an ONV is straightforward[75]

$$a^\dagger_{r\sigma}\left|\cdots n_{r\sigma}\cdots\right\rangle = (1-n_{r\sigma})\,(-1)^{\sum_{l<r} n_l}\left|\cdots n_{r\sigma}+1\cdots\right\rangle \quad n_r = 0,1, \tag{2.39}$$

where $n_{r\sigma}$ denotes the occupation number and $\sum_{l<i} n_l$ simply sums over all occupation numbers to the left of $n_{r\sigma}$ to count the necessary permutations needed to restore natural order. It is safe to assume that the ONVs are properly normalized. Consequently,

$$\langle n_{r\sigma}|n_{r\sigma}\rangle = \left(a^\dagger_{r\sigma}\left|\mathbf{0}\right\rangle\right)^\dagger \left|a^\dagger_{r\sigma}\left|\mathbf{0}\right\rangle\right. = \langle\mathbf{0}|\, a_{r\sigma}a^\dagger_{r\sigma}\left|\mathbf{0}\right\rangle = \langle\mathbf{0}|\, a_{r\sigma}\left|n_{r\sigma}\right\rangle \overset{!}{=} \langle\mathbf{0}|\mathbf{0}\rangle = 1, \tag{2.40}$$

where the annihilation operator was introduced as $\left(a^\dagger_{r\sigma}\right)^\dagger = a_{r\sigma}$. Its action on a ket state is determined by the LHS of the second to last equality

$$a_{r\sigma}\left|n_{r\sigma}\right\rangle = \left|\mathbf{0}\right\rangle$$

from which the general expression in the spirit of Eq. (2.39)

$$a_{r\sigma}\left|\cdots n_{r\sigma}\cdots\right\rangle = n_{r\sigma}\,(-1)^{\sum_{l<r} n_l}\left|\cdots n_{r\sigma}-1\cdots\right\rangle \qquad n_r = 0,1, \tag{2.41}$$

is easily deduced. Using the equations developed so far makes creating or annihilating particles from an ONV possible. However, for quantum chemistry it is more interesting

to know what happens on substitution of one particle state by another, as it never happens that a particle is removed completely from a chemical system[4]. Obviously, it is possible to deduce the action of chaining $a^\dagger_{r\sigma}$ and $a_{s\tau}$ together using Eq. (2.40) again. Reversing the order in the third-term would yield an element of the kernel $\ker(a_{r\sigma})$ as $|n_r\rangle$ is not present in $|\mathbf{0}\rangle$ by construction

$$\langle \mathbf{0}| \, a^\dagger_{r\sigma} a_{r\sigma} \, |\mathbf{0}\rangle = 0.$$

It can be concluded that

$$\begin{aligned} \left(a^\dagger_{r\sigma} a_{r\sigma} + a_{r\sigma} a^\dagger_{r\sigma}\right) |n_{r\sigma}\rangle &= |n_{r\sigma}\rangle \\ \rightarrow a^\dagger_{r\sigma} a_{r\sigma} + a_{r\sigma} a^\dagger_{r\sigma} &= 1 \end{aligned}$$

must hold. Constructing the general case is straightforward using Eqs. (2.41) and (2.39).

$$\begin{aligned} a^\dagger_{r\sigma} a_{r\sigma} \, |\cdots n_r \cdots\rangle &= n_r (-1)^{\sum_{l<r} n_l} a^\dagger_{r\sigma} \, |\cdots n_r - 1 \cdots\rangle \\ &= n_r \left(n_r - 1\right) (-1)^{2\sum_{l<r} n_l} \, |\cdots n_r \cdots\rangle \qquad \text{(a)} \\ &= n_r \, |\cdots n_r \cdots\rangle \\ a_{r\sigma} a^\dagger_{r\sigma} \, |\cdots n_r \cdots\rangle &= \left(1 - n_r\right) (-1)^{\sum_{l<r} n_l} a_{r\sigma} \, |\cdots n_r + 1 \cdots\rangle \\ &= \left(1 - n_r\right) \left(n_r + 1\right) (-1)^{2\sum_{l<r} n_l} \, |\cdots n_r \cdots\rangle \qquad \text{(b)} \\ &= \left(1 - n_r\right) |\cdots n_r \cdots\rangle \\ &\xrightarrow{\text{(a)+(b)}} \left(n_r + 1 - n_r\right) |\cdots n_r \cdots\rangle = |\cdots n_r \cdots\rangle \, , \qquad (2.42) \end{aligned}$$

[4]Obviously this would be the case if one limits the view on a species getting oxidized in a redox-reaction and *vice versa*. However, complete removal means a promotion to the continuum in this context, which is clearly not the case in a redox reaction. At least not the ones the author conducted.

where $n_r^2 = n_r$ was used, which is valid as $n_r = 0, 1$. Investigating the case $r\sigma \neq s\tau$ and assuming for simplicity $r < s$ yields

$$\begin{aligned} a^\dagger_{r\sigma} a_{s\tau} \left|\cdots n_r \cdots n_s \cdots\right\rangle &= n_s (-1)^{\sum_{l<s} n_l} a^\dagger_{r\sigma} \left|\cdots n_r \cdots n_s - 1 \cdots\right\rangle \\ &= n_s \left(1 - n_r\right) (-1)^{\sum_{l<s} n_l + \sum_{m<r} n_m} \left|\cdots n_r + 1 \cdots n_s - 1 \cdots\right\rangle \end{aligned} \tag{a}$$

$$\begin{aligned} a_{s\tau} a^\dagger_{r\sigma} \left|\cdots n_r \cdots n_s \cdots\right\rangle &= \left(1 - n_r\right) (-1)^{\sum_{m<r} n_m} a_{s\tau} \left|\cdots n_r + 1 \cdots n_s \cdots\right\rangle \\ &= n_s \left(1 - n_r\right) (-1)^{\sum_{m<r} n_m + \sum_{l<s} n_l} \left|\cdots \overbrace{n_r + 1}^{\text{+1 permutation for } a_{s\tau} \text{ compared to (a)}} \cdots n_s - 1 \cdots\right\rangle \end{aligned} \tag{b}$$

$$\xrightarrow{\text{(a)}=-\text{(b)}} \left(a^\dagger_{r\sigma} a_{s\tau} + a_{s\tau} a^\dagger_{r\sigma}\right) \left|\cdots n_r \cdots n_s \cdots\right\rangle = 0. \tag{2.43}$$

From Eqs. (2.42) and (2.43) the basic anti-commutation relations of the fermionic annihilation- and creation operators are given as

$$\left[a^\dagger_{r\sigma}, a^\dagger_{r\sigma}\right]_+ = \left[a_{r\sigma}, a_{r\sigma}\right]_+ = 0 \tag{2.44}$$

$$\left[a^\dagger_{r\sigma}, a_{s\tau}\right]_+ = \delta_{rs}\delta_{\sigma\tau}, \tag{2.45}$$

where $\delta^{r\sigma}_{s\tau}$ denotes the Kronecker-delta. Eq. (2.45) implies that the total number of particles N in an ONV can be obtained as

$$\sum^N a^\dagger_{r\sigma} a_{r\sigma} \left|\mathbf{k}\right\rangle = \sum^N \left(1 - a_{r\sigma} a^\dagger_{r\sigma}\right) \left|\mathbf{k}\right\rangle = \sum^N 1 \left|\mathbf{k}\right\rangle - \sum^N a_{r\sigma} a^\dagger_{r\sigma} \left|\mathbf{k}\right\rangle = N \left|\mathbf{k}\right\rangle, \tag{2.46}$$

which motivates the definition of the particle-number operator $\hat{N}$ and the number-operator $\hat{n}_r$

$$\hat{N} = \sum_N \sum_{\sigma=-\frac{1}{2}}^{\frac{1}{2}} \hat{n}_{r\sigma} = \sum_N \sum_{\sigma=-\frac{1}{2}}^{\frac{1}{2}} a^\dagger_{r\sigma} a_{r\sigma} \tag{2.47}$$

2.3.2 Expressing Operators

Now that the representation of states in the formalism is clear, one still needs to figure out how to express operator expressions in this framework. Fortunately, it is straightforward to do so[75]. Defining a (hermitian) single-particle operator $\hat{O}$, leads,

by using the completeness relation twice, to the expression

$$\begin{aligned}\hat{O} &= \sum_{r\sigma,s\tau} |r\sigma\rangle \langle r\sigma| \hat{O} |s\tau\rangle \langle s\tau| \\ &= \sum_{r\sigma,s\tau} o_{r\sigma s\tau} |r\sigma\rangle \langle s\tau| ,\end{aligned} \tag{2.48}$$

where $o_{r\sigma s\tau}$ are the matrix elements of the single particle operator in the chosen basis. Acting on any state vector $|\mathbf{k}\rangle$ yields

$$\begin{aligned}\hat{O} |\mathbf{k}\rangle &= \sum_{r\sigma,s\tau} o_{r\sigma s\tau} |r\sigma\rangle \langle s\tau| \cdots s\tau \cdots\rangle \\ &= \sum_{r\sigma,s\tau} o_{r\sigma s\tau}\gamma \langle s\tau|s\tau\rangle |r\sigma\rangle |\cdots\rangle \\ &= \sum_{r\sigma,s\tau} o_{r\sigma s\tau}\gamma \langle s\tau|s\tau\rangle |r\sigma\cdots\rangle \\ &= \sum_{r\sigma,s\tau} o_{r\sigma s\tau}\gamma^2 \langle s|s\rangle |\cdots r\sigma\cdots\rangle \\ &= \sum_{r\sigma,s\tau} o_{r\sigma s\tau} |\cdots r\sigma\cdots\rangle \\ &= \sum_{r\sigma,s\tau} o_{r\sigma,s\tau} a^\dagger_{r\sigma} a_{s\tau} |\mathbf{k}\rangle ,\end{aligned} \tag{2.49}$$

where γ was introduced as a condensed notation for the factor arising from permuting $|s\tau\rangle$ to the left and $|r\sigma\rangle$ to the right. Apparently, the expression $|r\sigma\rangle \langle s\tau|$ has the exact same effect as the annihilation and creation operators introduced in the previous paragraph, which is expressed in the last equality of Eq. (2.49), where spin- and space-indices are given explicitly again. The same procedure can be carried out for two-particle operators $\hat{Z}$, yielding the relation

$$\hat{Z} |\mathbf{k}\rangle = \sum_{\substack{r\rho,s\sigma \\ t\tau,u\upsilon}} \langle r\rho s\sigma|Z|t\tau u\nu\rangle \, a^\dagger_{r\rho} a^\dagger_{t\tau} a_{s\sigma} a_{u\upsilon} |\mathbf{k}\rangle . \tag{2.50}$$

According to Eqs. (2.49) and (2.50) the action of an operator in second quantization is given as the sum of all particle-substitutions weighted by an element of the operator's matrix representation in the one-particle basis. As discussed in the last section it is necessary to properly couple angular momentum eigenstates if a proper

total angular momentum state ought to be created. In accordance, the creation and annihilation operators can be understood as spherical tensor operators of half-integer rank $\left\{a^\dagger_{r;\frac{1}{2}}, a^\dagger_{r;-\frac{1}{2}}\right\}$. Using the machinery developed in the last section one gets right away

$$\left[S_z, a^\dagger_{r;m_s}\right] = m_s a^\dagger_{r;m_s} \tag{2.51a}$$

$$\left[S_\pm, a^\dagger_{r;m_s}\right] = \sqrt{\frac{3}{4} - m_s\left(m_s \pm 1\right)} a^\dagger_{r;m_s\pm1} = \left[a_{r;m_s}, S_\pm\right]^\dagger, \tag{2.51b}$$

where the dagger denotes complex conjugation. Coupling with the adjoint representation $\left\{a_{s;\frac{1}{2}}, -a_{s;-\frac{1}{2}}\right\}$ in the spirit of Tab. 2.1 one obtains for the component, transforming like a scalar under rotations

$$E^0_{rs} = \frac{1}{\sqrt{2}}\left(a^\dagger_{r;\frac{1}{2}} a_{s;\frac{1}{2}} + a^\dagger_{r;-\frac{1}{2}} a_{s;-\frac{1}{2}}\right) \tag{2.52}$$

and for the vector-like components

$$\begin{aligned} D^1_{rs} &= -a^\dagger_{r;\frac{1}{2}} a_{s;-\frac{1}{2}} \\ D^0_{rs} &= \frac{1}{\sqrt{2}}\left(a^\dagger_{r;\frac{1}{2}} a_{s;\frac{1}{2}} - a^\dagger_{r;-\frac{1}{2}} a_{s;-\frac{1}{2}}\right). \\ D^{-1}_{rs} &= a^\dagger_{r;-\frac{1}{2}} a_{s;\frac{1}{2}}. \end{aligned} \tag{2.53}$$

Note that all of the above operators describe appropriately coupled one-particle replacements The pair-creation operators, e.g $\frac{1}{\sqrt{2}}\left(a^\dagger_{r;\frac{1}{2}} a_{s;-\frac{1}{2}} - a^\dagger_{s;\frac{1}{2}} a_{r;-\frac{1}{2}}\right)$, are ignored here. It is common to define the orbital excitation operator E^r_s based on Eq. (2.52) as

$$E^r_s = \sqrt{2} E^0_{rs}, \tag{2.54}$$

which allows for a compact formulation of spin-free operators, e.g. Eq. (2.2) becomes

$$\hat{H} = \sum_{rs} h_{rs} E^r_s + \frac{1}{2} \sum_{\substack{rs \\ tu}} V_{rstu}\left(E^r_s E^t_u - \delta^t_s E^r_u\right) + V_{\text{nuc}}, \tag{2.55}$$

where the first two indices of four-index quantities refer to the first particle and the last two to the second. Furthermore, the lower index of E^r_s refers to the annihilation- and the upper to the creation operator. In this formalism the spin-spin dipole operator

is written as

$$\hat{\mathcal{H}}_{SS} = \sum_{q=-2}^{2} \sum_{\substack{rs \\ tu}}^{N_{orb.}} \sum_{\substack{\sigma\mu \\ \rho\lambda}}^{\frac{1}{2},-\frac{1}{2}} R^{(q)}_{rstu} S^{(q)}_{\sigma\mu\rho\lambda} a^{\dagger}_{r\sigma} a^{\dagger}_{t\rho} a_{u\lambda} a_{s\mu}. \tag{2.56}$$

$R^{(q)}_{rstu}$ and $S^{(q)}_{\sigma\mu\rho\lambda}$ collect all spatial- and spin matrix elements for a given value of q, respectively. While the presented framework is very helpful in manipulating equations, it does not provide a recipe on how to compute the one-particle states needed to obtain the desired eigenvalues of the discussed operators. Therefore, the next section is concerned with methods used in electronic structure theory to obtain (approximate) wave functions, serving as the basis for actual computations.

2.4 Approximations and Exact Solutions

In the preceding sections, approximations to the Hamiltonian have been discussed, and a framework was presented, which is very convenient in manipulating operator expressions and expressing many-body states. However, this framework is of little use if no one-particle functions are available, which can be used as a basis. In this section methods will be discussed to obtain one-particle states, followed by a short discussion of methods using the resulting states as a one-particle basis to yield more elaborate many-particle wave functions.

2.4.1 Hartree–Fock Theory

It is no exaggeration to say that the most influential concepts introduced in quantum chemistry are the orbital, the Slater-determinant (SD) and the Hartree-Fock (HF) model. While there is no theory using the orbital concept known to the author, not making use of SDs, the HF method itself is mainly still around for educational purposes. However, it serves as the starting point for the most accurate wave functions obtainable today. The wave function in HF theory is approximated with a single SD constructed from a spin-orbital basis $\{ \mid \phi_i \rangle \}$, which provides a formidable wave function if the particles are completely independent and should therefore be a reasonable approximation. However, a single determinant cannot describe arbitrary spin-angular momentum states of many-particle systems properly, which can be seen most easily by noting that the $\hat{n}_{r\sigma}$ defined in Eq. (2.47) and the ladder operators from Eq. (2.51b) cannot commute, as e.g.

$$\left[S_+, a^\dagger_{r;-\frac{1}{2}} a_{r-\frac{1}{2}}\right] = \left[S_+, a^\dagger_{r;-\frac{1}{2}}\right] a_{r;-\frac{1}{2}} + a^\dagger_{r;-\frac{1}{2}} \left[S_+, a_{r;-\frac{1}{2}}\right] \tag{2.57a}$$

$$= \left[S_+, a^\dagger_{r;-\frac{1}{2}}\right] a_{r;-\frac{1}{2}} + a^\dagger_{r;-\frac{1}{2}} \left[a_{r;-\frac{1}{2}}, S_-\right]^\dagger = a^\dagger_{r;\frac{1}{2}} a_{r;-\frac{1}{2}} \tag{2.57b}$$

In turn, any operator containing terms of ladder operators, such as $S^2 = S_+S_- + S_z\left(S_z + 1\right)$, cannot commute with a single $\hat{n}_\sigma$. As the SDs are eigenfunctions of the $\hat{n}_{r\sigma}$ the non-commutation is a hint that they cannot be eigenfunctions of S^2 as well. Obviously, this condition is not sufficient to show that this is truly the case, and there are two cases in which the operators share eigenfunctions. For an even number of particles it is possible to construct a case, where all available spatial orbitals are equally paired with $\frac{1}{2}$ and -$\frac{1}{2}$ spin functions, called the closed-shell case, which is an eigenfunction of S^2 and S_z. Secondly, one might construct a spin arrangement in

which all unpaired particles have the same spin, called the high-spin case, which is a simultaneous eigenvector of the two spin operators as well. It is straightforward[76] to show that for all remaining spin function arrangements appropriate linear combinations of determinants have to be considered if simultaneous eigenvectors of S^2 and S_z shall be constructed, as might be anticipated from the result in Eq. (2.57b). These linear combinations only concern the arrangement of spin functions for a given spatial configuration. Consequently, the functions are dubbed configuration state functions (CSFs). There are a couple of different ways to construct CSFs. For an overview the reader is referred to the book of Pauncz [77]. For a closed-shell arrangement the number of determinants and CSFs is equal. This is also the case for $S = M_S$, i.e. the high-spin case. In these cases, the single SD commutes with S^2, as already mentioned. In the following only the closed-shell scenario will be treated. Consequently, spin indices are omitted as they do not contain additional information in this case. Computing the expectation value of a single SD using the Hamiltonian of Eq. (2.55), eventually leads to a set of effective single particle equations called the HF equations. A single-particle operator, the Fock operator (Eq. (2.58)), is the central quantity of the scheme.

$$\hat{f} = \sum_{i,j}^{M} f_{ij} a_i^\dagger a_j = \sum_{i,j}^{M} \left[h_{ij} \sum_{r}^{N_{occ}} \left(V_{ijrr} - V_{irrj} \right) \right] a_i^\dagger a_j = \hat{T} + \hat{v}^{HF} \tag{2.58}$$

It consists of two terms h_{ij} and $\sum_r^{N_{occ}} (V_{ijrr} - V_{irrj})$. The first is the exact one-particle Hamiltonian, i.e. the kinetic energy and Coulomb interaction of the particle's charge with the nuclear charges, and the second expresses effective electron-electron interactions given through the Fock potential $\hat{v}^{HF}$. In this work the Mulliken notation is chosen. Consequently, the first two indices of V_{ijkl} refer to the coordinates of the first and indices three and four to the coordinates of the second particle. Note that the outer sum runs over the dimension of the spin orbital basis M, while the inner sum is only concerned with the occupied one-particle states N_{occ}. Due to the cancellation of terms in parentheses on equality of all four indices, any one-particle state from the occupied set is subject to the potential of $N - 1$ electrons. At the same time any state from the unoccupied set interacts with the full potential of all N particles, an argument becoming important in the later discussion of ionization- and excitation energies. Apparently, the positions of the electrons are not correlated explicitly, as they should be due to their repulsive charge interactions, but are treated as an averaged interaction of an electron's charge distribution with the distribution

of all other electrons. The spin correlation, however, is treated exactly as it arises from the antisymmetric character of the employed wave function. By definition the operator depends on its own solutions as they appear in the definition of the Fock potential. Therefore, it is common practice to solve the set of equations

$$\hat{f}\,|\psi_i\rangle = \epsilon_i \psi_i \tag{2.59}$$

iteratively[36], generating an optimal spin orbital basis $\{\,\phi_i\,\}$ and a so-called self-consistent field as a result. This approach yields matrix elements of the form $f_{ij} = \epsilon_i \delta_{ij}$, which plugged into Eq. (2.58) gives

$$\hat{f} = \sum_{i,j}^{M} \epsilon_{ij} \delta_{ij} a_i^\dagger a_j = \sum_{i}^{M} \epsilon_i a_i^\dagger a_i, \tag{2.60}$$

where the orbital energies ϵ_i were defined. The basis in which the Fock matrix is diagonal, is called the canonical basis and the basis functions canonical orbitals, respectively. The physical meaning of these quantities is established as the negative vertical ionization potentials and electron affinities. A result known as Koopman's theorem[36, 76] establishes that the canonical orbitals are optimal for the description of the ionization process in the single determinant approach, i.e.

$$\epsilon_i = E\,(N) - E\,(N-1) \approx -IP, \tag{2.61}$$

where $E\,(N)$ and $E\,(N-1)$ are the energies of the N and $N-1$ particle system evaluated in the canonical basis of the N electron system and ϵ_i represents the one-particle energy of the i-th particle missing in the wave function used to construct $E\,(N-1)$. The total HF energy is calculated as the expectation value of the SD Ψ^{HF} constructed from the orbitals obtained from solving Eqs. (2.59) giving

$$E^{HF} = \sum_i \epsilon_i - \frac{1}{2} \sum_{i,j} V_{iijj} - V_{ijji}, \tag{2.62}$$

where the constant term originating from the Coulomb interaction of the nuclei was omitted. While the introduction to HF theory is on the shorter side here, it should be understood that HF presents an adequate method to obtain a starting point for other wave function-based approaches, as it yields an optimal spin orbital basis for an independent-particle Hamiltonian. However, including many-particle effects is a must

for quantum chemistry and one therefore needs more sophisticated theories. Most of them employ the route of extending the SD or CSF space, leading to so-called multi-configurational theories, which will be discussed in a later section. Prior to that, another approach employing a single SD, which has become the *de facto* standard in quantum chemistry, shall be introduced.

2.4.2 Kohn–Sham Density Functional Theory

While wave functions contain all the information one needs to know in describing a system[78], they depend on $4N$ variables, where N is the number of particles. As already mentioned, it is an impossible task to find an analytical solution for the wave function due to the correlated motion of more than two bodies. However, at least in theory, there is no need to know the full wave function as it suffices to know the exact one- and two-particle density matrices, if one uses a Hamiltonian such as Eq. (2.55). Unfortunately, the only way known to compute the latter is *via* the exact wave function and therefore nothing can be gained from this statement, at least in practical calculations. A comparable dilemma is found in a theory known as density functional theory (DFT), which is based on the lemma of Hohenberg and Kohn [79]. It states that the ground state density $n(\vec{r})$ of an interacting electron system subject to an external potential $v_{ext}(\vec{r})$, determines $v_{ext}(\vec{r})$ up to a constant shift[80]. Additionally, it is guaranteed[81–84] that for any density associated with an antisymmetric wave function a universal functional can be found and minimized to give the exact ground state density, and correspondingly the exact, unique ground state energy. It follows that it is sufficient to know the exact electron density of the system to determine the Hamiltonian of the system and thus all the desired properties. This is particularly interesting as the density depends on only 3 spatial coordinates, simplifying the problem significantly. Unfortunately, there is no recipe for the search for the universal density functional. Approximations must be introduced to find a functional to be minimized. The common route taken is *via* self-consistent equations in the spirit of HF theory. This is rooted in the idea of Kohn and Sham [85] that one can decompose the universal functional into a sum of a kinetic energy density $T_{\mathrm{s}}[n]$ of a non-interacting auxiliary system subject to an external potential v_{ext} normally chosen as the electrostatic potential caused by the nuclei V_{ne}, the electrostatic energy of two-charge distributions $J[n]$, and a term containing all particle-particle interactions

called exchange-correlation energy E_{xc}.

$$E\left[\rho\right] = T_{\mathrm{s}}\left[\rho\right] + v_{ext}\left[\rho\right] + J\left[\rho\right] + E_{\mathrm{xc}}\left[\rho\right] \tag{2.63}$$

While this partitioning is straightforward and very successful, it only relocates the problematic term from the universal density functional to the exchange-correlation functional. Furthermore, it reintroduces the orbital concept[86] as the kinetic energy term of the non-interacting auxiliary system is calculated exactly by solving the respective one-particle SGLs

$$\left(-\frac{1}{2}\nabla^2 + V_{\mathrm{ne}} + V_J + V_{\mathrm{xc}}\right)\phi_i = \epsilon_i \phi_i \tag{2.64a}$$

$$n^{KS}\left(r\right) = \sum_{i=1}^{N_{occ}} \left|\phi_i\right|^2. \tag{2.64b}$$

The only term which needs to be approximated in Eq. (2.64a) is V_{xc}. After choosing an appropriate exchange-correlation functional the one-particle functions are used to generate the density according to Eq. (2.64b), which is per definition equal to the ground state density of the system. As this density has to fulfil certain variational conditions[36, 86] the equations have to be solved in a self-consistent way, similar to the HF equations[87]. An obvious downside of this approach is that the number of needed variables to describe the system is increased from 3 to 4N again. However, the success of the Kohn-Sham (KS) method greatly outweighs this. As a purely fictional model system is employed in KS theory, no meaning was assigned to the one-particle functions, i.e. KS orbitals, and to the associated energies, in the early days of the approach. However, it was realized by Janak [88] that the KS ϵ_i is proportional to the variation of the total KS energy E^{KS} w.r.t. the occupation k_i of the i-th ϕ_i, if one allows for fractional occupations

$$\frac{\partial E^{frac.}}{\partial k_i} = \epsilon_i, \tag{2.65}$$

where $E^{frac.}$ is given as[89]

$$E^{frac.}\left[\{k_i\}\right] = T_s^{frac.} + \int n^{frac.}(\vec{r}) v(\vec{r}) d^3r + E_H[n^{frac}] + E_{xc}[n^{frac}]$$
$$= \sum_i k_i \left\langle \phi_i \right| - \frac{\hbar^2}{2m_e}\nabla^2 \left|\phi_i\right\rangle + \int \sum_i \left|\phi_i\right|^2 v(\vec{r}) d^3r + E_H[n^{frac}] + E_{xc}[n^{frac}].$$

As the ground state density of any many-electron system decays exponentially in the asymptotic limit[90], it was realized[91–93] that the energy of the highest occupied molecular orbital (HOMO) ϵ_{HOMO} must be equal to the negative ionization potential of a neutral atom, as the KS-density represents the exact interacting density. This observation assigned a meaning to the KS eigenvalues and lead to further observations the exchange-correlation functional has to obey. With the aid of Janak's-theorem the ionization potential (IP) and electron affinity (EA) might be expressed as[94]

$$IP(M) = E(M-1) - E(M) = -\int_0^1 dk_i \epsilon_M(M-1+k_i) \tag{2.66a}$$

$$EA(M) = IP(M+1) = E(M) - E(M+1) = -\int_0^1 dk_i \epsilon_{M+1}(M+k_i), \tag{2.66b}$$

where M is any integer electron number and $\epsilon_{M/M+1}$ are the KS eigenvalues of the M electron system. It is clear that Eqs. (2.66a) and (2.66b) differ substantially from the corresponding interpretation of orbital energies in HF theory given by Eq. (2.61). In particular, it uses the occupation number k_i as a variational parameter, necessitating fractional occupation numbers, which are hard to reconcile with a discrete change in particle numbers as found in an ionization process. The validity of Janak's-theorem (Eq. (2.65)) has been debated in literature[89, 95], though it is frequently used to validate the Aufbau-principle in the framework of KS-DFT[88, 96], and has been used to justify the physical meaning of the lowest unoccupied molecular orbital (LUMO) in the KS framework[97]. However, finding an exchange-correlation functional which shows the correct behaviour on varying the occupation number is still an area of active research[98–101], as all known functionals do not describe the integer nature of electrons correctly[102]. In the review of Görling [103] it is nicely demonstrated that the aforementioned KS eigenvalues can be used as a zeroth-order approximation for excitation energies, which partially explains the success of time-dependent density functional theory (TD-DFT) in excited state calculations. Baerends et al. [98] gave the perspective that this is due to the stabilizing effect of the exchange-correlation hole potential, which mimics the hole left behind on excitation of an electron. However, it should be clear from the forgoing discussion that it is much more complicated to assign a meaning to orbitals in the framework of KS than it is in HF theory. Clearly, this does not diminish the usefulness of KS in electronic structure theory, as the total energy is the desired quantity to be computed. It has been found that KS is more accurate than HF, due to the inclusion of electron correlation effects, albeit only in an approximate

fashion. At the same time it is of comparable cost in terms of computational demands. The last point weighs particularly heavy as it becomes computationally expensive very quickly to include correlation in the HF framework. The following section will give a short introduction of possibilities to include correlation effects into HF.

2.4.3 *post*–Hartree–Fock Theory

As already mentioned, the HF method misses electron correlation caused by Coulomb repulsion of the electrons completely. Unfortunately, electron correlation beyond HF exchange is crucial for chemistry and photophysics. The smallest molecular example being the dissociation curve of H_2, which is neither described accurately by HF theory nor by approximate KS theory. Generally, there are two groups of correlation effects. The first arising from repulsive forces due to electrons' charges and the associated dependency of the positions, appropriately called dynamical correlation. It might be divided further into short- and long-range parts. The former is caused by the exchange- and Coulomb-holes associated with each electron, i.e. volume elements around the position of a defined electron, in which it is very unlikely to find another electron. To include such effects is a computationally demanding task in the framework of orbital theories and it has been found that the most efficient way of including short-range correlation is by equipping the orbitals with additional functions, leading to so-called explicitly correlated methods[104, 105]. The long-range class covers effects such as left-right correlation, in-out correlation and angular correlation, all making statements about electrons arranging themselves around a centre[106, 107], e.g. an atomic nucleus or a bond axis. Such effects can be incorporated by choosing flexible orbitals and linear combinations thereof to construct a wave function consisting of multiple SDs. The second group consists of correlation effects caused by near degeneracies of electronic states, making a description using one SD impossible. Such a situation is labeled as static correlation and requires the combination of multiple SDs Ψ^{SD} in the wave function expansion. Note that a strict separation of the two groups is generally not possible, but a separation may still be conceptually useful. The idea of expanding the wave function into a basis of multiple electronic configurations has been propagated by Löwdin [108]. Called configuration interaction (CI), the ansatz has been around for over half a century and is still a standard approach. The wave

function is simply written as

$$|\Psi\rangle^{FCI} = \sum_{i=0} t_i \Psi_i^{SD} = t_0 \Psi_0^{SD} + \sum_{i,r} t_i^r a_r^\dagger a_i \Psi_0^{SD} + \sum_{i<j,r<s} t_{ij}^{rs} a_r^\dagger a_s^\dagger a_j a_j \Psi_0^{SD} + \cdots , \quad (2.67)$$

where the zeroth-order term is commonly taken as the SD obtained from a preceding HF optimization and the excitation space is formulated using the non-spin-adapted one-particle substitution operators. Using the operators defined through Eq. (2.52) is of course possible, but uncommon. However, the method suffers from a debilitating deficiency. Given a number of one-particle states M and a number of fermions N, one might construct $\binom{M}{N}$ SDs, which becomes untraceable very quickly. Though proper spin adaption, by switching to the CSF basis, greatly reduces the number of basis functions, it does not remotely solve the dimensionality issue. Therefore, one is forced to introduce approximations into CI theory. The most obvious being a truncation of the expansion. It was recognized quite early[109], that a small expansion often suffices to get excellent results. Furthermore, it was recognized by Sinanoğlu [110][111] that most of the correlation energy is contained in interactions of particle pairs. In fact, it is straightforward[112] to show that the correlation energy, defined as difference to the ground state HF energy, might be expressed as a linear combination of matrix elements between the HF-determinant Ψ^{SD} and all double, i.e. pair, substitutions Ψ_{ij}^{ab} generated from Ψ^{SD}

$$E_{corr} = \sum t_{ij}^{ab} \langle \Psi_0 | \hat{H} | \Psi_{ij}^{ab} \rangle .$$

Unfortunately, the Ψ_{ij}^{ab} are coupled to singly- and triply-substituted SDs, leading to a hierarchical system of equations to be solved for the coupling amplitudes $t_{i\ldots}^{a\cdots}$. If one assumes decreasing contributions of highly substituted SDs in the expansion, which is certainly reasonable if the coefficient of the reference SD is already large, a truncation of the expansion given in Eq. (2.67) at the doubly excited level is only logical. Truncation leads to the size-consistency and -extensivity problems, which shall not be discussed here in detail. To put it in a nutshell, separated systems cannot be described properly by such truncated wave functions. For extensive discussions on the topic the reader is referred to the review of Bartlett [113]. Truncated CI methods employing a single SD as a reference are basically obsolete nowadays, as more sophisticated methods such as coupled-cluster are computationally traceable for ground state calculations. In computations of excited states the configuration interaction singles (CIS) variant is still used, due to its conceptual relation to TD-DFT[114], however it has

been basically replaced by the latter. The picture is a different one if one enters the regime of multi-reference wave functions. Multi-reference problems are intrinsically linked with the aforementioned phenomenon of static correlation, i.e. situations in different SDs become (near)-degenerate. In multi-reference configuration interaction (MRCI) theory a reference space is constructed, which often requires a lot of chemical insight from the user. Excited configurations are generated from all configurations of the reference space. Naturally, it is desirable to have all important configurations already contained in the reference space, such that the weight of the reference configurations is large and truncation covers the most important effects, in analogy to single reference theory. The wave function in MRCI theory can accordingly be written as

$$|\Psi^{MRCI}\rangle = \left(1 + \sum_{i,r} t_i^r \hat{T}_i^r + \sum_{\substack{i<j \\ r<s}} t_{ij}^{rs} \hat{T}_{ij}^{rs} + \dots\right) \sum_q^{N_{ref}} |\Psi_q^{(0)}\rangle \tag{2.68}$$

where the $\hat{T}$ denote operators generating the respective substitutions from the reference function $|\Psi_q^{(0)}\rangle$ and the $t_{i\dots}^{r\dots}$ are the associated weights of the generated functions. Though MRCI is conceptually very easy it poses a huge computational problem due to the size of the expansion needed to capture all correlation effects. Especially, the dynamical correlation effects require a lot of different determinants. In-out correlation, for example, surely needs SDs built from excitations into high-lying orbitals, as they are generally more diffuse. Obviously, there are many possibilities to realize such substitutions. As the spectrum gets denser at higher energies many similar configurations will enter Eq. (2.68) with a small weight. To reduce the number of configurations entering the expansion it is common practise to select important configurations either by means of perturbation theory[115–117] or statistical approaches[118, 119]. Other approximations include contraction schemes of which the internal contraction scheme promoted by Werner and Knowles [120] is a prominent example. In such methods, information contained in the reference space is used to reduce the number of coefficients to be optimized. Yet another famous group of MRCI schemes use (semi-)empirical considerations[121] to reduce the size of the expansion Eq. (2.68). One of them shall be the topic of the next section.

2.4.4 Multi–reference Configuration Interaction combined with Density Functional Theory

As mentioned before, DFT is a tremendously successful theory and has become the *de facto* standard in ground state computations. However, it has some short-comings in the computation of excited states mostly rooted in the approximate nature of the exchange-correlation functional[122]. Especially, states including charge-transfer configurations[123] are not well described by the commonly applied exchange-correlation approximations[101, 124], which is linked to deficiencies in the description of electron affinities. CI methods can describe such states well, however hit the exponential wall [125] quickly and are unfeasible for larger systems. DFT's success in ground state theory, due to the incorporation of correlation energy and good orbital energies by construction, motivated the design of semi-empirical methods[126, 127], which combine the wave function methodology with DFT to overcome the latter's shortcomings and to tame the expansion length of the former. A formulation of MRCI proposed by Segal et al. [128][129] was chosen as a starting point, and will be briefly reviewed below. The authors proposed to choose a closed-shell configuration $|A\rangle$ as an anchor point and to pre-tabulate all arising factors originating in spin-integration, as they are invariant to the underlying problem and follow certain patterns. This leads to a Hamiltonian of the form

$$\begin{aligned}\hat{H} = E_{\mathrm{SCF}} &- \sum_i \tilde{F}_{ii}\bar{w}_i + \frac{1}{2}\sum_{ij}\left(V_{iijj} - \frac{1}{2}V_{ijji}\right)\bar{w}_i\bar{w}_j \\ &+ \sum_{ij}\tilde{F}_{ij}E_i^j - \sum_{ijk}\left(V_{ijkk} - \frac{1}{2}V_{ikkj}\right)\bar{w}_k E_i^j \\ &+ \frac{1}{2}\sum_{ijkl}V_{ijkl}\left(E_i^j E_k^l - \delta_{jk}E_i^l\right),\end{aligned} \tag{2.69}$$

where E_{SCF} is the self-consistent energy of the chosen anchor $|A\rangle$ and $\tilde{F}_{rs}$ are elements of a Fock matrix, possibly modified to match the criterion of double occupation. Note, that E_{SCF} contains the unmodified, diagonal Fock matrix elements F_{ii} (c.f. Eqs.(2.59) and (2.62)), which obviously cancel assuming no modification of the Fock matrix was needed. In this case the $\tilde{F}_{ij}$ vanish as well, as the matrix representation of the Fock operator is diagonal in the canonical basis. The quantities equipped with a bar $\bar{w}_r$ in Eq. (2.69) denote the occupation numbers of the anchor configuration $|A\rangle$. The matrix representation of $\hat{H}$ of Eq. (2.69) in a CSF basis contains only occupation

number differences $\Delta w_q = w_q - \bar{w}_q$ w.r.t. the anchor, and operator coefficients η_i^j, depending solely on the spin part of the CSF, which can be tabulated. Explicitly, for configurations with the same spatial w and spin occupation ω, they read

$$\begin{aligned}\langle \omega w|\hat{\mathcal{H}}^{CI}|\omega w\rangle =& E^{SCF} + \sum_i \tilde{F}_{ii}\Delta w_i + \frac{1}{2}\sum_{i\neq j} V_{ijij}\Delta w_i \Delta w_j \\ &+ \frac{1}{2}\sum_{i\neq j} V_{ijji}\left(-\frac{1}{2}\Delta w_i \Delta w_j + \frac{1}{2}w_i w_j - w_i + \eta_{ij}^{ji}\right) \\ &+ \frac{1}{2}\sum_i V_{iiii}\left(\frac{1}{2}\Delta w_i \Delta w_i + \frac{1}{2}w_i w_i - w_i\right),\end{aligned} \tag{2.70}$$

configurations differing by a single occupation

$$\begin{aligned}\langle \omega w|\hat{\mathcal{H}}^{CI}|\omega' w'\rangle =& \tilde{F}_{ij}\eta_i^j + \sum_{k\neq i,j} V_{ikjk}\Delta w'_k \eta_i^j \\ &+ \sum_{k\neq i,j} V_{ikkj}\left(-\frac{1}{2}\Delta w'_k \eta_i^j + \frac{1}{2}w'_k \eta_i^j - \eta_i^j + \eta_{ik}^{kj}\right) \\ &+ V_{iiij}\left(\frac{1}{2}\Delta w'_i + \frac{1}{2}w'_i\right)\eta_i^j - V_{ijjj}\left(\frac{1}{2}\Delta w'_j + \frac{1}{2}w'_j - 1\right)\eta_i^j\end{aligned} \tag{2.71}$$

and differing by two occupations

$$\langle \omega w|\hat{\mathcal{H}}^{CI}|\omega'' w''\rangle = \left(V_{ikjl}\eta_{ik}^{jl} + V_{iklj}\eta_{ik}^{lj}\right)\left[(1+\delta_{ik})(1+\delta_{jl})\right]^{-1}. \tag{2.72}$$

The idea of Grimme and Waletzke [127] was to simply evaluate Eqs. (2.70)–(2.72) in the basis of KS orbitals and compensate the resulting, but unknown, surplus of correlation energy empirically. The general form of the approach can be written as

$$\begin{aligned}\langle \omega w|\hat{\mathcal{H}}^{DFT} - E^{KS}|\omega w\rangle =& \langle \omega w|\hat{\mathcal{H}}^{CI}|\omega w\rangle - E^{SCF} \\ &- \sum_i \Delta w_i F_{ii}^{HF} + \sum_i \Delta w_i F_{ii}^{KS} + \Delta E_{DFT/MRCI},\end{aligned} \tag{2.73}$$

where $\Delta E_{DFT/MRCI}$ differs for distinct variants of the method. Naturally, this leads to corrections of the two-electron integrals. Grimme and Waletzke [127] defined the two-electron corrections to be of the form

$$\Delta E_{DFT/MRCI}^{Grimme} = \frac{1}{n_{exc}}\sum_{i\in c}^{n_{exc}}\sum_{j\in a}^{n_{exc}}\left(p_J V_{iijj} - {}^m p[N_o] V_{ijji}\right), \tag{2.74}$$

where n_{exc} denotes the number of substitutions compared to the anchor configuration $|A\rangle$ and the sums run over created (c) and annihilated (a) orbitals. Comparing the last term with a diagonal element of CIS[114]

$$\langle \Phi_i^a | \hat{H} | \Phi_i^a \rangle = E^{HF} + F_{aa} - F_{ii} + V_{iiaa} - V_{iaai} \tag{2.75}$$

should make it clear that the correction term $\Delta E_{DFT/MRCI}$ of Eq. (2.74) can be interpreted as an averaged sum of two-electron interactions arising from single excitations. The parameters p_J and ${}^m p\,[N_o]$ scale the Coulomb- and exchange contributions and are determined empirically. As the contributions of exchange integrals are expected to vary strongly between different multiplicities m and number of open shells N_o the parameter ${}^m p\,[N_o]$ was chosen to be dependent on these two factors. BH-LYP is based on Becke [130]'s half-and-half approach, i.e. a 50/50 mixture of HF and local-density approximation (LDA)[131] exchange, for the exchange and the approximation formula of Lee et al. [132] for the correlation part. Interestingly, Grimme and Waletzke [127] found an optimal value for p_J of ≈0.5 if BH-LYP is employed, which corresponds well to the amount of non-local HF exchange used in the functional. In fact, they state to have obtained the best results in excited state calculations if the amount of exact exchange is somewhere between 40 and 50 %. They argued that this can be attributed to the rising non-local nature of the state on excitation into higher-lying orbitals. A similar argument was used later by Dreuw et al. [123] in the context of TD-DFT failing to accurately describe charge-transfer excitations. Additionally, they found that half-and-half functionals show the smallest error in the description of such states. Another benefit of employing BH-LYP is its relatively small self-interaction error[133, 134] compared to other approximate density functionals. Apparently, Grimme and Waletzke [127] showed a remarkable intuition in the choice of the underlying functional. This was also confirmed recently by investigations of Dombrowski [135]. The second ingredient of `mrci` is an energy difference dependent damping function premultiplied to the off-diagonal elements of Eqs (2.71) and (2.72)

$$\langle \omega w | \hat{\mathcal{H}}^{DFT/MRCI} | \kappa \neq \omega; k \neq w \rangle = \langle \omega w | \hat{\mathcal{H}}^{CI} | \kappa \neq \omega; k \neq w \rangle \cdot p_1 \exp\left(-p_2 \Delta E_{wk}\right). \tag{2.76}$$

The energy dependent term ΔE_{wk} in the exponent is computed as the difference between the diagonal elements associated with the CSFs $|\omega w\rangle$ and $|\kappa k\rangle$. If multiple CSFs belong to a spatial occupation w or k, the average value of the diagonal elements is used. Note that matrix elements between such CSFs are not corrected at all, but

calculated using the exact formula

$$\langle \omega w | \hat{\mathcal{H}}^{DFT/MRCI} | \kappa \neq \omega; k = w \rangle = \frac{1}{2} \sum_{i \neq j}^{N_{opn.}} V_{ijji} \eta_{ij}^{ji}. \tag{2.77}$$

In this case only exchange integrals between open shells $N_{opn.}$ contribute, which makes sense as this case describes the interaction of different spin-distributions in a given set of orbitals. The original approach showed small derivations ($\approx 0.25\,\mathrm{eV}$) in the simulation of excited state spectra of small- and medium-sized organic molecules and diatomics, which was confirmed in a broader study conducted by Silva-Junior et al. [136]. Later Escudero and Thiel [137] evaluated the ansatz for transition-metal (TM) complexes and found the method to deviate by up to 0.65 eV. Furthermore, they computed for the triply degenerate $T_{1/2}$ states of MnO_4^- deviations as large as 0.11 eV of the subcomponents. For the $Cr(CO)_6$ complex, transforming under the O_h point group, a similar magnitude of this degeneracy error (0.15 eV for T_{1g}) was obtained. Unfortunately, the authors did not comment on this, though the order of magnitude of this error is worryingly large. A point to be discussed shortly. What makes the method appealing is that the efficient inclusion of dynamical correlation through the KS orbital basis, allows for a drastic reduction of needed CSFs. The selection is carried out by a simple energy gap criterion

$$\sum_{q=1}^{N_{orb.}} (w_q - \bar{w}_q)\, \epsilon_q \leq \delta\varepsilon^{sel.} + \max\left(E^{ref}\right) = T^{sel.}, \tag{2.78}$$

making it particularly efficient. The first sum in Eq. (2.78) runs over all orbitals. Their respective energies are weighted with the occupation number differences of the created configuration and the anchor. $\delta\varepsilon^{sel.}$ is a user-given addition to the highest, user-requested energy computed in the reference space ($\max\left(E^{ref}\right)$). Together these quantities define an effective selection threshold T_{sel}. To achieve a further reduction of computational costs, another parameter set was developed[138], making a further truncation of the expansion possible[5]. Lyskov et al. [141] revised the method to rid the methods' parameters of their spin dependency, motivated by the failures of the original

[5]The parameter sets published in the works of Sanchez-Garcia et al. [139] and Crespo-Otero and Barbatti [140] are $p_1 = 0.629$, $p_2 = 0.611$, $p_J = 0.119$, ${}^1p[0] = 8.000$, $\alpha = 0.503$, which are seriously wrong. Employing this set would lead to a scaling of the exchange integrals by a factor of eight and the damping function would be strongly broadened. Presumably, ${}^1p[0]$ and p_2 were mixed up.

formulation in the description of dimer states. The authors claimed that a linear relation between HF-like exchange integrals computed in the basis of BH-LYP one-particle states and experimental singlet-triplet splitting exists and motivated a global scaling factor for exchange terms on these grounds. The correction term of Eq. (2.70) becomes[6]

$$\begin{aligned}\Delta E_{DFT/MRCI} = p_J &\left(-\sum_{\substack{i,j\in c\\ i>j}}^{n_{exc}} V_{ijij} - \sum_{\substack{i,j\in a\\ i>j}}^{n_{exc}} V_{ijij} + \sum_{i\in c}^{n_{exc}}\sum_{j\in a}^{n_{exc}} V_{ijij} + \frac{1}{2}\sum_{i\in s}^{n_{single}} V_{iiii}|\Delta w_i| \right) \\ - p_x &\left(\frac{1}{2}\sum_{i\in c}^{n_{exc}}\sum_{j\in a}^{n_{exc}} V_{ijji} - \frac{1}{2}\sum_{\substack{i\in c\\ j\in c,s}} V_{ijji} - \frac{1}{2}\sum_{\substack{i\in a\\ j\in a,s}} V_{ijji} + \sum_{\substack{i,j\in o\\ i>j}}^{N_o} V_{ijji}\eta_{ij}^{ji} \right),\end{aligned} \tag{2.79}$$

where the sums run over created (c) and annihilated (a) orbitals. The exponential function used in the original formulation to scale the off-diagonal elements was discarded and replaced by a new function with a less straightforward form

$$\begin{aligned}&\langle \omega w|\hat{\mathcal{H}}^{DFT/MRCI}|\kappa \neq \omega; k \neq w\rangle = \\ &\frac{p_1}{1+(p_2\cdot\delta\epsilon)^5 \arctan(p_2\cdot\delta\epsilon)^5}\,\langle \omega w|\hat{\mathcal{H}}^{CI}|\kappa \neq \omega; k \neq w\rangle\,.\end{aligned} \tag{2.80}$$

Unfortunately, no computations applying the exponential damping were given, making it difficult to judge the overall effect of this change. Investigating the damping function shown in Fig. 2.1 it is clear though, that the multiplicity-independent parametrization leads to a diminished consideration of off-diagonal elements, as the p_1 parameter is lower and the function profile much steeper in the interval $[0.4, 0.8]$. Especially, in the strong correlation region $[0, 0.2]$ less off-diagonal contributions are considered. This is accompanied by a sharp decrease in the exchange-like corrections taken into account in the diagonal element due to a drastic decrease of p_x, as can be seen from Tab. 2.2. Meanwhile, the considered Coulomb contributions p_J do not change nearly as much. A point which we will come back to shortly. While Lyskov et al. [141]'s formulation extended the scope of application fundamentally, the authors already stated that degeneracies cannot be described properly, still. The fundamental issue being the unbalanced treatment of off-diagonal and diagonal elements, due to a

[6] This is not the original equation derived by Lyskov et al. [141] but an extension formulated by Heil and Marian [142] containing an additional term for interactions of a singly occupied orbital in the anchor. However, the idea and motivation are similar to Lyskov et al. [141]'s.

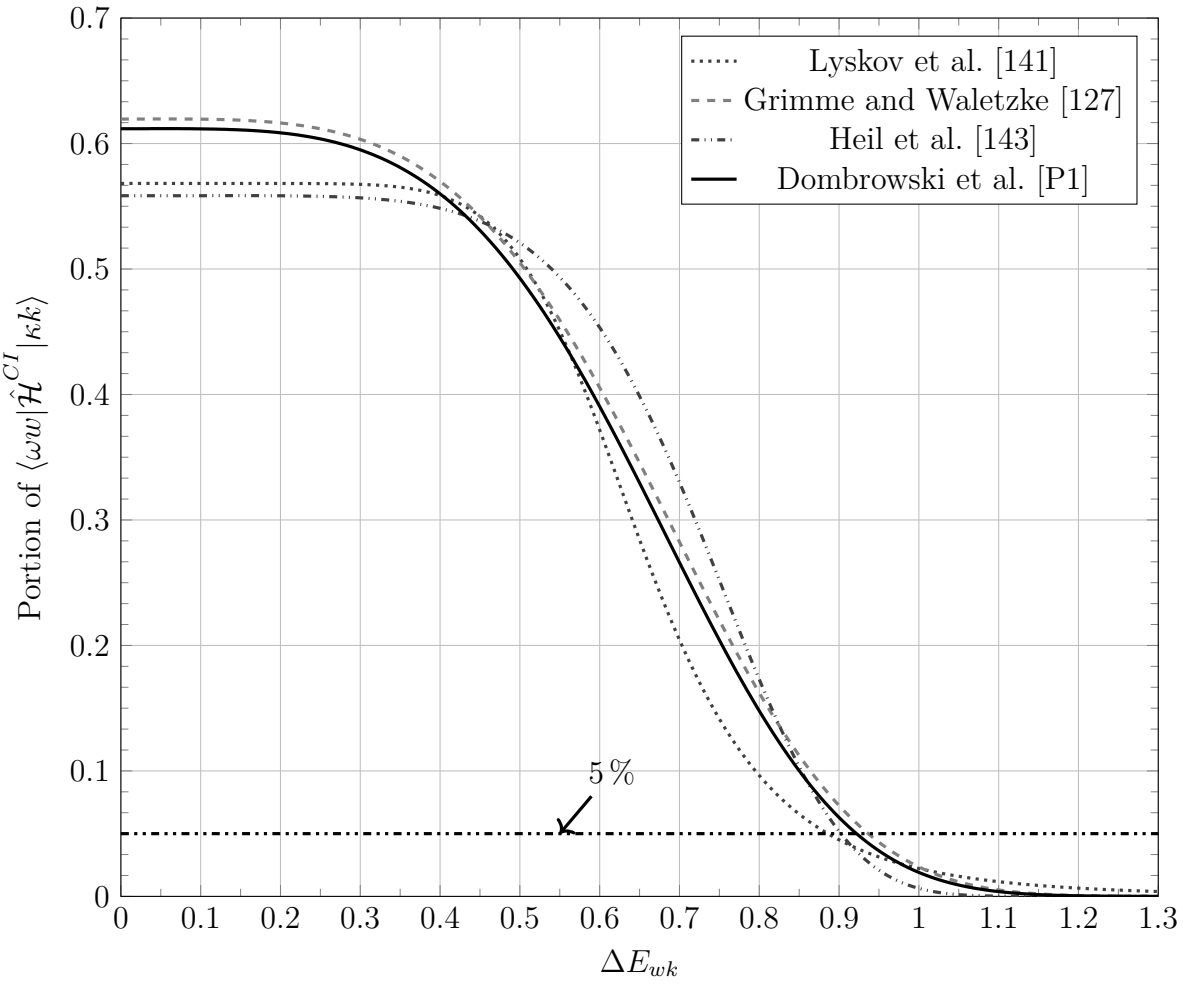

Figure 2.1: Plot of the damping functions employed in different formulations of the DFT/MRCI method for a $\delta\varepsilon = 1.0\,E_\mathrm{h}$

generally different scaling of the two in addition to a non-uniform scaling of the former. It was pointed out by the authors that p_1 is strongly dependent on the diagonal elements, as (near-)degeneracy of them equals to a mere scaling of the off-diagonal elements by this parameter. Indeed, the derivation given by Dombrowski et al. [P1], who reworked the DFT/MRCI formulas explicitly accounting for degeneracies of two states, resulted in an equation relating the scaling parameters employed in the construction of diagonal elements and the damping function's prefactor, yielding an equal correction in the case of strong static correlation. Furthermore, they found a value close to the original one for the prefactor of the damping function, leading to the interpretation of a general underestimation of correlation rooted in the off-diagonal elements in the redesigned Hamiltonian of [141]. This might explain the observa-

tion made by Heil et al. [143] for MnO_4^-. In contrast to computations carried out

Table 2.2: Parameter sets obtained by Grimme [126](original), Lyskov et al. [141](R2016) and Heil et al. [143](R2018) for a user defined selection threshold of $\delta\varepsilon^{sel.} = 1.0$. The p_x parameter of the original Hamiltonian given here is only valid for the closed-shell, singlet case, as it is defined to contain a linear correction term $p_x = p\,[0] + N_o\alpha$ depending on the number of open shells N_o

	diagonal		off-diagonal	
Hamiltonian	p_J	p_x	p_1	p_2
original	0.5102	0.5945[a]	0.6195	3.2719
R2016	0.5079	0.3559	0.5682	18.2960
R2018	0.5089	0.3624	0.558411	4.4717
R2022	0.5085/0.4649[b]	0.3426/0.5416[c]	0.6118[d]	3.4673

[a] $p\,[0]$; [b] p_J^{he}/p_J^{hhee} [c] p_x^{he}/p_x^{hhee} [d] $1 - 2p_J^{hhee} + p_x^{hhee}$

with the original formulation, they reported difficulties assigning the T_2 states, due to spurious contributions of doubly excited configurations. As these are comprised of degenerate configurations constructed from compact 3d and 2p orbitals[144], static correlation contributions are expected to be high. Remembering that the key idea is including the latter through the CI expansion, it makes sense that the methods of Heil et al. [143] and Lyskov et al. [141], considering the least portion of exact off-diagonal elements out of all DFT/MRCI methods, run into problems. Judging from the parameters shown in Tab. 2.2 the reduced static correlation goes along with a smaller weighting of correction terms applied to the HF-like exchange integrals in the CI-matrix element. Furthermore, a bias between exchange-like and Coulomb-like integral corrections seems to be introduced, as the latter are corrected in all formulations by roughly the same amount. Noteworthy, is the resemblance of the global parameters p_x used in the model Hamiltonians of Lyskov et al. [141] and Heil et al. [143], and the parameter used to correct exchange contributions originating in intra orbital particle-hole interactions p_x^{he} in the ansatz of Dombrowski et al. [P1]. At the same time, the correction parameter applied to interorbital particle-hole interactions p_x^{hhee} is close to the value used for the exchange correction in the original formulation. This might simply be a remarkable coincidence or points to a response of the parametrization and to the lack of correlation from the off-diagonal elements, through inclusion of intra orbital contributions, which presumably suffer from a higher self-

interaction error, mimicking static correlation[145], which would be in the sense of the foregoing discussion. Obviously it is too far-fetched to make definite statements based on similarities of the parameters. However, it might be worthwhile to investigate if the postulated connection exists to learn about correlation and maybe find a way to balance the treatments of off-diagonal and diagonal elements, solving the degeneracy issue.

3 Technical Details

In this chapter some technical details of the `mrci` program maintained in the theoretical chemistry group in Düsseldorf will be outlined. The coding of configurations as well as the general structure and algorithm of the program will be discussed, concluding with a brief presentation of possible parallelization strategies for the algorithm.

3.1 Sketch of the `mrci` Program

The key task in a selecting MRCI code employing CSFs as basis states, is to find a resourceful way of representing the spatial configurations, which are coupled to spin functions generated by using an appropriate scheme. A naive approach of storing lists off occupation number vectors would quickly lead to too high memory demands as one would need $M \times N \times B$ bytes, where M is the number of one-particle states, N the number of CSFs and B a factor in byte depending on the used data type, e.g. $\frac{1}{8}$ for an encoding in a single-bit[1] or 4 for a common 32-bit integer. Typical, medium-sized calculations are somewhere in the range of 1-5·10^6 CSFs and employ around 500 orbitals as basis states. This means such a storage scheme would quickly consume a few hundreds of MB to GB, depending on the factor B, and severely limit the applicability. Therefore, the configurations in the `mrci` program are stored in tree-like scheme to be introduced shortly. First a method to limit M shall be discussed. An approach used frequently is the frozen (anti)-core approximation[36, 76, 146]. As the core-orbitals are insensitive to the molecular environment and changes of it, the associated energy terms approximately cancel if relative energies are considered. For optical spectra, it is therefore often a good approximation to ignore orbitals below a certain energy threshold, often $< -10\,E_\mathrm{h}$, when distributing the particles in spatial orbitals. Similarly, it is often not necessary to substitute with very high-lying orbitals. Typical values for neglecting them being orbital energies $>2\,E_\mathrm{h}$. Freezing these orbitals often results in a large reduction in computational requirements

[1] which would only be possible using explicit spin-orbitals.

without introducing a too large an error[147]. Another approach shared by many multi-configurational theories is the separation into an active (internal)[148] and an external space. Dividing the orbital set into doubly-, variably- and un-occupied MOs gives this first, straightforward separation, as sketched in Fig. 3.1. The definition of

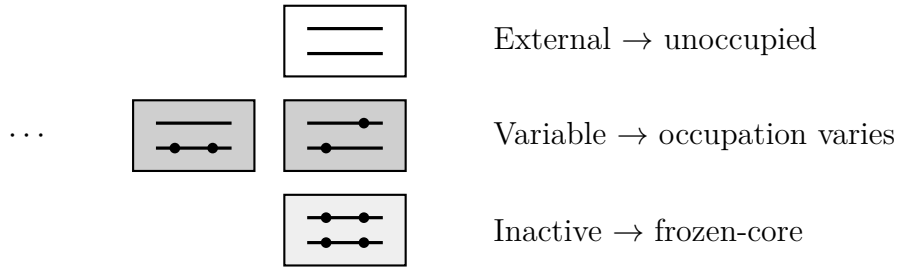

Figure 3.1: Partitioning of configuration space into different subspaces based on orbitals. Inactive or frozen-core orbitals are not used in the construction at all. The set of variably occupied orbitals defines the internal or active space. External orbitals are unoccupied in all generated configurations.

the active space necessitates input from the user and chemical insight. For instance, the single-particle functions serving as a basis must be rotated correctly to construct the desired configuration space. Special care must be taken if orbital degeneracies are to be addressed. Often, it is not an easy task to define a proper active space to cover all desired contributions. Nevertheless, the concept has been tremendously successful and is used in many electronic structure methods today. In the `mrci` program the reference space is generated from a complete or truncated active space, which means that all excitations or in the latter case a limited amount of configurations in the defined space are considered. The reference space is successively refined by excluding configurations with a weight lower than a user-defined threshold in the final CI vector. Configurations with squared coefficients larger than this threshold are included in the same step, if they were not present in the reference space beforehand. A simplified sketch of the program flow is given in Fig. 3.2. From the same figure it can also be seen, that the general structure is not particularly difficult. Most of the complexity in the code arises from managing the configurations as it is necessary to exclude redundancies, which occur very quickly. A very easy example for such redundancies is already found considering Fig. 3.3. Obviously, some configurations can be reached by different combinations of creation and annihilation operators which is to be avoided[2]. The full technical details of the configuration comparison can be found in the thesis

[2]Note that this is a purely technical statement and does not concern the interactions between the configurations.

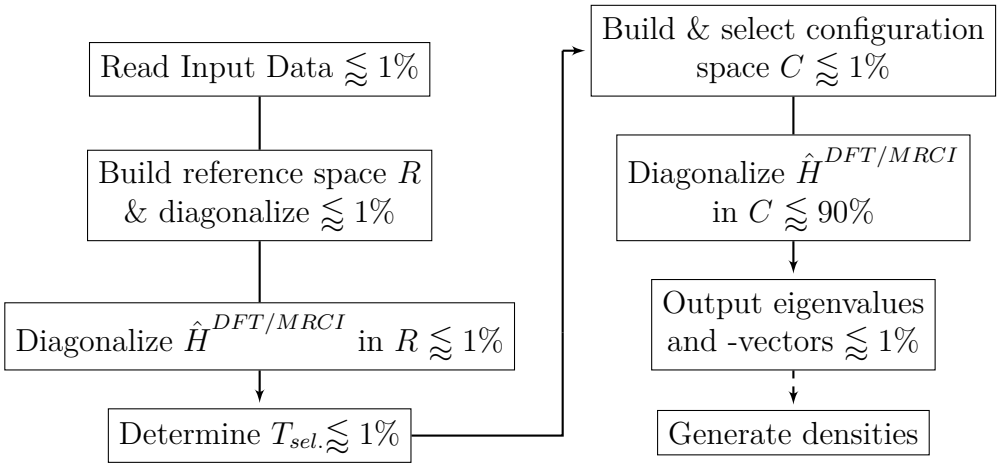

Figure 3.2: Layout of the mrci program and approximate share of total execution time.

of Waletzke [149]. In terms of needed computational resources the diagonalization of $\hat{H}^{DFT/MRCI}$ is the most demanding step. Therefore, it also poses the best entry point for trying to achieve computational gains through parallelization.

3.2 Parallelization Scheme in the mrci Program

As was already pointed out earlier, the matrix to be constructed in the CSF basis is enormous. In addition, it is also very sparse, which makes the use of iterative methods particularly attractive. The mrci program uses a multi-root generalization of the Davidson algorithm[150, 151], which allows solving the problem for a selected number of eigenvectors/-value pairs. The algorithm is given in Alg. 1. Being a projection method it yields approximation vectors in a small subspace S^m. The latter is enlarged iteratively to refine the computed, approximate vectors until a convergence criterion is met. While it would be straightforward to parallelize the individual steps of the algorithm it is not very meaningful. By far the most time is spent in one step, namely the generation of the σ vectors in line 5 of Alg. 1. Consequently, distributing the work here has the largest impact, as was already pointed out by Kleinschmidt et al. [152]. Another benefit of parallelizing the matrix-vector multiplication step in Alg. 1, is that it is easily adaptable to other problems, such as the computation of spin-spin matrix elements in the framework of the SPOCK.sistr program by Gilka [40]. Before proceeding with the discussion, it is necessary to consider how configurations used in the construction of H are grouped in the mrci code to achieve an efficient

Algorithm 1: Davidson-Liu algorithm implemented in the `mrci` program.

Input: Threshold t, Number of roots n

Select n orthonormal basis vectors $\{\vec{b}_j\}$ of S^m;
$N_{old} \leftarrow 0; N_{new} \leftarrow n;$
repeat
  `// Calculate representation of H on` $\{\vec{b}_j\}$
  for $q \leftarrow N_{old}+1$ **to** $N_{old}+N_{new}$ **do**
    $\vec{\sigma}_q \leftarrow H\vec{b}_q$; `// Computationally most expensive step`
    for $u \leftarrow 1$ **to** q **do**
      $A_{uq} \leftarrow \langle \vec{b}_u | \vec{\sigma}_q \rangle$;
    end
  end
  $N_{old} \leftarrow N_{old} + N_{new}$;
  Diagonalize A. Get N_{old} eigenpairs $(\vec{e}_k, \lambda_k)$ and select N_{new};
  for $i \leftarrow 1$ **to** N_{old} **do**
    for $j \leftarrow 1$ **to** N_{new} **do**
      $\vec{x}_j \leftarrow e_{i,j}\vec{b}_i$; `// Express the` $\vec{b}_i$ `in eigenbasis of A`
    end
  end
  $N_{iter} \leftarrow 0$;
  for $j \leftarrow 1$ **to** N_{new} **do**
    Calculate residual vector $\vec{r}_j \leftarrow H\vec{x}_j - \lambda_j \vec{x}_j$;
    if $||\vec{r}_j||_2 < t$ **then**
      Save $\vec{x}_j$ and discard from search;
    end
    else
      $N_{iter} \leftarrow N_{iter} + 1$;
    end
  end
  $N_{new} \leftarrow N_{iter}$;
  for $j \leftarrow 1$ **to** N_{new} **do**
    Precondition vector p_j by scaling r_j with $\left(\lambda_j - H^D\right)^{-1}$;
    `//` H^D `being the diagonal elements of` H
    Orthonormalize with $\{\vec{b}_j\}$ and append to set
  end
until $N_{new} = 0$;

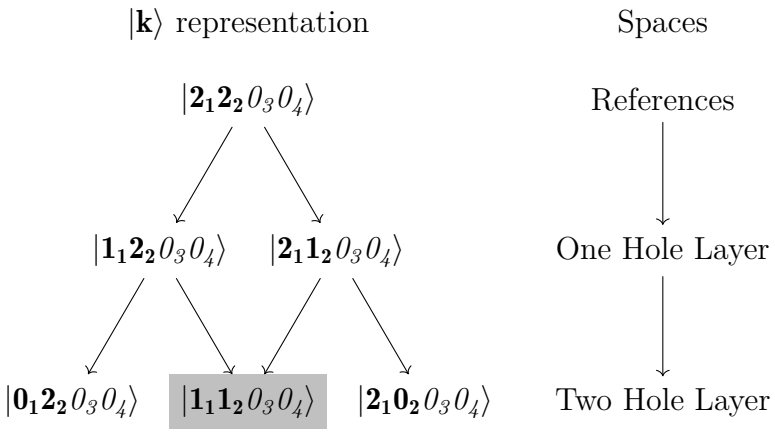

Figure 3.3: Sketch of the hierarchy of spatial hole configurations generated from a root configuration $|\mathbf{2_1 2_2} 0_3 0_4\rangle$. For simplicity the occupation number representation was chosen. The branches can be traversed in both directions by applying either annihilation (downward) or creation (upward) operators. The hole configuration in the grey box has two ingoing branches, exemplifying the necessity to take care of such redundant pathways.

calculation of matrix elements. Configurations differing by more than two occupations cannot interact in the first place due to the Slater-Condon rules. Therefore, grouping the configurations leading to interacting CSFs, thereby avoiding unnecessary computations and searches, is advantageous. To solve this logistic task, Hanrath and Engels [153] envisaged the MRCI wave function as a tree of configurations, as shown in Fig. 3.4. This approach results in a classification of generated configurations by the number of internal hole orbitals used in their construction. Eventually, this leads to three different subspaces consisting of configurations with zero, one or two hole orbitals, $\{\,\mathrm{int}0, \mathrm{int}-1, \mathrm{int}-2\,\}$. Therefore, interactions can be separated into similar or different hole-spaces, totalling to six classes. The basic algorithm, omitting all the logic used in constructing CSFs and determining configuration differences, is shown in Alg. 2. Two key points are to be recognized. First, the work can be shared by distributing the number of configurations. Second, in doing so care has to be taken when updating the component of the $\vec{\sigma}$ vector, as the distributed configurations might belong to similar CSFs. Kleinschmidt et al. [152] implemented an approach based on message passing interface (MPI). While this implementation is straightforward, it distributes all needed data to all processes, thereby avoiding any race condition, which is very memory consuming. The approach implemented in this work uses the OpenMP (OMP) application programming interface (API) to realize a shared-memory approach. Thereby, the needed memory in the generation of the $\vec{\sigma}$

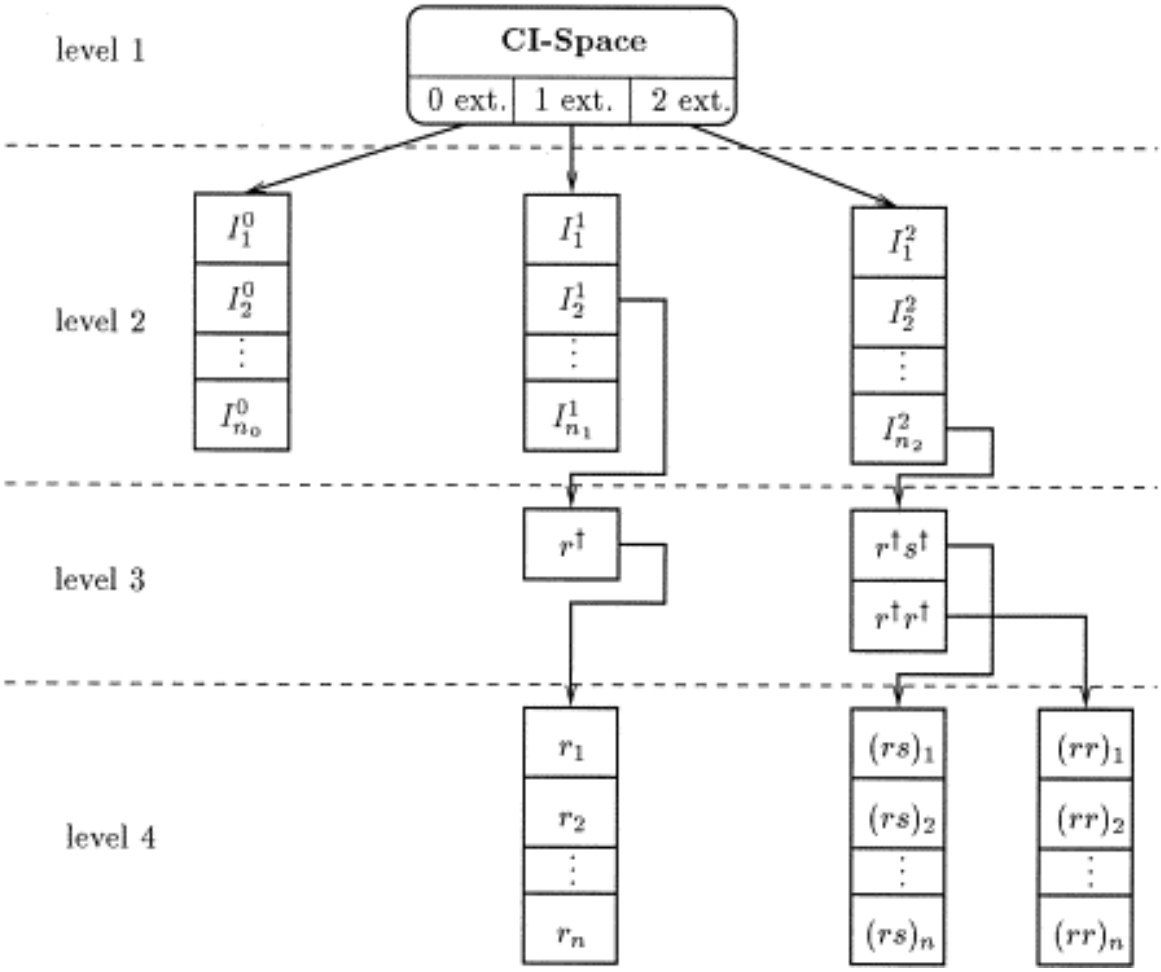

Figure 3.4: Representation of the MRCI wave function as a tree. Figure taken from Hanrath and Engels [153]

vectors should be reduced, enabling the treatment of larger systems. The benefit of sharing memory is best explained with an example. Imagine calculating the 20 lowest eigenvalues of $\hat{H}^{DFT/MRCI}$ in a basis of 10^7 CSFs, built from a MO basis in which the two-electron integrals consume 2 GB of memory, on a single compute node. For every iteration in Alg. 1, it is necessary to read some of the two-electron integrals, depending on the configuration processed by the current worker[3]. Unfortunately, it is not known until the very last step which integrals need to be loaded. It is therefore necessary to withhold all integral information. This information is read-only and no race condition ought to be feared. Therefore, it is clear that these 2 GB of memory need to be allocated once. However, in the distributed scheme this applies to every

[3]Worker will be used here as a placeholder for the entities performing work in parallel. Processes in MPI and threads in OMP.

Algorithm 2: Sketch of loop structure used in the `mrci` program to compute the $\vec{\sigma}$ used in the Davidsion-Liu algorithm (Alg. 1).

```
   Data: Hole configurations L ← { int0, int − 1, int − 2 }
 1 forall Configurations s ∈ L do
 2 |   Build up CSF c;
 3 |   Compute matrix element H; Compute component of σ⃗;
 4 |   forall Configurations s′ ≠ s ∈ L do
 5 |   |   Determine difference between s and s′;      // lots of logic needed
 6 |   |   if Interaction possible between s and s′ then
 7 |   |   |   Build up CSFs c and c′ ;                    // c = c′ possible!
 8 |   |   |   Compute matrix element H;
 9 |   |   |   Compute component of σ⃗;
10 |   |   end
11 |   end
12 end
```

worker as they cannot enter each others address spaces, consuming worker×2 GB of memory on the compute node. The second large quantity is the result of the iterative diagonalization, which is of dimension CSFs×20, as every eigenvalue belongs to an eigenvector. Each entry is stored as a double precision floating point number, consuming 8 B each, totalling to ≈1.5 GB. This amount has to be doubled[4] as this is also the initial dimension of the subspace S^m. Therefore, worker×2×1.5 GB need to be allocatable on the node using the distributed memory implementation of `mrci`. The final bill assuming 20 workers comes to 100 GB of consumed memory on a single node. In the new OpenMP version, the two-electron integrals are allocated only once, the result vector needs to be allocated for every worker to avoid race condition, and the subspace is allocated only once again as it is read-only. Concluding that the total bill of the shared memory implementation is only 33.5 GB again assuming 20 workers. Note that the exemplary balance sheet is not precise as arrays necessary to supply configuration information were ignored entirely. However, these are comparably modest in terms of memory consumption and normally do not tip the scales. The advantage in terms of memory should be apparent from the given example. However, if the computational performance is compromised, this advantage becomes insignificant. Obviously, one can assume the OpenMP implementation to be a bit slower as the memory allocation for the privatized vectors does not happen once, which is the

[4] in-fact the `mrci` code takes an additional vector into the search space, adding another ≈80 MB but this is going to be ignored here.

case in the distribution scheme, but in every iteration. To test the performance, a medium-sized calculation on pentacene was set up. The KS one-particle basis was created employing a def2-TZVP[154][155] basis on all atoms. Two-electron integrals were generated using the Resolution of the Identity approximation and a def2-TZVP auxiliary basis. The reference space was constructed by distributing eight electrons in 12 orbitals, allowing for single and double excitations, resulting in 569 reference functions. 21 eigenvalues were computed in this basis leading to an effective selection threshold of $1.225\,512\,65\,E_\mathrm{h}$[5]. After the configuration selection procedure 3 160 326 CSFs were left as a basis to solve the eigenvalue problem for the same amount of roots. The binaries were created with the Intel® Fortran Intel®64 Compiler Classic Version 2021.10.0 Build 20230609_000000 compiler[6] All computations were done on nodes equipped with two AMD EPYC™ 7402 24-core processors.

The scaling behaviour with the number of workers is found to be very similar to the MPI version, with the obvious difference of being much smoother, as can be seen from Fig.3.5. This is rooted in the different distribution strategies chosen. While the MPI implementation uses a step width dependent on the allocated number of processes in each outer-loop of Alg. 2, the OMP version uses the `dynamic` scheduling provided by the OpenMPAPI. Here a work pool is constructed, which can be accessed dynamically by every OpenMP thread. While this can cause significant overhead, likely the cause of the strong deviations for one worker in Fig. 3.6, it also provides a very good load balancing. The latter is likely the root of the strongly oscillating curve recorded for the MPI program. It can, and apparently does, happen that the MPI process loops over configurations, which do not contribute much, leading to many early exits of the loop structure, while another hits many important configurations, leading to increased computational labour. Though both got approximately the same amount of configurations, the work load is highly imbalanced. This is supported by the observation that the difference in absolute timings, shown in Fig. 3.6, shows

[5] Precision given for reproducibility.

[6] Used compilation flags:
OMP: `-I/apps/ql/intel/oneapi/mkl/2023.2.0/include -O3 -static -no-prec-div -fp-model fast=2 -march=core-avx2 -assume byterecl -qopenmp -qopenmp-link=static -fma -pad -fomit-frame-pointer -ftz -DOMPDOT -DONTMKLDOT -c -o main.o`, where `-DOMPDOT -DONTMKLDOT` are conditional compilation flags, activating memory checks on the given stack size and using Fortran `dot_product` instead of Intel® MKL `sdot`.
MPI: `-I/apps/ql/intel/oneapi/mpi/2021.10.0//include -I/apps/ql/intel/oneapi/mpi/2021.10.0/include -O3 -march=core-avx2 -align array64byte -fma -ftz -fomit-frame-pointer -DPARALLEL -assume byterecl -qopenmp-stubs -traceback -c -o main.o`, where `-DPARALLEL` activates the necessary MPI subroutine calls.

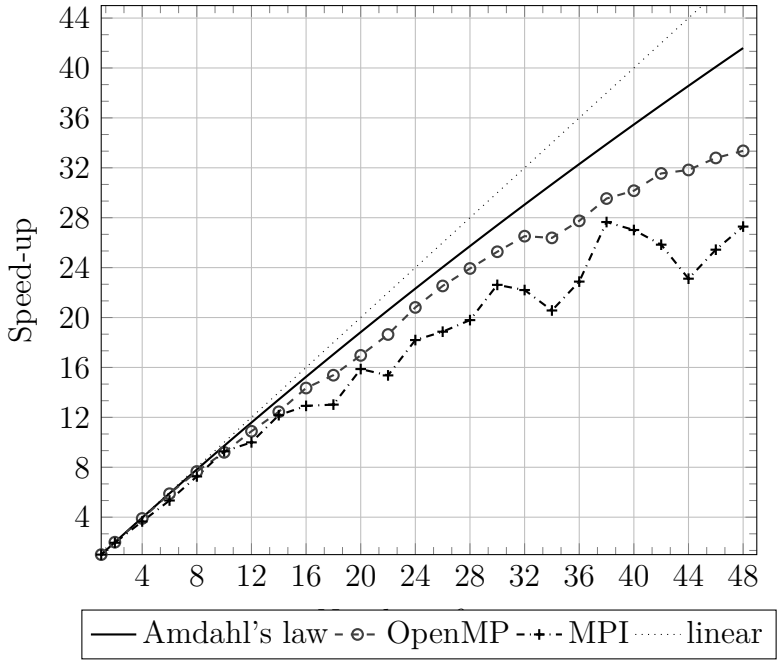

Figure 3.5: Obtained speed-ups for the test set-up described in the text.

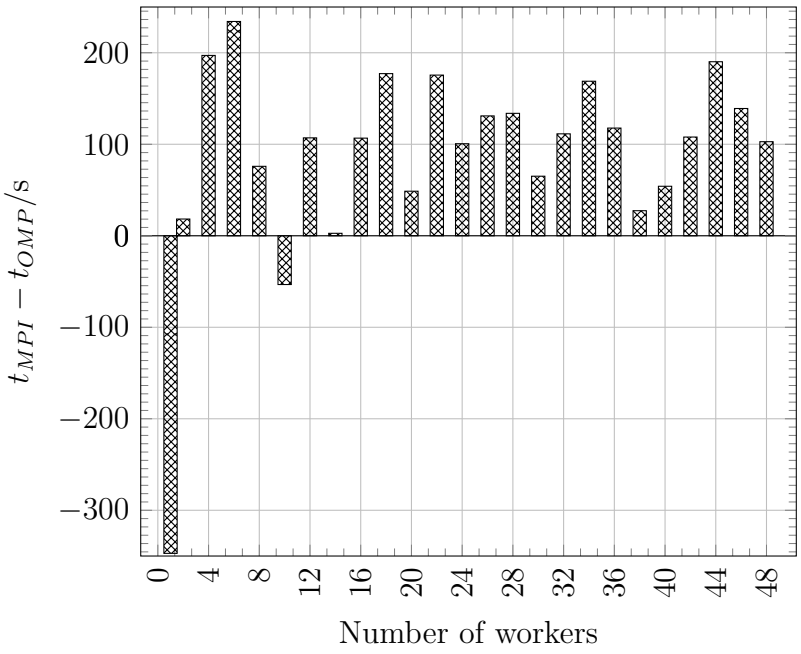

Figure 3.6: Differences in absolute timings of the MPI and the OMP obtained for the test set-up

oscillatory behaviour as well. It seems that the chosen set-up is very in favour of the OMP version. However, it is not guaranteed that this implementation is always faster,

as one can already surmise from the large difference for a single worker and the points where the performance is approximately similar. Furthermore, it should be pointed out that every data point represent just a single run of the respective binaries. To get more meaningful results, it would be necessary to carry out multiple runs to get a proper statistical estimate and smooth out (un-)beneficial effects. To put in a nutshell the newly implemented OpenMP parallel version of the `mrci` code is very similar to the MPI performance wise. Its biggest plus being the large reduction of memory needed. Therefore, the parallelization scheme was transferred to the `SPOCK.sistr` program, which has a much larger memory consumption in terms of two-electron integrals, thus enabling computations for larger systems in a reasonable amount of time. In the following chapters some applications on large systems will be discussed, which all utilized the OpenMP code. The original intention was to use these systems as a test of the capabilities of the new code, however it showed quickly, that these systems did not only push technical, but methodological boundaries.

4 Multi-Excitonic States and Degeneracies in DFT/MRCI

The performance benchmarks presented in the last section used pentacene as a test system. This was motivated by the fact that many known materials undergoing SF contain PT or its derivatives as building units. Specifically, the *regio*-isomers shown

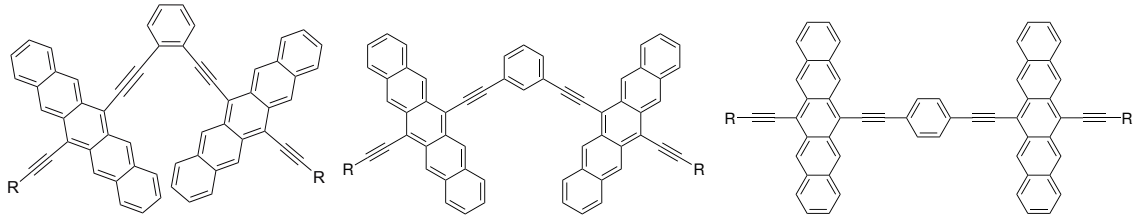

(a) *ortho* (b) *meta* (c) *para*

Figure 4.1: Skeletal formulas of the 6,6′-linked pentacene dimers. All computations were done on systems in which a methyl group was substituted for the triisopropylsilyl (TIPS) residues R in 13 and 13′ positions of the *ortho*, *meta* and *para* compounds, respectively.

in Fig. 4.1 were investigated to assess the applicability of the DFT/MRCI method. High-quality time-dependent and time-independent spectroscopic[156, 157] and computational data[156, 158] is available for these systems, making them good test subjects. Unfortunately, it was found at an early stage that the results obtained with the redesigned Hamiltonians of Lyskov et al. [141] and Heil et al. [143] are hard to interpret and likely flawed. In the following, it shall be argued why this is the case. The observations made are of similar nature for all three isomers. Therefore, the *meta*-linked derivative will be employed as a proxy in the discussion. An orbital energy diagram including plots of the MOs used as the one-particle basis in subsequent DFT/MRCI calculations is shown in Fig. 4.2. In the introduction, the significance of the anti-ferromagnetically coupled triplet pair ^{1}(TT) was highlighted in the description of Fig. 1.1. As ^{1}(TT) is imagined to be built from two coupled triplet states,

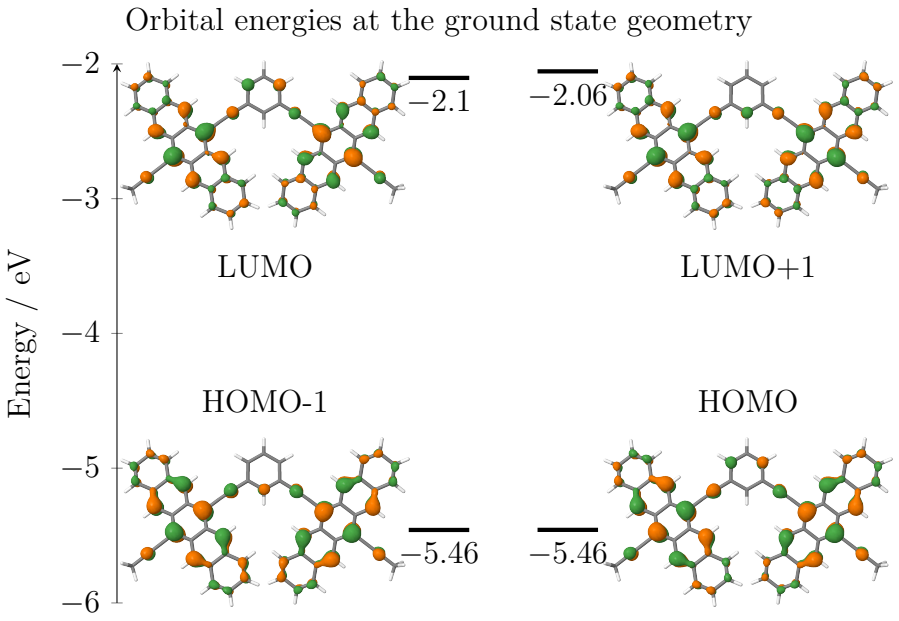

Figure 4.2: Energy levels of the two HOMOs and LUMOs computed with BH-LYP[130] in a def2-SVP[159] basis for *meta*. Full computational details are given in [P2].

the underlying configurations can be constructed by distributing four electrons in the spatial orbitals plotted in Fig 4.2. Furthermore, the initial step in the SF process occurs at energies corresponding to wavelengths of infrared and visible light. Therefore, it is anticipated that the valence orbitals of Fig. 4.2 will play a dominant role. Consequently, it is reasonable to restrict the preliminary stages of analysis to them. Some exemplary doubly excited configurations built in the valence space are shown in Fig. 4.3. Given that the spatial extent and energies of the HOMO and HOMO-1, and LUMO and LUMO+1 pairs, as shown in Fig. 4.2, are not significantly different, it is unlikely that any of the involved interaction integrals will be substantially different from any other. Consequently, all configurations shown in Fig. 4.3 should appear with a comparable weight in the MRCI vector. However, it was found that the configuration with four open-shells is weighted much stronger than the closed-shell ones, if either one of the redesigned model Hamiltonians is used. Additionally, it was found that the quintet states are computed at unexpectedly low energies with these Hamiltonians. A plot of the computed energy levels per multiplicity is shown in Fig. 4.4. Clearly, the results for the two model Hamiltonians differ strongly. Most striking is the energetic position of the lowest quintet state computed with Lyskov et al. [141]'s Hamiltonian, which is below the lowest triplet state. Investigation of the associated

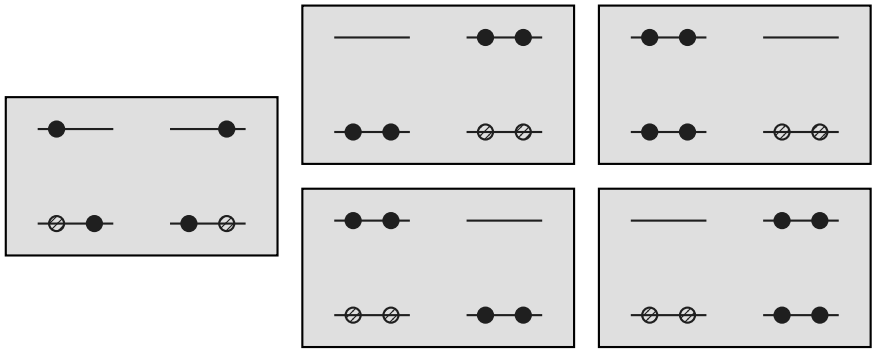

Figure 4.3: Exemplary spatial configurations constructed by distributing four electrons in the four valence orbitals shown in Fig. 4.2. Filled circles represent electrons, hatched the holes left behind on excitation.

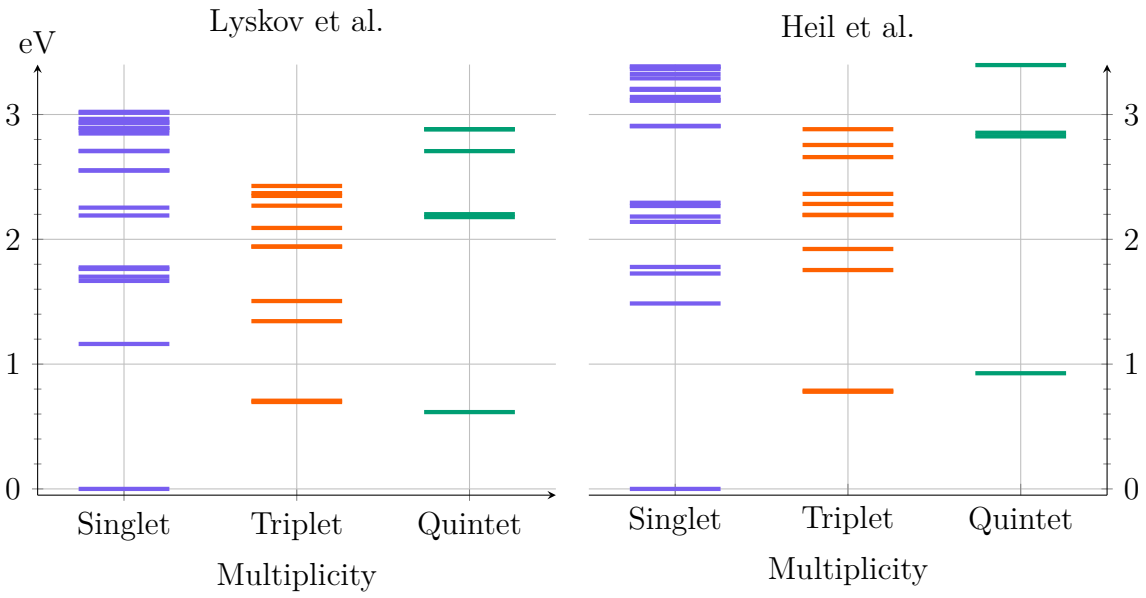

Figure 4.4: Energy level plot of the singlet, triplet and quintet state manifold found in *meta* computed with two different model hamiltonians.

wave function revealed dominant contributions of the configuration constructed by distributing four particles with like spin in the orbitals of Fig. 4.2. As this configuration can be understood as a single substitution on top of a triplet configuration this result can hardly be explained. Both hamiltonians predict the second excited singlet state to be the ^{1}(TT) state. Additionally, both predict the CI vector to be dominated by configurations with four open-shells. Based on the foregoing discussion of the similarities in the one-particle basis, this contradicts intuition and together with the low-lying quintet states points to an unbalanced treatment of configurations with four open-shells. Indeed, it was shown by Dombrowski et al. [P1] that states composed of such configurations are heavily underestimated by the redesigned Hamiltonians and proposed a new ansatz. Details can be found in the publication.

THE JOURNAL OF PHYSICAL CHEMISTRY A
A JOURNAL OF THE AMERICAN CHEMICAL SOCIETY

pubs.acs.org/JPCA Article

R2022: A DFT/MRCI Ansatz with Improved Performance for Double Excitations

Published as part of The Journal of Physical Chemistry virtual special issue "MQM 2022: The 10th Triennial Conference on Molecular Quantum Mechanics".

Dennis R. Dombrowski, Timo Schulz, Martin Kleinschmidt, and Christel M. Marian*

Cite This: *J. Phys. Chem. A* 2023, 127, 2011−2025 Read Online

ACCESS | Metrics & More | Article Recommendations | Supporting Information

ABSTRACT: A reformulation of the combined density functional theory and multireference configuration interaction method (DFT/MRCI) is presented. Expressions for ab initio matrix elements are used to derive correction terms for a new effective Hamiltonian. On the example of diatomic carbon, the correction terms are derived, focusing on the doubly excited $^1\Delta_g$ state, which was problematic in previous formulations of the method, as were double excitations in general. The derivation shows that a splitting of the parameters for intra- and interorbital interactions is necessary for a concise description of the underlying physics. Results for ^1L_a and ^1L_b states in polyacenes and ^1A_u and ^1A_g states in mini-β-carotenoids suggest that the presented formulation is superior to former effective Hamiltonians. Furthermore, statistical analysis reveals that all the benefits of the previous DFT/MRCI Hamiltonians are retained. Consequently, the here presented formulation should be considered as the new standard for DFT/MRCI calculations.

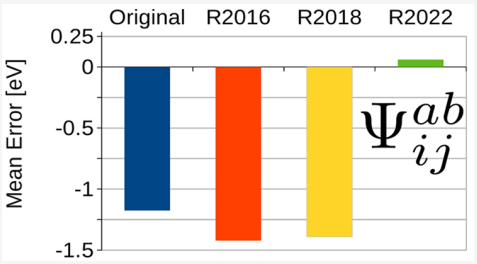

INTRODUCTION

The combined density functional theory and multireference configuration interaction method (DFT/MRCI) is a semi-empirical approach, which makes use of extensive configuration selection and introduces scaling parameters and damping functions to avoid double counting of electron correlation. Since its launch in 1999, it has developed from a powerful electronic structure method for computing spectral properties of singlet and triplet excited states of large molecules into a more general multireference method applicable to states of all spin multiplicities.[1−5] In its original formulation,[1] DFT/MRCI shows great efficiency in the evaluation of singlet and triplet excited states which mainly originate from local one-electron transitions.[6−8] Moreover, it is one of the few methods applicable to large systems that yields the correct ordering of adiabatic states in extended π-systems where double excitations play a significant role.[9−12] The redesigned DFT/MRCI Hamiltonians[2,4,5] extended the application range of the method to excited states of radicals with odd numbers of electrons[13] and to loosely coupled donor−acceptor systems[14−16] that play a central role in energy transfer cassettes and in organic light-emitting diodes based on thermally activated delayed fluorescence. In the course of time, it turned out, however, that certain types of double excitations are not handled well by the DFT/MRCI ansatz. Jovanović et al.[17] described several critical cases, comprising double excitations from nonbonding lone-pair orbitals to π orbitals ($n^2 \rightarrow \pi^{*2}$) and double excitations from different orbitals such as ($n, n' \rightarrow \pi^*\pi^{*\prime}$) or ($\pi, \pi' \rightarrow \pi^*\pi^{*\prime}$). In particular, the energies of doubly excited configurations with four open shells were severely underestimated by the original and redesigned DFT/MRCI Hamiltonians.

However, states of this kind play a key role in singlet fission (SF), the fission of a high-energy singlet exciton into two lower-energy triplet excitons,[18,19] and in triplet−triplet annihilation upconversion (TTA-UC), where low-energy photons are converted to higher-energy photons that can be collected by a solar cell.[20] Both processes are spin-allowed and involve singlet-coupled triplet-pair intermediates, ^{1}(T···T). To accomplish a proper modeling of SF and TTA-UC by quantum chemical methods, a balanced description of singly and doubly excited states is mandatory.[21−25] Doubly excited states also play a pivotal role for the light-harvesting and protective functions of carotenoids in photosynthetic complexes.[26,27] In these compounds, the S_1 state is characterized by a mixture of the two singly excited $\pi_{H-1} \rightarrow \pi_L$ and $\pi_H \rightarrow \pi_{L+1}$ configurations and the doubly excited $\pi_H^2 \rightarrow \pi_L^2$ configuration, while the optically bright S_2 state originates mainly from the $\pi_H \rightarrow \pi_L$ excitation.[28,29] The importance of double excitations is known to increase with growing conjugation lengths N.[30] Experimental results strongly

Received: November 11, 2022
Revised: February 2, 2023
Published: February 17, 2023

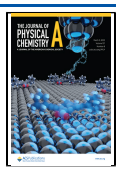

https://doi.org/10.1021/acs.jpca.2c07951
J. Phys. Chem. A 2023, 127, 2011−2025

suggest that in carotenoids with $N \geq 11$, an additional doubly excited dark state is located between S_2 and S_1, which speeds up the deactivation of the S_2 state.[31−35] Furthermore, a proper description of charge transfer states is desirable, since it was recently shown that intramolecular charge transfer (CT) states greatly speed-up the energy transfer to bacteriochlorophyll a.[36]

In this work, we set out for remedying the weaknesses of the previous DFT/MRCI Hamiltonians with regard to double excitations while retaining the good performance for CT, Rydberg, and singly excited states known from the previous formulations.[37−39] We will present a novel ansatz, which differentiates between double excitations involving the same spatial orbital twice and double excitations involving different spatial orbitals. By setting up a relationship between diagonal and off-diagonal corrections only one additional parameter needs to be introduced. After a careful assessment of the new effective Hamiltonian, dubbed R2022, we focus on its performance for two types of extended π-systems, namely, polyacenes and carotenoids, which are well investigated in the literature by other quantum chemical methods.[12,40−44]

THEORY

First we will recapitulate the basic idea of DFT/MRCI before lying focus on the modifications introduced in the R2022 Hamiltonian. In the DFT/MRCI method,[1,3] a Kohn−Sham (KS) one-particle basis and a closed- or single open-shell anchor configuration are used in the construction of the MRCI wave function. An efficient truncation of the CI expansion, without significant loss of accuracy, is achieved by utilizing a simple selection criterion based on orbital energies. The CI wave function is expanded into the basis of configuration state functions (CSFs), denoted $|w\omega\rangle$. Here w denotes the spatial- and ω is the spin-arrangement. To introduce corrections to the MRCI matrix elements, a formulation by Segal, Wetmore, and Wolf[45,46] was chosen. The latter groups the CI matrix into three different cases:

1. Diagonal elements with same spatial occupations

$$\begin{aligned}\langle \omega w|\hat{\mathcal{H}}^{\mathrm{CI}}|\omega w\rangle = {} & E^{\mathrm{HF}} + \sum_i F_{ii}\Delta w_i + \frac{1}{2}\sum_{i\neq j} V_{iijj}\Delta w_i \Delta w_j \\ & + \frac{1}{2}\sum_{i\neq j} V_{ijji}\left(-\frac{1}{2}\Delta w_i \Delta w_j + \frac{1}{2}w_i w_j - w_i + \eta_{ij}^{ji}\right) \\ & + \frac{1}{2}\sum_i V_{iiii}\left(\frac{1}{2}\Delta w_i \Delta w_i + \frac{1}{2}w_i w_i - w_i\right)\end{aligned} \tag{1}$$

2. One-electron occupation differences

$$\begin{aligned}\langle \omega w|\hat{\mathcal{H}}^{\mathrm{CI}}|\omega' w'\rangle = {} & F_{ij}\eta_i^{\ j} + \sum_{k\neq i,j} V_{ikjk}\Delta w'_k \eta_i^{\ j} \\ & + \sum_{k\neq i,j} V_{ikkj}\left(-\frac{1}{2}\Delta w'_k \eta_i^{\ j} + \frac{1}{2}w'_k \eta_i^{\ j} - \eta_i^{\ j} + \eta_{ik}^{kj}\right) \\ & + V_{iiij}\left(\frac{1}{2}\Delta w'_i + \frac{1}{2}w'_i\right)\eta_i^{\ j} \\ & - V_{ijjj}\left(\frac{1}{2}\Delta w'_j + \frac{1}{2}w'_j - 1\right)\eta_i^{\ j}\end{aligned} \tag{2}$$

3. Two-electron occupation differences

$$\langle \omega w|\hat{\mathcal{H}}^{\mathrm{CI}}|\omega'' w''\rangle = (V_{ikjl}\eta_{ik}^{\ jl} + V_{iklj}\eta_{ik}^{\ lj})[(1+\delta_{ik})(1+\delta_{jl})]^{-1} \tag{3}$$

where w_i denotes the occupation number of orbital i in the configuration w, Δw_i is the occupation difference of i with respect to the anchor configuration, η_i^j and η_{ij}^{ji} are the one- and two-electron spin-coupling coefficients, V_{ikjl} is the two-electron integrals $\langle i(1)k(2)|\frac{1}{r_{12}}|j(1)l(2)\rangle$, E^{HF} is the Hartree−Fock energy, F_{ij}^{HF} is the Fock matrix elements, and δ_{ij} is the Kronecker-Delta. In the DFT/MRCI method, a suitable parametrization of the Coulomb- and exchange-integrals for eq 1 as well as an energy-separation dependent scaling of the interacting configurations for eqs 2 and 3 is used to prevent double counting of the dynamical electron correlation. The latter being unquantifiably included in the KS one-particle basis. In the following subsections, we will introduce the corrections applied in DFT/MRCI to these matrix elements.

Diagonal Element Corrections in Previous Hamiltonians. First we concentrate on the corrections to the diagonal matrix elements, which are given in eq 1. They constitute the largest contribution to the MRCI energy because the CI matrix is diagonally dominant. In the DFT/MRCI method, the SCF energy E^{HF} and the diagonal elements of the Fock matrix F_{ii}^{HF}, i.e., the orbital energies in eq 1 are replaced by the KS energy of the anchor configuration E^{KS} and the KS canonical orbital energies F_{ii}^{KS}. Taking the difference of the modified and unmodified elements gives us the expression for a DFT/MRCI diagonal matrix element

$$\begin{aligned}&\langle \omega w|\hat{\mathcal{H}}^{\mathrm{DFT}} - E^{\mathrm{KS}}|\omega w\rangle \\ &= \langle \omega w|\hat{\mathcal{H}}^{\mathrm{CI}}|\omega w\rangle - E^{\mathrm{HF}} - \sum_i \Delta w_i F_{ii}^{\mathrm{HF}} + \sum_i \Delta w_i F_{ii}^{\mathrm{KS}} + \Delta E_{\mathrm{DFTMRCI}}\end{aligned} \tag{4}$$

where $\hat{\mathcal{H}}^{\mathrm{DFT}}$ denotes the modified Hamiltonian and $\Delta E_{\mathrm{DFTMRCI}}$ collects all empirical correction terms. Note that $-E^{\mathrm{HF}}$ and $-\sum_i \Delta w_i F_{ii}^{\mathrm{HF}}$ occur in $\langle \omega w|\hat{\mathcal{H}}^{\mathrm{CI}}|\omega w\rangle$ with opposite signs and cancel out. The two-electron correction terms collected in $\Delta E_{\mathrm{DFTMRCI}}$ constitute the major difference between the DFT/MRCI Hamiltonians and will be presented in the following. For the original Hamiltonian,[1] $\Delta E_{\mathrm{DFTMRCI}}$ is given by

$$\Delta E_{\mathrm{DFTMRCI}} = \frac{1}{n_{\mathrm{exc}}}\sum_{i\in c}^{n_{\mathrm{exc}}}\sum_{j\in a}^{n_{\mathrm{exc}}}(p_J V_{ijij} - {}^m p[N_o]V_{ijji}) \tag{5}$$

with p_J as the parameter for Coulomb- and ${}^m p[N_o]$ as the parameter for exchange-integral scaling. n_{exc} labels the excitation class and c and a denote creation and annihilation operators, respectively. ${}^m p[N_o]$ depends on the number of open shells N_o and takes different forms depending on the multiplicity m. The general idea of the original Hamiltonian is to express the correction term as an averaged sum of single excitation contributions. Note that this is also reflected in the summation over creation and annihilation operators applied to the anchor configuration. This is in contrast to the formulation in eq 1, where the summation is over orbitals. While the summation over operators has been partially retained in the redesigned Hamiltonians, although for different reasons, we chose to return to the summation over orbitals. The reason for this choice will become apparent shortly. In contrast to the original Hamiltonian, the redesigned Hamiltonians R2016,[2] R2017,[4] and R2018[5] correct the integrals according to their occurrence in the ab initio diagonal element. Furthermore, the dependency on a closed-shell anchor configuration and the multiplicity depend-

https://doi.org/10.1021/acs.jpca.2c07951
J. Phys. Chem. A 2023, 127, 2011−2025

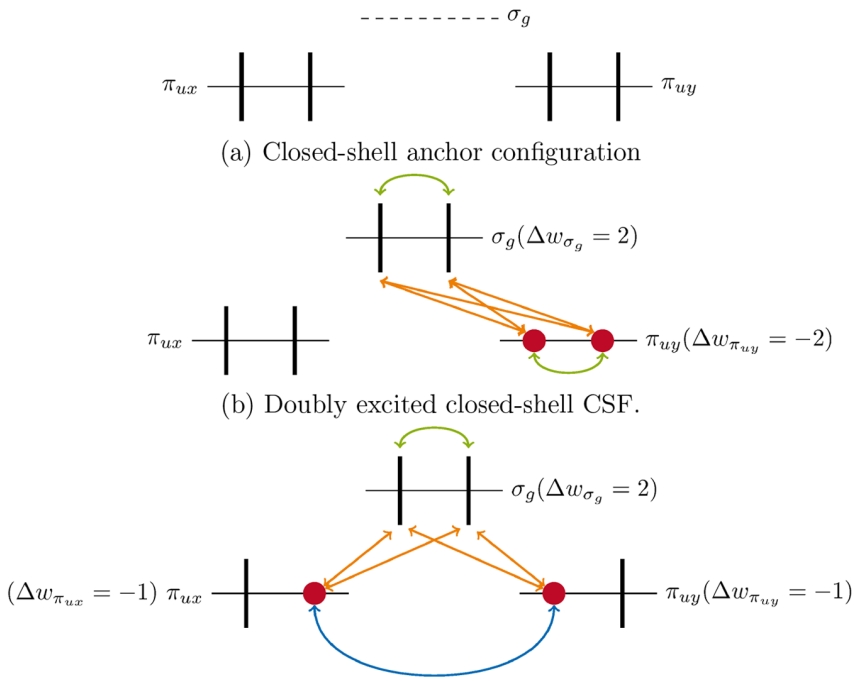

Figure 1. Possible double excitations in the valence orbitals of diatomic carbon. The black, thick, vertical lines symbolize electrons, the red circles symbolize holes. Interorbital interactions between electrons and holes are symbolized with a blue arrow. Intraorbital interactions between electrons or holes are marked with a green arrow, while the interactions between holes and electrons are symbolized with an orange arrow. In the parentheses, the change of occupation number, Δw_i w.r.t. the anchor configuration is given.

ence of the parameters were lifted. The R2017 and R2018 diagonal corrections are given by

$$\Delta E_{\mathrm{DFTMRCI}} = p_J\left(-\sum_{\substack{i,j\in c\\ i>j}}^{n_{\mathrm{exc}}} V_{ijij} - \sum_{\substack{i,j\in a\\ i>j}}^{n_{\mathrm{exc}}} V_{ijij} + \sum_{i\in c}^{n_{\mathrm{exc}}}\sum_{j\in a}^{n_{\mathrm{exc}}} V_{ijij} + \frac{1}{2}\sum_{i\in s}^{n_{\mathrm{single}}} V_{iiii}|\Delta w_i|\right) - p_x\left(\frac{1}{2}\sum_{i\in c}^{n_{\mathrm{exc}}}\sum_{j\in a}^{n_{\mathrm{exc}}} V_{ijji} - \frac{1}{2}\sum_{\substack{i\in c\\ j\in c,s}} V_{ijji} - \frac{1}{2}\sum_{\substack{i\in a\\ j\in a,s}} V_{ijji} + \sum_{\substack{i,j\in o\\ i>j}}^{N_o} V_{ijji}\eta_{ij}^{ji}\right) \tag{6}$$

Here, s denotes an open shell in the anchor configuration and p_x is the exchange integral correction parameter. Since the only difference to the R2016 formulation is the summations over the singly occupied orbitals in the anchor configuration, we refrain from repeating it here.

Derivation of the New Hamiltonian. In the newly proposed R2022 Hamiltonian, the two-electron correction parameters p_J and p_x of the former Hamiltonians are subdivided into cases in which different interactions are considered. The proposed ansatz is motivated by the physical nature of these interactions, which were averaged (eq 5) or not considered (eq 6) in previous formulations. We will illustrate the underlying idea with an example. Consider four electrons in three orbitals and an exemplary double excitation between them. As sketched in the valence MO diagram of diatomic carbon shown in Figure 1, one can roughly divide this situation into two cases, depicted in Figure 1b and c.

In one case, the two particles and holes, both reside in the same spatial orbital, leading to an intraorbital interaction (green arrows in Figure 1b). In the other case, the two particles and holes, reside in different spatial orbitals, leading to an interorbital interaction (blue arrows in Figure 1c). Dynamical correlation effects are expected to be larger in the intraorbital case, since the averaged distance between the interacting quantities is expected to be smaller, hence, the interaction is short-ranged. Therefore, it is advisable to use different scaling parameters for these interactions in the DFT/MRCI Hamiltonian. To derive an expression for such parameters, it is instructive to equip the expressions for the ab inito matrix elements with an arbitrary set of parameters q

$$\begin{aligned}\langle \omega w|\hat{\mathcal{H}}^{\mathrm{DFT}}|\omega w\rangle = {} & \sum_i F_{ii}\Delta w_i + \frac{1}{2}(1-q_J^{he}) \sum_{\substack{i\neq j\\ \Delta w_i\Delta w_j<0}} V_{ijij}\Delta w_i\Delta w_j \\ & + \frac{1}{2}(1-q_J^{hhee}) \sum_{\substack{i\neq j\\ \Delta w_i\Delta w_j>0}} V_{ijij}\Delta w_i\Delta w_j \\ & + \frac{1}{2}(1-q_x^{he}) \sum_{\substack{i\neq j\\ \Delta w_i\Delta w_j<0}} V_{ijji}\left(-\frac{1}{2}\Delta w_i\Delta w_j + \frac{1}{2}w_iw_j - w_i + \eta_{ij}^{ji}\right) + \frac{1}{2}(1-q_x^{hhee}) \sum_{\substack{i\neq j\\ \Delta w_i\Delta w_j>0}} V_{ijji} \\ & \times\left(-\frac{1}{2}\Delta w_i\Delta w_j + \frac{1}{2}w_iw_j - w_i + \eta_{ij}^{ji}\right) \\ & + \frac{1}{2}(1-q_J^{eeee}) \sum_i V_{iiii}\left(\frac{1}{2}\Delta w_i\Delta w_i + \frac{1}{2}w_iw_i - w_i\right)\end{aligned} \tag{7a}$$

https://doi.org/10.1021/acs.jpca.2c07951
J. Phys. Chem. A 2023, 127, 2011−2025

$$\langle \omega w|\hat{\mathcal{H}}^{\mathrm{DFT}}|\omega' w'\rangle = q_1 \cdot \langle \omega w|\hat{\mathcal{H}}^{\mathrm{CI}}|\omega' w'\rangle \tag{7b}$$

where we have split the second and third sums in eq 1 according to the signs of the $\Delta w_i \Delta w_j$ terms in eq 7a because they represent different cases, as illustrated in Figure 1. If two electrons are annihilated in different spatial orbitals, one will always get a positive sign (Figure 1c). This case is labeled *hhee*, where *h* denotes an electron hole and *e* denotes a particle. The other possible case (Figure 1b) in which electrons annihilated in the same spatial orbital, always leads to a negative sign and is labeled *he*.

To yield an expression for the parameters in eq 7, we will investigate the doubly degenerate $1\,^1\Delta_g$ state of diatomic carbon. The valence configuration in its $^1\Sigma_g^+$ ground state is given as $\pi_{u_x}^2 \pi_{u_y}^2 \sigma_g^0$. In a first approximation, one component Θ_1 is built from a linear combination of the two CSFs $|xx\rangle$ and $|yy\rangle$, whose spatial configurations are given by $\pi_{u_x}^2 \pi_{u_y}^0 \sigma_g^2$ and $\pi_{u_x}^0 \pi_{u_y}^2 \sigma_g^2$. The other component Θ_2 contains one CSF $|xy\rangle$, whose spatial configuration is given as $\pi_{u_x}^1 \pi_{u_y}^1 \sigma_g^2$. The energetic degeneracy condition requires $E(\Theta_1) = E(\Theta_2)$. Contained in these two quantities are the matrix elements shown in eq 8 for a generalized Hamiltonian $\hat{\mathcal{H}}^{\mathrm{DFT}}$.

$$\begin{aligned} E(\Theta_1) &= \frac{1}{2}\langle xx|\hat{\mathcal{H}}^{\mathrm{DFT}}|xx\rangle + \frac{1}{2}\langle yy|\hat{\mathcal{H}}^{\mathrm{DFT}}|yy\rangle - \langle xx|\hat{\mathcal{H}}^{\mathrm{DFT}}|yy\rangle \\ &= \langle xx|\hat{\mathcal{H}}^{\mathrm{DFT}}|xx\rangle - \langle xx|\hat{\mathcal{H}}^{\mathrm{DFT}}|yy\rangle \end{aligned} \tag{8a}$$

$$E(\Theta_2) = \langle xy|\hat{\mathcal{H}}^{\mathrm{DFT}}|xy\rangle \tag{8b}$$

The energetic degeneracy condition thus becomes

$$\langle xy|\hat{\mathcal{H}}^{\mathrm{DFT}}|xy\rangle = \langle xx|\hat{\mathcal{H}}^{\mathrm{DFT}}|xx\rangle - \langle xx|\hat{\mathcal{H}}^{\mathrm{DFT}}|yy\rangle \tag{9}$$

where the right-hand side has been simplified, using $\langle xx|\hat{\mathcal{H}}^{\mathrm{DFT}}|xx\rangle = \langle yy|\hat{\mathcal{H}}^{\mathrm{DFT}}|yy\rangle$. Inserting the expressions for $\hat{\mathcal{H}}^{\mathrm{DFT}}$ (eq 7) into eq 9 and using the equality of terms $F_{xx} = F_{yy}$, $V_{x\sigma x\sigma} = V_{y\sigma y\sigma}$, and $V_{x\sigma\sigma x} = V_{y\sigma\sigma y}$ leads to

$$(1 - q_J^{hhee})V_{xyxy} + (1 - q_x^{hhee})V_{xyyx} = (1 - q_J^{eeee})V_{xxxx} - q_1 V_{xyyx} \tag{10}$$

In the ab initio case, the integrals are in a fixed relationship, i.e.,

$$V_{xyxy} + V_{xyyx} = V_{xxxx} - V_{xyyx} \Leftrightarrow V_{xyxy} + 2V_{xyyx} = V_{xxxx} \tag{11}$$

Using this relation, we can eliminate one Coulomb integral in eq 10, giving

$$\begin{aligned} &(1 - q_J^{hhee})V_{xyxy} + (1 - q_x^{hhee})V_{xyyx} = (1 - q_J^{eeee})(V_{xyxy} + 2V_{xyyx}) - q_1 V_{xyyx} \\ &\Leftrightarrow (-q_J^{hhee} + q_J^{eeee})V_{xyxy} = (2\cdot(1 - q_J^{eeee}) - (1 - q_x^{hhee}) - q_1)V_{xyyx} \end{aligned} \tag{12}$$

The degeneracy condition can only be fulfilled if the expressions in the parentheses vanish, yielding the following relations:

$$q_J^{hhee} = q_J^{eeee} \tag{13a}$$

$$q_1 = 1 - 2q_J^{eeee} + q_x^{hhee} = 1 - 2q_J^{hhee} + q_x^{hhee} \tag{13b}$$

The consequences of the equalities in eq 13 are 2-fold. From eq 13a it follows that the parameters scaling the interorbital interactions between two created or two annihilated electrons (blue arrows Figure 1c) need to be treated in the same way as the intraorbital interactions between two created or two annihilated electrons (green arrows Figure 1c). Furthermore, it is evident from eq 13b that a fixed relation between the off-diagonal scaling parameter q_1 in eq 7b and the arbitrary diagonal correction parameters exists. Introducing the canonical KS orbital energies and the KS energy in the spirit of the DFT/MRCI ansatz (eq 4) and returning to the p_J/p_x nomenclature of the former Hamiltonians gives us the final expressions for the diagonal matrix elements of the R2022 Hamiltonian

$$\begin{aligned} \langle \omega w|\hat{\mathcal{H}}^{\mathrm{DFT}}|\omega w\rangle = {} & E^{\mathrm{KS}} + \sum_i F_{ii}^{\mathrm{KS}} \Delta w_i + \frac{1}{2}(1 - p_J^{he}) \sum_{\substack{i\neq j \\ \Delta w_i \Delta w_j < 0}} V_{ijij} \Delta w_i \Delta w_j \\ & + \frac{1}{2}(1 - p_J^{hhee}) \sum_{\substack{i\neq j \\ \Delta w_i \Delta w_j > 0}} V_{ijij} \Delta w_i \Delta w_j \\ & + \frac{1}{2}(1 - p_x^{he}) \sum_{\substack{i\neq j \\ \Delta w_i \Delta w_j < 0}} V_{ijji}\left(-\frac{1}{2}\Delta w_i \Delta w_j + \frac{1}{2} w_i w_j - w_i + \eta_{ij}^{ji}\right) \\ & + \frac{1}{2}(1 - p_x^{hhee}) \sum_{\substack{i\neq j \\ \Delta w_i \Delta w_j > 0}} V_{ijji} \times \left(-\frac{1}{2}\Delta w_i \Delta w_j + \frac{1}{2} w_i w_j - w_i + \eta_{ij}^{ji}\right) \\ & + \frac{1}{2}(1 - p_J^{eeee}) \sum_{i\notin s} V_{iiii}\left(\frac{1}{2}\Delta w_i \Delta w_i + \frac{1}{2} w_i w_i - w_i\right) \\ & + \frac{1}{4}(1 - p_J^{he}) \sum_{i\in s} V_{iiii}|\Delta w_i| + \frac{1}{4} p_x^{he} \sum_{\substack{i\neq j \\ \Delta w_i \Delta w_j < 0 \\ i,j\notin s}} V_{ijji} \Delta w_i \Delta w_j \end{aligned} \tag{14}$$

and a relation between them on the one side and the off-diagonal matrix elements on the other side for the case where the interacting configurations w and w' are energetically degenerate. The last term in eq 14 constitutes a correction term necessary to compute accurate results for triplet states. A thorough discussion of this term is given by Lyskov et al.[2]

To be consistent with the corrections in the diagonal elements, the parameter p_x scaling the matrix elements between different CSFs of the same configuration in the redesigned Hamiltonians is partitioned into p_x^{hhee} and p_x^{he} for R2022 in the same fashion, yielding

$$\begin{aligned} \langle w\omega|\hat{\mathcal{H}}^{\mathrm{DFT}}|w\omega'\rangle = {} & \frac{1}{2}(1 - p_x^{he}) \sum_{\substack{i\neq j \\ \Delta w_i \Delta w_j < 0}} V_{ijji} \eta_{ij}^{ji} + \frac{1}{2}(1 - p_x^{hhee}) \\ & \times \sum_{\substack{i\neq j \\ \Delta w_i \Delta w_j > 0}} V_{ijji} \eta_{ij}^{ji} \end{aligned} \tag{15}$$

Matrix elements coupling different configurations are scaled and damped in the R2022 Hamiltonian according to

$$\langle w\omega|\hat{\mathcal{H}}^{\mathrm{DFT}}|w'\omega'\rangle = p_1 \cdot \exp(-p_2 \cdot \Delta E_{ww'}^4) \cdot \langle w\omega|\hat{\mathcal{H}}^{\mathrm{CI}}|w'\omega'\rangle \tag{16}$$

where

$$p_1 = 1 - 2p_J^{hhee} + p_x^{hhee} \tag{17}$$

and $\Delta E_{ww'}$ denotes the energy difference between the diagonal elements of two interacting configurations. The energy-dependent damping is needed in the first place because interactions between two energetically distant CSFs contribute to the dynamical correlation, which is accounted for in DFT as well. The discussion of the degeneracy requirements for the $^1\Delta_g$ components of the C_2 molecule has taught us, however, that the

https://doi.org/10.1021/acs.jpca.2c07951
J. Phys. Chem. A 2023, 127, 2011−2025

parameter p_1 scaling the off-diagonal DFT/MRCI matrix elements ought not to be treated as an indepedent fit parameter. To avoid symmetry breaking of the $^1\Delta_g$ state, we eliminate p_1 in eq 16 and replace it by diagonal correction parameters yielding the final expression for the off-diagonal R2022 matrix elements

$$\langle w\omega|\hat{\mathcal{H}}^{\mathrm{DFT}}|w'\omega'\rangle = (1 - 2p_J^{hhee} + p_x^{hhee})\cdot\exp(-p_2\cdot\Delta E_{ww'}^4)\cdot\langle w\omega|\hat{\mathcal{H}}^{\mathrm{CI}}|w'\omega'\rangle \tag{18}$$

As the attentive reader might have noticed, the damping function used in eq 18 is similar to the one used in the original Hamiltonian. For the R2018 Hamiltonian, a damping function of the form $p_1\cdot\exp(-p_2\cdot\Delta E_{ww'}^6)$ had been used because the parametrization of the redesigned Hamiltonians in conjunction with an exponential damping depending on $\Delta E_{ww'}^4$ led to a too steep decline in the region of $\Delta E = 0.45E_h$. Comparison of the damping function profiles of the DFT/MRCI Hamiltonians (Figure 2), parametrized for a standard selection threshold E_{sel}

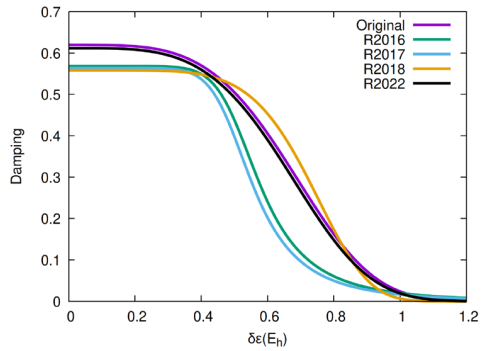

Figure 2. Damping decay for different Hamiltonians for the standard selection threshold $E_{sel} = 1.0E_h$ as a function of the energy difference.

of $1.0E_h$, shows that this is not the case for the R2022 Hamiltonian. Therefore, we decided to switch back to the function used in the original Hamiltonian.

A major advantage of the new formulation is that all terms contributing to the ab initio diagonal elements (eq 1) are corrected, which was not the case for the previous DFT/MRCI Hamiltonians. Let us consider the occurrence of the $V_{\pi_{ux}\pi_{uy}\pi_{uy}\pi_{ux}}$ term, i.e., the exchange interaction between the π electrons in Figure 1c, in the diagonal matrix elements. In this particular case, $w_{\pi_{ux}} = w_{\pi_{uy}} = 1$, and $\Delta w_{\pi_{ux}} = \Delta w_{\pi_{uy}} = -1$, since we start from a closed-shell anchor configuration (Figure 1a). The ab initio matrix element (eq 1) thus becomes

$$\begin{aligned} &V_{\pi_{ux}\pi_{uy}\pi_{uy}\pi_{ux}}\left(-\frac{1}{2}\Delta w_{\pi_{ux}}\Delta w_{\pi_{uy}} + \frac{1}{2}w_{\pi_{ux}}w_{\pi_{uy}} - w_{\pi_{ux}} + \eta_{\pi_{ux}\pi_{uy}}^{\pi_{uy}\pi_{ux}}\right) \\ &= V_{\pi_{ux}\pi_{uy}\pi_{uy}\pi_{ux}}\left(-\frac{1}{2}(-1)(-1) + \frac{1}{2}(1)(1) - (1) + \eta_{\pi_{ux}\pi_{uy}}^{\pi_{uy}\pi_{ux}}\right) \\ &= V_{\pi_{ux}\pi_{uy}\pi_{uy}\pi_{ux}}(-1 + \eta_{\pi_{ux}\pi_{uy}}^{\pi_{uy}\pi_{ux}}) \end{aligned} \tag{19}$$

where the symmetry relations between the integrals have been exploited. Evaluating the correction terms for this same example of the redesigned Hamiltonians of eq 6 shows that only one term

$$-p_x V_{\pi_{ux}\pi_{uy}\pi_{uy}\pi_{ux}}\eta_{\pi_{ux}\pi_{uy}}^{\pi_{uy}\pi_{ux}} \tag{20}$$

contributes, because the occupation numbers and their respective changes are not included in the correction. The missing term in comparison to eq 19 is apparent right away. Carrying out the same calculation for the R2022 Hamiltonian yields

$$\begin{aligned} &-p_x^{hhee}V_{\pi_{ux}\pi_{uy}\pi_{uy}\pi_{ux}}\left(-\frac{1}{2}\Delta w_{\pi_{u_x}}\Delta w_{\pi_{u_y}} + \frac{1}{2}w_{\pi_{u_x}}w_{\pi_{u_y}} - w_{\pi_{u_x}} + \eta_{\pi_{ux}\pi_{uy}}^{\pi_{uy}\pi_{ux}}\right) \\ &= -p_x^{hhee}V_{\pi_{ux}\pi_{uy}\pi_{uy}\pi_{ux}}\left(-\frac{1}{2}(-1)(-1) + \frac{1}{2}(1)(1) - (1) + \eta_{\pi_{ux}\pi_{uy}}^{\pi_{uy}\pi_{ux}}\right) \\ &= -p_x^{hhee}V_{\pi_{ux}\pi_{uy}\pi_{uy}\pi_{ux}}(-1 + \eta_{\pi_{ux}\pi_{uy}}^{\pi_{uy}\pi_{ux}}) \end{aligned} \tag{21}$$

where all integrals occurring in eq 19 are corrected. We want to stress again that, contrary to previous formulations,[1,2,4,5] the corrections in eq 14 are expressed in terms of molecular orbitals instead of annihilated and created electrons. This formulation emphasizes the influence of each term in the diagonal element and ensures that no integral is left uncorrected.

Computational Details. For most of the molecules contained in the fitting or assessment sets, the nuclear coordinates were taken from previous works[2,4,5,10,17,47] (see section S4 of the SI for further information). The geometries of the remaining compounds were optimized using the using the Turbomole package.[48,49] Unless stated otherwise, the optimizations were carried out on the DFT level employing the B3-LYP functional[50−52] together with Grimme's D3 correction[53] with Becke and Johnson damping.[54] The BH-LYP[55] functional in conjunction with a basis of triple-ζ quality, was used to generate the one-particle basis for DFT/MRCI calculations, except for some transition metals and larger molecules. A complete list of the used basis sets can be found in Tables S22−S25 of the SI. The orbital basis for molecules with doublet ground state was generated from restricted open-shell Kohn−Sham (ROKS) DFT calculations using the Dalton program.[56] The frozen (anti)core approximation has been applied throughout, consequently considering only orbitals with an energy ϵ of $-10.0E_h < \epsilon < 2.0E_h$. The reference space was generated iteratively using all configurations with coefficients larger than 0.003, starting from a carefully selected active space. A complete list of the starting active spaces can be found in Tables S27 and S28 of the SI. The number of selected configurations and CSFs is given in Tables S27 and S28 for the standard and tight selection thresholds, respectively.

Reference values for the assessment of the critical double excitation cases were generated using the second order fully internally contracted n-electron valence state perturbation theory (FIC-NEVPT2)[57−59] based on a complete-active space self-consistent field (CASSCF) wave function,[60−62] as implemented in the Orca 5.0[63] program. For all FIC-NEVPT2 calculations, the resolution of the identity (RI-JK) approximation was used. The auxiliary basis sets were generated using the AutoAux generation procedure.[64] In the state-averaging procedure, the required number of states from one irrep is used together with the ground state. The CAS spaces were set up to contain the most important orbitals as determined by a foregoing DFT/MRCI calculation. Further details on the CAS spaces can be found in Table S19 of the SI.

RESULTS AND DISCUSSION

Parameter Optimization. The parameters were optimized as described in ref 5. Using the Nelder−Mead simplex algorithm,[65] five parameters were fitted to give the lowest root mean-square deviation (RMSD) in the fitting set. The former fitting set was altered to reduce the computation time and to correct for errors, e.g., some doublet states were removed since

https://doi.org/10.1021/acs.jpca.2c07951
J. Phys. Chem. A 2023, 127, 2011−2025

their use in the parametrization was found to barely influence the resulting parameters, as one can see from the parameter differences in Table S1 between R2016 and R2017. All corrections made are indicated in the respective tables in the SI. To tune the newly introduced parameters for doubly excited states, 12 theoretical best estimates (TBEs) from Loos et al.[47] as well as two experimental energies of doubly excited states in hexatriene[66] and the magnesium atom[67] were added, leading to a training set comprising 55 singlet and 29 triplet states. A detailed list of all used states can be found in Tables S9−S18 of the SI. As in the case of the former Hamiltonians, two different parameter sets for the standard (E_{sel} = 1.0E_h) and the tight selection threshold (E_{sel} = 0.8E_h) were optimized (Table 1).

Table 1. Parameter Sets Optimized for the Standard and Tight Selection Thresholds of E_{sel} = 1.0E_h and E_{sel} = 0.8E_h

E_{sel} (E_h)	p_2	p_J^{he}	p_J^{hhee}	p_x^{he}	p_x^{hhee}
1.0	3.4673	0.5085	0.4649	0.3426	0.5416
0.8	4.5957	0.5051	0.4610	0.3375	0.5414

Note that the effective selection threshold T_{sel} for the inclusion of a configuration in the CI space is determined by adding the E_{sel} value to the excitation energy of the highest root in the reference space. Typical values for T_{sel} range between 1.2 and 1.35E_h for the standard parameter set and between 1.0 and 1.15E_h for the tight selection threshold.

The RMSDs and mean deviations of all states in the fitting set and its subsets are displayed in Figures 3 and 4. The corresponding numerical values are listed in Table S3 of the SI. The RMSDs and mean deviations of the singlet vertical excitations of all Hamiltonians are almost equal, with R2022 being slightly better than the other two. For triplet excited states, the performance of R2022 is marginally inferior. For the doubly excited states, R2022 vastly improves the performance of DFT/MRCI, lowering the RMSD from around 0.6 eV in R2016 and R2018 to 0.28 eV. Especially the description of $n^2 \rightarrow \pi^{*2}$ excitations are improved w.r.t. the other redesigned Hamiltonians. The largest differences are found in the excited state manifold of the C_2 molecule. Here, the two components of the $1^1\Delta_g$ state are at 0.77 and 0.85 eV in R2016, the energies being fairly similar for R2018, 1.86 and 2.28 eV for the original Hamiltonian, and 1.76 and 1.76 eV in R2022, while the TBE is at an excitation energy of 2.09 eV. Because the DFT/MRCI method is parametrized against experimental band maxima, in contrast to the TBEs from ab initio calculations of ref 68, it is expected and acceptable that the TBEs of the doubly excited state energies are slightly underestimated by the R2022 Hamiltonian. For the tight parameter set, the RMSDs are marginally inferior (Figure S1 and Table S4 of the SI).

General Assessment. Over the course of the development of R2016, R2017, and R2018, three different assessment sets had been assembled.[2,4,5] These contain 97 singlet and 63 triplet states of small metal-free compounds, 150 doublet states, and 67 states of transition metal complexes. To compare the performance of R2022 with the former Hamiltonians, all used states of these sets were combined, recomputed, and re-evaluated for all Hamiltonians. The RMSDs and mean deviations are visualized in Figures 5 and 6. A detailed list can be found in the SI (Tables S5−S8). We will start our analysis with the singlet and triplet assessment set by Lyskov et al.[2] The set contains $\pi \rightarrow \pi^*$, $n \rightarrow \pi^*$ as well as Rydberg vertical transition energies in small organic compounds and oxides. In comparison to the original set, some states were discarded, because they were already included in the parametrization set, leading to a total of 89 singlet and 50 triplet excitations. The overall performance remains the same for singlet and triplet states, which are dominated by singly excited configurations. For the doublet test set of Heil and Marian[4] the situation is similar. The set contains experimental values from photoelectron and electron absorption spectroscopy. Here R2022 performs as good as the other Hamiltonians without any outliers. Following the suggestion by Heil and Marian,[4] the transition metal complexes were subdivided into organometallic compounds, carrying organic ligands, and inorganic compounds comprising transition metal oxides, halides, cyanides and carbonyl complexes. The only modification to the inorganic assessment set is the exclusion of the CrF_6 molecule, since it is controversial whether this molecule is stable or not.[69,70] For the inorganic transition metal complexes, the results obtained with R2022 are improved w.r.t. R2018. This is mainly caused by a better description of the $\pi \rightarrow d^*/\pi^*$ ligand-to-metal charge

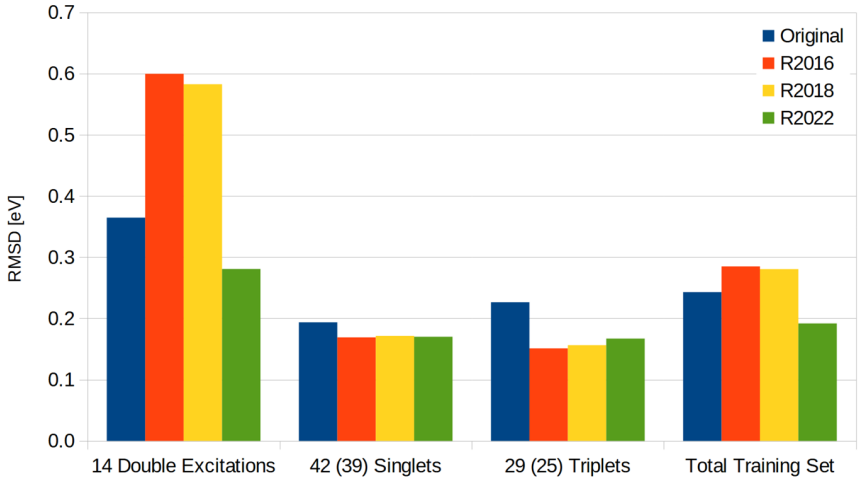

Figure 3. RMSD of the states in the fitting set sorted by type for the standard selection threshold of E_{sel} = 1.0E_h. R2016, R2018, and values for the original Hamiltonian are given for comparison. Doubly excited states are not included in the singlet or triplet subset. Values in brackets are the number of states for the original Hamiltonian, where dimer states were excluded. All values in eV.

https://doi.org/10.1021/acs.jpca.2c07951
J. Phys. Chem. A 2023, 127, 2011−2025

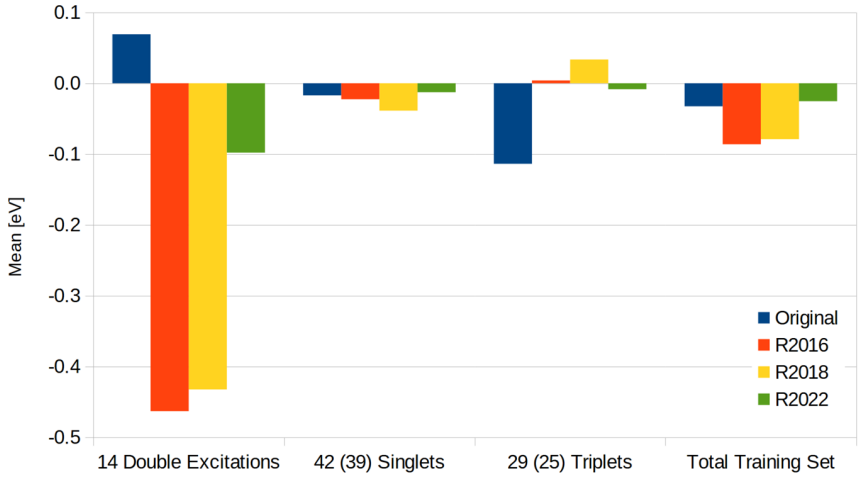

Figure 4. Mean deviation of the states in the fitting set sorted by type for the standard selection threshold of $E_{sel} = 1.0E_h$. R2016, R2018, and values for the original Hamiltonian are given for comparison. Doubly excited states are not included in the singlet or triplet subset. Values in brackets are the number of states for the original Hamiltonian, where dimer states were excluded. All values in eV.

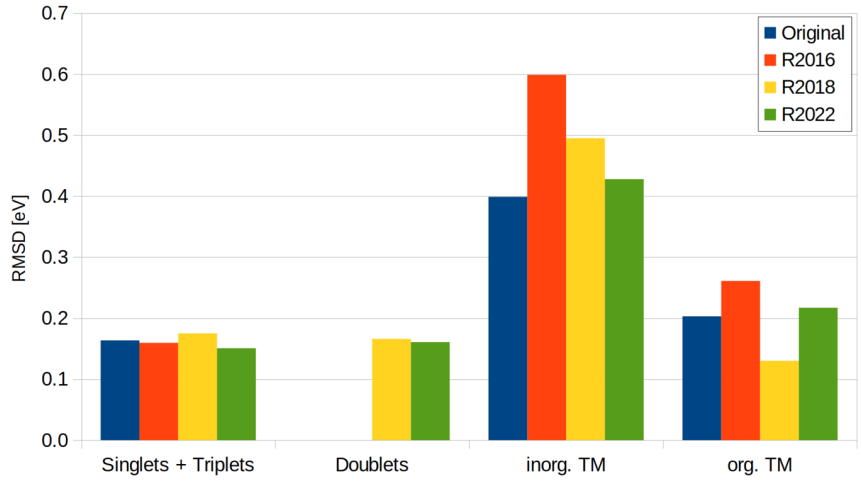

Figure 5. RMSD of the states in the assessment set sorted by type for the standard selection threshold of $\Delta E = 1.0E_h$. R2016, R2018, and values for the original Hamiltonian are given for comparison. Doubly excited states are not included in the singlet or triplet subset. All values in eV.

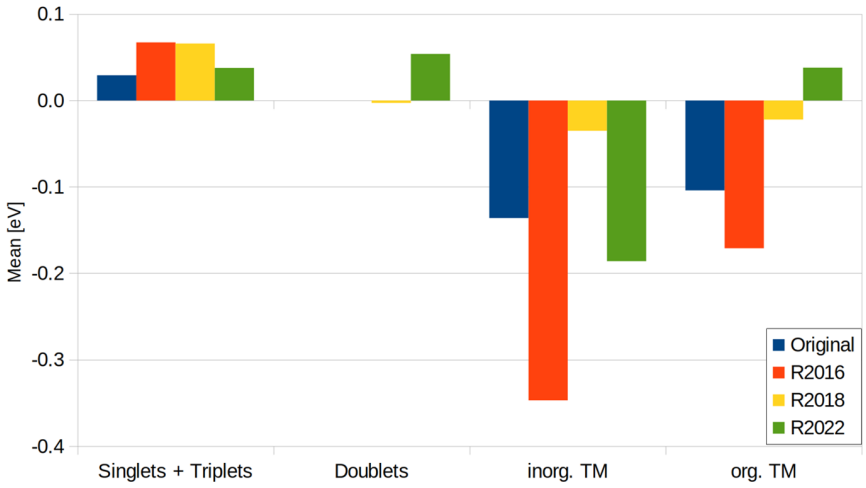

Figure 6. Mean deviation of the states in the assessment set sorted by type for the standard selection threshold of $\Delta E = 1.0E_h$. R2016, R2018, and values for the original Hamiltonian are given for comparison. Doubly excited states are not included in the singlet or triplet subset. All values in eV.

https://doi.org/10.1021/acs.jpca.2c07951
J. Phys. Chem. A 2023, 127, 2011−2025

transfer (LMCT) states in MnO_4^-, which could not be assigned in the R2018 assessment because of low-lying double excitations. In the case of organometallics, R2022 tends to slightly overestimate the excitation energy, which can be seen from the mean value given as 0.06 eV. This is in contrast to the marginal underestimation of the R2018 Hamiltonian, which yielded a mean value of −0.03 eV. Comparing the RMSDs for the two Hamiltonians, we find a comparable performance, with 0.19 eV for the R2022 and 0.14 eV for the R2018 Hamiltonian, respectively. All in all, the R2022 Hamiltonian performs better for the standard selection threshold as the previous Hamiltonians.

Basis Set Dependence of the DFT/MRCI Results. As stated above, typically an augmented TZVP basis set was used in the parametrization of the Hamiltonian. For large molecules, it might be necessary to choose smaller basis sets of valence double-ζ qualitiy, for example. The performance of the R2016 and R2022 Hamiltonians in conjunction with smaller basis sets was investigated for 27 $\pi \rightarrow \pi^*$ and $n \rightarrow \pi^*$ transitions taken from our training set. The used states are highlighted in Table S9. As can be seen in Figure 7, the here proposed R2022 Hamiltonian overestimates the vertical excitation energy by about 0.2 eV when a small basis set is used. The better performance of the R2016 Hamiltonian based on the SV(P) orbitals might be a bias to energy lowering by inclusion of doubly excited configurations in the former Hamiltonians. This bias can also lead to intruder states in the reference space, analogous to intruder states found in CAS-PT methods.[71−73] An extreme example can be found in the C_{60} molecule, whose spectra computed with the tight parameter set and various Hamiltonians, as well as two different basis sets, are shown in Figures S8−S10. The computed states were assigned according to the irreducible representations of the I_h ground state geometry and are shown in Table S21. The intruding doubly excited configurations in the reference space of R2016 lead to the unfortunate circumstance that only the first bright state is accessible, while the rest of the spectrum is spoiled with doubly substituted configurations of open shell character, preventing an assignment of higher excited states. Results obtained with the R2022 Hamiltonian do suffer from this problem as well, however not nearly as severely, and the second bright state is accessible. However, the state energies computed at the ground state geometry are overestimated by ≈0.6 eV using the R2022 Hamiltonian, compared to experimental band maxima. On the contrary the R2016 Hamiltonian shows good agreement with the energetic position of the experimental first bright state. We interpret this circumstance as an unfortunate loss of error cancellation in the new Hamiltonian. Although this does not fully explain the large deviation, a detailed analysis is subject of future work and will not be discussed here.

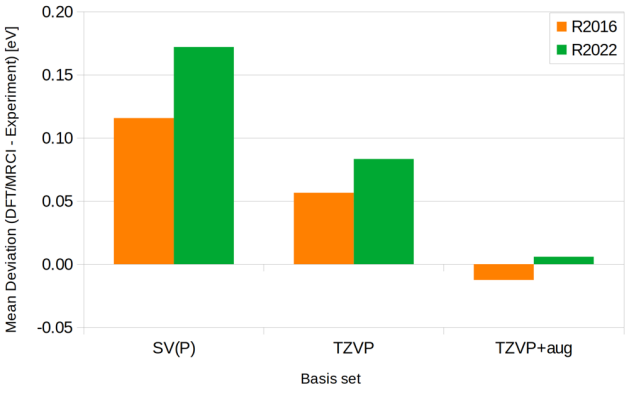

Figure 7. Mean deviation from experiment of 27 vertical excitation energies of $\pi \rightarrow \pi^*$ and $n \rightarrow \pi^*$ singlet transitions included in the training set computed using different basis sets. The used states were highlighted in Table S9.

Performance for Doubly Excited States. To assess the performance of the R2022 Hamiltonian for doubly excited states, it is useful to study its effect on the critical cases reported by Jovanović et al.[17] We decided to compare our results with vertical excitation energies calculated with NEVPT2, because this method was shown to give accurate excitation energies for doubly excited states.[47] As laid out in the Theory section, doubly excited states can be grouped into closed- and open-shell excitations (Figure 1).

Regarding the particular case of the C_2 molecule, we have shown that it is advisible to differentiate between intra- and interorbital interactions. While the original Hamiltonian does not consider the intraorbital interactions directly in its corrections, the redesigned Hamiltonians treat them on an equal footing as the interorbital ones and miss some corrections in open-shell cases (eq 20). Among the DFT/MRCI Hamiltonians, the here proposed R2022 Hamiltonian is the only one ensuring a balanced description of these cases per

Table 2. Vertical Excitation Energies in eV of Doubly Excited States[a]

molecule	state	character	NEVPT2	original	R2018	R2022
o-benzyne	$^1A_1$	$\pi, \pi' \rightarrow \pi^*, \pi^{*\prime}$	7.23	−2.99	−0.67	0.04
	$^1B_2$	$\pi, \pi' \rightarrow \pi^*, \pi^{*\prime}$	8.15	−2.41	−0.75	−0.04
	$^3A_1$	$\pi, \pi' \rightarrow \pi^*, \pi^{*\prime}$	7.12	−1.43	−0.61	0.03
thioformaldehyde	$^1A_1$	$n^2 \rightarrow \pi^{*2}$	7.37	0.58	−0.71	−0.44
	$^1A_2$	$n, \pi \rightarrow \pi^{*2}$	7.93	−0.74	−0.27	−0.28
	$^3A_2$	$n, \pi \rightarrow \pi^{*2}$	7.43	0.34	−0.20	−0.09
dithiosuccinimide	$^1A_1$	$n^2 \rightarrow \pi^{*2}$	5.85	0.22	−0.71	−0.36
	$^1A_1$	$n, n' \rightarrow \pi^*, \pi^{*\prime}$	7.13	−2.42	−3.65	0.33
	$^3B_2$	$n, n' \rightarrow \pi^{*2}$	5.86	−1.26	−2.34	0.37
	$^3A_1$	$n, n' \rightarrow \pi^*, \pi^{*\prime}$	6.99	−2.31	−3.49	0.40
nitromethane	$^3A'$	$n, n' \rightarrow \pi^{*2}$	8.79	−1.48	−2.35	0.60
dithiin	$^1A_1$	$\pi^2 \rightarrow \pi^{*2}$	4.91	−0.11	−0.20	0.17

[a]For the DFT/MRCI Hamiltonians the difference ΔE to the NEVPT2 results are given.

https://doi.org/10.1021/acs.jpca.2c07951
J. Phys. Chem. A 2023, 127, 2011−2025

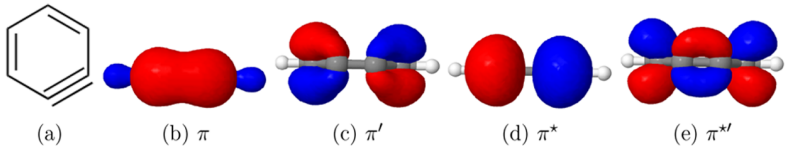

Figure 8. Chemical structure of *o*-benzyne and molecular orbitals involved in the $\pi, \pi' \rightarrow \pi^*, \pi^{*\prime}$ double excitation. The isosurface plots were generated with a cutoff of 0.05.

construction. As one can see from the results in Table 2, the new ansatz performs very well with regard to NEVPT2. A striking feature of the R2022 results is the drastically reduced number of outliers, compared to the other Hamiltonians. As can be seen from Table 2, the results obtained for the former DFT/MRCI Hamiltonians deviate strongly for the open-shell excitations, e.g., $\pi, \pi' \rightarrow \pi^*, \pi^{*\prime}$ in *o*-benzyne, while the difference to NEVPT2 is less in the closed-shell cases, e.g., $\pi^2 \rightarrow \pi^{*2}$ in dithiin. The R2022 Hamiltonian is of equal quality in both cases.

Comparing open-shell singlet and triplet excitations, e.g., the $^1A_1$ and $^3A_1$ exciations in *o*-benzyne in Table 2, it can be seen that the original Hamiltonian deviates less for the triplet state. This behavior is explained considering that the multiplicity-specific parameter sets are used for singlet and triplet excitations in the original Hamiltonian. Nevertheless, the deviations are large in the open-shell cases. These stem from the dependency of its diagonal exchange corrections on the number of open shells and the excitation class, as exemplified on the $^3B_2$ and $^3A_1$ exciations in dithiosuccinimide. The first is a state with two open shells N_o, while the latter has four open shells. The underestimation of the $^3A_1$ excitation is with −2.31 eV, almost twice as large as for the $^3B_2$ excitation. Considering the correction factor for diagonal elements in the original formulation $^3p_0[N_o] = \alpha N_o$ for triplets, we see that the increased error nicely corresponds to the N_o factor. A detailed discussion of the dependency of open shells in the original Hamiltonian can be found in the works of Lyskov et al.[2] or Jovanović et al.[17] The large deviations of the R2018 Hamiltonian in the dithiosuccinimide open-shell $^1A_1$ ($n, n' \rightarrow \pi^*, \pi^{*\prime}$) excitation can be explained by the missing exchange integral correction as outlined in the discussion of eq 20. We will illustrate this problem by comparing this case with the $\pi, \pi' \rightarrow \pi^*, \pi^{*\prime}$ excitation of *o*-benzyne, where the value computed with R2018 does not deviate as much. The excitation in *o*-benzyne occurs between the in-plane π/π^* orbitals and the out-of-plane $\pi'/\pi^{*\prime}$ orbitals, respectively, which are shown in Figure 8. Because the densities of the involved orbitals have negligible overlap, the interaction between a created electron in the out-of plane $\pi^{*\prime}$ orbital and the annihilated electron in the in-plane π-orbital will be close to zero. Analogously, the interaction between the created holes/particles will be close to zero. Therefore, the missing correction for the exchange intergrals does not influence the energy significantly.

In contrast, the exchange interaction of two electrons in the two *n* orbitals of dithiosuccinimide (Figure 9) will be much larger, because the associated densities overlap strongly. Therefore, the missing correction has a major impact on the excitation energy, which is found indeed.

The missing correction term is even more obvious considering the triplet excited states, e.g., $^3A_1$ excitation in dithiosuccinimide. This ought to be expected since electron exchange plays a larger role in these cases. Calculating the mean absolute errors (MAEs) for the cases in Table 2 yields a value of 0.26 eV for R2022, while for the original and the R2018

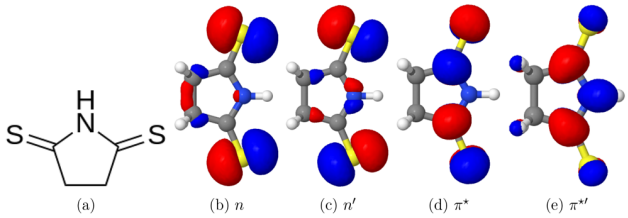

Figure 9. Chemical structure of dithiosuccinimide and molecular orbitals involved in the $n, n \rightarrow \pi^*, \pi^*$ excitation. The isosurface plots were generated with a cutoff of 0.05.

Hamitonians, the values are 1.34 and 1.39 eV, respectively. The RMSD of R2022 for all critical cases is 0.32 eV. The RMSDs for the original and R2018 Hamiltonians amount to 1.65 and 1.84 eV, respectively. Overall, we observe that the R2022 Hamiltonian notably reduces errors in doubly excited states and gives results comparable to NEVPT2, thus vastly outperforming the former Hamiltonians.

Extended π Systems. Polyacenes and carotenoids can be systematically extended to study the influence of doubly excited configurations on the energies of states. We will use the symmetry independent nomenclature introduced by Platt,[74] ^1L_a and ^1L_b, for the excited states of the investigated polyacenes. In the ^1L_a wave function, the $\pi_H \rightarrow \pi_L$ contribution prevails.[75,76] Its dominance remains essentially unaffected with increasing number of rings. Consequently, one would expect it to show a similar behavior as a particle in a box. This is indeed the case as can be seen from the curve generated from experimental values[9] shown Figure 10. The R2022 Hamiltonian reproduces this trend perfectly. Although the state does not change its main character, the R2016 curve starts to deviate from the experimental curve with increasing chain length. Clearly, the number of doubly excited configurations will increase with system size. Their

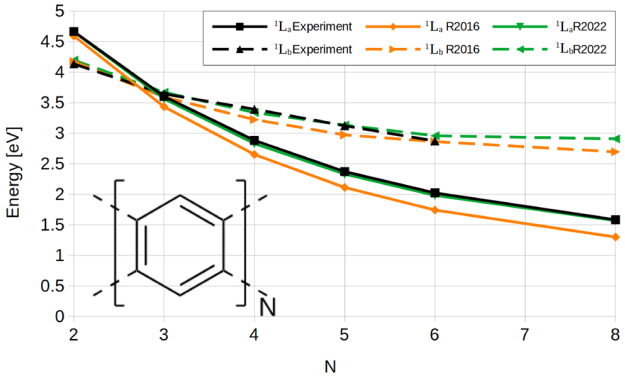

Figure 10. Calculated vertical excitation energies of polyacenes as a function of the number of rings *N*. Geometries and experimental values were taken from ref 9. The TZVP AO-basis was used for the DFT/MRCI calculation.

https://doi.org/10.1021/acs.jpca.2c07951
J. Phys. Chem. A 2023, 127, 2011−2025

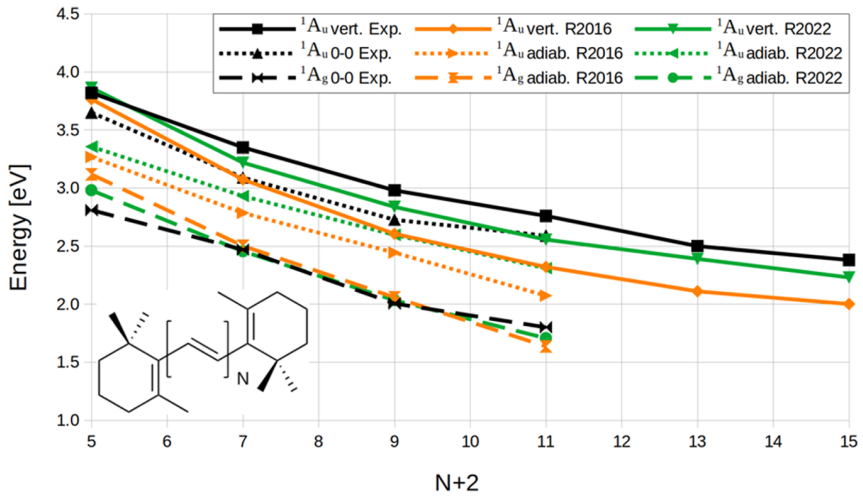

Figure 11. Calculated vertical and adiabatic excitation energies of *n*-carotenes as a function of the conjugation length *N*+2. Geometries and experimental values for mini-5-carotene to *β*-carotene were taken from ref 10. For M13 and M15, the geometries were optimized as described in ref 10 with B3-LYP/def-SV(P), and the experimental results were taken from ref 77. The def-SV(P) AO-basis was used for the DFT/MRCI calculation. The chemical structures of the molecules can be found in the SI, Figure S6.

diagonal elements are underestimated for the R2016 Hamiltonian, as outlined in the Theory section, thus explaining the increasing deviation from experiment. Comparing the R2022 energies of the ^1L_b state with the experimental curve, we find an excellent match again. This underpins the success of the new design strategy followed in this work.

Turning to carotenoids, we find a similar situation. Here, the low lying 2 ^1A_g state, which shows a pronounced double excitation character, and the optically bright 1 ^1A_u state, which is dominated by the $\pi_H \rightarrow \pi_L$ excitation, are investigated. The calculated vertical and adiabatic energies and the experimental values[10] are shown in Figure 11. On the abscissa, the conjugation length is given as $N + 2$, where N is the number of conjugated bonds in the polyene chain. This is done to stress that the double bonds in the terminal ionone groups are included. As discussed for the previous case, larger deviations with increasing number of double bonds are observed for former DFT/MRCI Hamiltonians, exemplified for the R2016 Hamiltonian in Figure 11. The deviations from experiment are approximately cut in half with the R2022 Hamiltonian, reducing the mean of the deviation from −0.23 to −0.10 eV.

To further support these findings and test the new Hamiltonian on a realistic example, the two extended carotenoids *β*-apo-8′-carotenal (BAC) and fucoxanthin (Fx) were investigated. Their chemical structures are shown in Figure 12. Both are found in the light-harvesting complexes of algae,

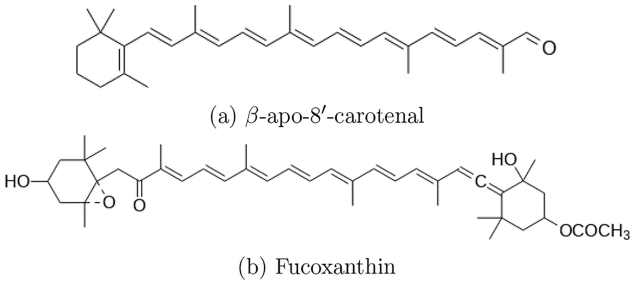

Figure 12. Chemical structures of *β*-apo-8′-carotenal and fucoxanthin.

showing efficient carotenoid to porphyrin energy transfer. A terminal allenic bond, a conjugated carbonyl group, an epoxy group and a backbone of eight conjugated double bonds bestow Fx a unique chemical structure and photophysics. In addition to the polyene-typical states, FX and BAC exhibit a low-lying $n \rightarrow \pi^*$ state close to the bright S_2 state due to the terminal aldehyde group on the polyene chain in the molecule. Here we want to give a very brief overview of the lowest excited states calculated at the ground state structure, since an exhaustive exploration of the excited state manifold is out of the scope of this work.

In Table 3, a comparison of excitation energies and oscillator strengths computed with R2016 and the newly developed R2022 Hamiltonian is shown. Difference density plots of the bright $\pi \rightarrow \pi^*$ and $n \rightarrow \pi^*$ states are displayed in Figure 13. The S_1 state exhibits strong contributions from doubly excited configurations, of which the $(\pi_H^2 \rightarrow \pi_L^2)$ excitation dominates and is delocalized along the polyene backbone. The bright S_2 state is mainly described by a $\pi_H \rightarrow \pi_L$ configuration and has a transition dipole directed along the polyene backbone.

In cyclohexane solution, the band maximum of this state is located at 2.61 eV in BAC.[79] As can be seen from Table 3 and the spectrum shown in Figure 14, the vertical excitation energy calculated with the R2016 Hamiltonian underestimates this value by around 0.2 eV. This is in line with the results shown in Figure 11 for *β*-carotenoids. The R2022 vertical excitation energy agrees well with the experimental result. Noteworthy is the ordering of the S_3 and S_4 states, which is reversed in R2016 and R2022. The S_3 state in the R2022 treatment results from a promotion of an electron from the in-plane nonbonding orbital at the carbonyl group to the polyene backbone and lies 0.2 eV above the S_2 state. A doubly excited state with two open shells consisting of $\pi_{H-1}\pi_H \rightarrow \pi_L^2$ and $\pi_H^2 \rightarrow \pi_L\pi_{L+1}$ is located 0.15 eV above the S_3 state. When the R2016 Hamiltonian is employed instead, this state is lowered in energy due to the open shell character of the double excitation and falls below the $n \rightarrow \pi^*$ state, which has the same energy in both Hamiltonians. For Fx, the situation is similar, as can be seen from Figure 15. The S_1 and S_2 states have the same character as in BAC and are located on the polyene backbone, too. Vertically, they are 0.2 and 0.1 eV

https://doi.org/10.1021/acs.jpca.2c07951
J. Phys. Chem. A 2023, 127, 2011−2025

Table 3. Vertical Excitation Energies and Oscillator Strengths of β-Apo-8′-Carotenal (BAC) and Fucoxanthin (Fx)[a]

molecule	state	character	R2016 (eV)	f (L)	R2022 (eV)	f (L)	exp. (eV)
β-apo-8′-carotenal	S_1	$\pi^2 \rightarrow \pi^{*2}$	2.14	0.26	2.41	0.35	
	S_2	$\pi \rightarrow \pi^*$	2.42	3.14	2.62	3.25	2.61[b]
	S_3	$n \rightarrow \pi^*$	2.83	0.00	2.82	0.00	
	S_4	$\pi, \pi' \rightarrow \pi^{*2}$	2.74	0.04	2.97	0.03	
fucoxanthin	S_1	$\pi^2 \rightarrow \pi^{*2}$	2.38	0.38	2.61	0.64	∼2.4[c]
	S_2	$\pi \rightarrow \pi^*$	2.56	3.25	2.74	3.11	2.74,[c] 2.76[d]
	S_3	$n \rightarrow \pi^*$	2.89	0.00	2.86	0.01	
	S_4	$\pi, \pi' \rightarrow \pi^{*2}$	3.00	0.00	3.19	0.00	

[a]Ground state geometry of Fx was taken from ref 78, while the geometry of BAC was optimized with B3LYP/def-SV(P). [b]Ref 79. [c]Ref 80. [d]Ref 81.

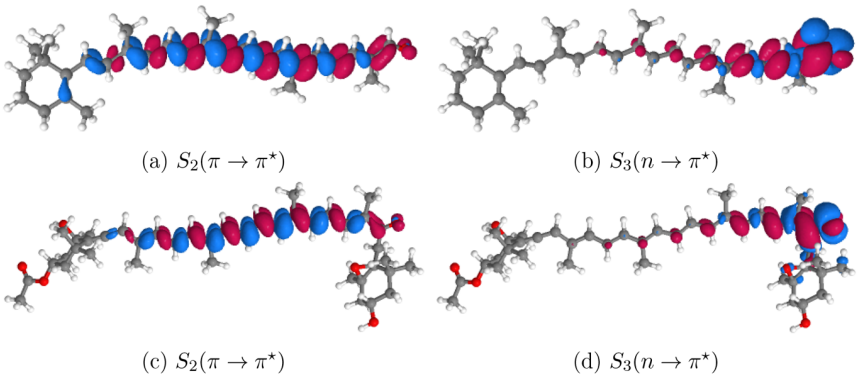

Figure 13. Difference densitiy plots (isosurface value of 0.001) between the ground and excited states of β-apo-8′-carotenal (top) and fucoxanthin (bottom). Blue (red) indicates a negative (positive) difference density. The state ordering was assigned on the basis of the R2022 results.

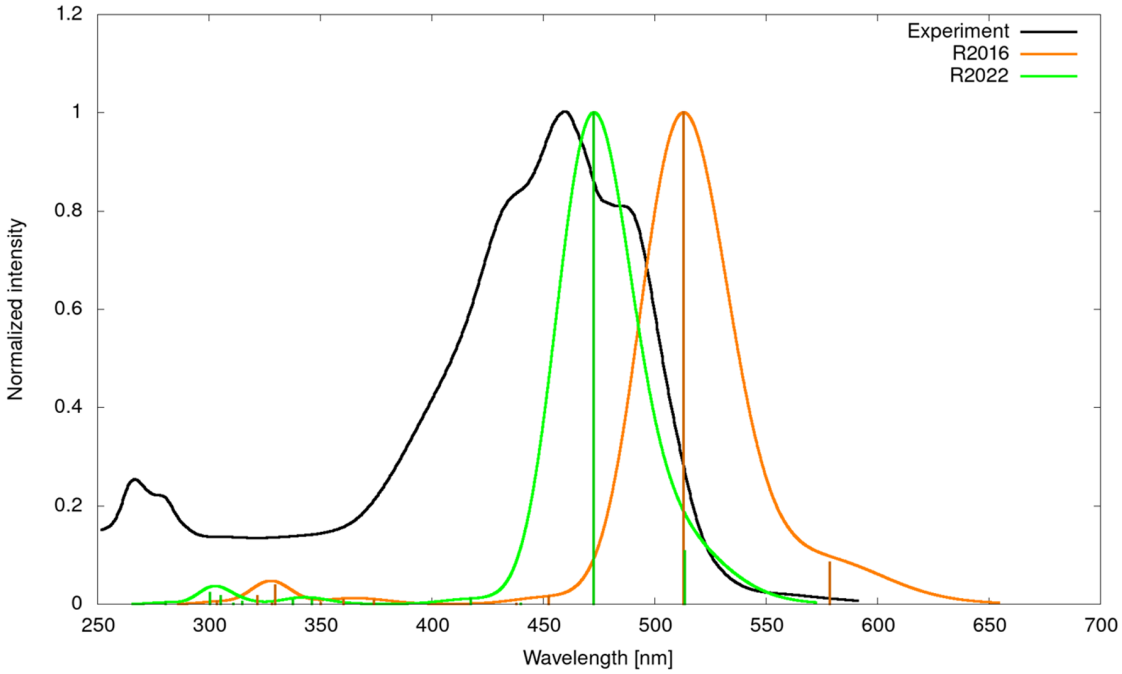

Figure 14. Calculated and experimental absorption spectrum of β-apo-8′-carotenal in cyclohexane solution. The calculated line spectrum was broadened by a Gaussian of 750 cm^{-1} full width at half-maximum. Note that the experimental spectrum, extracted from ref 79, shows a pronounced C−C stretching vibrational progression.

higher in energy compared to the states in BAC. The S_2 band maximum in tetrahydrofuran was experimentally determined at 2.74 eV[80] and in isopropanol at 2.76 eV.[81] Premvardhan et al.[80] estimated the energetic position of the dark S_1 state to be roughly around 2.4 eV from fluoresence studies. It is better predicted by R2016, contrary to the expectations. Since the R2016 Hamiltonian tends to underestimate these states in all previously discussed cases, this good agreement might be fortuitous. In comparison to BAC, the state ordering of the S_3 and S_4 states do not change. The S_3 state is the $n \rightarrow \pi^*$ transition

https://doi.org/10.1021/acs.jpca.2c07951
J. Phys. Chem. A 2023, 127, 2011−2025

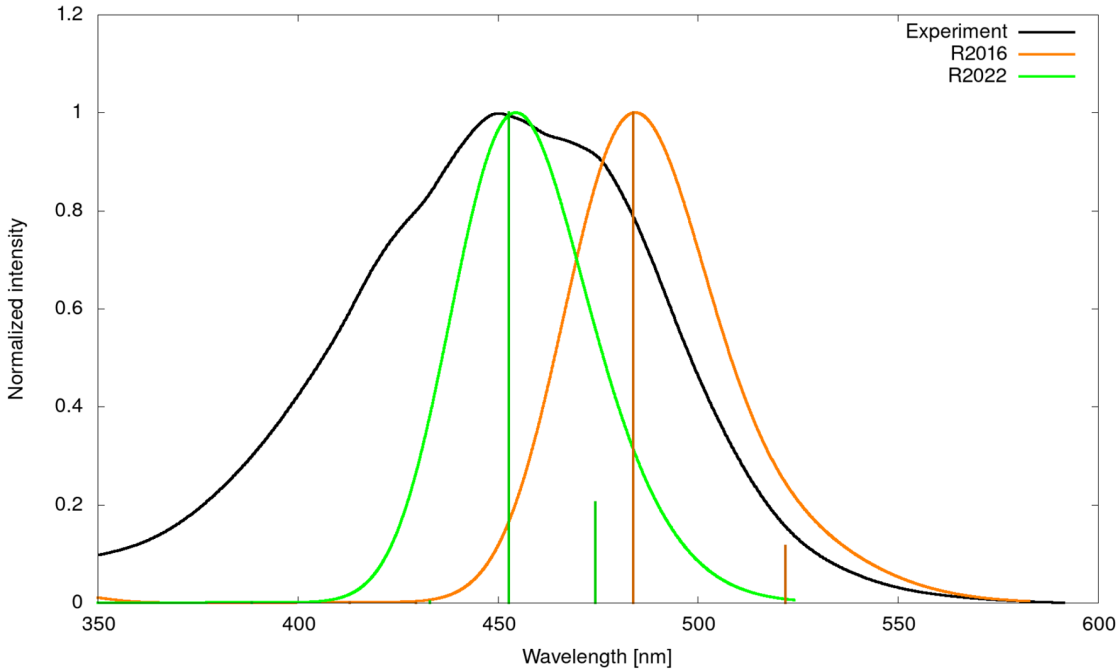

Figure 15. Calculated and experimental absorption spectrum of fucoxanthin in isopropanol solution. The calculated line spectrum was broadened by a Gaussian of 750 cm^{-1} full width at half-maximum. Note that the experimental spectrum, extracted from ref 81, shows a pronounced C−C stretching vibrational progression.

originating from the carbonyl group to the polyene backbone, while the S_4 is again the doubly excited $\pi_{H-1}\pi_H \rightarrow \pi_L^2$ state.

The phenalene derivatives heptazine and cycl[3.3.3]azine show an interesting excited state behavior. Due to the bipartite charge distribution in the HOMO and LUMO orbitals (Figure 16), the exchange interaction between π_H and π_L electrons

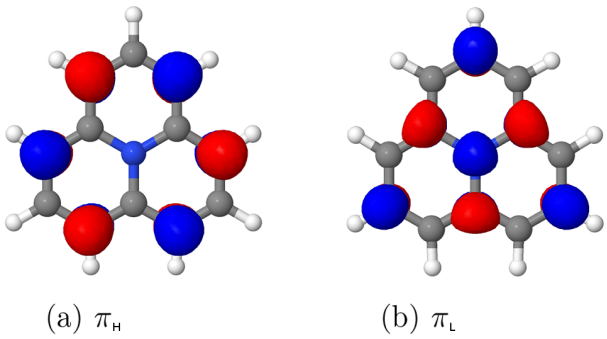

Figure 16. Frontier molecular orbitals of cycl[3.3.3]azine.

nearly vanishes, yielding a small S_1-T_1 gap. It was argued that double excitation contributions preferentially lower the S_1 energy and hence push it energetically below the T_1 state.[82−85] The inverted S_1-T_1 gap causes the reverse intersystem crossing to be a downhill process and therefore no thermal activation is needed. Results for heptazine, computed using the R2016 Hamiltonian were recently published by our group.[83] In this work we want to verify that an inverted S_1-T_1 gap is obtained with the new R2022 Hamiltonian as well. In Table 4, the excitation energies and resulting S_1-T_1 gaps computed at the ground state geometry of the respective molecules are given. The transitions are all dominated by single excitations of $\pi_H \rightarrow \pi_L$ character. As can be seen, the choice of the Hamiltonian hardly influences the determined S_1-T_1 gap in both molecules. However, the state energies are raised by approximately 0.15 eV, when using the R2022 Hamiltonian. This is might be a consequence of the different basis set behavior of the R2016 and R2022 Hamiltonian (vide supra).

These presented cases nicely illustrate the improvements gained with the new ansatz chosen in the R2022 Hamiltonian for double exciations. At the same time, they demonstrate that the good performance of the previous Hamiltonians for singly excited states is retained.

Table 4. Vertical Excitation Energies of Heptazine and Cycl[3.3.3]azine Calculated with Different Methods[a]

method	E_{S_1}	E_{T_1}	ΔE_{ST}
heptazine			
R2016	2.59	2.60	−0.01
R2022	2.74	2.78	−0.04
ADC(2)	2.57	2.85	−0.28
EOM-CCSD	2.78	2.96	−0.18
TDDFT/B3LYP	2.82	2.60	0.22
TDDFT/PBE0	2.92	2.68	0.24
cycl[3.3.3]azine			
R2016	0.96	0.97	−0.01
R2022	1.09	1.12	−0.03
ADC(2)	1.04	1.20	−0.16
EOM-CCSD	1.09	1.19	−0.10
TDDFT/B3LYP	1.26	1.05	0.21
TDDFT/PBE0	1.28	1.05	0.23

[a]The ADC(2), EOM-CCSD, and TDDFT results for heptazine and cycl[3.3.3]azine are taken from refs 82 and 84, respectively. All values in eV. The geometry of heptazine was taken from ref 83, while the geometry of cycl[3.3.3]azine was optimized with B3-LYP/TZVP.

https://doi.org/10.1021/acs.jpca.2c07951
J. Phys. Chem. A 2023, 127, 2011−2025

CONCLUSION

In this work, a new ansatz for the modification of the DFT/MRCI Hamiltonian has been presented. The ansatz remedies former errors made in the description of doubly excited and degenerate states. Especially the large underestimations of the $n^2 \rightarrow \pi^{*2}$ and $n, n' \rightarrow \pi^*, \pi^{*\prime}$ excitations in small organic compounds are removed, which is the largest improvement w.r.t. former approaches. Furthermore, it has been shown that for extended π-systems, specifically polyacenes and β-carotenoids, the description of the low-lying excited states gets much better. The experimental trends for the polyacenes are matched excellently, while the trends for the carotenoids are better reproduced compared to the redesigned Hamiltonians. The most important point to emphasize is that the new R2022 Hamiltonian leads to a balanced correction of ab initio CI-matrix elements, while losing nothing of the simplicity and strength of the DFT/MRCI method. This improvement is achieved with a moderate number of five parameters that have been derived in such a way that the underlying physics is reflected in the corrections at variance with former effective Hamiltonians used in DFT/MRCI. By requiring that the spatial components of the $^1\Delta$ state of C_2 remain degenerate, a fixed relationship between diagonal and off-diagonal scaling parameters was derived. As in previous formulations, the parametrization is independent of the particular chemical element and covers the most common multiplicities found in excited-state processes. Since the R2022 retains the same excellent performance for singly excited states as previous Hamiltonians, we conclude that the here presented formulation should be considered as the new standard for DFT/MRCI calculations. However, for small basis sets it might happen that the new ansatz overestimates excitation energies, although it was parametrized on experimental band maxima. A systematic study of the basis set behavior of the new Hamiltonian and DFT/MRCI in general is ongoing and will be the subject of future work.

ASSOCIATED CONTENT

Supporting Information

The Supporting Information is available free of charge at https://pubs.acs.org/doi/10.1021/acs.jpca.2c07951.

Statistical data, training data set, assessment data set, computational details, chemical structures of carotenoids, cycl[3.3.3]azine and heptazine, excitation energies, and spectra of C_{60} (PDF)

AUTHOR INFORMATION

Corresponding Author

Christel M. Marian − *Institute of Theoretical and Computational Chemistry, Heinrich-Heine-University Düsseldorf, 40225 Düsseldorf, Germany;* orcid.org/0000-0001-7148-0900; Email: christel.marian@hhu.de

Authors

Dennis R. Dombrowski − *Institute of Theoretical and Computational Chemistry, Heinrich-Heine-University Düsseldorf, 40225 Düsseldorf, Germany*

Timo Schulz − *Institute of Theoretical and Computational Chemistry, Heinrich-Heine-University Düsseldorf, 40225 Düsseldorf, Germany*

Martin Kleinschmidt − *Institute of Theoretical and Computational Chemistry, Heinrich-Heine-University Düsseldorf, 40225 Düsseldorf, Germany*

Complete contact information is available at: https://pubs.acs.org/10.1021/acs.jpca.2c07951

Notes

The authors declare no competing financial interest.

ACKNOWLEDGMENTS

Financial support by the Deutsche Forschungsgemeinschaft (DFG), Projects MA1051/14-2 and MA1051/19-1, is gratefully acknowledged.

REFERENCES

(1) Grimme, S.; Waletzke, M. A combination of Kohn-Sham density functional theory and multi-reference configuration interaction methods. *J. Chem. Phys.* **1999**, *111*, 5645−5655.

(2) Lyskov, I.; Kleinschmidt, M.; Marian, C. M. Redesign of the DFT/MRCI Hamiltonian. *J. Chem. Phys.* **2016**, *144*, 034104.

(3) Marian, C. M.; Heil, A.; Kleinschmidt, M. The DFT/MRCI method. *WIREs Comput. Mol. Sci.* **2019**, *9*, e1394.

(4) Heil, A.; Marian, C. M. DFT/MRCI Hamiltonian for odd and even numbers of electrons. *J. Chem. Phys.* **2017**, *147*, 194104.

(5) Heil, A.; Kleinschmidt, M.; Marian, C. M. On the performance of DFT/MRCI Hamiltonians for electronic excitations in transition metal complexes: The role of the damping function. *J. Chem. Phys.* **2018**, *149*, 164106.

(6) Grimme, S. *Rev. Comput. Chem.*; Wiley-Blackwell, 2004; Chapter 3, pp 153−218.

(7) Parusel, A. B. J.; Grimme, S. A Theoretical Study of the Excited States of Chlorophyll a and Pheophytin a. *J. Phys. Chem. B* **2000**, *104*, 5395−5398.

(8) Parusel, A. B. J.; Grimme, S. DFT/MRCI calculations on the excited states of porphyrin, hydroporphyrins, tetrazaporphyrins and metalloporphyrins. *J. Porphyr. Phthalocya.* **2001**, *05*, 225−232.

(9) Marian, C. M.; Gilka, N. Performance of the Density Functional Theory/Multireference Configuration Interaction Method on Electronic Excitation of Extended π-Systems. *J. Chem. Theory Comput.* **2008**, *4*, 1501−1515.

(10) Kleinschmidt, M.; Marian, C. M.; Waletzke, M.; Grimme, S. Parallel multireference configuration interaction calculations on mini-β-carotenes and β-carotene. *J. Chem. Phys.* **2009**, *130*, 044708.

(11) Knecht, S.; Marian, C. M.; Kongsted, J.; Mennucci, B. On the photophysics of carotenoids: A multireference DFT study of peridinin. *J. Phys. Chem. B* **2013**, *117*, 13808−13815.

(12) Andreussi, O.; Knecht, S.; Marian, C. M.; Kongsted, J.; Mennucci, B. Carotenoids and Light-Harvesting: From DFT/MRCI to the Tamm-Dancoff Approximation. *J. Chem. Theory Comput.* **2015**, *11*, 655−666.

(13) Heil, A.; Marian, C. M. DFT/MRCI-R2018 study of the photophysics of the zinc(II) tripyrrindione radical: non-Kasha emission? *Phys. Chem. Chem. Phys.* **2019**, *21*, 19857−19867.

(14) Spiegel, J. D.; Kleinschmidt, M.; Larbig, A.; Tatchen, J.; Marian, C. M. Quantum-Chemical Studies on Excitation Energy Transfer Processes in BODIPY-Based Donor-Acceptor Systems. *J. Chem. Theory Comput.* **2015**, *11*, 4316−4327.

(15) Lyskov, I.; Marian, C. M. Climbing up the ladder: Intermediate triplet states promote the reverse intersystem crossing in the efficient TADF emitter ACRSA. *J. Phys. Chem. C* **2017**, *121*, 21145−21153.

(16) Kaminski, J. M.; Rodriguez-Serrano, A.; Dinkelbach, F.; Miranda-Salinas, H.; Monkman, A. P.; Marian, C. M. Vibronic effects accelerate the intersystem crossing processes of the through-space charge transfer states in the triptycene bridged acridine-triazine donor-acceptor molecule TpAT-tFFO. *Chem. Sci.* **2022**, *13*, 7057−7066.

(17) Jovanović, V.; Lyskov, I.; Kleinschmidt, M.; Marian, C. M. On the performance of DFT/MRCI-R and MR-MP2 in spin-orbit coupling calculations on diatomics and polyatomic organic molecules. *Mol. Phys.* **2017**, *115*, 109−137.

(18) Smith, M. B.; Michl, J. Singlet Fission. *Chem. Rev.* **2010**, *110*, 6891−6936.

(19) Smith, M. B.; Michl, J. Recent Advances in Singlet Fission. *Annu. Rev. Phys. Chem.* **2013**, *64*, 361−386.
(20) Gray, V.; Dzebo, D.; Abrahamsson, M.; Albinsson, B.; Moth-Poulsen, K. Triplet-triplet annihilation photon-upconversion: Towards solar energy applications. *Phys. Chem. Chem. Phys.* **2014**, *16*, 10345−10352.
(21) Zimmerman, P. M.; Bell, F.; Casanova, D.; Head-Gordon, M. Mechanism for Singlet Fission in Pentacene and Tetracene: From Single Exciton to Two Triplets. *J. Am. Chem. Soc.* **2011**, *133*, 19944−19952.
(22) Casanova, D. Theoretical Modeling of Singlet Fission. *Chem. Rev.* **2018**, *118*, 7164−7207.
(23) Feng, X.; Krylov, A. I. On couplings and excimers: Lessons from studies of singlet fission in covalently linked tetracene dimers. *Phys. Chem. Chem. Phys.* **2016**, *18*, 7751−7761.
(24) Feng, X.; Casanova, D.; Krylov, A. I. Intra- and Intermolecular Singlet Fission in Covalently Linked Dimers. *J. Phys. Chem. C* **2016**, *120*, 19070−19077.
(25) C. A. Valente, D.; do Casal, M. T.; Barbatti, M.; Niehaus, T. A.; Aquino, A. J. A.; Lischka, H.; Cardozo, T. M. Excitonic and charge transfer interactions in tetracene stacked and T-shaped dimers. *J. Chem. Phys.* **2021**, *154*, 044306.
(26) Polívka, T.; Sundström, V. Ultrafast Dynamics of Carotenoid Excited States-From Solution to Natural and Artificial Systems. *Chem. Rev.* **2004**, *104*, 2021−2072.
(27) Hashimoto, H.; Uragami, C.; Yukihira, N.; Gardiner, A. T.; Cogdell, R. J. Understanding/unravelling carotenoid excited singlet states. *J. R. Soc. Interface* **2018**, *15*, 20180026.
(28) Tavan, P.; Schulten, K. The low-lying electronic excitations in long polyenes:A PPP-MRD-CI study. *J. Chem. Phys.* **1986**, *85*, 6602−6609.
(29) Tavan, P.; Schulten, K. Electronic excitations in finite and infinite polyenes. *Phys. Rev. B* **1987**, *36*, 4337−4358.
(30) Kurashige, Y.; Nakano, H.; Nakao, Y.; Hirao, K. The $\pi \rightarrow \pi^*$ excited states of long linear polyenes studied by the CASCI-MRMP method. *Chem. Phys. Lett.* **2004**, *400*, 425−429.
(31) Sashima, T.; Koyama, Y.; Yamada, T.; Hashimoto, H. The $1B_u^+$, $1B_u^-$, and $2A_g^-$ energies of crystalline lycopene, β-carotene, and mini-9-β-carotene as determined by resonance-Raman excitation profiles: Dependence of the $1B_u^-$ state energy on the conjugation length. *J. Phys. Chem. A* **2000**, *104*, 5011−5019.
(32) Fujii, R.; Inaba, T.; Watanabe, Y.; Koyama, Y.; Zhang, J.-P. Two different pathways of internal conversion in carotenoids depending on the length of the conjugated chain. *Chem. Phys. Lett.* **2003**, *369*, 165−172.
(33) Fujii, R.; Fujino, T.; Inaba, T.; Nagae, H.; Koyama, Y. Internal conversion of $1B_u^+ \rightarrow 1B_u^- \rightarrow 2A_g^-$ and fluorescence from the $1B_u^-$ state in all-trans-neurosporene as probed by up-conversion spectroscopy. *Chem. Phys. Lett.* **2004**, *384*, 9−15.
(34) Ostroumov, E.; Müller, M. G.; Marian, C. M.; Kleinschmidt, M.; Holzwarth, A. R. Electronic Coherence Provides a Direct Proof for Energy-Level Crossing in Photoexcited Lutein and β-Carotene. *Phys. Rev. Lett.* **2009**, *103*, 108302.
(35) Marek, M. S.; Buckup, T.; Motzkus, M. Direct Observation of a Dark State in Lycopene Using Pump-DFWM. *J. Phys. Chem. B* **2011**, *115*, 8328−8337.
(36) Yukihira, N.; Uragami, C.; Horiuchi, K.; Kosumi, D.; Gardiner, A. T.; Cogdell, R. J.; Hashimoto, H. Intramolecular charge-transfer enhances energy transfer efficiency in carotenoid-reconstituted light-harvesting 1 complex of purple photosynthetic bacteria. *Commun. Chem.* **2022**, *5*, 135.
(37) Diedrich, C.; Grimme, S. Systematic Investigation of Modern Quantum Chemical Methods to Predict Electronic Circular Dichroism Spectra. *J. Phys. Chem. A* **2003**, *107*, 2524−2539.
(38) Röder, A.; de Oliveira, N.; Grollau, F.; Mestdagh, J.-M.; Gaveau, M.-A.; Briant, M. Vacuum-Ultraviolet Absorption Spectrum of 3-Methoxyacrylonitrile. *J. Phys. Chem. A* **2020**, *124*, 9470−9477.
(39) Stojanović, L.; Alyoubi, A. O.; Aziz, S. G.; Hilal, R. H.; Barbatti, M. UV excitations of halons. *J. Chem. Phys.* **2016**, *145*, 184306.
(40) Khokhlov, D.; Belov, A. Ab Initio Study of Low-Lying Excited States of Carotenoid-Derived Polyenes. *J. Phys. Chem. A* **2020**, *124*, 5790−5803.
(41) Khokhlov, D.; Belov, A. Low-Lying Excited States of Natural Carotenoids Viewed by Ab Initio Methods. *J. Phys. Chem. A* **2022**, *126*, 4376−4391.
(42) Casanova, D.; Head-Gordon, M. Restricted active space spin-flip configuration interaction approach: theory, implementation and examples. *Phys. Chem. Chem. Phys.* **2009**, *11*, 9779−9790.
(43) Bettinger, H. F.; Tönshoff, C.; Doerr, M.; Sanchez-Garcia, E. Electronically Excited States of Higher Acenes up to Nonacene: A Density Functional Theory/Multireference Configuration Interaction Study. *J. Chem. Theory Comput.* **2016**, *12*, 305−312.
(44) Yang, Y.; Davidson, E. R.; Yang, W. Nature of ground and electronic excited states of higher acenes. *Proc. Natl. Acad. Sci. U.S.A.* **2016**, *113*, E5098−E5107.
(45) Segal, G. A.; Wetmore, R. W.; Wolf, K. Efficient methods for configuration interaction calculations. *Chem. Phys.* **1978**, *30*, 269−297.
(46) Wetmore, R. W.; Segal, G. A. Efficient generation of configuration interaction matrix elements. *Chem. Phys. Lett.* **1975**, *36*, 478−483.
(47) Loos, P.-F.; Boggio-Pasqua, M.; Scemama, A.; Caffarel, M.; Jacquemin, D. Reference Energies for Double Excitations. *J. Chem. Theory Comput.* **2019**, *15*, 1939−1956.
(48) TURBOMOLE V7.4 2019, a development of University of Karlsruhe and Forschungszentrum Karlsruhe GmbH, 1989−2007, TURBOMOLE GmbH, 2007; available from http://www.turbomole.com (visited on 01/23/23).
(49) Balasubramani, S. G.; Chen, G. P.; Coriani, S.; Diedenhofen, M.; Frank, M. S.; Franzke, Y. J.; Furche, F.; Grotjahn, R.; Harding, M. E.; Hättig, C.; et al. TURBOMOLE: Modular program suite for ab initio quantum-chemical and condensed-matter simulations. *J. Chem. Phys.* **2020**, *152*, 184107.
(50) Becke, A. D. Density-functional thermochemistry. III. The role of exact exchange. *J. Chem. Phys.* **1993**, *98*, 5648−5652.
(51) Stephens, P. J.; Devlin, F. J.; Chabalowski, C. F.; Frisch, M. J. *Ab initio* calculation of vibrational absorption and circular dichroism spectra using density functional force fields. *J. Phys. Chem.* **1994**, *98*, 11623−11627.
(52) Lee, C.; Yang, W.; Parr, R. G. Development of the Colle-Salvetti correlation-energy formula into a functional of the electron density. *Phys. Rev. B* **1988**, *37*, 785.
(53) Grimme, S.; Antony, J.; Ehrlich, S.; Krieg, H. A consistent and accurate ab initio parametrization of density functional dispersion correction (DFT-D) for the 94 elements H-Pu. *J. Chem. Phys.* **2010**, *132*, 154104.
(54) Grimme, S.; Ehrlich, S.; Goerigk, L. Effect of the damping function in dispersion corrected density functional theory. *J. Comput. Chem.* **2011**, *32*, 1456−1465.
(55) Becke, A. D. A new mixing of Hartree-Fock and local density-functional theories. *J. Chem. Phys.* **1993**, *98*, 1372−1377.
(56) Aidas, K.; Angeli, C.; Bak, K. L.; Bakken, V.; Bast, R.; Boman, L.; Christiansen, O.; Cimiraglia, R.; Coriani, S.; Dahle, P.; et al. The Dalton quantum chemistry program system. *WIREs Comput. Mol. Sci.* **2014**, *4*, 269−284.
(57) Angeli, C.; Cimiraglia, R.; Evangelisti, S.; Leininger, T.; Malrieu, J.-P. Introduction of n-electron valence states for multireference perturbation theory. *J. Chem. Phys.* **2001**, *114*, 10252−10264.
(58) Angeli, C.; Cimiraglia, R.; Malrieu, J.-P. n-electron valence state perturbation theory: A spinless formulation and an efficient implementation of the strongly contracted and of the partially contracted variants. *J. Chem. Phys.* **2002**, *117*, 9138−9153.
(59) Angeli, C.; Pastore, M.; Cimiraglia, R. New perspectives in multireference perturbation theory: the n-electron valence state approach. *Theor. Chem. Acc.* **2007**, *117*, 743−754.
(60) Roos, B. O.; Taylor, P. R.; Sigbahn, P. E. A complete active space SCF method (CASSCF) using a density matrix formulated super-CI approach. *Chem. Phys.* **1980**, *48*, 157−173.

https://doi.org/10.1021/acs.jpca.2c07951
J. Phys. Chem. A 2023, 127, 2011−2025

(61) Siegbahn, P. E.; Almlöf, J.; Heiberg, A.; Roos, B. O. The complete active space SCF (CASSCF) method in a Newton−Raphson formulation with application to the HNO molecule. *J. Chem. Phys.* **1981**, *74*, 2384−2396.
(62) Siegbahn, P.; Heiberg, A.; Roos, B.; Levy, B. A Comparison of the Super-CI and the Newton-Raphson Scheme in the Complete Active Space SCF Method. *Phys. Scr.* **1980**, *21*, 323.
(63) Neese, F.; Wennmohs, F.; Becker, U.; Riplinger, C. The ORCA quantum chemistry program package. *J. Chem. Phys.* **2020**, *152*, 224108.
(64) Stoychev, G. L.; Auer, A. A.; Neese, F. Automatic generation of auxiliary basis sets. *J. Chem. Theory Comput.* **2017**, *13*, 554−562.
(65) Nelder, J. A.; Mead, R. A Simplex Method for Function Minimization. *Comput. J.* **1965**, *7*, 308−313.
(66) Manna, S.; Chaudhuri, R. K.; Chattopadhyay, S. Taming the excited states of butadiene, hexatriene, and octatetraene using state specific multireference perturbation theory with density functional theory orbitals. *J. Chem. Phys.* **2020**, *152*, 244105.
(67) Martin, W. C.; Zalubas, R. Energy levels of magnesium, Mg I through Mg XII. *J. Phys. Chem. Ref. Data* **1980**, *9*, 1.
(68) Véril, M.; Scemama, A.; Caffarel, M.; Lipparini, F.; Boggio-Pasqua, M.; Jacquemin, D.; Loos, P.-F. QUESTDB: A database of highly accurate excitation energies for the electronic structure community. *WIREs Comput. Mol. Sci.* **2021**, *11*, e1517.
(69) Nikitin, M. I.; Malkerova, I. P.; Kayumova, D. B.; Alikhanyan, A. S. Enthalpies of Formation of Chromium Fluorides. II. Higher Fluorides CrF_4, CrF_5, and CrF_6. *Russ. J. Inorg. Chem.* **2021**, *66*, 1519−1526.
(70) Schlöder, T.; Brosi, F.; Freyh, B. J.; Vent-Schmidt, T.; Riedel, S. New Evidence in an Old Case: The Question of Chromium Hexafluoride Reinvestigated. *Inorg. Chem.* **2014**, *53*, 5820−5829.
(71) Roos, B. O.; Andersson, K. Multiconfigurational perturbation theory with level shift - the Cr_2 potential revisited. *Chem. Phys. Lett.* **1995**, *245*, 215−223.
(72) Forsberg, N.; Malmqvist, P.-Å. Multiconfiguration perturbation theory with imaginary level shift. *Chem. Phys. Lett.* **1997**, *274*, 196−204.
(73) Battaglia, S.; Fransén, L.; Fdez. Galván, I.; Lindh, R. Regularized CASPT2: an Intruder-State-Free Approach. *J. Chem. Theory Comput.* **2022**, *18*, 4814−4825.
(74) Platt, J. R. Classification of Spectra of Cata-Condensed Hydrocarbons. *J. Chem. Phys.* **1949**, *17*, 484−495.
(75) Parac, M.; Grimme, S. A TDDFT study of the lowest excitation energies of polycyclic aromatic hydrocarbons. *Chem. Phys.* **2003**, *292*, 11−21.
(76) Grimme, S.; Parac, M. Substantial Errors from Time-Dependent Density Functional Theory for the Calculation of Excited States of Large π Systems. *ChemPhysChem* **2003**, *4*, 292−295.
(77) Yoshizawa, M.; Aoki, H.; Ue, M.; Hashimoto, H. Ultrafast relaxation kinetics of excited states in a series of mini-and macro-β-carotenes. *Phys. Rev. B* **2003**, *67*, 174302.
(78) Spezia, R.; Knecht, S.; Mennucci, B. Excited state characterization of carbonyl containing carotenoids: a comparison between single and multireference descriptions. *Phys. Chem. Chem. Phys.* **2017**, *19*, 17156−17166.
(79) Pang, Y.; Fleming, G. R. Branching relaxation pathways from the hot S_2 state of 8′-apo-β-caroten-8′-al. *Phys. Chem. Chem. Phys.* **2010**, *12*, 6782−6788.
(80) Premvardhan, L.; Sandberg, D. J.; Fey, H.; Birge, R. R.; Büchel, C.; van Grondelle, R. The charge-transfer properties of the S2 state of fucoxanthin in solution and in fucoxanthin chlorophyll-a/c2 protein (FCP) based on stark spectroscopy and molecular-orbital theory. *J. Phys. Chem. B* **2008**, *112*, 11838−11853.
(81) West, R. G.; Fuciman, M.; Staleva-Musto, H.; Šebelík, V.; Bína, D.; Durchan, M.; Kuznetsova, V.; Polívka, T. Equilibration dependence of fucoxanthin S1 and ICT signatures on polarity, proticity, and temperature by multipulse femtosecond absorption spectroscopy. *J. Phys. Chem. B* **2018**, *122*, 7264−7276.
(82) Ehrmaier, J.; Rabe, E. J.; Pristash, S. R.; Corp, K. L.; Schlenker, C. W.; Sobolewski, A. L.; Domcke, W. Singlet-triplet inversion in heptazine and in polymeric carbon nitrides. *J. Phys. Chem. A* **2019**, *123*, 8099−8108.
(83) Dinkelbach, F.; Bracker, M.; Kleinschmidt, M.; Marian, C. M. Large Inverted Singlet-Triplet Energy Gaps Are Not Always Favorable for Triplet Harvesting: Vibronic Coupling Drives the (Reverse) Intersystem Crossing in Heptazine Derivatives. *J. Phys. Chem. A* **2021**, *125*, 10044−10051.
(84) de Silva, P. Inverted singlet-triplet gaps and their relevance to thermally activated delayed fluorescence. *J. Phys. Chem. Lett.* **2019**, *10*, 5674−5679.
(85) Sobolewski, A. L.; Domcke, W. Are heptazine-based organic light-emitting diode chromophores thermally activated delayed fluorescence or inverted singlet−triplet systems? *J. Phys. Chem. Lett.* **2021**, *12*, 6852−6860.

https://doi.org/10.1021/acs.jpca.2c07951
J. Phys. Chem. A 2023, 127, 2011−2025

Using the newly designed Hamiltonian yields entirely different results. In the range <3 eV above the DFT/MRCI ground state only one quintet state is found, which is in stark contrast to the other two calculations. Furthermore, the composition of the ^{1}(TT) wave function follows the intuitive reasoning given earlier, as the state is dominated by an equal mixture of the configurations shown in Fig. 4.3. With the new

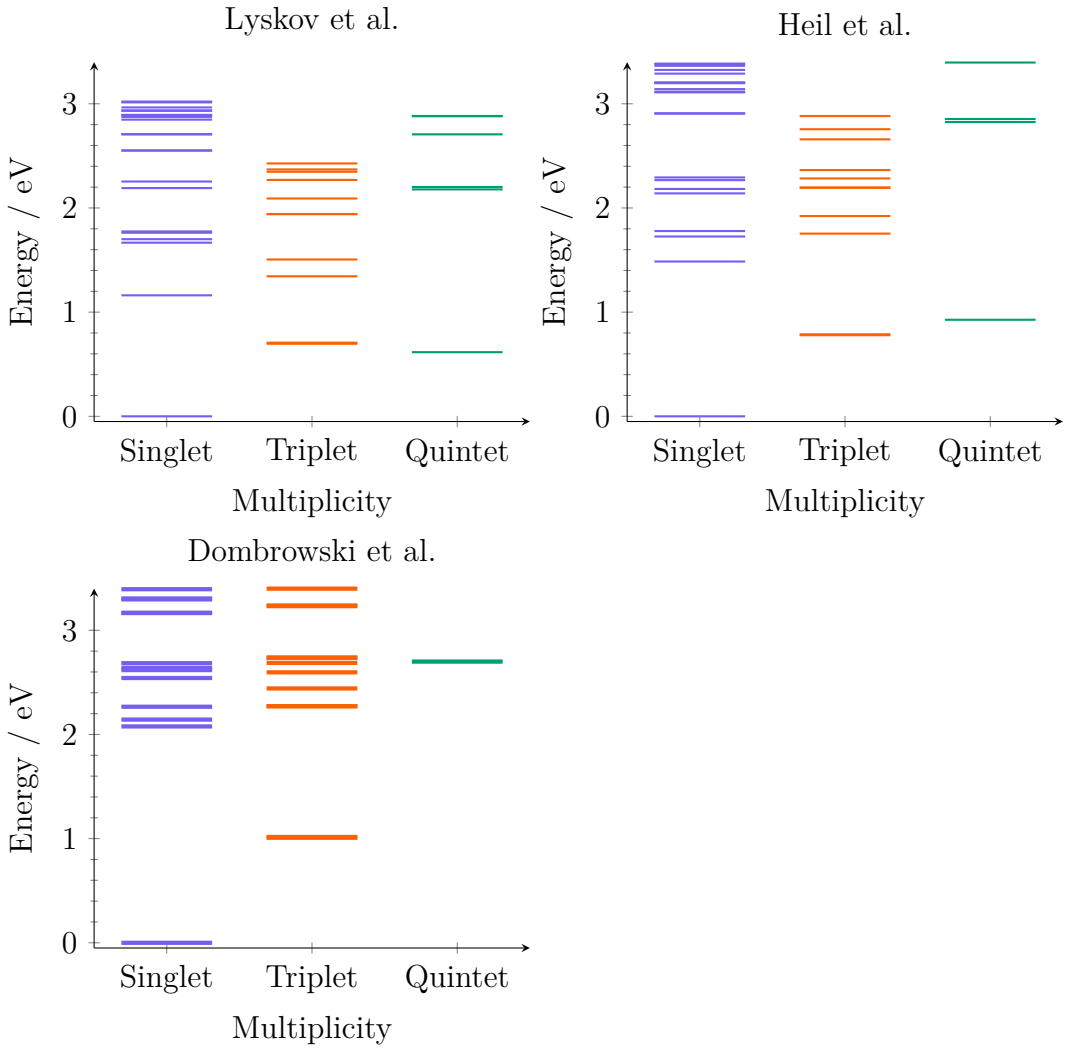

Figure 4.5: Energy level plot of the singlet, triplet and quintet state manifold found in *meta* computed with different model hamiltonians.

model Hamiltonian it was possible to investigate the energetic landscape of all three PT derivatives as outlined in [P2].

Journal of COMPUTATIONAL CHEMISTRY

Simulating the Full Spin Manifold of Triplet-Pair States in a Series of Covalently Linked TIPS-Pentacenes

Journal:	*Journal of Computational Chemistry*
Manuscript ID	JCC-24-0221
Wiley - Manuscript type:	Research Article
Date Submitted by the Author:	03-May-2024
Complete List of Authors:	Schulz, Timo; Heinrich Heine Universitat Dusseldorf Mathematisch-Naturwissenschaftliche Fakultat Marian, Christel; Heinrich Heine Universitat Dusseldorf Mathematisch-Naturwissenschaftliche Fakultat
Key Words:	singlet fission, multireference configuration interaction, pentacene dimers, regioisomer, direct mechanism, charge-resonance, multiexcitonic, triplet pair, quintet, double excitation
Selected Editor:	Europe - Prof. Frenking

Supporting Information for Simulating the Full Spin Manifold of Triplet-Pair States in a Series of Covalently Linked TIPS-Pentacenes

Timo Schulz and Christel M. Marian*

Institute of Theoretical and Computational Chemistry, Faculty of Mathematics and Natural Sciences, Heinrich Heine University Düsseldorf, 40204 Düsseldorf, Germany

E-mail: Christel.Marian@hhu.de

Table S1: Composition, coefficient and weight in % for states with contributions of doubly excited configurations of at least 10% and adiabatic energy less than 3 eV for the **ortho** regioisomer. Spatial configurations of $V^{l;l+1}_{h-1;h}$ excited character are highlighted green.

Geometry	Order	$E_{ad.}$	No.	**CSF**	**Composition**	**Coeff.**	**Weight**	$\mathbf{N}_{opn}$
			1	1	$(h)^1(l_{+1})^1$	0.5240	27.5	2
			2	1	$(h_{-1})^1(l)^1$	-0.4646	21.6	2
			3	1	$(h)^0(l)^2$	-0.3406	11.6	0
Gs	$\mathbf{1}_2$	2.16	4	1	$(h_{-1})^1(h)^1(l)^1(l_{+1})^1$	0.2614	6.8	4
			5	1	$(h_{-1})^0(l)^2$	0.2445	6.0	0
			6	1	$(h)^0(l_{+1})^2$	0.2424	5.9	0
			7	1	$(h_{-1})^0(l_{+1})^2$	-0.1549	2.4	0
			1	1	$(h)^1(l_{+1})^1$	-0.4041	16.3	2
			2	1	$(h_{-1})^1(l)^1$	0.3848	14.8	2
			3	1	$(h)^0(l)^2$	-0.3630	13.2	0
			4	1	$(h)^0(l_{+1})^2$	0.3055	9.3	0
Gs	$\mathbf{1}_5$	2.62	5	1	$(h_{-1})^0(l_{+1})^2$	-0.3044	9.3	0
			6	1	$(h_{-1})^1(h)^1(l)^1(l_{+1})^1$	0.2837	8.0	4
			7	1	$(h_{-1})^0(l)^2$	0.2801	7.8	0
			8	2	$(h_{-1})^1(h)^1(l)^1(l_{+1})^1$	0.0777	0.6	4
			1	1	$(h)^0(l)^1(l_{+1})^1$	0.4964	24.6	2
			2	1	$(h_{-1})^1(h)^1(l)^2$	-0.4872	23.7	2
Gs	$\mathbf{1}_6$	2.79	3	1	$(h_{-1})^1(h)^1(l_{+1})^2$	-0.3453	11.9	2
			4	1	$(h_{-1})^0(l)^1(l_{+1})^1$	0.3396	11.5	2
			5	1	$(h_{-10})^1(l)^1$	-0.0944	0.9	2

Continued on next page

Table S1: Composition, coefficient and weight in % for states with contributions of doubly excited configurations of at least 10% and adiabatic energy less than 3 eV for the **ortho** regioisomer. Spatial configurations of $V^{l;l+1}_{h-1;h}$ excited character are highlighted green.

Geometry	Order	$E_{ad.}$	No.	**CSF**	**Composition**	**Coeff.**	**Weight**	$\mathbf{N}_{opn}$
			1	2	$(h_{-1})^1(h)^1(l)^1(l_{+1})^1$	-0.5893	34.7	4
			2	1	$(h)^0(l)^2$	0.3362	11.3	0
Gs	$\mathbf{1}_7$	2.89	3	1	$(h)^0(l_{+1})^2$	0.2968	8.8	0
			4	1	$(h_{-1})^0(l)^2$	0.2842	8.1	0
			5	0	$(h)^2(l)^0$	0.2113	4.5	0
			1	1	$(h_{-1})^1(l_{+1})^1$	0.5397	29.1	2
			2	1	$(h)^1(l)^1$	-0.4217	17.8	2
			3	1	$(h_{-2})^1(l)^1$	-0.2699	7.3	2
Gs	$\mathbf{3}_2$	2.29	4	1	$(h_{-1})^1(h)^1(l)^2$	0.2429	5.9	2
			5	1	$(h)^0(l)^1(l_{+1})^1$	0.2353	5.5	2
			6	1	$(h)^1(l_{+3})^1$	-0.2033	4.1	2
			1	1	$(h)^0(l)^1(l_{+1})^1$	-0.3612	13.0	2
			2	1	$(h_{-1})^1(h)^1(l)^2$	-0.3502	12.3	2
			3	1	$(h_{-1})^1(h)^1(l_{+1})^2$	0.3337	11.1	2
			4	1	$(h_{-1})^0(l)^1(l_{+1})^1$	0.3225	10.4	2
Gs	$\mathbf{3}_6$	2.69	5	1	$(h)^1(l_{+2})^1$	0.2828	8.0	2
			6	1	$(h_{-1})^1(l_{+1})^1$	0.2551	6.5	2
			7	1	$(h_{-4})^1(l)^1$	0.2442	6.0	2
			8	1	$(h)^1(l)^1$	-0.2393	5.7	2

Continued on next page

Table S1: Composition, coefficient and weight in % for states with contributions of doubly excited configurations of at least 10% and adiabatic energy less than 3 eV for the **ortho** regioisomer. Spatial configurations of $V^{l;l+1}_{h-1;h}$ excited character are highlighted green.

Geometry	Order	$E_{ad.}$	No.	**CSF**	**Composition**	**Coeff.**	**Weight**	$\mathbf{N}_{opn}$
			9	1	$(h_{-7})^1(l_{+1})^1$	-0.1343	1.8	2
Q_1	$\mathbf{1}_1$	1.73	1	1	$(h)^0(l)^2$	0.4625	21.4	0
			2	1	$(h_{-1})^1(h)^1(l)^1(l_{+1})^1$	-0.3620	13.1	4
			3	1	$(h)^0(l_{+1})^2$	-0.3610	13.0	0
			4	1	$(h_{-1})^0(l)^2$	-0.3494	12.2	0
			5	1	$(h)^1(l_{+1})^1$	-0.2929	8.6	2
			6	1	$(h_{-1})^1(l)^1$	0.2774	7.7	2
			7	1	$(h_{-1})^0(l_{+1})^2$	0.2493	6.2	0
			8	2	$(h_{-2})^1(h)^1(l)^1(l_{+3})^1$	-0.0428	0.2	4
Q_1	$\mathbf{1}_4$	2.44	1	1	$(h_{-1})^1(h)^1(l)^2$	-0.5229	27.3	2
			2	1	$(h)^0(l)^1(l_{+1})^1$	0.4480	20.1	2
			3	1	$(h_{-1})^0(l)^1(l_{+1})^1$	0.3447	11.9	2
			4	1	$(h_{-1})^1(h)^1(l_{+1})^2$	-0.2987	8.9	2
			5	1	$(h_{-1})^1(l_{+1})^1$	-0.2136	4.6	2
Q_1	$\mathbf{1}_5$	2.45	1	1	$(h)^1(l_{+1})^1$	-0.5921	35.1	2
			2	1	$(h_{-1})^1(l)^1$	0.4664	21.8	2
			3	1	$(h_{-1})^0(l_{+1})^2$	-0.2699	7.3	0
			4	1	$(h)^0(l)^2$	-0.2260	5.1	0
			5	2	$(h_{-1})^1(h)^1(l)^1(l_{+1})^1$	0.2126	4.5	4

Continued on next page

Table S1: Composition, coefficient and weight in % for states with contributions of doubly excited configurations of at least 10% and adiabatic energy less than 3 eV for the **ortho** regioisomer. Spatial configurations of $V^{l;l_{+1}}_{h_{-1};h}$ excited character are highlighted green.

Geometry	Order	$E_{ad.}$	No.	**CSF**	**Composition**	**Coeff.**	**Weight**	$\mathbf{N}_{opn}$
Q_1	$\mathbf{1}_6$	2.50	1	1	$(h_{-1})^1(l_{+1})^1$	0.8313	69.1	2
			2	1	$(h)^0(l)^1(l_{+1})^1$	0.2761	7.6	2
			3	1	$(h_{-1})^1(h)^1(l_{+1})^2$	-0.1610	2.6	2
Q_1	$\mathbf{1}_7$	2.63	1	2	$(h_{-1})^1(h)^1(l)^1(l_{+1})^1$	0.5277	27.8	4
			2	1	$(h)^0(l)^2$	-0.3249	10.6	0
			3	1	$(h)^0(l_{+1})^2$	-0.3172	10.1	0
			4	0	$(h)^2(l)^0$	-0.3015	9.1	0
			5	1	$(h_{-1})^0(l)^2$	-0.2693	7.3	0
			6	1	$(h_{-1})^1(l)^1$	-0.2572	6.6	2
			7	1	$(h_{-1})^0(h)^0(l)^2(l_{+1})^2$	0.1558	2.4	0
Q_1	$\mathbf{3}_2$	1.95	1	1	$(h)^0(l)^1(l_{+1})^1$	-0.4689	22.0	2
			2	1	$(h_{-1})^1(h)^1(l)^2$	-0.4674	21.8	2
			3	1	$(h_{-1})^1(h)^1(l_{+1})^2$	0.3455	11.9	2
			4	1	$(h_{-1})^0(l)^1(l_{+1})^1$	0.3385	11.5	2
			5	1	$(h_{-1})^1(l_{+1})^1$	-0.3288	10.8	2
			6	1	$(h)^1(l)^1$	0.2066	4.3	2
Q_1	$\mathbf{3}_4$	2.55	1	1	$(h_{-1})^1(l_{+1})^1$	-0.5779	33.4	2
			2	1	$(h)^1(l)^1$	0.4586	21.0	2
			3	1	$(h_{-1})^1(h)^1(l_{+1})^2$	-0.2315	5.4	2

Continued on next page

Table S1: Composition, coefficient and weight in % for states with contributions of doubly excited configurations of at least 10% and adiabatic energy less than 3 eV for the **ortho** regioisomer. Spatial configurations of $V^{l;l+1}_{h-1;h}$ excited character are highlighted green.

Geometry	Order	$E_{ad.}$	No.	**CSF**	**Composition**	**Coeff.**	**Weight**	$\mathbf{N}_{opn}$
			4	1	$(h_{-1})^0(l)^1(l_{+1})^1$	-0.2160	4.7	2
S_1	$\mathbf{1}_1$	1.79	1	1	$(h)^1(l_{+1})^1$	-0.3898	15.2	2
			2	1	$(h_{-1})^1(l)^1$	0.3686	13.6	2
			3	1	$(h_{-1})^1(h)^1(l)^1(l_{+1})^1$	-0.3120	9.7	4
			4	1	$(h)^0(l)^1(l_{+1})^1$	-0.3103	9.6	2
			5	1	$(h)^0(l)^2$	0.3016	9.1	0
			6	1	$(h_{-1})^0(l)^2$	-0.2259	5.1	0
			7	1	$(h)^0(l_{+1})^2$	-0.2243	5.0	0
			8	1	$(h_{-1})^1(h)^1(l)^2$	0.2214	4.9	2
S_1	$\mathbf{1}_6$	2.53	1	1	$(h)^0(l)^2$	0.5209	27.1	0
			2	1	$(h_{-1})^1(h)^1(l)^2$	-0.4464	19.9	2
			3	1	$(h)^0(l)^1(l_{+1})^1$	0.3632	13.2	2
			4	2	$(h_{-1})^1(h)^1(l)^1(l_{+1})^1$	-0.1719	3.0	4
S_1	$\mathbf{1}_7$	2.84	1	2	$(h_{-1})^1(h)^1(l)^1(l_{+1})^1$	0.4207	17.7	4
			2	1	$(h_{-1})^1(h)^1(l_{+1})^2$	-0.4026	16.2	2
			3	1	$(h_{-1})^0(l)^1(l_{+1})^1$	0.3070	9.4	2
			4	1	$(h)^0(l_{+1})^2$	-0.2834	8.0	0
			5	1	$(h_{-1})^0(l_{+1})^2$	-0.2440	6.0	0
			6	1	$(h)^0(l)^1(l_{+1})^1$	0.1773	3.1	2

Continued on next page

Table S1: Composition, coefficient and weight in % for states with contributions of doubly excited configurations of at least 10% and adiabatic energy less than 3 eV for the **ortho** regioisomer. Spatial configurations of $V^{l;l+1}_{h-1;h}$ excited character are highlighted green.

Geometry	Order	$E_{ad.}$	No.	**CSF**	**Composition**	**Coeff.**	**Weight**	N_{opn}
			1	1	$(h_{-1})^1(l_{+1})^1$	-0.4170	17.4	2
			2	1	$(h)^0(l)^1(l_{+1})^1$	-0.3787	14.3	2
			3	1	$(h_{-1})^1(h)^1(l)^2$	-0.3457	12.0	2
S_1	$\mathbf{3}_2$	2.00	4	1	$(h)^1(l)^1$	0.2569	6.6	2
			5	1	$(h_{-1})^1(h)^1(l)^1(l_{+1})^1$	0.2425	5.9	4
			6	1	$(h_{-1})^0(l)^1(l_{+1})^1$	0.2367	5.6	2
			7	3	$(h_{-1})^1(h)^1(l)^1(l_{+1})^1$	-0.2199	4.8	4
			1	1	$(h)^1(l_{+1})^1$	-0.4212	17.7	2
			2	1	$(h)^0(l)^2$	0.4166	17.4	0
			3	1	$(h_{-1})^1(l)^1$	0.3677	13.5	2
S_2	$\mathbf{1}_1$	1.87	4	1	$(h_{-1})^1(h)^1(l)^1(l_{+1})^1$	-0.3181	10.1	4
			5	1	$(h)^0(l_{+1})^2$	-0.3110	9.7	0
			6	1	$(h_{-1})^0(l)^2$	-0.3009	9.1	0
			7	1	$(h_{-1})^0(l_{+1})^2$	0.2064	4.3	0
			1	1	$(h)^1(l_{+1})^1$	-0.4944	24.4	2
			2	1	$(h_{-1})^1(l)^1$	0.4780	22.8	2
			3	1	$(h)^0(l)^2$	-0.2949	8.7	0
S_2	$\mathbf{1}_5$	2.38	4	1	$(h_{-1})^0(l_{+1})^2$	-0.2806	7.9	0
			5	1	$(h)^0(l_{+1})^2$	0.2357	5.6	0

Continued on next page

Table S1: Composition, coefficient and weight in % for states with contributions of doubly excited configurations of at least 10% and adiabatic energy less than 3 eV for the **ortho** regioisomer. Spatial configurations of $V^{l;l_{+1}}_{h_{-1};h}$ excited character are highlighted green.

Geometry	Order	$E_{ad.}$	No.	**CSF**	**Composition**	**Coeff.**	**Weight**	$\mathbf{N}_{opn}$
			6	1	$(h_{-1})^1(h)^1(l)^1(l_{+1})^1$	0.2165	4.7	4
S_2	$\mathbf{1}_6$	2.49	1	1	$(h)^0(l)^1(l_{+1})^1$	-0.5140	26.4	2
			2	1	$(h_{-1})^1(h)^1(l)^2$	0.4932	24.3	2
			3	1	$(h_{-1})^1(h)^1(l_{+1})^2$	0.3434	11.8	2
			4	1	$(h_{-1})^0(l)^1(l_{+1})^1$	-0.3284	10.8	2
			5	1	$(h)^1(l_{+9})^1$	-0.0866	0.7	2
S_2	$\mathbf{1}_7$	2.61	1	2	$(h_{-1})^1(h)^1(l)^1(l_{+1})^1$	0.5777	33.4	4
			2	1	$(h)^0(l)^2$	-0.3348	11.2	0
			3	1	$(h)^0(l_{+1})^2$	-0.3125	9.8	0
			4	1	$(h_{-1})^0(l)^2$	-0.2823	8.0	0
			5	0	$(h)^2(l)^0$	-0.2442	6.0	0
			6	1	$(h_{-1})^0(h)^0(l)^2(l_{+1})^2$	0.1296	1.7	0
S_2	$\mathbf{3}_2$	2.05	1	1	$(h_{-1})^1(l_{+1})^1$	0.4827	23.3	2
			2	1	$(h_{-1})^1(h)^1(l)^2$	0.3903	15.2	2
			3	1	$(h)^0(l)^1(l_{+1})^1$	0.3878	15.0	2
			4	1	$(h)^1(l)^1$	-0.3514	12.4	2
			5	1	$(h_{-1})^1(h)^1(l_{+1})^2$	-0.2658	7.1	2
			6	1	$(h_{-1})^0(l)^1(l_{+1})^1$	-0.2620	6.9	2
			7	1	$(h_{-2})^1(l)^1$	-0.0887	0.8	2

Continued on next page

Table S1: Composition, coefficient and weight in % for states with contributions of doubly excited configurations of at least 10% and adiabatic energy less than 3 eV for the **ortho** regioisomer. Spatial configurations of $V^{l;l_{+1}}_{h_{-1};h}$ excited character are highlighted green.

Geometry	Order	$E_{ad.}$	No.	**CSF**	**Composition**	**Coeff.**	**Weight**	$\mathbf{N}_{opn}$
			1	1	$(h_{-1})^1(l_{+1})^1$	0.4647	21.6	2
			2	1	$(h)^1(l)^1$	-0.3872	15.0	2
			3	1	$(h_{-1})^1(h)^1(l_{+1})^2$	0.2848	8.1	2
S_2	$\mathbf{3}_6$	2.46	4	1	$(h)^0(l)^1(l_{+1})^1$	-0.2768	7.7	2
			5	1	$(h_{-1})^0(l)^1(l_{+1})^1$	0.2720	7.4	2
			6	1	$(h_{-1})^1(h)^1(l)^2$	-0.2487	6.2	2
			7	1	$(h)^1(l_{+2})^1$	-0.2060	4.2	2

Continued on next page

Table S1: Composition, coefficient and weight in % for states with contributions of doubly excited configurations of at least 10% and adiabatic energy less than 3 eV for the **ortho** regioisomer. Spatial configurations of $V^{l;l+1}_{h-1;h}$ excited character are highlighted green.

Geometry	Order	$E_{ad.}$	No.	**CSF**	**Composition**	**Coeff.**	**Weight**	$\mathbf{N}_{opn}$
T_1	$\mathbf{1}_1$	1.87	1	2	$(h_{-1})^1(h)^1(l)^1(l_{+1})^1$	0.3776	14.3	4
			2	1	$(h_{-1})^1(l)^1$	-0.3408	11.6	2
			3	1	$(h_{-1})^1(h)^1(l)^1(l_{+1})^1$	0.3391	11.5	4
			4	1	$(h)^0(l)^1(l_{+1})^1$	0.3353	11.2	2
			5	1	$(h)^1(l_{+1})^1$	0.3261	10.6	2
			6	1	$(h_{-1})^1(h)^1(l)^2$	-0.2834	8.0	2
			7	1	$(h_{-1})^0(l)^1(l_{+1})^1$	-0.1979	3.9	2
T_1	$\mathbf{1}_4$	2.42	1	1	$(h_{-1})^1(l)^1$	0.5439	29.6	2
			2	1	$(h)^1(l_{+1})^1$	-0.4923	24.2	2
			3	2	$(h_{-1})^1(h)^1(l)^1(l_{+1})^1$	0.2955	8.7	4
			4	1	$(h_{-1})^1(h)^1(l)^1(l_{+1})^1$	0.1881	3.5	4
T_1	$\mathbf{1}_6$	2.54	1	1	$(h)^0(l)^2$	-0.6916	47.8	0
			2	1	$(h_{-1})^1(h)^1(l)^2$	0.3303	10.9	2
			3	1	$(h)^0(l)^1(l_{+1})^1$	-0.2590	6.7	2
			4	0	$(h)^2(l)^0$	-0.1986	3.9	0

Continued on next page

Table S1: Composition, coefficient and weight in % for states with contributions of doubly excited configurations of at least 10% and adiabatic energy less than 3 eV for the **ortho** regioisomer. Spatial configurations of $V^{l;l_{+1}}_{h_{-1};h}$ excited character are highlighted green.

Geometry	Order	$E_{ad.}$	No.	**CSF**	**Composition**	**Coeff.**	**Weight**	$\mathbf{N}_{opn}$
T_1	$\mathbf{3}_2$	2.04	1	3	$(h_{-1})^1(h)^1(l)^1(l_{+1})^1$	0.3914	15.3	4
			2	1	$(h_{-1})^1(h)^1(l)^1(l_{+1})^1$	-0.3458	12.0	4
			3	1	$(h)^0(l)^1(l_{+1})^1$	0.3285	10.8	2
			4	1	$(h_{-1})^1(l_{+1})^1$	0.3042	9.3	2
			5	1	$(h_{-1})^1(h)^1(l)^2$	0.2913	8.5	2
			6	1	$(h_{-1})^1(l)^1$	0.2624	6.9	2
			7	2	$(h_{-1})^1(h)^1(l)^1(l_{+1})^1$	0.2404	5.8	4
			8	1	$(h_{-1})^0(l)^1(l_{+1})^1$	-0.1944	3.8	2
T_1	$\mathbf{3}_5$	2.47	1	1	$(h_{-1})^1(l_{+1})^1$	-0.3473	12.1	2
			2	1	$(h)^1(l_{+1})^1$	-0.3317	11.0	2
			3	1	$(h_{-1})^1(l)^1$	-0.3066	9.4	2
			4	1	$(h)^1(l)^1$	0.2436	5.9	2
			5	1	$(h_{-2})^1(l_{+1})^1$	-0.2376	5.6	2
			6	3	$(h_{-1})^1(h)^1(l)^1(l_{+1})^1$	0.2258	5.1	4
			7	1	$(h_{-1})^1(h)^1(l)^1(l_{+1})^1$	-0.1896	3.6	4

Table S2: Composition, coefficient and weight in % for states with contributions of doubly excited configurations of at least 10% and adiabatic energy less than 3 eV for the **meta** regioisomer. Spatial configurations of $V^{l;l+1}_{h-1;h}$ excited character are highlighted green.

Geometry	Order	$E_{ad.}$	No.	**CSF**	**Composition**	**Coeff.**	**Weight**	$\mathbf{N}_{opn}$
Gs	$\mathbf{1}_3$	2.27	1	1	$(h)^0(l)^2$	0.4133	17.1	0
			2	1	$(h_{-1})^0(l_{+1})^2$	0.4045	16.4	0
			3	1	$(h_{-1})^0(l)^2$	-0.4018	16.1	0
			4	1	$(h_{-1})^1(h)^1(l)^1(l_{+1})^1$	0.3898	15.2	4
			5	1	$(h)^0(l_{+1})^2$	-0.3871	15.0	0
			6	2	$(h_{-3})^1(h)^1(l)^1(l_{+3})^1$	0.0578	0.3	4
Gs	$\mathbf{1}_4$	2.54	1	1	$(h_{-1})^1(h)^1(l)^2$	-0.4432	19.6	2
			2	1	$(h)^0(l)^1(l_{+1})^1$	-0.4309	18.6	2
			3	1	$(h_{-1})^0(l)^1(l_{+1})^1$	-0.4072	16.6	2
			4	1	$(h_{-1})^1(h)^1(l_{+1})^2$	-0.3947	15.6	2
			5	1	$(h_{-1})^1(l)^1$	-0.1589	2.5	2
Gs	$\mathbf{1}_7$	2.68	1	2	$(h_{-1})^1(h)^1(l)^1(l_{+1})^1$	-0.5909	34.9	4
			2	1	$(h)^0(l_{+1})^2$	-0.2860	8.2	0
			3	1	$(h_{-1})^0(l)^2$	-0.2800	7.8	0
			4	1	$(h)^0(l)^2$	-0.2614	6.8	0
			5	1	$(h_{-1})^0(l_{+1})^2$	-0.2439	5.9	0
			6	0	$(h)^2(l)^0$	-0.2337	5.5	0
			7	1	$(h_{-1})^1(l_{+1})^1$	-0.1473	2.2	2

Continued on next page

Table S2: Composition, coefficient and weight in % for states with contributions of doubly excited configurations of at least 10% and adiabatic energy less than 3 eV for the **meta** regioisomer. Spatial configurations of $V^{l;l+1}_{h-1;h}$ excited character are highlighted green.

Geometry	Order	$E_{ad.}$	No.	**CSF**	**Composition**	**Coeff.**	**Weight**	$\mathbf{N}_{opn}$
Gs	$\mathbf{3}_4$	2.44	1	1	$(h_{-1})^1(h)^1(l)^2$	-0.4518	20.4	2
			2	1	$(h_{-1})^0(l)^1(l_{+1})^1$	-0.4476	20.0	2
			3	1	$(h)^0(l)^1(l_{+1})^1$	0.4436	19.7	2
			4	1	$(h_{-1})^1(h)^1(l_{+1})^2$	0.4402	19.4	2
			5	3	$(h_{-2})^1(h_{-1})^1(l_{+1})^1(l_{+3})^1$	0.0483	0.2	4
Q_1	$\mathbf{1}_1$	1.73	1	1	$(h)^0(l)^2$	-0.4113	16.9	0
			2	1	$(h_{-1})^0(l)^2$	0.4086	16.7	0
			3	1	$(h_{-1})^0(l_{+1})^2$	-0.4049	16.4	0
			4	1	$(h_{-1})^1(h)^1(l)^1(l_{+1})^1$	-0.4021	16.2	4
			5	1	$(h)^0(l_{+1})^2$	0.3941	15.5	0
			6	2	$(h_{-2})^1(h_{-1})^1(l)^1(l_{+3})^1$	0.0432	0.2	4
Q_1	$\mathbf{1}_2$	2.14	1	1	$(h_{-1})^1(l)^1$	-0.5561	30.9	2
			2	1	$(h)^1(l_{+1})^1$	0.5110	26.1	2
			3	1	$(h_{-1})^0(l)^1(l_{+1})^1$	0.2456	6.0	2
			4	1	$(h_{-1})^1(h)^1(l)^2$	0.2425	5.9	2
			5	1	$(h)^0(l)^1(l_{+1})^1$	0.2364	5.6	2
			6	1	$(h_{-1})^1(h)^1(l_{+1})^2$	0.2338	5.5	2
			7	1	$(h_{-1})^0(h)^1(l)^2(l_{+1})^1$	-0.0946	0.9	0

Continued on next page

Table S2: Composition, coefficient and weight in % for states with contributions of doubly excited configurations of at least 10% and adiabatic energy less than 3 eV for the **meta** regioisomer. Spatial configurations of $V^{l;l+1}_{h-1;h}$ excited character are highlighted green.

Geometry	Order	$E_{ad.}$	No.	**CSF**	**Composition**	**Coeff.**	**Weight**	$\mathbf{N}_{opn}$
			1	1	$(h_{-1})^1(l)^1$	-0.3890	15.1	2
			2	1	$(h_{-1})^1(h)^1(l)^2$	-0.3857	14.9	2
			3	1	$(h)^0(l)^1(l_{+1})^1$	-0.3699	13.7	2
Q_1	$\mathbf{1}_4$	2.27	4	1	$(h_{-1})^0(l)^1(l_{+1})^1$	-0.3599	13.0	2
			5	1	$(h_{-1})^1(h)^1(l_{+1})^2$	-0.3466	12.0	2
			6	1	$(h)^1(l_{+1})^1$	0.3023	9.1	2
			7	1	$(h)^1(l_{+9})^1$	0.0669	0.4	2
			1	2	$(h_{-1})^1(h)^1(l)^1(l_{+1})^1$	0.5639	31.8	4
			2	0	$(h)^2(l)^0$	0.3516	12.4	0
			3	1	$(h_{-1})^0(l)^2$	0.2845	8.1	0
Q_1	$\mathbf{1}_5$	2.48	4	1	$(h)^0(l_{+1})^2$	0.2466	6.1	0
			5	1	$(h)^0(l)^2$	0.2424	5.9	0
			6	1	$(h_{-1})^0(l_{+1})^2$	0.2324	5.4	0
			7	1	$(h)^1(l)^1$	-0.1831	3.4	2
			1	1	$(h_{-1})^1(h)^1(l)^2$	0.4588	21.1	2
			2	1	$(h_{-1})^0(l)^1(l_{+1})^1$	0.4535	20.6	2
Q_1	$\mathbf{3}_2$	1.95	3	1	$(h)^0(l)^1(l_{+1})^1$	-0.4490	20.2	2
			4	1	$(h_{-1})^1(h)^1(l_{+1})^2$	-0.4472	20.0	2
			5	3	$(h_{-2})^1(h_{-1})^1(l)^1(l_{+4})^1$	-0.0357	0.1	4

Continued on next page

Table S2: Composition, coefficient and weight in % for states with contributions of doubly excited configurations of at least 10% and adiabatic energy less than 3 eV for the **meta** regioisomer. Spatial configurations of $V^{l;l+1}_{h-1;h}$ excited character are highlighted green.

Geometry	Order	$E_{ad.}$	No.	**CSF**	**Composition**	**Coeff.**	**Weight**	$\mathbf{N}_{opn}$
S_1	$\mathbf{1}_2$	2.06	1	2	$(h_{-1})^1(h)^1(l)^1(l_{+1})^1$	0.7582	57.5	4
			2	1	$(h_{-1})^1(h)^1(l)^1(l_{+1})^1$	0.4422	19.6	4
			3	1	$(h_{-1})^1(h)^1(l)^2$	-0.1401	2.0	2
S_1	$\mathbf{1}_6$	2.59	1	1	$(h)^0(l)^2$	0.8059	65.0	0
			2	0	$(h)^2(l)^0$	0.1893	3.6	0
S_1	$\mathbf{3}_2$	2.11	1	3	$(h_{-1})^1(h)^1(l)^1(l_{+1})^1$	-0.6264	39.2	4
			2	1	$(h_{-1})^1(h)^1(l)^1(l_{+1})^1$	0.5098	26.0	4
			3	2	$(h_{-1})^1(h)^1(l)^1(l_{+1})^1$	-0.3601	13.0	4
			4	1	$(h_{-1})^1(h)^1(l)^2$	-0.1213	1.5	2
S_2	$\mathbf{1}_1$	1.91	1	1	$(h_{-1})^0(l)^2$	-0.4118	17.0	0
			2	1	$(h)^0(l)^2$	0.4058	16.5	0
			3	1	$(h)^0(l_{+1})^2$	-0.4046	16.4	0
			4	1	$(h_{-1})^1(h)^1(l)^1(l_{+1})^1$	0.3943	15.5	4
			5	1	$(h_{-1})^0(l_{+1})^2$	0.3903	15.2	0
			6	2	$(h_{-2})^1(h)^1(l)^1(l_{+3})^1$	0.0533	0.3	4
S_2	$\mathbf{1}_4$	2.26	1	1	$(h_{-1})^1(h)^1(l)^2$	-0.4444	19.7	2
			2	1	$(h_{-1})^0(l)^1(l_{+1})^1$	-0.4285	18.4	2
			3	1	$(h)^0(l)^1(l_{+1})^1$	-0.4234	17.9	2
			4	1	$(h_{-1})^1(h)^1(l_{+1})^2$	-0.4077	16.6	2

Continued on next page

Table S2: Composition, coefficient and weight in % for states with contributions of doubly excited configurations of at least 10% and adiabatic energy less than 3 eV for the **meta** regioisomer. Spatial configurations of $V^{l;l+1}_{h-1;h}$ excited character are highlighted green.

Geometry	Order	$E_{ad.}$	No.	**CSF**	**Composition**	**Coeff.**	**Weight**	$\mathbf{N}_{opn}$
			5	1	$(h)^1(l)^1$	-0.1361	1.9	2
			1	2	$(h_{-1})^1(h)^1(l)^1(l_{+1})^1$	0.5841	34.1	4
			2	1	$(h)^0(l)^2$	0.3022	9.1	0
			3	0	$(h)^2(l)^0$	0.2714	7.4	0
S_2	$\mathbf{1}_5$	2.43	4	1	$(h_{-1})^0(l)^2$	0.2535	6.4	0
			5	1	$(h_{-1})^0(l_{+1})^2$	0.2524	6.4	0
			6	1	$(h)^0(l_{+1})^2$	0.2461	6.1	0
			7	1	$(h_{-1})^1(l)^1$	-0.1757	3.1	2
			1	1	$(h_{-1})^1(h)^1(l)^2$	-0.4552	20.7	2
			2	1	$(h)^0(l)^1(l_{+1})^1$	0.4509	20.3	2
S_2	$\mathbf{3}_2$	2.12	3	1	$(h_{-1})^0(l)^1(l_{+1})^1$	-0.4458	19.9	2
			4	1	$(h_{-1})^1(h)^1(l_{+1})^2$	0.4437	19.7	2
			5	3	$(h_{-2})^1(h)^1(l_{+1})^1(l_{+3})^1$	-0.0442	0.2	4

Continued on next page

Table S2: Composition, coefficient and weight in % for states with contributions of doubly excited configurations of at least 10% and adiabatic energy less than 3 eV for the **meta** regioisomer. Spatial configurations of $V^{l;l_{+1}}_{h_{-1};h}$ excited character are highlighted green.

Geometry	Order	$E_{ad.}$	No.	**CSF**	**Composition**	**Coeff.**	**Weight**	$\mathbf{N}_{opn}$
T_1	$\mathbf{1}_2$	2.05	1	2	$(h_{-1})^1(h)^1(l)^1(l_{+1})^1$	0.7657	58.6	4
			2	1	$(h_{-1})^1(h)^1(l)^1(l_{+1})^1$	0.4443	19.7	4
			3	1	$(h_{-1})^1(h)^1(l)^2$	-0.1151	1.3	2
T_1	$\mathbf{1}_6$	2.55	1	1	$(h)^0(l)^2$	0.8094	65.5	0
			2	0	$(h)^2(l)^0$	0.2055	4.2	0
T_1	$\mathbf{3}_2$	2.11	1	3	$(h_{-1})^1(h)^1(l)^1(l_{+1})^1$	-0.6307	39.8	4
			2	1	$(h_{-1})^1(h)^1(l)^1(l_{+1})^1$	0.5136	26.4	4
			3	2	$(h_{-1})^1(h)^1(l)^1(l_{+1})^1$	-0.3628	13.2	4
			4	1	$(h_{-1})^1(h)^1(l)^2$	-0.0995	1.0	2

Table S3: Composition, coefficient and weight in % for states with contributions of doubly excited configurations of at least 10% and adiabatic energy less than 3 eV for the **para** regioisomer. Spatial configurations of $V^{l;l+1}_{h-1;h}$ excited character are highlighted green.

Geometry	Order	$E_{ad.}$	No.	**CSF**	**Composition**	**Coeff.**	**Weight**	$\mathbf{N}_{opn}$
Gs	$\mathbf{1}_2$	2.10	1	1	$(h)^0(l)^2$	-0.4694	22.0	0
			2	1	$(h_{-1})^1(l)^1$	-0.3850	14.8	2
			3	1	$(h_{-1})^1(h)^1(l)^1(l_{+1})^1$	-0.3486	12.2	4
			4	1	$(h_{-1})^0(l)^2$	0.3408	11.6	0
			5	1	$(h)^0(l_{+1})^2$	0.3276	10.7	0
			6	1	$(h_{-1})^0(l_{+1})^2$	-0.2499	6.2	0
			7	1	$(h)^1(l_{+1})^1$	-0.1538	2.4	2
Gs	$\mathbf{1}_4$	2.48	1	1	$(h_{-1})^1(h)^1(l)^2$	0.4953	24.5	2
			2	1	$(h)^0(l)^1(l_{+1})^1$	0.4831	23.3	2
			3	1	$(h_{-1})^0(l)^1(l_{+1})^1$	0.3538	12.5	2
			4	1	$(h_{-1})^1(h)^1(l_{+1})^2$	0.3445	11.9	2
			5	1	$(h_{-10})^1(l_{+1})^1$	0.1034	1.1	2
Gs	$\mathbf{1}_5$	2.63	1	2	$(h_{-1})^1(h)^1(l)^1(l_{+1})^1$	0.5576	31.1	4
			2	1	$(h)^0(l_{+1})^2$	0.3279	10.8	0
			3	1	$(h_{-1})^0(l)^2$	0.3264	10.7	0
			4	1	$(h)^0(l)^2$	0.2783	7.7	0
			5	0	$(h)^2(l)^0$	0.2283	5.2	0
			6	1	$(h_{-1})^1(l)^1$	0.1660	2.8	2

Continued on next page

Table S3: Composition, coefficient and weight in % for states with contributions of doubly excited configurations of at least 10% and adiabatic energy less than 3 eV for the **para** regioisomer. Spatial configurations of $V^{l;l+1}_{h-1;h}$ excited character are highlighted green.

Geometry	Order	$E_{ad.}$	**CSF** No.		**Composition**	**Coeff.**	**Weight**	$\mathbf{N}_{opn}$
Gs	$\mathbf{1}_6$	2.68	1	1	$(h)^1(l_{+1})^1$	-0.5375	28.9	2
			2	1	$(h_{-1})^1(l)^1$	-0.4674	21.8	2
			3	1	$(h_{-1})^0(l_{+1})^2$	0.2786	7.8	0
			4	1	$(h)^0(l)^2$	0.2139	4.6	0
Gs	$\mathbf{3}_4$	2.30	1	1	$(h_{-1})^1(l_{+1})^1$	-0.4171	17.4	2
			2	1	$(h_{-1})^1(h)^1(l)^2$	0.3615	13.1	2
			3	1	$(h)^0(l)^1(l_{+1})^1$	-0.3549	12.6	2
			4	1	$(h)^1(l)^1$	-0.3331	11.1	2
			5	1	$(h_{-4})^1(l)^1$	-0.2575	6.6	2
			6	1	$(h)^1(l_{+2})^1$	0.2549	6.5	2
			7	1	$(h_{-1})^0(l)^1(l_{+1})^1$	0.2312	5.3	2
			8	1	$(h_{-1})^1(h)^1(l_{+1})^2$	-0.2279	5.2	2
			9	1	$(h_{-7})^1(l_{+1})^1$	0.0822	0.7	2
Gs	$\mathbf{3}_5$	2.54	1	1	$(h_{-4})^1(l)^1$	0.3637	13.2	2
			2	1	$(h)^1(l_{+2})^1$	-0.3511	12.3	2
			3	1	$(h)^0(l)^1(l_{+1})^1$	-0.3226	10.4	2
			4	1	$(h_{-1})^1(h)^1(l)^2$	0.3175	10.1	2
			5	1	$(h_{-1})^1(h)^1(l_{+1})^2$	-0.2988	8.9	2
			6	1	$(h_{-1})^0(l)^1(l_{+1})^1$	0.2978	8.9	2
			7	1	$(h)^1(l)^1$	0.1848	3.4	2

Continued on next page

Table S3: Composition, coefficient and weight in % for states with contributions of doubly excited configurations of at least 10% and adiabatic energy less than 3 eV for the **para** regioisomer. Spatial configurations of $V^{l;l+1}_{h-1;h}$ excited character are highlighted green.

Geometry	Order	$E_{ad.}$	**CSF** No.	**Composition**	**Coeff.**	**Weight**	$\mathbf{N}_{opn}$
Q_1	$\mathbf{1}_1$	1.57	1 1	$(h)^0(l)^2$	-0.4927	24.3	0
			2 1	$(h_{-1})^1(h)^1(l)^1(l_{+1})^1$	-0.3732	13.9	4
			3 1	$(h)^0(l_{+1})^2$	0.3719	13.8	0
			4 1	$(h_{-1})^0(l)^2$	0.3708	13.8	0
			5 1	$(h_{-1})^0(l_{+1})^2$	-0.2716	7.4	0
			6 1	$(h)^1(l_{+1})^1$	-0.2048	4.2	2
Q_1	$\mathbf{1}_2$	2.03	1 1	$(h)^1(l)^1$	-0.7423	55.1	2
			2 1	$(h_{-1})^1(l_{+1})^1$	0.3303	10.9	2
			3 1	$(h)^0(l)^1(l_{+1})^1$	-0.2614	6.8	2
			4 1	$(h_{-1})^1(h)^1(l)^2$	-0.1837	3.4	2
Q_1	$\mathbf{1}_3$	2.18	1 1	$(h_{-1})^1(h)^1(l)^2$	-0.4835	23.4	2
			2 1	$(h)^0(l)^1(l_{+1})^1$	-0.4403	19.4	2
			3 1	$(h)^1(l)^1$	0.3611	13.0	2
			4 1	$(h_{-1})^0(l)^1(l_{+1})^1$	-0.3264	10.7	2
			5 1	$(h_{-1})^1(h)^1(l_{+1})^2$	-0.2999	9.0	2
			6 1	$(h_{-1})^1(l_{+1})^1$	-0.1390	1.9	2
Q_1	$\mathbf{1}_5$	2.41	1 2	$(h_{-1})^1(h)^1(l)^1(l_{+1})^1$	-0.5524	30.5	4
			2 0	$(h)^2(l)^0$	-0.3453	11.9	0
			3 1	$(h)^0(l)^2$	-0.3358	11.3	0
			4 1	$(h)^0(l_{+1})^2$	-0.2453	6.0	0

Continued on next page

Table S3: Composition, coefficient and weight in % for states with contributions of doubly excited configurations of at least 10% and adiabatic energy less than 3 eV for the **para** regioisomer. Spatial configurations of $V^{l;l+1}_{h-1;h}$ excited character are highlighted green.

Geometry	Order	$E_{ad.}$	No.	**CSF**	**Composition**	**Coeff.**	**Weight**	$\mathbf{N}_{opn}$
			5	1	$(h)^1(l_{+1})^1$	0.2328	5.4	2
			6	1	$(h_{-1})^0(l)^2$	-0.2233	5.0	0
Q_1	$\mathbf{1}_6$	2.60	1	1	$(h)^1(l_{+1})^1$	0.5354	28.7	2
			2	1	$(h_{-1})^1(l)^1$	0.5017	25.2	2
			3	1	$(h_{-1})^0(l_{+1})^2$	-0.2500	6.2	0
			4	1	$(h)^0(l_{+1})^2$	0.1880	3.5	0
Q_1	$\mathbf{3}_2$	1.83	1	1	$(h_{-1})^1(h)^1(l)^2$	-0.4861	23.6	2
			2	1	$(h)^0(l)^1(l_{+1})^1$	0.4843	23.5	2
			3	1	$(h_{-1})^1(h)^1(l_{+1})^2$	0.3602	13.0	2
			4	1	$(h_{-1})^0(l)^1(l_{+1})^1$	-0.3586	12.9	2
			5	1	$(h_{-1})^1(l_{+1})^1$	0.2564	6.6	2
			6	1	$(h)^1(l)^1$	0.1334	1.8	2
Q_1	$\mathbf{3}_6$	2.61	1	1	$(h)^1(l_{+1})^1$	-0.5883	34.6	2
			2	1	$(h_{-1})^1(l)^1$	-0.5863	34.4	2
			3	2	$(h_{-1})^1(h)^1(l)^1(l_{+1})^1$	-0.2828	8.0	4
			4	3	$(h_{-1})^1(h)^1(l)^1(l_{+1})^1$	0.1199	1.4	4

Continued on next page

Table S3: Composition, coefficient and weight in % for states with contributions of doubly excited configurations of at least 10% and adiabatic energy less than 3 eV for the **para** regioisomer. Spatial configurations of $V^{l;l+1}_{h-1;h}$ excited character are highlighted green.

Geometry	Order	$E_{ad.}$	No.	**CSF**	**Composition**	**Coeff.**	**Weight**	$\mathbf{N}_{opn}$
S_1	$\mathbf{1}_1$	1.60	1	1	$(h_{-1})^1(h)^1(l)^1(l_{+1})^1$	0.3517	12.4	4
			2	1	$(h)^0(l)^1(l_{+1})^1$	0.3411	11.6	2
			3	1	$(h_{-1})^1(h)^1(l)^2$	0.3042	9.3	2
			4	1	$(h)^0(l)^2$	0.3035	9.2	0
			5	1	$(h_{-1})^0(l)^2$	-0.2662	7.1	0
			6	1	$(h)^0(l_{+1})^2$	-0.2544	6.5	0
			7	1	$(h_{-1})^1(l)^1$	0.2337	5.5	2
			8	2	$(h_{-1})^1(h)^1(l)^1(l_{+1})^1$	0.2194	4.8	4
S_1	$\mathbf{1}_4$	2.25	1	1	$(h)^0(l)^2$	-0.5420	29.4	0
			2	1	$(h_{-1})^1(h)^1(l)^2$	0.4152	17.2	2
			3	1	$(h)^0(l)^1(l_{+1})^1$	0.3504	12.3	2
			4	0	$(h)^2(l)^0$	-0.1881	3.5	0
S_1	$\mathbf{1}_7$	2.65	1	2	$(h_{-1})^1(h)^1(l)^1(l_{+1})^1$	0.4537	20.6	4
			2	1	$(h_{-1})^1(h)^1(l_{+1})^2$	0.3397	11.5	2
			3	1	$(h_{-1})^0(l_{+1})^2$	0.3089	9.5	0
			4	1	$(h_{-1})^0(l)^1(l_{+1})^1$	0.2995	9.0	2
			5	1	$(h)^0(l_{+1})^2$	0.2120	4.5	0

Continued on next page

Table S3: Composition, coefficient and weight in % for states with contributions of doubly excited configurations of at least 10% and adiabatic energy less than 3 eV for the **para** regioisomer. Spatial configurations of $V^{l;l+1}_{h-1;h}$ excited character are highlighted green.

Geometry	Order	$E_{ad.}$	No.	**CSF**	**Composition**	**Coeff.**	**Weight**	$\mathbf{N}_{opn}$
S_1	$\mathbf{3}_2$	1.86	1	1	$(h)^0(l)^1(l_{+1})^1$	0.4080	16.6	2
			2	1	$(h_{-1})^1(h)^1(l)^2$	-0.3946	15.6	2
			3	3	$(h_{-1})^1(h)^1(l)^1(l_{+1})^1$	0.3075	9.5	4
			4	1	$(h_{-1})^1(h)^1(l)^1(l_{+1})^1$	-0.2804	7.9	4
			5	1	$(h_{-1})^0(l)^1(l_{+1})^1$	-0.2776	7.7	2
			6	1	$(h_{-1})^1(l_{+1})^1$	0.2631	6.9	2
			7	1	$(h_{-1})^1(h)^1(l_{+1})^2$	0.2590	6.7	2
			8	2	$(h_{-1})^1(h)^1(l)^1(l_{+1})^1$	0.1963	3.9	4
T_1	$\mathbf{1}_1$	1.62	1	1	$(h)^0(l)^1(l_{+1})^1$	0.3608	13.0	2
			2	1	$(h_{-1})^1(h)^1(l)^1(l_{+1})^1$	0.3598	12.9	4
			3	2	$(h_{-1})^1(h)^1(l)^1(l_{+1})^1$	0.3542	12.5	4
			4	1	$(h_{-1})^1(h)^1(l)^2$	0.3346	11.2	2
			5	1	$(h_{-1})^0(l)^1(l_{+1})^1$	-0.2257	5.1	2
			6	1	$(h_{-1})^1(l)^1$	0.2198	4.8	2
T_1	$\mathbf{1}_4$	2.31	1	1	$(h)^0(l)^2$	0.6440	41.5	0
			2	1	$(h_{-1})^1(h)^1(l)^2$	-0.3522	12.4	2
			3	1	$(h)^0(l)^1(l_{+1})^1$	-0.2925	8.6	2
			4	0	$(h)^2(l)^0$	0.2166	4.7	0

Continued on next page

Table S3: Composition, coefficient and weight in % for states with contributions of doubly excited configurations of at least 10% and adiabatic energy less than 3 eV for the **para** regioisomer. Spatial configurations of $V^{l;l_{+1}}_{h_{-1};h}$ excited character are highlighted green.

Geometry	Order	$E_{ad.}$	No.	**CSF**	**Composition**	**Coeff.**	**Weight**	$\mathbf{N}_{opn}$
T_1	$\mathbf{1}_7$	2.87	1	2	$(h_{-1})^1(h)^1(l)^1(l_{+1})^1$	-0.3792	14.4	4
			2	1	$(h_{-1})^1(h)^1(l_{+1})^2$	-0.3751	14.1	2
			3	1	$(h_{-1})^0(l_{+1})^2$	-0.3687	13.6	0
			4	1	$(h_{-1})^0(l)^1(l_{+1})^1$	-0.3343	11.2	2
			5	1	$(h)^0(l_{+1})^2$	-0.1978	3.9	0
T_1	$\mathbf{3}_2$	1.86	1	3	$(h_{-1})^1(h)^1(l)^1(l_{+1})^1$	-0.4034	16.3	4
			2	1	$(h)^0(l)^1(l_{+1})^1$	-0.3693	13.6	2
			3	1	$(h_{-1})^1(h)^1(l)^2$	0.3515	12.4	2
			4	1	$(h_{-1})^1(h)^1(l)^1(l_{+1})^1$	0.3471	12.0	4
			5	1	$(h_{-1})^0(l)^1(l_{+1})^1$	0.2441	6.0	2
			6	2	$(h_{-1})^1(h)^1(l)^1(l_{+1})^1$	-0.2434	5.9	4
			7	1	$(h_{-1})^1(l_{+1})^1$	-0.2245	5.0	2
			8	1	$(h_{-1})^1(h)^1(l_{+1})^2$	-0.2226	5.0	2

Table S4: Vertical- $E_{vert.}$ and Adiabatic-energy $E_{ad.}$ as well as oscillator strength f, squared Frobenius-Norm of the 1-TDM Ω, the participation ratio PR, averaged position of the exciton Pos., CT ratio ω_{CT}, particle-hole coherence length $\omega_{\mathrm{Coh.}}$ and netto CT length $\mathrm{CT_{net}}$, for the $S_0 \rightarrow S_n$ transitions of the *ortho*, *meta* and *para* isomers in the given geometries.

Isomer	Geo.	State	$E_{vert.}$	f	$E_{ad.}$	Ω	PR	Pos.	ω_{CT}	$\omega_{\mathrm{Coh.}}$	$\mathrm{CT_{net}}$	Assigned
ortho	Gs	A_2	2.04	0.2483	2.04	0.882	2.180	1.566	0.250	1.558	0.038	DL_{A+B}; S_h^{l+1} / S_{h-1}^{l}
		A_3	2.16	0.0004	2.16	0.498	2.179	1.566	0.965	1.169	0.022	DL_{A+B}; S_h^{l} / S_{h-1}^{l+1}
		A_4	2.22	0.4213	2.22	0.907	2.109	1.541	0.062	1.081	0.018	DL_{A+B}; S_{h-1}^{l} / S_h^{l+1}
		A_5	2.48	0.0008	2.49	0.828	2.121	1.545	0.775	1.663	0.010	DL_{A+B}; S_{h-1}^{l+1} / S_h^{l}
ortho	Q_1	A_2	1.39	0.0000	1.73	0.152	2.211	1.577	0.965	1.190	0.016	DL; N_h^{l} / S_h^{l+1} / N_h^{l+1} / $V_{h-1;h}^{l;l+1}$ / N_{h-1}^{l+1} / S_{h-1}^{l}
		A_3	1.74	0.2387	2.07	0.819	2.185	1.568	0.316	1.758	0.038	DL_{A+B}; S_h^{l}
		A_4	1.94	0.3258	2.28	0.875	2.120	1.545	0.073	1.097	0.022	DL; S_h^{l+1}
		A_5	2.10	0.0082	2.44	0.313	2.119	1.543	0.308	1.740	0.017	DL; S_{h-1}^{l} / S_h^{l+1}
ortho	T_1	A_2	1.76	0.0015	1.87	0.230	2.132	1.565	0.957	1.196	-0.139	DL_{A+B}; S_h^{l+1} / S_{h-1}^{l}
		A_3	1.80	0.2696	1.91	0.873	1.415	1.212	0.202	1.272	0.060	LE_A; S_h^{l}
		A_4	2.10	0.3129	2.21	0.866	1.929	1.713	0.314	1.658	0.015	LE_B; S_h^{l+1} / S_{h-1}^{l}

Continued on next page

Table S4: Vertical- $E_{vert.}$ and Adiabatic-energy $E_{ad.}$ as well as oscillator strength f, squared Frobenius-Norm of the 1-TDM Ω, the participation ratio PR, averaged position of the exciton Pos., CT ratio ω_{CT}, particle-hole coherence length $\omega_{\mathrm{Coh.}}$ and netto CT length $\mathrm{CT_{net}}$, for the $S_0 \rightarrow S_n$ transitions of the *ortho*, *meta* and *para* isomers in the given geometries.

Isomer	Geo.	State	$E_{vert.}$	f	$E_{ad.}$	Ω	PR	Pos.	ω_{CT}	$\omega_{\mathrm{Coh.}}$	$\mathrm{CT_{net}}$	Assigned
		A_5	2.31	0.0024	2.42	0.557	2.048	1.589	0.939	1.235	-0.237	$\mathrm{LE_B}$; S^{l+1}_{h-1}
ortho	S_1	A_2	1.73	0.0006	1.79	0.295	2.194	1.579	0.957	1.209	-0.075	DL; S^{l}_{h}
		A_3	1.82	0.2742	1.88	0.865	1.842	1.364	0.297	1.551	0.054	$\mathrm{DL_{A+B}}$; S^{l}_{h-1} / S^{l+1}_{h}
		A_4	2.08	0.3711	2.14	0.886	2.066	1.641	0.169	1.325	0.014	DL; N^{l}_{h} / N^{l}_{h-1} / $V^{l;l+1}_{h-1;h}$ / S^{l}_{h-1} / N^{l+1}_{h} / N^{l+1}_{h}
		A_5	2.33	0.0122	2.39	0.641	1.462	1.655	0.743	1.413	-0.665	$\mathrm{DL_{A+B}}$; S^{l+1}_{h} / S^{l}_{h-1}
ortho	S_2	A_2	1.87	0.0004	1.87	0.310	2.187	1.568	0.963	1.181	0.020	DL; S^{l+1}_{h} / N^{l}_{h} / S^{l}_{h-1} / $V^{l;l+1}_{h-1;h}$ / N^{l+1}_{h} / N^{l}_{h-1} / N^{l+1}_{h-1}
	S_2	A_3	1.90	0.2546	1.90	0.865	2.183	1.567	0.282	1.652	0.036	$\mathrm{DL_{A+B}}$; S^{l}_{h}
		A_4	2.09	0.3808	2.09	0.899	2.112	1.542	0.067	1.088	0.018	$\mathrm{LE_{A+B}}$; S^{l}_{h-1} / S^{l+1}_{h}

Continued on next page

Table S4: Vertical- $E_{vert.}$ and Adiabatic-energy $E_{ad.}$ as well as oscillator strength f, squared Frobenius-Norm of the 1-TDM Ω, the participation ratio PR, averaged position of the exciton Pos., CT ratio ω_{CT}, particle-hole coherence length $\omega_{\mathrm{Coh.}}$ and netto CT length $\mathrm{CT_{net}}$, for the $S_0 \rightarrow S_n$ transitions of the *ortho*, *meta* and *para* isomers in the given geometries.

Isomer	Geo.	State	$E_{vert.}$	f	$E_{ad.}$	Ω	PR	Pos.	ω_{CT}	$\omega_{\mathrm{Coh.}}$	$\mathrm{CT_{net}}$	Assigned
meta	Gs	A_2	2.08	0.5288	2.08	0.893	2.183	1.568	0.089	1.110	0.022	DL; S^l_{h-1} / S^{l+1}_h
		A_3	2.14	0.2145	2.14	0.904	2.138	1.551	0.070	1.085	0.015	DL; S^l_h / S^{l+1}_{h-1}
		A_4	2.27	0.0000	2.27	0.001	2.606	1.723	0.404	1.927	-0.054	^{1}DL; N^l_h / N^{l+1}_{h-1} / N^l_{h-1} /$V^{l;l+1}_{h-1;h}$ / N^{l+1}_h
		A_5	2.54	0.0033	2.54	0.197	2.118	1.539	0.271	1.635	-0.025	DL; $Z^l_{h-1;h}$ / $Z^{l;l+1}_h$ / $Z^{l;l+1}_{h-1}$ / $Z^{l+1}_{h-1;h}$
meta	Q_1	A_2	1.41	0.0000	1.73	0.001	2.477	1.677	0.300	1.609	-0.012	^{1}DL; N^l_h / $V^{l;l+1}_{h-1;h}$ / N^{l+1}_h / N^l_{h-1} / N^{l+1}_{h-1}
		A_3	1.82	0.3080	2.14	0.704	2.213	1.576	0.109	1.138	0.048	DL+$\mathrm{CT_{A+B\rightarrow L}}$; S^l_{h-1} / S^{l+1}_h / $Z^l_{h-1;h}$ / $Z^{l;l+1}_h$ / $Z^{l;l+1}_{h-1}$ / $Z^{l+1}_{h-1;h}$
		A_4	1.91	0.1710	2.23	0.865	2.164	1.560	0.087	1.107	0.022	DL; S^l_h / S^{l+1}_{h-1}
		A_5	1.95	0.1315	2.27	0.484	2.149	1.561	0.093	1.131	-0.030	DL+$\mathrm{CT_{L\rightarrow B+1}}$; S^l_{h-1} / S^{l+1}_h / $Z^l_{h-1;h}$ / $Z^{l;l+1}_h$ / $Z^{l;l+1}_{h-1}$ / $Z^{l+1}_{h-1;h}$

Continued on next page

Table S4: Vertical- $E_{vert.}$ and Adiabatic-energy $E_{ad.}$ as well as oscillator strength f, squared Frobenius-Norm of the 1-TDM Ω, the participation ratio PR, averaged position of the exciton Pos., CT ratio ω_{CT}, particle-hole coherence length $\omega_{\mathrm{Coh.}}$ and netto CT length $\mathrm{CT_{net}}$, for the $S_0 \rightarrow S_n$ transitions of the *ortho*, *meta* and *para* isomers in the given geometries.

Isomer	Geo.	State	$E_{vert.}$	f	$E_{ad.}$	Ω	PR	Pos.	ω_{CT}	$\omega_{\mathrm{Coh.}}$	$\mathrm{CT_{net}}$	Assigned
meta	T_1	A_2	1.82	0.3671	1.94	0.894	1.128	2.024	0.085	1.091	0.015	$\mathrm{DL_{A+L}}$; S_h^l
		A_3	1.94	0.0000	2.05	0.001	2.565	1.823	0.678	2.575	-0.001	$^1\mathrm{DL_{A+B}}$; $1/2\mathrm{V}_{h-1;h}^{l;l+1}$
	T_1	A_4	2.16	0.3592	2.28	0.904	1.168	1.117	0.108	1.121	0.054	$\mathrm{DL_{B+L}}$; S_{h-1}^{l+1}
		A_5	2.32	0.0158	2.44	0.766	1.869	1.583	0.945	1.250	0.455	$\mathrm{CT_{B\rightarrow A}}$; S_{h-1}^{l} / S_h^{l+1} / S_{h-1}^{l+1}
meta	S_1	A_2	1.86	0.3868	1.93	0.895	1.144	2.018	0.087	1.093	0.016	$\mathrm{DL_{A+L}}$; S_h^l
		A_3	2.00	0.0000	2.06	0.001	2.465	1.777	0.641	2.473	-0.117	$^1\mathrm{DL_{A+B}}$; $1/2\mathrm{V}_{h-1;h}^{l;l+1}$
	S_1	A_4	2.15	0.3502	2.21	0.905	1.178	1.120	0.106	1.120	0.049	$\mathrm{DL_{B+L}}$; S_{h-1}^{l+1}
		A_5	2.34	0.0147	2.41	0.774	2.100	1.585	0.949	1.256	0.285	$\mathrm{CT_{B\rightarrow A}}$; S_{h-1}^{l} / S_h^{l+1} / S_{h-1}^{l+1}
meta	S_2	A_2	1.92	0.0000	1.91	0.001	2.573	1.714	0.354	1.745	0.032	$^1\mathrm{DL}$; N_h^l / N_{h-1}^{l+1} / N_{h-1}^{l} / $\mathrm{V}_{h-1;h}^{l;l+1}$ / N_h^{l+1}
		A_3	1.96	0.4794	1.95	0.875	2.183	1.567	0.090	1.109	0.024	DL; S_h^l / S_{h-1}^{l+1}
		A_4	2.03	0.1995	2.02	0.895	2.141	1.552	0.072	1.085	0.016	DL; S_{h-1}^{l} / S_h^{l+1}

Continued on next page

Table S4: Vertical- $E_{vert.}$ and Adiabatic-energy $E_{ad.}$ as well as oscillator strength f, squared Frobenius-Norm of the 1-TDM Ω, the participation ratio PR, averaged position of the exciton Pos., CT ratio ω_{CT}, particle-hole coherence length $\omega_{\mathrm{Coh.}}$ and netto CT length $\mathrm{CT_{net}}$, for the $S_0 \rightarrow S_n$ transitions of the *ortho*, *meta* and *para* isomers in the given geometries.

Isomer	Geo.	State	$E_{vert.}$	f	$E_{ad.}$	Ω	PR	Pos.	ω_{CT}	$\omega_{\mathrm{Coh.}}$	$\mathrm{CT_{net}}$	Assigned
		A_5	2.28	0.0109	2.26	0.224	2.121	1.545	0.099	1.159	-0.011	DL; $Z^{l}_{h_{-1};h}$ / $Z^{l;l_{+1}}_{h}$ / $Z^{l;l_{+1}}_{h_{-1}}$ / $Z^{l_{+1}}_{h_{-1};h}$
para	Gs	A_2	1.98	1.1138	1.98	0.883	2.273	1.600	0.192	1.353	0.039	DL; S^{l}_{h} / $S^{l_{+1}}_{h_{-1}}$
		A_3	2.10	0.0000	2.10	0.185	2.336	1.623	0.793	1.845	0.080	^{1}DL; N^{l}_{h} / $S^{l}_{h_{-1}}$ / $V^{l;l_{+1}}_{h_{-1};h}$ / $N^{l_{+1}}_{h_{-1}}$ / $N^{l_{+1}}_{h_{-1}}$ / $N^{l_{+1}}_{h_{-1}}$
para	Q_1	A_2	1.26	0.0000	1.57	0.085	2.365	1.634	0.911	1.452	0.010	^{1}DL; N^{l}_{h} / $V^{l;l_{+1}}_{h_{-1};h}$ / $N^{l_{+1}}_{h}$ / $N^{l}_{h_{-1}}$ / $N^{l_{+1}}_{h_{-1}}$
		A_3	1.72	0.7822	2.03	0.746	2.259	1.595	0.212	1.411	0.054	$\mathrm{CT_{A+B\rightarrow L}}$; S^{l}_{h} / $S^{l_{+1}}_{h_{-1}}$
		A_4	1.87	0.1905	2.18	0.409	2.143	1.553	0.131	1.232	-0.026	DL+$\mathrm{CT_{L\rightarrow A+B}}$; $Z^{l}_{h_{-1};h}$ / $Z^{l;l_{+1}}_{h}$ / S^{l}_{h} / $Z^{l;l_{+1}}_{h_{-1}}$
		A_2	1.56	0.0001	1.62	0.092	2.327	1.615	0.942	1.336	-0.009	^{1}DL; $Z^{l;l_{+1}}_{h}$ / $_{1/2}V^{l;l_{+1}}_{h_{-1};h}$ / $Z^{l}_{h_{-1};h}$
para	T_1	A_3	1.77	0.7127	1.83	0.877	1.281	1.175	0.156	1.184	0.042	$\mathrm{DL_{A+L}}$; S^{l}_{h}

Continued on next page

Table S4: Vertical- $E_{vert.}$ and Adiabatic-energy $E_{ad.}$ as well as oscillator strength f, squared Frobenius-Norm of the 1-TDM Ω, the participation ratio PR, averaged position of the exciton Pos., CT ratio ω_{CT}, particle-hole coherence length $\omega_{\mathrm{Coh.}}$ and netto CT length $\mathrm{CT_{net}}$, for the $S_0 \rightarrow S_n$ transitions of the *ortho*, *meta* and *para* isomers in the given geometries.

Isomer	Geo.	State	$E_{vert.}$	f	$E_{ad.}$	Ω	PR	Pos.	ω_{CT}	$\omega_{\mathrm{Coh.}}$	$\mathrm{CT_{net}}$	Assigned
		A_4	2.04	0.4477	2.10	0.884	1.459	1.916	0.184	1.257	0.009	$\mathrm{DL_{B+L}}$; S^{l}_{h-1} / S^{l+1}_{h} / S^{l+1}_{h-1}
para	S_1	A_2	1.62	0.0002	1.60	0.106	2.354	1.634	0.940	1.360	0.063	$^{1}\mathrm{DL}$; $\mathrm{V}^{l;l+1}_{h-1;h}$ / $\mathrm{Z}^{l;l+1}_{h}$ / $\mathrm{Z}^{l}_{h-1;h}$ / N^{l}_{h} / N^{l}_{h-1} / N^{l+1}_{h} / S^{l}_{h-1}
		A_3	1.81	0.8844	1.79	0.873	1.453	1.944	0.190	1.244	0.026	$\mathrm{DL_{A+L}}$; S^{l}_{h} / S^{l+1}_{h-1}
		A_4	2.03	0.3059	2.01	0.891	1.559	1.265	0.148	1.209	0.047	$\mathrm{DL_{B+L}}$; S^{l}_{h-1} / S^{l+1}_{h} / S^{l+1}_{h-1}
para	S_2	A_2	1.77	0.0000	1.75	0.111	2.341	1.625	0.923	1.402	0.022	$^{1}\mathrm{ME_4}$; N^{l}_{h} / $\mathrm{V}^{l;l+1}_{h-1;h}$ / N^{l}_{h-1} / N^{l+1}_{h} / N^{l+1}_{h-1}
		B_1	1.87	1.0367	1.85	0.863	2.267	1.598	0.203	1.381	0.037	DL; S^{l}_{h} / S^{l+1}_{h-1}
		A_3	2.02	0.0000	2.00	0.890	2.134	1.549	0.078	1.102	0.022	$\mathrm{DL_{A+B}}$; S^{l}_{h-1} / S^{l+1}_{h}
		S_2	2.22	0.0253	2.20	0.218	2.110	1.539	0.132	1.246	0.003	$^{1}\mathrm{ME_2}$; $\mathrm{Z}^{l}_{h-1;h}$ / $\mathrm{Z}^{l;l+1}_{h}$ / $\mathrm{Z}^{l;l+1}_{h-1}$ / $\mathrm{Z}^{l+1}_{h-1;h}$
		A_4	2.39	0.0000	2.38	0.203	2.101	1.536	0.140	1.274	-0.006	$^{1}\mathrm{ME_4}$; $\mathrm{V}^{l;l+1}_{h-1;h}$ / N^{l}_{h} / N^{l+1}_{h} / N^{l}_{h-1}

Table S5: Vertical- $E_{vert.}$ and Adiabatic-energy $E_{ad.}$ as well as oscillator strength f, squared Frobenius-Norm of the 1-TDM Ω, the participation ratio PR, averaged position of the exciton Pos., CT ratio ω_{CT}, particle-hole coherence length $\omega_{\mathrm{Coh.}}$ and netto CT length $\mathrm{CT_{net}}$, for the $S_0 \rightarrow T_n$ transitions of the *ortho*, *meta* and *para* isomers in the given geometries.

Isomer	Geo.	State	$E_{vert.}$	f	$E_{ad.}$	Ω	PR	Pos.	ω_{CT}	$\omega_{\mathrm{Coh.}}$	$\mathrm{CT_{net}}$	Assigned
		A_1	1.09	0.0000	1.09	0.942	2.089	1.533	0.062	1.092	0.006	DL_{A+B}; T_h^l / T_{h-1}^{l+1}
		A_2	1.11	0.0000	1.11	0.940	2.078	1.529	0.049	1.065	0.004	DL_{A+B}; T_{h-1}^l / T_h^{l+1}
ortho	Gs	A_3	2.29	0.0015	2.29	0.694	2.156	1.558	0.633	2.041	0.026	DL_{A+B}; T_{h-1}^{l+1} / T_h^l / $Z_{h-1;h}^l$ / $Z_h^{l;l+1}$
		A_4	2.38	0.0308	2.38	0.903	2.028	1.510	0.072	1.140	0.008	DL_{A+B}; T_{h-2}^{l+1} / T_{h-3}^l / T_{h-1}^{l+3} / T_h^{l+4}
		A_{16}	3.62	0.5591	3.62	0.834	2.302	1.611	0.193	1.348	0.132	DL; T_h^{l+4} / T_{h-3}^l / T_{h-1}^{l+3} / T_{h-1}^{l+2}
		A_1	0.71	0.0000	1.05	0.826	2.121	1.544	0.084	1.128	-0.003	DL_{A+B}; T_h^l / T_{h-1}^{l+1}
		A_2	0.74	0.0000	1.08	0.819	2.112	1.541	0.072	1.101	-0.006	DL_{A+B}; T_h^{l+1} / T_{h-1}^l
ortho	Q_1	A_3	1.62	0.0000	1.95	0.126	2.206	1.575	0.895	1.378	0.005	^3DL; $Z_h^{l;l+1}$ / $Z_{h-1;h}^l$ / $Z_{h-1;h}^{l+1}$ / $Z_{h-1}^{l;l+1}$ / T_{h-1}^{l+1}
		A_4	2.09	0.1339	2.43	0.639	2.204	1.575	0.964	1.187	0.022	DL_{A+B}; T_{h-1}^l / T_h^{l+1} / $V_{h-1;h}^{l;l+1}$
		A_{12}	3.19	0.0228	3.53	0.109	2.210	1.579	0.497	2.174	0.080	^3DL; $Z_h^{l;l+1}$ / $Z_{h-1;h}^l$ / $Z_{h-1;h}^{l+1}$ / $Z_{h-1}^{l;l+1}$

Continued on next page

Table S5: Vertical- $E_{vert.}$ and Adiabatic-energy $E_{ad.}$ as well as oscillator strength f, squared Frobenius-Norm of the 1-TDM Ω, the participation ratio PR, averaged position of the exciton Pos., CT ratio ω_{CT}, particle-hole coherence length $\omega_{\mathrm{Coh.}}$ and netto CT length $\mathrm{CT_{net}}$, for the $S_0 \rightarrow T_n$ transitions of the *ortho*, *meta* and *para* isomers in the given geometries.

Isomer	Geo.	State	$E_{vert.}$	f	$E_{ad.}$	Ω	PR	Pos.	ω_{CT}	$\omega_{\mathrm{Coh.}}$	$\mathrm{CT_{net}}$	Assigned
ortho	T_1	A_1	0.75	0.0000	0.86	0.842	1.083	1.065	0.066	1.070	0.005	$\mathrm{LE_A}$; T_h^l
		A_2	1.14	0.0000	1.25	0.829	1.103	1.999	0.084	1.091	0.006	$\mathrm{LE_B}$; T_{h-1}^{l+1} / T_h^{l+1}
		A_3	1.93	0.0002	2.04	0.209	2.128	1.601	0.866	1.431	-0.138	$\mathrm{DL_{A+B}}$; $\mathrm{V}_{h-1;h}^{l;l+1}$ / $\mathrm{V}_{h-1;h}^{l;l+1}$ / $\mathrm{Z}_h^{l;l+1}$ / $\mathrm{Z}_{h-1;h}^{l}$ / $\mathrm{V}_{h-1;h}^{l;l+1}$ / $\mathrm{Z}_{h-1}^{l;l+1}$
		A_4	2.17	0.0261	2.28	0.704	2.182	1.565	0.956	1.197	-0.019	$\mathrm{DL_{A+B}}$; T_{h-1}^{l} / T_h^{l+1}
		A_{10}	3.15	0.1963	3.25	0.102	2.262	1.554	0.520	2.106	0.353	$\mathrm{CT_{A+B}}$; $\mathrm{Z}_h^{l;l+1}$ / $\mathrm{V}_{h-1;h}^{l;l+1}$ / $\mathrm{Z}_{h-1;h}^{l}$ / $\mathrm{V}_{h-1;h}^{l;l+1}$
ortho	S_1	A_1	0.82	0.0000	0.88	0.868	1.084	1.067	0.073	1.078	0.006	$\mathrm{LE_A}$; T_h^l / T_{h-1}^{l} / T_h^{l+1}
		A_2	1.04	0.0000	1.10	0.862	1.093	2.006	0.081	1.087	0.005	$\mathrm{LE_B}$; T_{h-1}^{l+1} / T_h^{l+1} / T_{h-1}^{l}
		A_3	1.94	0.0008	2.00	0.299	2.173	1.588	0.854	1.491	-0.110	$\mathrm{DL_{A+B}}$; T_{h-1}^{l+1} / $\mathrm{Z}_h^{l;l+1}$ / $\mathrm{Z}_{h-1;h}^{l}$ / $\mathrm{V}_{h-1;h}^{l;l+1}$ / $\mathrm{Z}_{h-1}^{l;l+1}$ / $\mathrm{V}_{h-1;h}^{l;l+1}$
		A_4	2.18	0.0588	2.24	0.730	2.203	1.568	0.939	1.252	0.003	$\mathrm{DL_{A+B}}$; T_{h-1}^{l} / T_h^{l+1}

Continued on next page

Table S5: Vertical- $E_{vert.}$ and Adiabatic-energy $E_{ad.}$ as well as oscillator strength f, squared Frobenius-Norm of the 1-TDM Ω, the participation ratio PR, averaged position of the exciton Pos., CT ratio ω_{CT}, particle-hole coherence length $\omega_{\mathrm{Coh.}}$ and netto CT length $\mathrm{CT_{net}}$, for the $S_0 \rightarrow T_n$ transitions of the *ortho*, *meta* and *para* isomers in the given geometries.

Isomer	Geo.	State	$E_{vert.}$	f	$E_{ad.}$	Ω	PR	Pos.	ω_{CT}	$\omega_{\mathrm{Coh.}}$	$\mathrm{CT_{net}}$	Assigned
		A_{10}	3.16	0.1270	3.22	0.209	2.398	1.603	0.464	2.045	0.312	DL; $Z_h^{l;l+1}$ / $Z_{h-1;h}^{l}$ / T_h^{l+2} / $V_{h-1;h}^{l;l+1}$ / $V_{h-1;h}^{l;l+1}$
	S_2	A_1	0.93	0.0000	0.92	0.845	2.096	1.535	0.069	1.105	0.006	$\mathrm{DL_{A+B}}$; T_h^{l} / T_{h-1}^{l+1}
		A_2	0.95	0.0000	0.95	0.842	2.086	1.531	0.055	1.075	0.003	$\mathrm{DL_{A+B}}$; T_h^{l+1} / T_{h-1}^{l}
ortho		A_3	2.05	0.0003	2.05	0.341	2.197	1.572	0.869	1.438	0.022	$\mathrm{DL_{A+B}}$; T_{h-1}^{l+1} / T_h^{l} / $Z_{h-1;h}^{l}$ / $Z_h^{l;l+1}$
		A_4	2.27	0.1181	2.27	0.717	2.179	1.566	0.927	1.270	0.027	$\mathrm{DL_{A+B}}$; T_{h-1}^{l} / T_h^{l+1}
	S_2	A_{13}	3.36	0.1025	3.36	0.516	2.899	1.882	0.348	1.995	0.125	DL; T_{h-8}^{l} / $Z_{h-1;h}^{l}$ / $Z_h^{l;l+1}$
		A_1	1.01	0.0000	1.01	0.807	2.152	1.557	0.082	1.109	-0.021	$\mathrm{DL_{A+B}}$; T_h^{l} / T_{h-1}^{l+1}
		A_2	1.02	0.0000	1.02	0.802	2.140	1.550	0.080	1.105	-0.022	$\mathrm{DL_{A+B}}$; T_{h-1}^{l} / T_h^{l+1}
meta	Gs	A_3	2.27	0.0056	2.27	0.776	2.031	1.516	0.037	1.060	-0.001	$\mathrm{DL_{A+B}}$; T_{h-2}^{l} / T_{h-3}^{l+1} / T_{h-1}^{l+3} / T_h^{l+4}
		A_4	2.27	0.0076	2.27	0.776	2.031	1.510	0.035	1.057	-0.002	$\mathrm{DL_{A+B}}$; T_{h-2}^{l+1} / T_{h-3}^{l} / T_{h-1}^{l+4} / T_h^{l+3}
		A_5	2.44	0.0000	2.44	0.001	2.591	1.726	0.336	1.704	0.103	^{3}DL; T_{h-1}^{l+1} / $Z_{h-1;h}^{l}$ / $Z_h^{l;l+1}$ / T_h^{l}

Continued on next page

Table S5: Vertical- $E_{vert.}$ and Adiabatic-energy $E_{ad.}$ as well as oscillator strength f, squared Frobenius-Norm of the 1-TDM Ω, the participation ratio PR, averaged position of the exciton Pos., CT ratio ω_{CT}, particle-hole coherence length $\omega_{\mathrm{Coh.}}$ and netto CT length $\mathrm{CT_{net}}$, for the $S_0 \rightarrow T_n$ transitions of the *ortho*, *meta* and *para* isomers in the given geometries.

Isomer	Geo.	State	$E_{vert.}$	f	$E_{ad.}$	Ω	PR	Pos.	ω_{CT}	$\omega_{\mathrm{Coh.}}$	$\mathrm{CT_{net}}$	Assigned
meta	Q_1	A_1	0.67	0.0000	0.99	0.837	2.172	1.563	0.085	1.110	-0.014	$\mathrm{DL_{A+B}}$; T_h^l / T_{h-1}^{l+1}
		A_2	0.68	0.0000	1.00	0.825	2.155	1.559	0.082	1.106	-0.014	$\mathrm{DL_{A+B}}$; T_{h-1}^l / T_h^{l+1}
	Q_1	A_3	1.62	0.0000	1.95	0.000	2.428	1.667	0.274	1.546	0.073	$^3\mathrm{DL}$; $\mathrm{Z}_{h-1;h}^l$ / $\mathrm{Z}_h^{l;l+1}$ / $\mathrm{Z}_{h-1}^{l;l+1}$ / $\mathrm{Z}_{h-1;h}^{l+1}$
		A_4	2.28	0.0075	2.60	0.691	2.184	1.567	0.368	1.913	0.026	$\mathrm{DL_{A+B}}$; T_{h-2}^{l+1} / T_{h-1}^{l+1} / T_h^l / T_{h-3}^l / T_{h-1}^{l+4}
meta	T_1	A_1	0.78	0.0000	0.90	0.862	1.083	2.024	0.070	1.075	0.007	$\mathrm{LE_A}$; T_h^l
		A_2	1.19	0.0000	1.30	0.860	1.072	1.062	0.061	1.064	-0.003	$\mathrm{LE_B}$; T_{h-1}^{l+1}
		A_3	2.00	0.0000	2.11	0.001	2.494	1.782	0.661	2.432	0.059	$^3\mathrm{DL}$; ${}_{3/1/2}\mathrm{V}_h^{l;l+1}$
	T_1	A_4	2.18	0.0223	2.30	0.800	1.064	1.987	0.055	1.057	0.029	$\mathrm{LE_A}$; T_{h-2}^l / T_{h-3}^l / T_h^{l+3}
		A_5	2.27	0.0002	2.39	0.710	2.052	1.652	0.936	1.298	0.403	$\mathrm{CT_{B\rightarrow A}}$; T_{h-1}^l / T_h^{l+1}

Continued on next page

Table S5: Vertical- $E_{vert.}$ and Adiabatic-energy $E_{ad.}$ as well as oscillator strength f, squared Frobenius-Norm of the 1-TDM Ω, the participation ratio PR, averaged position of the exciton Pos., CT ratio ω_{CT}, particle-hole coherence length $\omega_{\mathrm{Coh.}}$ and netto CT length $\mathrm{CT_{net}}$, for the $S_0 \rightarrow T_n$ transitions of the *ortho*, *meta* and *para* isomers in the given geometries.

Isomer	Geo.	State	$E_{vert.}$	f	$E_{ad.}$	Ω	PR	Pos.	ω_{CT}	$\omega_{\mathrm{Coh.}}$	$\mathrm{CT_{net}}$	Assigned
meta	S_1	A_1	0.84	0.0000	0.90	0.845	1.079	2.023	0.065	1.070	0.007	$\mathrm{LE_A}$; T^{l}_{h}
		A_2	1.17	0.0000	1.23	0.843	1.071	1.061	0.061	1.065	0.005	$\mathrm{LE_B}$; T^{l+1}_{h-1}
		A_3	2.04	0.0000	2.11	0.001	2.457	1.785	0.677	2.354	-0.001	^{3}DL; ${}_{3/1/2}\mathrm{V}^{l;l+1}_{h}$
		A_4	2.18	0.0206	2.25	0.796	1.065	1.988	0.053	1.054	0.022	$\mathrm{LE_A}$; T^{l}_{h-2} / T^{l+3}_{h} / T^{l}_{h-3}
		A_5	2.28	0.0007	2.35	0.706	2.321	1.652	0.928	1.336	0.198	$\mathrm{CT_{B\rightarrow A}}$; T^{l}_{h-1} / T^{l+1}_{h}
para	Gs	A_1	0.99	0.0000	0.99	0.845	2.170	1.563	0.101	1.147	0.002	$\mathrm{DL_{A+B}}$; T^{l}_{h} / T^{l+1}_{h-1}
		A_2	1.02	0.0000	1.02	0.841	2.134	1.549	0.082	1.115	-0.001	$\mathrm{DL_{A+B}}$; T^{l}_{h-1} / T^{l+1}_{h}
		A_3	2.30	0.0000	2.30	0.814	2.031	1.525	0.037	1.060	0.004	$\mathrm{DL_{A+B}}$; T^{l}_{h-2} / T^{l+1}_{h-3} / T^{l+3}_{h} / T^{l+4}_{h-1}
		A_4	2.30	0.0145	2.30	0.814	2.031	1.499	0.037	1.060	0.004	$\mathrm{DL_{A+B}}$; T^{l}_{h-3} / T^{l+1}_{h-2} / T^{l+4}_{h} / T^{l+3}_{h-1}
		A_5	2.30	0.0000	2.30	0.422	2.665	1.750	0.658	2.541	0.062	^{3}DL; T^{l+1}_{h-1} / $\mathrm{Z}^{l}_{h-1;h}$ / $\mathrm{Z}^{l;l+1}_{h}$ / T^{l}_{h}

Continued on next page

Table S5: Vertical- $E_{vert.}$ and Adiabatic-energy $E_{ad.}$ as well as oscillator strength f, squared Frobenius-Norm of the 1-TDM Ω, the participation ratio PR, averaged position of the exciton Pos., CT ratio ω_{CT}, particle-hole coherence length $\omega_{\mathrm{Coh.}}$ and netto CT length $\mathrm{CT_{net}}$, for the $S_0 \rightarrow T_n$ transitions of the *ortho*, *meta* and *para* isomers in the given geometries.

Isomer	Geo.	State	$E_{vert.}$	f	$E_{ad.}$	Ω	PR	Pos.	ω_{CT}	$\omega_{\mathrm{Coh.}}$	$\mathrm{CT_{net}}$	Assigned
para	Q_1	A_1	0.64	0.0000	0.94	0.832	2.185	1.569	0.111	1.166	0.013	$\mathrm{DL_{A+B}}$; T^{l}_{h} / T^{l+1}_{h-1}
		A_2	0.68	0.0000	0.99	0.814	2.157	1.558	0.097	1.139	0.008	$\mathrm{DL_{A+B}}$; T^{l}_{h-1} / T^{l+1}_{h}
		A_3	1.52	0.0000	1.83	0.076	2.327	1.619	0.799	1.797	0.008	$^3\mathrm{DL}$; $\mathrm{Z}^{l}_{h-1;h}$ / $\mathrm{Z}^{l;l+1}_{h}$ / $\mathrm{Z}^{l+1}_{h-1;h}$ / $\mathrm{Z}^{l;l+1}_{h-1}$ / T^{l+1}_{h-1}
	Q_1	A_4	2.26	0.0000	2.56	0.583	2.659	1.748	0.598	2.630	0.069	$\mathrm{LE_L}$; T^{l+1}_{h-1} / T^{l}_{h} / T^{l}_{h-4} / T^{l+2}_{h}
		A_5	2.27	0.0000	2.58	0.747	2.051	1.505	0.057	1.096	0.016	$\mathrm{DL_{A+B}}$; T^{l}_{h-2} / T^{l+1}_{h-3} / T^{l+3}_{h} / T^{l+4}_{h-1}

Continued on next page

Table S5: Vertical- $E_{vert.}$ and Adiabatic-energy $E_{ad.}$ as well as oscillator strength f, squared Frobenius-Norm of the 1-TDM Ω, the participation ratio PR, averaged position of the exciton Pos., CT ratio ω_{CT}, particle-hole coherence length $\omega_{\mathrm{Coh.}}$ and netto CT length $\mathrm{CT_{net}}$, for the $S_0 \rightarrow T_n$ transitions of the *ortho*, *meta* and *para* isomers in the given geometries.

Isomer	Geo.	State	$E_{vert.}$	f	$E_{ad.}$	Ω	PR	Pos.	ω_{CT}	$\omega_{\mathrm{Coh.}}$	$\mathrm{CT_{net}}$	Assigned
		A_1	0.65	0.0000	0.71	0.844	1.124	1.098	0.089	1.097	0.016	$\mathrm{LE_A}$; T_h^l / T_{h-1}^l / T_h^{l+1}
	T_1	A_2	1.03	0.0000	1.09	0.830	1.144	2.008	0.106	1.116	0.003	$\mathrm{LE_B}$; T_{h-1}^{l+1} / T_h^{l+1} / $\mathrm{T}_{h_1}^l$ / T_h^l
para		A_3	1.80	0.0000	1.86	0.093	2.333	1.672	0.763	1.903	-0.045	^{3}DL; $\mathrm{Z}_h^{l;l+1}$ / $\mathrm{Z}_{h-1;h}^l$ / $_{1/3}\mathrm{V}_{h-1;h}^{l;l+1}$ / $\mathrm{Z}_{h-1}^{l;l+1}$ / T_{h-1}^{l+1} / $\mathrm{Z}_{h-1;h}^{l+1}$
	T_1	A_4	2.25	0.0195	2.32	0.781	1.046	1.033	0.040	1.040	0.021	$\mathrm{LE_A}$; T_{h-2}^l / T_h^{l+3} / T_{h-2}^{l+1} / T_{h-1}^{l+3}
		A_5	2.33	0.0088	2.39	0.646	2.497	1.686	0.544	2.379	-0.138	$\mathrm{CT_{B\rightarrow A}}$+$\mathrm{DL_L}$; T_{h-3}^l / T_h^{l+2} / T_{h-1}^{l+1} / T_h^l / T_{h-1}^l
		A_1	0.71	0.0000	0.70	0.797	1.133	2.015	0.098	1.108	-0.005	$\mathrm{LE_A}$; T_h^l / T_{h-1}^l / T_h^{l+1}
	S_1	A_2	0.98	0.0000	0.97	0.793	1.146	1.107	0.110	1.120	0.016	$\mathrm{LE_B}$; T_{h-1}^{l+1} / T_h^{l+1} / $\mathrm{T}_{h_1}^l$ / T_h^l
para		A_3	1.88	0.0000	1.86	0.117	2.424	1.643	0.766	1.975	0.086	^{3}DL; $\mathrm{Z}_h^{l;l+1}$ / $\mathrm{Z}_{h-1;h}^l$ / $_{1/3}\mathrm{V}_{h-1;h}^{l;l+1}$ / $\mathrm{Z}_{h-1}^{l;l+1}$ / T_{h-1}^{l+1} / $\mathrm{Z}_{h-1;h}^{l+1}$

Continued on next page

Table S5: Vertical- $E_{vert.}$ and Adiabatic-energy $E_{ad.}$ as well as oscillator strength f, squared Frobenius-Norm of the 1-TDM Ω, the participation ratio PR, averaged position of the exciton Pos., CT ratio ω_{CT}, particle-hole coherence length $\omega_{\mathrm{Coh.}}$ and netto CT length $\mathrm{CT_{net}}$, for the $S_0 \rightarrow T_n$ transitions of the *ortho*, *meta* and *para* isomers in the given geometries.

Isomer	Geo.	State	$E_{vert.}$	f	$E_{ad.}$	Ω	PR	Pos.	ω_{CT}	$\omega_{\mathrm{Coh.}}$	$\mathrm{CT_{net}}$	Assigned
para	S_1	A_4	2.24	0.0182	2.22	0.748	1.059	1.994	0.050	1.051	-0.012	$\mathrm{LE_A}$; T^{l}_{h-2} / T^{l+3}_{h} / T^{l+1}_{h-2} / T^{l+3}_{h-1}
		A_5	2.33	0.0025	2.32	0.602	2.715	1.874	0.560	2.608	0.146	$\mathrm{CT_{B\rightarrow L}}$+$\mathrm{LE_A}$; T^{l}_{h-3} / T^{l+2}_{h} / T^{l+1}_{h-1} / T^{l}_{h} / T^{l}_{h-1}
	S_2	B_1	0.83	0.0000	0.82	0.840	2.650	1.807	0.694	2.590	-0.395	$\mathrm{DL_{A+B}}$; T^{l}_{h} / T^{l+1}_{h-1}
		A_1	0.87	0.0000	0.85	0.834	2.649	1.771	0.629	2.595	-0.294	$\mathrm{DL_{A+B}}$; T^{l+1}_{h} / T^{l}_{h-1}
		B_2	1.99	0.0000	1.98	0.149	2.587	1.726	0.641	2.587	-0.196	$\mathrm{DL_{A+B}}$; $\mathrm{Z}^{l}_{h-1;h}$ / $\mathrm{Z}^{l;l+1}_{h}$ / $\mathrm{Z}^{l;l+1}_{h-1}$ / $\mathrm{Z}^{l+1}_{h-1;h}$
	S_2	B_3	2.24	0.0000	2.22	0.795	2.582	1.716	0.623	2.598	-0.030	$\mathrm{DL_{A+B}}$; T^{l}_{h-2} / T^{l+1}_{h-3} / T^{l+3}_{h} / T^{l+4}_{h-1}

Table S6: Vertical- $E_{vert.}$ and Adiabatic-energy $E_{ad.}$ as well as oscillator strength f, squared Frobenius-Norm of the 1-TDM Ω, the participation ratio PR, averaged position of the exciton Pos., CT ratio ω_{CT}, particle-hole coherence length $\omega_{\mathrm{Coh.}}$ and netto CT length $\mathrm{CT_{net}}$, for the $\mathrm{T_1}\rightarrow\mathrm{T}_n$ transitions of the *ortho*, *meta* and *para* isomers in the given geometries.

Isomer	Geo.	State	$E_{vert.}$	f	$E_{ad.}$	Ω	PR	Pos.	ω_{CT}	$\omega_{\mathrm{Coh.}}$	$\mathrm{CT_{net}}$	Assigned
		A_2	0.02	0.0000	1.09	0.414	2.081	1.530	0.062	1.091	-0.002	$\mathrm{DL_{A+B}}$; T^{l}_{h} / T^{l+1}_{h-1}
		A_3	1.20	0.0000	1.11	0.296	2.199	1.573	0.796	1.670	0.020	$\mathrm{DL_{A+B}}$; T^{l}_{h-1} / T^{l+1}_{h}
ortho	Gs	A_4	1.29	0.0015	2.29	0.219	2.057	1.521	0.158	1.339	0.009	$\mathrm{DL_{A+B}}$; T^{l+1}_{h-1} / T^{l}_{h}
		A_5	1.31	0.0308	2.38	0.213	2.117	1.543	0.292	1.699	0.015	$\mathrm{DL_{A+B}}$; T^{l}_{h-1} / T^{l+1}_{h}
		A_{16}	2.52	0.1203	3.60	0.215	2.209	1.577	0.208	1.413	0.097	DL; T^{l}_{h-3}
		A_2	0.03	0.0000	1.05	0.385	2.100	1.537	0.078	1.117	-0.002	$\mathrm{DL_{A+B}}$; T^{l}_{h-1} / T^{l+1}_{h}
		A_3	0.91	0.0000	1.08	0.110	2.295	1.608	0.946	1.284	0.013	$\mathrm{DL_{A+B}}$; T^{l}_{h} / T^{l+1}_{h-1}
ortho	Q_1	A_4	1.38	0.0000	1.95	0.424	2.201	1.574	0.900	1.356	0.012	^{3}DL; $\mathrm{Z}^{l}_{h-1;h}$ / $\mathrm{Z}^{l;l+1}_{h}$ / $\mathrm{Z}^{l+1}_{h-1;h}$ / $\mathrm{Z}^{l;l+1}_{h-1}$ / T^{l+1}_{h-1} / $\mathrm{T}h^{l}$
		A_5	1.50	0.1339	2.43	0.292	2.255	1.593	0.856	1.523	0.035	$\mathrm{DL_{A+B}}$; T^{l}_{h-1} / T^{l+1}_{h}
		A_{13}	2.55	0.0228	3.53	0.281	2.124	1.545	0.619	2.043	0.032	^{3}DL; $\mathrm{V}^{l;l+1}_{h-1;h}$

Continued on next page

Table S6: Vertical- $E_{vert.}$ and Adiabatic-energy $E_{ad.}$ as well as oscillator strength f, squared Frobenius-Norm of the 1-TDM Ω, the participation ratio PR, averaged position of the exciton Pos., CT ratio ω_{CT}, particle-hole coherence length $\omega_{\mathrm{Coh.}}$ and netto CT length $\mathrm{CT_{net}}$, for the $T_1 \rightarrow T_n$ transitions of the *ortho*, *meta* and *para* isomers in the given geometries.

Isomer	Geo.	State	$E_{vert.}$	f	$E_{ad.}$	Ω	PR	Pos.	ω_{CT}	$\omega_{\mathrm{Coh.}}$	$\mathrm{CT_{net}}$	Assigned
ortho	T_1	A_2	0.39	0.0000	0.86	0.024	2.116	1.556	0.829	1.537	0.173	LE_A; T_h^l
		A_3	1.18	0.0000	1.25	0.116	2.151	1.573	0.947	1.233	-0.140	LE_B; T_{h-1}^{l+1} / T_h^{l+1}
		A_4	1.42	0.0002	2.04	0.420	2.167	1.572	0.928	1.267	-0.024	DL_{A+B}; T_{h-1}^{l} / T_h^{l+1} / T_{h-1}^{l+1} / $^{3/1/2}V_{h;h-1}^{l;l+1}$
		A_5	1.50	0.0261	2.28	0.402	1.096	1.061	0.086	1.092	0.058	DL_{A+B}; T_{h-1}^{l} / T_h^{l+1}
		A_{14}	2.64	0.0049	3.49	0.227	1.589	1.282	0.342	1.438	-0.293	CT_{A+B}; $Z_h^{l;l+1}$ / T_h^{l+2}
ortho	S_1	A_2	0.22	0.0000	0.88	0.025	2.087	1.569	0.955	1.203	0.228	DL_{A+B}; T_h^{l} / T_{h-1}^{l+1}
		A_3	1.12	0.0000	1.10	0.162	2.192	1.575	0.922	1.313	-0.116	DL_{A+B}; T_{h-1}^{l} / T_h^{l+1}
		A_4	1.35	0.0008	2.00	0.416	2.177	1.569	0.906	1.333	-0.015	DL_{A+B}; T_{h-1}^{l+1} / $Th_{-2}{}^{l}$ / T_h^l
		A_5	1.44	0.0588	2.24	0.398	1.080	1.052	0.071	1.075	0.050	DL_{A+B}; T_h^{l+1} / T_{h-1}^{l}
	S_1	A_{13}	2.49	0.0859	3.34	0.150	2.116	1.485	0.362	1.674	0.371	DL; T_{h-2}^{l} / T_{h-7}^{l} / T_{h-3}^{l+1} / T_h^{l+2} / T_h^{l+4} / $Z_{h-1;h}^{l}$ / $Z_h^{l;l+1}$

Continued on next page

Table S6: Vertical- $E_{vert.}$ and Adiabatic-energy $E_{ad.}$ as well as oscillator strength f, squared Frobenius-Norm of the 1-TDM Ω, the participation ratio PR, averaged position of the exciton Pos., CT ratio ω_{CT}, particle-hole coherence length $\omega_{\mathrm{Coh.}}$ and netto CT length $\mathrm{CT_{net}}$, for the $\mathrm{T_1 \rightarrow T}_n$ transitions of the *ortho*, *meta* and *para* isomers in the given geometries.

Isomer	Geo.	State	$E_{vert.}$	f	$E_{ad.}$	Ω	PR	Pos.	ω_{CT}	$\omega_{\mathrm{Coh.}}$	$\mathrm{CT_{net}}$	Assigned
ortho	S_2	A_2	0.03	0.0000	0.92	0.407	2.088	1.533	0.069	1.104	-0.002	$\mathrm{DL_{A+B}}$; T^{l}_{h} / T^{l+1}_{h-1}
		A_3	1.13	0.0000	0.95	0.209	2.256	1.594	0.933	1.296	0.018	$\mathrm{DL_{A+B}}$; T^{l+1}_{h} / T^{l}_{h-1}
		A_4	1.34	0.0003	2.05	0.415	2.170	1.563	0.905	1.322	0.010	$\mathrm{DL_{A+B}}$; T^{l+1}_{h-1} / T^{l}_{h} / $\mathrm{Z}^{l}_{h-1;h}$ / $\mathrm{Z}^{l;l+1}_{h}$
		A_5	1.38	0.1181	2.27	0.201	2.044	1.517	0.100	1.198	0.009	$\mathrm{DL_{A+B}}$; T^{l}_{h-1} / T^{l+1}_{h}
		A_{14}	2.53	0.1025	3.36	0.253	2.191	1.570	0.270	1.612	-0.070	DL; T^{l}_{h-8} / $\mathrm{Z}^{l}_{h-1;h}$ / $\mathrm{Z}^{l;l+1}_{h}$

Continued on next page

Table S6: Vertical- $E_{vert.}$ and Adiabatic-energy $E_{ad.}$ as well as oscillator strength f, squared Frobenius-Norm of the 1-TDM Ω, the participation ratio PR, averaged position of the exciton Pos., CT ratio ω_{CT}, particle-hole coherence length $\omega_{\mathrm{Coh.}}$ and netto CT length $\mathrm{CT_{net}}$, for the $\mathrm{T_1}\rightarrow\mathrm{T}_n$ transitions of the *ortho*, *meta* and *para* isomers in the given geometries.

Isomer	Geo.	State	$E_{vert.}$	f	$E_{ad.}$	Ω	PR	Pos.	ω_{CT}	$\omega_{\mathrm{Coh.}}$	$\mathrm{CT_{net}}$	Assigned
		A_2	0.01	0.0000	1.01	0.411	2.145	1.553	0.086	1.114	0.000	$\mathrm{DL_{A+B}}$; T^{l}_{h} / T^{l+1}_{h-1}
		A_3	1.26	0.0000	1.02	0.203	2.078	1.532	0.056	1.079	0.014	$\mathrm{DL_{A+B}}$; T^{l}_{h-1} / T^{l+1}_{h}
meta	Gs	A_4	1.26	0.0056	2.27	0.202	2.078	1.527	0.053	1.073	0.013	$\mathrm{DL_{A+B}}$; T^{l}_{h-2} / T^{l+1}_{h-3} / T^{l+3}_{h-1} / T^{l+4}_{h}
		A_5	1.43	0.0076	2.27	0.000	2.602	1.726	0.560	2.521	0.090	$\mathrm{DL_{A+B}}$; T^{l+1}_{h-2} / T^{l}_{h-3} / T^{l+4}_{h-1} / T^{l+3}_{h}
		A_6	1.59	0.0000	2.44	0.313	2.410	1.650	0.864	1.690	0.032	^{3}DL; T^{l+1}_{h-1} / $\mathrm{Z}^{l}_{h-1;h}$ / $\mathrm{Z}^{l;l+1}_{h}$ / T^{l}_{h}
		A_2	0.01	0.0000	0.99	0.381	2.137	1.550	0.074	1.088	0.000	$\mathrm{DL_{A+B}}$; T^{l}_{h} / T^{l+1}_{h-1}
	Q_1	A_3	0.95	0.0000	1.00	0.000	2.430	1.659	0.506	2.328	-0.005	$\mathrm{DL_{A+B}}$; T^{l}_{h-1} / T^{l+1}_{h}
meta		A_4	1.61	0.0000	1.95	0.270	2.185	1.565	0.569	2.181	0.030	^{3}DL; $\mathrm{Z}^{l}_{h-1;h}$ / $\mathrm{Z}^{l;l+1}_{h}$ / $\mathrm{Z}^{l;l+1}_{h-1}$ / $\mathrm{Z}^{l+1}_{h-1;h}$
	Q_1	A_5	1.61	0.0075	2.60	0.212	2.089	1.533	0.125	1.239	0.027	$\mathrm{DL_{A+B}}$; T^{l+1}_{h-2} / T^{l+1}_{h-1} / T^{l}_{h} / T^{l}_{h-3} / T^{l+4}_{h-1}
		A_{10}	2.22	0.3933	3.21	0.450	2.207	1.577	0.095	1.118	0.018	DL; $\mathrm{Z}^{l}_{h-1;h}$ / $\mathrm{Z}^{l;l+1}_{h-1}$ / $\mathrm{Z}^{l;l+1}_{h-1}$ / $\mathrm{Z}^{l+1}_{h-1;h}$

Continued on next page

Table S6: Vertical- $E_{vert.}$ and Adiabatic-energy $E_{ad.}$ as well as oscillator strength f, squared Frobenius-Norm of the 1-TDM Ω, the participation ratio PR, averaged position of the exciton Pos., CT ratio ω_{CT}, particle-hole coherence length $\omega_{\mathrm{Coh.}}$ and netto CT length $\mathrm{CT_{net}}$, for the $\mathrm{T_1}\rightarrow\mathrm{T}_n$ transitions of the *ortho*, *meta* and *para* isomers in the given geometries.

Isomer	Geo.	State	$E_{vert.}$	f	$E_{ad.}$	Ω	PR	Pos.	ω_{CT}	$\omega_{\mathrm{Coh.}}$	$\mathrm{CT_{net}}$	Assigned
meta	$\mathrm{T_1}$	$\mathrm{A_2}$	0.41	0.0000	0.90	0.001	1.800	1.617	0.760	1.664	0.478	$\mathrm{LE_A}$; T_h^l
		$\mathrm{A_3}$	1.22	0.0000	1.30	0.001	2.576	1.771	0.723	2.429	0.096	$\mathrm{LE_B}$; T_{h-1}^{l+1}
		$\mathrm{A_4}$	1.40	0.0000	2.11	0.411	1.077	2.003	0.071	1.075	0.026	$^3\mathrm{DL}$; ${}_{3/1/2}\mathrm{V}_h^{l;l+1}$
		$\mathrm{A_5}$	1.49	0.0223	2.30	0.399	1.965	1.626	0.956	1.243	0.403	$\mathrm{LE_A}$; T_{h-2}^l / T_{h-3}^l / T_h^{l+3}
	$\mathrm{T_1}$	$\mathrm{A_6}$	1.53	0.0002	2.39	0.325	1.940	1.596	0.984	1.157	-0.330	$\mathrm{CT_{B\rightarrow A}}$; T_{h-1}^l / T_h^{l+1}
		$\mathrm{A_{10}}$	2.40	0.5059	3.30	0.878	1.152	1.115	0.092	1.094	0.030	$^3\mathrm{LE}_A$; ${}_{1/3/2}\mathrm{V}_h^{l;l+1}$
meta	$\mathrm{S_1}$	$\mathrm{A_2}$	0.33	0.0000	0.90	0.001	1.939	1.598	0.626	1.938	0.353	$\mathrm{LE_A}$; T_h^l
		$\mathrm{A_3}$	1.21	0.0000	1.23	0.001	2.559	1.716	0.678	2.447	-0.010	$\mathrm{LE_B}$; T_{h-1}^{l+1}
		$\mathrm{A_4}$	1.34	0.0000	2.11	0.410	1.066	2.000	0.062	1.065	0.026	$^3\mathrm{DL}$; ${}_{3/1/2}\mathrm{V}_h^{l;l+1}$
		$\mathrm{A_5}$	1.44	0.0206	2.25	0.394	2.204	1.625	0.961	1.241	0.193	$\mathrm{LE_A}$; T_{h-2}^l / T_h^{l+3} / T_{h-3}^l
	$\mathrm{S_1}$	$\mathrm{A_6}$	1.48	0.0007	2.35	0.271	2.204	1.588	0.987	1.147	-0.066	$\mathrm{CT_{B\rightarrow A}}$; T_{h-1}^l / T_h^{l+1}
		$\mathrm{A_{10}}$	2.40	0.4868	3.30	0.847	1.192	1.136	0.101	1.102	0.033	$^3\mathrm{LE}_A$; ${}_{1/2}\mathrm{V}_{h-1;h}^{l;l+1}$

Continued on next page

Table S6: Vertical- $E_{vert.}$ and Adiabatic-energy $E_{ad.}$ as well as oscillator strength f, squared Frobenius-Norm of the 1-TDM Ω, the participation ratio PR, averaged position of the exciton Pos., CT ratio ω_{CT}, particle-hole coherence length $\omega_{\mathrm{Coh.}}$ and netto CT length $\mathrm{CT_{net}}$, for the $\mathrm{T_1}\rightarrow\mathrm{T}_n$ transitions of the *ortho*, *meta* and *para* isomers in the given geometries.

Isomer	Geo.	State	$E_{vert.}$	f	$E_{ad.}$	Ω	PR	Pos.	ω_{CT}	$\omega_{\mathrm{Coh.}}$	$\mathrm{CT_{net}}$	Assigned
meta	S_2	A_2	0.01	0.0000	0.87	0.406	2.112	1.541	0.062	1.075	0.000	$\mathrm{DL_{A+B}};\ \mathrm{T}^{l}_{h}\ /\ \mathrm{T}^{l+1}_{h-1}$
		A_3	1.26	0.0000	2.12	0.000	2.572	1.713	0.618	2.597	0.031	$^3\mathrm{DL};\ \mathrm{Z}^{l}_{h-1;h}\ /\ \mathrm{Z}^{l;l+1}_{h}\ /\ \mathrm{Z}^{l;l+1}_{h-1}\ /\ \mathrm{Z}^{l+1}_{h-1;h}$
		A_4	1.38	0.0069	2.25	0.205	2.061	1.515	0.049	1.072	0.013	$\mathrm{DL_{A+B}};\ \mathrm{T}^{l}_{h-2}\ /\ \mathrm{T}^{l+1}_{h-3}\ /\ \mathrm{T}^{l+3}_{h}\ /\ \mathrm{T}^{l+4}_{h-1}$
	S_2	A_5	1.38	0.0091	2.25	0.205	2.061	1.526	0.043	1.059	0.013	$\mathrm{DL_{A+B}};\ \mathrm{T}^{l+1}_{h-2}\ /\ \mathrm{T}^{l}_{h-3}\ /\ \mathrm{T}^{l+4}_{h}\ /\ \mathrm{T}^{l+3}_{h-1}$
		A_{12}	2.42	0.4300	3.28	0.449	2.205	1.576	0.090	1.111	0.024	$^3\mathrm{DL};\ \mathrm{Z}^{l}_{h-1;h}\ /\ \mathrm{Z}^{l;l+1}_{h}\ /\ \mathrm{Z}^{l;l+1}_{h-1}\ /\ \mathrm{Z}^{l+1}_{h-1;h}$

Continued on next page

Table S6: Vertical- $E_{vert.}$ and Adiabatic-energy $E_{ad.}$ as well as oscillator strength f, squared Frobenius-Norm of the 1-TDM Ω, the participation ratio PR, averaged position of the exciton Pos., CT ratio ω_{CT}, particle-hole coherence length $\omega_{Coh.}$ and netto CT length CT_{net}, for the $T_1 \rightarrow T_n$ transitions of the *ortho*, *meta* and *para* isomers in the given geometries.

Isomer	Geo.	State	$E_{vert.}$	f	$E_{ad.}$	Ω	PR	Pos.	ω_{CT}	$\omega_{Coh.}$	CT_{net}	Assigned
para	Gs	A_2	0.03	0.0000	0.99	0.413	2.139	1.552	0.092	1.130	-0.004	DL_{A+B}; T^{l}_{h} / T^{l+1}_{h-1}
		A_3	1.31	0.0000	1.02	0.204	2.073	1.540	0.070	1.114	0.015	DL_{A+B}; T^{l}_{h-1} / T^{l+1}_{h}
		A_4	1.31	0.0000	2.30	0.204	2.072	1.515	0.070	1.114	0.014	DL_{A+B}; T^{l}_{h-2} / T^{l+1}_{h-3} / T^{l+3}_{h} / T^{l+4}_{h-1}
		A_5	1.31	0.0145	2.30	0.213	2.633	1.736	0.804	2.140	0.039	DL_{A+B}; T^{l}_{h-3} / T^{l+1}_{h-2} / T^{l+4}_{h} / T^{l+3}_{h-1}
		A_6	1.55	0.0000	2.30	0.124	2.730	1.777	0.545	2.536	0.063	^{3}DL; T^{l+1}_{h-1} / $Z^{l}_{h-1;h}$ / $Z^{l;l+1}_{h}$ / T^{l}_{h}
para	Q_1	A_2	0.04	0.0000	0.94	0.381	2.149	1.555	0.102	1.149	-0.006	DL_{A+B}; T^{l}_{h} / T^{l+1}_{h-1}
		A_3	0.89	0.0000	0.99	0.082	2.495	1.682	0.896	1.602	0.009	DL_{A+B}; T^{l}_{h-1} / T^{l+1}_{h}
		A_4	1.62	0.0000	1.83	0.289	2.676	1.754	0.721	2.525	0.048	^{3}DL; $Z^{l}_{h-1;h}$ / $Z^{l;l+1}_{h}$ / $Z^{l+1}_{h-1;h}$ / $Z^{l;l+1}_{h-1}$ / T^{l+1}_{h-1}
		A_5	1.64	0.0000	2.56	0.208	2.097	1.523	0.090	1.147	0.007	LE_{L}; T^{l+1}_{h-1} / T^{l}_{h} / T^{l}_{h-4} / T^{l+2}_{h}
		A_6	1.64	0.0000	2.58	0.208	2.088	1.549	0.088	1.146	0.012	DL_{A+B}; T^{l}_{h-2} / T^{l+1}_{h-3} / T^{l+3}_{h} / T^{l+4}_{h-1}
	Q_1	A_{11}	2.46	0.1441	3.40	0.449	2.166	1.561	0.237	1.523	0.005	DL_{A+B}; $^{2/1/3}V^{l;l+1}_{h-1;h}$

Continued on next page

Table S6: Vertical- $E_{vert.}$ and Adiabatic-energy $E_{ad.}$ as well as oscillator strength f, squared Frobenius-Norm of the 1-TDM Ω, the participation ratio PR, averaged position of the exciton Pos., CT ratio ω_{CT}, particle-hole coherence length $\omega_{Coh.}$ and netto CT length CT_{net}, for the $T_1 \rightarrow T_n$ transitions of the *ortho*, *meta* and *para* isomers in the given geometries.

Isomer	Geo.	State	$E_{vert.}$	f	$E_{ad.}$	Ω	PR	Pos.	ω_{CT}	$\omega_{Coh.}$	CT_{net}	Assigned
para	T_1	A_2	0.39	0.0000	0.71	0.027	2.262	1.583	0.636	2.193	0.017	LE_A; T^l_h / T^l_{h-1} / T^{l+1}_h
		A_3	1.15	0.0000	1.09	0.053	2.367	1.621	0.890	1.545	-0.063	LE_B; T^{l+1}_{h-1} / T^{l+1}_h / $T^l_{h_1}$ / T^l_h
		A_4	1.61	0.0000	1.86	0.405	1.048	1.041	0.047	1.049	0.028	^3DL; $Z^{l;l+1}_h$ / $Z^l_{h-1;h}$ / $_{1/3}V^{l;l+1}_{h-1;h}$ / $Z^{l;l+1}_{h-1}$ / T^{l+1}_{h-1} / $Z^{l+1}_{h-1;h}$
		A_5	1.68	0.0195	2.32	0.296	2.018	1.489	0.632	2.003	-0.239	LE_A; T^l_{h-2} / T^{l+3}_h / T^{l+1}_{h-2} / T^{l+3}_{h-1}
		A_6	1.73	0.0088	2.39	0.409	2.278	1.631	0.853	1.630	0.253	$CT_{B\rightarrow A}$+DL_L; T^l_{h-3} / T^{l+2}_h / T^{l+1}_{h-1} / T^l_h / T^l_{h-1}
	T_1	A_{10}	2.36	0.6294	3.07	0.550	1.244	2.004	0.163	1.190	0.018	LE_A+DL_L; $Z^{l;l+1}_h$ / $_{1/3}V^{l+2}_{h-1;h}$ / $Z^l_{h-1;h}$ / $Z^{l+1}_{h-1;h}$

Continued on next page

Table S6: Vertical- $E_{vert.}$ and Adiabatic-energy $E_{ad.}$ as well as oscillator strength f, squared Frobenius-Norm of the 1-TDM Ω, the participation ratio PR, averaged position of the exciton Pos., CT ratio ω_{CT}, particle-hole coherence length $\omega_{\mathrm{Coh.}}$ and netto CT length $\mathrm{CT_{net}}$, for the $\mathrm{T_1}\rightarrow\mathrm{T}_n$ transitions of the *ortho*, *meta* and *para* isomers in the given geometries.

Isomer	Geo.	State	$E_{vert.}$	f	$E_{ad.}$	Ω	PR	Pos.	ω_{CT}	$\omega_{\mathrm{Coh.}}$	$\mathrm{CT_{net}}$	Assigned
para	S_1	A_2	0.27	0.0000	0.70	0.026	2.272	1.616	0.673	2.128	0.030	$\mathrm{LE_A}$; T^{l}_{h} / T^{l}_{h-1} / T^{l+1}_{h}
		A_3	1.16	0.0000	0.97	0.070	2.414	1.692	0.876	1.633	0.090	$\mathrm{LE_B}$; T^{l+1}_{h-1} / T^{l+1}_{h} / $\mathrm{T}^{l}_{h_1}$ / T^{l}_{h}
	S_1	A_4	1.52	0.0000	1.86	0.405	1.062	2.007	0.057	1.060	0.007	$^3\mathrm{DL}$; $\mathrm{Z}^{l;l+1}_{h}$ / $\mathrm{Z}^{l}_{h-1;h}$ / ${}_{1/3}\mathrm{V}^{l;l+1}_{h-1;h}$ / $\mathrm{Z}^{l;l+1}_{h-1}$ / T^{l+1}_{h-1} / $\mathrm{Z}^{l+1}_{h-1;h}$
		A_5	1.62	0.0182	2.22	0.268	2.069	1.966	0.647	2.220	0.149	$\mathrm{LE_A}$; T^{l}_{h-2} / T^{l+3}_{h} / T^{l+1}_{h-2} / T^{l+3}_{h-1}
	S_1	A_6	1.65	0.0025	2.32	0.009	1.782	1.392	0.723	1.539	0.413	$\mathrm{CT_{B\rightarrow L}}$+$\mathrm{LE_A}$; T^{l}_{h-3} / T^{l+2}_{h} / T^{l+1}_{h-1} / T^{l}_{h} / T^{l}_{h-1}
		A_{10}	2.35	0.6496	3.05	0.499	1.281	1.183	0.172	1.202	0.027	$\mathrm{LE_B}$+$\mathrm{DL_L}$; $\mathrm{Z}^{l;l+1}_{h}$ / ${}_{1/3}\mathrm{V}^{l+2}_{h-1;h}$ / $\mathrm{Z}^{l}_{h-1;h}$ / $\mathrm{Z}^{l+1}_{h-1;h}$
para	S_2	B_2	1.16	0.0000	0.82	0.110	2.539	1.697	0.882	1.695	0.025	$\mathrm{DL_{A+B}}$; T^{l}_{h} / T^{l+1}_{h-1}
		B_3	1.40	0.0000	0.85	0.206	2.076	1.528	0.064	1.099	0.016	$\mathrm{DL_{A+B}}$; T^{l+1}_{h} / T^{l}_{h-1}
	S_2	A_2	1.40	0.0000	1.98	0.206	2.075	1.528	0.064	1.099	0.016	$\mathrm{DL_{A+B}}$; $\mathrm{Z}^{l}_{h-1;h}$ / $\mathrm{Z}^{l;l+1}_{h}$ / $\mathrm{Z}^{l;l+1}_{h-1}$ / $\mathrm{Z}^{l+1}_{h-1;h}$

Continued on next page

Table S6: Vertical- $E_{vert.}$ and Adiabatic-energy $E_{ad.}$ as well as oscillator strength f, squared Frobenius-Norm of the 1-TDM Ω, the participation ratio PR, averaged position of the exciton Pos., CT ratio ω_{CT}, particle-hole coherence length $\omega_{\mathrm{Coh.}}$ and netto CT length $\mathrm{CT_{net}}$, for the $\mathrm{T_1 \rightarrow T}_n$ transitions of the *ortho*, *meta* and *para* isomers in the given geometries.

Isomer	Geo.	State	$E_{vert.}$	f	$E_{ad.}$	Ω	PR	Pos.	ω_{CT}	$\omega_{\mathrm{Coh.}}$	$\mathrm{CT_{net}}$	Assigned
		B_4	1.54	0.0000	2.22	0.233	2.722	1.773	0.660	2.724	0.054	$\mathrm{DL_{A+B}}$; T^{l}_{h-2} / T^{l+1}_{h-3} / T^{l+3}_{h} / T^{l+4}_{h-1}

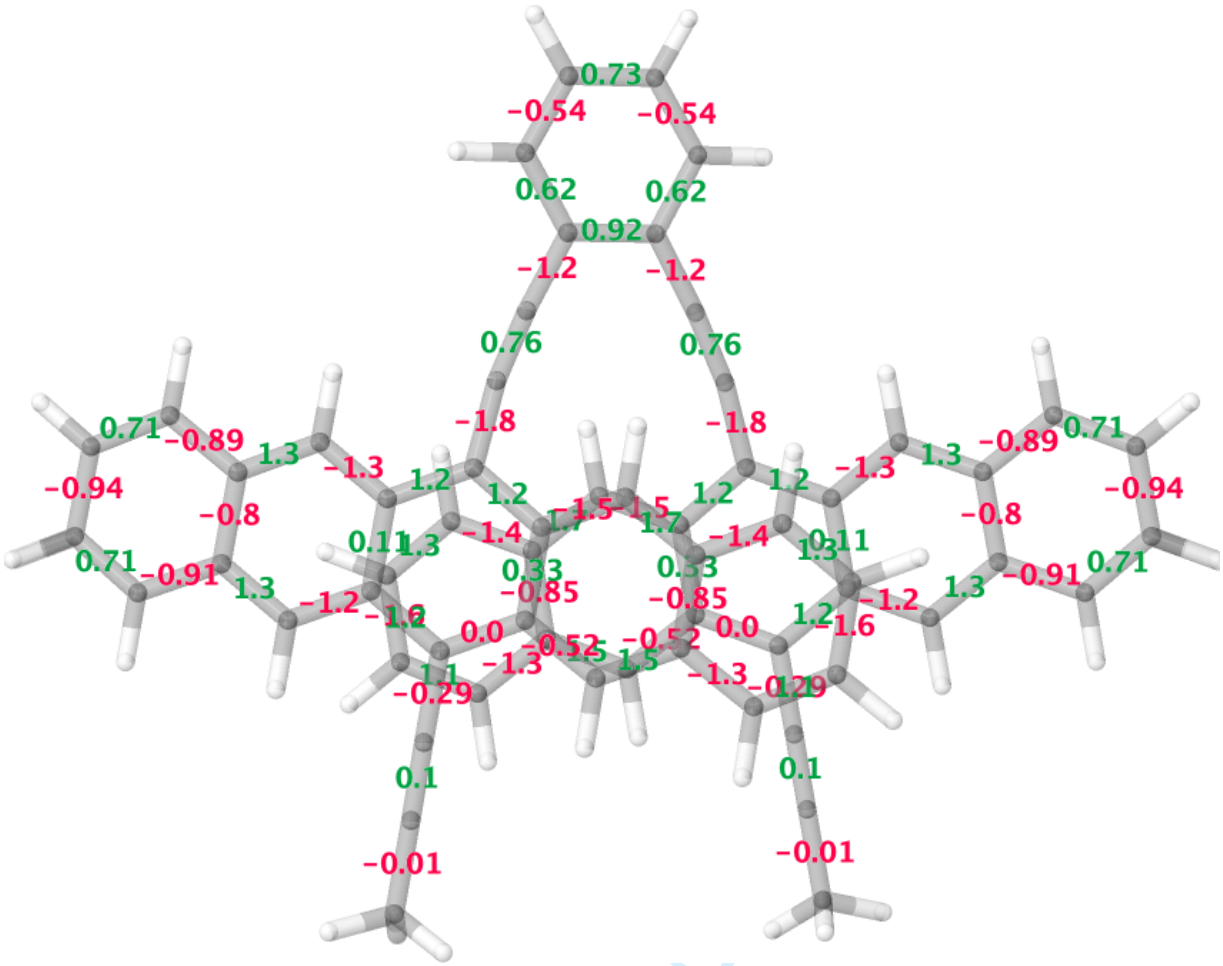

Figure S1: C–C bond distance changes between the ground state- and the optimized S_1-geometry of the *ortho* regio-isomer. All values are given in Å.

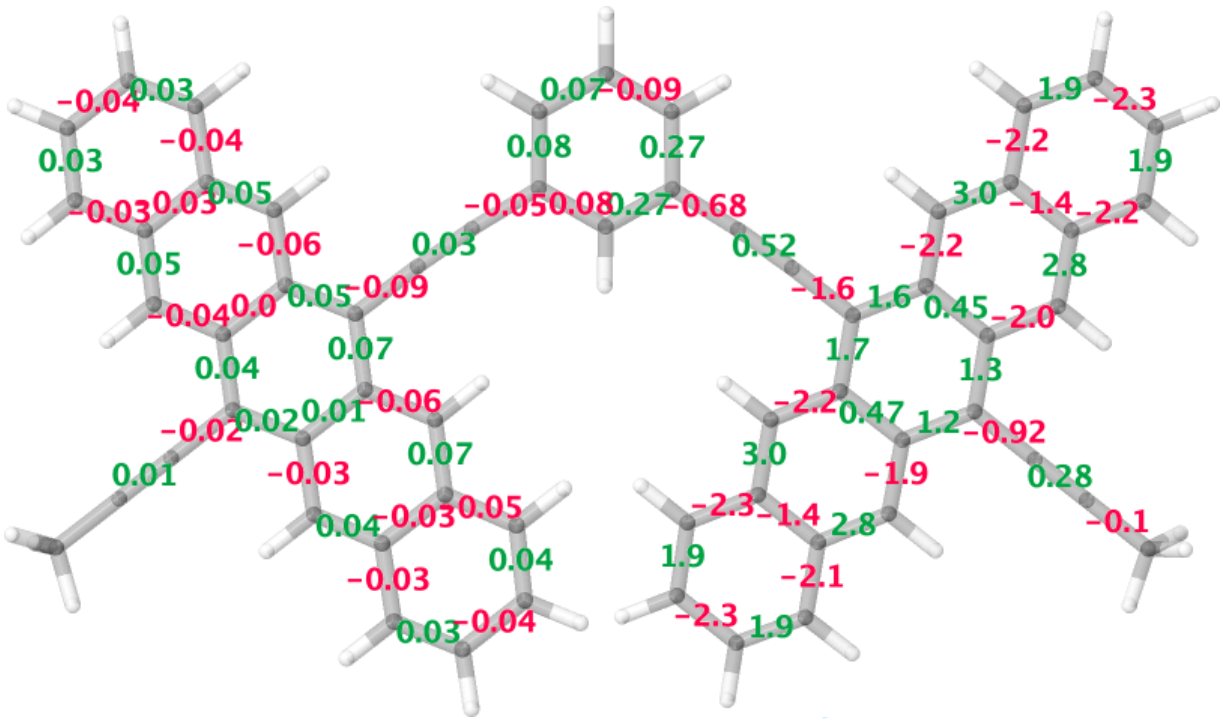

Figure S2: C–C bond distance changes between the ground state- and the optimized S_1-geometry of the *meta* regio-isomer. All values are given in Å.

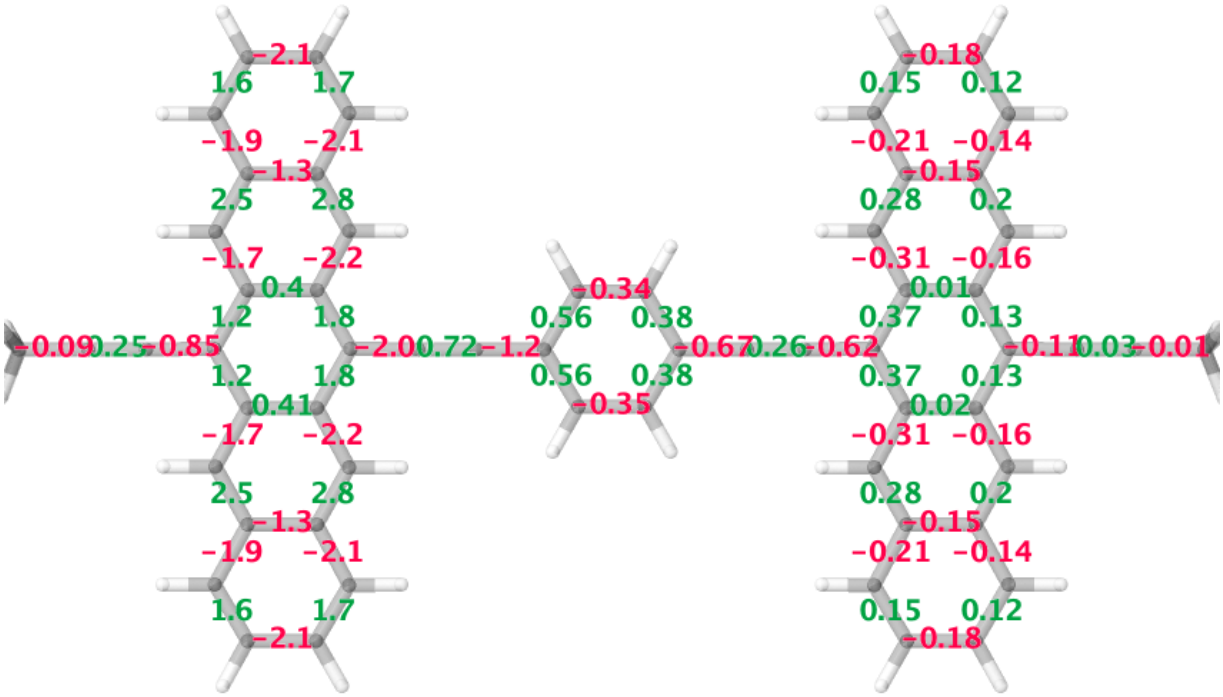

Figure S3: C–C bond distance changes between the ground state- and the optimized S_1-geometry of the *ortho* regio-isomer. All values are given in Å.

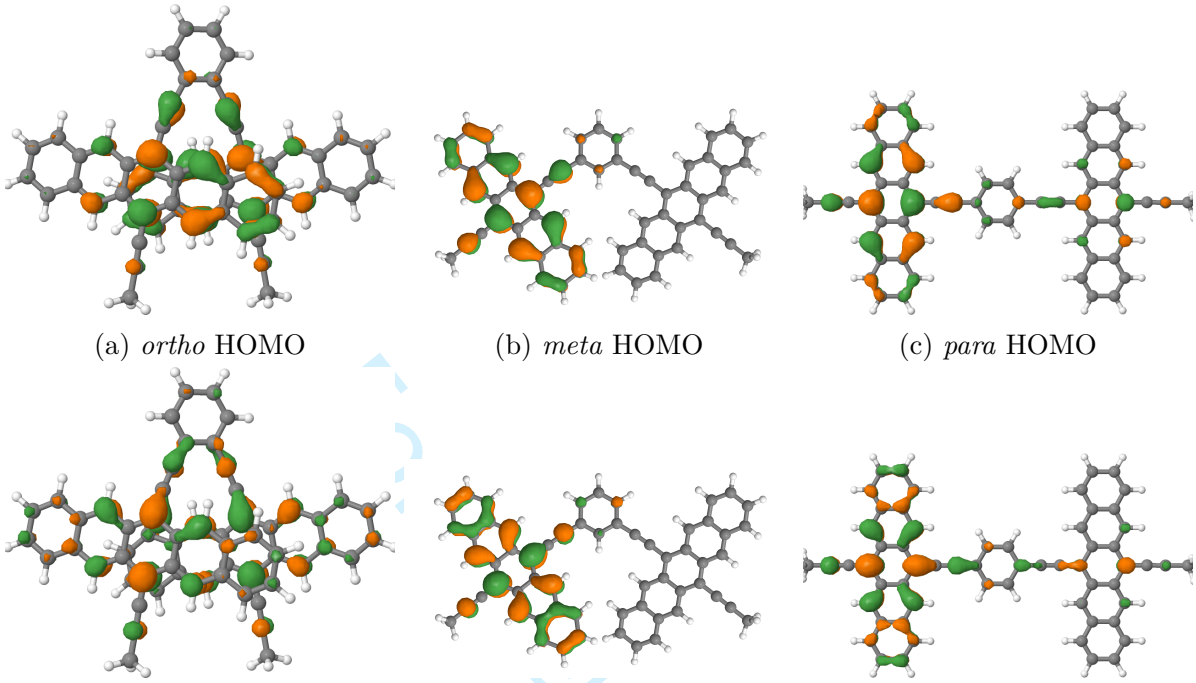

(a) *ortho* HOMO (b) *meta* HOMO (c) *para* HOMO

(d) *ortho* LUMO (e) *meta* LUMO (f) *para* LUMO

Figure S4: Valence orbitals of the three regio-isomers at their optimized S_1 geometries.

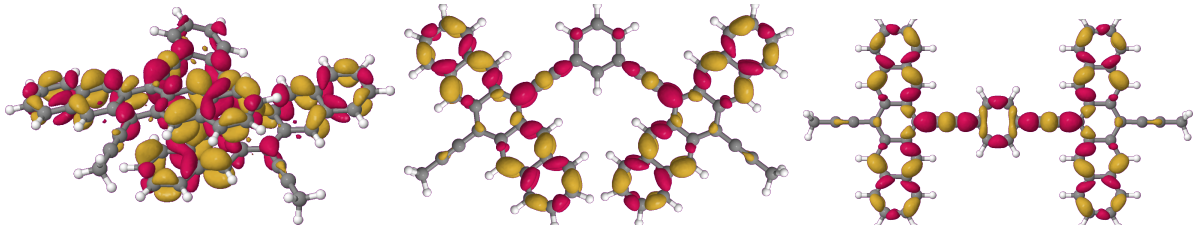

(a) *ortho* (b) *meta* (c) *para*

Figure S5: Density differences of the bright singlet transition state- and the ground state-density. Plotted with an *iso*-value of ± 0.0005.

Simulating the Full Spin Manifold of Triplet-Pair States in a Series of Covalently Linked TIPS-Pentacenes

Timo Schulz and Christel M. Marian*

Institute of Theoretical and Computational Chemistry, Faculty of Mathematics and Natural Sciences, Heinrich Heine University Düsseldorf, 40204 Düsseldorf, Germany

E-mail: Christel.Marian@hhu.de

Abstract

Combined density functional theory and multireference configuration interaction methods have been used to elucidate singlet fission (SF) pathways and mechanisms in three regioisomers of side-on linked pentacene dimers. In addition to the optically bright singlets (S_1 and S_2) and singly excited triplets (T_1 and T_2), the full spin manifold of multiexcitonic triplet-pair states (^{1}ME, ^{3}ME, ^{5}ME) has been considered. In the *ortho*- and *para*-regioisomers, the ^{1}ME and S_1 potentials intersect upon geometry relaxation of the S_1 excitation. In the *meta*-regioisomer, the crossing occurs upon delocalization of the optically bright excitation. The energetic accessibility of these conical intersections and the absence of low-lying charge-transfer states suggests a direct SF mechanism, assisted by charge-resonance effects in the ^{1}ME state. While the ^{5}ME state does not appear to play a role in the SF mechanism of the *ortho*- and *para*-regioisomers, its participation in the disentanglement of the triplet pair is conceivable in the *meta*-regioisomer.

1 Introduction

Singlet fission (SF) is a spin-allowed process in which one photon is converted into two triplet excitons. The reaction is supposed to involve an intermediate multiexcitonic singlet state, ^{1}ME, composed of an antiferromagnetically coupled triplet pair ^{1}(TT). Smith and Michl[1] pointed out that SF does not occur in small-molecule chromophores, but requires some sort of dimeric structure. Initially, SF was observed in molecular crystals where the two generated triplets reside on different molecules.[2] To outcompete other non-radiative pathways, the energy of the optically excited singlet state $E(S_1)$ should be slightly larger than twice the energy of the first excited triplet state $E(T_1)$, i.e. $E(S_1) \geq 2E(T_1)$. This requirement is met, for example, in thin microcrystalline pentacene films.[3] Intermolecular SF for 6,13-bis(triisopropylsilylethynyl)pentacene (TIPS-pentacene, TPc) in solution was reported by Walker et al.[4] who observed a transient bound excimer intermediate, producing triplets with a quantum yield $\Phi_{(T)}$ of 200%. The SF rate was approaching the diffusion limit in that experiment. Pump-depletion-probe experiments on the same system by Herz et al.[5] support a consecutive reaction mechanism for SF in TPc according to $S_1 \rightsquigarrow {}^1(TT) \rightsquigarrow 2T_1$, as opposed to a quantum coherent mechanism[6,7] in which the electronic coupling creates a quantum superposition of the locally excited singlet (^{1}LE) and the multiexcitonic ^{1}ME state immediately after optical excitation. The consecutive model of SF comes in two flavors: a direct and an indirect mechanism. The direct formation of the spin-entangled triplet pair from the primarily excited optically bright state comprises a simultaneous exchange of two electrons.[8,9] The nonadiabatic coupling between the S_1 and ^{1}(TT) states, required in this mechanism, is particularly strong at conical intersections of their respective potential energy surfaces (PESs). In the indirect mechanism, the electrons are exchanged in two steps according to $S_1 \rightsquigarrow {}^1CT \rightsquigarrow {}^1(TT)$ involving an intermediate charge-transfer (CT) state.[7,10] In both variants, the formation of the ^{1}(TT) state is eventually followed by a decoherence of the triplet pair, i.e., $^1(TT) \rightsquigarrow 2T_1$. While there is consensus that the antiferromagnetically coupled triplet-pair state, ^{1}(TT), represents an essential gateway state for SF, the participa-

tion of its ferromagnetically coupled congener, ^{5}(TT), in the disentanglement of the triplet excitons and the reverse process, triplet–triplet annihilation up conversion (TTA-UC), is a matter of debate.[11–16]

The quantum chemical description of SF pushes the boundaries of available electronic structure methods as the dimers are typically large and the spin-correlated triplet-pair states are doubly excited with respect to the electronic ground state: Correlated *ab initio* wave function methods are hardly affordable for molecular systems of this size and less expensive linear response methods such as time-dependent density functional theory (TDDFT) are not applicable as they can handle only singly excited states. Therefore, it is not surprising that many of the computational studies of SF in acene dimers building up on complete active space self-consistent field (CASSCF) wave functions employ very limited active orbital spaces[17–22] or rely on crude semiemprical Hamiltonians to account for dynamic electron correlation.[23–29] Other studies, including a benchmark study on tetracene dimers[30] and our recent work on the SF mechanism in pentacene crystals,[31] use a combination of density functional theory and multireference configuration interaction (DFT/MRCI)[32,33] for these purposes. The DFT/MRCI method, in particular when applied in conjunction with the R2022 Hamiltonian,[34] provides a balanced treatment of singly excited LE and CT states and of doubly excited (DE) and ME states in oligoacenes and their dimers at reasonable computational cost. It is therefore our method of choice when it comes to exploring the energetics of possible intramolecular SF pathways in a series of side-on linked pentacene dimers (*ortho*, *meta* and *para* in Figure 1) in the present work.

Three regioisomers of pentacene dimers (*o*-2, *m*-2 and *p*-2 in Figure 1), carrying one TIPS residue each in 13(13′) positions and covalently linked at their 6(6′) positions by a diethynylbenzene bridge, had been synthesized and spectroscopically characterized by Zirzlmeier et al.[19]. Their study aimed to unravel the influence of through-space vs. through-bond coupling of the pentacene units. Triplet rise times and quantum yields were found to depend on the relative orientation (*ortho*-, *meta*- or *para*-linkage) of the pentacene building

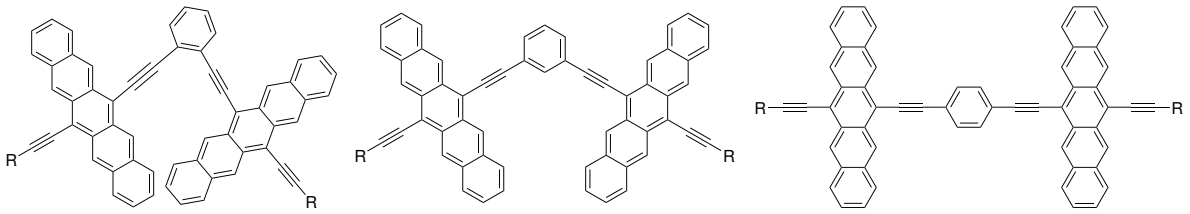

(a) *ortho*; *o*-2 (b) *meta*; *m*-2 (c) *para*; *p*-2

Figure 1: Chemical structures of the 6,6′-linked pentacene dimers. In the *ortho*-, *meta*- and *para*-regioisomers studied in this work, methyl groups were substituted for the triisopropylsilyl residues R in 13 and 13′ positions of the *o*-2, *m*-2 and *p*-2 compounds, respectively.

blocks and on the solvent environment. Time-resolved spectroscopy measurements gave clear indications for a two-step SF mechanism on the picosecond timescale in all regioisomers. Although SF was faster in the *o*-2 and *p*-2 regioisomers, the highest SF efficiency was observed for the *m*-2 regioisomer with a maximum of $\Phi_{(T)} = 145\pm10\%$ in benzonitrile solution and a somewhat lower value of $\Phi_{(T)} = 126\pm3\%$ in toluene. The authors concluded that the right balance between triplet formation and triplet decay optimizes the SF yield in *m*-2. The slight variation of the triplet quantum yield with the solvent polarity was interpreted as an indication for a CT mechanism, although electronic states with CT characteristics were not found among the low-lying electronic singlets in accompanying quantum chemical studies. Further time-resolved spectroscopic investigations by Ringström et al.[35] on the *p*-2 regioisomer and two derivatives thereof with bulky substituents on the phenylene bridge show that the rise and decay times of the triplet-pair depend also on the torsional angle between the pentacene units. Slightly increased rates in more polar solvents and the absence of low-lying CT states suggest that SF is mediated by virtual CT states (superexchange mechanism). Other side-on linked pentacene dimers studied by the Guldi group which are bridged by rigid aliphatic linkers in 6 and 6′ positions, respectively, provide evidence for a CT-mediated intramolecular SF as well.[36]

While complete active space second-order perturbation theory (CASPT2) calculations find the ^{1}ME state quasi degenerate with a bright ^{1}LE state in the simplified *ortho*-, *meta*- and *para*-regioisomers,[19] extended multiconfigurational quasidegenerate perturbation the-

ory (XMCQDPT) places the ^{1}ME state energetically markedly below the optically excited singlet state at all considered molecular geometries.[21,22] Conical intersections or avoided crossings between the S_1 and ^{1}ME PESs, which could promote the contribution of a direct channel in the SF mechanism, are therefore not accessible in subsequent quantum molecular dynamics calculations performed by the latter authors. All simulations were found to be unproductive unless additional higher-lying doubly excited singlet states ^{1}DE (*ortho* and *para*) or ^{1}CT states (*meta*) were included in the vibronic model space, thus suggesting a superexchange mechanism. Our recent theoretical work on the SF mechanism in crystalline pentacene employing the DFT/MRCI method painted a differentiated picture of SF in pentacene crystals.[31] The calculations support a CT-mediated SF mechanism for V-shaped pentacene dimers and the trimer subunit of the herringbone crystal structure. In the slip-stacked dimer, the S_1 and ^{1}ME PESs cross upon geometric relaxation of the optically bright state. The presence of this intersection in energetic and spatial proximity of the absorption region promotes a direct SF mechanism. Besides local excitations on the fragments, the analysis of the S_1 wave function reveals major contributions of charge resonance (CR) excitations, i.e., simultaneous CT excitations from fragment A to fragment B and *vice versa*. Applied to the present case of intermolecular SF in solution, the experimentally observed sensitivity of the SF efficiency with regard to the solvent polarity[19,35,36] does not automatically preclude the direct formation of the ^{1}(TT) triplet-pair state from the primarily excited S_1 state without the involvement of intermediate CT states. A participation of CR excitions in the multiexcitonic wave function could very well provide an alternative explanation of the solvent effects. In addition to the energetics of prospective SF pathways in the *ortho*-, *meta*- and *para*-regioisomers, a particular focus of the present quantum chemical investigation will therefore be a thorough analysis of their molecular wave function compositions in the excited state.

2 Computational Methods

All structures were optimized with the Gaussian 16 program[37] using density functional theory (DFT) in conjunction with the range-separated CAM-B3LYP[38] functional. The basis set comprised def2-SVP[39] contracted Gaussian-type orbitals on all atoms. Minima of the optically bright singlet excited states were determined using time-dependent DFT (TDDFT). Due to its double-excitation character, the nuclear arrangement of the ferromagnetically coupled triplet-pair state, ^{1}(TT), cannot be optimized with linear response TDDFT methods. As the closest proxy, we employ the minimum geometry of its ferromagnetically coupled counterpart, ^{5}(TT), which was optimized using unrestricted Kohn-Sham DFT. In the TDDFT triplet optimizations the Tamm-Dancoff approximation (TDA) was used. Generation of the one-particle basis for subsequent DFT/MRCI calculations employed the same AO basis set in conjunction with the BH-LYP[40] functional. The total energy was converged to 10^{-8}E$_h$, as a density cut-off 10^{-7} was chosen. The exchange-correlation functional was integrated numerically on a grid of size 5. The DFT/MRCI calculations were carried out employing the R2022 Hamiltonian.[34] For each DFT/MRCI calculation, the energy selection threshold was set to 0.8 E$_h$ above the highest desired, computed eigenvalue in the reference space. The short parameter set was employed, since it is optimized for this setup. At each geometry, 21 states of singlet, 20 of triplet and 6 states of quintet spin multiplicity were calculated. Franck–Condon (FC) spectra were generated using the VIBES program.[41,42]

Excited-state descriptors, derived from the DFT/MRCI one-particle transition density matrix (1-TDM), were generated with the TheoDORE toolkit.[43–46] To this end, we partitioned the molecules into three fragments: A and B label the left and right methylethynylpentacene units, respectively, and L the phenyl ring of the linker. The most important descriptors for characterizing the electronic structures are the Frobenius norm Ω of the 1-TDM, the signed net charge transfer length CT$_{\mathrm{net}}$, the CT-ratio ω_{CT}, the particle-hole coherence length ω_{coh}, the mean position of the electron-hole pair (exciton) Pos. and the participation ratio of the individual fragments PR. The Frobenius norm Ω measures the single-excitation

character of the transition and can vary between 0 (pure double or higher excitations) and 1 (pure single excitation). A value of $\mathrm{CT}_{\mathrm{net}} = 0$ in combination with $\omega_{\mathrm{CT}} = 0$ means that no charge displacement takes place upon excitation whereas $\mathrm{CT}_{\mathrm{net}} = 0$ in combination with $\omega_{\mathrm{CT}} \gg 0$ indicates a CR transition. A value of $\mathrm{CT}_{\mathrm{net}} = 1$ would imply a transfer of one electron from fragment A to fragment B, a value of $\mathrm{CT}_{\mathrm{net}} = -1$ a transfer in the opposite direction. The Pos. descriptor contains information about the final mean position of the particle and the initial mean position of the hole. The PR value measures how many fragments are involved in the transition. Detailed explanations of the mentioned quantities can be found in references 43–46.

In the following, singly excited configuration state functions are labelled according to their spin-multiplicity as S for singlets and T for triplets, with a lower case subscript encoding the hole and a lower case superscript specifying the particle molecular orbital (MO). A singlet state, dominated by a HOMO→LUMO single excitation, is denoted as S_h^l , the corresponding triplet state as T_h^l. For an easier characterization of the doubly excited states, we introduce a nomenclature that specifies the orbitals involved in the excitation and the number of open shells of the configuration. A doubly substituted closed-shell spatial configuration involving an excitation from the HOMO to the LUMO is denominated N_h^l, a double excitation with two open shells relocating the two HOMO electrons to LUMO and LUMO+1 is termed $\mathrm{Z}_h^{l;l+1}$ and a double excitation with four unpaired electrons in HOMO-1, HOMO, LUMO and LUMO+1 is referred to as $\mathrm{V}_{h-1;h}^{l;l+1}$. If necessary for the distinction, the resulting spin multiplicity is specified by an additional superscript preceding the capital letter. Using this nomenclature, the lowest quintet state, Q_1, would be denoted ${}^5\mathrm{V}_{h-1;h}^{l;l+1}$, for example.

3 Results and Discussion

3.1 The Franck–Condon region

Aside from the residues R, the *para*-isomer is planar and exhibits D_{2h}-symmetry in the electronic ground state. Due to spatial congestion, the *meta*-isomer and, even more so, the *ortho*-isomer have C_2-symmetric helical structures. Their coordinate systems are chosen such that the z-axis coincides with the symmetry axis, the x-axis lies in the molecular plane of the phenyl linker and the y-axis is perpendicular to it. For a consistent discussion of the absorption properties of the regioisomers, we kept this axis orientation for the *para*-isomer as well.

Due to the weak electronic coupling of the pentacene units by the diethynylphenyl bridges, the two highest occupied dimer orbitals, HOMO-1 and HOMO, have nearly equal energies. They are composed mainly of bonding or antibonding linear combinations of the pentacene monomer HOMOs, with minor contributions from the ethynyl and phenyl linkers (Figure 2). Similar considerations apply to the two lowest unoccupied dimer orbitals, LUMO and LUMO+1. As a consequence, even the singly excited wavefunctions of the optically bright states exhibit pronounced multiconfiguration character.

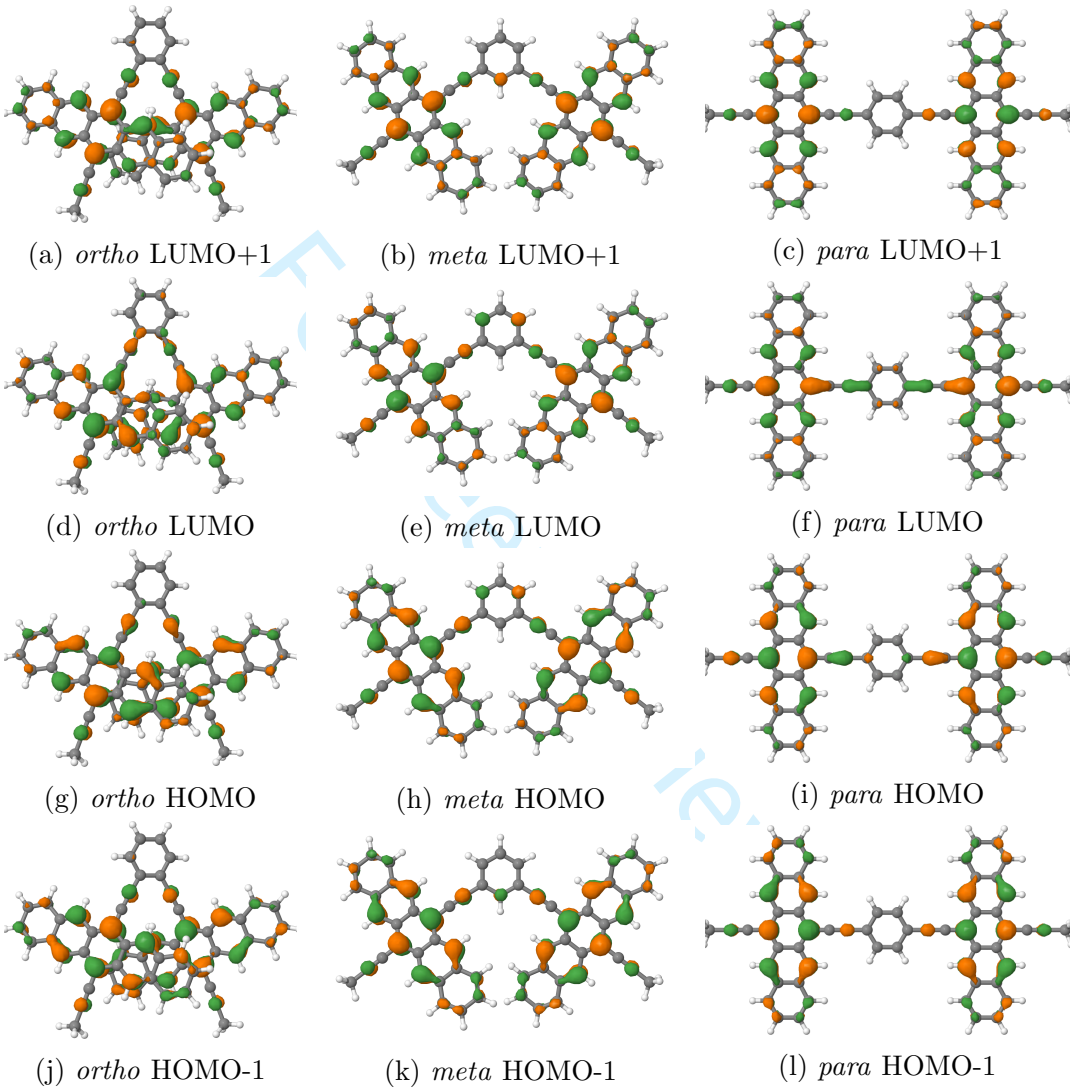

(a) *ortho* LUMO+1 (b) *meta* LUMO+1 (c) *para* LUMO+1

(d) *ortho* LUMO (e) *meta* LUMO (f) *para* LUMO

(g) *ortho* HOMO (h) *meta* HOMO (i) *para* HOMO

(j) *ortho* HOMO-1 (k) *meta* HOMO-1 (l) *para* HOMO-1

Figure 2: The two highest occupied and lowest unoccupied MOs of the regioisomers at the ground state geometry

The convoluted vertical absorption spectra in Figure 3 show two clear trends: A steady blue shift of the first band maximum from the *para*- to the *ortho*-regioisomer, accompanied by a decrease of the oscillator strength. While the energy shifts follow the expectations derived from a simple particle-in-a-box model, they do not reproduce the experimentally observed drifts of the first absorption peak (*para*: 1.79 eV, *meta*: 1.86 eV, *ortho*: 1.85 eV)[19] where a tiny red shift is found when moving from *meta* to *ortho*. One reason for this mismatch lies in the fact that two low-energetic bright transitions with different oscillator strengths form the first broad band in the convoluted absorption spectra of the *ortho*- and *meta*-isomers whereas there is only one in the *para*-isomer (Tables 1-3). The picture changes when we focus on state-specific information. The vertical DFT/MRCI energies of the $S_0 \rightarrow S_1$ transitions (*para*: 1.98 eV, *meta*: 2.08 eV, *ortho*: 2.04 eV) match the experimental trend very well, but they are somewhat too high on an absolute scale. Obviously, geometry relaxation effects in the excited state and vibrational corrections have to be taken into consideration for a fair comparison between theory and experiment (see Section 3.2).

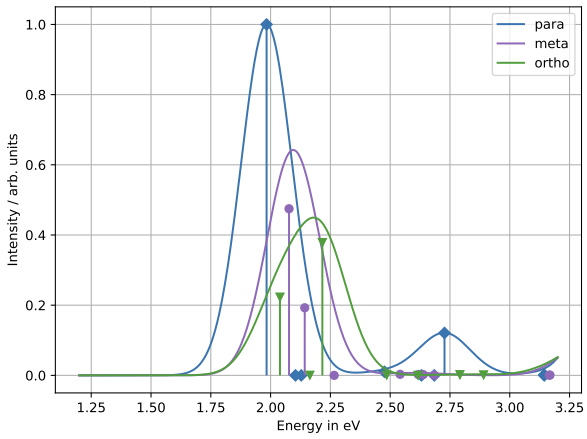

Figure 3: Calculated vertical absorption spectra of the three regioisomers. The DFT/MRCI line spectra were convoluted with Gaussian functions with a full-width at half maximum of 0.2 eV.

The trend in the $S_0 \rightarrow S_1$ absorption intensities of the regioisomers is in good agreement with the experimental results and can readily be understood by looking at the corresponding one-electron transition densities plotted in Figure 4. For all three regioisomers, the hole

Table 1: Adiabatic energies $E_{ad.}$, oscillator strengths f, polarizations and vertical energies $E_{vert.}$ of the transitions to the electronic ground state and descriptors derived from the one-particle transition density matrix for the three lowest excited singlet states of the *ortho*-isomer.

Isomer	**ortho**								
State No. @Geometry	**1**	**2**	**3**	**1**	**2**	**3**	**1**	**2**	**3**
		Gs			S_1			S_2	
$E_{ad.}$	2.04	2.16	2.22	1.79	1.88	2.14	1.87	1.90	2.09
f	0.248	0.000	0.421	0.000	0.274	0.371	0.000	0.255	0.381
Polarization	x	—	z	—	x	z	—	x	z
$E_{vert.}$	2.04	2.16	2.22	1.73	1.82	2.08	1.87	1.90	2.09
Ω	0.882	0.498	0.907	0.295	0.865	0.886	0.310	0.865	0.899
Pos.	1.566	1.566	1.541	1.579	1.364	1.641	1.568	1.567	1.542
PR	2.180	2.179	2.109	2.194	1.842	2.066	2.187	2.183	2.112
ω_{CT}	0.250	0.965	0.062	0.957	0.297	0.169	0.963	0.282	0.067
$\omega_{Coh.}$	1.558	1.169	1.081	1.209	1.551	1.325	1.181	1.652	1.088
CT_{net}	0.038	0.022	0.018	-0.075	0.054	0.014	0.020	0.036	0.018
Character	LE_{A+B}	DL /CR	LE_{A+B}	ME /CR	LE_{A+L}	LE_{B+L}	ME /CR	DL	DL

and particle densities are consistent with short-axis transitions of the individual pentacene building blocks.[31]

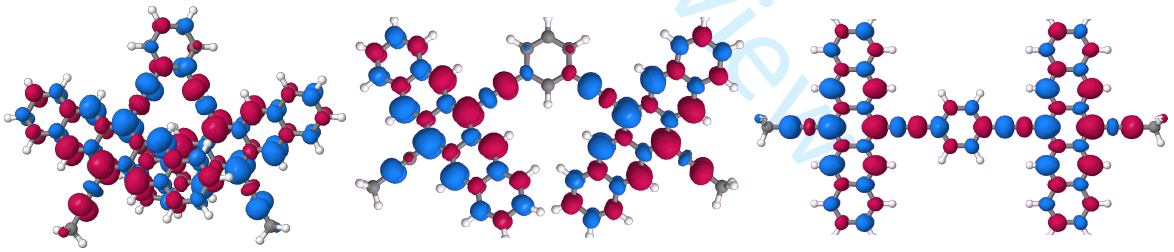

(a) *ortho* (b) *meta* (c) *para*

Figure 4: Transition densities of the $S_0 \rightarrow S_1$ transition at the ground state geometries of the respective regioisomers. Plotted with an *iso*-value of ± 0.0005.

In the *para*-isomer, the short-axis transitions are in a head-to-tail arrangement in the $S_0 \rightarrow S_1$ excitation, leading to a very strong x-polarized low-energy absorption (E_{vert}=1.98 eV, $f(r) = 1.1138$). The corresponding $S_0 \rightarrow S_3$ transition with a head-to-head orientation of the dipole vectors lies at higher energies and is completely dark (E_{vert}=2.13 eV). This behavior

Table 2: Adiabatic energies $E_{ad.}$, oscillator strengths f, polarizations and vertical energies $E_{vert.}$ of the transitions to the electronic ground state and polarization, vertical energies $E_{vert.}$ and descriptors derived from the one-particle transition density matrix for the three lowest excited singlet states of the *meta*-isomer.

Isomer	**meta**								
State No. @ Geometry	**1**	**2** Gs	**3**	**1**	**2** S_1	**3**	**1**	**2** S_2	**3**
$E_{ad.}$	2.08	2.14	2.27	1.93	2.06	2.21	1.91	1.95	2.02
f	0.529	0.215	—	0.387	—	0.350	—	0.479	0.200
Polarization	x	z	—	x	—	z	—	x	z
$E_{vert.}$	2.08	2.14	2.27	1.86	2.00	2.15	1.92	1.96	2.03
Ω	0.893	0.904	0.001	0.895	0.001	0.905	0.001	0.875	0.895
Pos.	1.568	1.551	1.723	2.018	1.777	1.120	1.714	1.567	1.552
PR	2.183	2.138	2.606	1.144	2.465	1.178	2.573	2.183	2.141
ω_{CT}	0.089	0.070	0.404	0.087	0.641	0.106	0.354	0.090	0.072
$\omega_{Coh.}$	1.110	1.085	1.927	1.093	2.473	1.120	1.745	1.109	1.085
CT_{net}	0.022	0.015	-0.054	0.016	-0.117	0.049	0.032	0.024	0.016
Character	LE_{A+B}	LE_{A+B}	ME /CR	LE_{A+L}	ME /CR	LE_{B+L}	ME /CR	LE_{A+B}	LE_{A+B}

is typical of J-aggregates where the transition dipoles point in the direction of the aggregate axis.[47] The S_1 wavefunction is dominated by the S^l_h configuration and exhibits smaller contributions from S^{l+1}_{h-1} whereas the S_3 wavefunctions features the S^l_{h-1} and S^{l+1}_h excitations as leading terms with nearly equal weights. With our choice of coordinate system, they transform according to the B_{2u} and A_{1g} irreducible representations, respectively.

The *meta*-linkage of the pentacene building blocks constitutes a case in which the individual transition dipoles deviate from collinearity and therefore partially cancel. The $S_0 \rightarrow S_1$ transition at E_{vert}=2.08 eV is x-polarized and exhibits larger oscillator strength than the z-polarized $S_0 \rightarrow S_2$ transition with a vertical excitation energy of E_{vert}=2.14 eV. In terms of orbital composition, the positive and negative linear combinations of the monomer LUMOs swap energetic order with regard to the *para*-isomer. Hence, S^l_{h-1} and S^{l+1}_h are B-symmetric excitations here and form the first optically bright singlet state while the A-symmetric S^l_h and S^{l+1}_{h-1} excitations give rise to the second low-lying optically bright state.

Table 3: Adiabatic energies $E_{ad.}$, oscillator strengths f, polarizations and vertical energies $E_{vert.}$ of the transitions to the electronic ground state and polarization, vertical energies $E_{vert.}$ and descriptors derived from the one-particle transition density matrix for the three lowest excited singlet states of the *para*-isomer.

Isomer	**para**								
State No.	**1**	**2**	**3**	**1**	**2**	**3**	**1**	**2**	**3**
@ Geometry	Gs			S_1			S_2[a]		
$E_{ad.}$	1.98	2.10	2.13	1.60	1.79	2.01	1.75	1.85	2.00
f	1.114	0.000	0.000	0.000	0.884	0.306	0.000	1.037	0.000
Polarization	x	—	—	—	x	x	—	x	—
$E_{vert.}$	1.98	2.10	2.13	1.62	1.81	2.03	1.77	1.87	2.02
Ω	0.883	0.185	0.874	0.106	0.873	0.891	0.111	0.863	0.890
Pos.	1.600	1.623	1.545	1.643	1.944	1.265	1.625	1.598	1.549
PR	2.273	2.336	2.121	2.327	1.453	1.559	2.341	2.267	2.134
ω_{CT}	0.192	0.793	0.072	0.940	0.190	0.148	0.923	0.203	0.078
$\omega_{Coh.}$	1.353	1.845	1.096	1.360	1.244	1.209	1.402	1.381	1.102
CT_{net}	0.039	0.080	0.009	0.063	0.026	0.047	0.022	0.037	0.022
Character	LE_{A+L+B}	ME /CR	DL	ME /CR	LE_{A+L}	LE_{B+L}	ME / CR	DL	DL

[a]Saddle point

Analyzing the low-lying singlet transitions of the *ortho*-isomer is more involved due to major contributions of doubly excited configurations to some of the low-lying A-symmetric wavefunctions. From purely geometrical considerations one might suspect that a z-polarized transition leads to the lowest excited singlet state of the *ortho*-isomer, but that is not the case. The S_1 state (E_{vert}=2.04 eV) originates from optically bright B-symmetric excitations even in this regioisomer. The A-symmetric S_2 state is dark. Its wavefunction is characterized by a mixture of $S^{l}_{h_{-1}}$ and S^{l+1}_{h} single excitations and multiexcitonic terms, mainly of N^{l}_{h}, $V^{l;l+1}_{h-1;h}$, N^{l}_{h-},N^{l+1}_{h} and N^{l+1}_{h-1} types. The optically bright z-polarized transition excites the A-symmetric S_3 state. With an angle of about 60° between the individual monomer transition dipoles, it carries higher oscillator strength than the x-polarized $S_0 \rightarrow S_1$ absorption, in agreement with a simple vector addition model. The increase of the relative absorption intensity of the z-polarized $S_0 \rightarrow S_3$ transition with regard to the x-polarized $S_0 \rightarrow S_1$ one is the true reason for the apparent blue shift of the first band in the convoluted absorption

spectrum (Figure 3), mentioned at the beginning of this section.

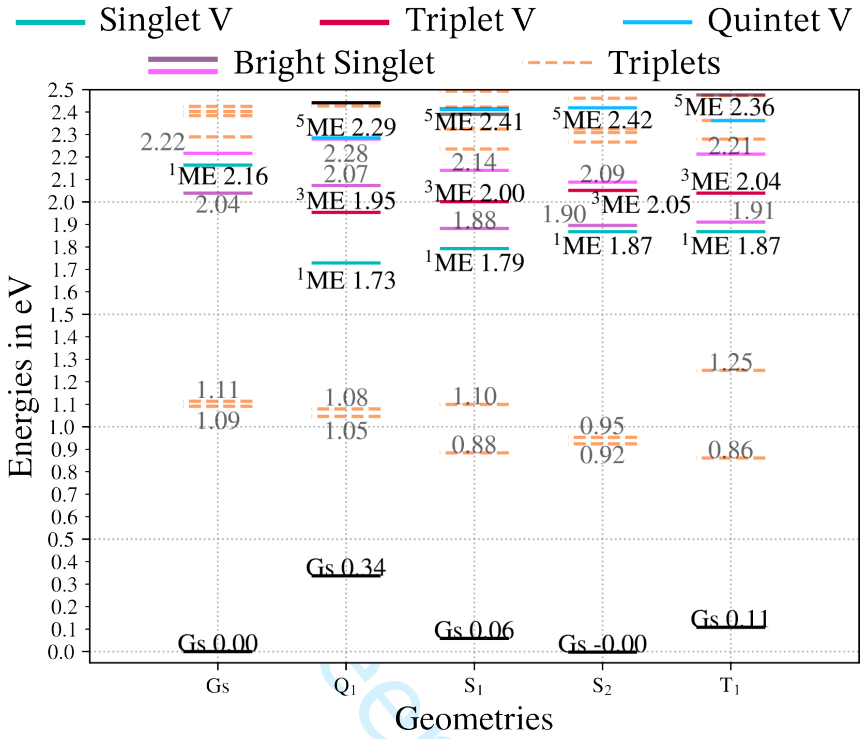

Figure 5: Level scheme of the adiabatic energies computed for the *ortho*-isomer at different optimized geometries. All values given in eV. The energy levels of the low-lying optically bright singlet states are plotted with pink or purple solid lines. For the first ^{1}ME state, teal solid lines have been used. Energy levels of singly excited triplet states are drawn with dashed orange lines. The energetic positions of the ^{3}ME and ^{5}ME states are indicated by red and light-blue solid lines, respectively.

Our calculations place the first ^{1}ME state of all regioisomers energetically above the corresponding optically bright S_1 state at the ground-state geometry (cp. Tables 1-3 and Figures 5-7). The lowest-lying ^{1}ME state (2.10 eV) is found for the *para*-isomer where it forms the S_2 state, located energetically only 0.12 eV above the optically bright S_1 state. Hence, excitation of one quantum of a C–C stretching mode in the $S_0 \rightarrow S_1$ absorption would suffice to make both states vibronically near degenerate. In the *meta*-isomer, S_3 (2.27 eV) can be identified with the ^{1}ME state at the DFT/MRCI level of theory, 0.19 eV above the optically bright S_1 state. While the electronic structures of the multiexcitonic and optically bright states can be clearly distinguished in the *meta*- and *para*-regioisomers, the higher-

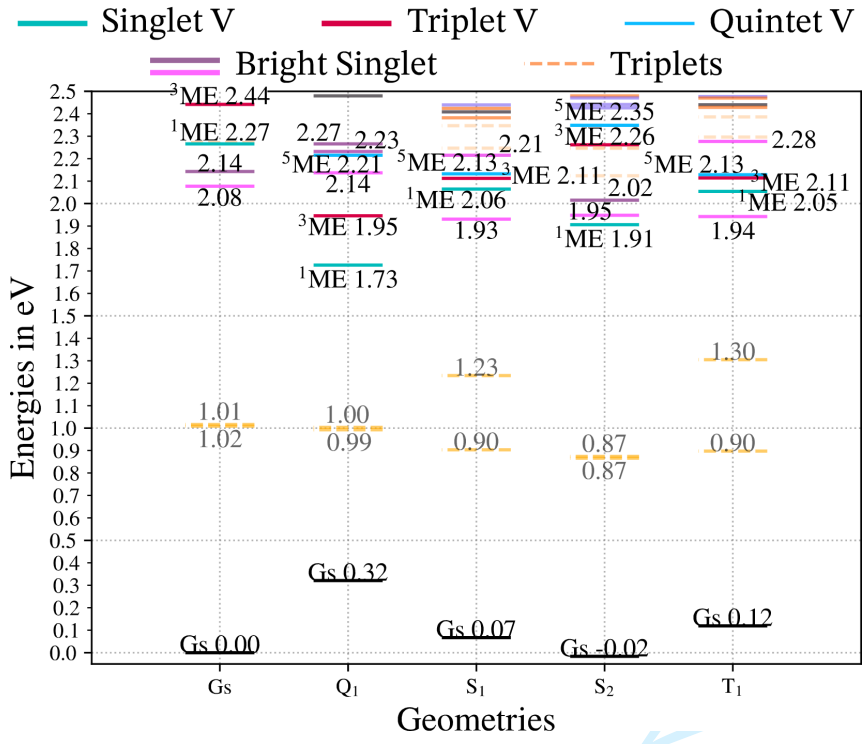

Figure 6: Level scheme of the adiabatic energies computed for the *meta*-isomer at different optimized geometries. All values given in eV. The color codes and line styles are explained in Figure 5.

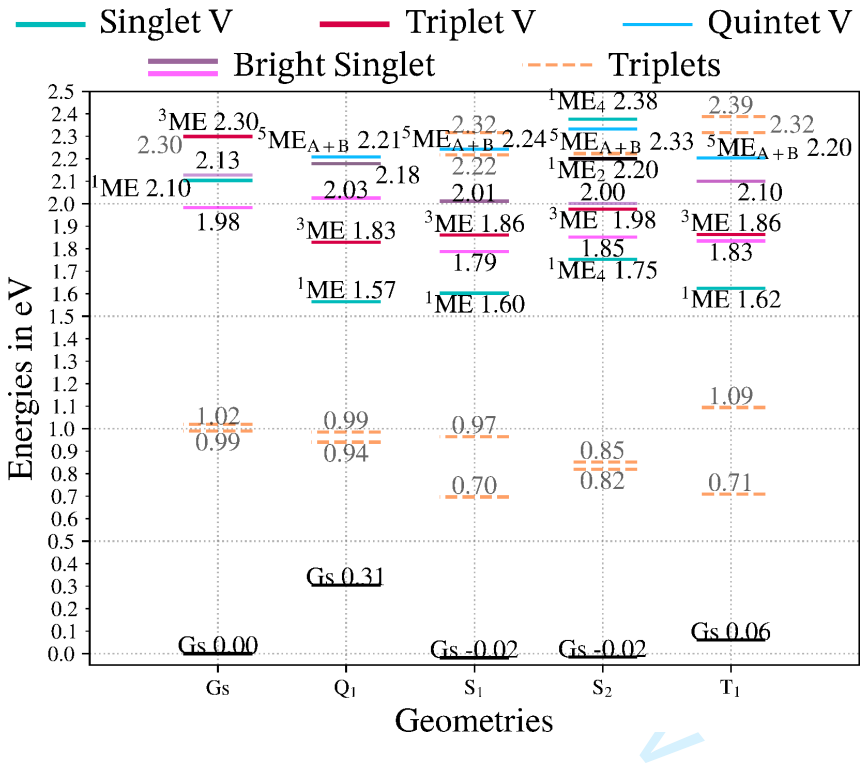

Figure 7: Level scheme of the adiabatic energies computed for the *para*-isomer at different optimized geometries. All values given in eV. The color codes and line styles are explained in Figure 5.

lying singlet states of the *ortho*-isomer have mixed character in the FC region. Here, major contributions of doubly excited configurations are found in the S_2 (2.16 eV) and S_5 (2.62 eV) states. As we will see below (cp. Section3.3), the energetic order of the singlet states in the absorption region and its reversal upon geometry relaxation in the excited state have important consequences on the mechanistic model of the SF process.

With a value of $\Delta E_{T_2-T_1} = 0.01$ eV, the energetic splitting of the T_1 and T_2 states is minuscule at the ground-state geometry of the *meta*-isomer, indicating a small electronic coupling between the T_1 states of the two buliding blocks. According to our calculations, the *meta*-isomer is the only regioisomer which fulfills the condition $E(S_1) \geq E(T_1) + E(T_2)$ even for the vertical excitation energies (cp. Figures 5-7). In the *ortho*- and *para*-isomers, $\Delta E_{T_2-T_1}$ is slightly larger. More importantly, the excess energy released upon geometry relaxation of the excited state is required to make the SF process exothermic. This also means that intramolecular TTA-UC is less endothermic in these regioisomers and could explain the lower net triplet quantum yield $\Phi_{(T)}$ of the *ortho*- and *para*-isomers. The vertical energy of the third triplet state varies between $2.27-2.30$ eV among the regioisomers. T_3 can therefore not be reached with an excitation wavelength of 610 nm, used in the experiments. Hence, it does not pose an additional (unwanted) nonradiative decay channel of the singlet population. The ferromagnetically coupled triplet-pair state, ^{5}ME, is not found among the low-lying states of any of the regioisomers at the respective ground-state geometry.

3.2 Geometry relaxation effects on the bright singlet states

Upon geometry relaxation of the S_1 states (x-polarized transitions), the excitations of the *ortho*-, *meta*- and *para*-regioisomers localize on one side. Only one of the pentacene units, henceforth denominated fragment A, and part of the linker L experience significant geometry changes at the minimum of the lowest optically bright state while fragment B mainly takes the role of a spectator (Figures S1-S3). Concomitantly, the valence orbitals localize at these geometries (see Figure S4). A similar behavior was observed by us when investigating pen-

tacene dimers and a trimer in crystalline surroundings[31] and points toward the importance of localization transitions in the photophysics of pentacene and its derivatives. Due to the spatial confinement, the participation ratio of the fragments remains quite high in the S_1 state of *ortho*-isomer (Table 1) whereas a PR value close to 1 is observed for the *meta*-isomer (Table 2). The PR value of 1.453 for the lowest optically bright state of the *para*-isomer (Table 3) is attributed to the stronger through-bond conjugation of the π-systems along the x-axis that is reflected in the amplitudes of the HOMO and LUMO orbitals (Figure S4) as well.

Investigation of Tables 1, 2 and 3 confirms that the adiabatic energies of the $S_0 \rightarrow S_1$ transition resemble the experimental trend and energetic positions of the first absorption peak much better than the vertical excitation energies do. Zero-point vibrational energy (ZPVE) corrections lower the adiabatic excitation energies additionally by 0.1 eV (*ortho*), 0.05 eV (*meta*) and 0.06 eV (*para*) yielding an almost perfect match between the computed 0–0 energies (*para*: 1.73 eV, *meta*: 1.88 eV, *ortho*: 1.78 eV) and the experimental values measured in benzonitrile (*para*: 1.79 eV, *meta*: 1.86 eV, *ortho*: 1.85 eV).[19]

In contrast to the x-polarized S_1 transitions, the z-polarized S_2 transitions of the *ortho*- and *meta*-regioisomers remain fully delocalized over both pentacene building blocks, reflected in PR values beyond 2. As the S_2 minimum structures play an essential role in our model of the SF process (see Section 3.3), we optimized the geometry of the singly excited ^1A_g-symmetric state even for the *para*-regioisomer which does not possess a low-lying z-polarized transition. In this case, the geometry labeled S_2 in Figure 7 and in Table 3 represents a saddle-point on the S_2 PES.

Pentacene monomers experience substantial C–C bond length alterations upon electronic excitation of the S_1 (^1L_a) state.[31] As the optically bright transitions of the covalently linked dimers, studied in the present work, can be interpreted as linear combinations of the monomer transitions with smaller contributions from the diethynylphenyl linker, the main geometrical changes upon $S_0 \rightarrow S_1$ or $S_0 \rightarrow S_2$ excitation are expected to occur in the C–C bond lengths.

Indeed, as exemplified for the *meta*-isomer, C–C bond-length alterations shape the most prominent vibrational progressions in the simulated FC spectra of the $S_0 \rightarrow S_1$ and $S_0 \rightarrow S_2$ transitions, which are shown in Figure 8 together with a digitized experimental absorption spectrum. The simulated spectrum matches the experimental one tremendously well,

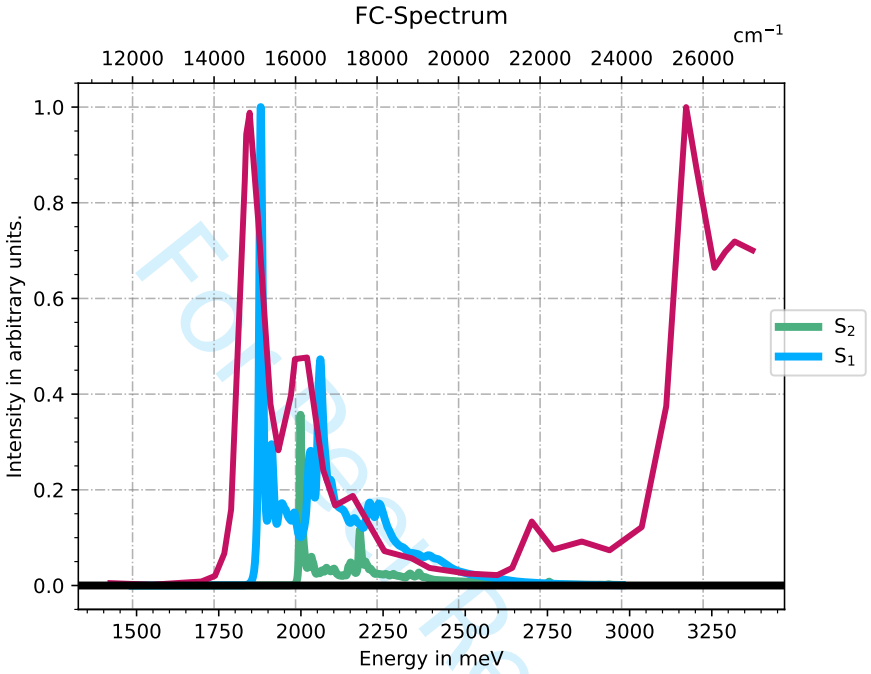

Figure 8: Simulated Franck-Condon spectra of the $S_0 \rightarrow S_1$ and $S_0 \rightarrow S_2$ transitions. A digitized experimental spectrum, extracted from Figure S14 in Ref. 19, is given for comparison.

revealing the $S_0 \rightarrow S_2$ transition hidden below the first progression of $S_0 \rightarrow S_1$ transition. Remarkably, both show comparable vibronic progressions. We find the largest displacements in the Duschinsky transformation of the normal coordinates related to $S_0 \rightarrow S_1$ for mode 2, a flapping mode with a vibrational energy of 4 cm^{-1} at the S_1 geometry. Other large displacements are observed for the concertina like vibration of the pentacene units (mode 37) at 266 cm^{-1} and a C–C stretch mode (mode 210) with an energy of 1471 cm^{-1} at the S_1 geometry, which we attribute to the main visible progression in the experiment. Normal modes with nearly identical harmonic vibrational energies are involved in the vibronic $S_0 \rightarrow S_2$ spectrum, as ought to be expected by visual inspection of Figure 8. Because the z-polarized electronic $S_0 \rightarrow S_2$ transition does not localize and hence preserves the C_2 molecular

point group symmetry, only *a*-symmetric vibrations contribute to the vibronic spectrum in first order, thus precluding a participation of the *b*-symmetric low-frequency mode 2 in the vibronic $S_0 \rightarrow S_2$ transitions. Due to technical problems in the Duschinsky transformation, meaningful FC spectra of the *ortho*- and *para*-isomers could not be generated: One of the methyl residues rotates by 60° upon geometry optimization in the excited state. While this rotation has a marginal effect on the electronic energy, it scrambles the Duschinsky matrix and leads to unreasonably long vibrational progressions of the related normal modes.

Due to ultrafast SF, steady-state fluorescence spectra were not measured in the *ortho*-isomer and *para*-isomers. The maximum fluorescence peak of the *meta*-isomer was determined to lie at 664 nm in toluene.[19] In benzonitirile it is located at ≈ 680 nm, showing a shoulder in the lower energy area. The solvent shift of 16 nm, corresponding to merely 0.04 eV in this wavelength regime, speaks against substantial CT contributions to the $S_1 \rightarrow S_0$ transition. And indeed, the analysis of the 1-TDM confirms that the transition has predominantly LE character with a minuscule net CT of about 2% (Table 2). The small experimentally observed solvent shift of the emission might instead be related to minor CR contributions: ω_{CT} values close to 0.09 are indicative of simultaneous small charge transfer from fragment A to fragment B and *vice versa*.

3.3 Mechanisms and energetics of singlet fission

The multiexcitonic ^{1}ME state forms either the first (*ortho* and *para*) or the second (*meta*) excited singlet state at the optimized geometry of the bright state (Tables 1-3). The apparent strong variation of its wavefunction composition among the regioisomers and nuclear geometries (Tables S1-S3) is a consequence of the localized vs. delocalized character of the frontier orbitals which hampers a definite one-to-one mapping of the electronic structures computed at different geometries. In this situation, state descriptors based on the one-particle transition density matrix, such as CT_{net} or ω_{CT}, give a much more consistent and hence reliable picture of the wavefunction characteristics than the coefficients of the leading configurations.

In all ^{1}ME states, CT_{net} and ω_{CT} values are found which indicate small net CT, but substantial CR character stemming from simultaneous A→B and B→A excitations, suggesting the involvement of a superexchange mechanism rather than a stepwise evolution of the optically bright to the multiexcitonic singlet state mediated by real CT state. However, as discussed in detail below, there are valid arguments for the participation of a direct mechanism in the formation of the ^{1}ME state as well.

In the *ortho*- and *para*-regioisomers, the optically bright S_h^l state and the ^{1}ME state swap energetic order upon evolution from the FC region to the vibrationally relaxed S_h^l structures according to our calculations (Figures 5 and 7). Consequently, their potential energy surfaces have to cross along this pathway. In the *meta*-regioisomer, the bright S_h^l state (pink solid lines in Figure 6) and the dark ^{1}ME state (teal solid lines in Figure 6) undergo a conical intersection when the S_h^l excitation switches from fragment A to fragment B. While the energy required for reaching the delocalized transition state from the localized minimum of the S_h^l state is very small ($\approx$ 0.02 eV), the multiexcitonic states is stabilized by 0.15 eV as it prefers a symmetric arrangement of the nuclei. Strong nonadiabatic coupling between the S_h^l and ^{1}ME potentials is expected when passing through these conical intersections or avoided crossings and should enable a direct SF process following the primary excitation of the optically bright singlet state. The fact that this direct SF channel is not observed in the quantum molecular dynamics simulations by Reddy et al.[21,22] is ascribed to the absence of energetically accessible conical intersections between the S_h^l and ^{1}ME states in the underlying XMCQDPT/CASSCSF model surfaces. Our results agree, however, with the findings of these studies in that the ^{1}ME state might form a trap if the molecular geometry can fully adapt to the electronic structure before SF has taken place.

Due to the spatial proximity of the two pentacene units, the energetic splitting between the ferro- and antiferromagnetically coupled triplet-pair states is high in the *ortho*-regioisomer, ranging between 0.5 and 0.6 eV at all considered nuclear arrangements. It may therefore safely be assumed that the ^{5}ME state is not involved in the SF mechanism of

this regioisomer. The interjacent ^{3}ME state is mainly composed of double excitations with two open shells at the S_1 minimum (Table S1). Although it is energetically accessible from the FC point in principle, it does not have the right electronic structure to promote SF. In the *meta*-regioisomer, the ^{5}ME state is located adiabatically at $E_{ad}(^5\text{ME}) = 2.21$ eV, substantially higher than the ^{1}ME and ^{3}ME states which adopt values of $E_{ad}(^1\text{ME}) = 1.73$ eV and $E_{ad}(^3\text{ME}) = 1.95$ eV, respectively, at the Q_1 geometry. Interestingly, the energetic splitting between the ^{1}ME and ^{5}ME states is quite small (0.07 eV) at the minimum of the optically bright S_1 state (cp. Figure 6). Moreover, the wave function of the interjacent ^{3}ME state is dominated by configurations with four open shells here (Table S2) and thus has an appropriate electronic structure for the disentanglement of the triplet pair. Like in the *meta*-substituted regioisomer of an end-on (2,2′)-linked TIPS-pentacene dimer, where indications for the involvement of a quintet state were found,[14] the contribution of spin-forbidden channels in the SF mechanism of the here investigated *meta*-substituted side-on (6,6′)-linked TIPS-pentacene dimer is conceivable. The strong through-bond interaction of the pentacene units in the *para*-regioisomer leads to energetic splittings of the ^{1}ME and ^{5}ME states of similar size as in the *ortho*-regioisomer and hence precludes the participation of the ^{5}ME in the SF process. The ^{3}ME state of the *para*-regioisomer lies in energetic proximity of the S_1 state at the optimized S_1, S_2 and T_1 geometries, though, and exhibits substantial contributions of four open-shell configurations (Table S3). It might therefore play a certain role in the SF mechanism of this isomer.

With regard to the energy balance between the singlet and triplet channels, intramolecular SF is not favored over TTA-UC in the *ortho*-regioisomer (cp. Figure 5). At the optimized S_h^l geometry, the T_1 and T_2 levels are split by 0.22 eV yielding a combined adiabatic energy of $E_{ad}(T_1) + E_{ad}(T_2) = 1.98$ eV compared to adiabatic singlet state energies of 1.79 eV (^{1}ME) and 1.88 eV (S_h^l). For this regioisomer, we find the lowest sum of T_1 and T_2 energies at the optimized $S_{h-1;h}^{l;l+1}$ geometry which represents a C_2 symmetric structure. Here, T_1 and T_2 are split by merely 0.03 eV, and their sum amounts to $E_{ad}(T_1) + E_{ad}(T_2) = 1.87$ eV. The

energetic proximity between the $E(S_1)$ and $E(T_1) + E(T_2)$ channels could explain the ultrafast SF process on the one hand and the high TTA-UC propensity of the *ortho*-regioisomer on the other hand, resulting in an overall low net triplet quantum yield $\Phi_{(T)}$.

As already mentioned in Section 3.1, the *meta*-coupled pentacene dimer is the only regioisomer for which the energy balance $E(S_1) - (E(T_1) + E(T_2))$ is positive in the FC region. Zirzlmeier et al. derived a value of 0.77 eV for the T_1 energy of this isomer in methyltetrahydrofuran at liquid nitrogen temperatures. A closer look shows, however, that this energy corresponds to the maximum of a broad phosphorescence band with a wavelength of 1610 nm, better comparable to the vertical energy at the T_1 minimum geometry than to the adiabatic or 0–0 energy of the $T_1 \rightarrow S_0$ transition. Our calculations find a vertical emission energy $E_{vert}(T_1)$ of 0.78 eV for this regioisomer, 0.12 eV lower than the adiabatic excitation energy $E_{ad}(T_1) = 0.90$ eV. Like its singlet counterpart, the T_h^l excitation localizes mainly on fragment A. At the T_1 minimum geometry, the energy of the local T_{h-1}^{l+1} excitation on the B fragment forming the T_2 state is markedly higher. Like in the *ortho*-regioisomer, the most favorable energetic situation for a simultaneous excitation of the T_1 and T_2 states is obtained for a C_2 symmetric nuclear arrangement at the S_2 minimum (cp. Figure 6). Here, $E_{ad}(T_1) + E_{ad}(T_2) = 1.74$ eV in comparison to adiabatic singlet state energies of 1.91 eV (^{1}ME) and 1.95 eV ($S_{h;h-1}^{l;l+1}$). From an energetic point of view, intramolecular SF should therefore proceed easily in the *meta*-regioisomer whereas TTA-UC is an endothermic process.

Due to π-conjugation effects, the strongest electronic coupling between the A and B fragments is found in the *para*-isomer. The respective adiabatic energies of the optically bright S_h^l, the multiexcitonic ^{1}ME and the T_1 states are lowest among all regioisomers. With a value of 1.67 eV, the total energy of the decoupled T_1 and T_2 states is equal at the S_h^l minimum and for a D_{2h}-symmetric structure which forms a first-order saddlepoint on the S_2 PES, although the energetic splitting between these states varies markedly (cp. Figure 7). While the energy of the vibrationally relaxed ^{1}ME state (1.57 eV) is not sufficient to reach this channel, SF is exothermic with regard to the optically bright S_h^l state which

adopts an adiabatic energy of 1.79 eV at the minimum of its potential well according to our calculations.

4 Conclusions

In this work, we have investigated three regioisomers of side-on linked pentacene dimers by means of combined DFT and MRCI methods to elucidate possible SF pathways and mechanisms. The R2022 Hamiltonian used in the DFT/MRCI calculations allows for a balanced description of singly excited and multiexcitonic configurations independent of their spin multiplicity. While the DFT/MRCI ansatz is not limited with regard to the number of orbitals included in the active space, most of the low-lying states are dominated by excitations involving the four frontier orbitals, mainly composed of the HOMO and LUMO orbitals of the individual pentacene units. Good agreement with experimental results is achieved for the spectral properties of the optically bright singlets and the first excited triplet state. Experimental reference values for the triplet-pair states (^{1}ME, ^{3}ME, ^{5}ME) of pentacene dimers do not exist, but their energetic positions and wave function compositions are reasonable. Benchmark calculations in previous work[34] had proven that the R2022 parametrization of the DFT/MRCI Hamiltonian is well suited for describing doubly excited states of organic molecules.

The *ortho*- and *meta*-regioisomers exhibit two low-lying optically bright singlet states, one polarized along the C_2 symmetry axis (z), the other polarized perpendicular to this axis (x). In all regioisomers, the x-polarized transition forms the first optically bright state and is denoted S_1 independent of its energetic position in the singlet ladder. The z-polarized transition (S_2) has lower intensity in the *ortho*- and *meta*-regioisomers and is electric dipole forbidden in the *para*-regioisomer. The fact that the x-polarized transitions localize on one side of the molecule while the z-polarized transitions do not, has some interesting consequences for the energy balance of the SF process. Localization of the S_h^l and T_h^l excitations

causes the T_1 and T_2 levels to split energetically which is less favorable for their combined energies $E(T_1) + E(T_2)$ than a delocalized excitation.

In all regioisomers, the net charge transfer from one pentacene unit to the other is minuscule in the optically bright S_h^l state. Also the state descriptors of the higher-lying states do not point toward a SF route involving intermediate real CT states. Instead, we attribute the experimentally observed solvent dependence of the triplet quantum yield to the substantial charge-resonance contributions to the multiexcitonic ^{1}ME wave function. While the ^{5}ME state does not appear to play a role in the SF mechanism of the *ortho*- and *para*-regioisomers, its participation in the disentaglement of the triplet pair is conceivable in the *meta*-regioisomer where the ^{1}ME, ^{3}ME and ^{5}ME states are energetically quite close at the S_h^l minimum. In the *ortho*- and *para*-regioisomers, the potential energy surfaces of the ^{1}ME and S_h^l states intersect upon geometry relaxation of the S_h^l excitation. In the *meta*-regioisomer, the crossing occurs upon delocalization of the optically bright excitation. Nonadiabatic coupling between two electronic states is typically very strong at conical intersections of the respective potential energy surfaces, thus favoring a direct SF mechanism in the regioisomers, assisted by charge-resonance effects.

Acknowledgement

The authors thank the Deutsche Forschungsgemeinschaft (DFG, German Research Foundation) for financial support—Grant No. MA 1051/20-1.

Supporting Information Available

For all regioisomers: Wave function composition of low-lying states with substantial double-excitation contributions, descriptors of the $S_0 \rightarrow S_n$, $S_0 \rightarrow T_n$ and $T_1 \rightarrow T_n$ transitions at optimized geometries, C-–C bond distance changes between the S_0 and S_1 minimum structures, frontier molecular orbitals and transition densities of the optically bright state

References

(1) Smith, M. B.; Michl, J. Singlet Fission. *Chem. Rev.* **2010**, *110*, 6891–6936.

(2) Singh, S.; Jones, W. J.; Siebrand, W.; Stoicheff, B. P.; Schneider, W. G. Laser Generation of Excitons and Fluorescence in Anthracene Crystals. *J. Chem. Phys.* **1965**, *42*, 330–342.

(3) Jundt, C.; Klein, G.; Sipp, B.; Le Moigne, J.; Joucla, M.; Villaeys, A. Exciton dynamics in pentacene thin films studied by pump-probe spectroscopy. *Chem. Phys. Lett.* **1995**, *241*, 84–88.

(4) Walker, B. J.; Musser, A. J.; Beljonne, D.; Friend, R. H. Singlet exciton fission in solution. *Nat. Chem.* **2013**, *5*, 1019–1024, 258hq Times Cited:386 Cited References Count:47.

(5) Herz, J.; Buckup, T.; Paulus, F.; Engelhart, J. U.; Bunz, U. H. F.; Motzkus, M. Unveiling Singlet Fission Mediating States in TIPS-pentacene and its Aza Derivatives. *J. Phys. Chem. A* **2015**, *119*, 6602–6610.

(6) Chan, W.-L.; Berkelbach, T. C.; Provorse, M. R.; Monahan, N. R.; Tritsch, J. R.; Hybertsen, M. S.; Reichman, D. R.; Gao, J.; Zhu, X.-Y. The Quantum Coherent Mechanism for Singlet Fission: Experiment and Theory. *Acc. Chem. Res.* **2013**, *46*, 1321–1329.

(7) Monahan, N.; Zhu, X.-Y. Charge Transfer–Mediated Singlet Fission. *Annu. Rev. Phys. Chem.* **2015**, *66*, 601–618.

(8) Musser, A. J.; Maiuri, M.; Brida, D.; Cerullo, G.; Friend, R. H.; Clark, J. The Nature of Singlet Exciton Fission in Carotenoid Aggregates. *J. Am. Chem. Soc.* **2015**, *137*, 5130–5139.

(9) Trinh, M. T.; Pinkard, A.; Pun, A. B.; Sanders, S. N.; Kumarasamy, E.; Sfeir, M. Y.; Campos, L. M.; Roy, X.; Zhu, X.-Y. Distinct properties of the triplet pair state from singlet fission. *Sci. Adv.* **2017**, *3*, e1700241.

(10) Burdett, J. J.; Bardeen, C. J. The Dynamics of Singlet Fission in Crystalline Tetracene and Covalent Analogs. *Acc. Chem. Res.* **2013**, *46*, 1312–1320.

(11) Cheng, Y. Y.; Fückel, B.; Khoury, T.; Clady, R. G. C. R.; Tayebjee, M. J. Y.; Ekins-Daukes, N. J.; Crossley, M. J.; Schmidt, T. W. Kinetic Analysis of Photochemical Upconversion by Triplet-Triplet Annihilation: Beyond Any Spin Statistical Limit. *J. Phys. Chem. Lett.* **2010**, *1*, 1795–1799.

(12) Tayebjee, M. J. Y.; Sanders, S. N.; Kumarasamy, E.; Campos, L. M.; Sfeir, M. Y.; McCamey, D. R. Quintet multiexciton dynamics in singlet fission. *Nat. Phys.* **2017**, *13*, 182.

(13) Basel, B. S.; Zirzlmeier, J.; Hetzer, C.; Phelan, B. T.; Krzyaniak, M. D.; Reddy, S. R.; Coto, P. B.; Horwitz, N. E.; Young, R. M.; White, F. J.; Hampel, F.; Clark, T.; Thoss, M.; Tykwinski, R. R.; Wasielewski, M. R.; Guldi, D. M. Unified model for singlet fission within a non-conjugated covalent pentacene dimer. *Nature Comm.* **2017**, *8*, 15171.

(14) Sakai, H.; Inaya, R.; Nagashima, H.; Nakamura, S.; Kobori, Y.; Tkachenko, N. V.; Hasobe, T. Multiexciton Dynamics Depending on Intramolecular Orientations in Pentacene Dimers: Recombination and Dissociation of Correlated Triplet Pairs. *J. Phys. Chem. Lett.* **2018**, *9*, 3354–3360.

(15) Casanova, D. Theoretical Modeling of Singlet Fission. *Chem. Rev.* **2018**, *118*, 7164–7207.

(16) Musser, A. J.; Clark, J. Triplet-Pair States in Organic Semiconductors. *Annu. Rev. Phys. Chem.* **2019**, *70*, 323–351.

(17) Zeng, T.; Hoffmann, R.; Ananth, N. The Low-Lying Electronic States of Pentacene and Their Roles in Singlet Fission. *J. Am. Chem. Soc.* **2014**, *136*, 5755–5764.

(18) Coto, P. B.; Sharifzadeh, S.; Neaton, J. B.; Thoss, M. Low-Lying Electronic Excited States of Pentacene Oligomers: A Comparative Electronic Structure Study in the Context of Singlet Fission. *J. Chem. Theory Compu.* **2015**, *11*, 147–156.

(19) Zirzlmeier, J.; Lehnherr, D.; Coto, P. B.; Chernick, E. T.; Casillas, R.; Basel, B. S.; Thoss, M.; Tykwinski, R. R.; Guldi, D. M. Singlet fission in pentacene dimers. *Proceedings of the National Academy of Sciences* **2015**, *112*, 5325–5330.

(20) Fuemmeler, E. G.; Sanders, S. N.; Pun, A. B.; Kumarasamy, E.; Zeng, T.; Miyata, K.; Steigerwald, M. L.; Zhu, X.-Y.; Sfeir, M. Y.; Campos, L. M.; Ananth, N. A Direct Mechanism of Ultrafast Intramolecular Singlet Fission in Pentacene Dimers. *ACS Cent. Sci.* **2016**, *2*, 316–324.

(21) Reddy, S. R.; Coto, P. B.; Thoss, M. Intramolecular Singlet Fission: Insights from Quantum Dynamical Simulations. *J. Phys. Chem. Lett.* **2018**, *9*, 5979–5986.

(22) Reddy, S. R.; Coto, P. B.; Thoss, M. Quantum dynamical simulation of intramolecular singlet fission in covalently coupled pentacene dimers. *J. Chem. Phys.* **2019**, *151*, 044307.

(23) Zimmerman, P.; Zhang, Z.; Musgrave, C. Singlet fission in pentacene through multi-exciton quantum states. *Nat. Chem.* **2010**, *2*, 648–652.

(24) Zimmerman, P. M.; Bell, F.; Casanova, D.; Head-Gordon, M. Mechanism for Singlet Fission in Pentacene and Tetracene: From Single Exciton to Two Triplets. *J. Am. Chem. Soc.* **2011**, *133*, 19944–19952.

(25) Aryanpour, K.; Shukla, A.; Mazumdar, S. Theory of Singlet Fission in Polyenes, Acene

Crystals, and Covalently Linked Acene Dimers. *J. Phys. Chem. C* **2015**, *119*, 6966–6979.

(26) Feng, X.; Krylov, A. I. On couplings and excimers: Lessons from studies of singlet fission in covalently linked tetracene dimers. *Phys. Chem. Chem. Phys.* **2016**, *18*, 7751–7761.

(27) Feng, X.; Casanova, D.; Krylov, A. I. Intra- and Intermolecular Singlet Fission in Covalently Linked Dimers. *J. Phys. Chem. C* **2016**, *120*, 19070–19077.

(28) Khan, S.; Mazumdar, S. Diagrammatic Exciton Basis Theory of the Photophysics of Pentacene Dimers. *J. Phys. Chem. Lett.* **2017**, *8*, 4468–4478.

(29) Hoche, J.; Flock, M.; Miao, X.; Philipp, L. N.; Wenzel, M.; Fischer, I.; Mitric, R. Excimer formation dynamics in the isolated tetracene dimer. *Chem. Sci.* **2021**, *12*, 11965–11975.

(30) C. A. Valente, D.; do Casal, M. T.; Barbatti, M.; Niehaus, T. A.; Aquino, A. J. A.; Lischka, H.; Cardozo, T. M. Excitonic and charge transfer interactions in tetracene stacked and T-shaped dimers. *J. Chem. Phys.* **2021**, *154*, 044306.

(31) Schulz, T.; Hédé, S.; Weingart, O.; Marian, C. M. Multiexcitonic and optically bright states in subunits of pentacene crystals: A hybrid DFT/MRCI and molecular mechanics study. *J. Chem. Phys.* **2024**, *160*, 144114.

(32) Grimme, S.; Waletzke, M. A combination of Kohn–Sham density functional theory and multi-reference configuration interaction methods. *J. Chem. Phys* **1999**, *111*, 5645–5655.

(33) Marian, C. M.; Heil, A.; Kleinschmidt, M. The DFT/MRCI Method. *WIREs Comput. Mol. Sci.* **2019**, *9*, e1394.

(34) Dombrowski, D. R.; Schulz, T.; Kleinschmidt, M.; Marian, C. M. R2022: A DFT/MRCI

Ansatz with Improved Performance for Double Excitations. *J. Phys. Chem. A* **2023**, *127*, 2011–2025.

(35) Ringström, R.; Edhborg, F.; Schroeder, Z. W.; Chen, L.; Ferguson, M. J.; Tykwinski, R. R.; Albinsson, B. Molecular rotational conformation controls the rate of singlet fission and triplet decay in pentacene dimers. *Chem. Sci.* **2022**, *13*, 4944–4954.

(36) Basel, B. S.; Zirzlmeier, J.; Hetzer, C.; Reddy, S. R.; Phelan, B. T.; Krzyaniak, M. D.; Volland, M. K.; Coto, P. B.; Young, R. M.; Clark, T.; Thoss, M.; Tykwinski, R. R.; Wasielewski, M. R.; Guldi, D. M. Evidence for Charge-Transfer Mediation in the Primary Events of Singlet Fission in a Weakly Coupled Pentacene Dimer. *Chem* **2018**, *4*, 1092 – 1111.

(37) Frisch, M. J.; Trucks, G. W.; Schlegel, H. B.; Scuseria, G. E.; Robb, M. A.; Cheeseman, J. R.; Scalmani, G.; Barone, V.; Petersson, G. A.; Nakatsuji, H.; Li, X.; Caricato, M.; Marenich, A. V.; Bloino, J.; Janesko, B. G.; Gomperts, R.; Mennucci, B.; Hratchian, H. P.; Ortiz, J. V.; Izmaylov, A. F.; Sonnenberg, J. L.; Williams-Young, D.; Ding, F.; Lipparini, F.; Egidi, F.; Goings, J.; Peng, B.; Petrone, A.; Henderson, T.; Ranasinghe, D.; Zakrzewski, V. G.; Gao, J.; Rega, N.; Zheng, G.; Liang, W.; Hada, M.; Ehara, M.; Toyota, K.; Fukuda, R.; Hasegawa, J.; Ishida, M.; Nakajima, T.; Honda, Y.; Kitao, O.; Nakai, H.; Vreven, T.; Throssell, K.; Montgomery, J. A., Jr.; Peralta, J. E.; Ogliaro, F.; Bearpark, M. J.; Heyd, J. J.; Brothers, E. N.; Kudin, K. N.; Staroverov, V. N.; Keith, T. A.; Kobayashi, R.; Normand, J.; Raghavachari, K.; Rendell, A. P.; Burant, J. C.; Iyengar, S. S.; Tomasi, J.; Cossi, M.; Millam, J. M.; Klene, M.; Adamo, C.; Cammi, R.; Ochterski, J. W.; Martin, R. L.; Morokuma, K.; Farkas, O.; Foresman, J. B.; Fox, D. J. Gaussian 16, Revision A.03. 2016; Gaussian Inc. Wallingford CT.

(38) Yanai, T.; Tew, D. P.; Handy, N. C. A new hybrid exchange–correlation functional

using the Coulomb-attenuating method (CAM-B3LYP). *Chem. Phys. Lett.* **2004**, *393*, 51–57.

(39) Weigend, F.; Ahlrichs, R. Balanced basis sets of split valence, triple zeta valence and quadruple zeta valence quality for H to Rn: Design and assessment of accuracy. *Phys. Chem. Chem. Phys.* **2005**, *7*, 3297.

(40) Becke, A. D. A new mixing of Hartree–Fock and local density-functional theories. *J. Chem. Phys.* **1993**, *98*, 1372–1377.

(41) Etinski, M.; Tatchen, J.; Marian, C. M. Time-dependent approaches for the calculation of intersystem crossing rates. *J. Chem. Phys* **2011**, *134*, 154105.

(42) Böhmer, T.; Kleinschmidt, M.; Marian, C. M. Toward the improvement of vibronic spectra and non-radiative rate constants using the vertical Hessian method.

(43) Plasser, F.; Lischka, H. Analysis of Excitonic and Charge Transfer Interactions from Quantum Chemical Calculations. *Journal of Chemical Theory and Computation* **2012**, *8*, 2777–2789.

(44) Plasser, F.; Bäppler, S. A.; Wormit, M.; Dreuw, A. New tools for the systematic analysis and visualization of electronic excitations. II. Applications. *J. Chem. Phys.* **2014**, *141*, 024107.

(45) Plasser, F.; Wormit, M.; Dreuw, A. New tools for the systematic analysis and visualization of electronic excitations. I. Formalism. *J. Chem. Phys.* **2014**, *141*, 024106.

(46) Plasser, F. TheoDORE: A toolbox for a detailed and automated analysis of electronic excited state computations. *J. Chem. Phys.* **2020**, *152*, 084108.

(47) Würthner, F.; Kaiser, T. E.; Saha-Möller, C. R. J-Aggregates: From Serendipitous Discovery to Supramolecular Engineering of Functional Dye Materials. *Angew. Chemie Int. Ed.* **2011**, *50*, 3376–3410.

While Dombrowski et al. [P1]'s newly designed Hamiltonian has shown to be a vast improvement for systems with low-lying doubly excited states, it still suffers from the degeneracy problem, already discussed in Sec. 2.4.4. It has been established at an early stage that C_{60} seems to be a system in which both kind of problems, manifest simultaneously. Therefore, it was hoped that the new model hamiltonian might remedy some of the problems. The buckminsterfullerene C_{60}, shown in Fig. 4.6, transforms according to the representations of the I_h point-group. Accordingly, the valence orbitals

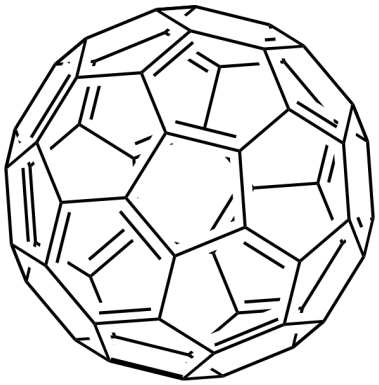

Figure 4.6: Skeletal formula of the Buckminsterfullerene C_{60}

show a high degree of degeneracy, as sketched in Fig. 4.7. This makes the system very

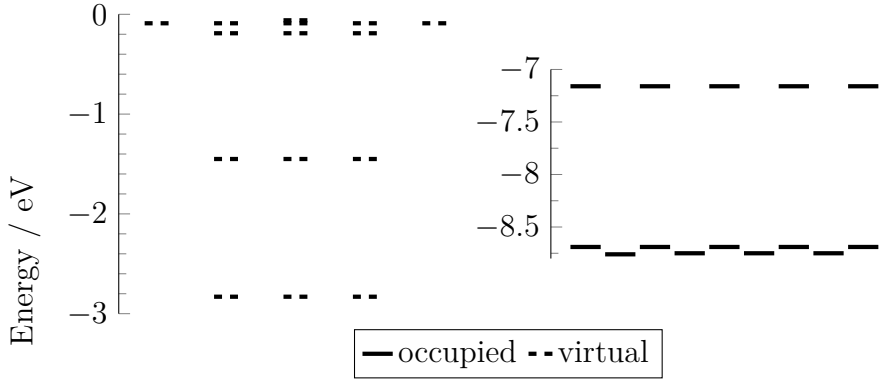

Figure 4.7: MO diagram for C_{60} computed on the DFT level using BH-LYP as the approximate functional and an augmented def2-SVP basis set. The reference space was constructed by distributing 28 electrons in the 29 shown orbitals, allowing for only single excitations.

interesting to study, as many different effects need to be taken into consideration. For example Jahn-Teller active modes have a strong influence on the spectroscopy of I_h symmetric systems[160, 161] and correlation effects are important already for

the ground state wave function[162–164]. Consequently, there is a lot of different experimental and computational data available[165–174] lending itself to comparison. Unfortunately, DFT/MRCI already struggles with the simulation of the vertical absorption spectrum, which becomes clear investigating Fig. 4.8. Additional spectra and computational details are given in the supporting information (SI) of publication Dombrowski et al. [P1]. The shown spectra were calculated using a KS-MO Basis generated with the BH-LYP functional, a SV(P)[159] basis set and symmetry restrictions of the D_{2h} point group. The basis set was augmented by putting diffuse functions[175, 176] into the centre of the molecule. Subsequent DFT/MRCI calculations for the A_g ground state, 20 A_u and 25 B_{1u}, B_{2u} and B_{3u} roots employed the different model Hamiltonians and the corresponding parameter set optimized for an energy-cut-off $\delta\varepsilon^{sel.} = 0.8$. While Dombrowski et al. [P1]'s Hamiltonian overestimates all energetic

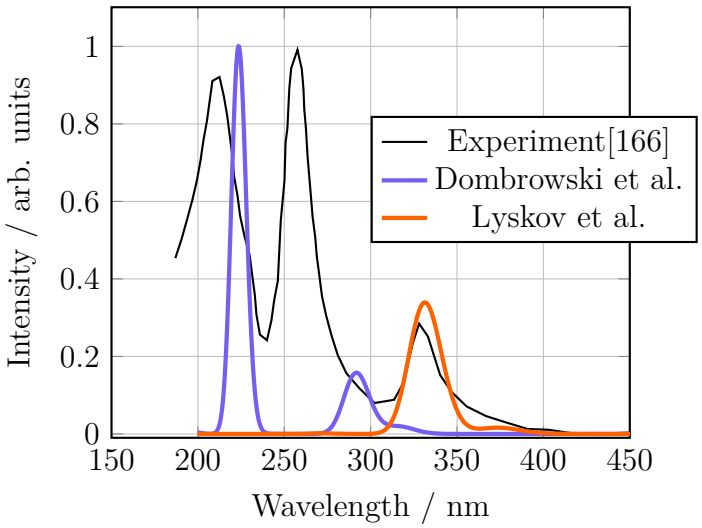

Figure 4.8: Plots of the digitalized experimental absorption spectrum recorded in toluene[166] and the Gaussian broadened vertical spectra calculated with Dombrowski et al. [P1]'s and Lyskov et al. [141]'s Hamiltonian, respectively. Gaussian functions with a full-width-at-half-maximum of 0.25 eV were used to broaden the stick spectra.

positions, Lyskov et al. [141]'s model Hamiltonian is not able to describe the energetic spectrum for energies larger than 4.70 eV even if the number of calculated eigenvalue is increased to 120. The reason can be found in the drastic increase of doubly excited configurations appearing in the CI vectors. As many of these are added to the reference space from run to run, they accumulate leading to faulty descriptions of the excited states. This is not as severe for the newly designed Hamiltonian, as is evident

from Table 4.1. Nevertheless, it is clear that the effect is present and will likely lead to the same result as for Lyskov et al. [141]'s Hamiltonian. Another detail can be ex-

Table 4.1: Comparison of the basis size of the reference space (# CSFs) in the DFT/MRCI method. The space for the first run is build by singly excited configurations constructed by distributing 28 electrons in 29 orbitals allowing for only single excitations (RAS). The second run uses the configurations with a weight greater than 3 % in the CI-vectors of the first run (Iterated). This iterative procedure is the standard way to build reference spaces in the `mrci` program.

(a) Lyskov et al. [141]

Ref. Space	Irrep.	# CSFs
RAS	A_g	28
	A_u	24
	B_{1u}	25
	B_{2u}	25
	B_{3u}	25
Iterated	A_g	1
	A_u	135
	B_{1u}	183
	B_{2u}	188
	B_{3u}	190

(b) Dombrowski et al. [P1]

Ref. Space	Irrep	# CSFs
RAS	A_g	28
	A_u	24
	B_{1u}	25
	B_{2u}	25
	B_{3u}	25
Iterated	A_g	1
	A_u	32
	B_{1u}	42
	B_{2u}	48
	B_{3u}	45

tracted from Tab. 4.1. The change of reference CSFs within the different irreducible representations is a sign for the loss of degeneracy. Due to the high symmetry of the computed states, this imbalance should not appear, but resemble the situation found in the first run. If the intruding doubly excited states are merely an artefact of the imbalanced parametrization of Lyskov et al. [141]'s Hamiltonian, or a general problem, maybe rooted in the crude selection procedure in such cases, which is indicated as it seemingly appears for the new Hamiltonian as well, can only be resolved by an in-depth analysis of the reference spaces between different runs. However, this is out of the scope of the present work. The overestimation of the energies with the new Hamiltonian is unfortunate, as well. Variations of the one-particle basis were investigated, e.g. by placing the augmented functions taken from Dunning's aug-cc-pVDZ basis[177, 178] in the centres of the pentagons, in the hope to obtain better results. However, the different basis sets investigated barely influenced the computed energies. Therefore, it is unknown at the moment why Dombrowski et al. [P1]'s Hamiltonian

appears to overestimate the absorption energies. Perhaps, including zero-point vibrational corrections will give a better estimate of the energetic positions. The next chapter will present work for which the inclusion of such effects yielded almost perfect matches to high-quality gas-phase data employing the new Hamiltonian.

5 Performance and Applications of the new Approach

In the last chapter it was discussed, how the previous DFT/MRCI formulations perform for doubly excited states. In particular, such with considerable contributions of configurations with four open shells. Whether the newly designed Hamiltonian performs better in such cases was tested by simulating the energy landscape of PT and TIPS-PT. Both were investigated in the gas-phase and electrostatically embedded to mimic a crystalline environment. The results of these studies will be presented in the last two sections of this chapter. At the beginning investigations used to evaluate the general performance of the new model Hamiltonian will be discussed. To do so, computations on *oligo-para*-phenylenes (Fig. 5.1), anthracene

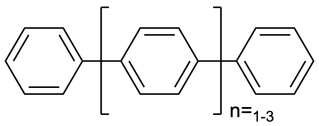

Figure 5.1: Skeletal structures of the investigated *oligo-para*-phenylenes

(An) and the An-derivatives 9-phenyl-anthracene (9PA), 9-(1-naphthyl)-anthracene (91NA), 9,9′-bis-anthracene (99pBA), 9,10-di-phenyl-anthracene (910dPA) and 2,6-di-phenyl-anthracene (26dPa) (Fig. 5.4) were conducted.
This was motivated by the availability of photodetachment-photoelectron spectroscopy (PD-PES) data recorded by Kosper[179] and Konieczny[180]. Furthermore, observations made by Meissner et al.[181] investigating PD-PES of acridon derivatives found that Lyskov et al.'s model Hamiltonian consistently underestimates all energies by $\approx$0.2 eV. Therefore, a comparison with the new Hamiltonian was close at hand.

5.1 *Oligo–para–*phenylenes

Oligo-para-phenylenes are well known in literature and have been discussed in the context of optoelectronics[182, 183], with respect to their dichroic behaviour[184] and the influence of their optical properties on the torsional angle between the phenyl-units [185]. A discussion of the energetic differences in the singlet and triplet manifold, and on the singlet-triplet gap can be found in the thesis of Dombrowski[135] and the publication [P3]. Here, focus will be laid on the EA and the vertical detachment energy (VDE), i.e. the doublet state manifold. PD-PES starting from the radical anion of the sample molecule is capable of probing all potential energy surfaces (PESs) connected to the radical parent state by a single detachment. The idea is sketched in Fig. 5.2. Apparently, the onset of the first peak in the spectrum can be interpreted as the EA of

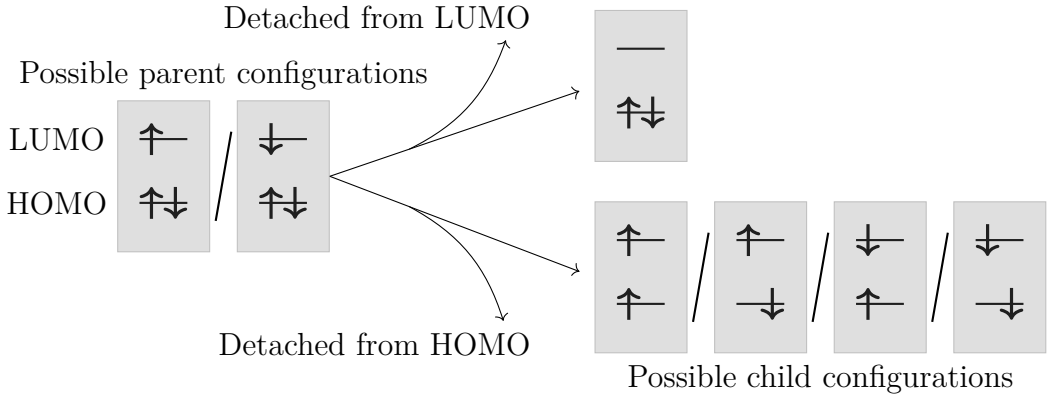

Figure 5.2: Reachable child configurations *via* a single detachment from the parent anion. Note that the orbitals are named according to the neutral child to avoid cluttering.

the neutral molecule, as it is equal to the binding energy of the electron in the highest occupied orbital, which is directly measured in PD-PES. As it is not always possible to identify the onset unambiguously the VDE is another valuable estimate to compare to experiment. Differentiating between both quantities makes computational support indispensable. An interfering effect in the identification of the energetic onset might be the auto-detachment from an anionic excited state. It occurs if the laser energy used for the detachment matches a vertical excitation of the anion. Consequently, an excited state of the anion is populated, and the electron is detached from this state, rather than the parent ground state. If the populated state is located above the ground state of the neutral child S_0, a fast decay to S_0 through auto-detachment will take place. Accordingly, signals governed by the overlap of the nuclear wave functions

of the parent excited state and the neutral ground state will occur in the spectrum. To identify such excited states and validate the postulated decay channel is greatly simplified by computational methods. Furthermore, it is possible to compute Dyson orbitals ϕ_D, defined as the overlap integral of the final and initial wave function[186]. The norm of the ϕ_D is proportional to the one-electron character of the transition. This property can be exploited to approximate the intensity of a transition in the PD-PES, which is strictly governed by the one-photon-one-electron principle. Note that a meaningful comparison is only possible, if the experimental spectrum was recorded at a single wavelength. This is not always the case, as the already mentioned anion excited states might interfere, necessitating the use of a different detachment wavelength. More details on the Dyson orbitals, their norms and how they are computed in the DFT/MRCI framework can be found in publication [P3].

PCCP

ROYAL SOCIETY OF CHEMISTRY

PAPER

View Article Online
View Journal | View Issue

Cite this: *Phys. Chem. Chem. Phys.*, 2023, **25**, 29850

Electron affinities and lowest triplet and singlet state properties of *para*-oligophenylenes (n = 3–5): theory and experiment†

Timo Schulz,‡[a] Paul Konieczny,‡[b] Dennis R. Dombrowski,[a] Simon Metz,[a] Christel M. Marian *[a] and Rainer Weinkauf *[b]

Received 4th July 2023,
Accepted 4th October 2023

DOI: 10.1039/d3cp03153e

rsc.li/pccp

We apply photodetachment–photoelectron spectroscopy to measure the electron affinities and the energetics of the lowest excited electronic states of the neutral molecules *para*-terphenyl (p3P), *para*-quaterphenyl (p4P) and *para*-quinquephenyl (p5P), including especially the triplet states below S_1. The interpretation of the experimental data is based on the comparison to calculated 0–0 energies and Dyson norms, using density functional theory and multireference configuration interaction methods, as well as Franck–Condon patterns. The comparison between calculated and experimental vibrational fine-structures reveals a twisted benzoid-like molecular structure of the S_0 ground state and nearly planar quinoid-like nuclear arrangements in the S_1 and T_1 excited states as well as in the D_0 anion ground state. For all *para*-oligophenylenes (ppPs) in this series, at least two triplet states have been identified in the energy regime below the S_1 state. The large optical S_0–S_1 cross sections of the ppPs are rationalised by the nodal structure of the molecular orbitals involved in the transition. The measured electron affinities range from 380 meV (p3P) over 620 meV (p4P) to 805 meV (p5P). A saturation of the electron binding energy with the increasing number of phenyl units is thus not yet in sight.

1 Introduction

The chemical structures of the *para*-terphenyl (p3P), *para*-quaterphenyl (p4P) and *para*-quinquephenyl (p5P) molecules are shown in Fig. 1.

Because of their high fluorescence quantum yields *para*-oligophenylenes (ppPs) are used as UV-laser dyes. For example, p3P was the gain medium in one of the first tunable UV dye lasers.[1–4] In the search for higher laser efficiencies, broader wavelengths tunabilities and new wavelength ranges it was found that modified p3P chromophores[5] and longer ppPs can be also used as laser dyes.[6] Already in 1976, a fluorescence quantum yield of 0.93 was measured for p3P in solution, although its S_1 lifetime was found to be rather short (1.2 ns).[3]

In 1982, a resonant multi-photon ionisation (REMPI) gas phase spectrum of the $S_0 \rightarrow S_1$ transition of cold p3P molecules was reported by Murakami *et al.*[7] In their spectrum, two long progressions of low-frequency vibrations are built upon the origin transition at 4.024 eV. These modes have been assigned to the in-phase and out-of-phase torsional twist modes around the C–C bonds which connect the phenyl rings. As explanation for the occurrence of the long progressions, the authors propose that in the S_0 state the benzene rings are twisted against each other, but lie in one plane in the S_1 state. Other experimental and theoretical publications dealing with the twisted S_0

[a] *Institute of Theoretical and Computational Chemistry, Heinrich-Heine-University Düsseldorf, Universitätsstr. 1, 40225 Düsseldorf, Germany. E-mail: Christel.Marian@hhu.de; Tel: +49 211 8113209*
[b] *Institute of Physical Chemistry, Heinrich-Heine-University Düsseldorf, Universitätsstr. 1, 40225 Düsseldorf, Germany. E-mail: Rainer.Weinkauf@hhu.de; Tel: +49 211 8111729*

† Electronic supplementary information (ESI) available: *xyz* coordinates of all optimised structures, torsional angles of ground and excited state structures, electron density differences, energies and calculated spectra of conformers, displacement vectors of selected normal mode vibrations, additional computational details, qualitative simulation of "peak-attraction" effect in T_1 of p3P. See DOI: https://doi.org/10.1039/d3cp03153e

‡ These authors contributed equally to this work.

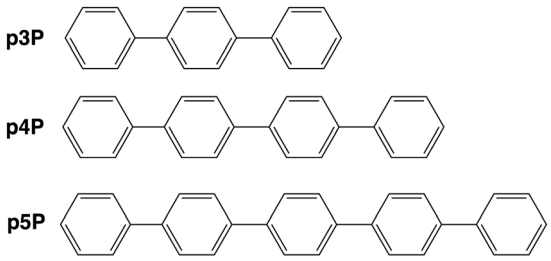

Fig. 1 Chemical structures of *para*-terphenyl (p3P), *para*-quaterphenyl (p4P) and *para*-quinquephenyl (p5P).

geometry of p3P have been reviewed by Baraldi and Ponterini.[8] Using semiempirical calculations, they found for p3P two nearly isoenergetic conformers: (1) a C_{2h} symmetric conformer with alternating signs of the inter-ring twist angles and (2) a helical conformer with D_2 symmetry. For p3P the angles of the inter-ring twist were calculated to be 35°. The barrier separating the two minima was predicted to be low enough to allow a thermal equilibration of the rotamer populations at room temperature. Interestingly, in the above-mentioned REMPI S_0–S_1 gas phase spectrum of p3P, despite of the high spectral resolution, no evidence for a second conformer can be found.[7] This means that either only one conformer is thermally populated or, more plausible, that the two conformers have identical $S_0 \rightarrow S_1$ transition energies.

The role of the inter-ring twist modes on the absorption and emission spectra of p3P were further investigated by Schneider *et al.*[5] They investigated p3P derivatives with and without additional bridges between the rings and confirmed that the S_0–S_1 Stokes shifts are relatively large for the non-bridged compounds but considerably smaller if the torsional angle between the phenyl rings is reduced due to the presence of the bridges.[5] Employing a combination of Hartree–Fock theory and configuration interaction singles Heimel *et al.*[9] calculated twist angles between 30 and 40 degrees for the S_0 state of p3P. However, the large Stokes shift and the observed violation of the mirror-image-rule in p3P could be only explained when they included the anharmonicities of the torsional potentials in the S_0 and the S_1 states in their Franck–Condon (FC) simulations. Heimel *et al.*[9] also find in their S_0–S_1 FC spectrum four members of a sequence of the inter-ring stretch vibration (spacing $\sim$1400 cm^{-1}). This sequence and its combination bands with the torsion modes then explain, why in solution the emission spectrum of p3P is so broad and completely structure-less. Investigations by Lukeš *et al.*[10] performed later with time-dependent density functional theory (TDDFT) came to the conclusion that the π system of the S_1 state adopts a quinoid double-bond structure in p3P.

In a more recent experimental investigation of p3P, p4P, p5P and *para*-sexyphenyl (p6P) by Nijegorodov *et al.*[11] the fluorescence quantum efficiencies were measured to be 0.84 (p3P), 0.81 (p4P); 0.89 (p5P) and 0.93 (p6P) and the corresponding fluorescence lifetimes are 1.0 ns (p3P), 0.85 ns (p4P), 0.82 ns (p5P) and 0.78 ns (p6P). Note that in this work no error bars were given despite the small differences between the values. If we assume that the small differences are correct, both series of data follow roughly the same line: the optical S_1–S_0 transition cross section, being already high for p3P, still increases with chain length and is directly responsible for the increase in the fluorescence quantum efficiencies and the shortening of the S_1 lifetimes.

The larger the molecules become, the more non-radiative decay channels should be accessible. Typically, only the electronic ground state and triplet states are situated below S_1. The experimental determination of the energetic position of triplet states by conventional methods is difficult in pure hydrocarbons because the electronic singlet–triplet coupling is weak. The T_1 triplet state energies of p3P (3.1 eV) and p4P (2.3 eV) were measured for the first time by electron energy loss spectroscopy (EELS),[12] a method which competes with photodetachment–photoelectron spectroscopy (PD–PES), used in our investigation. Both methods can access triplet and singlet states of the neutral molecules on an equal footing. Strangely, by EELS no triplet states above T_1 have been found, although the energy range of the EELS spectra includes the S_1 (p3P: 4.9 eV; p4P: 4.6 eV), S_2 and even higher singlet states. Also by transient triplet absorption spectroscopy, no further triplet state was found below S_1 for p3P.[13]

To answer the open questions for the ppPs, we apply PD–PES to intact parent radical ppP anions. The fact that triplet states of the neutral molecule can be directly probed by removal of an electron from an intact radical anion has been known for a long time[14–17] and was applied by us to anthracene,[18] azulene,[19] *N*-methylacridone and *N*,*N*-dimethylquinacridone.[20] With the same method, the electron affinities (EAs) of p3P and p4P were determined by Nakamura *et al.* in 2006.[21] They also presented theoretical EA values, which agree reasonably well with their experimental values. By using UV lasers, we measure the lowest electronic excited states including S_1 and especially the T_1 and the T_2 states in this work. Finally, we compare calculated FC spectra with the shape of the measured spectra with the aim to gain new insights into the energetics as well as the geometric and electronic structures of the observed electronic states.

2 Methods

2.1 Anion photodetachment–photoelectron spectroscopy: the experimental setup

The sample molecules have been purchased from TCI. The apparatus used in this work for conducting photodetachment–photoelectron spectroscopy (PD–PES) has been described elsewhere.[19,20] In short, the apparatus consists of four vacuum chambers in a sequence to stepwise reduce the vacuum pressure from the inlet chamber (chamber 1) to the photoelectron spectrometer (chamber 4). At the beginning of each measurement cycle, a heated and pulsed stainless steel gas nozzle releases a short gas pulse of argon (20 bar back pressure) with a small percentage of thermally evaporated sample molecules. As a result a pulsed co-expansion takes place through the small orifice (diameter 300 μm) into the first vacuum chamber (pressure in average better than 5×10^{-5} mbar). During expansion, radical anion formation by electron attachment to the sample molecules is performed. During the ongoing expansion, the initially hot radical anions then quickly undergo many collisions with the dense Ar gas. By this, the anions are energetically stabilised and strongly cooled. The slow neutral atoms and molecules as well as all the negative sample anions and the positive Ar ions contained in the centre of the expansion pass after about 10 mm through a skimmer orifice into the second vacuum chamber. The latter is used for vacuum pressure reduction between the chambers.

Despite that most of the sample radical anions are intact parent anions, mass selection is required before the

photodetachment, because many aggregates are formed. In chamber number two, for this reason, the ions enter a pulsed linear time-of-flight mass spectrometer (ToF-MS) which includes chambers 3 and 4. After passing several ion focussing lenses and several deflection plates in chamber 3, the anion cloud of interest crosses the PE spectrometer in chamber 4 and is detected at the rear side of chamber 4 on a micro-channel-plate (MCP) ion detector. The mass resolution is at this stage about 200. When crossing chamber 4, in the middle of the perpendicular μ-metal-shielded and therefore field-free PE spectrometer the anions interact with the pulsed detachment laser beam, which comes from above, perpendicular to the ion beam and the PE-spectrometer. Only these electrons which are emitted perpendicular to the ion and the laser beams are detected on a MCP-detector. The energy of the electrons is then determined by a start-stop ToF measurement. To achieve a high accuracy in the time measurement, the slightly focussed detachment laser has a pulse width below 1 ns (fundamental and higher harmonics of a post-amplified Piccolo laser, Innolas, Germany, pulse width 800 ps).

In order to be able to hit as many anions as possible with the laser beam, after mass identification and selection by a mass gate, the anions of interest are post-accelerated before chamber 4 and by this compressed in time and space.[22] Photoelectron spectra are recorded by measuring the ToF which the electrons take for the 60 cm long field-free drift tube form the detachment site to the MCP electron detector. The advantage of such a ToF-energy analyser is, that for each cycle the PE spectrum covers always the full electron energy range, which depends on the molecular EA and the photon energy. The disadvantages are (i) a low transmission and (ii) the fact that the smallest peak width (best energy resolution) is only achieved for relatively low-energetic electrons ($E \leq 200$ meV).

To present a good energy resolution, for most of the accessible electronic states of the neutral sample molecule the overview anion PD–PE spectra are composed of sections of sub-spectra recorded with different detachment wavelengths. The disadvantage of this procedure is unfortunately that the relative electronic state intensities in the sub-spectra are different due to Wigner's threshold law[23] and difficult to adjust to each other. However, since we are especially interested in the energetics, such as electron affinities and triplet state energies, a comparison of the intensities is of minor importance.

In the ideal case, a photo excitation of a radical anion would excite into the detachment continuum and the intensities of the vibronic transitions of the final neutral electronic state would be exclusively given by the FC factors between the anion ground state and the neutral electronic state to which the detachment process leads. Unfortunately, anions can have anion-excited states even above the electron detachment threshold. These states, if accidentally resonantly photoexcited, can autoionise. Since in this case the resonant anion excited electronic state is involved, it can (i) either disturb the anion-to-neutral FC factors,[24–26] or (ii) lead to a vibronically induced delayed autodetachment.[27]

To avoid surface effects as much as possible, the inner spectrometer wall is heated to 340 K and the PE spectrometer is energy-calibrated from time to time with the two spin–orbit transitions of atomic iodide.[28–30] We found that the experimental accuracy concerning the absolute energy is ±5 meV for electrons with energies below 300 meV, but the relative accuracy is much better than this. The accuracy to determine the energy of the adiabatic origin of an electronic state may, however, be less than the experimental accuracy because the shape of the observed spectral structures might be weak or/and broad and thus make an assignment of the exact origin transition of an electronic state difficult. This is especially the case for the adiabatic positions of the S_0 ground states of the ppPs (see Section 3.1).

2.2 Theoretical methods and computational details

All geometry optimisations and frequency analyses were performed with the Gaussian 16 program[31] using the PBE0 density functional,[32,33] which is known to give accurate ground- and excited-state geometries for this class of compounds,[34] and a valence triple-zeta basis set with polarisation functions (TZVP)[35] for carbon and hydrogen. The geometries of the anionic ground states (D_0) were optimised at the level of unrestricted Kohn–Sham density functional theory (KS-DFT) whereas closed-shell KS-DFT was employed for the neutral ground states (S_0). The minima of the excited singlet states were determined with time-dependent density functional theory (TDDFT), those of the triplet states with TDDFT in the Tamm–Dancoff approximation. Unless stated otherwise, all electronic excitation energies and molecular wavefunctions at the optimised geometries were calculated with the combined DFT and multireference configuration interaction (DFT/MRCI) method[36,37] employing the recently presented R2022 Hamiltonian[38] which is particularly well suited for extended π-systems. DFT/MRCI is a semi-empirical multireference configuration interaction ansatz based on KS orbitals and orbital energies of a closed-shell BH-LYP functional[39,40] determinant. For the construction of the two-electron integrals in the resolution-of-the-identity approximation, the auxiliary basis sets from the Turbomole library[41,42] were employed. Computational details concerning the DFT/MRCI parameter set, the selection thresholds for including configuration in the variational space and the number of roots determined in the Davidson diagonalisation procedure can be found in the ESI.† FC spectra were calculated *via* a fast Fourier transformation ansatz employing the Vibes program.[43,44] Besides adiabatic energies and FC patterns of the excitation, photoionisation cross sections are especially valuable for assigning closely spaced electronic states. To obtain an estimate for the photoionisation probabilities, often Dyson orbitals ϕ_{IF}^{Dyson} and their respective squared norms σ_{IF} are used, disregarding the overlap between the outgoing electron and the ionisation continuum states.[45–48] In the context of PES, Dyson orbitals are defined as the overlap between an initial N-electron state and a final $N-1$-electron state.

$$\phi_{IF}^{Dyson}(x_1) = \sqrt{N}\int \psi_F^{N-1}(x_2, x_3, \ldots, x_N)\psi_I^N \times (x_1, x_2, x_3, \ldots, x_N)\mathrm{d}x_2, \mathrm{d}x_3, \ldots, \mathrm{d}x_N \quad (1)$$

Dyson orbitals can also be written as a linear combination of the molecular orbital set of the initial wave function $\{\phi_p\}$:

$$\phi_{\mathrm{IF}}^{\mathrm{Dyson}}(x_1) = \sum_p \gamma_p \phi_p(x_1) \quad (2)$$

where the expansion coefficients, also called Dyson amplitudes, are defined as:

$$\gamma_p = \langle \psi_{\mathrm{F}}^{N-1} | a_p | \psi_I^N \rangle \quad (3)$$

Possible values range between 0 for states that cannot be described by a one-electron transition and 1 for two states that differ exactly by the occupation of one spin orbital. Note, that a value of 1 is only possible if the electron is detached from a singly occupied molecular orbital of the anion. If the electron is removed from a doubly occupied shell, at most a Dyson amplitude of 0.5 can be expected. (For further explanations, see the ESI.†) The squared Dyson norm can be described as the sum over the squared coefficients

$$\sigma_{\mathrm{IF}} = \left\| \phi_{\mathrm{IF}}^{\mathrm{Dyson}} \right\|^2 = \sum_p {\gamma_p}^2 \quad (4)$$

and is a measure for the probability of a photoionisation. In this work, DFT/MRCI wavefunctions of the anionic ground state and the ground and excited states of the respective neutral molecules have been used to determine the pole strengths.

3 Results and discussion

In the following section, we present the experimental PD–PE overview spectra of p3P, p4P and p5P, explain their specialities and propose first assignments. Subsequently, we report on the results of our quantum chemical calculations before we compare them with the experimental data and discuss the resulting consequences.

3.1 Photodetachment–photoelectron overview spectra

The overview PD–PE spectra of p3P, p4P and p5P (Fig. 2) show the transitions from the anion ground states to the S_0 and to the excited electronic states of the neutral molecules. Note that they are composed of sub-spectra recorded with different detachment wavelengths in order to show spectra with the best possible electron energy resolution and to avoid strange vibrational FC effects as caused by the resonance of the detachment laser with an anion-excited electronic state. Labels with the detachment wavelengths are included in Fig. 2. The relative intensites of the subspectra have been adapted to each other according to graphical aspects. Between two electronic states they can be only interpreted if their spectral structures have been recorded with the same wavelength and if the two states lie rather close in energy. The estimated origin positions of the S_0 states are set to the zero position of the energy scale which is—as a consequence—the energy scale of the neutral molecules. As a result of the definition of the energy axis, the anion ground states lie to the left of the zero point of the *x*-axis (S_0)

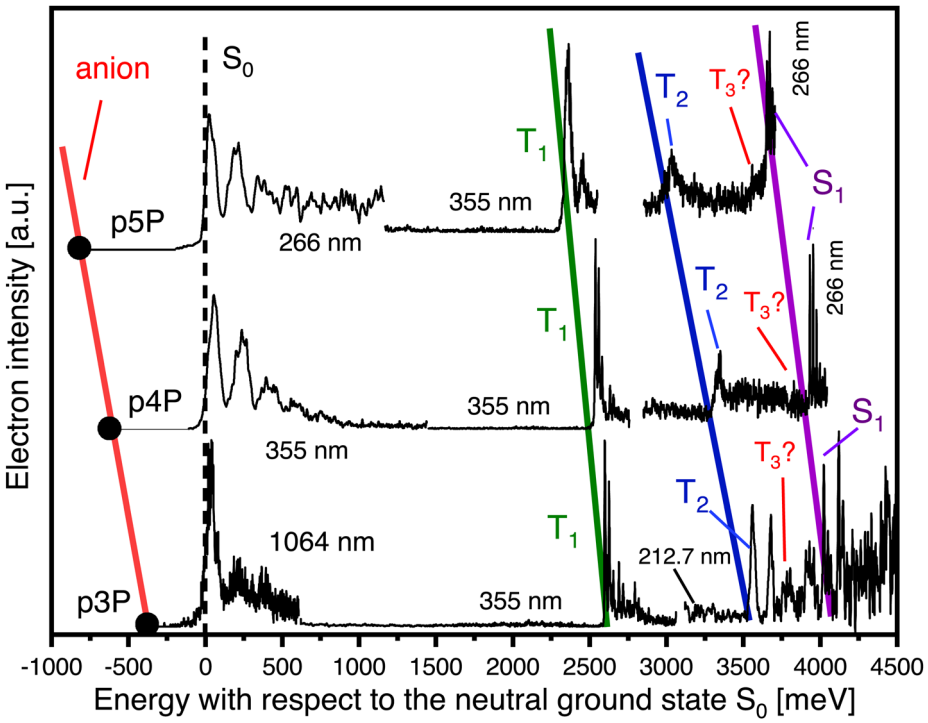

Fig. 2 Composed PD–PE overview spectra of p3P, p4P and p5P illustrating the energetic trends. The coloured lines are only meant to guide the eye. For a better comparison to the spectroscopy of the neutral molecules the energies are given with respect to the neutral S_0 ground state. The positions of the anion D_0 ground states are marked by bullets (for values, see Table 1). The EA increases with increasing size of the molecules, the S_1 and T_1 bands shift slightly to lower energies whereas a stronger shift is observed for T_2. The assignment of the T_3 band is tentative only.

and the electronically excited states of the neutral molecules to the right side. As expected, the EAs increase and the electronic excited state energies decrease with the increase of the number of phenyl rings.

The assignments included in Fig. 2 are based on simple spectroscopic principles and literature data. The lowest-energetic transition from the radical anion to the neutral molecule leads to the S_0 state. The assignment of the next spectral PE structures is also obvious: in a closed-shell molecule, the T_1 state is usually the first excited state above S_0 and does not appear in UV-VIS spectra. The assignment of the S_1 states can be performed on the basis of their energetics which agree with S_0–S_1 transition energies known from literature (see Table 1). Since the isolated transitions which are located between T_1 and S_1 have not been observed in the UV-VIS spectra,[5] they are attributed to T_2. In addition, further peaks are assigned tentatively to the T_3 state.

The EA values and the excited-state energies of all three molecules are summarised in Table 1 and compared to experimental literature data. In all investigated ppPs, definitively the T_2 states and possibly even the T_3 states lie below the respective S_1 states and the S_1–T_2 energy gap is relatively small. In Fig. 2 one can see that the vibrational structures of the individual electronic states are rather different. For example, in p3P the first transition to S_0 is much broader (this sub-spectrum was recorded with 1064 nm, providing the best experimental resolution) than the peaks of the transitions to T_1, T_2 and S_1. If autodetachment effects were absent, these individual vibrational patterns should be correlated with structural changes between the molecular anion geometry and the geometries of the individual electronic states of the neutral molecules. In Section 3.3, expanded PD–PE spectra of most of the transitions to the individual electronic states of the neutral molecules are shown and compared to corresponding theoretical spectra.

3.2 Quantum chemical results

According to former investigations,[7–9,21] the changes of the torsional angles, which are allocated between the phenyl rings, play an important role for the interpretation of the electronic and vibronic spectra of the ppPs. Moreover, these twist angles seem to be correlated with C–C bond length alterations. Lukeš *et al.* postulated that ppPs exhibit a quinoid structure in the first excited singlet state and that the double-bond character of the C–C bond between the phenyl rings causes the planarity in S_1.[10] We here take these statements as a motivation for a more general investigation on the equilibrium geometry changes in the ground and excited electronic states of the neutral ppPs with regard to the anion ground state. In the following, the trends will be discussed in a qualitative manner.

As mentioned earlier, for the neutral *para*-phenylenes two or more stable rotamers exist which differ in the relative orientation of the phenyl rings, *i.e.*, alternating or helical. Within the error bars of our experiment and our quantum chemical calculations we do not find energetic differences between the two (p3P) and multiple (p4P and p5P) possible conformers of the investigated ppPs, neither in the anions nor in the neutral electronic states. Inter-conformer transitions have very similar transition energies as intra-conformer transitions but have typically broader vibrational structures due to the larger geometry changes. To simplify the complex discussions, we only present the results for the conformers alternating in the sign of the torsion angles.

3.2.1 Quantum chemical results on p3P. The analysis of the twist angles in the equilibrium structures (Fig. 3) shows that D_0, S_1, S_2 and T_1 are nearly planar and that S_0 is strongly non-planar. For the S_0 and S_1 states these finding agree well with the results of Lukeš *et al.*[10] and explain the large and irregular S_0–S_1 Stokes shifts determined in optical spectroscopy.[5] The minimum structure of the T_3 state could not be determined because the geometry optimisation converges towards a conical intersection with the T_2 potential energy surface.

In Fig. 4, the calculated bond length changes with respect to the anion ground state D_0 are shown. These changes will be rationalised based on the leading configurations of the wavefunctions. To avoid confusion, we designate the molecular orbitals (MOs) according to their occupations in the ground state of the neutral molecule: the highest occupied molecular orbital (HOMO, H) is doubly occupied in both, S_0 and D_0, whereas the lowest unoccupied molecular orbital (LUMO, L) is empty in S_0 and singly occupied in D_0.

The leading term of the totally symmetric S_0 state is related to the D_0 state by the ejection of the LUMO electron. The LUMO has bonding character with regard to the inter-ring C–C bonds 4 and 8 (see Fig. 5), where we have used the bond labelling introduced in Fig. 4. Also the C–C bond 6 in the central phenyl

Table 1 Electron affinities and electronic state energies of p3P, p4P and p5P with respect to the neutral ground state S_0. Experimental data from this work and literature data. All values are given in meV. Note that the energy error in this work is given by the accuracy with which the origin of the S_0 state can be determined (about ±50 meV)

	p3P		p4P		p5P	
State	Lit.	This work	Lit.	This work	Lit.	This work
EA/S_0	390[a]	379	660[a]	620	—	805
S_1	4024[b], 3962[c], 4900[d]	4024	3731[c], 4600[d]	3872	3602[c]	3688
S_2	6500[d]	—	4029[c], 6400[d]	—	3967[c]	—
T_1	2541[c], 3100[d], 2529[e]	2598	2392[c], 2300[d]	2478	2318[c]	2375
T_2	—	3558	—	3260	—	3073
T_3	—	3930 (?)	—	3771 (?)	—	3597 (?)

[a] Ref. 21 PD–PES. [b] Ref. 7 REMPI, gas phase. [c] Ref. 11 solution phase. [d] Ref. 12 electron beam, gas phase. [e] Ref. 49 crystal.

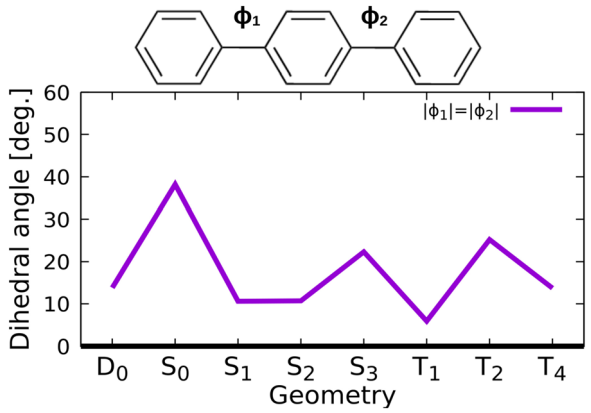

Fig. 3 Calculated torsional angles in the equilibrium geometries of selected anionic and neutral electronic states of p3P.

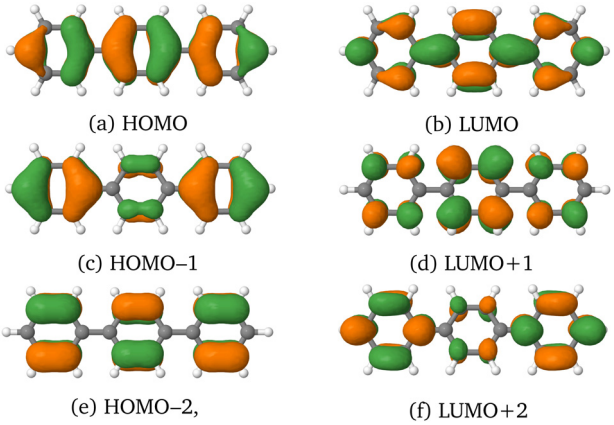

Fig. 5 Important MOs of p3P at the anion ground state geometry. Images of further MOs may be found in the ESI.†

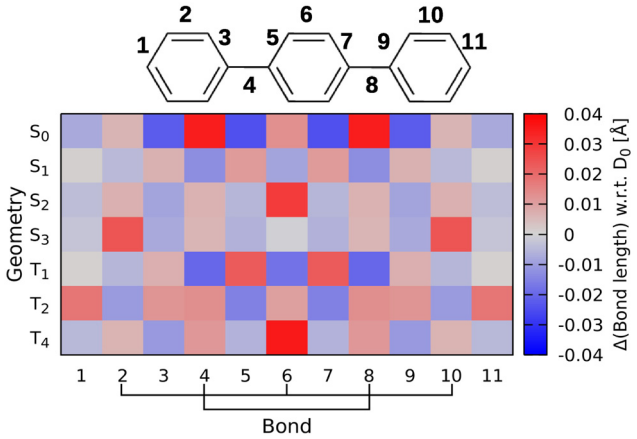

Fig. 4 Bond length differences between the respective neutral states and the D_0 anion state of p3P. The colour bar at the right side gives the correlation between the colours and the bond length changes (in Å).

ring and, to a minor extent, the C–C bonds 2 and 10 in the terminal phenyl rings experience bonding interactions in LUMO. All other C–C bonds of p3P are intersected by nodal planes in the LUMO and therefore have antibonding character. The pattern of the bond length alterations, shown in Fig. 4, exactly follows the expected trends: if one electron is removed from the LUMO, the inter-ring C–C bonds 4 and 8 lose their double-bond character. Accordingly, the steric strain caused by the repulsion between the hydrogen atoms of two neighbouring phenyl rings prevails over the bonding forces and leads to an out-of-plane twist, as may be seen when comparing the torsional angles of the D_0 and the S_0 states in Fig. 3. Also the central bond 6 is strongly elongated in S_0 with respect to D_0 while the bonds carrying odd labels are shortened, but these bond length changes do not have a major impact on the dihedral angles.

If instead an electron is removed from the HOMO, the A_u-symmetric T_1 or S_1 states are reached, depending on the spin orientation of the outgoing electron. Although both states are well represented by the $(H)^1(L)^1$ configuration, the bonding patterns (Fig. 4) are not identical. We notice stronger bond length alterations in the triplet state, a phenomenon already observed for the $(H)^1(L)^1$ states of polyene chains.[50] Nodal planes intersect the even numbered bonds whereas high electron density is found between the carbon atoms connected by odd numbered bonds (see Fig. 4). In the S_1 and T_1 states, therefore the inter-ring C–C bonds are strengthened and shortened whereas the neighbouring bonds are elongated. Even the bonds 2, 6 and 10 acquire partial double bond character, thus giving the three phenyl rings a quinoid structure.

The geometry changes of the higher-lying electronic states are not as easily deduced because they have multiconfigurational character. The wavefunction of the T_2 state exhibits A_g symmetry and is dominated by an almost equal mixture of $(H-1)^1(L)^1$ and $(H)^1(L+2)^1$ configurations. HOMO−1 and LUMO+2 have larger amplitudes on the terminal phenyl rings than on the central one (see Fig. 5c and f). Ejection of an electron from HOMO−1 and occupation of LUMO+2 both lead to a pronounced elongation of the terminal C–C bonds 1 and 11, other geometry changes are less obvious. Inter-ring twist angles intermediate between the D_0 and S_0 are found for the equilibrium geometry of this state. S_2 and T_4 transform according to the B_u irreducible representation with leading $(H)^1(L+1)^1$ and $(H-2)^1(L)^1$ terms. LUMO+1 and HOMO−2 do not involve the carbon atoms connecting the phenyl rings (see Fig. 5d and e). Therefore, the small twist angles (Fig. 3) are mainly caused by the removal of a HOMO electron in the first case and the remaining electron in the LUMO in the second case. The most pronounced bond length change involves the central C–C bond 6 which is markedly weakened with respect to the anion ground state (Fig. 4).

3.2.2 Quantum chemical results on p4P. The structural differences between the electronic states of p4P show similar patterns as those of p3P (Fig. 6 and 7), save for a few distinct peculiarities concerning the central C–C bond and the related torsional angle Φ_2. In the anionic ground state, the torsional angles vary between 15° for Φ_2 and −20° for Φ_1 and Φ_3. The S_0 minimum geometry is again strongly non-planar and the inter-ring bonds are elongated with regard to the D_0 structure.

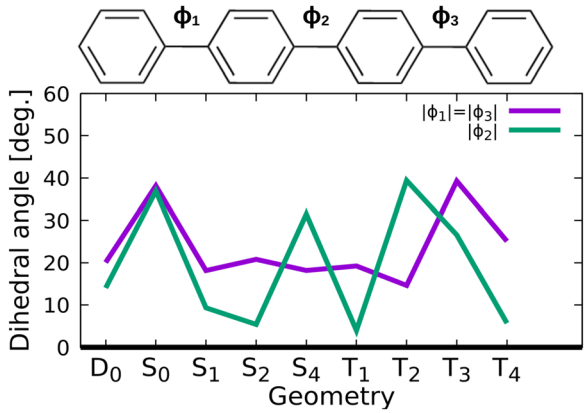

Fig. 6 Torsional angles in the different electronic states of p4P. Note the different behaviour of the outer angles Φ_1 and Φ_3 in comparison to Φ_2.

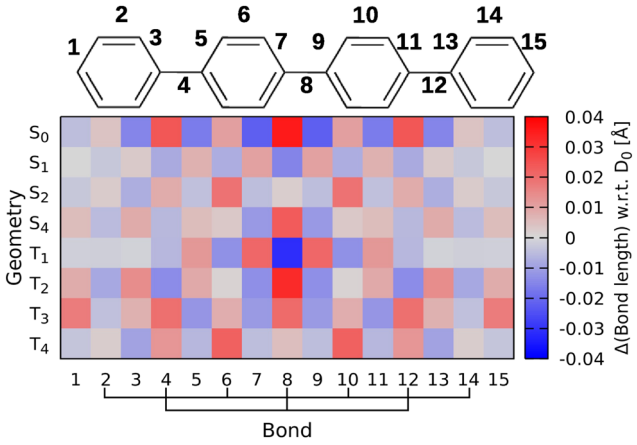

Fig. 7 Bond length differences between the neutral states of p4P with respect to D_0. For further explanations, see Fig. 4.

The effect is more pronounced for the central bond 8 because the electron density in the LUMO (Fig. 8b), from which the electron is ejected, is higher than for the terminal inter-ring bonds 4 and 12. The S_1 and T_1 states of p4P adopt a quinoidal structure, again with stronger alterations for the central bond and the related twist angle due to the larger orbital amplitudes of the HOMO (Fig. 8a) in that spatial region.

T_2 and S_4 are interesting cases because here opposite tendencies are observed for the outer and inner phenyl rings and the related geometry parameters (Fig. 6 and 7) which can be traced back to the electron density distribution in the involved MOs. Like in p3P, T_2 and S_4 are multiconfigurational wavefunctions with the $(H-1)^1(L)^1$ and $(H)^1(L+1)^1$ configurations as leading terms. Inspection of Fig. 8c reveals bonding character for 8 and antibonding character for 4 and 12 in HOMO−1. Annihilation of an electron in HOMO−1 therefore weakens the central inter-ring bond and strengthens the outer ones. The second configuration cannot be reached from D_0 by a single electron excitation, but requires the removal of an electron from HOMO accompanied by an excitation from LUMO to LUMO+1. While the geometric effects caused by the

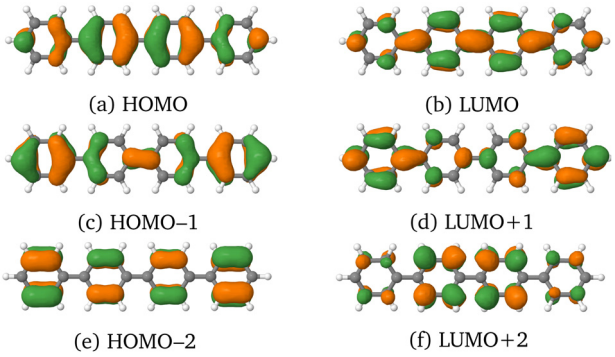

Fig. 8 Important MOs of p4P at the anion ground state geometry. Images of further MOs may be found in the ESI.†

lowering of the HOMO and LUMO populations nearly cancel, occupation of LUMO+1 (Fig. 8d) results in an elongation of the central C–C bond. While the electronic states of neutral p4P, discussed so far, are symmetric with respect to a rotation through 180° about the long C_2 axis (z axis), S_2 and T_4 are antisymmetric. To reach their leading $(H)^1(L+2)^1$ configuration from the D_0 state, again a two-electron process is necessary. Their secondary configuration, $(H-2)^1(L)^1$, is generated by PES through the ejection of an electron from HOMO−2. Neither HOMO−2 (Fig. 8e) nor LUMO+2 (Fig. 8f) exhibit notable amplitudes on the inter-ring C–C bonds. Ejection of an electron from HOMO−2 and occupation of LUMO+2 rather lead to a weakening of the bonds 6 and 10 (Fig. 7) without essentially changing the torsional angles with regard to the anion ground state (Fig. 6).

3.2.3 Quantum chemical results on p5P. Without repeating this kind of detailed discussion for p5P, we notice that for some electronic states the outer ($\Phi_1 = \Phi_4$) and the inner torsional angles ($\Phi_2 = \Phi_3$) differ considerably (Fig. 9). In the D_0 anion ground state, all twist angles are around 20° while the S_0 state of p5P is strongly twisted, with all torsional angles close to 40°. In S_1 (configuration $(H)^1(L)^1$), the inner two twist angles are smaller than the outer ones, an effect which is even more pronounced in the T_1 state. The degree of torsion finds its direct correspondence in the inter-ring C–C bond distance (Fig. 10).

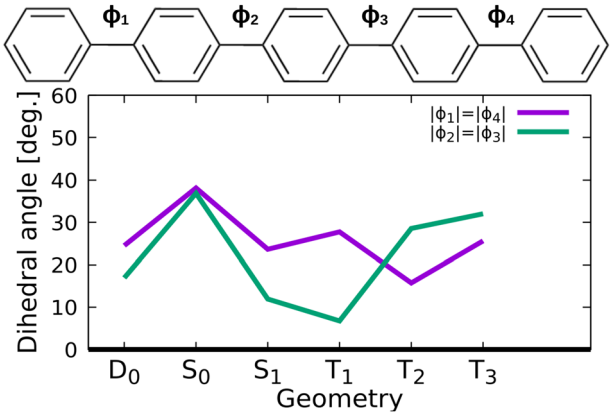

Fig. 9 Torsional angles in the different electronic states of p5P.

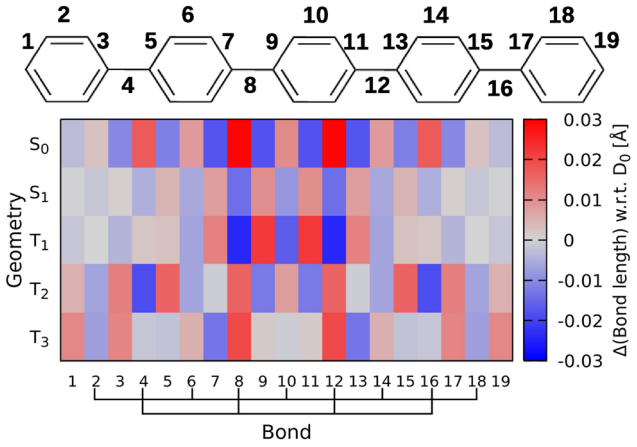

Fig. 10 Bond length differences between the neutral states of p5P with respect to D_0. For further explanations, see Fig. 4.

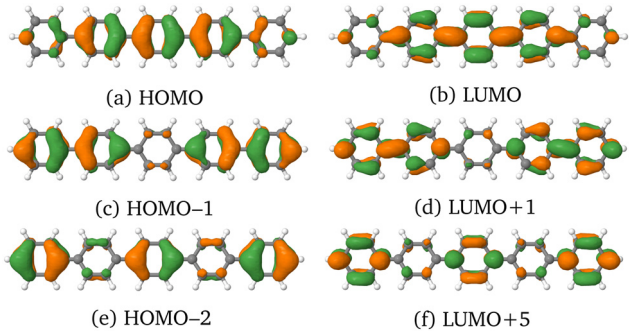

Fig. 11 Important MOs of p5P at the anion ground state geometry. Images of further MOs may be found in the ESI.†

The quinoidal structure appears to extend over the three innermost phenyl rings only. These trends are related to the observation that the electron densities in the HOMO (Fig. 11a) and LUMO (Fig. 11b) orbitals are mainly localised in this part of the molecule. In contrast, HOMO−1 (Fig. 11c) and LUMO+1 (Fig. 11d) have large amplitudes on the outermost phenyl rings and their neighbours and almost zero coefficients on the central phenyl ring. For that reason, the inner inter-ring bonds No. 8 and 12 are weakened whereas the outer inter-ring bonds (No. 4 and 16) are strengthened at the T_2 minimum where the $(H-1)^1(L)^1$ and $(H)^1(L+1)^1$ configurations have nearly equal weights. As a consequence, the outer twist angles are smaller than the inner ones, essentially reversed to the situation in the T_1 state. Also T_3 is not planar. It exhibits a nearly equal mixture of $(H-2)^1(L)^1$, $(H-1)^1(L+1)^1$ and $(H)^1(L+5)^1$ configurations (for orbitals see Fig. 11). Like in T_2, its inter-ring bonds 8 and 12 are elongated with respect to the D_0 structure, but the bond length alterations in the central ring nearly level out.

In conclusion of this section, with increasing chain length of the ppP, more and more local effects are observed where the inner and outer molecular sections behave differently in individual electronic states. The tendency that a nearly planar quinoidal structure in the S_1 state is restricted to the central parts of the molecule has been reported even for longer *para*-phenylene oligomers.[51] While trends for the first excited singlet state were discussed in detail by Lukeš *et al.*,[10] we extended our investigation of the structural changes to several low-lying triplet states.

3.3 Comparison of the experimental and computed spectra

In this chapter we present our theoretical results based on the DFT/MRCI method and compare them to the experimental data. The absolute error for the experimental electronic state energies with respect to the S_0 state is determined by the error with which the exact position of the transition to the S_0 origin can be determined. Due the broad unresolved structure of this transition, the S_0 origin position may have only an accuracy of roughly 50 meV. Root mean square deviations of the DFT/MRCI method are typically in the 200 meV range for organic molecules with a closed-shell ground state when the R2022 Hamiltonian is employed.[38]

3.3.1 *para*-Terphenyl (p3P). The agreement between the calculated and measured 0–0 energies is relatively good (Table 2). This applies even to the EA, computed as ΔSCF value at the PBE0/TZVP level of theory, whereas DFT/MRCI underestimates the EA. With the exception of T_1, which matches the experimental value perfectly, the calculations appear to underestimate the experimental 0–0 energies by about 0.1 eV, whereas adiabatic DFT/MRCI energies which do not include ZPVE corrections are a bit too high. The theoretical value of the T_3 energy, provided in Table 2, has been obtained for a C_s-symmetric saddlepoint structure with a small imaginary frequency (-13 cm^{-1}). Despite many attempts, a proper minimum could not be determined for the T_3 potential energy surface because it undergoes a conical intersection with the T_2 potential. According to the calculations, this saddlepoint lies energetically below the S_1 minimum if ZPVE corrections are taken into consideration. The strong vibronic coupling between two triplet states is held responsible for the irregular vibrational pattern observed between T_2 and S_1 in the overview spectrum.

The very different vibrational substructures of the individual transitions in the experimental p3P PD–PE spectrum shown in Fig. 2 indicate that some electronic states of the neutral molecule exhibit strong structural differences with respect to the anion ground state, an effect which is worth to be further investigated by calculations of FC patterns. As discussed in Sections 3.2.1, p3P is almost planar in the anion ground state, strongly twisted in the neutral ground state S_0 and nearly planar in the S_1 state. A quick look at the overview spectrum of p3P (see Fig. 2) confirms qualitatively these theoretical results: in contrast to the broad anion to S_0 transition, the transitions to excited electronic states, such as T_1 and S_1, contain intense origin transitions and relatively small intensities for the low-frequency vibrations.

For a more detailed analysis, individual expanded experimental spectra and the corresponding theoretical calculated FC transition spectra have been juxtaposed. Displacement vectors of the most important normal coordinates are visualised in the ESI.†

Table 2 Theoretical and experimental results for p3P: coefficients (absolute values) of leading MO configurations, calculated vertical transition energies $\Delta E_{vert.}$ at the S_0 geometry, calculated adiabatic transition energies $\Delta E_{adiab.}$ and ZPVE corrected transition energies ΔE_{0-0} with respect to S_0, experimental energies $\Delta E_{exp.}$ (this work only), oscillator strengths f, calculated vertical electron detachment energies $\Delta E_{det.}$ and Dyson intensities σ at the D_0 geometry. All energies in eV. In the first row of the table body, the experimental and the ZPVE corrected theoretical EAs are displayed. Experimentally not observed transitions are labelled as 'n.o.'

State		Configurations	$\Delta E_{vert.}$	$\Delta E_{adiab.}$	ΔE_{0-0}	$\Delta E_{exp.}$	f	$\Delta E_{det.}{}^{b}$	$\Delta E_{det.}{}^{c}$	σ
S_0	1^1A_g	0.97 GS			EA: 0.42[b]	EA: 0.380	—	0.53	0.53	0.95
S_1	1^1A_u	0.95 $(H)^1(L)^1$	4.61	4.03	3.91	4.024	1.15	4.27	4.36	0.46
S_2	1^1B_u	0.67 $(H)^1(L+1)^1$ 0.50 $(H-2)^1(L)^1$ 0.28 $(H-4)^1(L)^1$	4.54	4.21	4.09	n.o.	0.00	4.87	4.59	0.17
S_3	1^1B_g	0.60 $(H-3)^1(L)^1$ 0.54 $(H)^1(L+3)^1$	4.63	4.50	4.34	n.o	0.00	5.19	4.85	0.18
T_1	1^3A_u	0.91 $(H)^1(L)^1$	3.36	2.74	2.60	2.598	—	3.08	3.12	0.43
T_2	1^3A_g	0.65 $(H-1)^1(L)^1$ 0.60 $(H)^1(L+2)^1$	3.83	3.64	3.45	3.558	—	4.13	3.03	0.21
T_3	2^3A_u	0.47 $(H-3)^1(L+3)^1$ 0.41 $(H-5)^1(L)^1$	4.17	4.04[a]	3.81[a]	3.93 (?)	—	4.88	4.75	0.09
T_4	1^3B_u	0.69 $(H)^1(L+1)^1$ 0.50 $(H-2)^1(L)^1$ 0.24 $(H-4)^1(L)^1$	4.27	4.01	3.95	n.o.	—	4.44	4.40	0.16

[a] No minimum was found. In C_s symmetry, still a small imaginary frequency with -13 cm^{-1} is present at the saddlepoint. [b] Computed at the (TD-)PBE0/TZVP level of theory. [c] DFT/MRCI energies at the D_0 geometry, shifted by 0.38 eV, the difference between the PBE0/TZVP and DFT/MRCI computed vertical detachment energy of the S_0 state.

The experimental spectrum in Fig. 12a shows at the low-energetic side a smooth onset, then a steep rise at about 400 meV followed by some distinct peaks with spacings of about 54 cm^{-1} before the signal declines again. The width at half height of a fictive envelope of the complete S_0 structure would be about 50 meV. The important question now is where does the S_0 origin transition lie? Remember that the exact position of the S_0 origin affects the determination of the electron affinity and the derived energetic positions with respect to the neutral S_0 state. The first observed weak transition of the S_0–S_1 spectrum of Murakami *et al.* has been determined by laser spectroscopy (4.024 eV).[7] We can use this value to qualitatively locate the S_0 origin at about 380 meV above the anion ground state. This position is marked with a black vertical line in Fig. 12a. Since the theoretical spectrum in Fig. 12b essentially predicts a very low intensity for the D_0–S_0 0–0 transition, the exact position of the experimental origin should lie considerably to the left of the distinct sharp first peak indicated as "S_0?" in Fig. 12a. Because the exact determination of the S_0 origin position is impossible on the basis of the presently available information, we set our error bars to ±50 meV.

If one compares the experimental with the calculated FC spectrum (see Fig. 12b), the peak spacings are roughly similar, however, the agreement of the peak intensities is rather poor: (i) in the theoretical FC spectrum the width of the envelope over the vibrational fine structure is about 100 meV and therefore much broader than that of the experimental spectrum (50 meV) and (ii) there are also no sudden intensity-changes in the calculated spectrum as observed in the experimental spectrum. Possible reasons for the deviations between experiment and theory could lie on the experimental or theoretical side. As mentioned in Section 1, resonant anion excited states could manipulate the anion-to-neutral FC factors. The absorption

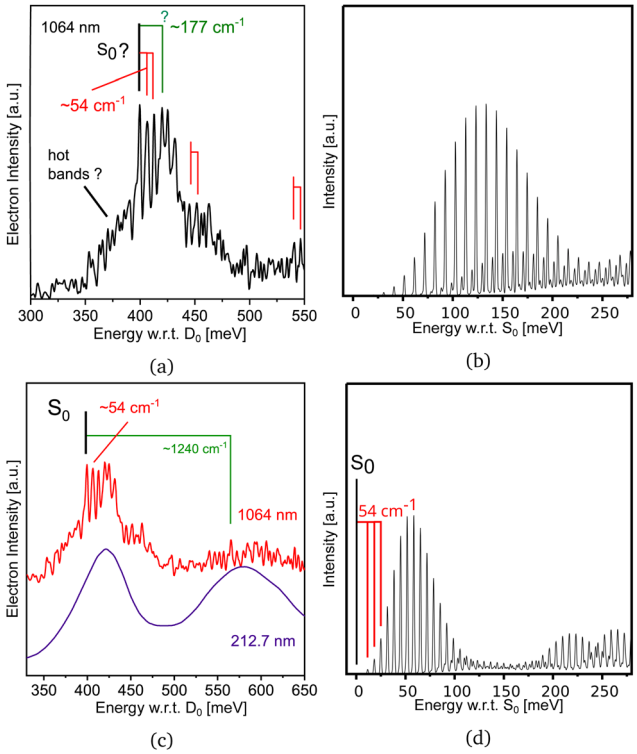

Fig. 12 p3P: experimental and calculated spectra of the transition from D_0 to S_0. (a) Experimental spectrum recorded with PD wavelength 1064 nm. The vertical black line indicates the expected position of the D_0–S_0 origin position as derived from the difference between our D_0–S_1 origin and the S_0–S_1 origin transition measured by Murakami *et al.*[7] (b) Simulated FC spectrum (c) PD–PE spectra recorded with 1064 and for comparison with 212.7 nm. (d) Simulated FC-spectrum with the torsional potential scaled to the experimental value of 54 cm^{-1}. For further discussion, see text.

spectrum of p3P anions published by Shida[52] shows only very small to vanishing absorption at 1064 nm, the wavelength used

for photodetachment, which makes a strong influence on the vibronic intensities very improbable. This indicates that the theoretical treatment of the low-frequency torsional modes is inaccurate. To explain the deviation of the calculated FC spectra from the experiment, it should be noted that the harmonic oscillator model used to determine the FC spectra is not well suited for describing large-amplitude motions. Due to the large displacements in the torsional coordinates by about 30°, a long vibrational progression can be expected. Because the low-frequency torsion modes at 83 cm^{-1} (observed at 54 cm^{-1}) and 217 cm^{-1} (observed at 177 cm^{-1}), exhibit too high wavenumbers, the envelopes of the torsional potentials are too wide. If the potential of the torsional mode in S_1 is adjusted by using the experimental vibrational frequency of 54 cm^{-1} in the FC calculation (Fig. 12d), the vibrational structure is not only compressed because of the lower vibrational frequency, but also the FC factors for the quantum numbers change.

Since the equilibrium structures of the D_0 anionic ground state and the T_1 state of the neutral molecule both are quasi planar, the calculated FC spectra are supposed to be more reliable. Indeed, Fig. 13 shows that the agreement between experiment (left side) and theory (right side) is quite good. The peak observed with a spacing of 225 cm^{-1} above the origin (see green line) can be identified with the calculated inter-ring vibration of 231 cm^{-1}. The next vibration identified in the experimental spectrum lies at 742 cm^{-1} and corresponds nicely to the calculated collective phenyl-ring breathing mode with an energy of 767 cm^{-1}. The first two main peaks in the experimental spectrum have each two satellite peaks somewhat shifted to higher energies (red and orange lines), one directly in the shoulder of the first highest peak (peak position: 24 cm^{-1}) and another one at a distance of about 89 cm^{-1}. Because the first main peak and its neighbouring satellite peak overlap, it is difficult to derive the exact underlying energetic spacing between the molecular vibronic states. Our FC simulations reveal that the three-fold structure might be attributed to a symmetric torsional mode with a calculated frequency of 41 cm^{-1}. To explain this discrepancy of computation and experiment, especially considering the third peak (89 cm^{-1}) we carried out a qualitative simulation (Fig. S12 in the ESI†) of a potential peak attraction effect caused by overlapping peaks. This resulted in a correction for the experimental 28 cm^{-1} value to 32 cm^{-1}. Obviously, even this fitted frequency of 89 cm^{-1} does not fit into a regular progression. As we did not find another FC active mode in our computations, tentatively matching this frequency, its origin remains inconclusive. However, it is reasonable to assume that anharmonicities are responsible for the observed peak structures.

In Fig. 14 the expanded experimental PD–PES recorded with 212.7 nm and the corresponding calculated FC spectra of the spectral range covering the transition to T_2 up to the transition to S_1 is displayed. The experimental spectrum in Fig. 14 is a good example for the effect that the resolution of ToF PES strongly depends on the electron excess energy: the closer the spectrum comes to the low-energy electron range (from left to right) the better the energy resolution becomes. Wigner's threshold law for photodetachment[23] predicts an intensity loss for structures close to the detachment threshold. This holds especially true for the excitation to the S_1 state.

The experimental transition spectrum to T_2 essentially consists of two equally strong broad peaks with a spacing of 960 cm^{-1} followed by two bunches of threefold structures. This peak pattern is unexpected. As the first two peaks are intense, one would expect a third member of the vibrational progression to follow. Instead, an irregular pattern is observed. In our calculations, we find an intersection between the T_2 and T_3 potential energy surfaces in this energy range which might explain these irregularities. As a consequence, we are not able to locate the minimum geometry of the T_3 state which is why no FC spectrum is plotted for this state in Fig. 14 (right). We first concentrate on the two strong broad peaks in the experimental spectrum. They are both asymmetric and the second peak has clearly a second close side-peak. This indicates that also the first peak has a weak underlying satellite peak shifted slightly to the blue. On the left side, the calculated FC spectrum shows a comb-like structure with a small energy spacing of 83 cm^{-1} corresponding to a torsional mode. Note, however, that the resolution of the computed spectrum depends on the width of the Gaussisan damping function (here 5 cm^{-1} full width a half maximum) used in the Fourier transformation of the

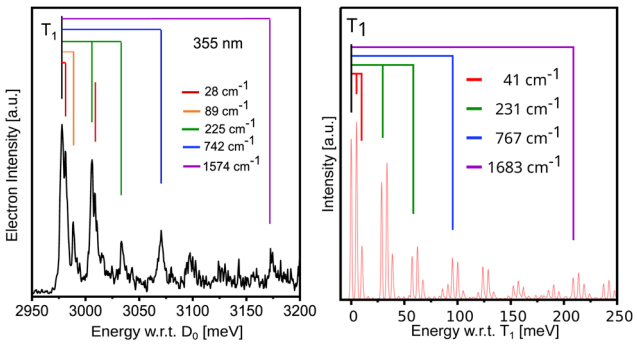

Fig. 13 Experimental (left side) and calculated (right side) spectra of the transition to the T_1 state of p3P.

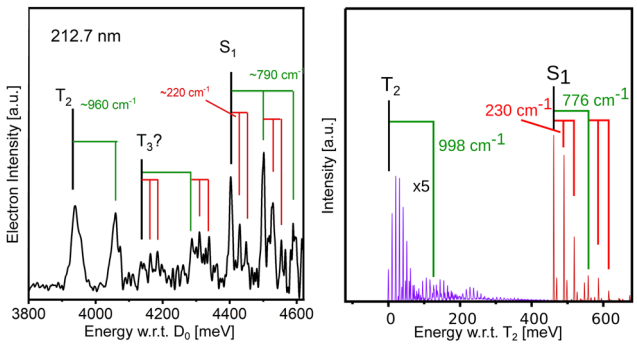

Fig. 14 Experimental (left side) and calculated (right side) spectra of the transitions to the T_2 and the S_1 states in p3P. Note that the T_3 state was omitted from the calculated spectrum because its origin position was not found. For further explanations see text.

correlation function. The small satellite peaks presumably arise from the excitation of a concertina-like stretching motion of the molecule along the C_2 symmetry axis with a frequency of 222 cm^{-1} in the computed spectrum (Fig. 14 right). The comb of peaks starting 998 cm^{-1} above the 0–0 transition in the theoretical spectrum possibly corresponds to the second peak in the experimental spectrum, but has a much too low intensity in comparison to the spectrum on the left side. Obviously, the harmonic force calculations do not properly describe the properties of the T_2 state in this energy range due to the conical intersection.

The agreement between the experimental and the theoretical S_1 spectra is very good. The first three peaks in the experimental S_1 spectrum (spacing about 220 cm^{-1}) nicely correspond to the first three intense peaks in the theoretical spectrum (spacing 230 cm^{-1}). Note that the anion ground state and the S_1 state are nearly planar. The repetition of this threefold structure shifted by 790 cm^{-1} to the blue (experimental value) is somewhat too weak in intensity in the theoretical spectrum (found at 776 cm^{-1} above the origin). It corresponds to an inter-ring C–C stretch vibration, which appears here as a result of the quinoidal reconstruction of the nuclear frame in the S_1 state. Interestingly, in the optical $S_0 \rightarrow S_1$ spectrum of Murakami *et al.*[7] the symmetric (62 cm^{-1}) and asymmetric (89 cm^{-1}) inter-ring torsion modes have been observed with long progressions. Both vibrations are not observed by us in the $D_0 \rightarrow S_1$ spectrum of Fig. 14 because the displacements in the torsional coordinates between the anion and the S_1 states are very small and the excitation of these modes hence does not gain much intensity.

The tentative assignment of the T_3 transitions needs a detailed explanation. Since the energy spacing between the two three-fold comb-like structures roughly fits in position and spacing in a series with the two strong peaks of T_2, one could argue that they correspond to T_2 and continue its peak progression. This explanation seems, however, implausible since the structures in T_2 and in the tentatively assigned T_3 are too different for this. Interestingly, the small spacings of their close-lying sub-structures are similar to the distances of the peaks corresponding to the low-energy vibration in S_1, only the intensities of the substructures are different. Note that also their spacings are such, that they seem to be part of a progression of the S_1 state. However, they cannot correspond to the transition to S_1, since the energy of the $S_0 \rightarrow S_1$ transition is accurately known from a gas phase experiment[7] and even then the FC-intensities would not fit. Even assuming a large inaccuracy in the determination of the S_0 origin of 50 meV or more would not bring the S_1 origin in the neighbourhood of the peaks attributed by us to T_3. Also hot bands can be excluded as explanation because (i) the other hot band transition we observe are usually weak in intensity and (ii) they should lie in the direct vicinity of the origin peak of S_1 and not hundreds of meV away. In conclusion we tentatively attribute them – on the basis of spectroscopic reasons alone – to the transitions to T_3. Indeed, according to theory (see Table 2), T_3 is expected to lie below the S_1 origin and even the T_4 transition is close-by. The Dyson intensity for the photodetachment to T_3 is considerably weaker (0.09) than for the transition to T_2 (0.21), which is in qualitative agreement with the small intensity of the observed complex structure above T_2 (see Fig. 14). The PD–PE spectrum of the T_4 state (Dyson norm 0.16) is presumably buried beneath the S_1 bands because the two states are near degenerate according to the calculations. Unfortunately, the identity of these tridental structures between T_2 and S_1 cannot be unambiguously clarified with the help of FC calculations, because T_3 undergoes a conical intersection with T_2 upon geometry optimisation and the true minimum of its potential energy surface could not be located. The strong vibronic coupling in the neighbourhood of the intersection impedes a meaningful computation of spectral envelopes in a static approach and would require a quantum dynamical treatment which is, however, far beyond the scope of this work.

3.3.2 *para*-Quaterphenyl (p4P). In the PD–PE overview spectrum of p4P in Fig. 2, there is at first glance considerably less peak activity in the energy range between T_1 and S_1 than in the spectrum of p3P. In the high-energetic range again the transitions to T_1 (neutral energy: 2478 $\pm$ 50 meV), T_2 (neutral energy: 3260 $\pm$ 50 meV) and S_1 (neutral energy: 3872 $\pm$ 50 meV) are observed. Only a small peak in front of S_1 might be due to the transition to T_3, an assignment which, however, needs further support by computational data.

In Table 3 the theoretical results are presented and compared to the experimental data. The calculated electron affinity is somewhat too high (703 meV, compared to $\sim$620 meV in the experiment), which is unexpected from a theoretical point of view, but has been observed for oligothiophenes[53] and other compounds[20] as well. The Dyson norm for the photodetachment of an electron from the singly occupied anion MO (LUMO in the nomenclature used here) has a value close to 1. The ratio of the Dyson intensities for the transitions to T_1 and to T_2 are about 2 : 1, in nice agreement with the spectrum recorded with 266 nm (not shown as a complete spectrum here). The transition to T_3 has a very low Dyson intensity of 0.12 (for comparison: the neighbouring transition to S_1 has a Dyson intensity of 0.44), which would qualitatively agree with the very small intensity of these peaks in the overview spectrum. The 0–0 transition energy of 3.55 eV, determined in the DFT/MRCI calculations, supports the tentative assignment of T_3 closely below S_1.

In p4P, the singlet-coupled HOMO–LUMO excitation forms the first excited singlet state. The computed oscillator strength f of its optical $S_0 \rightarrow S_1$ transition is 1.67 and thus has considerably increased in comparison to p3P (f = 1.15). The nodal structure of the MOs involved in the $S_0 \rightarrow S_1$ transition is similar in both molecules (cp. Fig. 5 and 8). HOMO and LUMO both exhibit b symmetry with regard to the $C_2(z)$ symmetry axis. Hence, the transition moment for the $S_0 \rightarrow S_1$ transition lies, as in p3P, parallel to the long axis. As in p3P, the oscillator strengths for the transitions to the multiconfigurational S_2 and S_3 states are close to zero.

On the left side of Fig. 15, the PD–PE spectra of the transition to S_0, recorded with the wavelengths 1064, 355 and

Table 3 Theoretical and experimental results for p4P: coefficients (absolute values) of leading MO configurations, calculated vertical transition energies $\Delta E_{vert.}$ at the S_0 geometry, calculated adiabatic transition energies $\Delta E_{adiab.}$ and ZPVE corrected transition energies ΔE_{0-0} with respect to S_0, experimental energies $\Delta E_{exp.}$ (this work only), oscillator strengths f, calculated vertical electron detachment energies $\Delta E_{det.}$ and Dyson intensities σ at the D_0 geometry. All energies in eV. In the first row of the table body, the experimental and the ZPVE corrected theoretical EAs are displayed. Experimentally not observed transitions are labelled as 'n.o.'

State		Configurations	$\Delta E_{vert.}$	$\Delta E_{adiab.}$	ΔE_{0-0}	$\Delta E_{exp.}$	f	$\Delta E_{det.}$ [b]	$\Delta E_{det.}$ [c]	σ
S_0	1^1A	0.96 $H^2(L)^0$		—	EA: 0.70 [b]	EA: 0.620	—	0.82	0.82	0.93
S_1	1^1B_1	0.94 $(H)^1(L)^1$	4.31	3.75	3.65	3.872	1.67	4.25	4.38	0.44
S_2	1^1B_2	0.66 $(H)^1(L+2)^1$ 0.41 $(H-2)^1(L)^1$ 0.35 $(H-4)^1(L)^1$	4.46	4.14	3.98	n.o.	0.00	5.06	4.79	0.15
S_3	1^1B_3	0.52 $(H)^1(L+3)^1$ 0.42 $(H-3)^1(L)^1$ 0.38 $(H-5)^1(L)^1$	4.49	[a]	[a]	n.o.	0.00	5.31	5.00	0.16
S_4	2^1A	0.66 $(H-1)^1(L)^1$ 0.43 $(H)^1(L+1)^1$	4.99	4.69	4.56	n.o.	0.00	5.15	5.17	0.23
T_1	1^3B_1	0.89 $(H)^1(L)^1$	3.20	2.63	2.51	2.478	—	3.24	3.31	0.41
T_2	1^3A	0.64 $(H-1)^1(L)^1$ 0.60 $(H)^1(L+1)^1$	3.54	3.24	3.13	3.260	—	4.03	3.95	0.21
T_3	2^3B_1	0.51 $(H-6)^1(L)^1$ 0.48 $(H-1)^1(L+1)^1$ 0.44 $(H)^1(L+6)^1$	3.94	3.86	3.55	3.771 (?)	—	4.74	4.62	0.12
T_4	1^3B_2	0.68 $(H)^1(L+2)^1$ 0.40 $(H-2)^1(L)^1$ 0.32 $(H-4)^1(L)^1$	4.19	3.94	3.79	n.o.	—	4.65	4.71	0.13

[a] No minimum was found in the calculations. At the converged structure still an imaginary frequency is present. [b] Computed at the (TD-)PBE0/TZVP level of theory. [c] DFT/MRCI energies at the D_0 geometry, shifted by the difference between the PBE0/TZVP and DFT/MRCI computed vertical detachment energy of the S_0 state.

266 nm, are presented. The fact that the spectrum recorded with 266 nm looks very similar in vibrational intensity to the spectrum recorded with 355 nm proves that the wavelength 1064 nm performs a resonant excitation of an anion-excited state which then decays *via* autodetachment. The p4P anion absorption spectrum of Shida in tetrahydrofuran[52] shows strong absorptions at 1220 nm and 1115 nm. Our detachment wavelength of 1064 nm then would be overlapping with Shida's second broad peak at 1115 nm. The 355 nm spectrum, displayed in Fig. 15 (left side), shows a strong first peak followed by two or more peaks with spacings of about 1475 cm^{-1}. The corresponding calculated FC spectrum is displayed in Fig. 15 (right side). It shows a dense peak structure with very small spacings of 88 cm^{-1} (inter-ring twist mode) which has a nearly Gaussian envelope. The width at half height of the envelope is about 100 meV and only slightly broader than the first peak in the experimental spectrum. A second comb of low-energetic vibrations shifted by about 1535 cm^{-1} follows. These are combination bands with a high-energetic vibration (experiment: 1475 cm^{-1}, collective inter-ring stretch mode). The broader envelopes of the two structures in the FC spectrum in comparison to the experiment are—as in p3P—presumably also due to the overestimation of the force constant of the twist potential.

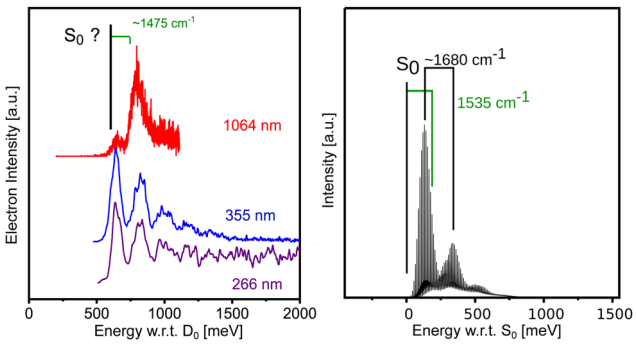

Fig. 15 p4P: experimental (left side, detachment wavelengths 1064 nm, 355 nm and 266 nm) and calculated (right side) spectra of the transition to the S_0 state.

In Fig. 16, two experimental spectra and one calculated FC spectrum of the transition to T_1 are displayed. If the theoretical spectrum would be broadened the two spectra would agree well in shape and relative energetic positions and only slightly differ in intensities. This is an example showing that typically the spectra recorded with high excitation energies are not or not much influenced by anion-excited states. The observed mode with a frequency of 170 cm^{-1} can be assigned to a global stretching mode (calculated frequency: 174 cm^{-1}). The next observed mode with 766 cm^{-1} can be assigned to a collective breathing mode with a calculated frequency of 787 cm^{-1}. The most displaced mode, an antisymmetric torsional mode with a frequency of 30 cm^{-1}, which appears as a progression with three strong and two smaller peaks in the calculated spectrum, is not identified in the experimental spectrum due to lack in energy resolution.

In Fig. 17, the experimental and theoretical FC spectra of the transition to the S_1 state are juxtaposed. The first observed mode has an energy of 160 cm^{-1} in the experimental spectrum (left side) and can be identified with the calculated symmetric collective stretching mode along the molecular axis (calculated frequency: 175 cm^{-1}). The weakly observed mode with a

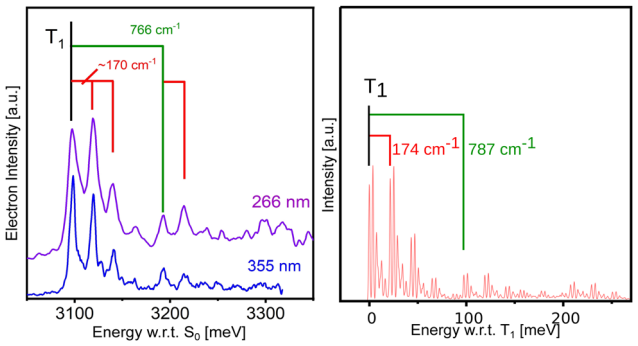

Fig. 16 Experimental spectra recorded with 355 nm and 266 nm (left side) and calculated (right side) FC spectra of the transition to the T_1 state in p4P. For discussion see text.

frequency of 766 cm^{-1} presumably corresponds to the mode with the calculated frequency of 795 cm^{-1}, which is a collective inter-ring breathing mode, at which especially the two inner phenyl rings participate. The intensity of the latter transition is presumably only so extremely small, because it may be affected by Wigner's threshold law.[23] This would mean that the calculated intensity of this transition is somewhat too small. The low-energetic torsion mode with a calculated energy of 78 cm^{-1} appears in the calculated spectrum as a very weak progression of 4 peaks. The transitions of this mode cannot be identified and assigned in the experimental spectrum. They presumably are buried in the background socket behind and between the strong transitions. Overall, for the transition to the S_1 the agreement between experiment and theory can be considered very good.

3.3.3 ***para*-Quinquephenyl (p5P).** Except for the very broad transition to the S_0, the appearance of the spectrum of p5P (Fig. 2) is very similar to that of p4P. The right side of the spectrum is rather simple to explain. The transitions to T_1 (neutral energy: 2340 ± 50 meV), T_2 (neutral energy: 3038 ± 50 meV) and S_1 (neutral energy: 3653 ± 50 meV) are observed. A very small additional structure in front of S_1 is found which could be tentatively assigned to T_3 because its energetic position is in agreement with the calculations. The ratio of the Dyson intensities of the transitions to T_3 and to S_1 are 0.13/0.44 = 0.29. This small value can explain why the intensity of the observed T_3 structure is so small (Table 4).

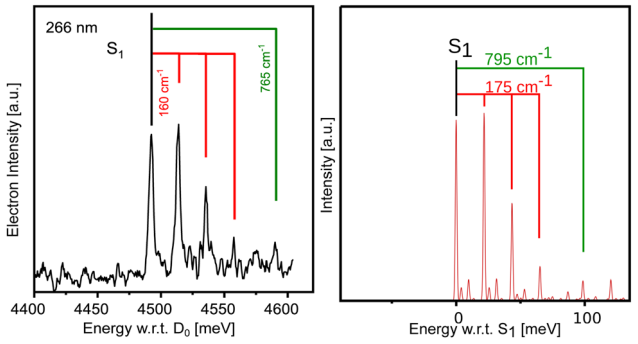

Fig. 17 p4P: experimental (left side) and calculated (right side) spectrum of the transition to S_1.

In Fig. 18 we present expanded experimental PD–PE spectra (detachment wavelengths 1064 nm (red), 532 nm (green) and 266 nm (violet)) of p5P. The vibrational peak patterns are very different. The strong rise of the second peak in the PD–PE spectrum recorded with 1064 nm and the many intense peaks in the spectrum recorded with 532 nm are obviously—similar as in p4P—due to resonant photoabsorptions channels for the detachment wavelengths 1064 nm and 532 nm in the anionic species of p5P. Unfortunately, no anion absorption spectrum exists for p5P. In the following, we tentatively take the first strong transition in the 266 nm spectrum as the S_0 origin (EA = 805 ± 50 meV).

The calculated transition spectrum to S_0 (Fig. 18) shows very dense combs of peaks with a spacing which corresponds to a symmetric twist mode (calculated energy: 90 cm^{-1}). The envelopes of these twist mode peaks reproduce roughly the structures of the first three peaks in the experimental spectrum recorded with 266 nm. As in p3P and p4P, also here the envelope in the theoretical spectrum is somewhat broader than the peak width in the 266 nm spectrum. The high-energetic spacing between the two comb of peaks in the experimental spectrum is about 1420 cm^{-1} which best agrees with a collective stretching mode (calculated energy: 1338 cm^{-1}).

In Fig. 19, the experimental spectrum of the transition to T_1 of p5P, recorded with 355 nm (left side), and the calculated FC spectrum (right side) are displayed. Note that the origin transition seems to be not the highest peak. Besides a comb of small peaks with a spacing of 40 cm^{-1} in the first part of the experimental spectrum at the blue side, some peaks with spacings of 85 cm^{-1} are observed. In addition, a vibration with an energy of about 742 cm^{-1} is present. A look at the FC simulation shows that a low-frequency mode of 55 cm^{-1} has the highest displacement and forms a comb of nine vibronic close-lying transitions. It should correspond to the observed peak spacing of about 40 cm^{-1} at the rise of the hump. If one takes the envelopes of the peaks in the calculated spectrum, it roughly fits the experimental features. The measured peak spacings of 85 cm^{-1} appearing on the blue side of the hump in the experimental spectrum remain unclear. The observed mode at about 742 cm^{-1} (measured between two well identified combination band peaks) is in an astonishing agreement with the calculated FC-active mode at 741 cm^{-1}. In conclusion, the calculated FC spectrum reasonably well agrees with the experimental spectrum.

One remaining question is, however, why in p5P—in contrast to the corresponding p3P and p4P spectra—the transition to T_1 is relatively broad. A resonant excitation to an anion-excited state with 355 nm seems not to apply here since the spectrum recorded with 266 nm (not shown here) is also broad. In Section 3.2 we had noticed for p5P that the inner three and the outer two torsional angles of equilibrium structures can differ considerably (Fig. 9). Indeed, in the T_1 state, the quinoidal structure appears to be confined to the three innermost phenyl rings, resulting in an almost co-planar orientation of the

Table 4 Theoretical and experimental results for p5P: coefficients (absolute values) of leading MO configurations, calculated vertical transition energies $\Delta E_{vert.}$ at the S_0 geometry, calculated adiabatic transition energies $\Delta E_{adiab.}$ and ZPVE corrected transition energies ΔE_{0-0} with respect to S_0, experimental energies $\Delta E_{exp.}$ (this work only), oscillator strengths f, calculated vertical electron detachment energies $\Delta E_{det.}$ and Dyson intensities σ at the D_0 geometry. All energies in eV. In the first row of the table body, the experimental and the ZPVE corrected theoretical EAs are displayed

State		Configurations	$\Delta E_{vert.}$	$\Delta E_{adiab.}$	ΔE_{0-0}	$\Delta E_{exp.}$	f	$\Delta E_{det.}{}^{a}$	$\Delta E_{det.}{}^{b}$	σ
S_0	1^1A_g	0.95 GS			EA: 0.88[b]	EA: 0.805[b]	—	0.99	0.99	0.93
S_1	1^1A_u	0.92 $(H)^1(L)^1$	4.13	3.59	3.49	3.69	2.17	4.26	4.41	0.44
T_1	1^3A_u	0.86 $(H)^1(L)^1$	3.10	2.56	2.40	2.38	—	3.37	3.43	0.39
T_2	1^3A_g	0.63 $(H-1)^1(L)^1$ 0.60 $(H)^1(L+1)^1$	3.33	3.02	2.94	3.07	—	3.97	3.91	0.20
T_3	2^3A_u	0.51 $(H-2)^1(L)^1$ 0.50 $(H-1)^1(L+1)^1$ 0.46 $(H)^1(L+5)^1$	3.70	3.58	3.41	3.60 (?)	—	4.57	4.45	0.13

[a] Computed at the (TD-)PBE0/TZVP level of theory. [b] DFT/MRCI energies at the D_0 geometry, shifted by the difference between the PBE0/TZVP and DFT/MRCI computed vertical detachment energy of the S_0 state.

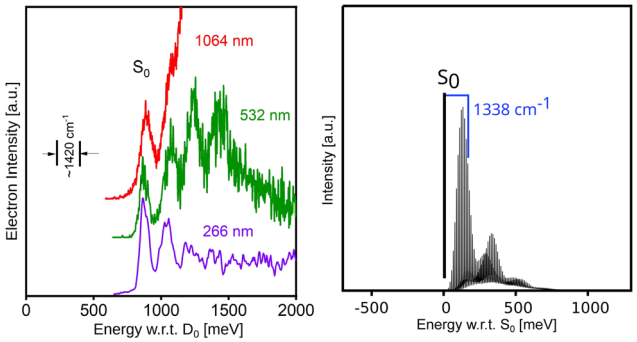

Fig. 18 p5P: experimental (left side) and calculated (right side) spectra of the transition to S_0. For discussion of the different intensities of the three experimental spectra, see text.

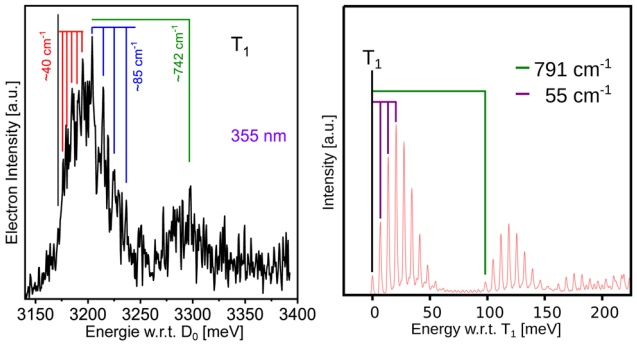

Fig. 19 p5P: experimental (left side) and calculated (right side) spectrum of the transition to T_1. For explanations see text.

rings (twist angles around 7°), whereas the outer two twist angles are considerably larger (about 24°). Interestingly, in the equilibrium geometry of the D_0 anion ground state the outer twist angles are almost the same as in T_1 (about 22°). However, the two inner twist angles in the anion ground state (about 17°) are much larger than in T_1. It is therefore not unlikely that, in addition to global stretch modes, also torsional modes are excited, as observed in the photodetachment spectrum of the T_1 state in p5P.

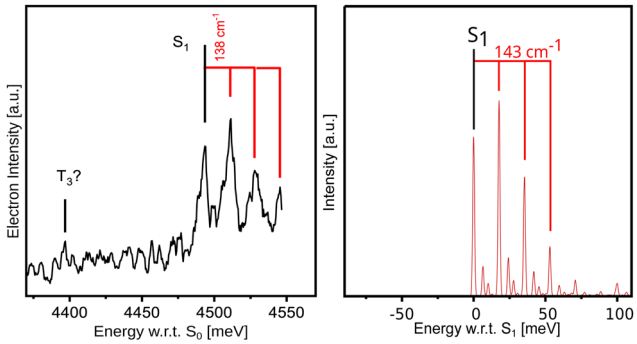

Fig. 20 p5P: experimental (left side) and calculated (right side) spectrum of the transition to S_1. For assignments see text.

In the S_1 state, the geometry difference with respect to the D_0 structure are less pronounced than in the T_1 state. In the sharp PD–PE spectrum of S_1 (Fig. 20) four quanta of a progression of a vibration with an energy of about 138 cm^{-1} are observed. Since the S_1 state lies very close to the detachment energy of the laser wavelength 266 nm, the intensities of the latter peaks may be affected by Wigner's threshold law[23] and may be smaller than given by the FC factors. The observed mode with an energy of 138 cm^{-1} agrees well with a global stretch mode calculated to have an energy of 143 cm^{-1}. Also the agreement between the intensities in the experimental and the calculated spectrum is very good.

4 Summary and conclusions

In this work, it was possible to record and assign PD–PE spectra of p3P, p4P and p5P. The experimental PD–PE spectra are partly vibrationally resolved and provide—in combination with calculated FC spectra—valuable information on the geometrical structures of the investigated ppPs in their lowest electronic states. No indications for spectral differences between the different possible rotamers in the ppPs have been found in the experimental spectra. The EA values, the oscillator strengths and the energetic positions of the electronic states follow the expectations for an increase in the π-conjugation

length. For most of the electronic states, the calculated energies and structures are qualitatively confirmed by the experimental results, thus strengthening the credibility of these theoretical data, which cannot be directly derived from the experimental data. For example, the calculations provide an understanding why in most of the electronic states bond length changes as well as twist angle changes occur. Surprisingly, for some electronic states in p4P and p5P these displacements are localised on the inner and for others on the outer parts of the molecules. Dyson norms have been evaluated at the DFT/MRCI level of theory to estimate the individual photodetachment probabilities, which are especially interesting for the assignments of the structures attributed to the T_2 states. For high kinetic energies of the photoelectron, the ratios of the Dyson norms compare well with measured photodetachment intensities, but the agreement is less satisfactory for slow photoelectrons due to Wigner's threshold law for photodetachment.[23] To include the latter effect in the model, the overlap between the wavefunction of the outgoing photoelectron and the ionisation continuum would have to be taken into account, which is, however, beyond the scope of this work.

The calculations show that the character of the optical $S_0 \rightarrow S_1$ transition is the same in all molecules: the electric dipole transition moment is parallel to the long molecular axis. The calculated oscillator strengths increase almost linearly with increasing molecular length: p3P: $f = 1.15$, p4P: $f = 1.67$ and p5P: $f = 2.17$ but are somewhat smaller than the values calculated from experimental data (p3P: $f_{exp} = 2.060$; p4P: $f_{exp} = 2.360$; p5P: $f_{exp} = 2.600$).[11] Interestingly, a saturation of f with the molecular length does not occur. The MOs involved in the $S_0 \rightarrow S_1$ transition are similar in shape in all investigated ppPs (compare Fig. 5, 8 and 11): the HOMO exhibits along the long axis $2n - 1$ nodal planes (aligned perpendicular to the long molecular axis), $n - 1$ of them cutting the inter-ring C–C bonds (n is here the number of phenyl rings in the molecule). The LUMO has exactly one additional node plane, thus shifting the pattern of double and single bonds by one unit along the C_2 symmetry axis. Both HOMO and LUMO orbitals have in each benzene unit essentially the same density and the same sign concerning the plane formed by the long molecular axis and the axis perpendicular to the benzene ring. This pattern complies with the $\Delta n = \pm 1$ preferences for electric dipole transitions in the quasi-one-dimensional particle-in-the-box model and explains the very high oscillator strengths. As our calculations show and the experiment tentatively confirms, in all investigated ppP molecules definitively two or even possibly three triplet states lie below S_1. Typically, in a molecule with such an electronic state energy scheme, one would expect high rates for intersystem crossing (ISC) transitions from the S_1 state to the triplet manifold. However, due to the absence of heteroatoms in the molecules, spin–orbit coupling between the excited states is obviously so small that ISC cannot compete against the rapid radiative deactivation on the nanosecond time scale. Our theoretical analysis thus supports the explanation given by Godard and de Witte[3] and by Nijegorodov *et al.*[11] that the S_1 lifetimes in ppPs are primarily determined by the high oscillator strengths of the $S_1 \rightarrow S_0$ transitions.

In a former paper, we investigated the size of the singlet–triplet splittings in azulene and found that the energy separation between singlet and triplet states of the same spatial MO configuration strongly depends on the overlap between the electron densities in the involved semi-occupied MOs.[19] In the investigated ppPs, S_1 and T_1 both originate from a HOMO–LUMO transition. Since the oscillator strengths of their S_1–S_0 transitions are very high—which is only possible if the HOMO–LUMO orbital densities strongly overlap[19]—their S_1–T_1 energy gap should be large. In addition, it is expected that the gap decreases in longer molecular chains where the two unpaired electrons are more and more efficiently able to avoid each other. Indeed, the experimentally observed S_1–T_1 splitting in the ppPs is large and – interestingly – decreases very slowly in this molecular series (1.43 eV (p3P) over 1.39 eV (p4P) to 1.31 eV (p5P)). The quantum chemical calculations predict much faster decreases of the 0–0 energy splittings (1.31 eV (p3P) over 1.14 eV (p4P) to 1.09 eV (p5P)). A similar trend results if the vertical S_1–T_1 DFT/MRCI energy differences at the respective ground state geometries are compared. Hence, a strong impact of the molecular geometry on the S_1–T_1 splitting can be excluded. The fact that the S_1–T_1 energy separation is increasingly underestimated as the chain length grows, rather points towards a more general problem of the applied quantum chemical methods. While the energetic positions of the T_1 0–0 transitions match the experimental values almost perfectly, the 0–0 energies of the S_1 states appear to be underestimated by about 0.1–0.2 eV. The number of samples (3 in this case) is, however, too small for a valid analysis. Forthcoming studies investigating the performance of the DFT/MRCI R2022 Hamiltonian[38] on excitation energies of other molecules with extended π-systems will have to prove whether the observed deviation is systematic or coincidental.

In this work, we could show that the twist angles between the phenyl moieties and the bond lengths of the inter-ring C–C bonds are correlated. While the anion ground state, as well as S_1 and T_1 of the neutral molecule are practically planar in p3P, the quinoidal structure in the S_1 and T_1 states of p5P is essentially confined to the innermost three phenyl rings. The twist angles between the terminal rings are considerably larger than those of the central rings in the S_1 and T_1 states of this compound. We interpret these findings in terms of competing forces: while in general the H–H repulsion between neighbouring phenyl units stays the same, the effect of an electron in an orbital with strong bonding contributions in the inter-ring C–C bonds (here LUMO) washes out, because in a large-sized molecule the electron density is distributed over more atoms and bonds, thus less affecting individual bonds.

If one lists the EA values of the ppPs, still no saturation effect with regard to the number of phenyl rings (n) is found: EA(p3P) = 380 ± 50 meV, EA(p4P) = 620 ± 50 meV and EA(p5P) = 805 ± 50 meV. Obviously, the increment, which has to be added to the EA if an additional phenyl ring is attached, decreases but the EA would still considerably increase for longer ppPs. Remembering that the ppP anions are nearly planar and that the neutral ppP molecules are twisted in the S_0 ground state,

such a high EA for long ppPs could provide an alternative explanation for the intereresting experimental findings of Yuan *et al.*[54] By AFM and STM methods, these authors observed twisted (benzoid) and planar (quinoid) structures in long ppPs on metal surfaces and proposed a proton tunneling mechanism for the observed benzoid-to-quinoid transitions. Having in mind the high EAs of longer ppP chains or segments, as proposed in our work, an alternative explanation suggests itself, namely, the involvement of a ''surface-to-molecule'' charge transfer (CT) state. In such a case, the charge separation takes place only over a very small distance d ($\approx$3.2 Å) so that the work function of the metal has to be reduced by the Coulomb integral from infinity to d,[55] totalling in a very low or even negative CT state energy with respect to the benzoid neutral ground state.

Conflicts of interest

There are no conflicts to declare.

Acknowledgements

The authors gratefully acknowledge financial support by the Deutsche Forschungsgemeinschaft (DFG, German Research Foundation) through MA 1051/20-1 and 396890929/GRK 2482.

References

1 K. Kato, *Jpn. J. Appl. Phys.*, 1972, **11**, 912–913.
2 G. A. Abakumov, V. V. Padeev, R. V. Khokhlov and A. P. Simonov, *Spectrosc. Lett.*, 1975, **8**, 651–667.
3 B. Godard and O. de Witte, *Opt. Commun.*, 1976, **19**, 325–328.
4 H. Bücher and W. Chow, *Appl. Phys.*, 1977, **13**, 267–269.
5 D. J. Schneider, D. A. Landis, P. A. Fleitz, J. M. Kauffman and R. N. Steppel, *Laser Chem.*, 1991, **11**, 49–62.
6 C. J. Seliskar, D. A. Landis, J. M. Kauffman, R. N. Aziz, M. A. Steppel, C. J. Kelly, Y. Qin and A. Chiorghis, *Laser Chem.*, 1993, **13**, 9–28.
7 J. Murakami, M. Okuyama and K. Ito, *Bull. Chem. Soc. Jpn.*, 1982, **55**, 3422–3423.
8 I. Baraldi and G. Ponterini, *THEOCHEM*, 1985, **122**, 287–298.
9 G. Heimel, M. Daghofer, J. Gierschner, E. J. W. List, A. C. Grimsdale, K. Müllen, D. Beljonne, J.-L. Brédas and E. Zojer, *J. Chem. Phys.*, 2005, **122**, 054501.
10 V. Lukeš, A. J. A. Aquino, H. Lischka and H.-F. Kauffmann, *J. Phys. Chem. B*, 2007, **111**, 7954–7962.
11 N. Nijegorodov, W. Downey and M. Danilov, *Spectrochim. Acta, Part A*, 2000, **56**, 783–793.
12 N. A. Borisevich, S. M. Kazakov, É. É. Kolesnik, A. V. Kukhto, A. I. Mit'kovets, D. V. Murtazaliev and O. V. Khristoforov, *J. Appl. Spectrosc.*, 2001, **68**, 447–454.
13 X. Cai, M. Sakamoto, M. Hara, S. Tojo, K. Kawai, M. Endo, M. Fujitsuka and T. Majima, *J. Phys. Chem. A*, 2004, **108**, 9361–9364.
14 P. G. Wendthold, J. Hu, R. R. Squires and W. C. Lineberger, *J. Am. Chem. Soc.*, 1996, **118**, 475–476.
15 T. R. Taylor, R. T. Bise, K. R. Asmis and D. M. Neumark, *Chem. Phys. Lett.*, 1999, **301**, 413–416.
16 R. Busani, M. Folkers and O. Cheshnovsky, *Phys. Rev. Lett.*, 1998, **81**, 3836–3839.
17 M. Kohno, S. Suzuki, H. Shiromaru and Y. Achiba, *J. Chem. Phys.*, 1999, **110**, 3781–3784.
18 J. Schiedt and R. Weinkauf, *Chem. Phys. Lett.*, 1997, **266**, 201–205.
19 S. Vosskötter, P. Konieczny, C. M. Marian and R. Weinkauf, *Phys. Chem. Chem. Phys.*, 2015, **17**, 23573–23581.
20 J. Meissner, B. Kosper, C. M. Marian and R. Weinkauf, *J. Phys. Chem. A*, 2021, **125**, 8777–8790.
21 T. Nakamura, N. Ando, Y. Matsumoto, S. Furuse, M. Mitsui and A. Nakajima, *Chem. Lett.*, 2006, **35**, 888–889.
22 G. R. Kinsel and M. V. Johnston, *Int. J. Mass Spectrom. Ion Processes*, 1989, **91**, 157–176.
23 E. P. Wigner, *Phys. Rev.*, 1948, 1002–1009.
24 J. Schiedt and R. Weinkauf, *J. Chem. Phys.*, 1999, 304–314.
25 C. R. Sagan, C. S. Anstöter, M. Thodika, S. Wilson and K. D. Matsika, *J. Phys. Chem. Lett.*, 2022, **13**, 10245–10252.
26 A. Jalehdoost and B. von Issendorff, *J. Chem. Phys.*, 2023, **158**, 194302.
27 L. G. Christophorou, J. G. Carter and A. A. Christodoulides, *Chem. Phys. Lett.*, 1969, **3**, 237–240.
28 E. Luc-Koenig, C. Morillon and J. Vergès, *Phys. Scr.*, 1975, **12**, 199–219.
29 D. Hanstorp and M. Gustafsson, *J. Phys. B: At. Mol. Opt. Phys.*, 1992, **25**, 1773–1783.
30 R. Peláez, C. Blondel, C. Delsart and C. Drag, *J. Phys. B: At., Mol. Opt. Phys.*, 2009, **42**, 125001.
31 M. J. Frisch, G. W. Trucks, H. B. Schlegel, G. E. Scuseria, M. A. Robb, J. R. Cheeseman, G. Scalmani, V. Barone, G. A. Petersson, H. Nakatsuji, X. Li, M. Caricato, A. V. Marenich, J. Bloino, B. G. Janesko, R. Gomperts, B. Mennucci, H. P. Hratchian, J. V. Ortiz, A. F. Izmaylov, J. L. Sonnenberg, D. Williams-Young, F. Ding, F. Lipparini, F. Egidi, J. Goings, B. Peng, A. Petrone, T. Henderson, D. Ranasinghe, V. G. Zakrzewski, J. Gao, N. Rega, G. Zheng, W. Liang, M. Hada, M. Ehara, K. Toyota, R. Fukuda, J. Hasegawa, M. Ishida, T. Nakajima, Y. Honda, O. Kitao, H. Nakai, T. Vreven, K. Throssell, J. A. Montgomery, Jr., J. E. Peralta, F. Ogliaro, M. J. Bearpark, J. J. Heyd, E. N. Brothers, K. N. Kudin, V. N. Staroverov, T. A. Keith, R. Kobayashi, J. Normand, K. Raghavachari, A. P. Rendell, J. C. Burant, S. S. Iyengar, J. Tomasi, M. Cossi, J. M. Millam, M. Klene, C. Adamo, R. Cammi, J. W. Ochterski, R. L. Martin, K. Morokuma, O. Farkas, J. B. Foresman and D. J. Fox, *Gaussian 16, Revision A.03*, Gaussian Inc., Wallingford CT, 2016.
32 J. P. Perdew, K. Burke and M. Ernzerhof, *Phys. Rev. Lett.*, 1996, **77**, 3865–3868.
33 C. Adamo and V. Barone, *J. Chem. Phys.*, 1999, **110**, 6158–6170.
34 E. Brémond, M. Savarese, C. Adamo and D. Jacquemin, *J. Chem. Theory Comput.*, 2018, **14**, 3715–3727.
35 A. Schäfer, H. Horn and R. Ahlrichs, *J. Chem. Phys.*, 1992, **97**, 2571–2577.

36 S. Grimme and M. Waletzke, *J. Chem. Phys.*, 1999, **111**, 5645–5655.
37 C. M. Marian, A. Heil and M. Kleinschmidt, *Wiley Interdiscip. Rev.: Comput. Mol. Sci.*, 2019, **9**, e1394.
38 D. Dombrowski, T. Schulz, M. Kleinschmidt and C. M. Marian, *J. Phys. Chem. A*, 2023, **1127**, 2011–2025.
39 C. Lee, W. Yang and R. G. Parr, *Phys. Rev. B: Condens. Matter Mater. Phys.*, 1988, **37**, 785–789.
40 A. D. Becke, *J. Chem. Phys.*, 1993, **98**, 1372–1377.
41 TURBOMOLE V7.5.1 2021, a development of University of Karlsruhe and Forschungszentrum Karlsruhe GmbH, 1989-2007, TURBOMOLE GmbH, since 2007; available from **https://www.turbomole.com**.
42 F. Weigend, M. Häser, H. Patzelt and R. Ahlrichs, *Chem. Phys. Lett.*, 1998, **294**, 143–152.
43 M. Etinski, J. Tatchen and C. M. Marian, *J. Chem. Phys.*, 2011, **134**, 154105.
44 M. Etinski, J. Tatchen and C. M. Marian, *Phys. Chem. Chem. Phys.*, 2014, **16**, 4740–4751.
45 M. Spanner, S. Patchkovskii, C. Zhou, S. Matsika, M. Kotur and T. C. Weinacht, *Phys. Rev. A: At., Mol., Opt. Phys.*, 2012, **86**, 053406.
46 W. Arbelo-González, R. Crespo-Otero and M. Barbatti, *J. Chem. Theory Comput.*, 2016, **12**, 5037–5049.
47 M. L. Vidal, A. I. Krylov and S. Coriani, *Phys. Chem. Chem. Phys.*, 2020, **22**, 2693–2703.
48 B. N. C. Tenorio, A. Ponzi, S. Coriani and P. Decleva, *Molecules*, 2022, **27**, 1203.
49 E. Morikawa and M. Kotani, *Z. Naturforsch.*, 1980, **35a**, 823–827.
50 C. M. Marian and N. Gilka, *J. Chem. Theory Comput.*, 2008, **4**, 1501–1515.
51 E. Artacho, M. Rohlfing, M. Côté, P. D. Haynes, R. J. Needs and C. Molteni, *Phys. Rev. Lett.*, 2004, **93**, 116401.
52 T. Shida, *Phys. Sci. Data*, 1988, **34**, 1–308.
53 R. Weinkauf, L. Lehr, E. W. Schlag, S. Salzmann and C. M. Marian, *Phys. Chem. Chem. Phys.*, 2008, **10**, 393–404.
54 B. Yuan, C. Li, Y. Zhao, O. Gröning, X. Zhou, P. Zhang, D. Guan, Y. Li, H. Zheng, C. Liu, Y. Mai, P. Liu, W. Ji, J. Jia and S. Wang, *J. Am. Chem. Soc.*, 2020, **142**, 10034–10041.
55 R. Weinkauf and J. Schiedt, *Photochem. Photobiol.*, 1997, **66**, 569–575.

An important detail is the MO basis chosen for the Dyson orbitals and consequently their norms. The current implementation enforces the used MOs for the anionic parent and neutral child wave functions to be identical. Consequently, orbital relaxation effects are fully neglected. This greatly simplifies the calculation of certain terms in the computations of excitation-energy transfer rates in the monomer transition density combined with transfer integral (MTD-TI) method[187]. As this approach invokes charge-transfer states between donor and acceptor molecules, it is necessary that the used method is able to describe the ionization of the donor and the acceptor appropriately. Accordingly, the applied method must be able to give reasonable estimates of the VDEs and vertical attachment energies. The PD-PES data is obviously very well suited to evaluate the capability of DFT/MRCI to describe EAs and VDEs. Fig. 5.3 shows a sketch of the different quantities and how they are computed. The calculated VDEs using the same MO basis for the anionic parent and the neutral

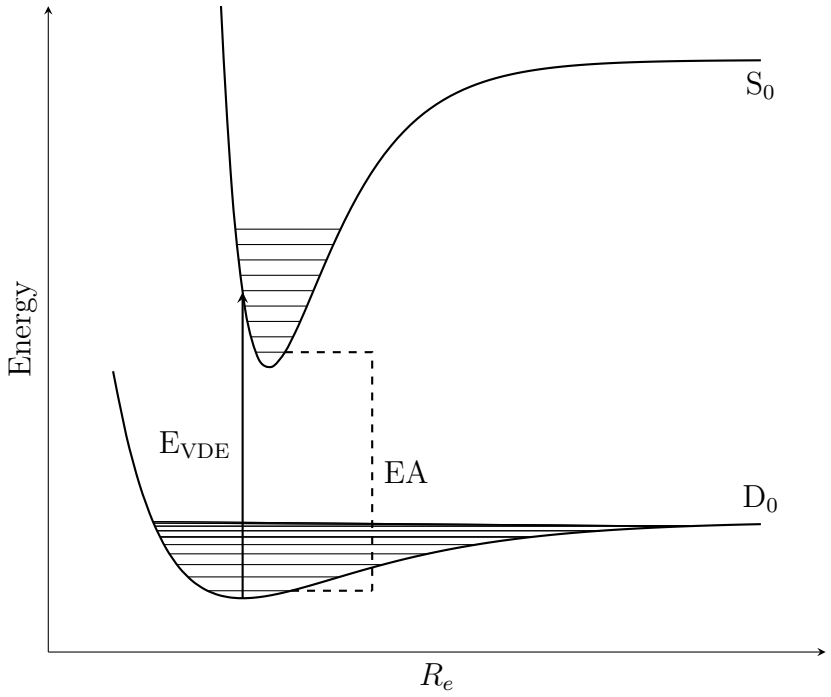

Figure 5.3: Sketch of the PESs for the anionic parent species, D_0, and a neutral child ground state, S_0. Here it is assumed that the parent is lower in energy than the child, which is necessary to conduct PD-PES. Solid horizontal lines depict possible vibrational levels.

child species, differ by up to 0.8 eV from the experiment, as can be seen from Tab. 5.1. This implies missing contributions, possibly due to geometrical or orbital relaxation energies. Using restricted open-shell Kohn-Sham (ROKS)-MOs[188] as basis states

for the DFT/MRCI calculations on the anion, thereby including orbital relaxation effects, gave results close to the experimental EAs. This suggests that orbital relaxation effects cannot be well accounted for by the DFT/MRCI expansion alone, considering that the geometrical relaxation is of the order of 0.15 eV (cf. Tab. 5.1) and therefore cannot explain the large deviation. The ROKS basis was generated using the `Dalton` program[189][190] employing the same basis set and functional as in KS computations[P3]. `Dalton` is interfaced[142] to the `mrci` code to enable calculations using an anchor configuration with a single open-shell. The differing results using ROKS-MOs illustrate the importance of the one-particle basis for the DFT/MRCI calculation. Though, the closer resemblance does not appear to be attributable to the DFT/M-

Table 5.1: Computed VDEs and EAs for *para*-ter- (n=1), -quater- (n=2) and -quinque-phenyl (n=3). Columns labelled ROKS were obtained using relaxed MO bases. Others were calculated in the basis of the neutral child species. Values superscripted with $S_0 - D_0$ denote adiabatic energies. The calculated zero-point vibrational energy (ZPVE) differences E_{ZPVE} used to calculate the EAs are given. E_{DFT} labels the VDE computed as the difference of the anionic ROKS- and the neutral childs' KS-ground state energy. Experimental values[P3] $E_{exp.}$ recorded with PD-PES are given in the last column. For comparison the LUMO energy of the employed MO basis in the MRCI computed at the KS and ROKS level of theory are also given. All values in eV.

n=	ϵ	ϵ^{ROKS}	E_{MRCI}	E_{MRCI}^{ROKS}	E_{DFT}	$E_{MRCI}^{S_0-D_0}$	$E_{ZPVE}^{S_0-D_0}$	EA	$E_{exp.}$
1	-0.87	1.79	0.031	0.183	0.177	-0.090	0.139	0.049	0.380
2	-1.02	1.32	0.053	0.457	0.418	0.197	0.129	0.326	0.620
3	-1.10	1.02	0.072	0.634	0.553	0.391	0.123	0.515	0.805

RCI method in the first place. Consideration of column E_{DFT} in Tab. 5.1, clearly shows that the large shift is already present on the DFT level. DFT/MRCI corrects this energy only marginally. The energies of the LUMOs in the KS basis generated with the BH-LYP functional are given in Tab. 5.1 as well. In HF theory this value would correspond to the first electron affinity of the neutral child species. However, as pointed out in Sec. 2.4.2, this represents only a crude approximation and lacks physical meaning in the KS framework. Apparently, the KS-LUMO energies in the neutral case, show a severe overbinding. This is rooted in the exchange-correlation hole present in KS theory as outlined in Sec. 2.4.2. In contrast, the ROKS orbitals produce a non-bound LUMO, albeit too high in energy if used in a Koopman's-like argument. Interestingly, both methods produce a similar trend. The LUMO becomes

more strongly bound with increasing system size, which is in accordance with experiment. Inclusion of ZPVE corrections has a large influence on the EA in these systems. Often the structures of the anionic parent and the neutral child are quite similar, allowing to neglect such corrections[191]. Clearly this is not the case here, as the order of the correction is around 0.13 eV in all systems. This is in agreement with the value given by Rienstra-Kiracofe et al.[191] for condensed polycyclic aromatic hydrocarbons. The error in the EAs computed with DFT/MRCI is found to be ≈0.3 eV for these systems, which is acceptable. Most importantly, the experimental trend is accurately reproduced. To gain further insight, An and An-derivatives, whose skeletal structures are shown in Fig. 5.4, were studied.

5.2 Anthracene Derivatives

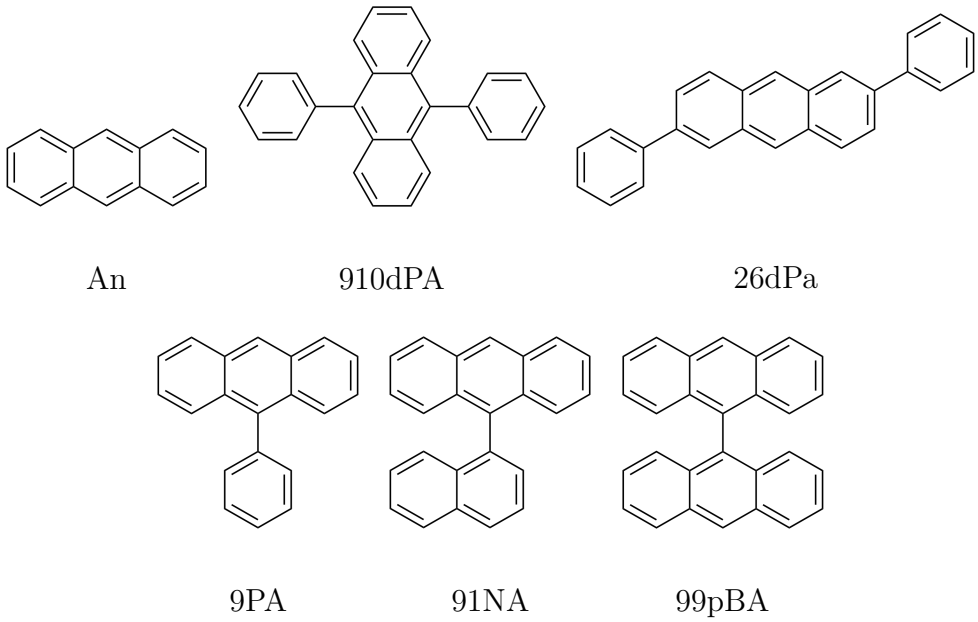

Figure 5.4: Skeletal structures anthracene An and its investigated derivatives.

Anthracene (An) is a very well characterized polycyclic aromatic hydrocarbon for which a lot of literature data is available[192–196]. This is due to its broad range of possible applications, easy availability and toxicity[197]. Furthermore, An, has been highly functionalized with various substituents to tune its photo- [198–200] and electronic[201] properties. Here, the influence of different aryl-substitution patterns on the An core is investigated. Similar to the studies presented in the last section,

PD-PES data was backed with computations on the DFT/MRCI level of theory. One might expect different influences of the core substitution with either one or two aryl-substituents. The direct participation of the residue's π-system in the π-system of the An-core, effectively increasing the electronic delocalization in the system, would lead to a large shift of the electronic energies with respect to the non-substituted An. On the other hand, assuming little participation of the substituents is reasonable as well, as they are expected to be (almost) orthogonal to the An-core. This is caused by the steric strain induced by the repulsion of the residues' hydrogens and the core hydrogens in the positions adjacent to the bridge carbon atom. Therefore, the possible influence to static or dynamic polarizability effects of the substituents would be limited. Accordingly, the energetic shifts with respect to bare An would be small. Obviously, these two effects can act complementary as well. One question to address is how these two possibilities influence the electronic states in the investigated systems by direct comparison with the measured energetic shifts recorded by PD-PES. To do so the interpretation of experimental data is combined with a thorough discussion of optimized geometries and simulated electronic, as well as Franck-Condon (FC) spectra. However, most of these results will be presented elsewhere[202]. Another question to be addressed, and for which the PD-PES method is particularly well suited, is the influence of substitution patterns on the EA. A substituent's impact on the anion is expected to be larger than in the neutral molecule. An aryl-substituent may overtake a fraction of the surplus charge by rearranging its electronic system, effectively carrying a partial charge. This shift should become larger with increasing number and/or size of the aryl substituent. Larger residues (phenyl $\rightarrow$ naphthyl $\rightarrow$ anthryl) correspond to the alignment of orbital energies of the latter to those of the An-core. In the case of 99pBA one might imagine an energetically favourable charge-resonance effect by delocalisation of the surplus electron over two equal subunits, in the spirit of cationic arene dimers[203–205]. Especially, since 99pBA serves as a model system for symmetry-breaking charge-transfer[206]. Clearly, the EA of 99pBA would be considerably increased with respect to An if such a stabilization would occur. All the investigated An-derivatives have potential applications as organic semiconductors[207], optically active materials[208] or triplet up-converters[209–212]. Therefore, it is of great interest to better understand their energetic landscape. Geometry optimizations and frequency analyses of the anionic and neutral molecular states were performed with a similar setup as for the *oligo-para*-phenylenes. PBE0[213–216] was used as approximate exchange-correlation functional. The basis set was chosen to

be of TZVP[159] quality. Electronic excitation energies and molecular properties at the optimized geometries were calculated with the DFT/MRCI method employing the standard parametrization of the new model hamiltonian[P1]. Dyson orbitals were generated as described in publication [P3]. FC spectra were calculated using the `VIBES` program[217, 218]. As large parts of the discussions in the following subsections will relate to the electronic situation in bare An a short discussion of the latter will be given. PD-PES data of An were recorded by Schiedt and Weinkauf [194] and Konieczny [180]. The latter is shown in Fig. 5.5a. For details of the experimental setup and used detachment wavelengths see the thesis of Konieczny [180]. The EA of An was determined to be 530 meV in various experiments[194, 219, 220], making it the smallest polyacene with a stable anionic valence state[221]. The PD-PES measurements[180] confirmed this value, as can be seen in Fig. 5.5a. From the same figure a pronounced vibrational progression in the S_0 peak is evident. The signal consists of a well resolved peak triplet with a spacing of $\approx$400 cm^{-1}[192, 194, 219] and a second structure $\approx$1410 cm^{-1} above the peak origin. FC simulations reproduce the main spectral features well, as can be seen from the overview spectrum shown in Fig. 5.5b and the close-up of the $D_0 \rightarrow S_0$ transition shown in Fig. 5.6. Dominant normal modes contributing to the vibronic pattern of the $D_0 \rightarrow S_0$ transition are shown in Fig. 5.7. A concertina-like mode of the An core and a C–C stretch mode show the greatest displacements in the Duschinsky-transformation. Detailed discussions on the vibronic signatures, energetic landscape and characterization of all investigated molecules and states can be found elsewhere[202]. Here only an overview will be given. The signals recorded at 3443 meV and two triplet states below it at 1869 meV and 3286 meV are assigned to the S_1-, T_1- and T_2-states, respectively. Investigating Fig. 5.5b reveals that this is in full agreement with the computations. A signal right above 4000 meV found in the experimental spectrum can be assigned to the T_4 state, based on the calculations. It is constructed from the positive linear combination of the T_h^{l+1} and T_{h-1}^{l} configurations making it the counterpart of T_3, which is built as the negative linear combination. T_2 is of B_{1g} symmetry and a linear combination of T_{h-2}^{l} and T_h^{l+2} making it the triplet counterpart of the energetically much higher S_4 state. Unfortunately, the T_3 state of An could not be optimized with the chosen setup. During the optimization the T_3 and T_2 PES cross, hampering finding a minimum of the former. It was possible to obtain a geometry for T_3 using the CAM-B3LYP[130–132, 222, 223] functional, however details are discussed elsewhere[202].

Judging from the transition densities of the lowest singlet transitions, shown in

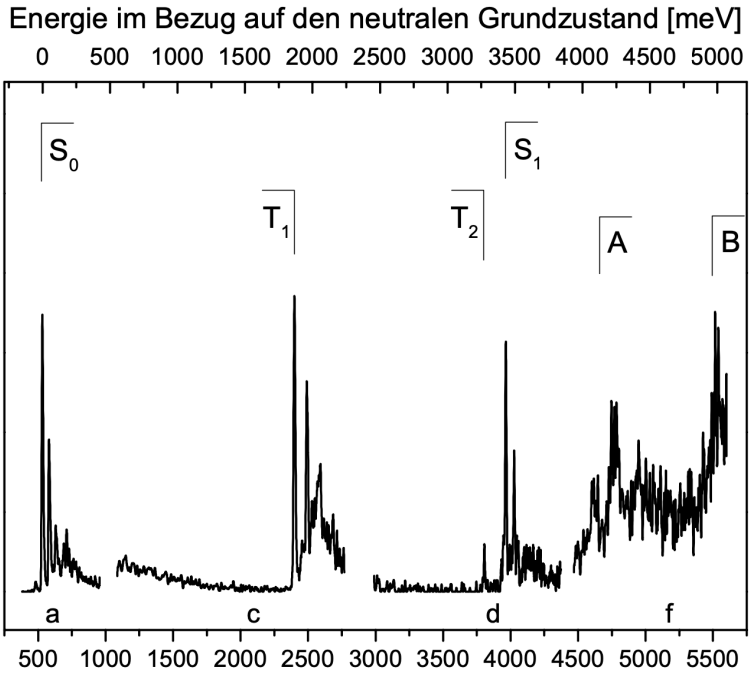

(a) PD-PES on An. Note that the spectrum is composed of different sub-spectra, using varying detachment wavelengths. Copied from the thesis of Konieczny [180].

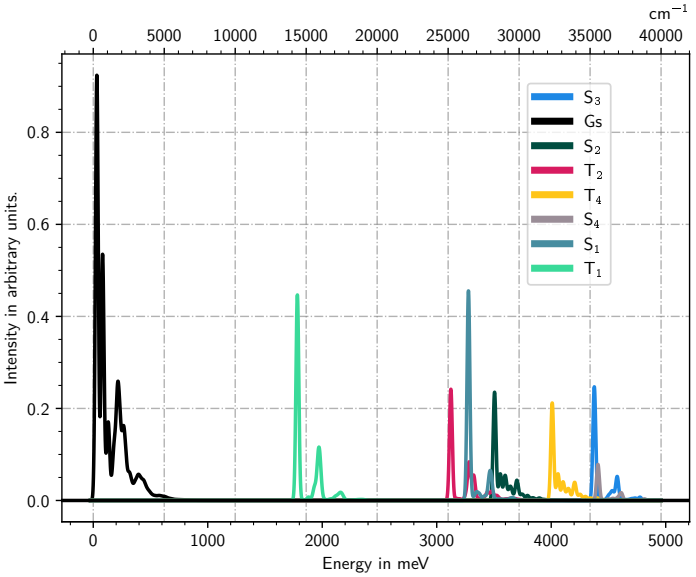

(b) Simulated FC spectrum of An with respect to the D_0 geometry.

Figure 5.5: Comparison of the spectrum recorded with PD-PES and the simulated FC spectrum.

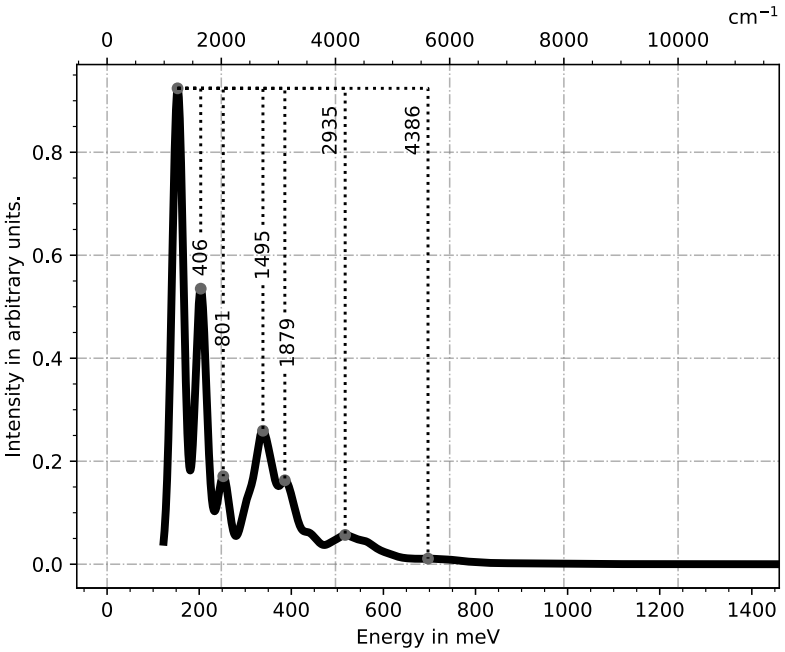

Figure 5.6: Simulated FC spectrum of the $D_0 \rightarrow S_0$ of An. Peaks are annotated with their distance in wave numbers from the highest maximum.

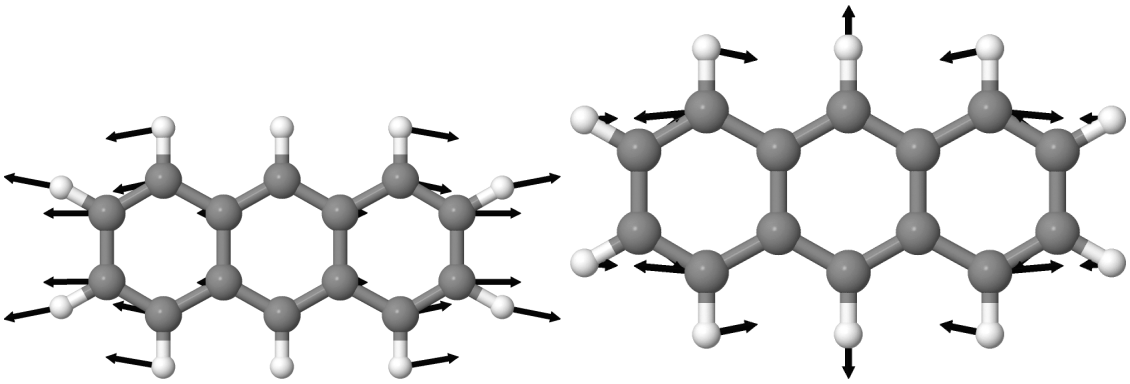

(a) Mode number 8 with a frequency of $403\,\mathrm{cm}^{-1}$ and a displacement of 1.07.

(b) Mode number 48 with a frequency of $1462\,\mathrm{cm}^{-1}$ and a displacement of -0.65.

Figure 5.7: Dominant modes contributing to the FC spectrum of Fig. 5.6. Energies are given at the ground state geometry.

Fig. 5.8, it ought to be expected that the largest influence on the $S_0 \rightarrow S_1$ transition, dominated almost exclusively by a S_h^l configuration, is exerted by the substitutions in positions nine and ten. In contrast, the long-axis $S_0 \rightarrow S_2$ transition, shown in Fig. 5.8b, will be stronger influenced on substitution in positions two and six. Tabulating oscillator strengths $f_{abs.}$ and transition dipole vectors $\vec{\mu}$ (Tab. 5.2) for the molecules in question provides evidence to support this assertion. The dipole transition moment

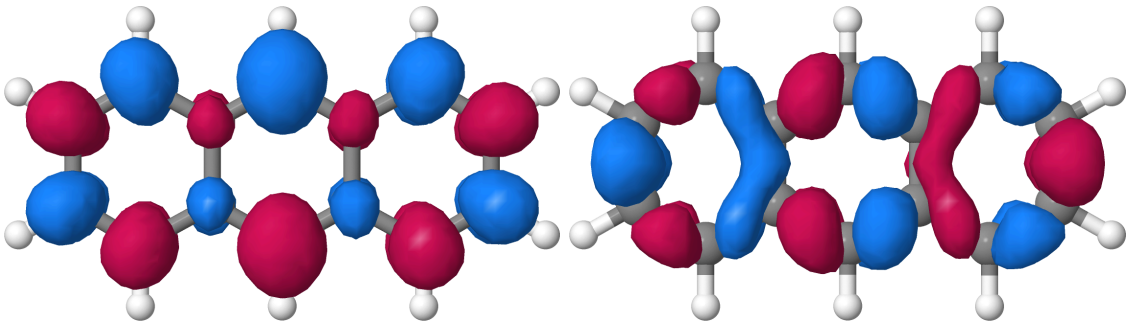

(a) $S_0 \rightarrow S_1$ (b) $S_0 \rightarrow S_2$

Figure 5.8: DFT/MRCI transition densities plotted with an *iso*-value of 0.0004 of a the short axis transition and b the long axis transition from the ground state of anthracene. Red are positive, blue negative values of the transition density.

Table 5.2: Vertical excitation energies in eV, as well as transition dipole vector $\vec{\mu}$ components and oscillator strength $f_{abs.}$ for the $S_0 \rightarrow S_m$ of investigated molecules at their respective ground state geometry. μ_l, μ_s and $\mu_\perp$ denote the long-, short- and perpendicular axes w.r.t. the An-core. Values are given in bohr.

Molecule	$\Delta E_{S_0}^{vert.}$	μ_l	μ_s	$\mu_\perp$	f_{abs}
An	3.570	0.000	1.210	0.000	0.129
9PA	3.510	0.000	1.470	0.000	0.186
91NA	3.510	0.000	1.510	-0.280	0.202
99pBA	3.430	0.000	2.080	0.000	0.364
910dPA	3.440	0.000	1.760	0.000	0.261
26dPa	3.360	1.210	0.680	0.020	0.160

increases systematically on extension of the short axis of the An core and is barely influenced by the phenyl substitution in the two and six positions. Here, the vector component along the long axis acquires a significant magnitude. Consequently, the transition dipole moment vector is tilted away from the short axis, as can be seen from Fig. 5.10, only resulting in a negligible enhancement of the oscillator strength. The increased influence of the long axis is clearly visible in the strong red-shift of the energy, as well. Comparing to a particle-in-a-box model fits the observed energetic shift very well. The substitution in positions two and six causes the largest increase in box length, accompanied by an increased delocalization of the one-particle wave functions, compared to the nine/ten substitution. On substitution of the hydrogen in position nine with 1-naphthyl the transition dipole acquires a component along the perpendic-

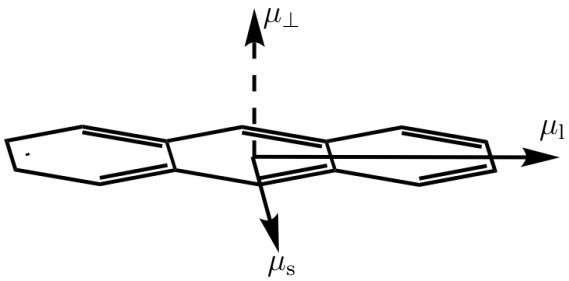

Figure 5.9: Used axis system in the characterization of the transition vectors.

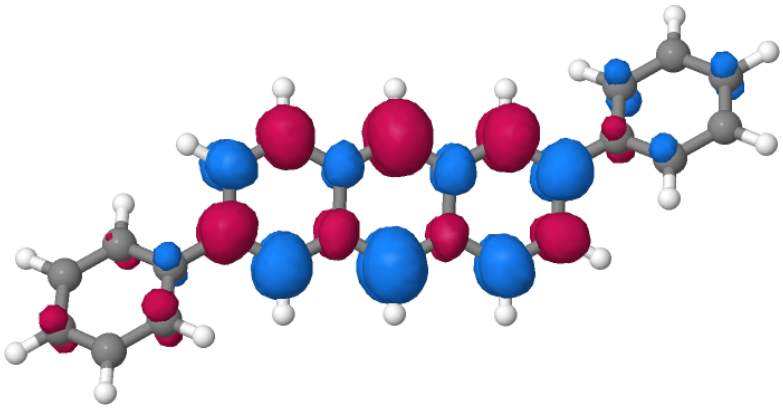

Figure 5.10: DFT/MRCI transition density of the vertical $S_0 \rightarrow S_1$ transition in 26dPa plotted with an *iso*-value of 0.001. Red are positive, blue negative values of the transition density.

ular axis of the An-core. However, it is not evident at first sight why this is the case. Judging from the transition density plotted in Fig. 5.11a the main contributions are directed along the short axis, explaining the increased oscillator strength. The perpendicular component $\mu_\perp$coincidences with the long axis of the naphthyl substituent. It is generally accepted that the lowest transition of naphthalene is polarized along this axis[224][225]. Consequently, it is reasonable to interpret the occurrence of the perpendicular component as a combination of the long-axis transition of naphthalene and the short-axis transition of anthracene. Plotting with a smaller *iso*-value supports this interpretation as the component along the long axis of the naphthyl substituent becomes clearly visible. 91NA provides an interesting example how the transition moments of the monomers influence each other when combined. A behaviour, which is mostly discussed in the context of non-covalently linked molecular aggregates[226–228]. In particular, the behaviour of 99pBA is analogous to that of a J-aggregate when the bond axis is considered to be the aggregation axis. The short axes of the two An fragments and the aggregation axis are congruent and the respective transition dipole

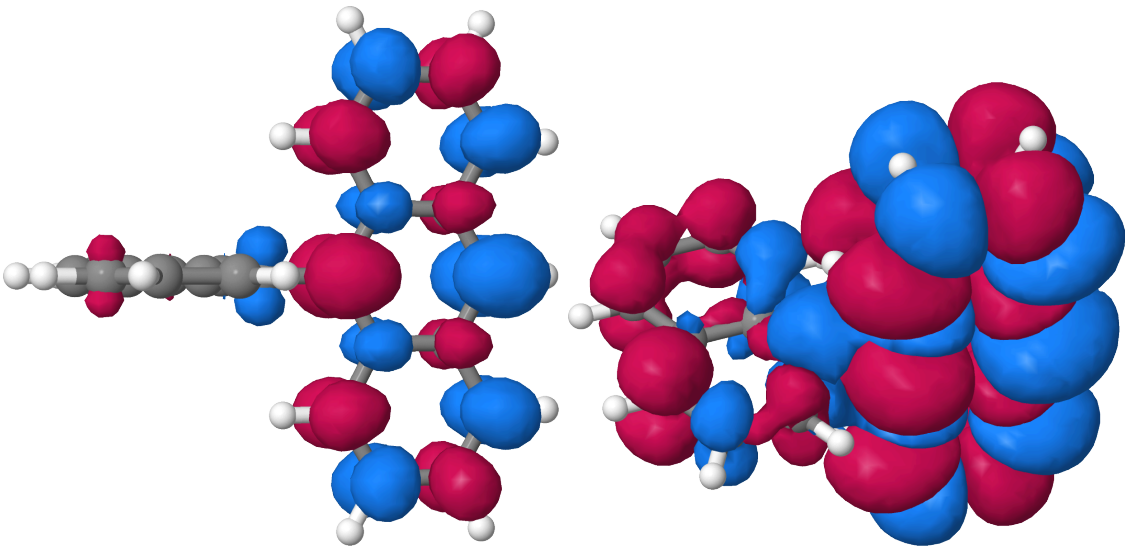

(a) $S_0 \rightarrow S_1$ transition. (b) $S_0 \rightarrow S_1$ transition.

Figure 5.11: DFT/MRCI transition densities of the lowest singlet transition of 91NA. Fig. (a) was plotted with an *iso*-value of 0.001, while a value of 0.0001 was used to generate Fig. (b). Red are positive, blue negative values of the transition density.

moments are in a head-to-tail arrangement, as can be seen from Fig. 5.12a. Consequently, the oscillator strength is enhanced. Accordingly, the transition dipoles of the $S_0 \rightarrow S_2$ transition, whose associated density is shown in Fig. 5.12b, are in the tail-to-tail arrangement, leading to a completely dark state. Another interesting observation can be made characterizing the orthogonality of the An-core and its substituents using the torsional angles sketched in Figs. 5.13 and 5.15, respectively. Bar plots of the measured dihedral angles for different optimized geometries of the investigated molecules are given in Figs. 5.14 and 5.16. Investigating the dihedral angles found in the optimized S_1 and D_0 geometries shows similar values. The commonality between the two states can be found in the character of the leading configurations in the CI vectors of the states. In all investigated molecules the eigenvector of the S_1 is dominated by a singlet CSF built from a S_h^l configuration. It can be concluded that the main electronic influence on the S_1 and D_0 geometries is the occupation of the LUMO. The depletion hole present in the HOMO in the S_1 state does not seem to have a large influence. However, as the values deviate slightly more from orthogonality as in the D_0 geometry, it is reasonable to assume a partial localization of the hole on the substituent or the An-core pulls the substituent more into the plane of the An-core, due to charge attraction. Analysing the particle-hole densities, as de-

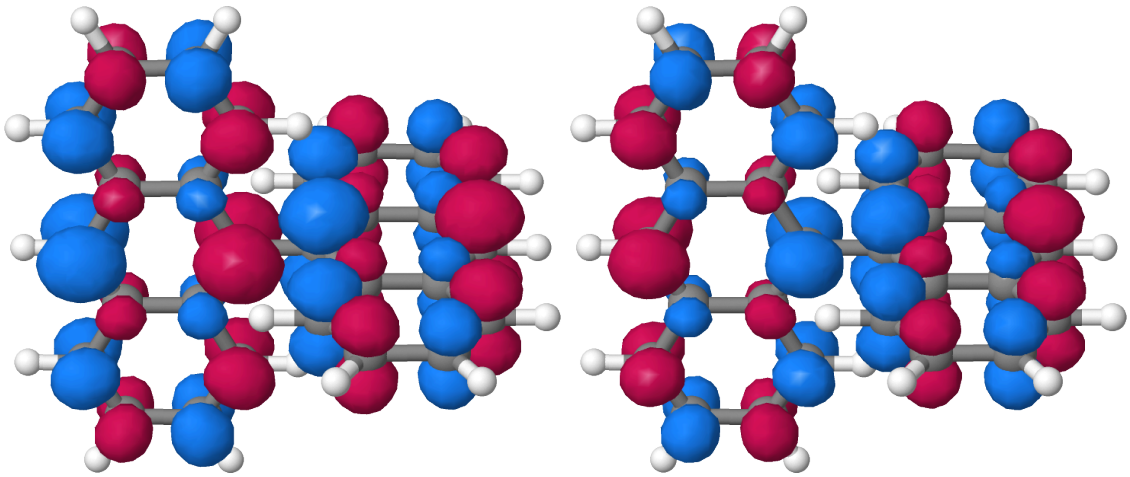

(a) Head-to-tail arrangement of the $\vec{\mu}$ in the $S_0 \rightarrow S_1$ transition.

(b) Tail-to-tail arrangement of $\vec{\mu}$ in the $S_0 \rightarrow S_2$ transition.

Figure 5.12: DFT/MRCI transition densities plotted with an *iso*-value of 0.001 of two lowest singlet transition of 99pBA at the ground state geometry. Red are positive, blue negative values of the transition density.

Table 5.3: Particle e^- and hole h^+ populations for the substituent (subscript *sub*) and the An-core (no subscript) computed from the DFT/MRCI densities at the S_1 geometry of the respective An-derivative.

Molecule	h^+_{sub}	e^-_{sub}	h^+	e^-
99pBA	0.390	0.195	0.501	0.697
91NA	0.063	0.036	0.847	0.874
9PA	0.052	0.035	0.857	0.875

scribed in Sec. 5.3 reveals that the proportion of the hole density on the substituent is indeed slightly larger than the particle density. The particle-hole populations for 9PA, 91NA and 99pBA are shown in Tab. 5.3 Apparently, the stronger tilt into the plane of the An-core can be explained by the excess hole-charge on the substituent. Though, the main excitation obviously takes place on the An-core. Although, 26dPa shows a different behaviour in the vertical excitation energies than the other derivatives it follows the same geometrical trend with respect to the similarity of the D_0 and S_1 PES minima, as can be seen from Fig. 5.16. Furthermore, the tendency of the two phenyl substituents to tilt into the plane of the An-core, thereby increasing the degree of conjugation, is clearly visible. This lowers the energy and fits the aforementioned particle-in-a-box-like behaviour. As 26dPa has the lowest-lying S_1 state (c.f. Tab. 5.2), a stabilization of the D_0 state ought to be expected, if the S_1/D_0 analogy

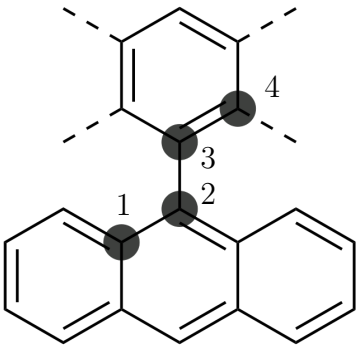

Figure 5.13: Generic structure of the mono-substituted anthracene derivatives. Building atoms used to measure the torsional angles are marked with dots and annotated.

holds. Both, experiment and computation confirm the expected highest EA out of all investigated An-derivatives, as can be seen from Tab. 5.4. Similar to the *oligo-para-*

Table 5.4: Computed VDEs and EAs for all investigated An-derivatives and An. Values in columns labelled ROKS were obtained using relaxed MO bases. Others were calculated in the basis of the neutral child species. Values superscripted with $S_0 - D_0$ denote adiabatic energies. The calculated ZPVE differences E_{ZPVE} used to calculate the EAs are given. E_{DFT} labels the VDE computed as the difference of the anionic ROKS- and the neutral child's KS-ground state energy. Experimental values[179][180] E_{exp} recorded with PD-PES are given in the last column. All values in eV.

Molecule	E_{MRCI}	E_{MRCI}^{ROKS}	E_{DFT}^{ROKS}	$E_{MRCI}^{S_0-D_0}$	$E_{DFT}^{S_0-D_0}$	$E_{ZPVE}^{S_0-D_0}$	EA_{MRCI}	$E_{exp.}$
An	-0.037	0.269	0.310	0.164	0.136	0.153	0.318	0.530
9PA	-0.029	0.420	0.451	0.275	0.239	0.144	0.418	0.576
91NA	-0.080	0.455	0.497	0.308	0.288	0.147	0.454	0.652
99pBA	0.384	0.523	0.516	0.416	0.346	0.145	0.561	0.728
910dPA	-0.052	0.533	0.565	0.368	0.328	0.125	0.493	0.750
26dPa	0.018	0.693	0.706	0.556	0.508	0.131	0.687	0.884

phenylenes (cf. Tab. 5.1) it is found that DFT/MRCI does not improve significantly on the VDEs computed on the DFT level. Quite the opposite. Naturally the added correlation energy does not lead to a uniform shift of the D_0 and S_0 energies. In this case this leads to a further lowering of the VDE. In accordance with Tab. 5.1, the VDEs computed in the neutral basis, deviate strongly from experiment. However, an outlier is found in 99pBA. Here, the VDE is at least in the same order of magnitude as the experimental values. The reason for this can likely be found in the strongly

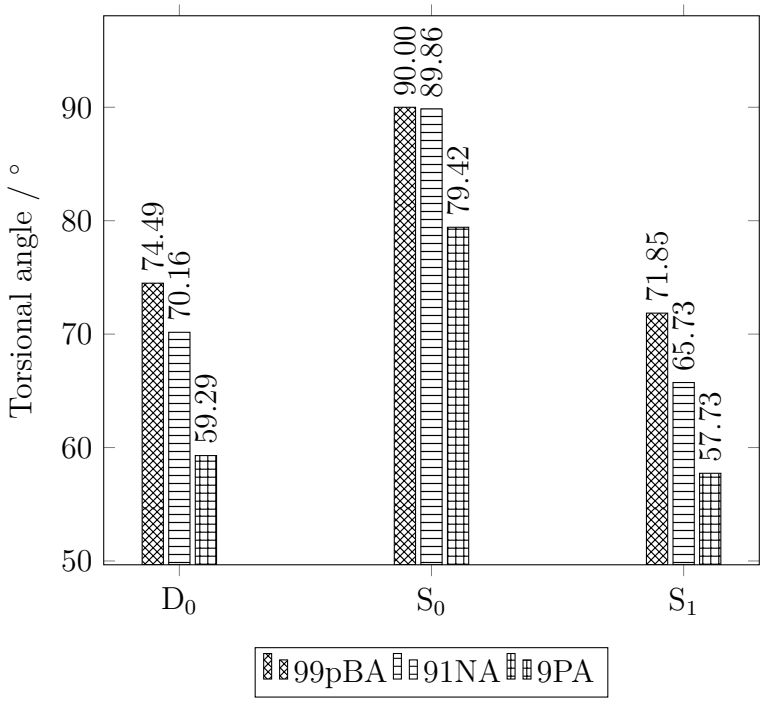

Figure 5.14: Torsional angle measured at different optimized geometries of 99pBA, 9PA and 91NA. All values given in degree.

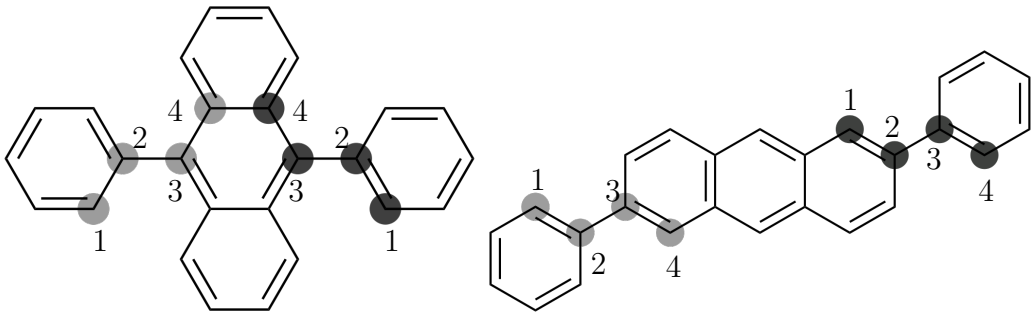

Figure 5.15: The atoms marked light-gray constitute group A, while the dark-gray constitute group B.

bound LUMO+1. Configurations populating LUMO+1 will lead to a larger energy gain than in the other investigated cases. In the case of 99pBA, this even leads to a flip of the D_0, dominated by the KS anchor configuration with the LUMO singly occupied, and the D_1 state, mainly consisting of the LUMO→LUMO+1 configuration. Apparently, DFT/MRCI predicts a different anionic ground state than ROKS-theory. Ionization in PD-PES would consequently take place from LUMO+1. Although this result contradicts intuition, it is not possible to say whether it is wrong on the basis of the available data in the neutral basis. Neither the energetic positions of the associ-

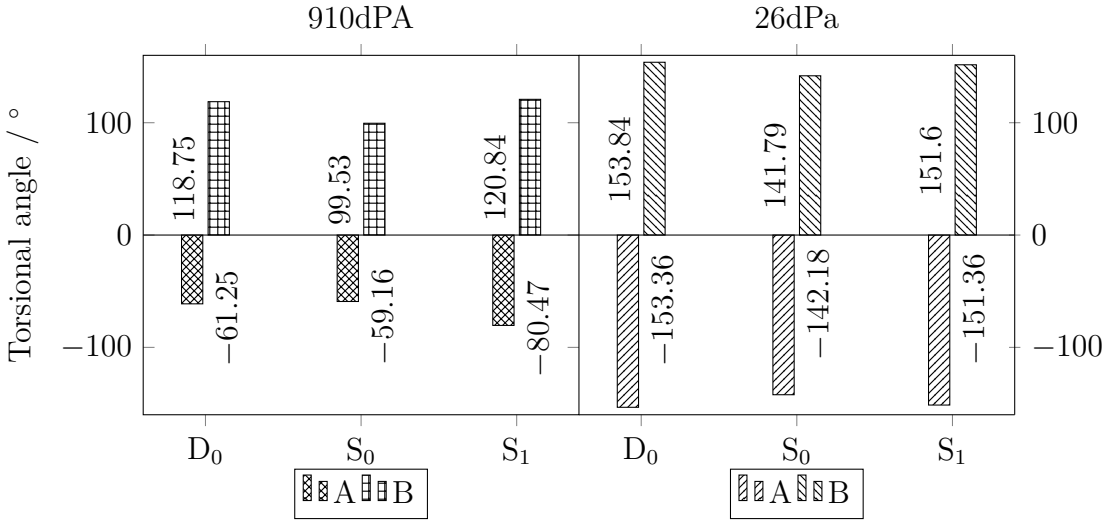

Figure 5.16: Torsional angles measured at different optimized geometries of 910dPA and 26dPa. Groups A and B are defined through the differently marked atoms in Fig. 5.15. All values are given in degree.

ated singlets, nor the Dyson norms differ substantially. Only the DFT/MRCI vector computed in the relaxed anion basis objects this results, as it predicts the ground state to be of similar character as computed using ROKS-theory. A bound LUMO+1 is found for 26dPa and 91NA, as well. However, in these two cases the anionic ground state is dominated by the open-shell ROKS-anchor configuration, as expected, and no switching of D_1 and D_0 is observed. It can be concluded, that DFT/MRCI in its current formulation is not capable of reasonable approximations to the VDE in the basis of neutral orbitals. This can clearly be traced back to the employed one-particle basis. Especially, the virtual orbitals LUMO and LUMO+1 are too strongly bound in KS-theory employing the BH-LYP functional on which DFT/MRCI is built. While the generated wave functions for the anion seem to be reasonable, judged on the Dyson norms compute for the *oligo-para*-phenylenes[P3], it is possible to generate unphysical anion ground states as demonstrated by the calculations on 99pBA. Consequently, special attention must be paid if homodimers are to be investigated. In such calculations it ought to be expected that the two virtual orbitals LUMO and LUMO+1 differ only slightly, especially if a symmetry is present between the two subunits. A possible improvement for calculating VDEs with DFT/MRCI might be achieved by extrapolating the orbital energies in the spirit of Dombrowski [135], who tried to adapt the DFT/MRCI method for other functionals. Zhan et al. [229] have shown that it is indeed possible to find a linear relationship between KS-MO ener-

gies and the EA. Unfortunately, the behaviour of DFT/MRCI computing the EAs does not follow the one found for the *oligo-para*-phenylenes, as the increments do not match the experimental ones. In particular, the EA of 910dPA is much too low and does not fit experimental data at all. A reason for this is not apparent and further investigation will be necessary. The analysis of the DFT/MRCI densities using the tools presented in the subsequent section may provide a first step to gain insight into the nature of the error.

5.3 Analysis of DFT/MRCI Densities

As was worked out by Plasser [230] in a series of publications [231–233], it is possible to extract a great deal of information from the one-particle reduced transition density matrix (1-TDM) γ. For a transition from the ground state $|\Psi_0\rangle$ to an arbitrary excited state $|\Psi_L\rangle$ γ reads

$$\gamma^{0L}\left(\kappa_1', \kappa\right) = N \int d\kappa_2 \ldots d\kappa_N \bar{\Psi}_0\left(\kappa_1', \kappa_2, \ldots \kappa_N\right) \Psi\left(\kappa_1, \kappa_2 \ldots \kappa_N\right)$$

in position basis, where the bar indicates complex conjugation. Here κ_i collects all position- and spin variables of the i-th particle. Integration over spin for all κ_i yields the spin-free transition density matrix

$$\gamma^{0L}\left(r_1', r_1\right) = N \int dr_2 \ldots dr_N \bar{\Psi}_0\left(r_1', r_2, \ldots, r_N\right) \Psi\left(r_1, r_2 \ldots r_N\right)$$

The square of this matrix can be associated with the exciton wave function[232] and in turn with the electron and hole densities $\rho_e\left(r_e\right)$ and $\rho_h\left(r_h\right)$ as

$$\begin{aligned}
\rho_e\left(r_e\right) &= \int dr_h \left[\gamma^{0L}\left(r_e, r_h\right)\right]^2 \\
\rho_h\left(r_h\right) &= \int dr_e \left[\gamma^{0L}\left(r_e, r_h\right)\right]^2
\end{aligned}$$

$\rho_e\left(r_e\right)$ is interpreted as the conditional probability of finding an electron around the coordinate of the hole r_h, *vice versa* for ρ_h. The combined conditional probability of finding a hole around r_h while an electron is around r_e can therefore be expressed as

$$\Omega = \int dr_e \rho_e\left(r_e\right) \tag{5.1}$$

$$\int dr_h \rho_h\left(r_h\right) = \iint dr_e r_h \left[\gamma^{0L}\left(r_e, r_h\right)\right]^2 \tag{5.2}$$

Note that $\gamma^{0L}\left(r_e, r_h\right)$ can be expressed in terms of single-particle creation and annihilation operators as

$$\begin{aligned}
\gamma^{0L}\left(r_e, r_h\right) &= \sum_{i,r} \langle \Psi_0 | a_i^\dagger a_r | \Psi_L \rangle \, \bar{\phi}_i\left(r_h\right) \phi_r\left(r_e\right) \\
\gamma^{0L}\left(r_e, r_h\right) &= \sum_{i,r} \left[\mathbf{D}^{0L}\mathbf{S}\right]_{ir}
\end{aligned} \tag{5.3}$$

where $\phi_i(r_h)$ and $\phi_r(r_e)$ are the hole and electron orbitals, $\mathbf{S}$ their overlap matrix and $\mathbf{D^{0L}}$ is the transition density matrix. Inserting this expression into Eq. (5.2) gives

$$\begin{aligned}\sum_{i,r}\left[\mathbf{D}^{0L}\mathbf{S}\right]_{ir}^{T}\left[\mathbf{D}^{0L}\mathbf{S}\right]_{ir} &= \sum_{i,r}\left[\mathbf{S}^{T}\left\{\mathbf{D}^{0L}\right\}^{T}\right]_{ri}\left[\mathbf{D}^{0L}\mathbf{S}\right]_{ir} = \mathrm{Tr}\left[\mathbf{S}^{T}\left\{\mathbf{D}^{0L}\right\}^{T}\mathbf{D}^{0L}\mathbf{S}\right] \\ &= \mathrm{Tr}\left[\left\{\mathbf{D}^{0L}\right\}^{T}\mathbf{D}^{0L}\right]\end{aligned} \tag{5.4}$$

where the last equality only holds if an orthogonal basis is used. If the ground state is composed of a single configuration and only single substitutions in the underlying basis are made, it should be clear from Eq. (5.3) and Eq.(5.5) that the maximal value of Ω is 1 if the function is normalized and strictly zero for higher excitations. Conclusively, Ω can be viewed as a measure for the amount of single excitation character of a state $|\Psi_L(\kappa)\rangle$. By partitioning the electron-hole distribution Ω into contributions from defined fragments A and B Plasser et al. [232] derived the charge-transfer number Ω_{AB}, which is defined by subdividing the integration over the whole space in Eq. (5.2) into integrations over volumes around the fragments.

$$\Omega_{AB} = \int_A dr_h \int_B dr_e \left[\gamma^{0L}(r_e, r_h)\right]^2 \tag{5.5}$$

which can now be interpreted as the probability of finding the electron in the volume element containing fragment A and the electron around B. Obviously, $0 \leq \Omega_{AB} \leq 1$ holds and summing up all fragment probabilities must give the total Ω again

$$\sum_{A,B}\Omega_{AB} = \Omega$$

One can immediately conclude that $\Omega_{AB} \propto \frac{1}{F}$ if all F defined fragments contribute equally. Furthermore, the diagonal elements Ω_{XX} are nothing but the electron-hole distributions on the X-th fragment, i.e. the conditional probability of finding the electron on X while the hole is also around X. From the definition of Ω_{AB} further quantities were defined by Plasser [230]. Straightforward is the charge-transfer ratio ω_{CT}, which is nothing but the proportion of off-diagonal elements in the whole distribution Ω.

$$\omega_{CT} = \frac{1}{\Omega}\sum_{A\neq B}\Omega_{AB} \tag{5.6}$$

If only diagonal elements exist, i.e. there are no charge-transfer configurations, ω_{CT} is obviously zero. Accordingly, all $\Omega_{XX} = 0$ means there are only charge-transfer configurations, from which one can conclude that $\Omega = \sum_{A \neq B} \Omega_{AB}$ and $\omega_{CT} = 1$. A further descriptor, the participation ratio PR of the fragments, is computed as the average of the participation ratios of the hole PR_H and the electron PR_E, respectively.

$$\mathrm{PR} = \frac{\mathrm{PR}_H + \mathrm{PR}_E}{2} \tag{5.7}$$

where PR_H and PR_E are computed as the proportion of the squared Ω value and the sum of the squared charge-transfer numbers Ω_{AB}^2

$$\mathrm{PR}_H = \frac{\left(\sum_{A,B} \Omega_{AB}\right)^2}{\sum_A \left(\sum_B \Omega_{AB}^2\right)}$$
$$\mathrm{PR}_E = \frac{\left(\sum_{A,B} \Omega_{AB}\right)^2}{\sum_B \left(\sum_A \Omega_{AB}^2\right)}$$

Note, the order of summation in the denominator only matters for a non-symmetric Ω matrix. Remembering that $\Omega_{AB} \propto \frac{1}{F}$ if all F defined fragments contribute equally, leads to the realization that PR_H and PR_E have maximum values equal to the number of defined fragments, as the numerator becomes 1 and the denominator reads $\sum_{A,B} \frac{1}{F^2} = F \frac{1}{F^2} = \frac{1}{F}$. Obviously, PR also takes the value F in that case. Finally, it is possible to define the average position of the exciton Pos as the average fragment wise positions of the electron and the hole Pos_E and Pos_H[231]. The latter constitute weighted fragment coordinates of the form

$$\mathrm{Pos}_H = \frac{\sum_A A \left(\sum_B \Omega_{AB}\right)}{\Omega}$$
$$\mathrm{Pos}_E = \frac{\sum_B B \left(\sum_A \Omega_{AB}\right)}{\Omega}$$
$$\mathrm{Pos} = \frac{\mathrm{Pos}_H + \mathrm{Pos}_E}{2}$$

To exemplify the usefulness of these descriptors, especially in the case of delocalized orbitals, we sketched possible situations for two fragments in Fig. 5.17. The presented quantities are a great aid in extracting useful information from a DFT/MRCI density. Consequently, they were employed in analysing the electronic influences in a trimer of pentacene and a dimer of a pentacene derivative, presented in the next section.

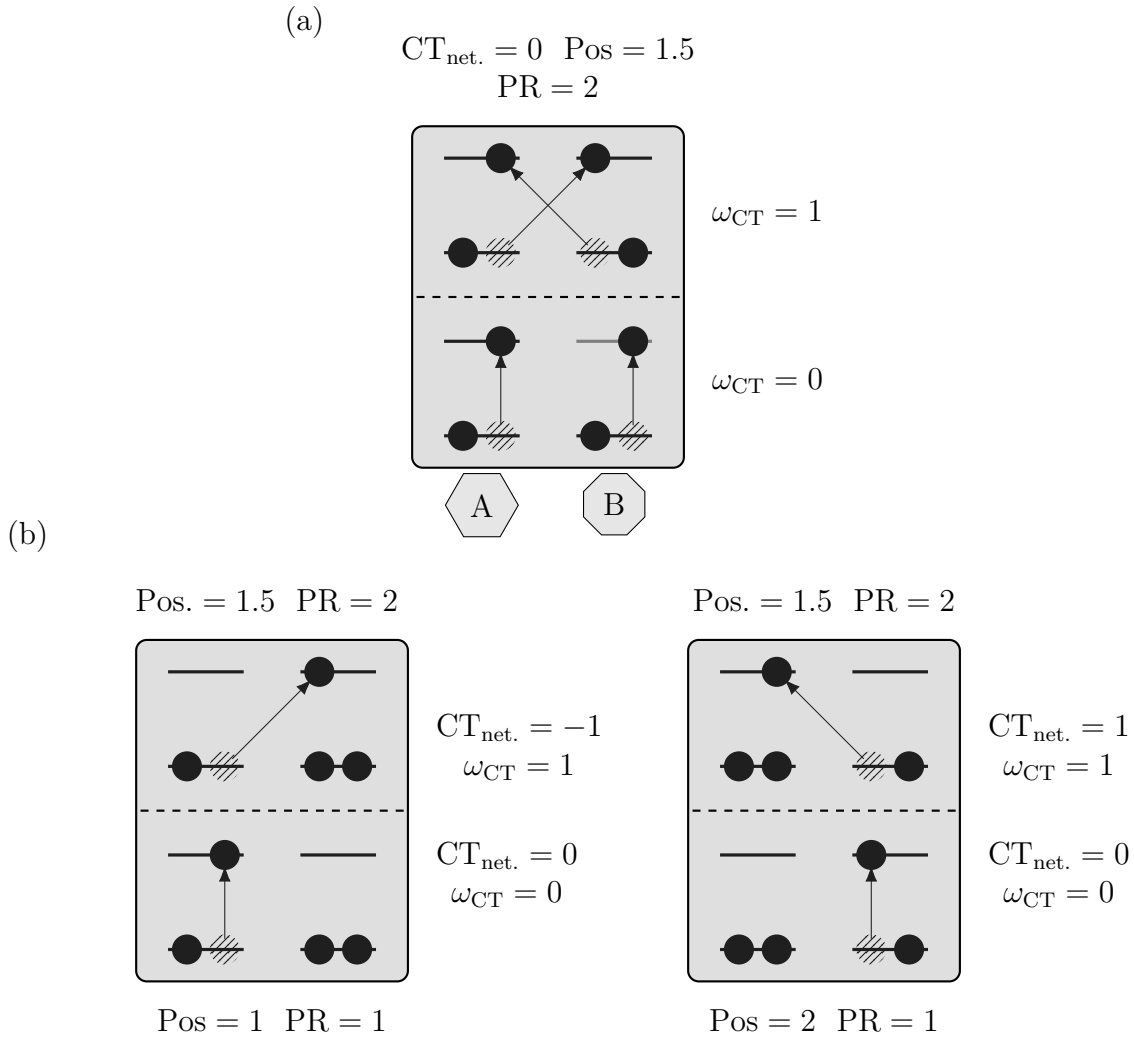

Figure 5.17: Example of possible single excitations on two defined fragments A and B and the resulting descriptors. Hatched circles depict holes, filled electrons. The connectors symbolize the direction of the excitation. Part (a) shows the usefulness of the ω_{CT} value, if one needs to distinguish a charge-resonance configuration (upper panel) from an excitonic-resonance state (lower panel). Part (b) shows the idealized cases of a pure local (lower panels) and pure charge-transfer excitation (upper panels) on the respective fragments.

5.4 Pentacene and TIPS–Pentacene in Crystalline Surrounding

Similar to An and its derivatives discussed in Sec. 5.2 PT has promising applications in organic electronics[234–236]. Crystal packing does play a key role in maximizing the desired properties of PT materials[237–239]. Consequently, modification of the PT-core with the aim of controlling crystal morphology is a promising way to synthesize materials with the desired property boosted. Straightforward, are substitutions in position 6 and 13, as the central ring is the most reactive[240–242]. A prominent example being TIPS-PT. Both, PT and TIPS-PT, were found to undergo SF[243–248] after initial photoexcitation. As discussed in the introduction and in Sec. 4 a crucial state in the SF process is the multi-excitonic[247] singlet state ^{1}(TT). In addition, it has been argued that the model Hamiltonian of Dombrowski et al. [P1] gives more physically intuitive results for this state. As the ^{1}(TT) is a doubly excited state with respect to the closed-shell ground state, there is little spectroscopic data available for comparison. For a comprehensive review of the spectroscopic signatures of ^{1}(TT) in different methods, the reader is referred to the review by Miyata et al. [15]. Recently, Neef et al. [249][250] published time- and angle-resolved photo-emission spectroscopy (trARPES) data for crystalline PT, providing high quality data for the first step of the SF process in which ^{1}(TT) is involved. This allows estimating the energetic position and character of the ^{1}(TT) state. Motivated by their results, calculations on PT seemed to be a nice test case for probing the capabilities of the new Hamiltonian. Particularly, interesting in this context was the question, whether different arrangements allow for different decay pathways in the SF process. As was already mentioned in the introduction, different mechanisms are discussed for the transfer of the excited state population from the bright S_1 to the optically dark ^{1}(TT) state, i.e. the first step after photoexcitation in SF. The first possibility is the crossing of the PESs leading to a nonadiabatic transition[251] which readily explains the ultrafast kinetics of the process. Here, the population is transferred directly to the ^{1}(TT) state. Experimental hints for this pathway have been provided for PT by Chan et al. [252] using time-resolved two-photon photoemission spectroscopy. Based on multi-state DFT calculations, these authors found that charge-transfer states are also involved in the process. They suggested that they act as virtual states in a superexchange-like mechanism. However, the trARPES experiments of Neef et al. [249] give a clear indication of a charge-transfer mediated mechanism (Step 3 in Fig. 5.18) in crystalline

PT with its herringbone crystal structure. The direct population of ^{1}(TT) (Step 2 in Fig. 5.18) was thereby ruled out. However, in other systems such as rubrene[253,

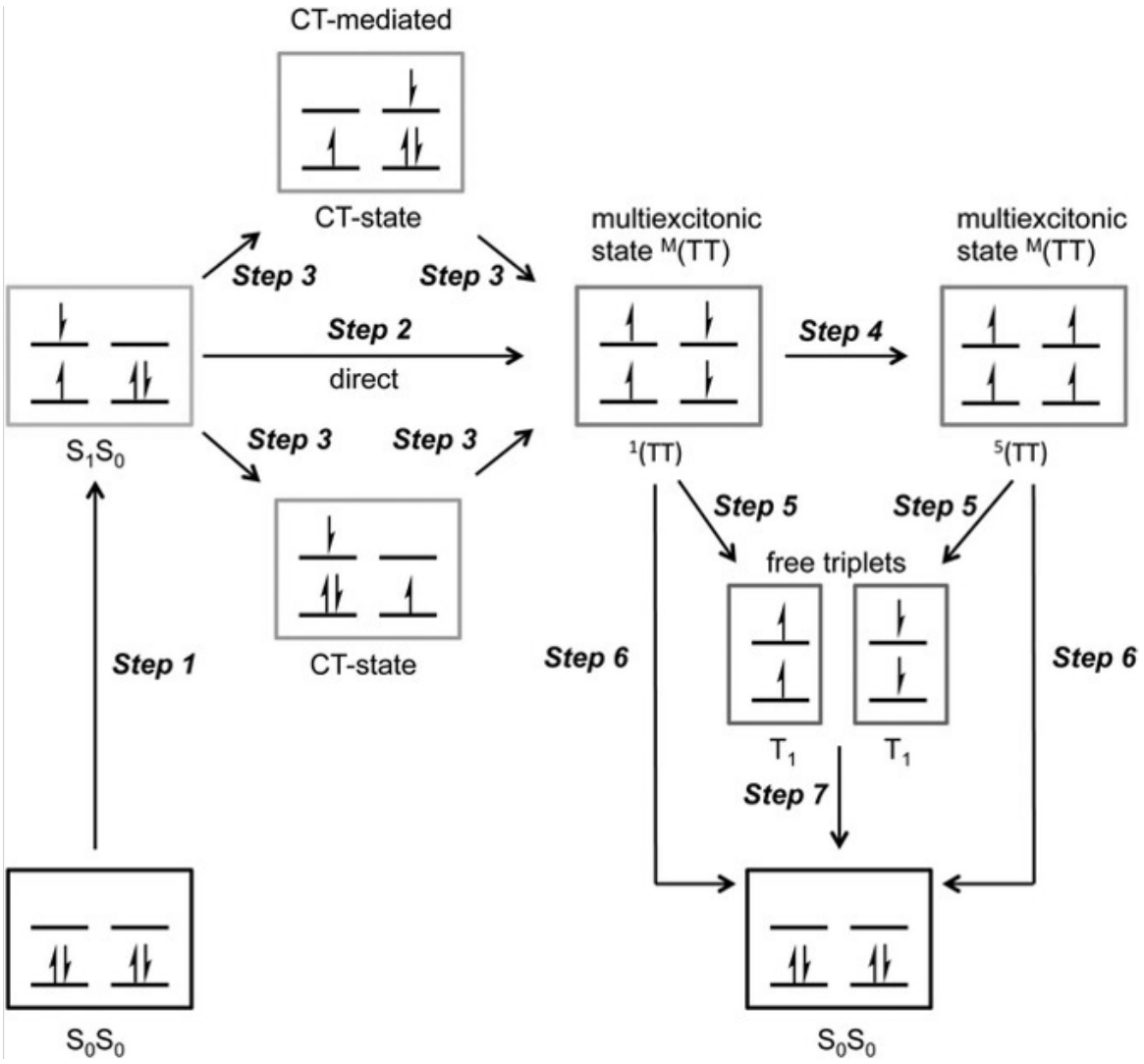

Figure 5.18: Different possible mechanism for the SF process. Copied with permission from Hetzer et al. [19].

254] and end-linked pentacene dimers[255] there is clear evidence for a direct mechanism. This again stresses the elementary influence of morphology[256–259] in the SF process. While the ^{1}(TT) state is a commonly accepted first intermediate, due to the conservation of spin angular momentum, it is not guaranteed that it is the final intermediate before the separation into free triplets (Step 5 in Fig. 5.18). In fact, there is no need for the state to be involved at all. Although there are no experimental indications for this and the ultrafast kinetics also tend to favour a spin-allowed

process. The population might flow through other channels leading to the ^{3}(TT) or the ^{5}(TT) state[15, 260] While the former is accessible by intersystem crossing[261, 262] from ^{1}(TT) or S_1, the latter must be coupled to ^{1}(TT) or S_1 by a second order tensor operator, such as the Breit-Pauli spin-spin dipole operator introduced in Sec. 2.2. Population of ^{3}(TT) is actually undesirable as it offers the possibility for adjacent triplet states to annihilate, as has been demonstrated using time-resolved electron paramagnetic resonance spectroscopy by Chen et al. [263]. The same authors

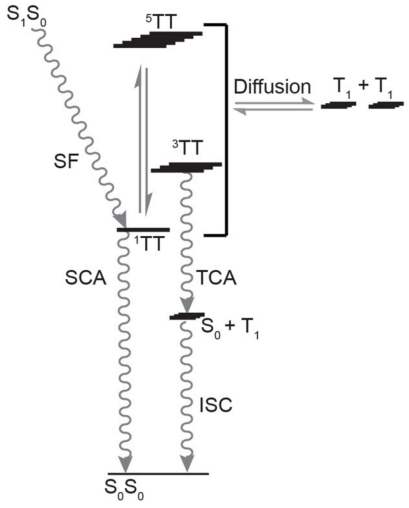

Figure 5.19: Model showing the formation of ^{1}(TT) and possible deactivation mechanism. The deactivation might happen *via* singlet-channel annihilation (SCA), possibly leading to luminesence[264], and ending in the system's ground state. The triplet-channel annihilation (TCA) leads to the T_1 state of the system. Diffusion into two triplets represents the desired productive channel, resulting in two separated triplet states. The equilibrium between ^{5}(TT) and ^{1}(TT), possibly mediated by spin-spin dipole coupling is implied. Adapted with permission from Dill et al. [265].

also found that ^{5}(TT) and ^{3}(TT) are mixed at room temperature when studying a terylene dimer. They concluded that this opens a channel for ^{3}(TT), leading to the annihilation of the triplets mentioned above. Experimental evidence for the ^{5}(TT) state has been found using time-resolved electron spin resonance for various covalently linked PT dimers[25, 266–268] differing in the orientations of the PT units, but also in TIPS-tetracene[26]. However, its specific role in SF is not yet fully understood. It may serve as an intermediate on the way to free triplets[269], or it may be a port to the loss channel through coupling to ^{3}(TT). Furthermore, it ought to be recognized that the applied spectroscopic techniques to detect these states have a time resolution

in the ns regime[260]. Therefore, the possibility that ^{5}(TT) is only populated as a result of the fusion of triplets generated by ultra-fast SF and plays no role in the actual SF mechanism is also a possibility. Obviously, it is necessary to be able to describe the energetic positions and possible couplings in the full spin manifold of the multi-excitonic state, i.e. ^{1}(TT), ^{3}(TT) and ^{5}(TT), if one wants to explore effects of crystal morphology or specific geometrical parameters. This is a major challenge for computational methods. Especially if the coupling between these states is to be described. A method is needed that can be used to calculate spin-orbit or spin-spin matrix elements between these states. DFT/MRCI serves as a good basis for this, since it is able to describe double excitations as well as the triplet and quintet spin manifold, as mentioned above. Furthermore, it is one of the few methods that allows the calculation of Breit-Pauli spin-spin matrix elements between states of different multiplicity[40]. In addition, DFT/MRCI wave functions have proven to be a robust platform for the calculation of spin-orbit matrix elements[270]. To evaluate how well the new model Hamiltonian performs and to elucidate the possible role of ^{3}(TT) and ^{5}(TT) in different arrangements, we considered a PT monomer, three different arrangements[248] of dimers and a trimer in a crystalline environment. Due to the large size of the full system, this investigation provided nice test cases for the OMP implementations of the `SPOCK.sistr` and `mrci` programs. Further details can be found in the publication[P4]. A comparable investigation was carried out by Aguilar Suarez et al. [271] on tetracene using different levels of theory. These authors identified subunit arrangements in which low-lying charge-transfer states are mixed with locally excited states, favouring the S_1 to ^{1}(TT). However, they focused only on the singlet spin manifold.

The Journal of Chemical Physics ARTICLE pubs.aip.org/aip/jcp

Multiexcitonic and optically bright states in subunits of pentacene crystals: A hybrid DFT/MRCI and molecular mechanics study

Cite as: J. Chem. Phys. 160, 144114 (2024); doi: 10.1063/5.0203006
Submitted: 8 February 2024 • Accepted: 22 March 2024 •
Published Online: 10 April 2024

Timo Schulz,[a] Simon Hédé,[b] Oliver Weingart,[c] and Christel M. Marian[d]

AFFILIATIONS

Institute of Theoretical and Computational Chemistry, Faculty of Mathematics and Natural Sciences, Heinrich Heine University Düsseldorf, Düsseldorf, Germany

[a]**Electronic mail:** timo.schulz@hhu.de
[b]**Electronic mail:** simon.hede@hhu.de
[c]**Electronic mail:** weingart@hhu.de. **Present address:** Center for Information and Media Technology, Heinrich Heine University Düsseldorf, Düsseldorf, Germany.
[d]**Author to whom correspondence should be addressed:** christel.marian@hhu.de

ABSTRACT

A hybrid quantum mechanics/molecular mechanics setup was used to model electronically excited pentacene in the crystal phase. Particularly interesting in the context of singlet fission (SF) is the energetic location of the antiferromagnetically coupled multiexcitonic singlet state, ^{1}(TT), and the ferromagnetically coupled analog in relation to the optically bright singlet state. To provide photophysical properties of the accessible spin manifold, combined density functional theory and multi-reference configuration interaction calculations were performed on pentacene dimers and a trimer, electrostatically embedded in the crystal. The likelihood of a quintet intermediate in the SF process was estimated by computing singlet–quintet electron spin–spin couplings employing the Breit–Pauli Hamiltonian. The performance of the applied methods was assessed on the pentacene monomer. The character of the optically bright state and the energetic location of the ^{1}(TT) state depend strongly on the relative orientation of the pentacene units. In the V-shaped dimers and in the trimer, the optically bright state is dominated by local and charge transfer (CT) excitations, with admixtures of doubly excited configurations. The CT excitations gain weight upon geometry relaxation, thus supporting a CT-mediated SF mechanism as the primary step of the SF process. For the slip-stacked dimer, the energetic order of the bright and the ^{1}(TT) states swaps upon geometry relaxation, indicating strong nonadiabatic coupling close to the Franck–Condon region—a prerequisite for a coherent SF process. The multiexcitonic singlet, triplet, and quintet states are energetically too far apart and their spin–spin couplings are too small to bring about a noteworthy multiplicity mixing.

I. INTRODUCTION

Oligoacenes have stirred the interest of experimental and computational chemists alike, as they have remarkable photophysical and electrical properties. Prominent in recent research is the process of singlet fission (SF) due to its potential to lead to efficient third generation solar cells.[1,2] In this process, a singlet excited state (or singlet exciton) evolves into two triplet states on very short time scales and can thus address wavelength regions of the solar radiation spectrum that are otherwise unusable for generating electric current in photovoltaic (PV) devices. In this way, the Shockley–Queisser limit[3] of 33.7% efficiency for an ideal single-junction solar cell can be overcome.[4] Comprehensive reviews on the topic were given by Casanova,[5] Monahan and Zhu,[6] and Smith and Michl.[7,8]

While there is agreement on the basic mechanism, which involves an optically bright singlet excited state as well as a dark, spatially confined singlet-coupled bitriplet exciton, ^{1}(TT), losing spatial-, but retaining spin-coherence,[9,10] details have been heavily debated. Whether the initial step forming the ^{1}(TT) state is a coherent process[11] or follows a stepwise charge transfer (CT)-mediated mechanism[12–15] has been controversially discussed. Very recently, the authors of the work of Neef *et al.*[16,17] presented clear experimental evidence supporting the CT-mediated route in pentacene crystals. It remains unclear, however, how the antiferromagnetically

coupled triplet pair evolves into free triplets. Mechanisms involving a ferromagnetically coupled triplet pair, ^{5}(T...T), seem to be a plausible variant.[18] Experimental indications for the formation of an intermediate quintet state come from transient electron paramagnetic resonance (EPR) spectroscopy of pentacene films[19] and covalently linked pentacene dimers.[20–22]

Although pentacene dimers have been extensively studied computationally,[23–28] very few computational studies have investigated the full spin manifold, i.e., singlet, triplet, and quintet states, possibly involved in the SF process. One of the main problems has been the quality of the electronic structure methods that are applicable to dimers or even trimers: Accurate *ab initio* methods that can handle double excitations, such as equation-of-motion coupled cluster singles and doubles (EOM-CCSD) or complete active space self-consistent field methods with perturbative second-order correlation corrections (CASSCF/MRPT2), are prohibitively expensive; cheaper methods such as linear response time-dependent density functional theory (TDDFT) are limited to single excitations and hence miss the biexcitonic states completely. Our group recently presented a cost-efficient approach[29] to reliably compute doubly excited states containing open-shell configurations in the framework of combined density functional theory and multi-reference configuration interaction (DFT/MRCI), which has proven to be a robust and fast method in the computation of excited states of varying character.[30,31] In this work, we apply the DFT/MRCI method in a hybrid QM/MM (quantum mechanics/molecular mechanics) setup to model pentacene in the crystal phase and to investigate the full spin manifold, accessible to an entangled triplet pair, and analyze their interactions.

II. COMPUTATIONAL DETAILS

A. Gas-phase geometries

The ground, quintet, and excited state geometries of pentacene were optimized using the Gaussian 16 program suite. Ground state geometries were obtained with Kohn–Sham density functional theory (KS-DFT).[32] Excited singlet state geometries were optimized using time-dependent density functional theory.[33,34] In triplet state computations, the Tamm–Dancoff approximation (TDA)[35] was employed. The minima of lowest quintet states were determined with unrestricted KS-DFT. In all cases, PBE0[36–40] was used as an approximation to the exchange–correlation functional. All centers were equipped with a def2-SV(P)[41] basis set. Grimme's D3 dispersion correction[42] with Becke–Johnson damping[43] (D3-BJ) was used throughout.

B. QM/MM methodology

The crystal structure of pentacene (CCDC no./Refcode PENCEN04/170187)[44] was taken from the CCDC website. The unit cell was then refined through Quantum Espresso[45] using the generalized gradient approximation with PBE exchange–correlation[40] and RRKJ pseudopotentials.[46] Additionally, the D3-BJ dispersion correction was employed. The periodic boundary calculations were performed only at the gamma point and using a kinetic energy cutoff of 40 eV, with the cell size fixed to the experimental values. To create the bulk from the optimized unit cell, a $4 \times 4 \times 4$ supercell was generated and all molecules whose centroids were located strictly inside the supercell were kept, resulting in a bulk of 7380 atoms in total. Atomic partial charges, to be employed in subsequent QM/MM calculations, were computed using restricted Hartree–Fock, the 6-31G* basis set, and the Merz-Kollmann scheme[47] for a nuclear arrangement extracted from the pentacene crystal. Force-field parameters were obtained from the Generalized Amber Force Field (GAFF), the parameters for nonbonding interactions (van der Waals parameters) were taken from the third set in the work of Singh and Kollman.[47] QM/MM geometry optimizations were performed with the COBRAMM2.0[48] package using Gaussian16 for the QM part and AMBER16 for the MM part. The geometries of the states in the QM layer, consisting of one, two, or three pentacene molecules, respectively, were optimized employing the same methods and technical parameters as in the gas-phase calculations. Vibrational analyses were performed in order to validate that the obtained structures were true minima for all S_0 and Q_1 states and for the S_1 and T_1 states of pentacene monomers and dimers. A vibrational frequency calculation was not performed for pentacene trimers due to the high demand on computational resources.

C. DFT/MRCI setup

DFT/MRCI[30,49] is a semiempirical electronic structure method for computing the properties of electronically excited states in large molecular systems. It employs KS-DFT orbitals and orbital energies of a closed-shell anchor configuration in combination with a multi-reference configuration interaction (MRCI) expansion of the wavefunction. The idea behind this approach is to use the dynamical correlation, included in DFT by construction, to efficiently truncate the otherwise necessary large MRCI expansion. To avoid double counting of electron correlation, the approach makes use of extensive configuration selection and inserts scaling parameters and damping functions into the MRCI Hamiltonian. The R2022 ansatz[29] improves a description of doubly excited and degenerate states with respect to former DFT/MRCI parametrizations. In particular, good agreement with experimental trends for the low-lying excited states of polyacenes, β-carotenoids, and *para*-oligophenylenes was achieved with the R2022 approach.[29,50] Unless noted otherwise, an energy selection threshold of 0.8 E_h and the *tight* parameter set optimized for this threshold was used in the present calculations. The one-particle basis was generated using the BH-LYP[37,39,51–53] functional, again with a def2-SV(P) basis and an integration grid of 5, as implemented in the TURBOMOLE program suite.[54,55] The MM surrounding was incorporated through point charges generated by COBRAMM2.0 in the previous step. Convergence criteria were met when the energy was converged to 10^{-7} E_h and the density to 10^{-7}. The frozen orbital approximation was employed in the DFT/MRCI calculations. Orbitals with an energy less than -10 E_h and higher than 2 E_h were excluded from the correlation treatment. All DFT/MRCI calculations were carried out using a revised implementation of the program, which uses the OpenMP implementation of multithreading, instead of message passing as specified Message Passing Interface standard. Performance benchmarks and technical details of the OpenMP implementation will be published elsewhere. For the monomer, we calculated 21, 20, and 16 roots for the singlet, triplet, and quintet multiplicity, respectively. In the dimer cases, these numbers were reduced to 11 singlets, 10 triplets, and 5 quintets. Due to high demands on the computational resources, the

number of CI vectors was further reduced in the trimer case to 6 singlets, 7 triplets, and 2 quintets. The energy of the highest root in the reference space has an impact on the effective configuration selection threshold (tsel) in the DFT/MRCI method.[49] To obtain DFT/MRCI energies of comparable quality for the dimers and the trimer, the selection parameter was chosen such that an effective tsel value of ≈ 0.93 E_h resulted in both cases. Further information from the DFT/MRCI wavefunctions were extracted by means of the TheoDORE program.[56] In this context, molecular fragments were auto-generated using the interface to Open Babel[57] and transition densities were computed using ORBKIT.[58] All plots of molecular orbitals and densities were created with Jmol.[59]

D. Electronic spin–spin coupling

Electron spin–spin dipole coupling (SSC) calculations were performed at the DFT/MRCI level using an OpenMP implementation of the `SPOCK.SISTR`[60] program, employing spin–spin integrals computed in the resolution-of-the-identity framework[61] in a def2-SV(P) basis set. Second-order spin–orbit coupling (SOC) effects were evaluated perturbationally with `SPOCK`[62] in the atomic mean-field approximation[63] of the Breit–Pauli Hamiltonian. SSC and SOC matrix elements were calculated for the five, ten, and eleven lowest quintet, triplet, and singlet states, respectively. The SSC Hamiltonian has the power to couple states of singlet and quintet spin multiplicity directly, thus enabling transitions between an antiferromagnetically (singlet) and ferromagnetically (quintet) coupled triplet pair states. Unlike SOC, SSC leads to first-order zero-field splitting (ZFS) of triplet and quintet states, even if they are orbitally nondegenerate as in the present case of pentacene. The same effect can be brought about by second-order SOC interactions. Experimentally, these two effects can be hardly told apart because both exhibit the same tensorial structure. For this reason, typically two fine structure parameters, D and E, are used to define an effective dipolar electron spin magnetic interaction Hamiltonian in spin multiplets.[64–66] To avoid any possibility of confusion with symbols employed for doubly excited states or energy, we will use D_T and E_T in conjunction with the ZFS in triplet states and D_Q and E_Q for quintets, respectively. Due to symmetry selection rules, only the diagonal elements of the second-rank tensor contribute to the ZFS in D_{2h} molecular point groups.[65]

III. RESULTS

To begin this section, we wish to introduce the nomenclature used in the following subsections. Commonly, the excited states of oligoacenes are labeled according to the nomenclature introduced by Platt,[67] which was derived for a simple perimeter model. However, as we deal not only with monomeric systems but also with dimers (and trimers) in which the situation is rather complex and the states have mixed character, we decided not to transfer this nomenclature as it would be too inflexible. Instead, we equipped all labels with a super- and a subscript encoding the leading configurations of the state, similar to the notation of excited determinants or configuration state functions in the context of configuration interaction. Singly excited states are labeled according to their spin multiplicity as S for singlets and T for triplets, as is common practice. A singlet excited state dominated by a single substitution in the highest occupied molecular orbital (HOMO) and the lowest unoccupied orbital (LUMO) would be denoted as S_h^l, the corresponding triplet state as T_h^l in this nomenclature. $S_{h-1;h}^{l;l+1}$ denotes a singlet state featuring two singly excited configurations as leading terms, i.e., HOMO-1 to LUMO and HOMO to LUMO+1. Doubly excited states are differentiated by the number of open shells in their spatial configurations. Configurations with zero, two, or four open shells are denoted as N, Z, and V, based on the German words Null, Zwei, and Vier, respectively. A doubly substituted closed-shell spatial configuration involving an excitation from the HOMO to the LUMO, for example, would be denominated N_h^l, a double excitation from the HOMO to the LUMO and LUMO+1 with two open shells would be called $Z_h^{l;l-1}$, and finally a double excitation from the HOMO-1 and HOMO to LUMO and LUMO+1 featuring four open shells would be denoted as $V_{h-1;h}^{l;l+1}$.

A. Monomers

To assess the performance of the theoretical methods, we first discuss the excited states of the pentacene monomer. The four lowest excited singlet and triplet states are of interest to us, in the quintet manifold we will focus on the lowest electronic state only. It is commonly accepted that the lowest singlet excited transition S_h^l (^1L_a, B_{2u}) of pentacene is polarized along the short molecular axis,[67] has ionic character,[68–70] and is governed by a configuration constructed from a single substitution from the HOMO to the LUMO.[25,71] Moreover, it is established that the long-axis transition $S_{h-2;h}^{l;l+2}$ (^1L_b, B_{3u}) is located above the S_h^l and has a much weaker oscillator strength f. A third, yet less often discussed singlet state, $S_{h-1;h}^{l;l+1}$ (B_{1g}), is located close to the $S_{h-2;h}^{l;l+2}$ state and is dipole forbidden. Lastly, a doubly excited singlet state of A_g symmetry owing multiconfiguration character has been discussed in the vicinity of these two states due to its potential role in the SF mechanism.[23,26] In Table I, this state is listed as N_h^l according to its leading configuration in our calculations. In the triplet manifold, the T_1 state (T_h^l, ^3L_a, B_{2u}) has been studied by various experimental[72,73] and theoretical methods.[25,74–77] The T_2 state transforms according to the B_{1g} irreducible representation and is denoted here as $T_{h-1;h}^{l;l+1}$. Energetically, it is located far above T_h^l [$\Delta E(T_2 - T_1) \approx 1.4$ eV].[77] The second triplet state of B_{1g} symmetry is composed of the same leading terms as T_2 but exhibits a much higher oscillator strength in the triplet absorption spectrum and is therefore experimentally well known,[78] in contrast to the $T_{h-2;h}^{l;l+2}$ state (^3L_b, B_{3u}), which cannot be reached from the T_1 state by a dipole-allowed transition. For a meaningful comparison of our results with literature data, it is mandatory to recognize whether the cited excitation energies refer to vertical, adiabatic, or 0–0 transition energies. For this reason, we annotated the literature data in Table I by specifying the experimental or computational method, respectively. Our calculations reproduce the state energies and their characters well, as can be seen from Table I. The crystal environment stabilizes the monomer by 0.46 eV in the electronic ground state but appears to have a minor impact on its excitation energies and oscillator strengths. The transition densities, displayed in Fig. 1, confirm that the $S_0 \rightarrow S_h^l$ (^1L_a) transition dipole is oriented along the short molecular axes, whereas it points in the

TABLE I. Calculated vertical energies at the S_0 ($E_{vert.}$) and T_1 geometries ($E_{vert.}$[a]) as well as adiabatic ($E_{ad.}$) energies of selected states of a pentacene monomer in crystal and gas-phase environments in comparison to literature values. All energies in eV. Oscillator strengths f of singlet transitions refer to the S_0 geometry, those of triplet transitions to the T_1 geometry.

State		$E_{ad.}$		$E_{vert.}$ (f)		$E_{vert.}$ (f)[a]		Literature	
		Crystal	Gas	Crystal	Gas	Crystal	Gas	Experiments	Computations
1^3B_{2u}	T_h^l	0.89	0.88	1.10	1.09	0.00	0.00	0.86,[b] 0.95[c]	0.98,[d] 1.07[e] 0.87,[f] 0.72[g]
1^3B_{1g}	$T_{h-1;h}^{l;l+1}$	⋯	2.00	2.19	2.15	1.28 (0.0009)	1.25 (0.0017)	1.4[h]	1.24,[i] 1.37,[j] 1.41[g]
1^3B_{3u}	$T_{h-2;h}^{l;l+2}$	⋯	⋯	3.19	3.11	2.34	2.27	⋯	⋯
2^3B_{1g}	$T_{h-1;h}^{l;l+1}$	⋯	⋯	3.57	3.54	2.60 (1.0322)	2.58 (0.9948)	2.46[k]	2.53,[d] 2.67[g]
1^1B_{2u}	S_h^l	2.21	2.20	2.34 (0.1100)	2.34 (0.1087)			2.21,[l] 2.31[m]	2.34,[n] 2.31,[o] 2.31[e]
2^1A_g	N_h^l	⋯	⋯	2.97	2.94			⋯	2.63,[e] 2.52,[d] 2.88[o]
1^1B_{3u}	$S_{h-2;h}^{l;l+2}$	⋯	⋯	3.22 (0.0000)	3.16 (0.0086)			2.94[l]	3.29,[n] 3.14[o]
1^1B_{1g}	$S_{h-1;h}^{l;l+1}$	⋯	⋯	3.30	3.24			⋯	⋯
1^5A_g	$V_{h-1;h}^{l;l+1}$	4.24	4.19	4.78	4.70			⋯	⋯

[a] $T_1 \rightarrow T_n$.
[b] Extracted from kinetic data in crystal.[73]
[c] In cyclohexane, UV–vis absorption.[72]
[d] Vertical/pp-RPA.[69]
[e] Vertical/SS-CAS(12π,12)SCF+MRMP2, S_0 geometry.[26]
[f] Adiabatic/SS-CAS(12π,12)SCF+MRMP2.[26]
[g] Vertical/RI-CC2, T_1 geometry.[83]
[h] Transient triplet absorption in crystal.[80]
[i] Vertical/CAS(12,12)SCF+MRMP2.[23]
[j] Vertical/EOM-CCSD, S_0 geometry.[77]
[k] Flash photolysis in benzene, lowest energy band of triplet absorption.[78]
[l] In argon matrix at 10 K, lowest energy band within a system.[81]
[m] Supersonic beam, band origin.[82]
[n] Vertical/CC2, S_0 geometry.[84]
[o] Vertical/SA-CAS(14,14)SCF+CASPT2.[25]

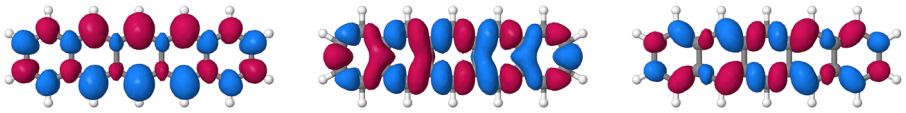

(a) S_h^l (b) $S_{h-2;h}^{l;l+2}$ (c) $S_{h-1;h}^{l;l+1}$

FIG. 1. Transition densities of the $S_0 \rightarrow S_h^l$, $S_{h-2;h}^{l;l+2}$, and $S_{h-1;h}^{l;l+1}$ excitations of monomeric pentacene. Isosurfaces were plotted with an absolute cutoff of 0.0004. Positive values are colored red and negative values blue.

direction of the long molecular axis in case of the $S_0 \rightarrow S_{h-2;h}^{l;l+2}$ (^1L_b) excitation.

The singlet and triplet states of pentacene originating from $\pi\pi^*$ single excitations follow a principle introduced by Klán and Wirz[79] that relates the size of the singlet–triplet energy gap ΔE_{ST} to the overlap of the electron densities of the orbitals involved in the transition. The electron densities of HOMO and LUMO strongly overlap (see Fig. 2), with the result that the singlet–triplet splitting of the S_h^l and T_h^l states is very large, as required for efficient SF. In contrast, the ΔE_{ST} value of the $S_{h-2;h}^{l;l+2}$ and $T_{h-2;h}^{l;l+2}$ states is very small. The $S_{h-2;h}^{l;l+2}$ and $T_{h-2;h}^{l;l+2}$ wavefunctions are composed of nearly equal contributions of HOMO-2 → LUMO and HOMO → LUMO+2 excitations. Klán and Wirz show that very small singlet–triplet splittings cannot only be achieved when donor and acceptor orbitals are spatially far apart but also in cases where the local electron densities in the orbitals involved in the electronic transition peak at different atoms.[79]

Considering the 2^1A_g state of pentacene, we find dominant contributions of the doubly excited $(h)^0(l)^2$ and the ground state $(h)^2(l)^0$ configurations. While the former dominates with a weight of ≈70%, the ground state configuration contributes ≈5%

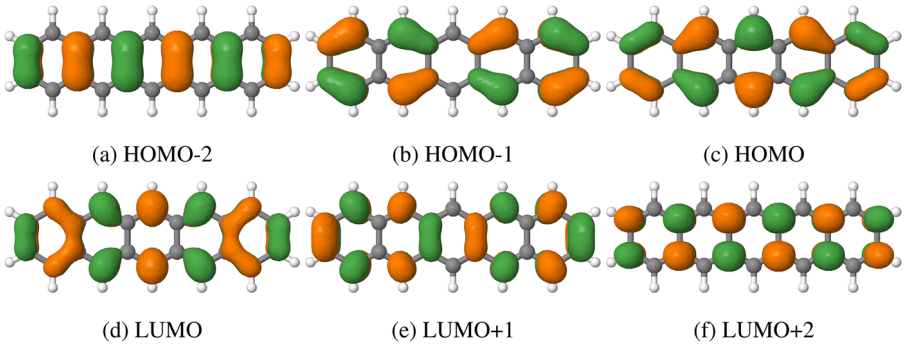

FIG. 2. Selected molecular orbitals in the ground state geometry of pentacene. Isosurfaces were plotted with a cutoff of 0.03. The electron densities of HOMO and LUMO strongly overlap, resulting in a large ΔE_{ST} value of the S_h^l and T_h^l states (1^1B_{2u}–1^3B_{2u}). In contrast, the electron density of HOMO-2 and LUMO and those of HOMO and LUMO+2 overlaps only slightly, explaining the tiny energy gap between the $S_{h_{-2};h}^{l;l_{+2}}$ and $T_{h_{-2};h}^{l;l_{+2}}$ states (1^1B_{3u}–1^3B_{3u}). The energetic splitting of the $S_{h_{-1};h}^{l;l_{+1}}$ and $T_{h_{-1};h}^{l;l_{+1}}$ states (1^1B_{1g}–1^3B_{1g}) is in-between.

to the wavefunction. 2^1A_g is likely the state labeled D by Zimmerman, Zhang, and Musgrave[23] using multi-reference perturbation theory (MRMP). They found the ground state configuration to contribute with 7% and report large amplitudes of doubly excited configurations involving HOMO-1, HOMO, LUMO, and LUMO+1. Unfortunately, the authors do not state whether their computed configurations are of closed- or open-shell character. The extra ordinarily low energetic position of their D state of 1.95 eV (lying below the bright S_h^l state in their calculation) is likely due to an intruder state problem, as discussed by Zeng, Hoffmann, and Ananth.[26] The latter authors determined the D state's energy at 2.63 eV, which is much closer to our computed value of 2.94 eV.

As a general trend, the C–C bonds perpendicular to the main molecular axis shorten upon electronic excitation (see Sec. S1.4 of the supplementary material). In the S_1 state, the C–C bonds at angles of ±60° with respect to this axis widen in the central ring while elongations and shortenings alternate in the neighboring rings. These atomic displacements clearly shape the first absorption band of pentacene (see below). Similar trends are seen for excitation to the T_1 state. Because the high-spin coupled electrons in the open shells tend to avoid each other, the shift in electron density away from the center toward the terminal rings is more pronounced in comparison to S_1, thus resulting in stronger C–C bond elongations in the central ring. The Q_1 state is dominated by a double excitation involving the HOMO-1, HOMO, LUMO, and LUMO+1 orbitals (see Table I). Here, the Fermi correlation effect on the molecular geometry is even more pronounced than in the triplet states. As a consequence, its minimum nuclear arrangement shows extreme deformations of the terminal rings with displacements of the carbon centers by up to ±5.4 pm.

The Franck–Condon (FC) spectrum of the $S_0 \rightarrow S_1$ absorption in the gas phase (Fig. 3) is dominated by a C–C stretch mode of the pentacene core with a progression of 1495 cm^{-1}, which fits the experimental results of 1514 cm^{-1} measured in a Ne matrix[85] very well. The second clearly visible structure peaking at 756 cm^{-1} to the blue-side of the 0–0 maximum matches the structure found by the authors of the work of Halasinski *et al.*[85] at 734 cm^{-1}. It is assigned to a C–C concertina-like motion with a computed energy of 772 cm^{-1} in the electronic ground state. The shoulder at about 1200 cm^{-1} can be attributed to the A_g in-plane C–H bending vibration, which was measured by the same authors[85] at 1181 cm^{-1} and in the work of He *et al.*[86] at 1177 cm^{-1} in resonance Raman experiments. We identified it as mode 60 in pentacene. Figure S4 shows vectors of normal modes with a non-negligible dimensionless displacement in the Duschinsky transformation.

Before turning our attention to the pentacene dimers and the trimer, we want to present ZFS parameters of the T_1 state of

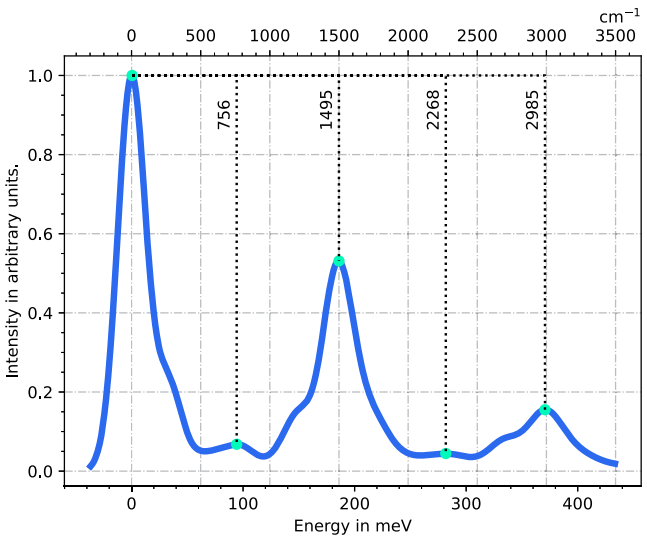

FIG. 3. Simulated Franck–Condon spectrum of the $S_0 \rightarrow S_1$ absorption of pentacene for a temperature of 10 K. Peak maxima are marked by green dots and their distances to the maximum of the largest peak are given in cm^{-1}. The correlation function was damped with a Gaussian of 100 cm^{-1} full width at half maximum before Fourier transformation. The numerical integration was performed for a time interval of 3000 fs and 262 144 grid points.

TABLE II. Comparison of calculated zero-field splitting parameters D_T and E_T of the T_1 state of monomeric pentacene at the optimized T_1 geometry with literature values. All values are given in cm^{-1}.

	This work	Other calculations				Experiments	
D_T	0.032 126	0.0303[a]	0.0305[b]	0.0600[c]	0.0327[d]	0.046 510[e]	0.046 519[f]
E_T	0.001 237	0.0111[a]	0.0079[b]	−0.0042[c]	−0.0008[d]	0.001 823[e]	0.001 778[f]

[a]ROHF@TZVPP.[61]
[b]ROHF@DZP.[87]
[c]DDCI@TZVPP.[61]
[d]DFT/MRCI(original)@def2-SV(P).[61]
[e]Pulsed EPR free induction decay (FID) after laser excitation of pentacene-h_{14} in benzoic acid.[88]
[f]Pulsed EPR free induction decay (FID) after laser excitation of pentacene-h_{14} in *p*-terphenyl crystals.[88]

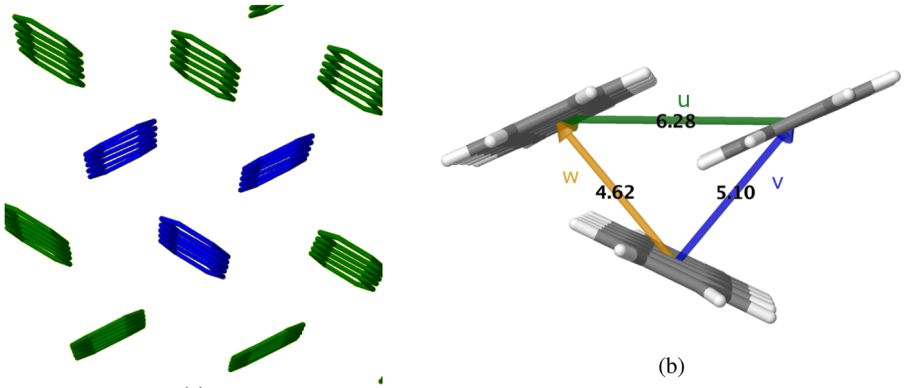

FIG. 4. (a) Herringbone structure of the pentacene crystal. The trimer is marked in blue. (b) Definition of the dimer interaction patterns **u**, **v**, and **w**. The distances between the molecular centroids are given in Å.

the monomer computed with a newly developed OpenMP parallel version of our group's spin–spin coupling program, employing DFT/MRCI(R2022) vectors.

In the absence of an external field, the triplet spin of a nonlinear molecule is quantized in the direction of the principal axes of the spin–spin dipolar tensor **x**, **y**, **z**. In D_{2h}-symmetric molecules, these axes coincide with the C_2 symmetry axes of the point group. The model spin Hamiltonian in a zero field can then be written as[66]

$$\hat{\mathcal{H}}_{SS} = -\left(X\hat{\mathcal{S}}_x^2 + Y\hat{\mathcal{S}}_y^2 + Z\hat{\mathcal{S}}_z^2\right), \tag{1}$$

where X, Y, and Z are the energies of the triplet sublevels arising from the ZFS. For the triplet ZFS parameters, one then obtains

$$D_T = \frac{1}{2}(X+Y) - Z = -\frac{3}{2}Z, \tag{2}$$

$$E_T = \frac{1}{2}(Y-X). \tag{3}$$

As can be seen from Table II, the agreement of the computed and experimental values is very good. Especially, the better agreement of the E_T value compared to the value computed with the original Hamiltonian is noteworthy. Second-order SOC contributions to the ZFS were found to be negligible.

B. Trimer and dimer subpatterns

In the crystalline phase, the pentacene molecules are arranged in a herringbone structure [Fig. 4(a)]. The authors of the work of Nagami *et al.*[89] identified three distinct interaction patterns, **u**, **v**, and **w**, in dimer subsets of herringbone pentacene structures [Fig. 4(b)].

1. Geometries and binding energies

The S_0 interaction energies of the respective subpatterns at the optimized ground state are given in Table III. Each value was computed as the difference between twice (or three times) the S_0 energy of a monomer in the crystalline environment E_{mon} and the S_0 state energy of the subpattern E_{pat}, i.e., $E_{int} = n \times E_{mon} - E_{pat}$, where $n = 2$ (dimers) or $n = 3$ (trimer). While the interaction energies

TABLE III. Ground state interaction energy E_{int} of the subpatterns in the crystal. All values in eV.

Pattern	Trimer	u	v	w
Geometry				
S_0	−0.55	0.14	−0.16	−0.23

of the **v** and **w** patterns are fairly similar, the **u** energy differs substantially. Furthermore, it is noteworthy that the interaction energy of the trimer differs from the sum of the pair interaction energies. The positive, i.e., repulsive interaction of the monomers in the **u**-pattern at the ground state geometry may be traced back to the slip-stacked orientation of the monomeric units and the electrostatic repulsion of their negatively charged π-electron systems. The attractive interactions of the **v** and **w** subpatterns are readily explained with a small overlap of the π-systems of the subunits and the proximity between the negatively charged π-electron cloud of one pentacene and the partially positive hydrogen atoms of the other, as can be seen exemplarily from the highest occupied molecular orbitals at the respective nuclear arrangements (Fig. 5). Illustrations of other molecular orbitals can be found in Figs. S7, S10, and S14.

A view along the long and short molecular axes of a reference pentacene (Fig. 6) reveals why the interaction energy is somewhat larger in the **w** than in the **v** pattern. The onset of the long axes in the **v** subpattern is slightly shifted with respect to the onset of the reference long axis, while the onsets of the long axes in the **w** configuration are almost congruent, leading to a larger interaction surface in the **w** pattern.

Comparing the electronic structures of the **u**-dimer at the ground, S_1, T_1, and Q_1 state minima, we notice that the MOs localize on the individual pentacenes in the S_1 and T_1 minimum nuclear arrangements (Fig. 7). Nevertheless, the excitation is delocalized over both pentacene molecules in the bright singlet state. The unidirectional polarization of the transition dipoles [Fig. 8(a)] effectuates a reduction of the monomer repulsion energy and leads to a slight decrease in the intermolecular separation between the slip-stacked units (see Sec. II B). C–C bond elongations and shortenings in the individual pentacene units follow the same pattern as in the monomer S_1 state, but they are less pronounced. In the T_1 state, the excitation localizes on one of the pentacene molecules while the other acts as a spectator. The C–C bond length alterations in the Q_1 state of the **u**-dimer are indicative of a high-spin coupled triplet excitation on two adjacent pentacene units, hence featuring less drastic atomic displacements than the Q_1 state of the monomer and a similar distortion pattern as in the T_1 state in both units. The intermolecular separation of the pentacenes at the T_1 and Q_1 minima is nearly unaltered with respect to the electronic ground state configuration. Similar trends are observed for the geometry changes upon electronic excitation of the **v**- and **w**-dimers, but the trend of the exciton to localize or delocalize is less distinctive here.

2. Absorption in the Franck–Condon region

Investigating the transition densities of the lowest bright singlet excitation of the dimers at their ground state geometries (Fig. 8), we find short-axis transitions on the individual subunits, in agreement with expectations. Accordingly, the lowest transition in the full trimer is a combination of short-axis transitions on the three monomers, as shown in Fig. 8(d). Although the transitions have similar characters, their oscillator strengths f vary significantly among the different subpatterns (Table IV). Comparing with the oscillator strength of the monomer $S_0 \rightarrow S_h^l$ transition (Table I), it is clear that the subunits do not behave independently. While the oscillator strength of the first bright transition almost triples in the **u**-pattern, it decreases in the **w** and **v** patterns, respectively.

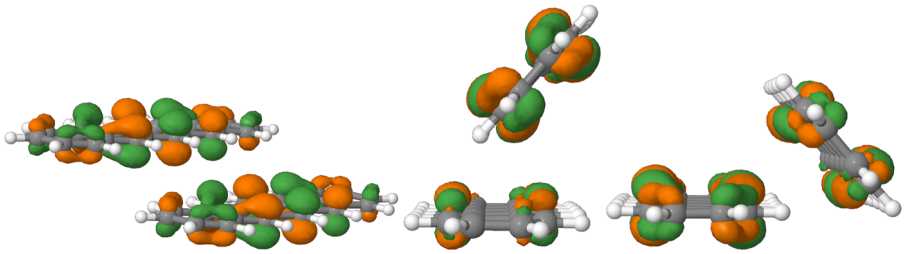

(a) HOMO **u** (b) HOMO **v** (c) HOMO **w**

FIG. 5. The highest occupied molecular orbital of the subpatterns at their respective optimized ground state geometries. Isosurfaces were plotted with an absolute cutoff of 0.03.

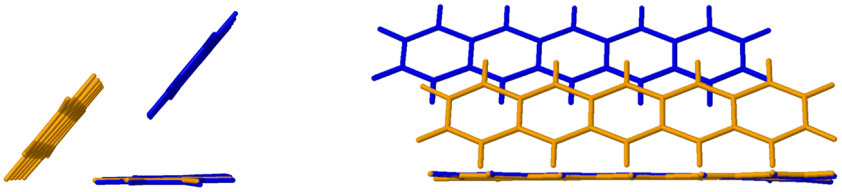

(a) View along the long molecular axis (b) View along the short molecular axis

FIG. 6. Views along the (a) long and (b) short molecular axes of a reference pentacene in a trimer. The **v**-dimer is drawn in blue, the **w**-dimer in gold.

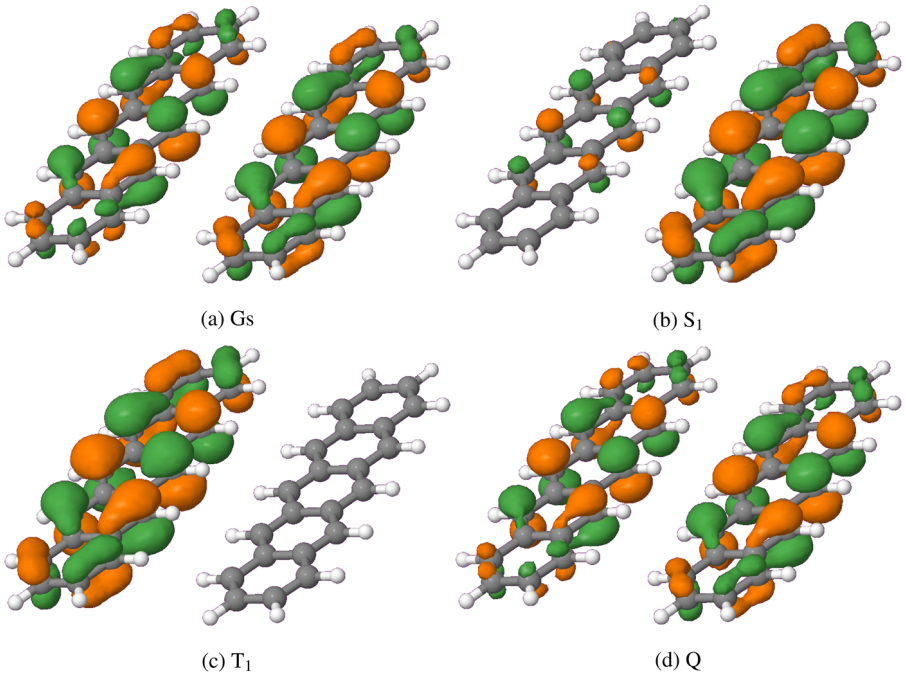

FIG. 7. Highest occupied molecular orbital at different optimized geometries of the **u** subpattern. Isosurfaces were plotted with a cutoff of 0.03.

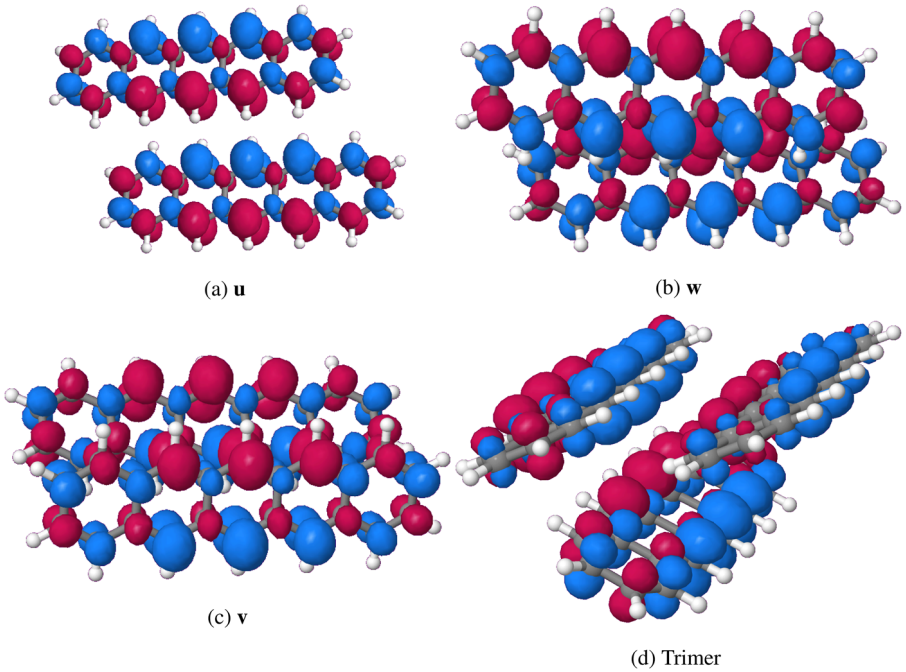

FIG. 8. Plots of the transition densities of the $S_0 \rightarrow S_h^l$ transition at the ground state geometries of the **u**, **v**, and **w** subpatterns and the trimer.

TABLE IV. Vertical energies at the respective geometries $E_{vert.}$, adiabatic energies $E_{ad.}$, oscillator strength f, and characterization of the singlet excited states with an oscillator strength larger than 0.05. All energies in eV. States are characterized as delocalized (DL), locally excited (LE), charge-resonance (CR), or charge transfer (CT) excitation.

Subpattern	u		v			w			Trimer			
Exc. state no.	1	2	1	1	2	1	1	2	1	3	1	5
At geometry	S_0	S_1	S_0	S_1		S_0	S_1		S_0		S_1	
$E_{vert.}$	2.31	2.14	2.25	2.02	2.09	2.21	1.99	2.07	2.24	2.37	2.14	2.44
f	0.2733	0.2486	0.1708	0.0533	0.1042	0.1664	0.0779	0.0732	0.2414	0.0921	0.1694	0.1599
Character	DL	LE + CR	CT + LE	CT	CT + LE	CT	CT	CT + LE	$(DL + CR)_{\mathbf{w}}$	$DL_{\mathbf{v}} + CT_{A\to\mathbf{v}}$	$(CT + LE)_{\mathbf{w}}$	$LE_B + CT_{C\to B}$
Assignment	$S^{l_{+1};l}_{h_{-1};h}$	$S^{l;l;l_{+1}}_{h;h_{-1};}$	S^{l}_{h}	S^{l}_{h}	$S^{l;l_{+1}}_{h;h_{-1}}$	S^{l}_{h}	S^{l}_{h}	$S^{l}_{h;h_{-1}}/N^{l}_{h}$	S^{l}_{h}	$S^{l_{+1};l}_{h_{-1};h;h_{-2}}$	S^{l}_{h}	$S^{l_{+1};l_{+2}}_{h_{-1};h}$

In the **u**-dimer, the subunits obviously form a J-type aggregate with singlet excitation energies of 2.31 and 2.37 eV, respectively, at the ground state geometry compared to 2.34 eV for the monomer in the crystal environment. The transition dipoles of the lower of the Davydov-split excitonic states lie parallel and hence increase the transition strength whereas they are antiparallel in the upper one and nearly cancel. As is evident from Table IV and Fig. 8, the transition dipoles of the $S_0 \rightarrow S_1$ excitations form acute angles in the **v** and **w** substructures, thus leading to a mild increase in the oscillator strength compared to the S^l_h monomer absorption. The obtuse angle of the $S_0 \rightarrow S_2$ transition dipoles does not lead to a complete cancellation but a significant reduction of the electric dipole oscillator strength. In the trimer, the first bright absorption mainly involves local excitations on the A and C building blocks [Fig. 8(d)]. The situation therefore resembles the picture in the **w** subpattern. However, smaller contributions from an L_a-type transition on the B building block add to the transition dipole vector and enhance the oscillator strength compared to **w**. The $S_0 \rightarrow S_2$ transition of the trimer

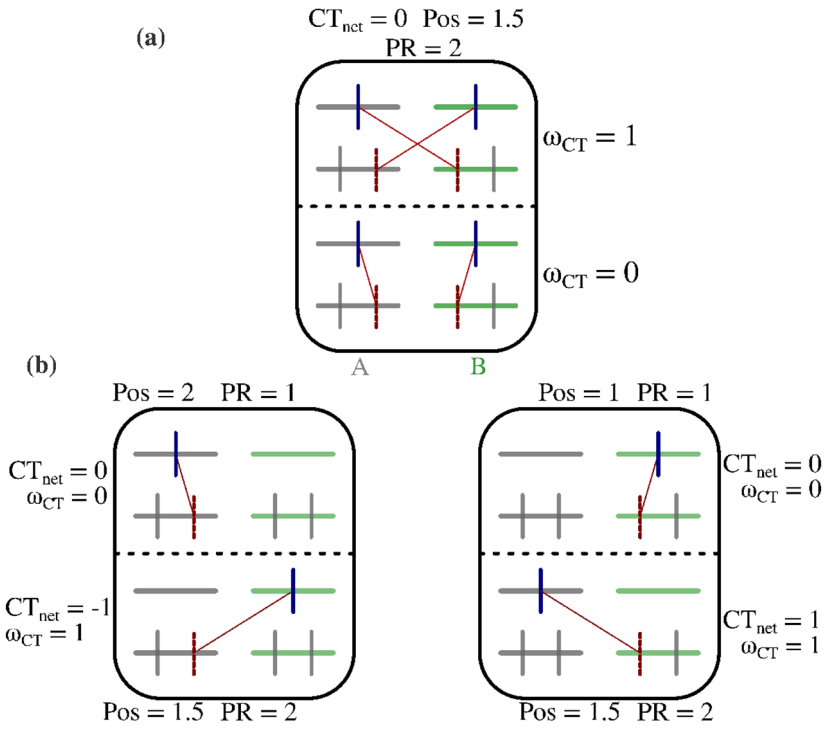

FIG. 9. Types of single excitations on two predefined fragments A and B and the resulting descriptors. Red vertical lines depict holes, blue vertical lines electrons. Red connectors symbolize the direction of the excitation. Part (a) shows the usefulness of the ω_{CT} value if one needs to distinguish a charge-resonance configuration (upper panel) from an excitonic-resonance state (lower panel). Part (b) shows the idealized cases of pure local (upper panels) vs pure charge transfer excitations (lower panel) on the respective fragments.

(Fig. S30) resembles the corresponding transition of the **u**-dimer at the ground state geometry where the transition dipoles largely cancel. The transition dipole vector of the $S_0 \rightarrow S_3$ trimer excitation can be thought of as a positive linear combination of the individual vectors on the parallel A and B units, diminished by the transition vector of the C building block forming an obtuse angle with the former two.

3. Emission/photoexcitation decay

Due the pronounced multiconfiguration character of the excited state wavefunctions, an analysis based on the hole (donor) and particle (acceptor) MOs involved in the transition is elusive. First, we computed the difference densities[90] with respect to the ground state density, but this diagnostic is not suitable in all cases. For example, it does not allow us to distinguish a charge resonance (CR) transition, i.e., two simultaneous CT excitations from fragment 1 to fragment 2 and from fragment 2 to fragment 1, from two local excitations (LEs) on the fragments. To further characterize the states, we employed additional descriptors deduced from a fragment analysis of the one-particle transition density matrix (1-TDM).[56,91–93] A full list of the computed descriptors can be found in Tables S4–S6 for selected states. The most important ones for our interpretation of the electronic structures are the Frobenius norm Ω of the 1-TDM, the signed net charge transfer length CT_{net}, the CT-ratio ω_{CT}, the mean position of the electron–hole pair (exciton), Pos., and the participation ratio of the individual fragments, PR. The Frobenius norm Ω is a measure of the single excitation character of the transition and can vary between 0 (pure double and higher excitations) and 1 (pure single excitation). A value of $CT_{net} = 0$ in combination with $\omega_{CT} = 0$ means that no charge displacement took place upon excitation whereas $CT_{net} = 0$ in combination with $\omega_{CT} \gg 0$ indicates a charge resonance. A value of $CT_{net} = 1$ would imply a transfer of one electron from fragment 1 to fragment 2, a value of $CT_{net} = -1$ a transfer in the opposite direction. Pos. contains information about the final mean position of the particle and the initial mean position of the hole. The PR value measures how many fragments are involved in the transition. Detailed explanations of the

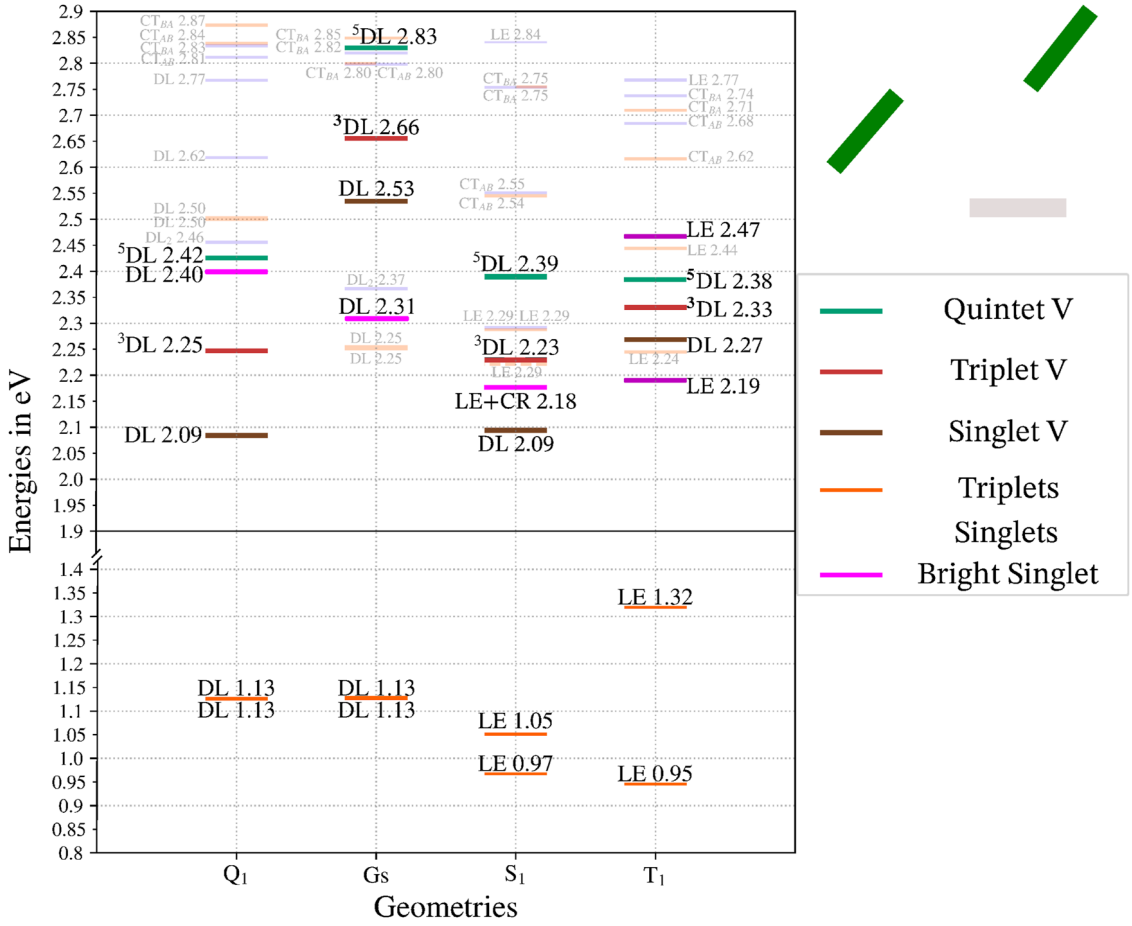

FIG. 10. Energy level scheme of the **u** subpattern. In the upper right corner, the position of the **u**-dimer within the trimer is indicated by thick green bars. All energies are given in eV and are calculated with respect to the ground state energy of this subpattern. States are characterized as either delocalized (DL), locally excited (LE), charge-resonance (CR), or as a charge transfer (CT) excitation.

mentioned quantities can be found in Refs. 56 and 91–93. To exemplify the usefulness of these descriptors, especially in the case of delocalized orbitals, we sketched possible situations for two fragments in Fig. 9.

a. Bright state. Although the MOs localize at the TDDFT-optimized S_1 geometry of the **u**-dimer (Fig. 7), the net charge transfer (−0.025) is very small in the bright state and the excitation remains delocalized over both units. Correspondingly, the oscillator strength remains high. With an interlayer spacing of >6 Å, the interaction between the two pentacenes in the **u**-dimer is significantly smaller (computed Davydov splitting of the $S^{l;l+1}_{h-1;h}$ excitation 0.06/0.11 eV at the S_0/S_1 geometry) than in films with more than 10% pentacence concentration where an interlayer spacing of ≈3.5 Å was assumed.[19] Note, however, that a state with predominant double excitation character forms the lowest excited singlet state at the optimized $S^{l;l+1}_{h-1;h}$ geometry according to the DFT/MRCI calculations (Fig. 10). The nonequivalence of the two pentacene subunits at this geometry is evident from the energetic splitting of the corresponding triplet states, which is small [$\Delta E(T_2 - T_1) = 0.08$ eV] at this nuclear arrangement.

For the **v** pattern, the bright singlet excited state S^l_h contains minor CT contributions in addition to local or charge resonance configurations, as indicated by the difference density plotted in Fig. 14(c) as well as the CT_{net} and ω_{CT} descriptors in Table S4. At the TDDFT-optimized S_1 geometry, we find a noticeable increase in the CT character for the S^l_h state as well as a mixing with the second excited state, which itself consists of ≈22% doubly excited configurations. Out of these double excitations, 16% are of type $N^l_h/N^l_{h_{-1}}$, while the remaining 6% can be attributed to the $V^{l;l_{+1}}_{h;h_{-1}}$ configuration. This admixture is also seen clearly in the diagnostics. The PR drops from 1.928 at the S_0 geometry to 1.450 at the S_1 geometry while the CT_{net} greatly increases. The Frobenius norm Ω of the first excited singlet state value drops from 0.880 at the ground state geometry, indicating a dominantly single excitation character in the FC region, to 0.501 at the relaxed S^l_h geometry. Concomitantly, the oscillator strength is reduced from 0.1708 to 0.0533. The largest oscillator strength (0.1042) is found for the S_2 wavefunction at the S_1 minimum geometry. Similar trends are observed for the **w** pattern, but the single excitation character

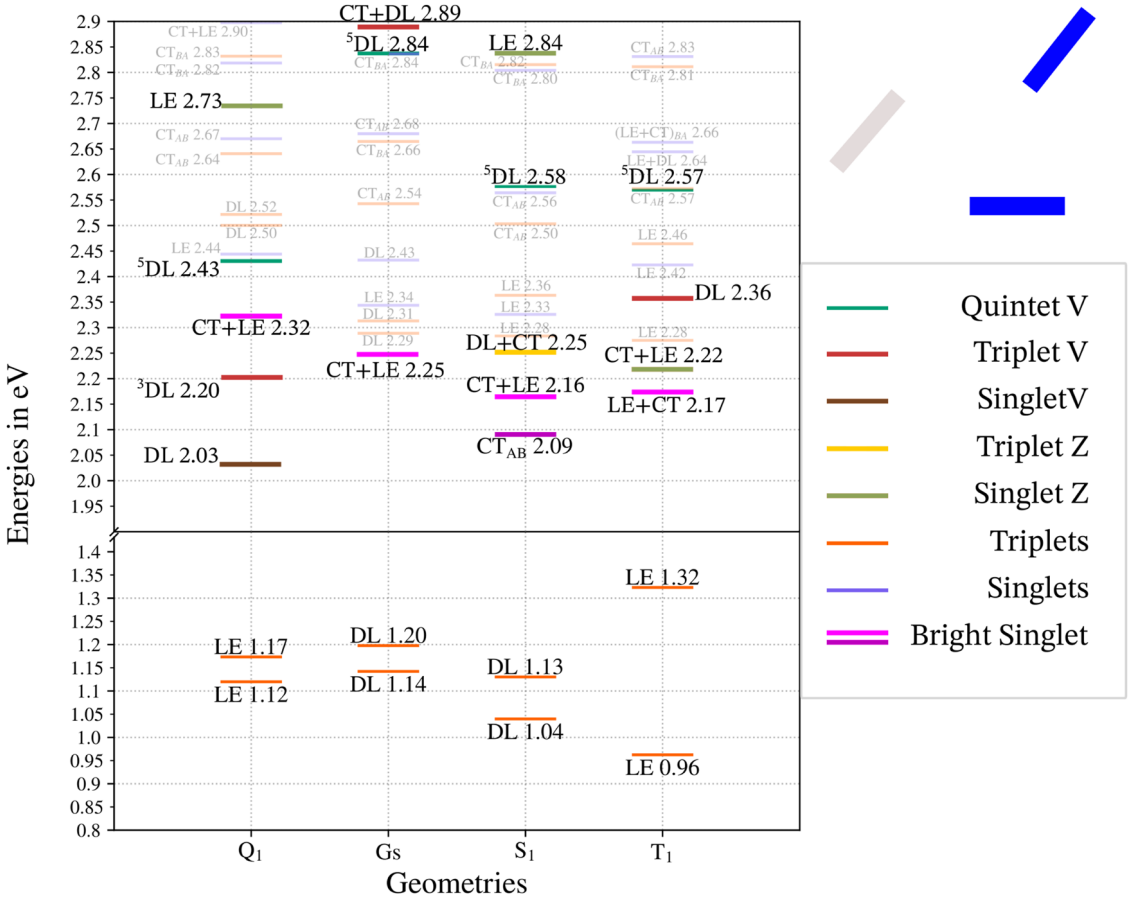

FIG. 11. Energy level scheme of the **v** subpattern. In the upper right corner, the position of the **v**-dimer within the trimer is indicated by thick blue bars. All energies are given in eV and are calculated with respect to the ground state energy of this subpattern.

remains dominant in the lowest excited singlet state, as exemplified by an Ω value of 0.631 and an oscillator strength of 0.0779 (Table S4). In this case, the second excited singlet state carries more double excitation character. The S_1 state of the trimer is also the brightest among the low-lying excited singlet states. At the S_1 geometry, it mainly involves the A and C units, similar to the **w** subpattern, and may be characterized as CT + LE. This state localizes on the C unit at the optimized T_1 geometry without changing the adiabatic excitation energy significantly. In all considered cases, the adiabatic excitation energy of the brightest singlet state ($E_{ad.dimer,trimer} \approx 2.15$ eV) (cp. Figs. 10–13) is somewhat lower than the corresponding monomer energy ($E_{ad.mono} = 2.21$ eV), i.e., the S_h^l state is stabilized by the delocalization of the excitation.

b. Doubly excited singlet state. As already mentioned, a singlet composed predominantly of double substitutions in the HOMO-1, HOMO, LUMO, and LUMO+1, as shown in Table V, becomes the lowest singlet state at the S_1 geometry of the **u**-dimer. We associate this state with the singlet entangled bi-triplet exciton. This state is of utmost importance for the fission of the singlet exciton to independent triplets as it shares the same spatial occupation as two antiferromagnetically coupled triplet states. At first sight, the S_h^l state does not mix with this doubly excited state in the **u**-dimer, neither at the S_0 nor at the S_1 geometry. Note, however, that a conical intersection between the optically bright and the dark multiexcitonic singlet state must occur on the pathway between the absorption region and the minimum of S_h^l state (Fig. 10), thus providing the strong electronic coupling between the two singlet states that is required for a coherent mechanism as postulated in the work of Chan *et al.*[11] Figure 14(d) suggests that the excitation is completely delocalized over the two adjacent pentacene units in the dark state. However, the PR of 1.751 and the Frobenius norm of 0.348 indicate the participation of further configurations at the S_1 geometry. Remembering that the MO pairs HOMO/LUMO+1 and HOMO-1/LUMO of the **u**-dimer are mainly localized on one of the pentacene building units at the S_1 geometry, it is evident that the configurations number 3–7

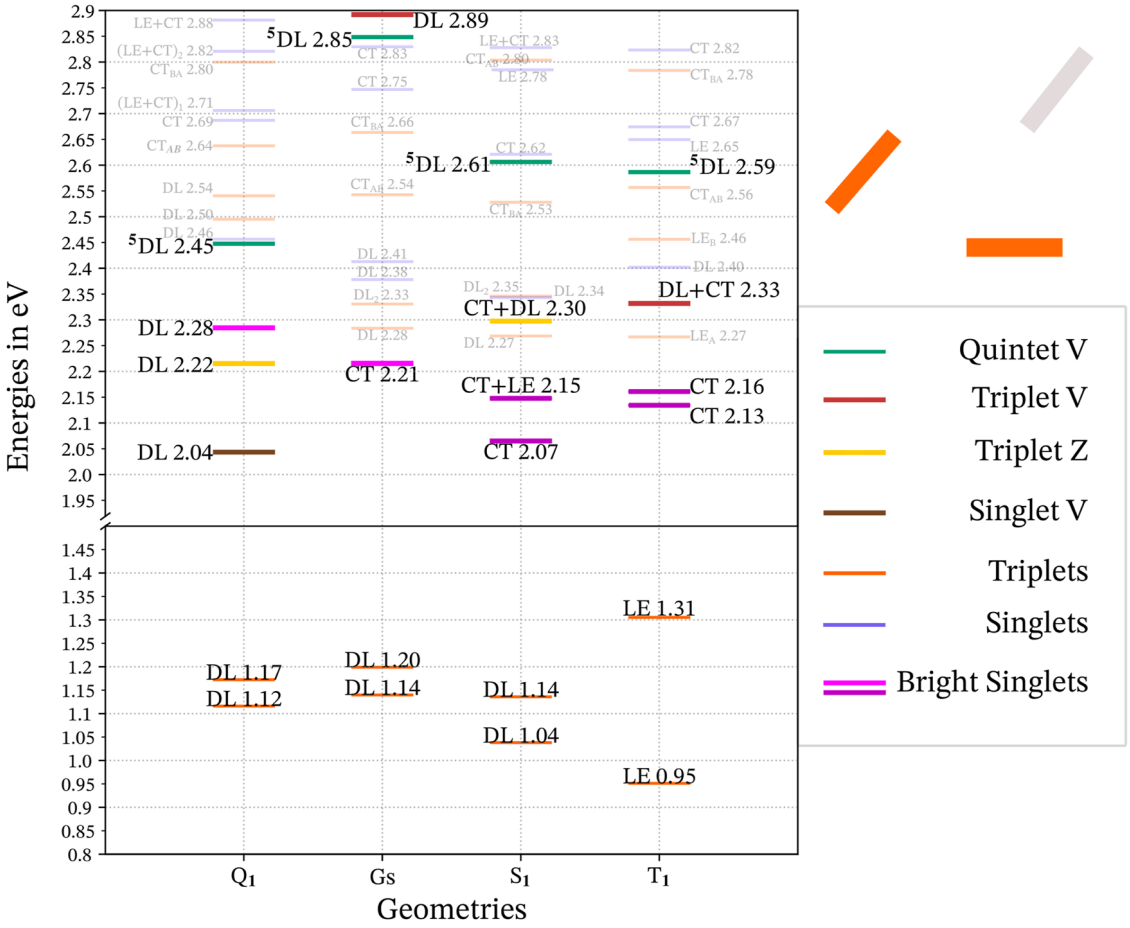

FIG. 12. Energy level scheme of the **w** subpattern. In the upper right corner, the position of the **w**-dimer within the trimer is indicated by thick orange bars. All energies are given in eV and are calculated with respect to the ground state energy of this subpattern. States are characterized as delocalized (DL), locally excited (LE), charge-resonance (CR), or as a charge transfer (CT) excitation.

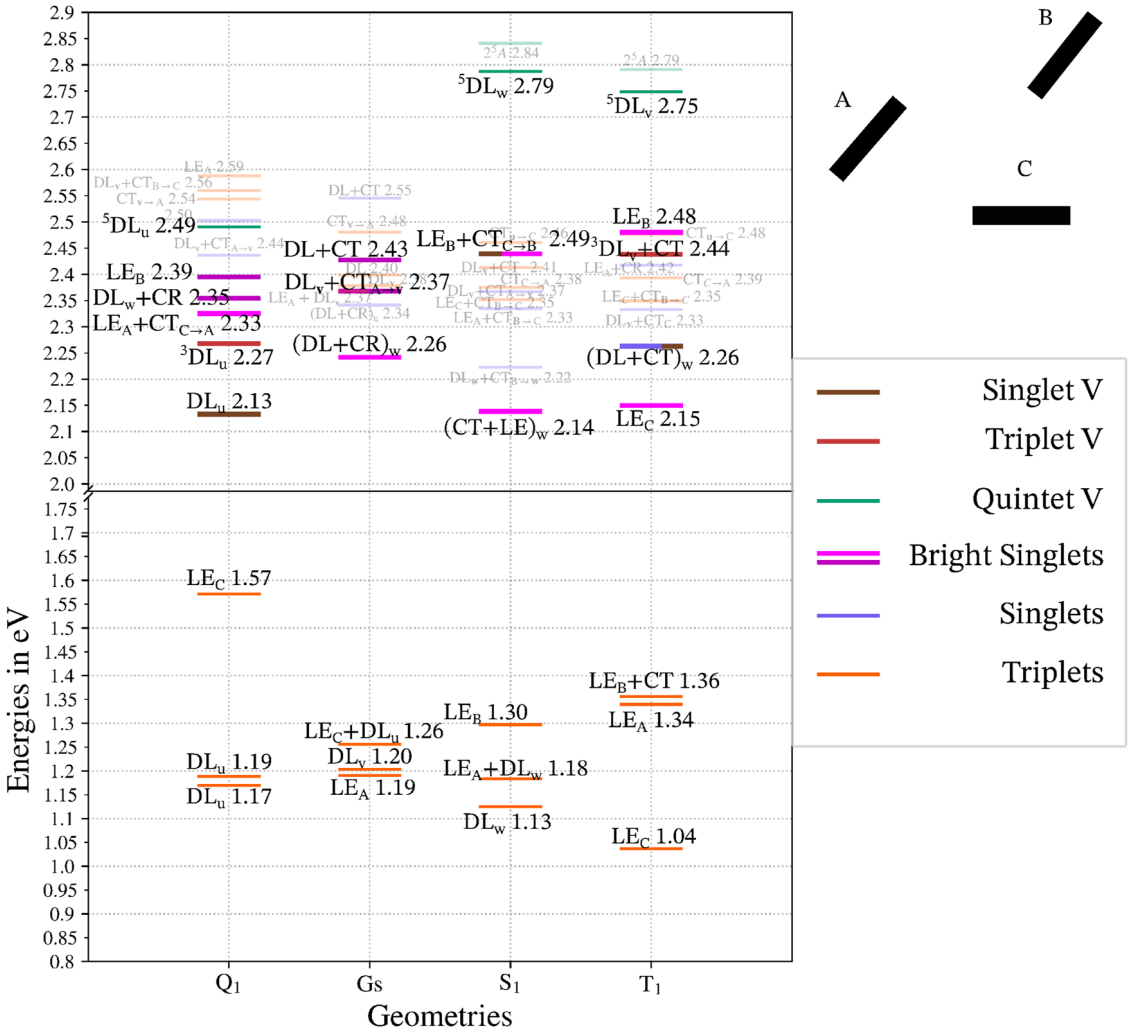

FIG. 13. Energy level scheme of the trimer. The position of the monomers A, B, and C within the trimer is indicated in the upper right corner. All energies are given in eV and are calculated with respect to the ground state energy. States are characterized as delocalized (DL), locally excited (LE), charge-resonance (CR) character, or as a charge transfer (CT) excitation.

in Table V all have an ionic component, i.e., are of CT or CR type, respectively. The CT_{net} value is found to be −0.377 at this geometry.

At the Q_1 geometry, which corresponds to the minimum of two ferromagnetically coupled triplet states and is our closest proxy for the minimum of the singlet-coupled triplet pair state, ^{1}(TT), the Ω value reduces to 0.018 as ought to be expected for a dominantly doubly excited state. With a value of 1.995, the PR is close to its maximum (2.0) for a completely delocalized dimer state and the net CT reduces to 0.050. Interestingly, the adiabatic energy of the ^{1}(TT) state (2.09 eV) hardly changes when moving from the S_1 to the Q_1 geometry.

Considering the already discussed CT states at the **v** and **w** patterns, we find noteworthy admixtures of the $V^{l,l+1}_{h-1;h}$ configuration and a double excitation of type N^l_h (Table V). These findings support the experimental results presented in the work of Neef *et al.*,[16] which point toward a CT-mediated mechanism with a hybridization of Frenkel and CT states in the primary step of the SF process in single-crystal pentacene.

In the trimer, the optically bright singlet state and the ^{1}(TT) state are adiabatically degenerate, but they localize on different subpatterns. As described above, the bright state is dominated by excitations on the A and C units [Fig. 14(h)], thus resembling the excitation of the **w**-dimer. Its minimum geometry appears to be unfavorable for the triplet pair states (Fig. 13). The first singlet state with noteworthy contributions from $V^{l,l+1}_{h-1;h}$ configurations is S_5 with an energy of 2.49 eV at this geometry. In contrast, the ^{1}(TT) forms the lowest excited state at the Q_1 geometry [Fig. 14(i)] where the excitation is delocalized over the A and B units, just like in the case of the **u**-dimer.

TABLE V. Composition, label, adiabatic energy $E_{ad.}$ (eV), coefficient, and weight in the CI vector of the lowest state with a double excitation character larger than 10% at the optimized S_1 geometry. The place in the energetic order is also given.

Subpattern	Order	$E_{ad.}$	No.	CSF	Composition	Coeff.	Weight	Label
u	1	2.09	1	1	$(h_{-1})^1(h)^1(l)^1(l_{+1})^1$	−0.3750	14.1	$\mathbf{V}^{l;l_{+1}}_{h_{-1};h}$
			2	2	$(h_{-1})^1(h)^1(l)^1(l_{+1})^1$	0.3654	13.3	$\mathbf{V}^{l;l_{+1}}_{h_{-1};h}$
			3	1	$(h)^0(l)^1(l_{+1})^1$	−0.3213	10.3	$\mathrm{Z}^{l;l_{+1}}_{h}$
			4	1	$(h_{-1})^1(h)^1(l)^2$	0.3097	9.6	$\mathrm{Z}^{l}_{h_{-1};h}$
			5	1	$(h_{-1})^0(l)^1(l_{+1})^1$	0.2729	7.4	$\mathrm{Z}^{l;l_{+1}}_{h_{-1}}$
			6	1	$(h)^0(l)^2$	−0.2596	6.7	N^{l}_{h}
			7	1	$(h_{-1})^1(h)^1(l_{+1})^2$	−0.2447	6.0	$\mathrm{Z}^{l}_{h;h_{-1}}$
			8	1	$(h)^1(l)^1$	0.1809	3.3	S^{l}_{h}
v	1	2.09	1	1	$(h)^1(l)^1$	0.6521	42.5	S^{l}_{h}
			2	1	$(h)^0(l)^2$	−0.3080	9.5	N^{l}_{h}
			3	1	$(h_{-1})^1(h)^1(l)^1(l_{+1})^1$	0.2410	5.8	$\mathbf{V}^{l;l_{+1}}_{h_{-1};h}$
			4	1	$(h_{-1})^1(l)^1$	−0.2026	4.1	$\mathrm{S}^{l}_{h_{-1}}$
w	1	2.07	1	1	$(h)^1(l)^1$	−0.7532	56.7	S^{l}_{h}
			2	1	$(h)^0(l)^2$	−0.2861	8.2	N^{l}_{h}
			3	1	$(h_{-1})^1(h)^1(l)^1(l_{+1})^1$	−0.1908	3.6	$\mathbf{V}^{l;l_{+1}}_{h_{-1};h}$
Trimer	2	2.22	1	1	$(h)^1(l)^1$	0.5677	32.2	$\mathrm{S}^{l_{+1}}_{h}$
			2	1	$(h)^0(l)^2$	−0.2966	8.8	N^{l}_{h}
			3	1	$(h)^1(l)^1$	0.2206	4.9	$\mathbf{S}^{l}_{h}$

c. Triplet states. The two lowest states in the triplet manifold, T^{l}_{h} and $\mathrm{T}^{l;l_{+1}}_{h_{-1};h}$, exhibit negligible CT character (Table S6). Energetically, they are almost degenerate at the ground state and the quintet geometries in all subpatterns and the excitations are delocalized. At the minimum geometries of the bright singlet states, the energetic splitting between the T_1 and T_2 states is still small, ranging from 0.08 eV in the **u**-dimer to 0.10 eV in the **w**-dimer as can be seen from the energy level plots shown in Figs. 10–12. More importantly, however, the requirement for an exothermal SF process, namely that the energy of the optically bright singlet state is larger than the sum of the two triplet energies, is fulfilled for the **u**-dimer. For the other two dimers, this process is slightly endothermic according to our calculations. In the **u**-dimer, the exothermicity of the SF holds true even for the multiexcitonic singlet state, i.e., $E(^1(\mathrm{TT})) > E(\mathrm{T}_1) + E(\mathrm{T}_2)$.

Upon geometry relaxation, the triplet excitations localize, as is evident from the energy schemes in Figs. 10–12 and the descriptors in Table S6. The adiabatic T_1 dimer excitation energy ($E_{ad.dimer} \approx 0.95$ eV) is somewhat higher than the corresponding monomer value ($E_{ad.mono} = 0.89$ eV) in the crystal surrounding. This might have technical reasons caused by slightly different effective configuration selection thresholds in the DFT/MRCI runs of the monomer and the dimers, but we note that the trend is opposite to what is found for the bright singlet. In the **u**-dimer, the T_1 is represented by a LE on fragment 1, i.e., the A unit. While the localization has a minor stabilization effect on T_1 with respect to the S_1 geometry (ΔE = −0.02 eV), it causes a marked upshift of the T_2 excitation energy that localizes on fragment 2, i.e., unit B. The relaxation effect is somewhat larger in the **v** (0.08 eV, LE on B) and **w** patterns (0.09 eV, LE on C), but even in these dimers the sum of the T_1 and T_2 excitation energies is higher than at the relaxed geometry of the bright singlet state (cp. Figs. 10–12). In the trimer, the T_1 excitation localizes on unit C while the T_2 (LE on A) and T_3 (LE on B) states are almost uniformly upshifted. Hence, there seems to be a small driving force for a spatial separation of the two triplet excitons. We did not carry out dynamics simulations, but it appears plausible that the localization promotes the disentanglement of the triplet pair.

Particularly interesting in the context of SF is the energetic location of the triplet analog of the multiexcitonic singlet state, characterized by the $^3\mathrm{V}^{l;l_{+1}}_{h;h_{-1}}$ configuration. At the Q_1 geometries of the **u**- and **v**-dimers and of the trimer, we find a triplet state with this electronic structure in the energetic vicinity of the primary absorption transition. In contrast, a doubly excited triplet state with merely two open shells is observed in the **w**-dimer. Remarkably, the multi-excitonic state of the trimer seems to favor the **u** arrangement in all three possible spin manifolds, i.e., singlet, triplet, and quintet.

d. Quintet states. The quintet manifold allows for a compact discussion, as the situation for every subpattern is clear. A state dominated by a $\mathrm{V}^{l;l_{+1}}_{h_{-1};h}$ spatial configuration constitutes the lowest quintet, as ought to be expected. Adiabatically, it is located between

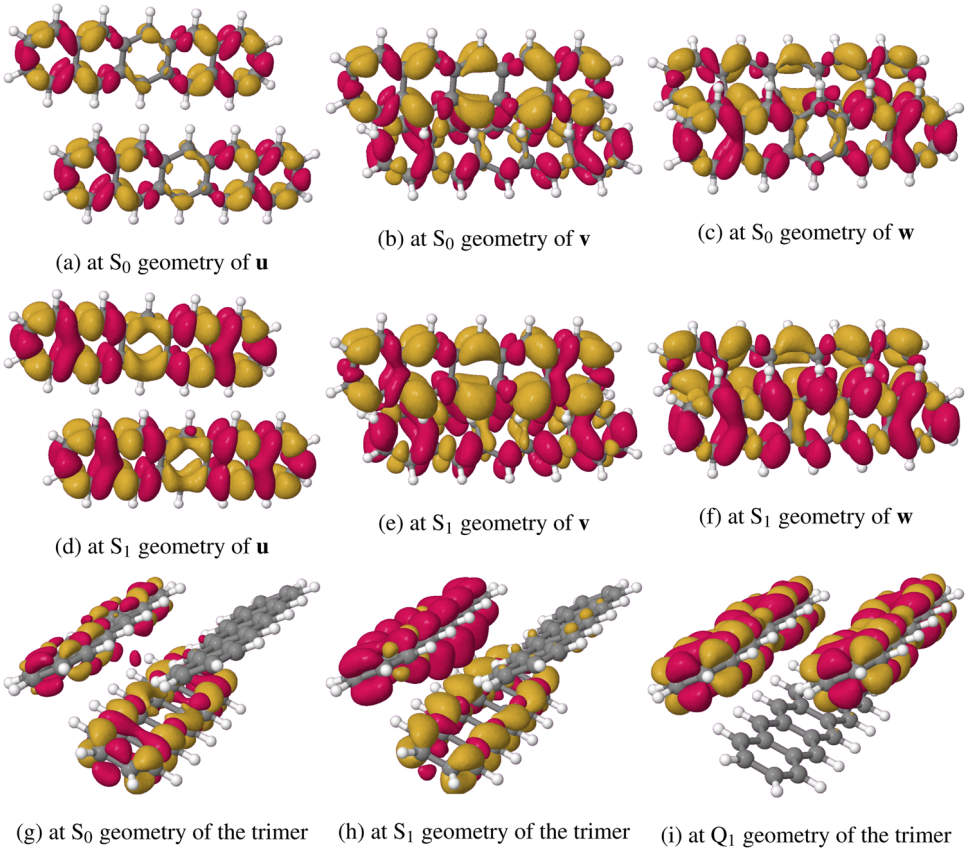

FIG. 14. Difference densities with respect to the ground state density (isovalue 0.0004) for the lowest singlet excited states at different geometries of the subpatterns.

2.42 and 2.45 eV above the electronic ground state in the dimers (Figs. 10–12) and at 2.49 eV in the trimer (Fig. 13). The gap to the next quintet state is larger than 1.1 eV in all investigated cases, ruling out the participation of any other quintet state than the lowest one. A look at the level schemes further reveals that a direct involvement of the Q_1 state in the SF process, as discussed in the work of Lubert-Perquel *et al.*[19] for dilute pentacene films, is unlikely in spatially confined dimers composed of adjacent pentacene molecules. The energy separations of the ^{1}(TT) and ^{5}(TT) states are substantial in the **u**-, **v**-, and **w**-dimers as well as in the trimer. For the **u** subpattern, exhibiting the smallest energy gap (0.31 eV) among the dimers, we explicitly computed the spin–spin coupling matrix elements. In the limiting case of a large electrostatic energy splitting, the couplings between the spin pair functions are expected to be weak, but the spin multiplets split individually due to the fine structure interaction.[65] The computed off-diagonal SSC matrix elements are negligible ($\leq 10^{-6}$ cm^{-1}), indeed, and no singlet–quintet multiplicity mixing is apparent in the perturbed wavefunctions. As the coordinate axes do not coincide with the symmetry axes of the dimer, a transformation of the fine structure tensor to principal axes (x'', y'', z'') is required to express the calculated ZFSs in terms of the effective SSC parameters D_Q and E_Q:[65]

$$\begin{aligned} E(Q_{1z''}) &= 2D_Q\sqrt{1+3E_Q^2/D_Q^2}, & E(Q_{2z''}) &= 2D_Q, \\ E(Q_{x''}) &= -D_Q + 3E_Q, & E(Q_{y''}) &= -D_Q - 3E_Q, \\ E(Q_{x''y''}) &= -2D_Q\sqrt{1+3E_Q^2/D_Q^2}. \end{aligned} \quad (4)$$

Here, $E(Q_{j''})$ denotes the energy of the quintet fine structure level $Q_{j''}$ with respect to the energy of the unperturbed quintet state. Comparing our computed energies of the $^5V^{l;l_{+1}}_{h_{-1};h}$ sublevels with the expressions in Eq. (4), we arrive at ZFS parameters of $V^{l;l_{+1}}_{h_{-1};h}$ of D_Q = 0.009 28 cm^{-1} and E_Q = 0.005 11 cm^{-1}. The ^{3}(TT) state of the **u**-dimer is located energetically about halfway between the ^{1}(TT) and ^{5}(TT) states but does not play a role in the spin multiplicity mixing either. Interestingly, its ZFS parameters (D_{TV} = 0.029 28 cm^{-1}, E_{TV} = 0.002 61 cm^{-1}) have similar magnitudes as those of the monomer T_1 state (Table II) and dimer (D_{T1} = 0.030 67 cm^{-1}, E_{T1} = 0.001 72 cm^{-1}) T_1 states although the excitation is delocalized over both pentacene molecules at the Q_1 geometry.

IV. CONCLUSION

In this work, we performed combined density functional theory and multi-reference configuration interaction (DFT/MRCI)

calculations on the energetics and photophysical properties of the low-lying electronic states of a pentacene monomer, three dimers, and a trimer structure, electrostatically embedded in a crystal surrounding. The quantum chemically treated dimer and trimer models are chosen such that they represent different spatially confined subpatterns of the herringbone crystal structure of pentacene. While the **u**-dimer consists of adjacent, parallelly arranged pentacene molecules, the constituting pentacene units form an acute angle in the **v**- and **w**-dimers. To evaluate the likelihood of a quintet intermediate in the disentanglement of the triplet pair state, electron spin–spin coupling calculations were carried out on the **u**-dimer. The performance of the applied methods was assessed on the pentacene monomer where numerous theoretical and experimental reference values are at hand.

In the **u**-dimer, the optically bright $S^{l;l+1}_{h-1;h}$ and the multiexcitonic ^{1}(TT) states are clearly separated at the ground state and optimized $S^{l;l+1}_{h-1;h}$ geometries. Their wavefunctions show no apparent mixing in the absorption and emission regions, but their energetic order swaps. Hence, a conical intersection between the $S^{l;l+1}_{h-1;h}$ and ^{1}(TT) potential energy surfaces must have occurred upon geometry relaxation of the primarily excited singlet state. In the other dimers and in the trimer, this is not the case. Strong nonadiabatic coupling of the optically bright state and the dark multiexcitonic states close to the absorption region is a prerequisite for a coherent process. Consequently, we postulate that the **u**-pattern plays a fundamental role in the direct SF mechanism. A parallel orientation of the molecules in the spirit of the **u**-pattern is observed in 6,13-bis-(triisopropylsilylethinyl)-pentacene (TIPS-pentacene) crystals that exhibit a brickwork structure[94] and is imaginable in pentacene films and covalently linked pentacene dimers as well. The results of our calculations do not support, however, the involvement of a ferromagnetically coupled triplet pair state in the SF process: The multiexcitonic singlet, triplet, and quintet states on spatially confined dimers, consisting of adjacent pentacene molecules, are energetically too far apart and their off-diagonal spin–spin couplings are too small to bring about a noteworthy multiplicity mixing observed in transient EPR spectroscopies of films with high pentacene concentrations.[19]

A pattern, reminiscent of the **w**-dimer, hosts the lowest excited singlet state in the trimer. Here and in the **w**-dimer, the two lowest excited singlet states are mixtures of $S^{l;l+1}_{h-1;h}$ and ^{1}(TT) configurations. The folded nuclear arrangement of the two pentacene units facilitates CT excitations, which are relatively small in the absorption region but increase markedly upon geometry relaxation in the S_1 state. Excitation of the **w**-dimer therefore supports a CT-mediated SF mechanism with a hybridization of Frenkel and CT states in the primary step of the SF process in pentacene crystals, as postulated in the work of Neef *et al.*[17] on the basis of their time- and angle-resolved photoemission spectroscopy investigations of single-crystal pentacene.

SUPPLEMENTARY MATERIAL

See the supplementary material for more information on molecular orbitals, selected geometry parameters and normal mode displacements, transition densities, difference densities, state descriptors, and wavefunction composition of states with substantial double excitation character.

ACKNOWLEDGMENTS

This research was funded by the Deutsche Forschungsgemeinschaft (DFG, German Research Foundation)—Grant Nos. MA-1051/20-1 and 396890929/GRK 2482. Parts of the calculations were carried out on the central HPC system "HILBERT" at the Heinrich Heine University Düsseldorf.

AUTHOR DECLARATIONS

Conflict of Interest

The authors have no conflicts to disclose.

Author Contributions

Timo Schulz: Conceptualization (lead); Data curation (equal); Software (lead); Visualization (lead); Writing – original draft (lead); Writing – review & editing (supporting). **Simon Hédé**: Data curation (equal); Software (supporting); Visualization (supporting); Writing – original draft (supporting). **Oliver Weingart**: Funding acquisition (supporting); Supervision (supporting). **Christel M. Marian**: Conceptualization (supporting); Funding acquisition (lead); Supervision (lead); Writing – review & editing (lead).

DATA AVAILABILITY

The data that support the findings of this study are available within this article and its supplementary material. Additional data are available from the corresponding author upon reasonable request.

REFERENCES

[1] N. Shah, A. A. Shah, P. K. Leung, S. Khan, K. Sun, X. Zhu, and Q. Liao, Processes **11**, 1852 (2023).
[2] D. N. Congreve, J. Lee, N. J. Thompson, E. Hontz, S. R. Yost, P. D. Reusswig, M. E. Bahlke, S. Reineke, T. Van Voorhis, and M. A. Baldo, Science **340**, 334 (2013).
[3] W. Shockley and H. J. Queisser, J. Appl. Phys. **32**, 510 (1961).
[4] M. C. Hanna and A. J. Nozik, J. Appl. Phys. **100**, 074510 (2006).
[5] D. Casanova, Chem. Rev. **118**, 7164 (2018).
[6] N. Monahan and X.-Y. Zhu, Annu. Rev. Phys. Chem. **66**, 601 (2015).
[7] M. B. Smith and J. Michl, Chem. Rev. **110**, 6891 (2010).
[8] M. B. Smith and J. Michl, Annu. Rev. Phys. Chem. **64**, 361 (2013).
[9] R. D. Pensack, E. E. Ostroumov, A. J. Tilley, S. Mazza, C. Grieco, K. J. Thorley, J. B. Asbury, D. S. Seferos, J. E. Anthony, and G. D. Scholes, J. Phys. Chem. Lett. **7**, 2370 (2016).
[10] C. K. Yong, A. J. Musser, S. L. Bayliss, S. Lukman, H. Tamura, O. Bubnova, R. K. Hallani, A. Meneau, R. Resel, M. Maruyama, S. Hotta, L. M. Herz, D. Beljonne, J. E. Anthony, J. Clark, and H. Sirringhaus, Nat. Commun. **8**, 15953 (2017).
[11] W.-L. Chan, T. C. Berkelbach, M. R. Provorse, N. R. Monahan, J. R. Tritsch, M. S. Hybertsen, D. R. Reichman, J. Gao, and X.-Y. Zhu, Acc. Chem. Res. **46**, 1321 (2013).
[12] S. M. Hart, W. R. Silva, and R. R. Frontiera, Chem. Sci. **9**, 1242 (2018).
[13] T. C. Berkelbach, M. S. Hybertsen, and D. R. Reichman, J. Chem. Phys. **138**, 114102 (2013).

[14]T. C. Berkelbach, M. S. Hybertsen, and D. R. Reichman, J. Chem. Phys. **138**, 114103 (2013).
[15]T. C. Berkelbach, M. S. Hybertsen, and D. R. Reichman, J. Chem. Phys. **141**, 074705 (2014).
[16]A. Neef, S. Beaulieu, S. Hammer, S. Dong, J. Maklar, T. Pincelli, R. P. Xian, M. Wolf, L. Rettig, J. Pflaum, and R. Ernstorfer, Nature **616**, 275 (2023).
[17]A. Neef, M. Rossi, M. Wolf, R. Ernstorfer, and H. Seiler, Phys. Status Solidi A **221**, 2300304 (2024).
[18]M. I. Collins, F. Campaioli, M. J. Tayebjee, J. H. Cole, and D. R. McCamey, Commun. Phys. **6**, 64 (2023).
[19]D. Lubert-Perquel, E. Salvadori, M. Dyson, P. N. Stavrinou, R. Montis, H. Nagashima, Y. Kobori, S. Heutz, and C. W. M. Kay, Nat. Commun. **9**, 4222 (2018).
[20]B. S. Basel, J. Zirzlmeier, C. Hetzer, B. T. Phelan, M. D. Krzyaniak, S. R. Reddy, P. B. Coto, N. E. Horwitz, R. M. Young, F. J. White, F. Hampel, T. Clark, M. Thoss, R. R. Tykwinski, M. R. Wasielewski, and D. M. Guldi, Nat. Commun. **8**, 15171 (2017).
[21]M. J. Y. Tayebjee, S. N. Sanders, E. Kumarasamy, L. M. Campos, M. Y. Sfeir, and D. R. McCamey, Nat. Phys. **13**, 182 (2017).
[22]H. Sakai, R. Inaya, H. Nagashima, S. Nakamura, Y. Kobori, N. V. Tkachenko, and T. Hasobe, J. Phys. Chem. Lett. **9**, 3354 (2018).
[23]P. M. Zimmerman, Z. Zhang, and C. B. Musgrave, Nat. Chem. **2**, 648 (2010).
[24]P. M. Zimmerman, F. Bell, D. Casanova, and M. Head-Gordon, J. Am. Chem. Soc. **133**, 19944 (2011).
[25]P. B. Coto, S. Sharifzadeh, J. B. Neaton, and M. Thoss, J. Chem. Theory Comput. **11**, 147 (2014).
[26]T. Zeng, R. Hoffmann, and N. Ananth, J. Am. Chem. Soc. **136**, 5755 (2014).
[27]P. Petelenz, M. Snamina, and G. Mazur, J. Phys. Chem. C **119**, 14338 (2015).
[28]P. Petelenz and M. Snamina, J. Phys. Chem. C **119**, 28570 (2015).
[29]D. R. Dombrowski, T. Schulz, M. Kleinschmidt, and C. M. Marian, J. Phys. Chem. A **127**, 2011 (2023).
[30]C. M. Marian, A. Heil, and M. Kleinschmidt, Wiley Interdiscip. Rev.: Comput. Mol. Sci. **9**, e1394 (2019).
[31]D. C. A. Valente, M. T. do Casal, M. Barbatti, T. A. Niehaus, A. J. A. Aquino, H. Lischka, and T. M. Cardozo, J. Chem. Phys. **154**, 044306 (2021).
[32]W. Kohn and L. J. Sham, Phys. Rev. **140**, A1133 (1965).
[33]E. Runge and E. K. U. Gross, Phys. Rev. Lett. **52**, 997 (1984).
[34]E. K. U. Gross and W. Kohn, Phys. Rev. Lett. **55**, 2850 (1985).
[35]S. Hirata and M. Head-Gordon, Chem. Phys. Lett. **314**, 291 (1999).
[36]J. P. Perdew and Y. Wang, Phys. Rev. B **45**, 13244 (1992).
[37]J. C. Slater, Phys. Rev. **81**, 385 (1951).
[38]J. P. Perdew, K. Burke, and M. Ernzerhof, Phys. Rev. Lett. **77**, 3865 (1996).
[39]P. A. M. Dirac Proc. R. Soc. London, Ser. A **123**, 714 (1929).
[40]J. P. Perdew, M. Ernzerhof, and K. Burke, J. Chem. Phys. **105**, 9982 (1996).
[41]F. Weigend and R. Ahlrichs, Phys. Chem. Chem. Phys. **7**, 3297 (2005).
[42]S. Grimme, J. Antony, S. Ehrlich, and H. Krieg, J. Chem. Phys. **132**, 154104 (2010).
[43]S. Grimme, S. Ehrlich, and L. Goerigk, J. Comput. Chem. **32**, 1456 (2011).
[44]C. Mattheus, A. Dros, J. Baas, A. Meetsma, J. De Boer, and T. Palstra, "CCDC 170187: Experimental crystal structure determination," Acta Cryst. C **57**, 939 (2001).
[45]P. Giannozzi, S. Baroni, N. Bonini, M. Calandra, R. Car, C. Cavazzoni, D. Ceresoli, G. L. Chiarotti, M. Cococcioni, I. Dabo, A. D. Corso, S. de Gironcoli, S. Fabris, G. Fratesi, R. Gebauer, U. Gerstmann, C. Gougoussis, A. Kokalj, M. Lazzeri, L. Martin-Samos, N. Marzari, F. Mauri, R. Mazzarello, S. Paolini, A. Pasquarello, L. Paulatto, C. Sbraccia, S. Scandolo, G. Sclauzero, A. P. Seitsonen, A. Smogunov, P. Umari, and R. M. Wentzcovitch, J. Phys.: Condens. Matter **21**, 395502 (2009).
[46]A. M. Rappe, K. M. Rabe, E. Kaxiras, and J. D. Joannopoulos, Phys. Rev. B **41**, 1227 (1990).
[47]U. C. Singh and P. A. Kollman, J. Comput. Chem. **5**, 129 (1984).
[48]O. Weingart, A. Nenov, P. Altoè, I. Rivalta, J. Segarra-Martí, I. Dokukina, and M. Garavelli, J. Mol. Model. **24**, 271 (2018).
[49]S. Grimme and M. Waletzke, J. Chem. Phys. **111**, 5645 (1999).
[50]T. Schulz, P. Konieczny, D. R. Dombrowski, S. Metz, C. M. Marian, and R. Weinkauf, Phys. Chem. Chem. Phys. **25**, 29850 (2023).
[51]A. D. Becke, J. Chem. Phys. **98**, 1372 (1993).
[52]A. D. Becke, Phys. Rev. A **38**, 3098 (1988).
[53]C. Lee, W. Yang, and R. G. Parr, Phys. Rev. B **37**, 785 (1988).
[54]TURBOMOLE V7.5.1 2021, a development of University of Karlsruhe and Forschungszentrum Karlsruhe GmbH, 1989–2007, TURBOMOLE GmbH, since 2007; available at https://www.turbomole.org.
[55]S. G. Balasubramani, G. P. Chen, S. Coriani, M. Diedenhofen, M. S. Frank, Y. J. Franzke, F. Furche, R. Grotjahn, M. E. Harding, C. Hättig, A. Hellweg, B. Helmich-Paris, C. Holzer, U. Huniar, M. Kaupp, A. M. Khah, S. K. Khani, T. Müller, F. Mack, B. D. Nguyen, S. M. Parker, E. Perlt, D. Rappoport, K. Reiter, S. Roy, M. Rückert, G. Schmitz, M. Sierka, E. Tapavicza, D. P. Tew, C. van Wüllen, V. K. Voora, F. Weigend, A. Wodyński, and J. M. Yu, J. Chem. Phys. **152**, 184107 (2020).
[56]F. Plasser, J. Chem. Phys. **152**, 084108 (2020).
[57]N. M. O'Boyle, M. Banck, C. A. James, C. Morley, T. Vandermeersch, and G. R. Hutchison, J. Cheminf. **3**, 33 (2011).
[58]G. Hermann, V. Pohl, J. C. Tremblay, B. Paulus, H. Hege, and A. Schild, J. Comput. Chem. **37**, 1511 (2016).
[59]See http://www.jmol.org/ for Jmol: An open-source java viewer for chemical structures in 3D.
[60]N. Gilka, P. R. Taylor, and C. M. Marian, J. Chem. Phys. **129**, 044102 (2008).
[61]D. Ganyushin, N. Gilka, P. R. Taylor, C. M. Marian, and F. Neese, J. Chem. Phys. **132**, 144111 (2010).
[62]M. Kleinschmidt, J. Tatchen, and C. M. Marian, J. Chem. Phys. **124**, 124101 (2006).
[63]AMFI is an atomic spin–orbit integral program written by B. Schimmelpfennig, University of Stockholm, 1996.
[64]A. McLachlan, Mol. Phys. **6**, 441 (1963).
[65]H. Benk and H. Sixl, Mol. Phys. **42**, 779 (1981).
[66]J. van der Waals, Appl. Magn. Reson. **20**, 545–561 (2001).
[67]J. R. Platt, J. Chem. Phys. **17**, 484 (1949).
[68]M. Parac and S. Grimme, Chem. Phys. **292**, 11 (2003).
[69]Y. Yang, E. R. Davidson, and W. Yang, Proc. Natl. Acad. Sci. U. S. A. **113**, E5098 (2016).
[70]L. Salem and C. Rowland, Angew Chem., Int. Ed. Engl. **11**, 92 (1972).
[71]C. M. Marian and N. Gilka, J. Chem. Theory Comput. **4**, 1501 (2008).
[72]N. Nijegorodov, V. Ramachandran, and D. Winkoun, Spectrochim. Acta, Part A **53**, 1813 (1997).
[73]J. Burgos, M. Pope, C. E. Swenberg, and R. R. Alfano, Phys. Status Solidi B **83**, 249 (1977).
[74]E. S. Kadantsev, M. J. Stott, and A. Rubio, J. Chem. Phys. **124**, 134901 (2006).
[75]H. Chakraborty and A. Shukla, J. Chem. Phys. **141**, 164301 (2014).
[76]J. Hachmann, J. J. Dorando, M. Avilés, and G. K.-L. Chan, J. Chem. Phys. **127**, 134309 (2007).
[77]Y. Y. Pan, J. Huang, Z. Wang, D. W. Yu, B. Yang, and Y. G. Ma, RSC Adv. **7**, 26697 (2017).
[78]C. Hellner, L. Lindqvist, and P. C. Roberge, J. Chem. Soc., Faraday Trans. 2 **68**, 1928 (1972).
[79]P. Klán and J. Wirz, *Photochemistry of Organic Compounds* (John Wiley & Sons, Ltd., 2009).
[80]V. K. Thorsmølle, R. D. Averitt, J. Demsar, D. L. Smith, S. Tretiak, R. L. Martin, X. Chi, B. K. Crone, A. P. Ramirez, and A. J. Taylor, Phys. Rev. Lett. **102**, 017401 (2009).
[81]R. Mondal, C. Tönshoff, D. Khon, D. C. Neckers, and H. F. Bettinger, J. Am. Chem. Soc. **131**, 14281 (2009).
[82]E. Heinecke, D. Hartmann, R. Müller, and A. Hese, J. Chem. Phys. **109**, 906 (1998).
[83]M. Pabst and A. Köhn, J. Chem. Phys. **129**, 214101 (2008).
[84]I. Benkyi, E. Tapavicza, H. Fliegl, and D. Sundholm, Phys. Chem. Chem. Phys. **21**, 21094 (2019).
[85]T. M. Halasinski, D. M. Hudgins, F. Salama, L. J. Allamandola, and T. Bally, J. Phys. Chem. A **104**, 7484 (2000).

[86]R. He, N. G. Tassi, G. B. Blanchet, and A. Pinczuk, Phys. Rev. B **83**, 115452 (2011).
[87]O. Loboda, B. Minaev, O. Vahtras, B. Schimmelpfennig, H. Ågren, K. Ruud, and D. Jonsson, Chem. Phys. **286**, 127 (2003).
[88]T.-C. Yang, D. J. Sloop, S. I. Weissman, and T.-S. Lin, J. Chem. Phys. **113**, 11194 (2000).
[89]T. Nagami, H. Miyamoto, R. Sakai, and M. Nakano, J. Phys. Chem. C **125**, 2264 (2021).
[90]K. B. Wiberg, C. M. Hadad, J. B. Foresman, and W. A. Chupka, J. Phys. Chem. **96**, 10756 (1992).
[91]F. Plasser and H. Lischka, J. Chem. Theory Comput. **8**, 2777 (2012).
[92]F. Plasser, S. A. Bäppler, M. Wormit, and A. Dreuw, J. Chem. Phys. **141**, 024107 (2014).
[93]F. Plasser, M. Wormit, and A. Dreuw, J. Chem. Phys. **141**, 024106 (2014).
[94]J. Anthony, J. Brooks, D. Eaton, and S. Parkin, "CCDC 172476: Experimental crystal structure determination," J. Am. Chem. Soc. **123**, 9482 (2001).

A key observation of [P4] was that a coherent SF mechanism is imaginable, if the PT units are in a parallel orientation. Consequently, it was postulated that TIPS-PT, owning a brickwork-like crystal structure shown in Fig. 5.20, might follow a different decay channel in the SF process than PT. Consequently, the same investigations car-

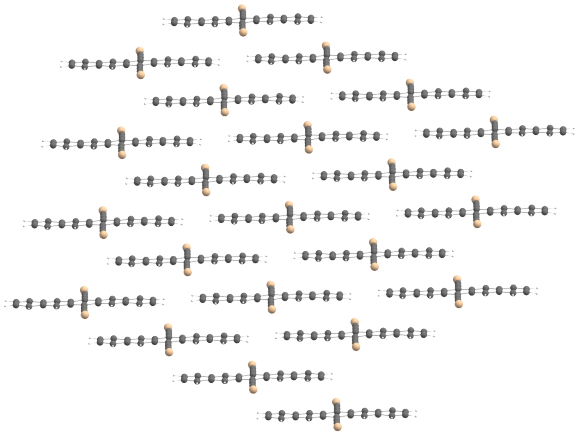

Figure 5.20: Cut out of the TIPS-PT crystal structure[272]. Hydrogens and TIPS residues were omitted for clarity.

ried out for PT were conducted for TIPS-PT. Details on structural changes can be found in [273]. Before presenting results obtained for TIPS-PT in crystalline environment, some computational approximations need to be discussed, which simplify the calculations considerably.

5.4.1 Studies on Monomers

In the following, the electronic changes introduced by the addition of triisopropylsilylethynyl (TIPSet) residues to the PT-core shall be discussed. All computations were carried out with the same setup described in publication [P4]. As the added substituents prolong the short axis of the PT-core, an increased magnitude of the electric transition dipole vector and a lowering of the transition energy, due to increased conjugation, ought to be expected for the $S_0 \rightarrow S_1$transition. As can be seen from Tab. 5.5 the excitation energy to the first bright state in TIPS-PT is lowered by 0.27 eV compared to PT. In both cases the S_1 state is dominated by a S_h^l configuration. Both HOMO and LUMO have contributions from the functions centred at the ethynyl group carbons, as can be seen from Fig. 5.21. This supports the expected

Table 5.5: Comparison of the first bright singlet transitions of PT and TIPS-PT. Tabulated are the vertical excitation energies E_{vert} at the S_0 geometries, the adiabatic $E_{ad.}$ and the 0–0 E_{0-0} energies.

Molecule	State	$E_{vert.}$	$E_{ad.}$	E_{0-0}	$E_{exp.}$	f	μ_s	μ_l	$\mu_\perp$
PT	S_1	2.34	2.20	2.16	2.21[a]	0.109	1.33	0.00	0.00
	S_3	3.16	–	–	–	0.009	0.00	0.33	0.00
	S_4	3.24	–	–	–	0.000	0.00	0.00	0.00
TIPS-PT	S_1	2.07	1.96	1.92	1.90[b]	0.297	2.42	0.00	0.00
	S_3	3.03	–	–	–	0.000	0.00	0.00	0.00
	S_4	3.18	–	–	–	0.048	0.00	-0.78	0.00

[a] In Ar matrix at 10 K[274]
[b] Steady-state absorption in $CHCl_3$[275]

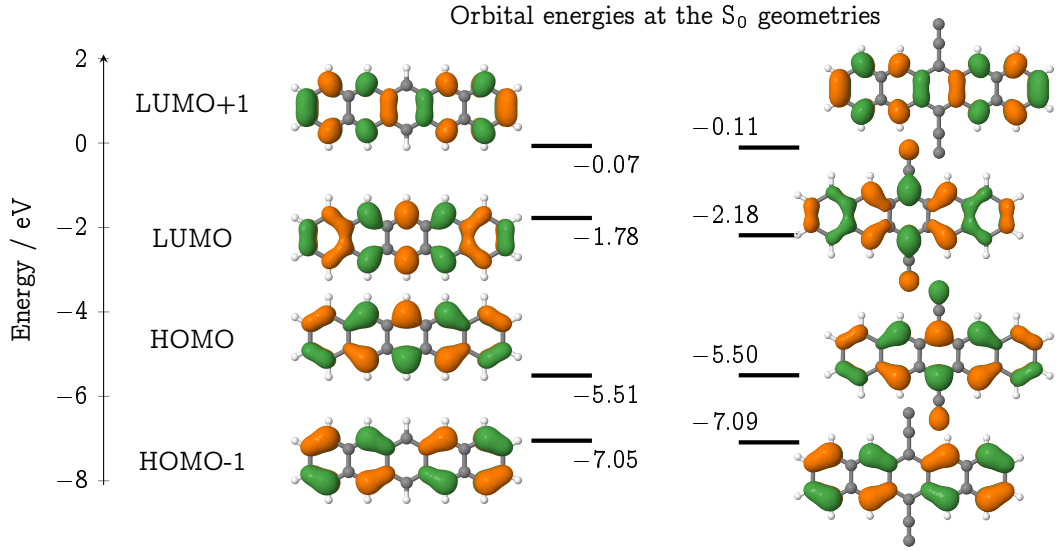

Figure 5.21: Energy levels and *iso*-surfaces of valence KS-MOs for PT and TIPS-PT computed with the BH-LYP def2-SV(P) approximation. The TIPS residues are not shown for clarity.

increased conjugation and explains the energy lowering. Similar considerations apply for the T_1 state, however the energy decrease is not as pronounced (≈0.2 eV). Investigating the oscillator strength for the $S_0 \rightarrow S_1$ transition, given in Tab. 5.5, shows an almost tripling in magnitude. Plotting the transition densities (Fig. 5.22) suggests, that this is indeed rooted in the prolonged short axis. This observation is in complete analogy to the findings for the An-derivatives discussed in Sec. 5.2. In contrast to HOMO and LUMO, the HOMO-2, HOMO-1, LUMO+1 and LUMO+2 are cen-

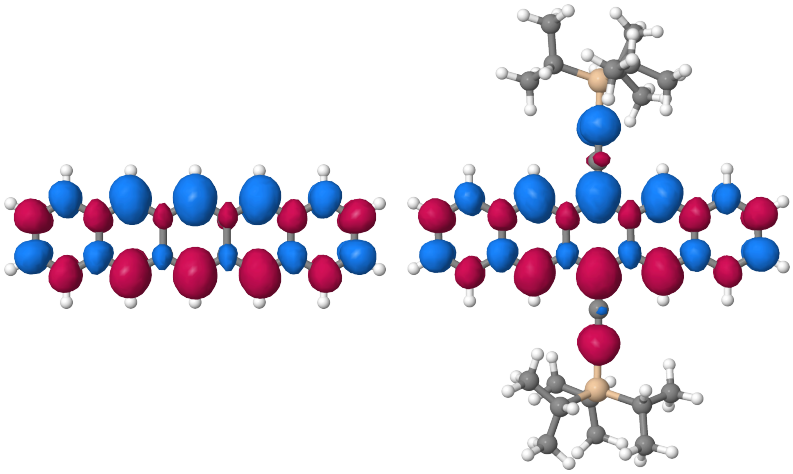

(a) PT (b) TIPS-PT

Figure 5.22: Transition densities of the $S_0 \rightarrow S_1$ of PT and TIPS-PT. *Iso*-surfaces were plotted with an absolute cut-off of 0.0004. Red are positive, blue negative values of the transition density.

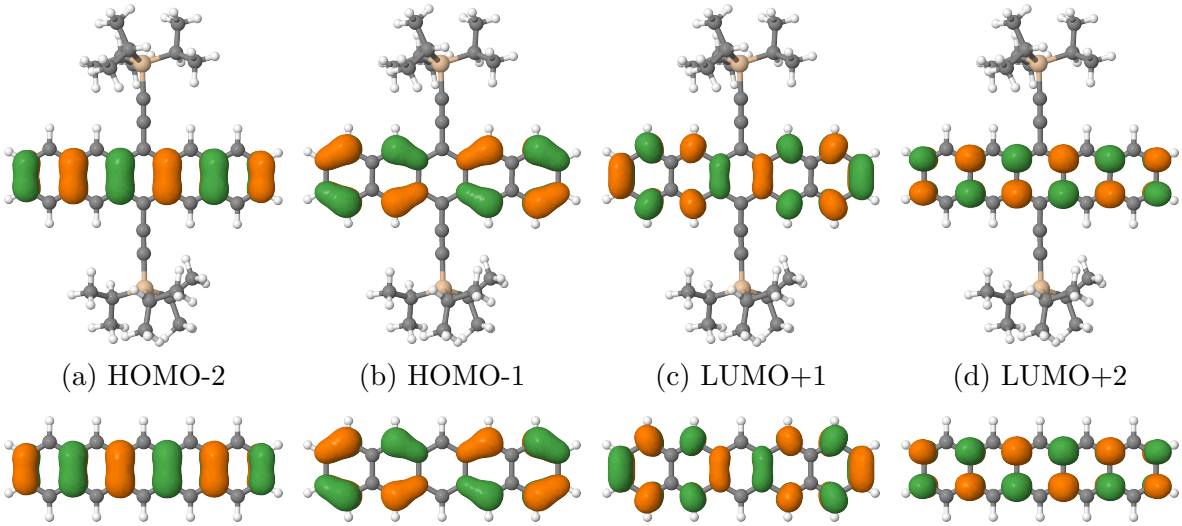

(a) HOMO-2 (b) HOMO-1 (c) LUMO+1 (d) LUMO+2

(e) HOMO-2 (f) HOMO-1 (g) LUMO+1 (h) LUMO+2

Figure 5.23: Comparison of the second and third highest occupied and lowest unoccupied MOs of TIPS-PT (a-d) and PT (e-h). All *iso*-surfaces were plotted with a cut-off of 0.03.

tred on the PT-core and resemble the respective PT-orbitals closely, as can be seen from Fig. 5.23. Therefore, the long axis polarized $S_0 \rightarrow S_3$ transition, whose transition density is shown in Fig. 5.24a, does not benefit from the possibility of increasing

delocalization, as it is mainly made up of substitutions from the core centred MOs ($S^{l+2;l}_{h;h-2}$). Consequently, the energetic position of the state barely changes, as can be seen from Tab. 5.5. A similar observation holds for the dark S_2 state composed of $S^{l+1;l}_{h;h-1}$ configurations, which is of *gerade* symmetry in the case of PT. In this case, the weights of the included configurations change drastically. The calculations reveal that the weight of the $(h)\,(l_{+1})$ configuration is reduced from $\approx 42\%$ in PT to $\approx 2\%$ in TIPS-PT. Meanwhile, the weight of the $(h_{-1})\,(l)$ configuration almost doubles from $\approx 42\%$ to $\approx 79\%$. Investigating the sketch of the orbital energies of PT and TIPS-PT

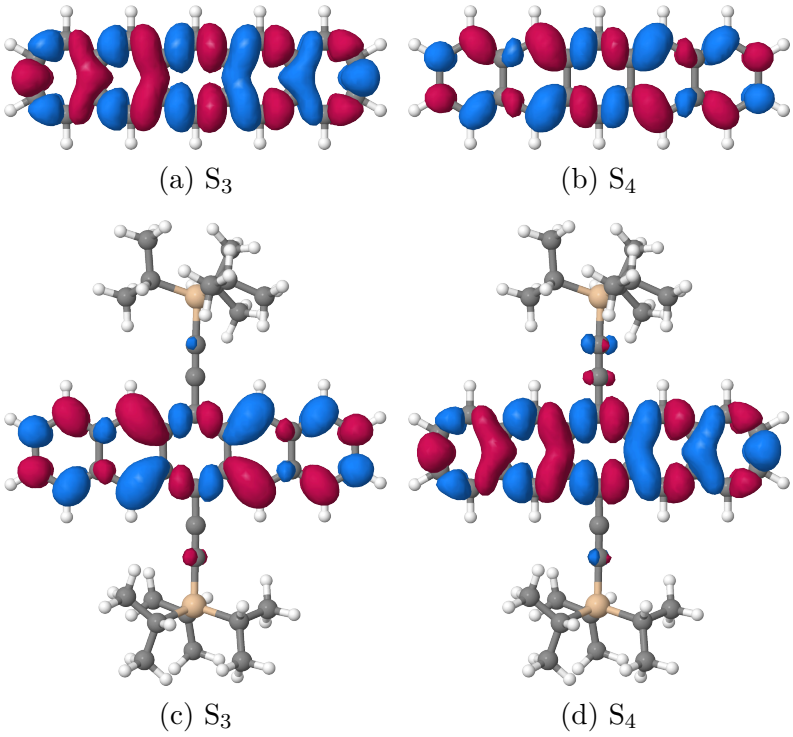

(a) S_3 (b) S_4

(c) S_3 (d) S_4

Figure 5.24: Transition densities of the $S_0 \rightarrow S_3$ and S_4 transitions of PT and TIPS-PT. *Iso*-surfaces were plotted with an absolute cut-off of 0.0004. Red are positive, blue negative values of the transition density.

in Fig. 5.21 offers an explanation. While the HOMO and LUMO+1 are barely changed in energy, the HOMO-1 is slightly raised and the LUMO is lowered in energy. Hence, the S^{l+1}_{h} configuration becomes more beneficial and consequently gains a larger weight in the DFT/MRCI vector. Turning to the Franck-Condon spectra computed for the *in vacuo* structures we find similar main features. Both spectra are dominated by a progression of $1495\,\mathrm{cm}^{-1}$ ($1484\,\mathrm{cm}^{-1}$ in TIPS-PT), originating from a C–C stretch mode of the PT-core. This result fits the experimental value of $1514\,\mathrm{cm}^{-1}$, measured in a Ne

matrix[274] at 10 K, very well. The shoulder right before the second peak maximum can be attributed to the A_g in plane C–H bending vibration, which was measured by the same authors [274] at 1181 cm^{-1} and by He et al. [276] at 1177 cm^{-1} in resonance Raman experiments. It was identified as mode 60 in PT and mode 156 in TIPS-PT with energies of 1172 cm^{-1} and 1168 cm^{-1} , respectively. The second clearly visible peak to the blue-side of the 0–0 maximum is assigned to a C–C concertina like motion with a computed energy of 772 cm^{-1}, which was found by Halasinski et al. [274] at 734 cm^{-1}. As one would expect the computed mode's frequency is slightly red-shifted to 730 cm^{-1} in TIPS-PT as the mass is increased close the centre of mass by TIPSet residues. The bathochromic shift is accompanied by a notable broadening, making the peak markedly less intense. Considering the alkynyl residue, the symmetric and antisymmetric stretching modes are of interest. Grieco et al. [277] used them as a vibrational probe for the triplet exciton dynamics. Using Fourier-transformed infra-red spectroscopy (FTIR) the authors located the bands at 2130 cm^{-1} and 2090 cm^{-1}. The computed values of 2256 cm^{-1} for the symmetric and 2261 cm^{-1} for the antisymmetric stretch mode, are too hypsochromic. In summary, the selected computational setup proved to be adequate for the description and investigation of the electronic structure of both TIPS-PT and PT. As the TIPS-residues are fairly large from a computational point of view and no significant contributions to the valence MOs were found, we checked whether the TIPS-PT system might be further simplified.

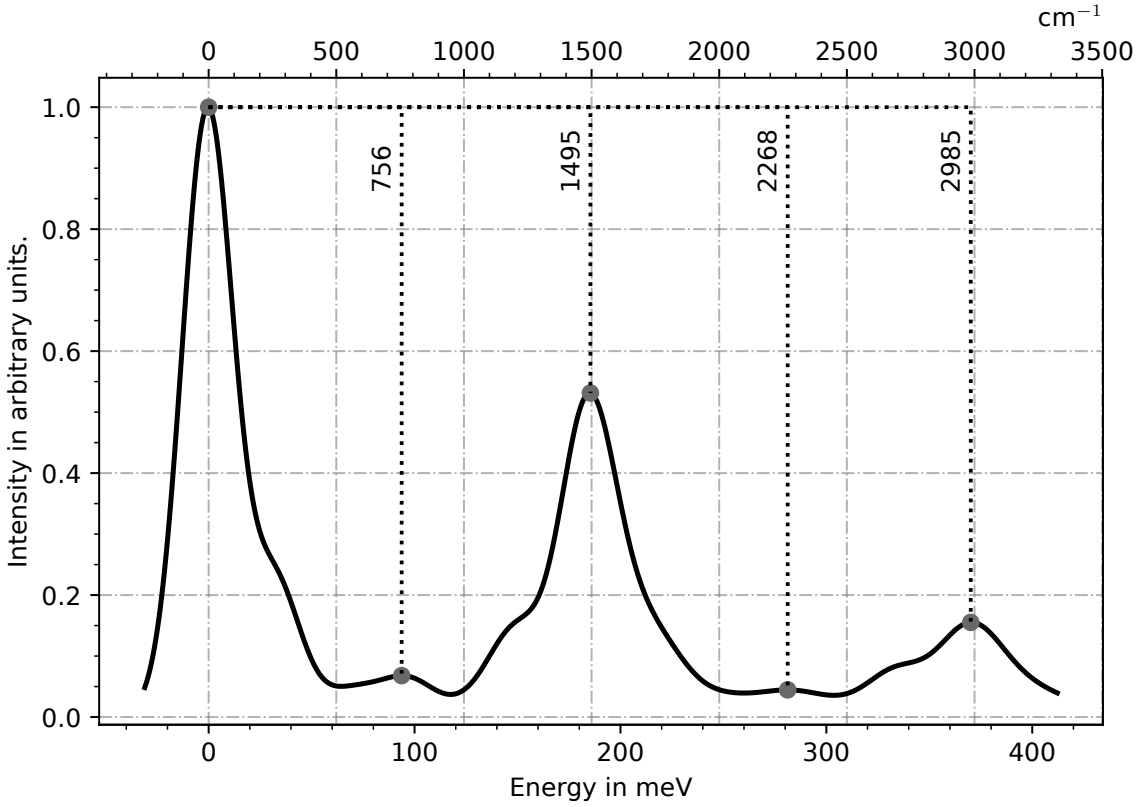

(a) PT

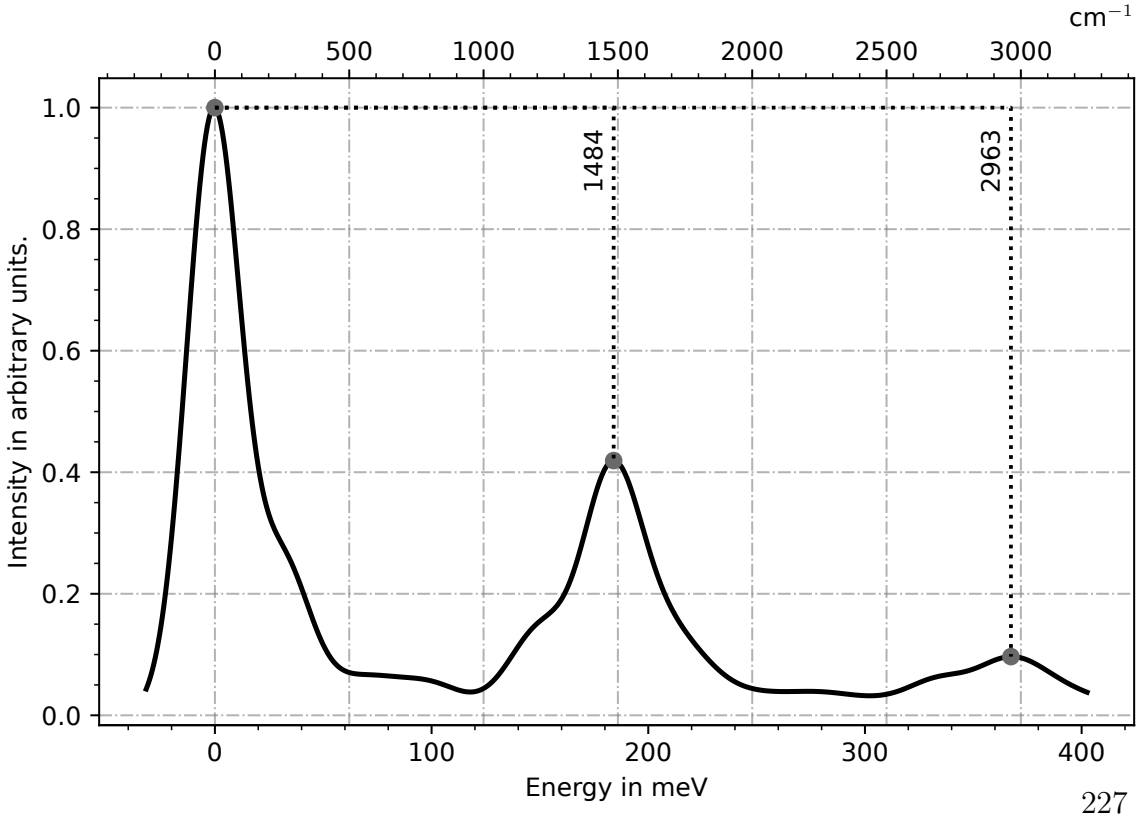

(b) TIPS-PT

Figure 5.25: Simulated FC spectra of the $S_0 \rightarrow S_1$ transitions of PT and TIPS-PT. Only maxima with an intensity greater than 0.04 were marked.

5.4.2 Preliminary Screening of Necessary Structural Features

More than 50% of the atomic centres in TIPS-PT are not part of the PT-core or ethynyl part of the TIPSet substituents, which are most relevant for the electronic structure of the states of interest, as discussed in the last section. From a computational perspective, it is interesting to see how much of the molecule one might substitute with smaller and computationally less demanding groups without altering the character of the involved states. However, it is clear that the geometry optimizations for the dimers must be done on the full system as the steric demands of the TIPS-residues are not negligible. Using the optimized gas-phase structure of TIPS-PT as a scaffold, the influence of the TIPS-groups on the electronic structure was investigated by successively replacing them with other groups. At the same time the PT-core as well as the ethynyl carbons were left fixed in space. Here, results for methyl residues and hydrogen atoms shall be presented. Plotting a Gaussian-broadened absorption spectrum clearly shows that the main spectral features are conserved despite the substitution. None of the investigated states is significantly altered, as is apparent

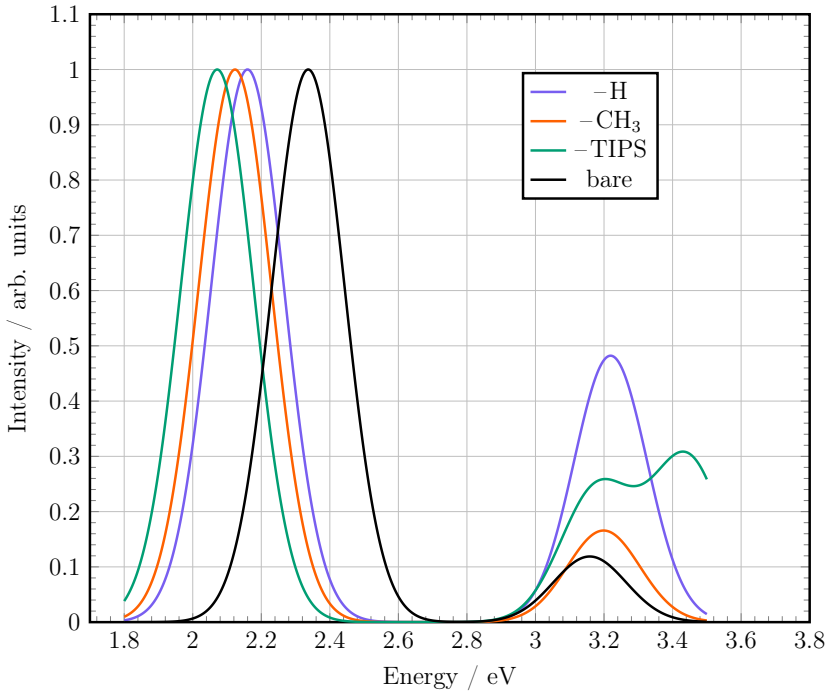

Figure 5.26: Gaussian-broadened vertical absorption spectra at the S_0 geometries. The TIPS residues were substituted by H and CH_3. All computed values were convoluted using Gaussian functions with a full-width-at-half-maximum of 0.25 eV. Bare PT is given as a reference.

from Tab. 5.6. Neither in composition, nor in energy. Therefore, it was concluded

Table 5.6: Adiabatic- E_{ad} and vertical energies E_{vert} computed after substituting the residue. All energy values are given in eV. The leading configurations (Comp.) and their weights $|c_i|^2$ in the DFT/MRCI vector are also given.

Residue	State	$E_{vert.}$	$E_{ad.}$	Comp.	$\|c_i\|^2$
–H	S_1	2.16	2.03	S_h^l	88.42%
	S_2	2.76	–	N_h^l	69.51%
	T_1	0.99	0.83	T_h^l	87.79%
	T_2	2.26	–	T_{h-1}^l	54.31%
		–	–	T_h^{l+1}	27.98%
	Q_1	4.68	4.26	$V_{h-1;h}^{l;l+1}$	78.67%
$-CH_3$	S_1	2.12	2.03	S_h^l	88.61%
	S_2	2.74	–	N_h^l	69.70%
	T_1	0.97	0.80	T_h^l	88.02%
	T_2	2.24	–	T_{h-1}^l	51.39%
		–	–	T_h^{l+1}	30.27%
	Q_1	4.65	4.23	$V_{h-1;h}^{l;l+1}$	78.25%
–TIPS	S_1	2.07	1.96	S_h^l	88.38%
	S_2	2.70	–	N_h^l	69.49%
	T_1	0.97	0.79	T_h^l	88.05%
	T_2	2.23	–	T_{h-1}^l	53.69%
		–	–	T_h^{l+1}	27.89%
	Q_1	4.64	4.23	$V_{h-1;h}^{l;l+1}$	77.41%

that substituting the TIPS-residues by hydrogen atoms, in DFT/MRCI and, more importantly, possible spin-spin calculations on the dimeric system, ought to be unproblematic. Computations of TIPS-PT embedded in a crystalline environment will be subject of the next section.

5.4.3 6,13–bis(triisopropylsilylethynyl)pentacene–Dimer in Crystalline Surrounding

The crystal structure of TIPS-PT shows two different arrangements of neighbouring monomer units. As should be evident from Fig. 5.27, the main difference is the overlap of the monomer building blocks. In the **large** overlap (Fig. 5.27a) situation the closest C–C distance at the optimized ground state geometry was measured to be 0.325 nm,

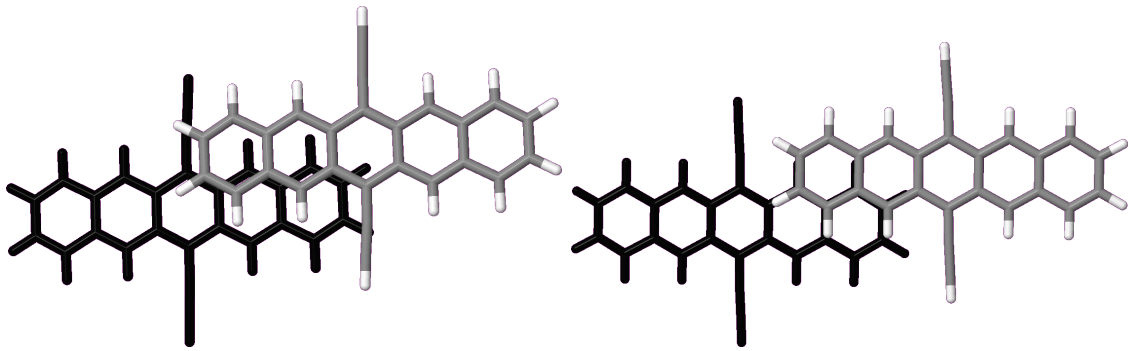

(a) **large** (b) **small**

Figure 5.27: **Large** (a) and **small** (b) overlap of two TIPS-PT building blocks in the crystal structure[272].

while 0.331 nm were determined for the **small** overlap (Fig. 5.27b). The average C−C distance between the subunits was found to be 0.917 nm for the **large** and 1.030 nm for the **small** overlap. Therefore, one ought to expect an energy lowering caused by stronger interactions of the π-systems of the two TIPS-PT units for the **large** overlap. Indeed, it was found to be more stable by 0.26 eV computed on the DFT/MRCI level. Though, as can be seen from the level plots Figs. 5.28 and 5.29, the excited state manifold does not differ markedly between the two arrangements. One exception was found in the ^{1}(TT) state. While the vertical energies of the bright state S_1 and the dark, first singlet state S_1^{dark} are similar for both arrangements, it seems that relaxation to ^{1}(TT) is energetically more favourable in the dimer with a **large** overlap. A point to be discussed shortly. The similarity of the $S_0 \rightarrow S_1$ transitions is readily understood investigating the transition densities in Fig. 5.30 and the descriptors tabulated in Tabs. 5.7 and 5.8. From Figs. 5.30 the analogy to a J-aggregate is apparent. The bright vertical singlet transition $S_0 \rightarrow S_1$ is the parallel alignment of the two short-axis transition dipole vectors, while the dark state S_1^{dark} is the anti-parallel alignment with respect to the polarization axis.

Relaxing the excited state geometry of the S_1 leads to the two subunits moving closer. The shortest distance decreases further to 0.318 nm in the large and 0.314 nm in the **small** pattern. This means the TIPS-PT subunits compress much more strongly in the **small** overlap than in the **large**, where the minimal distance barely changes. However, investigating the average C−C distances between the subunits reveals that only a few carbons actually move closer together, as the value slightly increases to 1.043 nm. As can be seen from the side-view in Fig. 5.31, the upper unit tilts towards the lower. In contrast, the average distance in the **large** overlap decreases signifi-

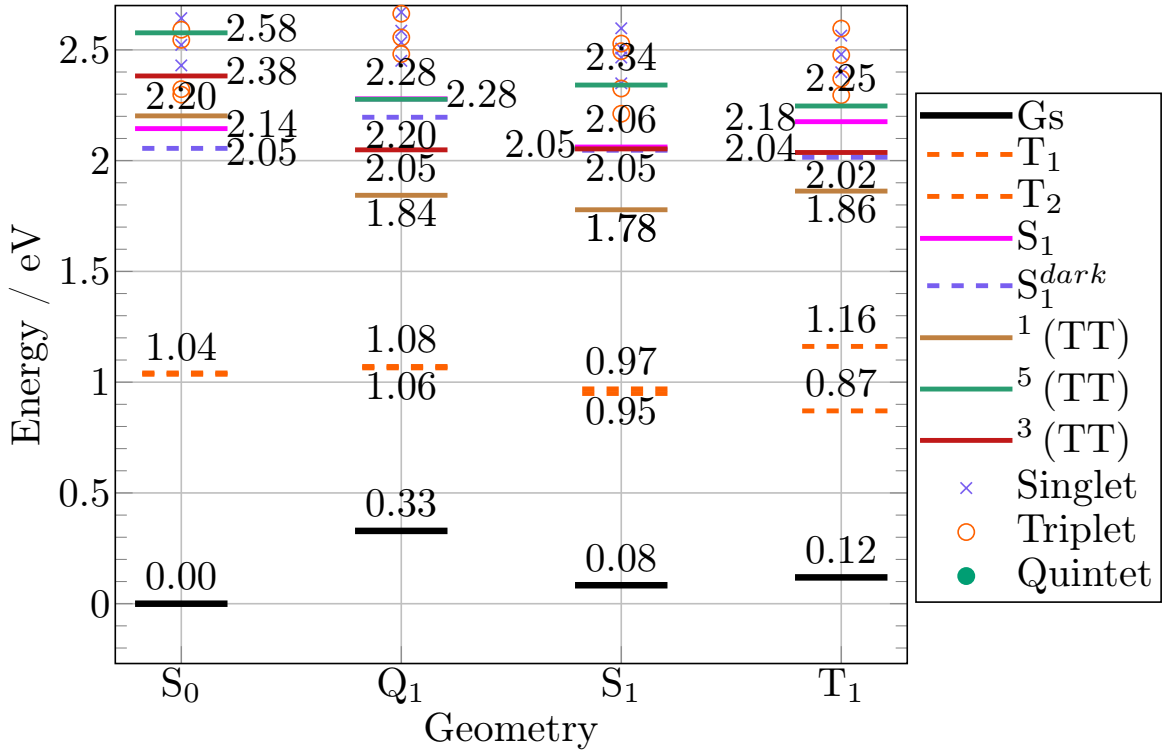

Figure 5.28: Level plot for the **large** overlap of the TIPS-PT building blocks. Selected energy levels are annotated with energy values in eV.

Table 5.7: Vertical energy $E_{vert.}$, oscillator strength f and descriptors derived from the 1-TDM for singlet excited states with an oscillator strength greater than 0.005 at the optimized singlet geometries of **large**.

Overlap	**large**				
Exc. state No.	**2**	**4**	**3**	**4**	**5**
At Geometry	**S_0**			**S_1**	
f	0.385	0.049	0.306	0.112	0.019
$E_{vert.}$	2.14	2.43	1.98	2.27	2.38
Ω	0.899	0.810	0.873	0.708	0.313
Pos.	1.490	1.505	1.499	1.520	1.614
PR	1.999	1.945	2.000	1.984	1.741
ω_{CT}	0.039	0.952	0.239	0.674	0.413
$\omega_{\mathrm{Coh.}}$	1.081	1.098	1.571	1.774	1.677
$\mathrm{CT_{net}}$	0.001	-0.167	-0.005	-0.080	-0.343
Character	DL	DL	DL	DL	DL+CR
Assignment	$S^{l;l+1}_{h-1;h}$	$S^{l+1;l}_{h;h-1}$	S^{l}_{h-1}	S^{l+1}_{h}	$Z/S^{l+1}_{h}y$

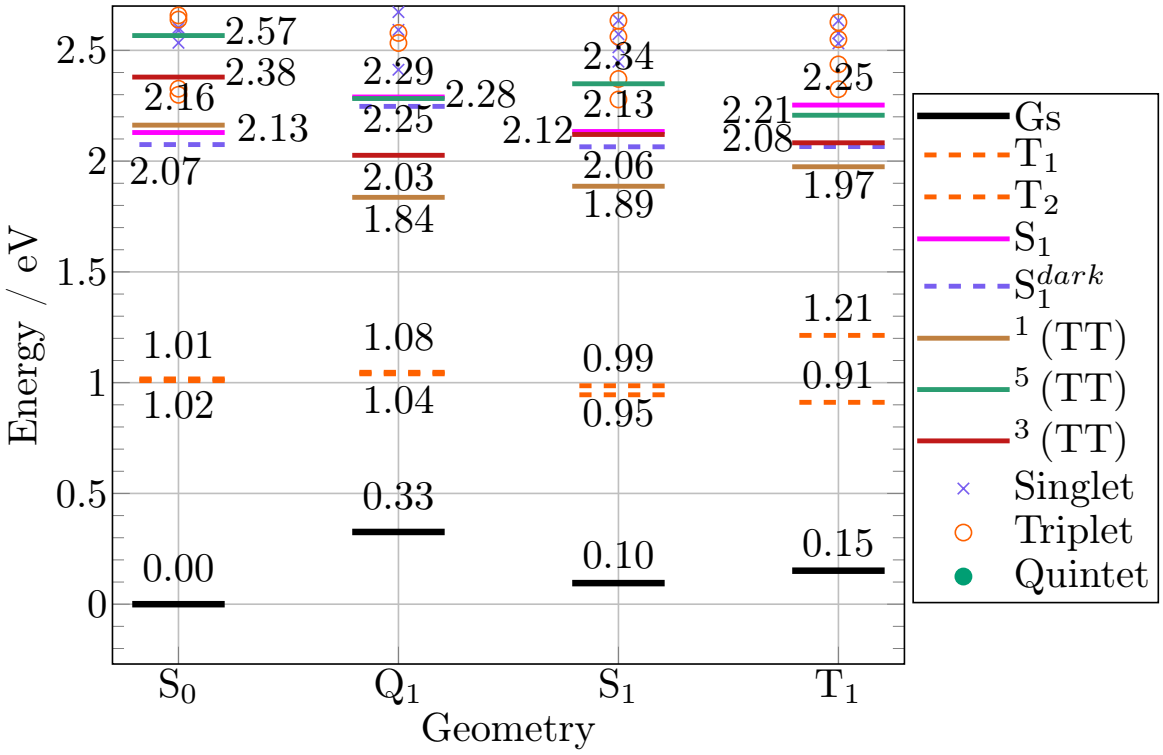

Figure 5.29: Level plot for the **small** overlap of the TIPS-PT building blocks. Selected energy levels are annotated with energy values in eV.

Table 5.8: Vertical energy $E_{vert.}$, oscillator strength f and descriptors derived from the 1-TDM for singlet excited states with f greater than 0.005 at the optimized singlet geometries of **small**.

Overlap	**small**							
Exc. state No.	**2**	**4**	**5**	**6**	**3**	**4**	**5**	**6**
At Geometry			**S_0**				**S_1**	
f	0.395	0.023	0.005	0.018	0.378	0.016	0.010	0.014
$E_{vert.}$	2.13	2.53	2.59	2.60	2.04	2.35	2.42	2.48
Ω	0.896	0.499	0.597	0.565	0.892	0.456	0.532	0.574
Pos.	1.519	1.505	1.460	1.538	1.520	1.482	1.437	1.557
PR	1.997	1.951	1.430	1.236	1.997	1.706	1.324	1.270
ω_{CT}	0.037	0.819	0.844	0.844	0.048	0.727	0.758	0.798
$\omega_{Coh.}$	1.077	1.406	1.223	1.187	1.100	1.510	1.296	1.239
CT_{net}	0.004	0.158	0.632	-0.788	-0.002	0.414	0.718	-0.762
Character	DL	DL	CT	CT	DL	CR	CT	CT
Assignment	$S^{l;l+1}_{h-1;h}$	$S^{l+1;l}_{h;h-1}$	$S^{l+1;l}_{h-1;h}$	$S^{l+1;l+1;l}_{h-1;h;h-1}$	$S^{l;l+1}_{h-1;h}$	Z/S^{l+1}_{h}	S^{l+1}_{h}	S^{l+1}_{h-1}

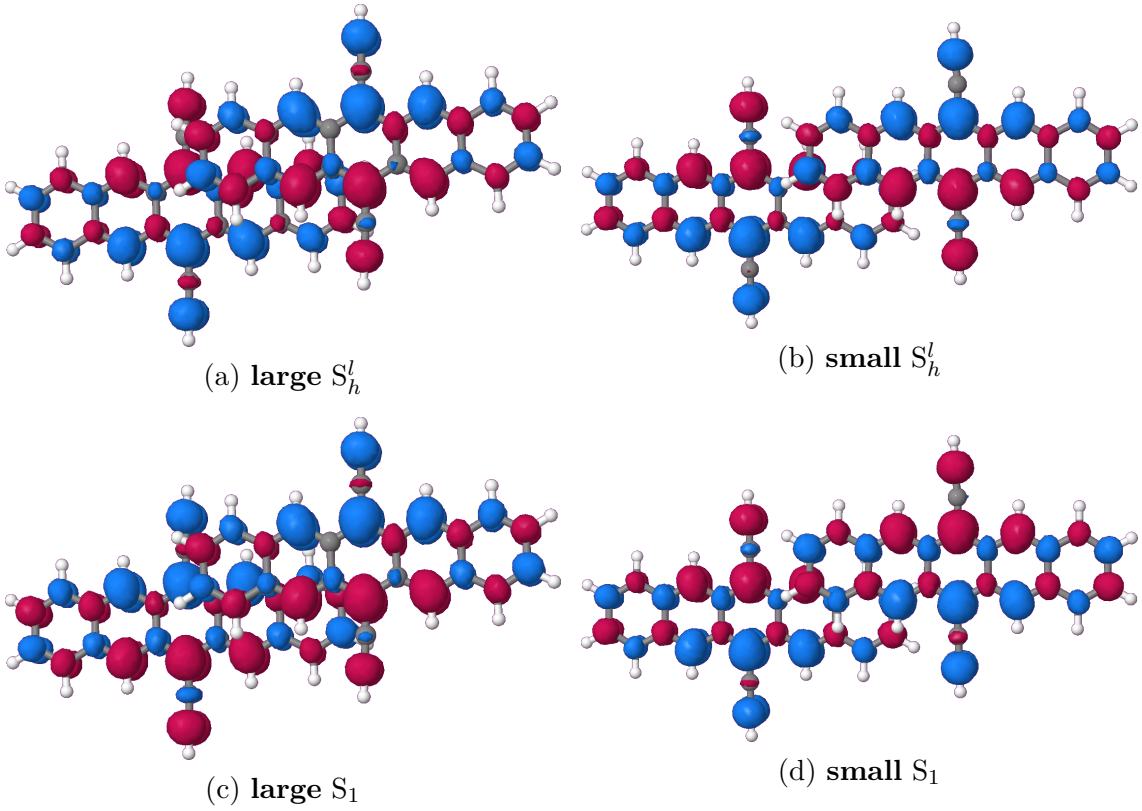

(a) **large** S_h^l (b) **small** S_h^l

(c) **large** S_1 (d) **small** S_1

Figure 5.30: Transition densities of the $S_0 \rightarrow S_1$ (c-d) $S_0 \rightarrow S_h^l$ (a-b) transitions of the **large** and **small** overlaps of two TIPS-PTs. *Iso*-surfaces were plotted with an absolute cut-off of 0.0004. Black are positive, gray negative values of the transition density.

cantly to 0.880 nm. Combined with the barely changed minimal distance, this finding can be interpreted as a shearing motion, which is clearly visible after overlaying the structures, as in Fig. 5.32. Consequently, the contact surface of the building units increases, leading to stronger $\pi - \pi$ interactions, accompanied by a stabilization of all states compared to the **small** overlap. The beneficial interaction influences the ^{1}(TT) state the most. Evidently, ^{1}(TT) is completely delocalized in both cases, as can be seen from the difference density plotted in Fig. 5.33, offering a good explanation of its energetic lowering through increased overlap. Additionally, this leads to a strong mixing with the dark S_h^l state, as can be seen from Tab. 5.9. Note that the singlet states with a noteworthy charge-transfer character are all located ≈0.4 eV above the S_1 state, which agrees with computations by Casillas et al. [278], and is in stark contrast to the situation in PT[P4]. This makes a charge-transfer mediated SF mechanism unlikely. Furthermore, it is evident that the bright S_1 and the ^{1}(TT)

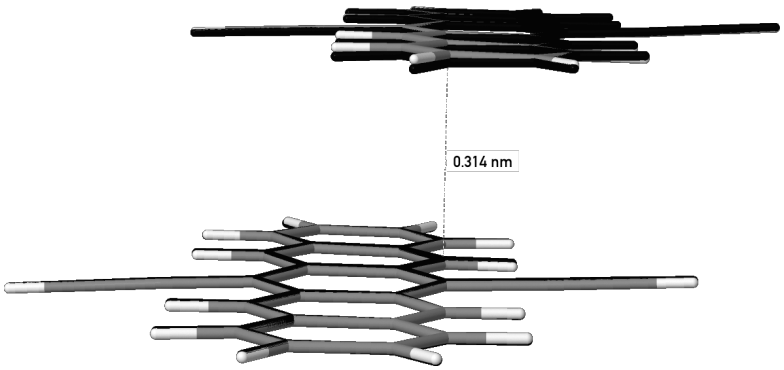

(a) Side-view. Shortest distance between the units is given in nm.

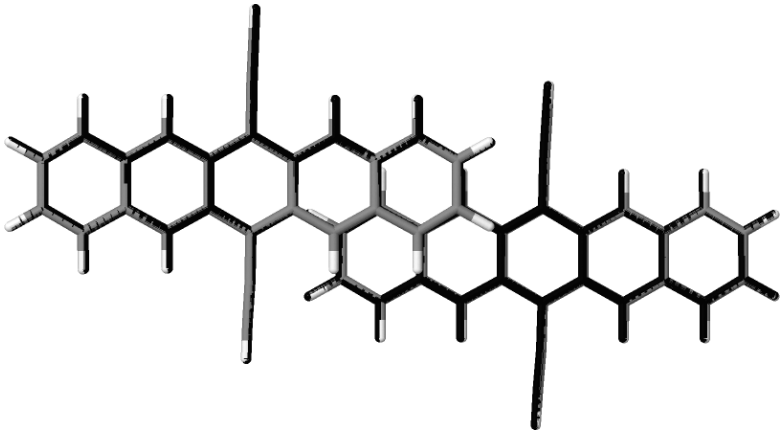

(b) Top-view.

Figure 5.31: Overlay of the optimized ground- and S_1 state structure (black) of the **small** overlap. The shortest distance between the units is given in nm. The only movement is the tiliting of the upper pentacene unit toward the lower.

PESs must cross upon relaxation to the S_1 geometry, supporting a direct SF mechanism for TIPS-PT as postulated by Schulz et al. [P4]. Similar to PT, the ^{5}(TT) is far above the relevant states for SF. Therefore, a participation of ^{5}(TT) through spin-spin coupling can be ruled out with the same reasoning already given for PT in [P4]. The triplet state manifold behaves similar to the triplet manifold of the **u** arrangement of PT in the same publication. Therefore, it is refrained from repeating the discussion here and the reader is referred to the publication [P4].

Apparently, the geometrical arrangement of PT units is a key factor in determining the SF mechanism. As postulated based on observations made for the side-on arrangement of PTs, TIPS-PT seems to follow a different SF mechanism than found for PT. Furthermore, it was found that a key motion to stabilize the ^{1}(TT) state, is

Table 5.9: Composition Comp., coefficients c_i and weights $|c_i|^2$ in % for the lowest singlet state with contributions of doubly excited configurations of at least 10% and adiabatic energy E_{ad} less than 3 eV for the **large** overlap of the TIPS-PT monomers. Spatial configurations of $V^{l;l_{+1}}_{h_{-1};h}$ excited character are highlighted gray.

Geom.	Order	$E_{ad.}$	No.	CSF	Comp.	c_i	$\|c_i\|^2$	N_{opn}
			1	1	$(h_{-1})^1(l_{+1})^1$	-0.47	21.9	2
			2	1	$(h)^0(l)^2$	0.37	14.0	0
			3	1	$(h_{-1})^0(l)^2$	-0.35	12.2	0
$\mathbf{S}_0$	3	2.20	4	1	$(h_{-1})^1(h)^1(l)^1(l_{+1})^1$	-0.33	11.1	4
			5	1	$(h)^0(l_{+1})^2$	-0.31	9.8	0
			6	1	$(h_{-1})^0(l_{+1})^2$	0.30	9.1	0
			7	1	$(h)^1(l)^1$	-0.12	1.5	2
			1	1	$(h)^1(l)^1$	-0.68	46.4	2
			2	1	$(h)^0(l)^2$	-0.36	13.3	0
$\mathbf{S}_1$	1	1.78	3	1	$(h_{-1})^0(l)^2$	0.27	7.3	0
			4	1	$(h_{-1})^1(h)^1(l)^1(l_{+1})^1$	0.25	6.2	4
			5	1	$(h)^0(l_{+1})^2$	0.19	3.5	0
			1	1	$(h)^1(l)^1$	0.48	23.2	2
			2	1	$(h_{-1})^1(h)^1(l)^2$	-0.38	14.4	2
			3	2	$(h_{-1})^1(h)^1(l)^1(l_{+1})^1$	-0.33	11.0	4
$\mathbf{T}_1$	1	1.86	4	1	$(h_{-1})^1(h)^1(l)^1(l_{+1})^1$	-0.32	10.0	4
			5	1	$(h_{-1})^1(h)^1(l_{+1})^2$	0.25	6.0	2
			6	1	$(h_{-1})^1(l)^1$	0.23	5.4	2
			7	1	$(h)^0(l)^2$	0.19	3.6	0
			1	1	$(h)^0(l)^2$	-0.45	20.6	0
			2	1	$(h_{-1})^0(l)^2$	0.4	16.0	0
			3	1	$(h_{-1})^1(h)^1(l)^1(l_{+1})^1$	0.38	14.3	4
$\mathbf{Q}_1$	1	1.84	4	1	$(h)^0(l_{+1})^2$	0.34	11.4	0
			5	1	$(h_{-1})^0(l_{+1})^2$	-0.32	10.1	0
			6	1	$(h)^1(l)^1$	-0.27	7.4	2
			7	1	$(h_{-1})^1(l_{+1})^1$	0.11	1.1	2

Table 5.10: Composition Comp., coefficients c_i and weights $|c_i|^2$ in % for the lowest singlet state with contributions of doubly excited configurations of at least 10% and adiabatic energy E_{ad} less than 3 eV for the **small** overlap of the TIPS-PT monomers. Spatial configurations of $V^{l;l_{+1}}_{h_{-1};h}$ excited character are highlighted gray.

Geom.	Order	$E_{ad.}$	No.	CSF	Comp.	c_i	$\|c_i\|^2$	N_{opn}
			1	1	$(h)^0(l)^2$	-0.39	14.9	0
			2	1	$(h_{-1})^0(l)^2$	0.37	13.8	0
			3	1	$(h_{-1})^1(h)^1(l)^1(l_{+1})^1$	0.35	12.2	4
$\mathbf{S}_0$	3	2.16	4	1	$(h_{-1})^1(l_{+1})^1$	-0.34	11.6	2
			5	1	$(h)^0(l_{+1})^2$	0.32	10.2	0
			6	1	$(h_{-1})^0(l_{+1})^2$	-0.32	9.9	0
			7	1	$(h)^1(l)^1$	-0.20	4.0	2
			1	1	$(h)^0(l)^2$	0.39	15.5	0
			2	1	$(h_{-1})^1(h)^1(l)^1(l_{+1})^1$	-0.36	13.1	4
			3	1	$(h_{-1})^1(h)^1(l)^2$	-0.33	10.8	2
			4	1	$(h_{-1})^0(l)^2$	-0.32	10.0	0
$\mathbf{S}_1$	1	1.89	5	1	$(h)^1(l)^1$	-0.28	7.8	2
			6	1	$(h)^0(l_{+1})^2$	-0.27	7.5	0
			7	1	$(h_{-1})^0(l_{+1})^2$	0.27	7.4	0
			8	1	$(h_{-1})^1(h)^1(l_{+1})^2$	0.25	6.1	2
			9	1	$(h)^0(l)^1(l_{+1})^1$	-0.12	1.5	2
			1	2	$(h_{-1})^1(h)^1(l)^1(l_{+1})^1$	-0.55	29.7	4
			2	1	$(h_{-1})^1(h)^1(l)^2$	0.39	15.5	2
$\mathbf{T}_1$	1	1.97	3	1	$(h_{-1})^1(h)^1(l)^1(l_{+1})^1$	-0.39	15.4	4
			4	1	$(h_{-1})^1(h)^1(l_{+1})^2$	-0.29	8.1	2
			5	1	$(h)^1(l)^1$	-0.21	4.5	2
			1	1	$(h)^0(l)^2$	0.43	18.8	0
			2	1	$(h_{-1})^0(l)^2$	-0.41	16.7	0
			3	1	$(h_{-1})^1(h)^1(l)^1(l_{+1})^1$	-0.39	15.4	4
$\mathbf{Q}_1$	1	1.84	4	1	$(h)^0(l_{+1})^2$	-0.36	12.8	0
			5	1	$(h_{-1})^0(l_{+1})^2$	0.35	12.1	0
			6	1	$(h_{-1})^1(h)^1(l)^2$	-0.17	2.8	2

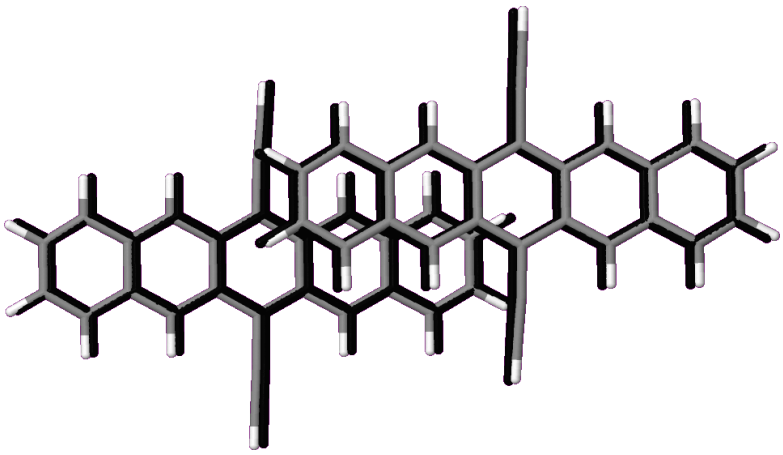

Figure 5.32: Overlay of the optimized ground- and S_1 state structure (black) of the **large** overlap. The shearing motion of the building blocks should be obvious.

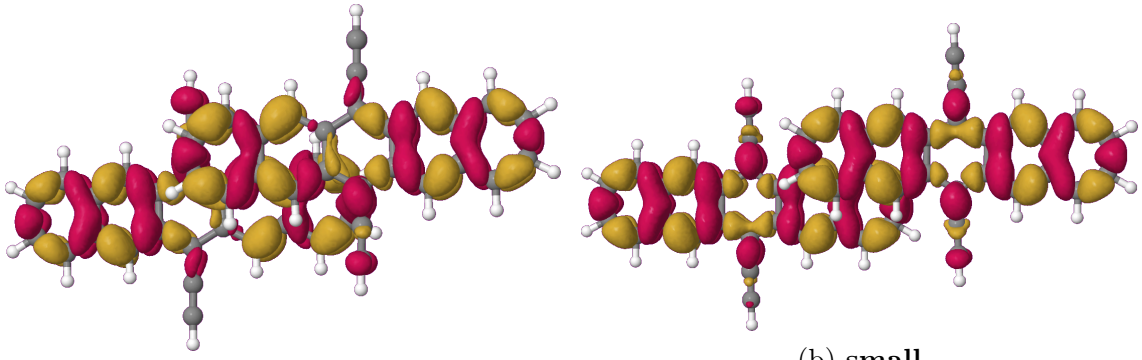

(a) **large** (b) **small**

Figure 5.33: Density difference of the ^{1}(TT) and S_0 densities at the S_1 geometries of the **large** (a) and **small** overlap (b), respectively. Red depicts a density increase, yellow a decrease.

the shearing of two TIPS-PT building blocks in the **large** overlap situation. This directly necessitates the treatment of at least three TIPS-PT units, as it is not apparent what happens if the **small** and **long** overlap patterns are both present. However, the made observations show that maximizing the $\pi - \pi$ interactions between two parallel aligned PTs should lead to a large stabilization of the ^{1}(TT) state. This likely comes with a downside as a too stable ^{1}(TT) has time to deactivate *via* different pathways, than the diffusion into two uncorrelated triplet states. Further investigations in this direction ought to be made, to gain more insight into the SF process and find an optimal design pattern.

6 Conclusion and Outlook

The aim of this work was to gain a deeper insight into the singlet exciton fission (SF) process and to evaluate a newly formulated DFT/MRCI model Hamiltonian on photodetachment-photoelectron spectroscopy (PD-PES) data. A particular focus of the SF studies has been on the ^{5}(TT) state, which could open up spin-forbidden pathways. As this state and its singlet counterpart ^{1}(TT) can only be properly studied if the chosen computational framework is able to describe the intrinsic doubly excited nature of the underlying configurations, it was necessary to use a newly designed Hamiltonian for the density functional theory combined with multi-reference configuration interaction (DFT/MRCI) method. This was because all other formulations of the method failed in such cases. Although the new Hamiltonian performs better overall than its predecessors, the example of C_{60} showed that the conceptual flaw in the DFT/MRCI formulation prevents meaningful results when highly degenerate states have to be treated. Evidence was also found that the iterative construction of the reference spaces commonly used in the DFT/MRCI program in the `mrci` programme may be affected by the intrusion of configurations that could potentially compromise the results. Nevertheless, the new Hamiltonian was found to be a valuable tool to elucidate the origins of peaks recorded with PD-PES. The calculation of Dyson orbital norms based on the calculated DFT/MRCI vectors proved particularly useful, as it was possible to reproduce the experimentally observed intensities almost perfectly. It was possible to identify the states involved and the associated electronic configurations. However, it was also found that the calculation of vertical detachment energies with the same basis as for the Dyson orbitals yields unintuitive results. Although one would expect at least rough estimates to be possible, only large, unsystematic deviations from the experiment were found. The use of relaxed orbitals for the anionic parent gave good results for both the investigated *oligo-para* phenylenes and anthracene (An) derivatives, with deviations from experiment of only $\approx$0.3 eV. It has been shown that DFT/MRCI in conjunction with a suitable orbital basis is a valuable tool for the calculation of electron affinitys (EAs), which are often difficult to calcu-

late by other methods. Finally, studies have been carried out on pentacene (PT) and 6,13-bis(triisopropylsilylethynyl)pentacene (TIPS-PT) embedded in crystalline environments. It was found that the ^{5}(TT) is too high in energy to play a fundamental role in the SF mechanism. Computations of Breit-Pauli spin-spin matrix elements using DFT/MRCI vectors for PT confirmed that the interaction between the ^{5}(TT) state and relevant singlet states is too small for the involvement of a spin-forbidden SF pathway. Further investigation is needed on other test systems, such as the end-linked PTs, also known from the literature. This could help to clarify whether the ^{5}(TT) is a result of the fusion of the generated triplet pair rather than a participant in the SF mechanism, as suggested by the calculations carried out in this paper. The latter imply that PT and TIPS-PT follow two different spin-allowed SF pathways. Dombrowski's Hamiltonian has proved to be a valuable tool for such calculations. In particular, the ability to calculate Breit-Pauli spin-spin matrix elements between different multiplicities and spin-orbit couplings using the same level of theory is a major advantage of the DFT/MRCI method. While PT favours a charge-transfer-mediated route, evidence for a coherent process *via* a crossing of the potential energy surface (PES) of the bright singlet and the ^{1}(TT) state has been found in TIPS-PT. All calculations were performed with new implementations of the `mrci` and `SPOCK.sistr` programs, using the OpenMP application programming interface (API) for shared memory parallelization. Using PT as an example, it was shown for the `mrci` program that the OpenMP implementation has comparable performance to the older message passing interface (MPI) version, while drastically reducing memory consumption. While DFT/MRCI is certainly a good and robust method for most excited state manifolds, it has been shown that it still has some shortcomings in special cases. The incorrect treatment of degeneracies is probably the most difficult to improve, as it is a conceptual problem of the method. One point that should certainly be investigated more thoroughly in the future is the construction of the reference space, as too much dependence could lead to misinterpretation of the results. In the case of C_{60} the problem was obvious, but this may not always be the case. An extended investigation of the convergence behaviour with respect to the selection threshold is also a good idea. Dombrowski's Hamiltonian gives different results for states with a strong double excitation character, including quintet states, compared to the previous formulations of DFT/MRCI. The convergence behaviour of different states was used in the original formulation to justify the chosen energy selection cut-off. Therefore, it is interesting to see if the values found in the original formulation are still valid for such states despite the large differences in

the formulations of the Hamiltonians. To investigate the SF process further, it would seem that quantum or molecular dynamics simulations would need to be carried out. As DFT/MRCI does not provide analytical gradients, it may not be the ideal tool for this. However, it is certainly worth a try, as the results computed at stationary points are very promising and numerical gradients are available. DFT/MRCI can certainly be used to investigate the influence of vibrations when scanning along normal modes, which are also expected to be of great importance. For this application it is of particular interest to know whether triplet, quintet and singlet states have the same convergence behaviour with the selection cut-off, as it is advisable to reduce the computational cost of these investigations as far as possible. The present work represents the first investigation of quintet states using DFT/MRCI, which does not involve a simple model system, but large molecular systems. Due to the lack of spectroscopic data, no quintet is included in the parameterisation procedure. Nevertheless, the results obtained with Dombrowski's Hamiltonian seem reasonable, judging from the close resemblance of the calculated and experimental zero-field splitting parameters of PT, again showing the robustness of the method. As these results are already promising, it would be very helpful to extend the DFT/MRCI method to anchor configurations with open shells. This would further broaden the range of applications and is currently under investigation.

Glossary

Angular correlation If one particle is above the nuclear plane it is likely to find the other one on the opposite site[105, 279]. 31

Atomic units A unit system in which lengths are measured as multiples of the radius of the lowest orbit in the Hydrogen atom derived from the Bohr model, charges as multiples of the charge of an electron and masses as multiples of the mass of an electron[280]. For an overview table see Andre [281, p. 110]. 6

Basis While mathematicians can live happily ever after without specifying a basis in most of the cases, physicists and quantum chemists cannot. If a set of vectors spans a vector space $\mathcal{V}$ and are linear independent, they constitute a basis of $\mathcal{V}$. One might define the completeness relation

$$\sum_i |a_i\rangle \langle a_i| = \mathbb{I},$$

where a_i are basis vectors and $\mathbb{I}$ is the unit element of $\mathcal{V}$. 158, 251, 252, 255, 256

Charge–transfer The electron is transferred from a donor D to an acceptor A. The energy can be approximated by

$$E_{CT} = I_D + E_A - 1/R,$$

where I_D is the ionization potential (IP) of the donor D, E the EA of the acceptor, and $1/R$ the Coulomb coupling between the two.. 34, 36, 181, 184, 231, 238

Correlation energy In most textbooks on quantum chemistry[112] defined as the difference between the exact energy E_{exact} and the HF energy. However, this definition suggests that HF does not include any kind of particle correlation,

which is not true. Through the exchange operator of HF particles carrying the same spin avoid each other, thereby correlating their positions. In general only two-body interactions are meant when talking of correlation in the context of quantum chemistry. An elegant formulation of the correlation problem can be obtained using the reduced density matrix formalism as was outlined by Löwdin [108][282] and in the book of McWeeny [283]. The key quantity is the two-particle reduced density matrix $\Gamma\left(\kappa_1'\kappa_2'|\kappa_1\kappa_2\right)$ (see reduced density matrix), which for antisymmetric wavefunctions obeys the permutation relations

$$\Gamma\left(\kappa_1'\kappa_2'|\kappa_1\kappa_2\right) = -\Gamma\left(\kappa_2'\kappa_1'|\kappa_1\kappa_2\right) = -\Gamma\left(\kappa_1'\kappa_2'|\kappa_2\kappa_1\right) \tag{1}$$

from which immediately follows

$$\Gamma\left(\kappa_1'\kappa_2'|\kappa_1\kappa_2\right) = 0 \quad \forall \quad \kappa_1' = \kappa_2', \kappa_1 = \kappa_2 \tag{2}$$

as e.g.

$$\Gamma\left(\kappa_1'\kappa_1'|\kappa_1\kappa_2\right) = -\Gamma\left(\kappa_1'\kappa_1'|\kappa_1\kappa_2\right) \tag{3}$$

Remembering that κ is used here to represent spatial and spin degrees of freedom it follows that the probability of finding particles of like coordinate sets, i.e. similar space and spin coordinate, around the same point in space is exactly zero, which is the well known result from Hartree-Fock theory. Treating Coulomb correlation is bit more intricate, as the actual hole carried around by the charged electron is due to the singularity of the Coulomb operator $\frac{1}{|r_2-r_1|}$, when $r_2 \to r_1$ and cannot directly be linked to Γ. However, an obvious implication is that Γ must be very small, when $r_2 \to r_1$. A key insight for a single-determinant wavefunction is that such functions do not treat Coulomb correlation at all. For a thorough discussion on the matter see McWeeny [283, 284] and Pilar [279]. 31–35

Coulomb gauge $\mathrm{div}\vec{A} = \vec{\nabla}\cdot\vec{A} = 0$. 9, 11

Dirac relation Vector identity attributed to Dirac [285].

$$\left(\sigma\cdot\vec{p}\right)\left(\sigma\cdot\vec{q}\right) = \left(p\cdot q\right)\mathbb{I}_2 - i\cdot\sigma\left(\vec{p}\times\vec{q}\right),$$

where $\mathbb{I}$ denotes the two-dimensional matrix representation of the identity, $\vec{\sigma}$ is a vector of the Pauli spin-matrices $\sigma_1, \vec{\sigma_2}, \sigma_3$ and $\vec{p}, \vec{q}$ any two operators commuting with $\vec{\sigma}$. 9, 10

Dual vector The dual space $\mathcal{V}^\star$ of a vector space $\mathcal{V}$ is defined as the space of all linear maps taking an element $|a\rangle$ in $\mathcal{V}$ to the underlying field of numbers $\mathbb{F}$. The elements of $\mathcal{V}^\star$ are thus all of the form $f : \mathcal{V} \mapsto \mathbb{F}$ and are called dual vectors[58, 62, 286]. A common definition for a dual vector f^i is given by: $f^i(v) = v^i$ where v^i is the i-th component of the vector v. This implies $f^i(e_j)\,\delta^i{}_j$, where $\delta^i{}_j$ is the Kronecker-delta. . 256

Einstein summation convention Repeated indices imply a summation, e.g. $v_i e^i = \sum_i v_i e^i$. 256

Electronic configuration Thinking in terms of occupation vectors, presented in Section 2.3, a specific occupation pattern. Using atomic one-particle states $\{\, 1s, 2s \,\}$ as an example one can understand the occupation vectors $|1_{1s}; 1_{2s}\rangle$ and $|2_{1s}; 0_{2s}\rangle$ as two different electronic configurations. The 2 indicates that both spin-states are combined with the spatial orbtial $1s$. 5, 26, 31, 33–37, 40, 44, 47, 50, 51, 158, 162

Exchange–correlation hole The two-particle reduced density matrix Γ_2 maybe split[287, p. 17] into a one-particle density $n(\mathbf{r})$ and a conditional density $n_2(\mathbf{r}, \mathbf{r}')$ interpreted as the density of N-1 particles around $\mathbf{r}'$ if one particle is definitly around $\mathbf{r}$[86].

$$\Gamma_2 = n(\mathbf{r})\, n_2(\mathbf{r}, \mathbf{r}')$$
$$\int d\mathbf{r} n(r) = N \quad \int d\mathbf{r}' n_2(\mathbf{r}, \mathbf{r}') = N - 1 \tag{4}$$

This can be further subdivided into the total density around $\mathbf{r}'$ and an exchange-correlation hole density $n_{xc}(\mathbf{r}, \mathbf{r}')$,

$$n_2(\mathbf{r}, \mathbf{r}') = n(\mathbf{r}') + n_{xc}(\mathbf{r}, \mathbf{r}')$$

which by means of Eq. (4) obeys

$$\int d\mathbf{r}' n_{xc}(\mathbf{r}, \mathbf{r}') = -1$$

As pointed out by [98] this hole potential leads to a stabilizing effect for virtual orbitals in KOHN-SHAM (KS) theory, which is in stark contrast to HARTREE-FOCK (HF) theory. 30

Excition Quasi-particle description of a bound particle-hole pair[288]. Used in the description of excitations in condensed matter. 1

Hamiltonian In classical mechanics the hamilton function is a function of generalized momentum and space coordinates and is directly related to the energy of a system[57]. If the Hamilton function does not have an explicit time dependence the law of energy conservation follows directly from the formalism. It is therefore only natural that it pops up in the context of quantum mechanics when investigating the time-evolution of a state as the hermitian operator associated with energy[59]. It can generally be written as the sum of kinetic $\hat{T}$ and potential energy operators $\hat{V}$ $\hat{H} = \hat{T} + \hat{V}$. 6, 7, 10, 11, 26, 39, 40, 72, 158, 159, 161, 200, 237, 249, 287

Hermitian If the complex conjugate of an operator is equal to the operator itself, the operator is said to be hermitian. The following relation holds

$$\hat{O} = \hat{O}^{\dagger}$$

where the dagger denotes complex conjugation. Hermitian operators are guaranteed to have real eigenvalues and a complete set of eigenfunctions. If instead

$$\hat{O} = -\hat{O}^{\dagger}$$

holds, the operator is said to be anti-hermitian. 12

Hilbert space A space $\mathcal{H}$ defined over a field of numbers $\mathbb{F}$, e.g. the real numbers $\mathbb{R}$, which obeys the following rules:

1. Closed under scalar multiplication: $z \cdot |a\rangle \in \mathcal{H} \quad \forall z \in \mathbb{F}$
2. Distributive under scalar multiplication:

$$\begin{aligned} (|a\rangle + |b\rangle)\, z &= |a\rangle \cdot z + |b\rangle \cdot z \quad \forall z \in \mathbb{F} \\ (y + z)\, |a\rangle &= y \cdot |a\rangle + z \cdot |a\rangle \quad \forall y, z \in \mathbb{F} \end{aligned}$$

3. Closed under addition: $|a\rangle + |b\rangle = |c\rangle \Rightarrow |c\rangle \in \mathcal{H}$
4. Associative under addition: $(|a\rangle + |b\rangle) + |c\rangle = |a\rangle + (|b\rangle + |c\rangle)$
5. An additive identity $|0\rangle$ is $\in \mathcal{H}$: $|a\rangle + |0\rangle = |a\rangle$
6. An additive inverse exists $\forall\, |a\rangle$: $|a\rangle + (-|a\rangle) = -|a\rangle + |a\rangle = |0\rangle$
7. Every pair of elements $\langle a \ |b\rangle$ can be associated with a scalar, commonly called inner product. Connected with this is the notion of the norm $|||a\rangle|| = \sqrt{\langle a|a\rangle}$ and the metric D. The latter is defined such that $D(|a\rangle, |b\rangle) = |||a\rangle - |b\rangle||$ represents the distance between the elements $|a\rangle$ and $|b\rangle$
8. The space is closed under the metric D generated by $\langle a|b\rangle$

where $|a\rangle, |b\rangle, |c\rangle \in \mathcal{H}$ is implied in the above definitions. For a complete treatment the reader is referred to the books of Hassani [62], Jeevanjee [58] or Akhiezer and Glazman [289] . 5, 254, 255

In–out correlation If a particle is close to a centre it is unlikely to find another one a that centre as the present particle repells the others through its electric field[105]. . 31, 33

Irreducible representation If one cannot reduce the subspaces of the underlying vector space of a representation of a group further, the representation is called irreducible[58, 60]. This abstract definition is often made clear considering the matrix representation, where one can show that if no similarity transformation reduces the block form of a matrix further, the matrix representation is irreducible. 15, 16, 159

Iterative Methods Approaches to solve matrix-vector equation of the form $\underline{\underline{A}}\vec{x} = \vec{b}$, where $\underline{\underline{A}} \in \mathbb{C}^{n\times n}$ and $\vec{x}, \vec{b} \in \mathbb{C}^n$, are grouped into iterative and direct methods. The matrix $\underline{\underline{A}}$ is assumed to be non-singular, i.e. $\det\left(\underline{\underline{A}}\right) \neq 0$. While direct methods are in principle exact they often cannot be used for solving large, sparse linear equations[290]. Iterative methods on the other hand only provide approximate solutions, though the precision of the approximation can be controlled. For an overview the reader is reffered to the books of Dahmen [290] or Saad [291]. All of these methods follow the principle where $Q(x_i, b)$ is a map connecting the approximate vector $\vec{x}_i$ and the known vector $\vec{b}$. Iterative methods largely differ in the choice of the convergence criterion and of the map $Q\left(\vec{x}_i, \vec{b}\right)$.

Algorithm 3: General algorithm of an iterative method

1 Pick any start vector $x_0 \in \mathbb{C}^n$;
2 **repeat**
3 | Compute approximation to x $= \underline{\underline{A}}^{-1}\vec{b}$ by $\vec{x}_{i+1} = Q\left(\vec{x}_i, \vec{b}\right)$
4 **until** *Convergence criterion is met*;

The two most prominent members of the class of iterative algorithms are surely the projection methods conjugate gradient and steepest descent, which are used in many areas of computational simulation. In computational chemistry the so-called Davidson-algorithm is widely employed. 45, 49

Kernel Given a linear map $\mathrm{T} : \mathcal{V} \mapsto \mathcal{W}$, where $\mathcal{V}$ and $\mathcal{W}$ are vector spaces, the kernel[286] ker of T is defined as the set of all vectors $v \in \mathcal{V}$ for which $\mathrm{T}(v) = 0_{\mathcal{W}}$, where $0_{\mathcal{W}}$ is the identity element for addition in $\mathcal{W}$. 19, 20

Kronecker–delta Defined by the relation

$$\delta^i{}_j = \begin{cases} 1 & i = j \\ 0 & i \neq j \end{cases} \tag{5}$$

. 21, 243, 248, 256

Left–right correlation Describes the ability of two electrons to avoid each other by staying on opposite sides of a nodal plane[279] . 31

Linear independent A set of vectors $\{ q_i \}$ is said to be *linear independent* if for any element in span q_i $z_1 q_1 + \ldots z_i q_i = 0$ implies $z_1 = z_2 = \cdots = z_i = 0$, where z_k are numbers. 241

Linear operator A (multi-)linear map of the form $L : V \mapsto V$. 5, 244

Message Passing Interface A message-passing standard for usage on parallel computing architectures. Message-passing is a concurrency model where processors synchronize by sending chunks of data (messages) amongst each other. Each processor has a private physical address space. . 260

Minimal coupling When a charged particle, such as an electron is subjected to an electromagnetic field, i.e. a quantity linked to a vector potential $\vec{A}$, one must

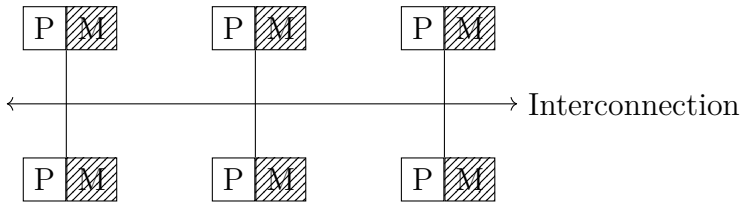

Figure 1: Layout of the distributed memory model. Every process P owns its own address space M. The processes communicate over the network by passing messages among each other

modify the momentum $\vec{p}$ of the particle according to $\pi = \vec{p} + q\vec{A}$, where q is the particle's charge[292]. As only the latter is involved in the coupling it is called *minimal*. See [41] for a detailed discussion of the topic. 8

Nabla operator A vector operator of the form $\left(\frac{\partial}{\partial q_1}, \cdots, \frac{\partial}{\partial q_N}\right)$, where $\frac{\partial}{\partial q_l}$ is the partial derivative with respect to coordinate q_l. 6

Normalizable A function Ψ for which

$$\int_{-\infty}^{\infty} \bar{\Psi}\Psi d\tau = 1 \tag{6}$$

, where the bar denotes complex conjugation and τ collects all varibales the function depends on, has a solution is called normalizable.. 252

Observable If the states associated with a dynamical variable $a \in \mathbb{R}^{\mathrm{n}}$ form a complete set, this variable is called observable[**1947**]. Furthermore, if this variable does not change of the course of time, i.e. $\frac{d}{\mathrm{dt}}a = 0$ it is called a constant of motion. . 5, 12, 13, 252

OpenMP Offers an API supporting shared-memory multiprocessing in different programming languages. A high focus lies on portability and scalability. The underlying design is a fork-join model, sketched in Fig. 2, which means a master thread spawns teams of threads as needed. The shared-memory perspective, shown in Fig. 3, means that all threads share an address space and each owns a small private patch in this space, called stack.

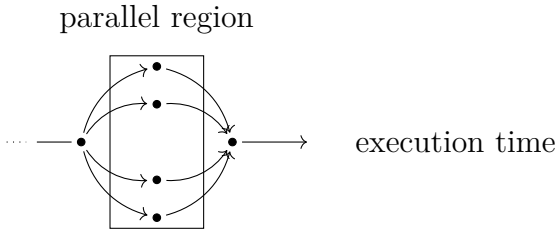

Figure 2: Fork-join model for four spawned threads

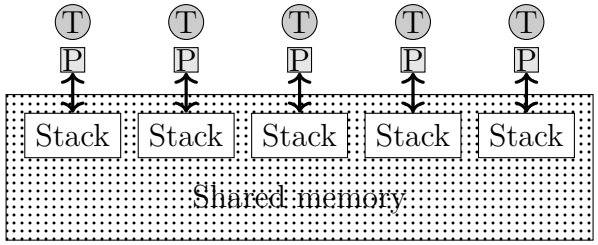

Figure 3: Sketch of a shared memory architecture assuming a one-to-one mapping of threads (T) and processors (P). The threads are scheduled to processors by the operating system. In this work no differentiation between P and T will be made

. vii, ix, 49–52, 238, 260

Orbital Different name for a one-particle wavefunction. Introduced into quantum chemistry by Mulliken [293]. 23, 25, 27, 31, 43, 44, 47, 53, 54, 255, 260

Pair theory Theories based on observations made for two-electron wavefunctions. It is assumed that only pair-interactions are to be incorporated, e.g. assuming completely independent pairs (IEPA) or approximating coupled-pairs (CEPA). For reviews of the method see Szabó [112, chap. 5] or Ahlrichs in [294]. 10

Pauli spin–matrices Set of complex 2×2 matrices $\{ \sigma_1, \sigma_2, \sigma_3 \}$, which can be written as

$$\sigma_j = \begin{pmatrix} \delta_{j3} & \delta_{j1} - i\,\delta_{j2} \\ \delta_{j1} + i\,\delta_{j2} & -\delta_{j3} \end{pmatrix} \tag{7}$$

, where $j = 1, 2, 3$ and δ_{ji} is the Kronecker-delta. They play a fundamental role in quantum mechanics as they are related to the components of the spin angular momentum operator. 8, 243

Perturbation theory Perturbation theory is arguably the most useful tool in quantum mechanics, as it often provides a straightforward insight into the basic

physics of a problem. The idea is simply to split a complicated operator into a simple part, which is easy to solve[1], and a remainder which is seen as a perturbation of the system. Most common for time-independent perturbations is surely Rayleigh-Schrödinger perturbation theory, which will be dealt with briefly here in the line of the discussions given by Sakurai and Napolitano [59] and Helgaker et al. [76]. As a first step the Hamiltonian is separated as

$$\hat{H} = \hat{H}_0 + \lambda\hat{U}$$

where $0 \leq \lambda \leq 1$ is a continuous parameter varying the strength of the perturbation $\hat{U}$. Furthermore, one assumes that the $\hat{U} = 0$ cases' solutions are known. Inserting into the SGL

$$\left(\hat{H}_0 + \lambda\hat{U}\right)|\Psi\rangle_n^\lambda = E_n^\lambda \Psi_n$$

gives an eigenvalue equation, where it is assumed that the states $|\Psi\rangle_n^\lambda$ and associated eigenvalues E_n^λ are continuous functions of the perturbation parameter λ. Expanding $|\Psi\rangle_n^\lambda$ and E_n^λ in orders of λ

$$|\Psi\rangle_n^\lambda = \sum_{k=0}^{\infty} |\psi\rangle_n^k$$
$$E_n^\lambda = \sum_{k=0}^{\infty} E_n^k$$

and inserting gives

$$\left(\hat{H}_0 + \lambda\hat{U}\right)\sum_{k=0}^{\infty}|\psi\rangle_n^k = \left(\sum_{k=0}^{\infty}E_n^k\right)\sum_{k=0}^{\infty}|\psi\rangle_n^k$$

Truncating this expression at an arbitrary order o and rearranging gives the working equation

$$\left(\hat{H}_0 - E_n^0\right)|\psi\rangle_n^o = -\hat{U}\,|\psi\rangle_n^{o-1} + \sum_{k=1}^{o} E^k\,|\psi\rangle^{o-k} \tag{8}$$

Introducing the complementary projection operator $\phi = 1 - |\psi\rangle_n^0\,\langle\psi|_n^0 = \sum_{k\neq n}|\theta\rangle_k^0\,\langle\theta|_k^0$,

[1] or at least simply to approximate

which is nothing but excluding one term from the resolution of the identity in the basis of unperturbed vectors, to guarantee the LEFT-HAND SIDE (LHS) to be invertible gives for the perturbed function of o-th order

$$|\psi\rangle_n^o = -\phi\left(\hat{H}_0 - E_n^0\right)^{-1}\phi\left(\hat{U}\,|\psi\rangle^{o-1} - \sum_{k=1}^{o-1} E^k\,|\psi\rangle^{o-k}\right)$$

The expressions for the energies of n-th order, can be obtained by feeding an arbitrary basis vector $\langle\psi|_i^0$ into Eq (8)

$$\langle\psi|_i^0\left(\hat{H}_0 - E_n^0\right)|\psi\rangle_n^o = -\langle\psi_i^0|\hat{U}|\psi^{o-1}\rangle + \sum_{k=1}^{o} E^k\,\langle\psi_i^0|\psi^{o-k}\rangle$$
$$E^n = \langle\psi_i^0|\hat{U}|\psi^{o-1}\rangle$$

where $\langle\psi_i^0|\psi^n\rangle = 0$ for $n \neq 0$ is assumed. For questions on the topic which one never dared to ask, e.g. why λ can be used in the first place, convergence of the expansion and the like, the reader is referred the brilliant book of Katō [295]. 33

Projection method The goal is to find approximate solutions of $A\vec{\tau} = \lambda\vec{\tau}$, with $A \in \mathbb{R}^{n\times n}$ and $\vec{\tau} \in \mathbb{R}^n$ by searching some approximate eigenvector $\vec{\rho}$, which is an element of some subspace S^m of $\mathbb{R}^n$[290], with $m \leq n$, and the associated eigenvalues b. Generally it is imposed[291] that

$$(A - bI)\,\vec{\rho} \perp S^m, \text{ i.e. } \langle(A - bI)\,\vec{\rho}|\vec{v}\rangle = 0 \quad \forall v \in S^m, \tag{9}$$

where $\langle\cdot|\cdot\rangle$ denotes the inner product. Given some basis $\{\,q_i\,\}$ of S^m one might transform the searched vector's components into this basis according to

$$\vec{\rho} = Q\vec{\xi}$$

where Q is the column matrix of basis vectors[296] $\{\,\vec{q}_1, \vec{q}_2, \ldots, \vec{q}_m\,\}$. It can be concluded that

$$(A - bI)\,Q\vec{\xi} \perp S^m \Leftrightarrow AQ\vec{\xi} = bQ\vec{\xi} \Leftrightarrow Q^{-1}AQ\vec{\xi} = b\vec{\xi},$$

which defines a relation to be forefilled by the pair $\left(b, \vec{\xi}\right)$. A famous example of computing all necessary quantities is the Rayleigh-Ritz procedure . 45, 246

Projection operator A linear map[62] of the form $P : \mathcal{V} \mapsto \mathcal{W}$, where $\mathcal{W}$ is a subspace of $\mathcal{V}$, i.e. $\mathcal{V} = \mathcal{U} \oplus \mathcal{W}$, where $\oplus$ denotes the direct sum, is called a projection operator if it is idempotent, i.e. $P^2 = P$, and hermitian $P = P^\dagger$. 249, 251

Race condition The time-ordering of operations, e.g. read from memory and write to memory, matters. Consider the example of incrementing a variable value x twice, but splitting the work between to processors

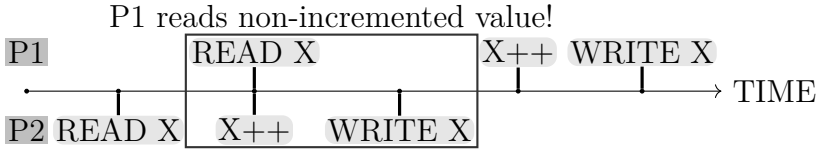

clearly P1 reads the old value of x as P2 has not yet written the incremented value to memory. Therefore, one would get the wrong result. 48, 49

Rayleigh–Ritz procedure Let $A\tau = \lambda\tau$ be an eigenvalue problem with $\lambda \in \mathbb{C}$, $A \in \mathbb{C}^{n\times n}$ and $\tau \in \mathbb{C}^n$. The task is to find approximate solutions $\tilde{\tau}, \tilde{\lambda}$ in some subspace S of dimension d, such that $\langle A\tilde{\tau} - \tilde{\lambda}\tilde{\tau}|v\rangle = 0 \quad \forall v \in S$. This can be achieved with the following procedure . 250

---

1 Construct orthonormal basis $\{ b_i \}_{i=1,\dots,m}$of S ;
2 Construct change-of-basis matrix $Q = [b_1, \dots, b_m]$;
3 Compute matrix representation of A in basis $B_m = Q^\dagger AQ$;
4 Compute eigenvalues $\tilde{\lambda}$ of B_m and select $k \leq m$ desired ones;
5 Compute eigenvectors $\vec{v}_i$ of B_m for every $\tilde{\lambda}$;
6 Compute $\tilde{\tau}_i = V\vec{v}_i$;

Reduced density matrix In the description of quantum states which contain a certain degree of randomness, e.g. an unpolarized light beam, introduction of the density operator $\hat{\rho}$ has proven useful[59, 297]. $\hat{\rho}$ has the following form

$$\hat{\rho}_i = |\psi_i\rangle \langle\psi^i|$$

and is nothing but a projection operator onto the i-th state. Choosing a set of

Basis vectors $\{v_q\}$ and acting with $\hat{\rho}$ gives

$$\hat{\rho}^r{}_s = \langle v^s|\hat{\rho}|v_r\rangle = \langle v^r|\psi_i\rangle\langle\psi^i|v_s\rangle = \langle v^r|\sum_q c^q v_q\rangle\langle\sum_m \bar{c}_m v^m|v_s\rangle = c^r\bar{c}_s$$

after expansion of ψ_i into the orthonormal Basis $\{\, v_a \,\}$, where $\bar{c}$ denotes complex conjugation. As the state ψ_i must be normalizable and the vector space acted on obeys the completeness relation[62], i.e.$\sum_i |i\rangle\langle i| = 1$, it immediately follows $\mathrm{Tr}\,(\rho) = 1$, where Tr is the trace, as

$$\langle\psi^i|\psi_i\rangle = \sum_q \langle\psi^i|u_q\rangle\langle u^q|\psi_i\rangle = \sum_q \bar{c}^q c_q = 1 \rightarrow \sum_m \bar{c}^q c_q = 1.$$

Therefore, the expectation value for any observable $\hat{O}$ can be expressed with $\hat{\rho}$ as $\mathrm{Tr}\,(\rho O)$

$$\begin{aligned}\langle\hat{O}\rangle = \langle\psi^i|\hat{O}|\psi_i\rangle &= \langle\sum_{m,q}\langle\psi^i|u_m\rangle\langle u^m|\hat{O}|u_q\rangle\langle u^q|\psi_i\rangle\rangle \\ &= \langle\sum_{m,q}\langle u^q|\psi_i\rangle\langle\psi^i|u_m\rangle\langle u^m|\hat{O}|u_q\rangle\rangle \\ &= \sum_{m,q}\rho^m{}_q\, O^q{}_m = \sum_q [\rho O]_q{}^q = \mathrm{Tr}\,(\rho O)\end{aligned}$$

where the last step is a simple matrix multiplication between the m-th row of the matrix-representation of $\hat{\rho}$ and the m-th column of the matrix-representation of $\hat{O}$. This result holds for an arbitrary choice of basis vectors as Tr is independent of the chosen basis. Using the continuous position vectors $\{\ |\,\mathbf{r}\rangle\,\}$ as a basis, where $|\mathbf{r}\rangle = \int d^3\mathbf{r}\psi\,(\mathbf{r})$ and $\int d^3\mathbf{r}\,|\mathbf{r}\rangle\langle\mathbf{r}| = 1$, one obtains for the matrix representation of the density operator

$$\begin{aligned}\langle\mathbf{r}'|\hat{\rho}|\mathbf{r}\rangle &= \langle\mathbf{r}'\,|\phi_i\rangle\langle\phi^i|\,\mathbf{r}\rangle \\ &= \iint d^3\mathbf{r}'d^3\mathbf{r}\,\langle\mathbf{r}'\,|\mathbf{r}'\rangle\langle\mathbf{r}'|\phi_i\rangle\langle\phi^i|\mathbf{r}\rangle\langle\mathbf{r}|\,\mathbf{r}\rangle \\ &= \iint d^3\mathbf{r}'d^3\mathbf{r}\bar{\psi}^i\,(\mathbf{r}')\,\psi_i\,(\mathbf{r})\end{aligned}$$

on inserting the completeness relation twice and using $\langle\mathbf{r}'|\phi_i\rangle = \bar{\psi}^i\,(\mathbf{r})$. Letting $\mathbf{r} = \mathbf{r}'$ gives $\int d^3\mathbf{r}\bar{\psi}^i\,(\mathbf{r})\,\psi_i\,(\mathbf{r})$, which is just the probability density $\int |\psi_i|^2$ of

finding the particle in the i-th state in the volume element $d^3\mathbf{r}$. The expressions are easily generalized for a system consisting of N particles, by the same procedure. Letting $\kappa = \{\,\kappa_i\,\}$ denote the collection of all variables κ_i occurring in the many-particle wavefunction $\Psi\left(\kappa\right)$ leads to

$$\begin{aligned}&\iint d\kappa d\kappa' \bar{\Psi}\left(\kappa'\right)\Psi\left(\kappa\right) = \\ &\int d\kappa_1 d\kappa_2 \ldots d\kappa_N \int d\kappa'_1 \ldots d\kappa'_N \bar{\Psi}\left(\kappa'_1, \ldots \kappa'_N\right)\Psi\left(\kappa_1, \ldots \kappa_N\right)\end{aligned}$$

Letting $\kappa'_1 = \kappa_1; \kappa'_2 = \kappa_2; \ldots$ in the spirit of the discussion given above leads to the same result for the diagonal elements. As we assumed the particles to be indistinguishable we can associate κ_1 with any one of the N particles. Similarly, as soon as we made our choice for κ_1, we can associate κ_2 with any one of the $N-1$ particles left. One can easily see that we are left with $N!$ choices in total, which motivates the definition of the N-particle density[284] matrix commonly denoted Γ^N[279]

$$\Gamma_N = N!\rho\left(\kappa'|\kappa\right)$$

where we made the dependency of ρ on κ' and κ explicit, similarly to the discussion given by Pilar [279, p. 291]. Löwdin [108] introduced the concept of a reduced density matrix Γ^p_N

$$\begin{aligned}\Gamma^p_N &= p!\binom{N}{p}\int \rho\left(\kappa'|\kappa\right) d\kappa_{p+1} d\kappa_{p+2} \ldots d\kappa_N \\ &= p!\binom{N}{p}\int \big[\bar{\Psi}\left(\kappa'_1, \ldots, \kappa'_p, \kappa_{p+1}, \ldots\right) \\ &\Psi\left(\kappa_1, \ldots, \kappa_p, \kappa_{p+1}, \ldots\right) d\kappa'_1 d\kappa_1 \ldots d\kappa'_p d\kappa_p\big]\, d\kappa_{p+1} d\kappa_{p+2} \ldots d\kappa_N\end{aligned}$$

This is motivated by the fact, that the complete matrix consists of particle subblocks. For example the one-particle block consists solely of matrix elements of the form $\rho\left(\kappa'_i|\kappa_i\right)$, while the two-particle block has elements of type $\rho\left(\kappa'_i\kappa'_j|\kappa_i\kappa_j\right)$

$$\begin{aligned}\gamma^1 &= N\int \rho\left(\kappa'_1|\kappa_1\right) d\kappa_2 \ldots d\kappa_N \\ \Gamma^2 &= N\left(N-1\right)\int \rho\left(\kappa'_1\kappa'_2|\kappa_1\kappa_2\right) d\kappa_3 \ldots d\kappa_N\end{aligned}$$

28, 242, 243

Resolution of the Identity Different phrasing for the completeness relation of the underlying Hilbert space $\sum |a\rangle \langle a| = 1$. 22, 249, 254

Resolution of the Identity approximation Used to approximate two-center integrals by inserting the resolution of the identity. The approximation lies in the unavoidable truncation of the latter[298, 299].

$$\langle ij|kl\rangle \approx \langle ij \sum_{a}^{M} |a\rangle \langle a| kl\rangle$$

The computational effort is formally reduced from N^4 to N^3, where N is the number of orbitals. For a discussion on the true scaling see e.g. [300]. 50

Schrödinger picture Interpretation of quantum mechanics in which the time-evolution of a system is fully described in terms of the wavefunction $|\Psi(t, \mathbf{r})\rangle$. 260

Self–interaction error An error arising in density functional theory (DFT) due to an incomplete cancellation of the Hartree-like Coulomb interaction $J[\rho] = \frac{1}{2}\int d^3r_1 d^3r_2 \frac{\rho(\vec{r}_1)\rho(\vec{r}_2)}{r_1 2}$, where $\rho(r_i)$ is the total electron density. Writing the Kohn-Sham (KS)-energy functional as

$$E[\rho] = T_{\mathrm{s}}[\rho] + J[\rho] + E_{\mathrm{xc}}[\rho] \tag{10}$$

and simply assuming a true non-interacting system, e.g. a single electron, immediately shows that

$$J[\rho] = -E_{\mathrm{xc}}[\rho] \tag{11}$$

must hold for the exact exchange-correlation functional. For approximate functionals this is often not the case leading to spurious interactions. 36, 41

Slater–Condon rules Set of rules for matrix elements of one- and two-body operators[76, 112], which are readily shown with the tools of second quantization (Sec.2.3). Let $\hat{O}^{(2)} = \sum_{pqrs} O_{pqrs} a_p^\dagger a_r^\dagger a_s a_q$ be a two-particle operator and $\langle a| = \langle \mathbf{0}| a_i a_j, |b\rangle = a_k^\dagger a_l^\dagger |\mathbf{0}\rangle$ two eigenfunctions of the number operator, i.e. $\hat{N}^p |b\rangle = k_p |b\rangle$. Denoting their difference in occupation with Δ_{occ} the possible

matrix elements for a two-electron operator become

$$\langle a|\sum_{pqrs}^{max} O_{pqrs}a_p^\dagger a_r^\dagger a_s a_q|b\rangle = \begin{cases} \sum_{pr} k_p k_r \left(O_{pprr} - O_{prrp}\right) & \text{if a = b} \\ \Lambda_i\Lambda_j \sum_r k_r \left(g_{ijrr} - g_{irrj}\right) & \Delta_{occ} = 1 \\ \Lambda_i\Lambda_j\Lambda_k\Lambda_l \left(g_{ikjl} - g_{iljk}\right) & \Delta_{occ} = 2 \\ 0 & \text{else} \end{cases} \tag{12}$$

, where Λ_I denotes the sign resulting due to the necessary permutations of the differing occupations. That it is not possible to generate a full line-up of the operator string $a_p^\dagger a_r^\dagger a_s a_q$ if a and b differ by more than two orbitals should be apparent. 47

Slater determinant Anti-symmetrized product of orbitals introduced by Slater [301], as ansatz for the fermionic many-particle wavefunction. The author's favourite discussion of the concept can be found in the educationally valuable book of Szabó [112]. 25–28, 31–33

Span Given a vector space $\mathcal{V}$ and a list of vectors $\{\, q_i \,\}$ living in $\mathcal{V}$ one can start constructing linear combinations of the $\{\, q_i \,\}$, i.e. constructs of the form $z_1 q_1 + z_2 q_2 + \cdots + z_i q_q$, where z is a number. The set of all linear combinations on $\{\, q_i \,\}$ is called the span of $\{\, q_i \,\}$. If span q_i is similar to $\mathcal{V}$ it is said that $\{\, q_i \,\}$ *spans* $\mathcal{V}$. For a good introduction on the subject see Axler [286]. 241, 246

Spinor Fundamental representations of the matrix Lie-groups SU(2) and SL(2,$\mathbb{C}$). For a concise treatment of basic representation theory see Jeevanjee [58, ch. 5]. 8

State In contrast to classical mechanics where a state is fully defined through six parameters at all times, one needs to consider a whole function in quantum mechanics. This sets up the stage for the involvement of complex vector spaces, whose members are called state vectors and are represented by a $|\cdot\rangle$. If A is a linear map on such a complex vector space $\mathcal{V}$ and its effect on an arbitrary element $|q\rangle$ of $\mathcal{V}$ is simply multiplying it by constant

$$A\,|q\rangle = q\,|q\rangle \tag{13}$$

one calls $|q\rangle$ an eigenstate and q an eigenvalue of the linear operator A. It can be shown that the set of all eigenstates forms a Basis of $\mathcal{V}$. Consequently, an

arbitrary state $|\Pi\rangle$ can be expanded in the basis formed by the eigenstates of an operator

$$|\Pi\rangle = \sum_i \langle q^i|\Pi\rangle \, |q_i\rangle = \sum_i c_q^i \, |q\rangle \tag{14}$$

where the dual vector $\langle q|$ was introduced. Note $\langle q^i|q_j\rangle = \delta_{ij}$, where δ_{ij} is the Kronecker-delta.. 247

Stationary state An eigenstate associated with the observable energy E. Its time dependence is fully described by a phase-factor $e^{\frac{-itE}{\hbar}} \forall t \in \mathbb{R}$[302]. 5

Tensor A multilinear map of the form $T : \mathcal{V}_s \times \mathcal{V}_r^\star \mapsto \mathbb{F}$ where $\mathbb{F}$ denotes a field of numbers and $\mathcal{V}_s \times \mathcal{V}_r^\star$ represents s-times the Cartesian product of the vector space $\mathcal{V}$ ($\mathcal{V}_1 \times \mathcal{V}_2 \times \cdots \times \mathcal{V}_s$) and r-times the dual vector space $\mathcal{V}^\star$ ($\mathcal{V}_1^\star \times \mathcal{V}_2^\star \times \cdots \times \mathcal{V}_r^\star$). Consequently a tensor can be classified by the notation $T\,(r, s)$ or T_r^s, where r denotes the number of vectors and s the number of dual vectors as every dual vector must be paired with a vector from $\mathcal{V}$ and *vice versa*. All tensors of type (r, s) acting on a vector space $\mathcal{Q}$ again form a vector space denoted $\mathcal{T}_r^s\,(\mathcal{Q})$. An more intuitive way of understanding on what kind of spaces a tensor acts is to simply consider an example. For $r = 2$ and $s = 0$ we would get $\mathcal{V} \times \mathcal{V}$ from the given definition. This space has elements of the form $(v_1, v_1)\,, (v_1, v_2)\,, \ldots (v_2, v_1)\,, (v_2, v_2) \ldots$. A prominent represent of such a space would be $\mathbb{R}^2 = \mathbb{R} \times \mathbb{R}$, which obviously contains tuples of the shown form. The space of all maps T taking an element of $\mathbb{R}^2$ as input and outputting a number, e.g., is denoted $T_2^0\,(\mathbb{R}^2)$ Multilineality simply means that $T\,(q_1 \ldots z q_o + y q_p \ldots q_r) \;=\; zT\,(q_1 \ldots q_o \ldots q_r) + yT\,(q_1 \ldots q_p \ldots q_r)$ holds for every argument of T. Tensors are said to have a rank k, which is simply the count of arguments they take $k = r + s$ as inputs. As a consequence, a tensor of rank 2 can either be of type (2, 0), (1, 1) or (0, 2). Acting on a set of Basis vectors yields the tensor's components, which are often quantities of physical interest. For example acting on the vector v and the dual vector t with a (1, 1) tensor gives

$$T_1^1\,(v, t) = T_1^1\left(v^i e_i, t_k f^k\right) = v^i t_k T_1^1\left(e_i, f^k\right) = v^i t_k T_i{}^k$$

where the Einstein summation convention has been used, and e_i / f^k denote basis vectors of $\mathcal{V}$ and $\mathcal{V}^\star$, respectively. Similarly one might expand T_1^1 using

the tensor product.

$$T_1^1(v,t) = T_k{}^l\left(e_k \otimes f^l\right)(v,t) = T_k{}^l v^j t_i e_k\left(f^i\right) f^l(e_j) = v^i t_k T_i{}^k$$

. 15, 246, 257

Tensor product One of the axioms of quantum mechanics is that adding degrees of freedom to the system corresponds to taking the tensor product[58, 297] of the subspaces. Generally taking the tensor product is denoted by $\otimes$ and is nothing but another tensor on the connected spaces. Given two tensors $A(r,s)$ and $Z(o,p)$, one can construct the composite map

$$(A \otimes Z)(r+o, s+p) \equiv A(v_1,\ldots,v_r,t_1,\ldots,t_s)\, Z(v_{r+1},\ldots,v_o,t_{s+1},\ldots,t_p)$$

acting on $\mathcal{V}^\star_{r+o} \times \mathcal{V}_{s+p}$. A very useful consequence from the introduction of the tensor product is that one can show that the set of all tensor products between basis vectors of $\mathcal{V}$ and $\mathcal{V}^\star$, whose Cartesian product is acted upon by the tensor, can be used to define a basis for the vector space $\mathcal{T}^s_r$.

$$A = A^{t_1;t_2;\ldots;t_r}_{i_1;i_2;\ldots;i_s} e_1 \otimes e_2 \otimes \cdots \otimes e_r \otimes f^1 \otimes f^2 \otimes \cdots \otimes f^s$$

. 5, 14, 16, 257

Acronyms and Abbreviations

26dPa 2,6-Di-phenyl-anthracene. 161, 183, 189, 191–194, 283

910dPA 9,10-Di-phenyl-anthracene. 161, 183, 189, 192, 194, 195, 283

91NA 9-(1-Naphthyl)-anthracene. 161, 183, 188–193, 283

99pBA 9,9′-Bis-anthracene. 161, 183, 184, 189, 191–194, 283

9PA 9-Phenyl-anthracene. 161, 183, 189, 191–193, 283

An Anthracene. 161, 183–187, 189–192, 200, 220, 237, 282, 288

API Application programming interface. vii, ix, 48, 50, 238, 247

CI Configuration interaction. 31, 32, 34, 40, 44, 56, 158, 159, 190, 287

CIS Configuration interaction singles. 32, 36

CSF Configuration state function. 26, 28, 32, 34–37, 43, 45, 47–50, 159, 190, 287

DFT Density functional theory. ix, 28, 30, 34, 157, 182, 192, 254, 282

DFT/MRCI Density functional theory combined with multi-reference configuration interaction. ix, xv, 39, 40, 53, 72, 158, 159, 161, 163, 181–183, 185, 188–199, 221, 225, 227, 228, 237–239, 281, 283, 287, 288

EA Electron affinity. 30, 162, 181–185, 192, 195, 241, 288

FC Franck-Condon. 184–188, 224, 282–284

HF Hartree-Fock. 25–32, 36, 38, 40, 182, 241, 244

HHU Heinrich Heine University. 3

HOMO Highest occupied molecular orbital. 30, 54, 162, 190, 219, 221, 282

IP Ionization potential. 30, 241

KS Kohn-Sham. ix, 29–31, 35, 37, 50, 158, 182, 192–195, 220, 244, 254, 260, 284, 288

LDA Local-density approximation. 36

LHS Left-hand side. 16, 19, 250

LUMO Lowest unoccupied molecular orbital. 30, 54, 162, 182, 190, 193, 194, 219, 221, 282, 288

MO Molecular orbital. ix, 18, 44, 48, 53, 157, 158, 181, 182, 192, 195, 220–223, 282, 284, 288

MPI Message Passing Interface. 48–51, 238, 281

MRCI Multi-reference configuration interaction. ix, 33, 34, 43, 47, 48, 54, 182, 281, 288

OMP OpenMP. 48–51, 200, 281

ONV Occupation number vector. 18, 19, 21

PD–PES Photodetachment-photoelectron spectroscopy. ix, 161–163, 181, 183–186, 193, 237, 282

PES Potential energy surface. 162, 181, 185, 191, 231, 238, 282

PT Pentacene. viii–x, 3, 53, 72, 161, 200, 219–226, 231, 232, 237, 238, 284, 288

ROKS KS. 182, 192, 193, 288

SF Singlet exciton fission. ix, 1–3, 53, 54, 200, 219, 231, 232, 237, 238, 281

SGL Schrödinger picture. 10, 29, 249

SI Supporting information. 158

TD–DFT Time-dependent density functional theory. ix, 30, 33, 36

TIPS Triisopropylsilyl. 53, 219, 220, 223, 225, 226, 281, 283, 284

TIPS–PT 6,13-Bis(triisopropylsilylethynyl)pentacene. viii, ix, 3, 161, 200, 219–225, 228–234, 237, 238, 283, 284, 288

TIPSet Triisopropylsilylethynyl. 219, 222, 225

TM Transition-metal. 37

trARPES Time- and angle-resolved photo-emission spectroscopy. 200

VDE Vertical detachment energy. 162, 181, 182, 192–194, 238, 288

WET Wigner-Eckart Theorem. 15, 17

ZPVE Zero-point vibrational energy. 182, 192, 288

Bibliography

[5] M. Guarnieri, *IEEE Industrial Electronics Magazine* **2015**, *9*, 58–61.

[6] B. Berger, C. Hanisch, Öffentliche Stromerzeugung 2023: Erneuerbare Energien Decken Erstmals Großteil des Stromverbrauchs [pressemeldung], tech. rep., Frauenhofer ISE, Fraunhofer ISE, Heidenhofstr. 2, 79110 Freiburg, **2024**.

[7] H. Wirth, Aktuelle Fakten zur Photovoltaik in Deutschland, tech. rep., Photovoltaische Module und Kraftwerke, Fraunhofer ISE, Fraunhofer ISE, Heidenhofstr. 2, 79110 Freiburg, **2024**.

[8] M. A. Green, E. D. Dunlop, G. Siefer, M. Yoshita, N. Kopidakis, K. Bothe, X. Hao, *Progress in Photovoltaics: Research and Applications* **2022**, *31*, 3–16.

[9] W. Shockley, H. J. Queisser, *Journal of Applied Physics* **1961**, *32*, 510–519.

[10] J.-F. Guillemoles, T. Kirchartz, D. Cahen, U. Rau, *Nature Photonics* **2019**, *13*, 501–505.

[11] D. Meissner, *Solarzellen, Physikalische Grundlagen und Anwendungen in der Photovoltaik*, Springer Vieweg. in Springer Fachmedien Wiesbaden GmbH, Wiesbaden, **1993**.

[12] M. C. Hanna, A. J. Nozik, *Journal of Applied Physics* **2006**, *100*.

[13] M. B. Smith, J. Michl, *Chemical Reviews* **2010**, *110*, 6891–6936.

[14] M. B. Smith, J. Michl, *Annual Review of Physical Chemistry* **2013**, *64*, 361–386.

[15] K. Miyata, F. S. Conrad-Burton, F. L. Geyer, X.-Y. Zhu, *Chemical Reviews* **2019**, *119*, 4261–4292.

[16] N. V. Korovina, N. F. Pompetti, J. C. Johnson, *The Journal of Chemical Physics* **2020**, *152*.

[17] N. Monahan, X.-Y. Zhu, *Annual Review of Physical Chemistry* **2015**, *66*, 601–618.

[18] D. Casanova, *Chemical Reviews* **2018**, *118*, 7164–7207.

[19] C. Hetzer, D. M. Guldi, R. R. Tykwinski, *Chemistry – A European Journal* **2018**, *24*, 8245–8257.

[20] J. J. Burdett, C. J. Bardeen, *Accounts of Chemical Research* **2013**, *46*, 1312–1320.

[21] C. Grieco, E. R. Kennehan, H. Kim, R. D. Pensack, A. N. Brigeman, A. Rimshaw, M. M. Payne, J. E. Anthony, N. C. Giebink, G. D. Scholes, J. B. Asbury, *The Journal of Physical Chemistry C* **2018**, *122*, 2012–2022.

[22] G. D. Scholes, *The Journal of Physical Chemistry A* **2015**, *119*, 12699–12705.

[23] W.-L. Chan, M. Ligges, A. Jailaubekov, L. Kaake, L. Miaja-Avila, X.-Y. Zhu, *Science* **2011**, *334*, 1541–1545.

[24] M. I. Collins, F. Campaioli, M. J. Y. Tayebjee, J. H. Cole, D. R. McCamey, *Communications Physics* **2023**, *6*.

[25] M. J. Y. Tayebjee, S. N. Sanders, E. Kumarasamy, L. M. Campos, M. Y. Sfeir, D. R. McCamey, *Nature Physics* **2016**, *13*, 182–188.

[26] L. R. Weiss, S. L. Bayliss, F. Kraffert, K. J. Thorley, J. E. Anthony, R. Bittl, R. H. Friend, A. Rao, N. C. Greenham, J. Behrends, *Nature Physics* **2016**, *13*, 176–181.

[27] B. S. Basel, I. Papadopoulos, D. Thiel, R. Casillas, J. Zirzlmeier, T. Clark, D. M. Guldi, R. R. Tykwinski, *Trends in Chemistry* **2019**, *1*, 11–21.

[28] T. Sakuma, H. Sakai, Y. Araki, T. Mori, T. Wada, N. V. Tkachenko, T. Hasobe, *The Journal of Physical Chemistry A* **2016**, *120*, 1867–1875.

[29] C. K. Yong, A. J. Musser, S. L. Bayliss, S. Lukman, H. Tamura, O. Bubnova, R. K. Hallani, A. Meneau, R. Resel, M. Maruyama, S. Hotta, L. M. Herz, D. Beljonne, J. E. Anthony, J. Clark, H. Sirringhaus, *Nature Communications* **2017**, *8*.

[30] H.-w. Bahng, C. D. Ertl, J. Yuan, M. O. Wolf, *The Journal of Physical Chemistry Letters* **2023**, *14*, 10369–10377.

[31] M. H. Farag, A. I. Krylov, *The Journal of Physical Chemistry C* **2018**, *122*, 25753–25763.

[32] B. Friedrich, D. Herschbach, *Physics Today* **2003**, *56*, 53–59.

[33] T. Lancaster, S. Blundell, *Quantum Field Theory for the Gifted Amateur*, OUP Oxford, **2014**.

[34] H. C. Ohanian, *American Journal of Physics* **1986**, *54*, 500–505.

[35] W. Kutzelnigg, *Chemical Physics* **2012**, *395*, 16–34.

[36] F. Jensen, *Introduction to Computational Chemistry*, 2nd ed., Wiley, Chichester [u.a.], **2007**.

[37] H. Haken, *Molekülphysik Und Quantenchemie, Einführung in die experimentellen und theoretischen Grundlagen*, 5th ed., (Ed.: H. C. Wolf), Springer, Berlin, **2006**.

[38] J.-M. Lévy-Leblond, *Communications in Mathematical Physics* **1967**, *6*, 286–311.

[39] W. Kutzelnigg, *Theoretica Chimica Acta* **1988**, *73*, 173–200.

[40] N. Gilka, PhD thesis, Düsseldorf, Univ., Diss., 2008, **2008**.

[41] M. Reiher, A. Wolf, *Relativistic Quantum Chemistry: The Fundamental Theory of Molecular Science*, Wiley, **2014**.

[42] K. G. Dyall, *Introduction to Relativistic Quantum Chemistry*, (Ed.: K. Faegri), Oxford University Press, New York, **2020**.

[43] J. J. Sakurai, *Advanced Quantum Mechanics*, Addison-Wesley, Reading, Mass., **1999**.

[44] M. Barysz, Y. Ishikawa, *Relativistic Methods for Chemists*, Springer Netherlands, **2010**.

[45] M. Gell-Mann, *Il Nuovo Cimento* **1956**, *4*, 848–866.

[46] A. Messiah, *Quantum Mechanics, Two volumes bound as one*, Dover Publications, Inc., Garden City, New York, **2020**.

[47] W. Kutzelnigg, *Chemical Physics* **1997**, *225*, 203–222.

[48] W. Kutzelnigg, *Zeitschrift für Physik D Atoms Molecules and Clusters* **1989**, *11*, 15–28.

[49] W. Kutzelnigg, *Zeitschrift für Physik D Atoms Molecules and Clusters* **1990**, *15*, 27–50.

[50] T. Saue, *ChemPhysChem* **2011**, *12*, 3077–3094.

[51] W. Liu, *Molecular Physics* **2010**, *108*, 1679–1706.

[52] G. Breit, *Physical Review* **1929**, *34*, 553–573.

[53] G. Breit, *Physical Review* **1930**, *35*, 569–578.

[54] G. Breit, *Physical Review* **1932**, *39*, 616–624.

[55] *Handbook of Relativistic Quantum Chemistry*, (Ed.: W. Liu), Springer, Berlin, Heidelberg, **2017**.

[56] H. Bethe, E. Salpeter, *Quantum Mechanics of One- and Two-Electron Atoms*, Springer Berlin Heidelberg, **1957**.

[57] L. D. Landau, E. M. Lifschitz, *Band 1 Mechanik*, (Ed.: G. Heber), De Gruyter, Berlin, Boston, **1962**.

[58] N. Jeevanjee, *An Introduction to Tensors and Group Theory for Physicists*, Springer International Publishing, **2015**.

[59] J. J. Sakurai, J. Napolitano, *Modern Quantum Mechanics*, 3rd ed., Cambridge University Press, Cambridge, United Kingdom, **2021**.

[60] M. Tinkham, *Group Theory and Quantum Mechanics*, Dover Publications, Incorporated, Newburyport, **2003**.

[61] J. S. Rose, *A Course on Group Theory*, 1st ed., Dover Publications, New York, **1994**.

[62] S. Hassani, *Mathematical Physics: A Modern Introduction to Its Foundations*, Springer International Publishing, **2013**.

[63] F. Iachello, *Lie Algebras and Applications*, 2nd ed., Springer, Berlin, Heidelberg, **2015**.

[64] B. C. Hall, *Quantum Theory for Mathematicians*, 1st ed., Springer New York, New York, NY, **2013**.

[65] V. Devanathan, *Angular Momentum Techniques in Quantum Mechanics*, Kluwer Academic Publishers, Dordrecht, **2002**.

[66] M. E. Rose, *Elementary Theory of Angular Momentum*, Wiley, New York u.a., **1957**.

[67] F. Schwabl, *Quantenmechanik (qm I) – Eine Einführung*, 7th ed., Springer Berlin Heidelberg, **2007**.

[68] A. R. Edmonds, *Angular Momentum in Quantum Mechanics*, Princeton University Press, Princeton, NJ, **2016**.

[69] G. Racah, *Physical Review* **1942**, *62*, 438–462.

[70] G. Racah, *Physical Review* **1942**, *61*, 186–197.

[71] G. Racah, *Physical Review* **1943**, *63*, 367–382.

[72] P. R. Fontana, *Physical Review* **1962**, *125*, 220–228.

[73] P. R. Fontana, W. J. Meath, *Journal of Mathematical Physics* **1968**, *9*, 1357–1364.

[74] H. Rollnik, *Quantentheorie 2*, Springer Berlin Heidelberg, Berlin, Heidelberg, **2003**.

[75] H. Reinhardt, *Quantenmechanik 2, Pfadintegralformulierung und Operatorformalismus*, Oldenbourg Verlag, München, **2013**.

[76] T. Helgaker, P. Jorgensen, J. Olsen, *Molecular Electronic-Structure Theory*, Wiley, Hoboken, **2014**.

[77] R. Pauncz, *Spin Eigenfunctions, Construction and Use*, Springer, New York, NY, **1979**.

[78] D. A. Mazziotti, *Accounts of Chemical Research* **2006**, *39*, 207–215.

[79] P. Hohenberg, W. Kohn, *Physical Review* **1964**, *136*, B864–B871.

[80] R. M. Dreizler, *Density Functional Methods in Physics*, (Ed.: J. da Providência), Springer, New York, NY, **1985**.

[81] M. Levy, *Proceedings of the National Academy of Sciences* **1979**, *76*, 6062–6065.

[82] M. Levy, *Physical Review A* **1982**, *26*, 1200–1208.

[83] E. H. Lieb, *International Journal of Quantum Chemistry* **1983**, *24*, 243–277.

[84] J. E. Harriman, *Physical Review A* **1981**, *24*, 680–682.

[85] W. Kohn, L. J. Sham, *Physical Review* **1965**, *140*, A1133–A1138.

[86] R. O. Jones, O. Gunnarsson, *Reviews of Modern Physics* **1989**, *61*, 689–746.

[87] A. J. Cohen, P. Mori-Sánchez, W. Yang, *Chemical Reviews* **2011**, *112*, 289–320.

[88] J. F. Janak, *Physical Review B* **1978**, *18*, 7165–7168.

[89] E. Kraisler, G. Makov, N. Argaman, I. Kelson, *Physical Review A* **2009**, *80*, 032115.

[90] J. Katriel, E. R. Davidson, *Proceedings of the National Academy of Sciences* **1980**, *77*, 4403–4406.

[91] J. P. Perdew, R. G. Parr, M. Levy, J. L. Balduz, *Physical Review Letters* **1982**, *49*, 1691–1694.

[92] M. Levy, R. G. Parr, *The Journal of Chemical Physics* **1976**, *64*, 2707–2708.

[93] M. Levy, J. P. Perdew, V. Sahni, *Physical Review A* **1984**, *30*, 2745–2748.

[94] J. P. Perdew, M. Levy, *Physical Review Letters* **1983**, *51*, 1884–1887.

[95] M. M. Valiev, G. W. Fernando, *Physical Review B* **1995**, *52*, 10697–10700.

[96] J. P. Perdew, A. Zunger, *Physical Review B* **1981**, *23*, 5048–5079.

[97] A. J. Cohen, P. Mori-Sánchez, W. Yang, *Physical Review B* **2008**, *77*, 115123.

[98] E. J. Baerends, O. V. Gritsenko, R. van Meer, *Physical Chemistry Chemical Physics* **2013**, *15*, 16408.

[99] E. J. Baerends, *Physical Chemistry Chemical Physics* **2017**, *19*, 15639–15656.

[100] E. J. Baerends, *The Journal of Chemical Physics* **2018**, *149*.

[101] D. Mester, M. Kállay, *Journal of Chemical Theory and Computation* **2022**, *18*, 1646–1662.

[102] P. Mori-Sánchez, A. J. Cohen, *Physical Chemistry Chemical Physics* **2014**, *16*, 14378–14387.

[103] A. Görling, *Physical Review A* **1996**, *54*, 3912–3915.

[104] A. Grüneis, S. Hirata, Y.-y. Ohnishi, S. Ten-no, *The Journal of Chemical Physics* **2017**, *146*.

[105] L. Kong, F. A. Bischoff, E. F. Valeev, *Chemical Reviews* **2011**, *112*, 75–107.

[106] C. Eckart, *Physical Review* **1930**, *36*, 878–892.

[107] W.-K. Li, *Journal of Chemical Education* **1987**, *64*, 128.

[108] P.-O. Löwdin, *Physical Review* **1955**, *97*, 1474–1489.

[109] A. D. McLean, A. Weiss, M. Yoshimine, *Reviews of Modern Physics* **1960**, *32*, 211–218.

[110] O. Sinanoğlu, *The Journal of Chemical Physics* **1962**, *36*, 706–717.

[111] O. Sinanoğlu, *Advances in Chemical Physics* **1964**, 315–412.

[112] A. Szabó, *Modern Quantum Chemistry Introduction to Advanced Electronic Structure Theory*, 1st ed., McGraw-Hill, New York u.a., **1989**.

[113] R. J. Bartlett, *Annual Review of Physical Chemistry* **1981**, *32*, 359–401.

[114] A. Dreuw, M. Head-Gordon, *Chemical Reviews* **2005**, *105*, 4009–4037.

[115] C. F. Bender, E. R. Davidson, *Physical Review* **1969**, *183*, 23–30.

[116] B. Huron, J. P. Malrieu, P. Rancurel, *The Journal of Chemical Physics* **1973**, *58*, 5745–5759.

[117] R. J. Buenker, S. D. Peyerimhoff, *Theoretica Chimica Acta* **1974**, *35*, 33–58.

[118] A. A. Holmes, N. M. Tubman, C. J. Umrigar, *Journal of Chemical Theory and Computation* **2016**, *12*, 3674–3680.

[119] J. C. Greer, *The Journal of Chemical Physics* **1995**, *103*, 1821–1828.

[120] H.-J. Werner, P. J. Knowles, *The Journal of Chemical Physics* **1988**, *89*, 5803–5814.

[121] W. Thiel, *WIREs Computational Molecular Science* **2013**, *4*, 145–157.

[122] M. E. Casida, *Journal of Molecular Structure: THEOCHEM* **2009**, *914*, 3–18.

[123] A. Dreuw, J. L. Weisman, M. Head-Gordon, *The Journal of Chemical Physics* **2003**, *119*, 2943–2946.

[124] N. T. Maitra, *Annual Review of Physical Chemistry* **2022**, *73*, 117–140.

[125] P. Fulde, H. Stoll, *The Journal of Chemical Physics* **2017**, *146*.

[126] S. Grimme, *Chemical Physics Letters* **1996**, *259*, 128–137.

[127] S. Grimme, M. Waletzke, *The Journal of Chemical Physics* **1999**, *111*, 5645–5655.

[128] G. A. Segal, R. W. Wetmore, K. Wolf, *Chemical Physics* **1978**, *30*, 269–297.

[129] R. W. Wetmore, G. A. Segal, *Chemical Physics Letters* **1975**, *36*, 478–483.

[130] A. D. Becke, *The Journal of Chemical Physics* **1993**, *98*, 1372–1377.

[131] A. D. Becke, *Physical Review A* **1988**, *38*, 3098–3100.

[132] C. Lee, W. Yang, R. G. Parr, *Physical Review B* **1988**, *37*, 785–789.

[133] A. D. Dutoi, M. Head-Gordon, *Chemical Physics Letters* **2006**, *422*, 230–233.

[134] D. R. Lonsdale, L. Goerigk, *Physical Chemistry Chemical Physics* **2020**, *22*, 15805–15830.

[135] D. R. Dombrowski, PhD thesis, Heinrich Heine University, Düsseldorf, Düsseldorf, **2023**.

[136] M. R. Silva-Junior, M. Schreiber, S. P. A. Sauer, W. Thiel, *The Journal of Chemical Physics* **2008**, *129*.

[137] D. Escudero, W. Thiel, *The Journal of Chemical Physics* **2014**, *140*.

[138] M. Gerenkamp, PhD thesis, Westfälische Wilhelms-Universität Münster, **2005**.

[139] E. Sanchez-Garcia, M. Doerr, Y.-W. Hsiao, W. Thiel, *The Journal of Physical Chemistry B* **2009**, *113*, 16622–16631.

[140] R. Crespo-Otero, M. Barbatti, *The Journal of Chemical Physics* **2011**, *134*.

[141] I. Lyskov, M. Kleinschmidt, C. M. Marian, *The Journal of Chemical Physics* **2016**, *144*.

[142] A. Heil, C. M. Marian, *The Journal of Chemical Physics* **2017**, *147*.

[143] A. Heil, M. Kleinschmidt, C. M. Marian, *The Journal of Chemical Physics* **2018**, *149*.

[144] M. A. Buijse, E. J. Baerends, *The Journal of Chemical Physics* **1990**, *93*, 4129–4141.

[145] T. M. Henderson, G. E. Scuseria, *Molecular Physics* **2010**, *108*, 2511–2517.

[146] E. S. Sachs, J. Hinze, N. H. Sabelli, *The Journal of Chemical Physics* **1975**, *62*, 3393–3398.

[147] V. W.-z. Yu, J. Moussa, V. Blum, *The Journal of Chemical Physics* **2021**, *154*.

[148] B. O. Roos, P. R. Taylor, P. E. Sigbahn, *Chemical Physics* **1980**, *48*, 157–173.

[149] M. Waletzke, PhD thesis, Rheinischen Friedrich-Wilhelms-Universität Bonn, **2001**.

[150] E. R. Davidson, *Journal of Computational Physics* **1975**, *17*, 87–94.

[151] C. Moler, I. Shavitt in Numerical Algorithms in Chemistry: Algebraic Methods. [workshop, August 9-11, 1978], **1978**.

[152] M. Kleinschmidt, C. M. Marian, M. Waletzke, S. Grimme, *The Journal of Chemical Physics* **2009**, *130*, 044708.

[153] M. Hanrath, B. Engels, *Chemical Physics* **1997**, *225*, 197–202.

[154] F. Weigend, M. Häser, H. Patzelt, R. Ahlrichs, *Chemical Physics Letters* **1998**, *294*, 143–152.

[155] C. Hättig, *Physical Chemistry Chemical Physics* **2005**, *7*, 59–66.

[156] J. Zirzlmeier, D. Lehnherr, P. B. Coto, E. T. Chernick, R. Casillas, B. S. Basel, M. Thoss, R. R. Tykwinski, D. M. Guldi, *Proceedings of the National Academy of Sciences* **2015**, *112*, 5325–5330.

[157] R. Ringström, F. Edhborg, Z. W. Schroeder, L. Chen, M. J. Ferguson, R. R. Tykwinski, B. Albinsson, *Chemical Science* **2022**, *13*, 4944–4954.

[158] S. R. Reddy, P. B. Coto, M. Thoss, *The Journal of Chemical Physics* **2019**, *151*.

[159] F. Weigend, R. Ahlrichs, *Physical Chemistry Chemical Physics* **2005**, *7*, 3297.

[160] P. Surján, L. Udvardi, K. Németh in *Frontier Topics in Nuclear Physics*, Springer US, **1994**, pp. 487–488.

[161] C. C. Chancey, *The Jahn-Teller Effect in C_{60} and Other Icosahedral Complexes*, (Ed.: M. C. O'Brien), Princeton University Press, Princeton, NJ, **2022**.

[162] M. Häser, J. Almlöf, G. E. Scuseria, *Chemical Physics Letters* **1991**, *181*, 497–500.

[163] B. Paulus, *International Journal of Quantum Chemistry* **2004**, *100*, 1026–1032.

[164] D. Stück, T. A. Baker, P. Zimmerman, W. Kurlancheek, M. Head-Gordon, *The Journal of Chemical Physics* **2011**, *135*.

[165] R. E. Haufler, Y. Chai, L. P. F. Chibante, M. R. Fraelich, R. B. Weisman, R. F. Curl, R. E. Smalley, *The Journal of Chemical Physics* **1991**, *95*, 2197–2199.

[166] S. Leach, M. Vervloet, A. Desprès, E. Bréheret, J. P. Hare, T. John Dennis, H. W. Kroto, R. Taylor, D. R. Walton, *Chemical Physics* **1992**, *160*, 451–466.

[167] R. Abouaf, J. Pommier, S. Cvejanovic, *Chemical Physics Letters* **1993**, *213*, 503–508.

[168] C. Bulliard, M. Allan, S. Leach, *Chemical Physics Letters* **1993**, *209*, 434–438.

[169] J. Catalán, *Chemical Physics Letters* **1994**, *223*, 159–161.

[170] R. Bauernschmitt, R. Ahlrichs, F. H. Hennrich, M. M. Kappes, *Journal of the American Chemical Society* **1998**, *120*, 5052–5059.

[171] R. Fukuda, M. Ehara, *The Journal of Chemical Physics* **2012**, *137*, 134304.

[172] E. Menéndez-Proupin, A. Delgado, A. L. Montero-Alejo, J. García de la Vega, *Chemical Physics Letters* **2014**, *593*, 72–76.

[173] S. Grimme, M. Waletzke, *Physical Chemistry Chemical Physics* **2000**, *2*, 2075–2081.

[174] G. Orlandi, F. Negri, *Photochemical & Photobiological Sciences* **2002**, *1*, 289–308.

[175] A. J. Sadlej, *Collection of Czechoslovak Chemical Communications* **1988**, *53*, 1995–2016.

[176] M. E. Casida, C. Jamorski, K. C. Casida, D. R. Salahub, *The Journal of Chemical Physics* **1998**, *108*, 4439–4449.

[177] T. H. Dunning, *The Journal of Chemical Physics* **1989**, *90*, 1007–1023.

[178] R. A. Kendall, T. H. Dunning, R. J. Harrison, *The Journal of Chemical Physics* **1992**, *96*, 6796–6806.

[179] B. Kosper, PhD thesis, Heinrich Heine University, Düsseldorf, **2022**.

[180] P. Konieczny, PhD thesis, Heinrich Heine University, Düsseldorf, **2017**.

[181] J. Meissner, B. Kosper, C. M. Marian, R. Weinkauf, *The Journal of Physical Chemistry A* **2021**, *125*, 8777–8790.

[182] V. Enkelmann in *Electronic Materials: The Oligomer Approach*, (Eds.: K. Müllen, G. Wegner), Electronic Materials: The Oligomer Approach, Wiley, **1998**, Chapter 5, pp. 295–344.

[183] H. Bässler in *Electronic Materials: The Oligomer Approach*, (Eds.: K. Müllen, G. Wegner), Wiley, **1998**, Chapter 7, pp. 404–447.

[184] G. Zerbi, C. Castiglioni, M. Del Zoppo in *Electronic Materials: The Oligomer Approach*, (Eds.: K. Müllen, G. Wegner), Electronic Materials: The Oligomer Approach, Wiley, **1998**, Chapter 6, pp. 345–402.

[185] V. Lukeš, A. J. A. Aquino, H. Lischka, H.-F. Kauffmann, *The Journal of Physical Chemistry B* **2007**, *111*, 7954–7962.

[186] C. Melania Oana, A. I. Krylov, *The Journal of Chemical Physics* **2007**, *127*.

[187] F. Meitza, PhD thesis, Heinrich Heine University, Düsseldorf, Düsseldorf, **2023**.

[188] M. Filatov, S. Shaik, *Chemical Physics Letters* **1998**, *288*, 689–697.

[189] K. Aidas, C. Angeli, K. L. Bak, V. Bakken, R. Bast, L. Boman, O. Christiansen, R. Cimiraglia, S. Coriani, P. Dahle, E. K. Dalskov, U. Ekström, T. Enevoldsen, J. J. Eriksen, P. Ettenhuber, B. Fernández, L. Ferrighi, H. Fliegl, L. Frediani, K. Hald, A. Halkier, C. Hättig, H. Heiberg, T. Helgaker, A. C. Hennum, H. Hettema, E. Hjertenæs, S. Høst, I.-M. Høyvik, M. F. Iozzi, B. Jansík, H. J. A. Jensen, D. Jonsson, P. Jørgensen, J. Kauczor, S. Kirpekar, T. Kjærgaard, W. Klopper, S. Knecht, R. Kobayashi, H. Koch, J. Kongsted, A. Krapp, K. Kristensen, A. Ligabue, O. B. Lutnæs, J. I. Melo, K. V. Mikkelsen, R. H. Myhre, C. Neiss, C. B. Nielsen, P. Norman, J. Olsen, J. M. H. Olsen, A. Osted, M. J. Packer, F. Pawlowski, T. B. Pedersen, P. F. Provasi, S. Reine, Z. Rinkevicius, T. A. Ruden, K. Ruud, V. V. Rybkin, P. Sałek, C. C. M. Samson, A. S. de Merás, T. Saue, S. P. A. Sauer, B. Schimmelpfennig, K. Sneskov, A. H. Steindal, K. O. Sylvester-Hvid, P. R. Taylor, A. M. Teale, E. I. Tellgren, D. P. Tew, A. J. Thorvaldsen, L. Thøgersen, O. Vahtras, M. A. Watson, D. J. D. Wilson, M. Ziolkowski, H. Ågren, *Wiley Interdisciplinary Reviews: Computational Molecular Science* **2016**, *4*, 269–284.

[190] Dalton, a Molecular Electronic Structure Program, Release Dalton2018.0 (2018), See Http://daltonprogram.org.

[191] J. C. Rienstra-Kiracofe, G. S. Tschumper, H. F. Schaefer, S. Nandi, G. B. Ellison, *Chemical Reviews* **2002**, *102*, 231–282.

[192] W. R. Lambert, P. M. Felker, J. A. Syage, A. H. Zewail, *The Journal of Chemical Physics* **1984**, *81*, 2195–2208.

[193] H. Muddasir, Z.-m. Wang, B. Yang, P. Lu, Y.-g. Ma, *Chemical Research in Chinese Universities* **2013**, *29*, 110–115.

[194] J. Schiedt, R. Weinkauf, *Chemical Physics Letters* **1997**, *266*, 201–205.

[195] J. Wolf, G. Hohlneicher, *Chemical Physics* **1994**, *181*, 185–208.

[196] C. Zimmermann, M. Mohr, H. Zipse, R. Eichberger, W. Schnabel, *Journal of Photochemistry and Photobiology A: Chemistry* **1999**, *125*, 47–56.

[197] J. R. Polli, B. R. Rushing, L. Lish, L. Lewis, M. I. Selim, X. Pan, *The Science of the total environment* **2020**, *745*, 140639.

[198] A. R. Collins, B. Zhang, M. J. Bennison, R. C. Evans, *Journal of Materials Chemistry C* **2024**, *12*, 6310–6318.

[199] Z. Feng, F. Liu, Z. Cheng, S. Ge, Y. Wang, Z. Yan, X. Ma, Y. Wang, P. Lu, *Journal of Materials Chemistry C* **2024**, *12*, 3881–3887.

[200] P.-T. Li, R. Yang, Y.-P. Ma, J.-L. Zhao, S.-N. Liu, Z.-D. Qiu, Y.-T. Ding, Z.-F. Shi, Y. Miao, M. Zhao, X.-P. Cao, *Dyes and Pigments* **2024**, *224*, 112041.

[201] D. Khan, Z. Xiaotao, M. H. Jameel, M. A. B. Agam, M. S. B. Roslan, M. A. Bajaber, *Micro and Nano Systems Letters* **2023**, *11*.

[202] T. Schulz, B. Kosper, D. Dombrowski, R. Weinkauf, C. M. Marian, **in preparation**.

[203] B. Badger, B. Brocklehurst, *Nature* **1968**, *219*, 263–263.

[204] A. Chandra, K. Bhanuprakash, V. J. Bhasu, D. Srikanthan, *Molecular Physics* **1984**, *52*, 733–741.

[205] P. L. Maguères, S. V. Lindeman, J. K. Kochi, *Journal of the Chemical Society Perkin Transactions 2* **2001**, 1180–1185.

[206] C. Lee, T. Lyu, C. H. Choi, T. Joo, *EPJ Web of Conferences* **2019**, *205*, (Eds.: G. Cerullo, J. Ogilvie, F. Kärtner, M. Khalil, R. Li), 09008.

[207] M. Vorona, PhD thesis, Université d'Ottawa / University of Ottawa, **2020**.

[208] H. Iwahara, T. Kushida, S. Yamaguchi, *Chemical Communications* **2016**, *52*, 1124–1127.

[209] Z. Li, G. Gan, Z. Ling, K. Guo, C. Si, X. Lv, H. Wang, B. Wei, Y. Hao, *Organic Electronics* **2019**, *66*, 24–31.

[210] G. Mu, S. Zhuang, W. Zhang, Y. Wang, B. Wang, L. Wang, X. Zhu, *Organic Electronics* **2015**, *21*, 9–18.

[211] P. Xia, J. Schwan, T. W. Dugger, L. Mangolini, M. L. Tang, *Advanced Optical Materials* **2021**, 2100453.

[212] X. Zhao, A. A. Sukhanov, K. Chen, X. Geng, Y. Dong, V. K. Voronkova, J. Zhao, L. Liu, *Dyes and Pigments* **2021**, *187*, 109121.

[213] P. A. M. Dirac, *Proceedings of the Royal Society of London. Series A Containing Papers of a Mathematical and Physical Character* **1929**, *123*, 714–733.

[214] J. C. Slater, *Physical Review* **1951**, *81*, 385–390.

[215] J. P. Perdew, Y. Wang, *Physical Review B* **1992**, *45*, 13244–13249.

[216] J. P. Perdew, M. Ernzerhof, K. Burke, *The Journal of Chemical Physics* **1996**, *105*, 9982–9985.

[217] M. Etinski, J. Tatchen, C. M. Marian, *The Journal of Chemical Physics* **2011**, *134*, 154105.

[218] M. Etinski, J. Tatchen, C. M. Marian, *Physical Chemistry Chemical Physics* **2014**, *16*, 4740–4751.

[219] J. K. Song, N. K. Lee, S. K. Kim, *Angewandte Chemie International Edition* **2003**, *42*, 213–216.

[220] N. Ando, M. Mitsui, A. Nakajima, *The Journal of Chemical Physics* **2007**, *127*.

[221] B. Hajgató, M. S. Deleuze, D. J. Tozer, F. De Proft, *The Journal of Chemical Physics* **2008**, *129*.

[222] S. H. Vosko, L. Wilk, M. Nusair, *Canadian Journal of Physics* **1980**, *58*, 1200–1211.

[223] T. Yanai, D. P. Tew, N. C. Handy, *Chemical Physics Letters* **2004**, *393*, 51–57.

[224] J. R. Platt, *The Journal of Chemical Physics* **1949**, *17*, 484–495.

[225] D. S. McClure, *The Journal of Chemical Physics* **1954**, *22*, 1668–1675.

[226] V. Czikklely, H. Forsterling, H. Kuhn, *Chemical Physics Letters* **1970**, *6*, 207–210.

[227] F. Würthner, T. E. Kaiser, C. R. Saha-Möller, *Angewandte Chemie International Edition* **2011**, *50*, 3376–3410.

[228] N. J. Hestand, F. C. Spano, *Chemical Reviews* **2018**, *118*, 7069–7163.

[229] C.-G. Zhan, J. A. Nichols, D. A. Dixon, *The Journal of Physical Chemistry A* **2003**, *107*, 4184–4195.

[230] F. Plasser, *The Journal of Chemical Physics* **2020**, *152*.

[231] F. Plasser, H. Lischka, *Journal of Chemical Theory and Computation* **2012**, *8*, 2777–2789.

[232] F. Plasser, M. Wormit, A. Dreuw, *The Journal of Chemical Physics* **2014**, *141*.

[233] F. Plasser, S. A. Bäppler, M. Wormit, A. Dreuw, *The Journal of Chemical Physics* **2014**, *141*.

[234] J. Anthony, *Angewandte Chemie International Edition* **2007**, *47*, 452–483.

[235] A. R. Murphy, J. M. J. Fréchet, *Chemical Reviews* **2007**, *107*, 1066–1096.

[236] M. Kitamura, Y. Arakawa, *Journal of Physics: Condensed Matter* **2008**, *20*, 184011.

[237] T. Siegrist, C. Kloc, J. H. Schön, B. Batlogg, R. C. Haddon, S. Berg, G. A. Thomas, *Angewandte Chemie International Edition* **2001**, *40*, 1732–1736.

[238] C. Wang, H. Dong, L. Jiang, W. Hu, *Chemical Society Reviews* **2018**, *47*, 422–500.

[239] R. C. Haddon, X. Chi, M. E. Itkis, J. E. Anthony, D. L. Eaton, T. Siegrist, C. C. Mattheus, T. T. M. Palstra, *The Journal of Physical Chemistry B* **2002**, *106*, 8288–8292.

[240] M. Bendikov, F. Wudl, D. F. Perepichka, *Chemical Reviews* **2004**, *104*, 4891–4946.

[241] P. v. R. Schleyer, M. Manoharan, H. Jiao, F. Stahl, *Organic Letters* **2001**, *3*, 3643–3646.

[242] S. S. Zade, M. Bendikov, *Journal of Physical Organic Chemistry* **2012**, *25*, 452–461.

[243] M. Dvořák, S. K. K. Prasad, C. B. Dover, C. R. Forest, A. Kaleem, R. W. MacQueen, A. J. Petty, R. Forecast, J. E. Beves, J. E. Anthony, M. J. Y. Tayebjee, A. Widmer-Cooper, P. Thordarson, T. W. Schmidt, *Journal of the American Chemical Society* **2021**, *143*, 13749–13758.

[244] R. J. Hudson, A. N. Stuart, J. M. de la Perrelle, D. M. Huang, T. W. Kee, *The Journal of Physical Chemistry C* **2021**, *125*, 21559–21570.

[245] L. Yang, M. Tabachnyk, S. L. Bayliss, M. L. Böhm, K. Broch, N. C. Greenham, R. H. Friend, B. Ehrler, *Nano Letters* **2014**, *15*, 354–358.

[246] T. Zeng, R. Hoffmann, N. Ananth, *Journal of the American Chemical Society* **2014**, *136*, 5755–5764.

[247] P. M. Zimmerman, Z. Zhang, C. B. Musgrave, *Nature Chemistry* **2010**, *2*, 648–652.

[248] T. Nagami, H. Miyamoto, R. Sakai, M. Nakano, *The Journal of Physical Chemistry C* **2021**, *125*, 2264–2275.

[249] A. Neef, S. Beaulieu, S. Hammer, S. Dong, J. Maklar, T. Pincelli, R. P. Xian, M. Wolf, L. Rettig, J. Pflaum, R. Ernstorfer, *Nature* **2023**, *616*, 275–279.

[250] A. Neef, M. Rossi, M. Wolf, R. Ernstorfer, H. Seiler, *Physica Status Solidi A* **2023**, *221*.

[251] P. M. Zimmerman, F. Bell, D. Casanova, M. Head-Gordon, *Journal of the American Chemical Society* **2011**, *133*, 19944–19952.

[252] W.-L. Chan, T. C. Berkelbach, M. R. Provorse, N. R. Monahan, J. R. Tritsch, M. S. Hybertsen, D. R. Reichman, J. Gao, X.-Y. Zhu, *Accounts of Chemical Research* **2013**, *46*, 1321–1329.

[253] K. Miyata, Y. Kurashige, K. Watanabe, T. Sugimoto, S. Takahashi, S. Tanaka, J. Takeya, T. Yanai, Y. Matsumoto, *Nature Chemistry* **2017**, *9*, 983–989.

[254] K. A. McGarry, W. Xie, C. Sutton, C. Risko, Y. Wu, V. G. Young, J.-L. Brédas, C. D. Frisbie, C. J. Douglas, *Chemistry of Materials* **2013**, *25*, 2254–2263.

[255] M. T. Trinh, A. Pinkard, A. B. Pun, S. N. Sanders, E. Kumarasamy, M. Y. Sfeir, L. M. Campos, X. Roy, X.-Y. Zhu, *Science Advances* **2017**, *3*.

[256] D. H. Arias, J. L. Ryerson, J. D. Cook, N. H. Damrauer, J. C. Johnson, *Chemical Science* **2016**, *7*, 1185–1191.

[257] K. Yoshino, H. Sakai, Y. Shoji, T. Kajitani, H. Anetai, T. Akutagawa, T. Fukushima, N. V. Tkachenko, T. Hasobe, *The Journal of Physical Chemistry B* **2020**, *124*, 11910–11918.

[258] X. Feng, A. B. Kolomeisky, A. I. Krylov, *The Journal of Physical Chemistry C* **2014**, *118*, 19608–19617.

[259] K. Kolata, T. Breuer, G. Witte, S. Chatterjee, *ACS Nano* **2014**, *8*, 7377–7383.

[260] J. C. Johnson, *Communications Chemistry* **2021**, *4*.

[261] C. M. Marian, *WIREs Computational Molecular Science* **2011**, *2*, 187–203.

[262] C. M. Marian, *Annual Review of Physical Chemistry* **2021**, *72*, 617–640.

[263] M. Chen, M. D. Krzyaniak, J. N. Nelson, Y. J. Bae, S. M. Harvey, R. D. Schaller, R. M. Young, M. R. Wasielewski, *Proceedings of the National Academy of Sciences* **2019**, *116*, 8178–8183.

[264] J. Hausch, N. Hofeditz, J. Bredehöft, S. Hammer, J. Pflaum, K. Broch, M. Gerhard, F. Schreiber, *The Journal of Physical Chemistry C* **2023**, *127*, 3778–3786.

[265] R. D. Dill, G. Joshi, K. J. Thorley, J. E. Anthony, B. Fluegel, J. C. Johnson, O. G. Reid, *The Journal of Physical Chemistry Letters* **2023**, *14*, 2387–2394.

[266] H. Sakai, R. Inaya, H. Nagashima, S. Nakamura, Y. Kobori, N. V. Tkachenko, T. Hasobe, *The Journal of Physical Chemistry Letters* **2018**, *9*, 3354–3360.

[267] R. D. Dill, K. E. Smyser, B. K. Rugg, N. H. Damrauer, J. D. Eaves, *Nature Communications* **2023**, *14*.

[268] B. S. Basel, J. Zirzlmeier, C. Hetzer, B. T. Phelan, M. D. Krzyaniak, S. R. Reddy, P. B. Coto, N. E. Horwitz, R. M. Young, F. J. White, F. Hampel, T. Clark, M. Thoss, R. R. Tykwinski, M. R. Wasielewski, D. M. Guldi, *Nature Communications* **2017**, *8*.

[269] A. J. Musser, J. Clark, *Annual Review of Physical Chemistry* **2019**, *70*, 323–351.

[270] C. M. Marian, A. Heil, M. Kleinschmidt, *WIREs Computational Molecular Science* **2018**, *9*.

[271] L. E. Aguilar Suarez, M. F. S. J. Menger, S. Faraji, *Molecular Physics* **2020**, *118*.

[272] A. J.E., B. J.S., E. D.L., P. S.R., CCDC 172476: Experimental Crystal Structure Determination, **2001**.

[273] S. Hédé, PhD thesis, Heinrich-Heine University, Düsseldorf, Düsseldorf, **in preparation**.

[274] T. M. Halasinski, D. M. Hudgins, F. Salama, L. J. Allamandola, T. Bally, *The Journal of Physical Chemistry A* **2000**, *104*, 7484–7491.

[275] B. J. Walker, A. J. Musser, D. Beljonne, R. H. Friend, *Nature Chemistry* **2013**, *5*, 1019–1024.

[276] R. He, N. G. Tassi, G. B. Blanchet, A. Pinczuk, *Physical Review B* **2011**, *83*, 115452.

[277] C. Grieco, G. S. Doucette, K. T. Munson, J. R. Swartzfager, J. M. Munro, J. E. Anthony, I. Dabo, J. B. Asbury, *The Journal of Chemical Physics* **2019**, *151*.

[278] R. Casillas, M. Adam, P. B. Coto, A. R. Waterloo, J. Zirzlmeier, S. R. Reddy, F. Hampel, R. McDonald, R. R. Tykwinski, M. Thoss, D. M. Guldi, *Advanced Energy Materials* **2018**, *9*.

[279] F. L. Pilar, *Elementary Quantum Chemistry*, Dover Publications, **2001**.

[280] D. R. Hartree, *Mathematical Proceedings of the Cambridge Philosophical Society* **1928**, *24*, 89–110.

[281] *Hans Hellmann: Einführung in Die Quantenchemie: Mit Biografischen Notizen Von Hans Hellmann Jr.* 1st ed., (Ed.: D. Andre), Springer Berlin Heidelberg, **2015**.

[282] P.-O. Löwdin, *Physical Review* **1955**, *97*, 1509–1520.

[283] R. McWeeny, *Methods of Molecular Quantum Mechanics*, Academic Press, **1992**.

[284] R. McWeeny, *Reviews of Modern Physics* **1960**, *32*, 335–369.

[285] P. A. M. Dirac, *Proceedings of the Royal Society of London. Series A Containing Papers of a Mathematical and Physical Character* **1928**, *117*, 610–624.

[286] S. J. Axler, *Linear Algebra Done Right*, 3rd ed., Springer, Cham, **2015**.

[287] *A Primer in Density Functional Theory*, (Eds.: C. Fiolhais, A. L. M. Marques, F. Nogueira), Springer Berlin Heidelberg, **2003**.

[288] C. Kittel, *Einführung in die Festkörperphysik*, 6th ed., (Ed.: R. Oldenbourg), Oldenbourg, München [u.a.], **1983**.

[289] N. I. Akhiezer, I. M. Glazman, *Theory of Linear Operators in Hilbert Space*, Courier Corporation, **2013**.

[290] W. Dahmen, *Numerik Für Ingenieure Und Naturwissenschaftler, Methoden, Konzepte, Matlab-Demos, E-Learning*, 3rd ed., (Ed.: A. Reusken), Springer Berlin Heidelberg, Berlin, Heidelberg, **2022**.

[291] Y. Saad, *Numerical Methods for Large Eigenvalue Problems*, Rev. ed, Society for Industrial and Applied Mathematics (SIAM, 3600 Market Street, Floor 6, Philadelphia, PA 19104), Philadelphia, Pa., **2011**.

[292] W. Nolting, *Grundkurs Theoretische Physik 2*, Springer-Verlag, **2006**.

[293] R. S. Mulliken, *Physical Review* **1928**, *32*, 186–222.

[294] *Methods in Computational Molecular Physics*, (Eds.: G. H. F. Diercksen, S. Wilson), D. Reidel Publishing Company, Dordrecht, [Netherlands], **1983**.

[295] T. Katō, *Perturbation Theory for Linear Operators*, Springer-Verlag, Berlin, [Germany] ; **1976**.

[296] I. Savov, *No Bullshit Guide to Linear Algebra*, Minireference Co., p. 570.

[297] C. Cohen-Tannoudji, B. Diu, F. Laloë, *Quantenmechanik: Band 1*, De Gruyter, **2019**.

[298] K. Eichkorn, O. Treutler, H. Öhm, M. Häser, R. Ahlrichs, *Chemical Physics Letters* **1995**, *240*, 283–290.

[299] R. A. Kendall, H. A. Früchtl, *Theoretical Chemistry Accounts: Theory Computation and Modeling (Theoretica Chimica Acta)* **1997**, *97*, 158–163.

[300] A. Sodt, M. Head-Gordon, *The Journal of Chemical Physics* **2008**, *128*.

[301] J. C. Slater, *Physical Review* **1929**, *34*, 1293–1322.

[302] A. Dawydow, *Quantenmechanik*, 6th ed., (Ed.: R. R. und Ernst Schmutzer), VEB Deutscher Verlag der Wissenschaften, **1981**.

List of Figures

List of Tables